Systematic *s*-process sensitivity studies

Dissertation

zur Erlangung des Doktorgrades

der Naturwissenschaften

vorgelegt beim Fachbereich Physik

der Johann Wolfgang Goethe-Universität

in Frankfurt am Main

von

Alexander Koloczek

aus Frankfurt am Main

Frankfurt am Main 2014

(D 30)

vom Fachbereich Physik der

Johann Wolfgang Goethe-Universität als Dissertation angenommen.

Dekan: Prof. Dr. René Reifarth

Gutachter: Prof. Dr. René Reifarth
Dr. Kerstin Sonnabend

Datum der Disputation:

Zusammenfassung

Seit der Entdeckung der schweren, instabilen Isotope des Technetiums in der Atmosphäre eines roten Riesen im Jahre 1952 wurde nach Erklärungen gesucht, wie Elemente, die nicht durch Fusion geladener Teilchen erzeugt werden können, entstehen. Der langsame Neutroneneinfangprozess (*s*-Prozess) wurde fünf Jahre später als eine Lösung präsentiert. Mehrere Jahrzehnte mit experimenteller Bestimmung von Wirkungsquerschnitten haben die *s*-Prozessmodelle so weit verbessert, dass diese nun verwendet werden können, um wichtige, bislang ungemessene Wirkungsquerschnitte zu identifizieren. In dieser Arbeit werden auf dem neusten Stand der Technik vier *s*-Prozessszenarien mit systematischen Sensitivitätsstudien untersucht. Dabei werden alle Reaktionsraten identifiziert, die einen globalen Einfluss auf die *s*-Prozesshäufigkeiten haben und zusätzlich alle Verzweigungspunkte gesucht, die zur Verbesserung der *s*-Prozessmodelle dienen können. Darüber hinaus wird der größte Einfluss aller Wirkungsquerschnitte auf die Häufigkeiten jedes stabile Isotop in den verschiedenen Szenarien untersucht. Die gleiche Untersuchung wird ebenfalls auf den *i*-Prozess, einen kürzlich postulierten Prozess mit mittleren Neutronendichten, angewandt. Von allen untersuchten Prozessen wird der Einfluss auf die LEPP-Isotope (Lighter Element Primary Process), Sr, Y und Zr, betrachtet, um mögliche Kandidaten für den noch unbestimmten LEPP zu finden.

Abstract

The discovery of the heavy, unstable technetium isotopes in the atmosphere of a red giant in 1952 raised the question about their origin. Five years later, the slow neutron capture process (*s* process) was presented as one solution to the formation of elements heavier than iron. The *s* process creates elements, which cannot be produced by fusion reactions of charged particles. Several decades of experimental determination of cross sections refined *s*-process models in a way that these models can nowadays be used to identify crucial reactions, which should be measured in the future. In this work, four state-of-the-art *s*-process scenarios were analysed with systematic sensitivity studies. All reaction rates with a global impact on the overall abundance distribution as well as branching points, which can be used to refine these models were identified for each scenario. Furthermore, the rates with the highest impact on every stable isotope in each scenario were deduced. The same study was applied to the *i* process, a recently postulated process with intermediate neutron densities. All processes studied in this thesis are evaluated with respect to their impact on the LEPP isotopes (Lighter Element Primary Process isotopes), Sr, Y, and Zr, in order to obtain possible candidates for the so far unidentified LEPP.

Contents

1 Introduction **3**

1.1 Motivation . . . 3

1.2 Nucleosynthesis . . . 5

1.2.1 Solar abundance distribution . . . 5

1.2.2 Primordial nucleosynthesis . . . 6

1.2.3 Fusion . . . 6

1.2.4 Neutron capture reactions . . . 12

1.3 Stellar evolution . . . 27

1.3.1 Stellar evolution of a 3 solar-mass star . . . 27

1.3.2 Stellar evolution of a 25 solar-mass star . . . 29

2 Simulation & analysis tools **33**

2.1 Simulation codes . . . 33

2.1.1 Stellar evolution calculation . . . 33

2.1.2 Post processing . . . 34

2.2 Stellar simulations . . . 35
2.2.1 3 Solar-mass stellar model . . . 36
2.2.2 25 Solar-mass stellar model . . . 41
2.2.3 Low metallicity stars . . . 42
2.2.4 The *i* process . . . 44
2.3 Sensitivity . . . 46
2.3.1 Definition . . . 46
2.3.2 Sensitivity plots . . . 47
2.3.3 Sensitivity tables . . . 49

3 Results **51**
3.1 Main component . . . 52
3.1.1 ^{13}C-pocket . . . 52
3.1.2 Thermal pulse . . . 60
3.2 Weak component . . . 69
3.2.1 Weak *s* process . . . 70
3.2.2 Convective carbon shell burning . . . 80
3.3 The *i* process . . . 89
3.4 Lighter element primary process – LEPP . . . 97

4 Conclusion and outlook **101**
4.1 Conclusion . . . 101
4.2 Outlook . . . 104

5 Zusammenfassung **107**

Bibliography **113**

List of figures **121**

List of tables **134**

A Appendix **139**

A.1 Main component . . . 140

A.1.1 ^{13}C-pocket . . . 140

A.1.2 Thermal pulse . . . 154

A.2 Weak component . . . 174

A.2.1 Weak *s* process . . . 174

A.2.2 Convective C shell burning . . . 216

A.3 *i* process . . . 230

A.4 LEPP . . . 250

Danksagung **259**

Curriculum Vitae **261**

1 Introduction

1.1 Motivation

"*Look deep into nature, and then you will understand everything better.*" — Albert Einstein.

Gathering knowledge is the foundation of understanding. Since ancient times generations of scientists work for a greater understanding of the universe and all its content. Ancient civilisations used astronomy to obtain precise calendars, measure the radius of earth and distance to the sun and moon. These are great achievements and even greater, considering the tools available at this time. The technological revolutions during the modern era revolutionised astronomy and opened new fields to study with astrophysics. The current state where technology is the basis of our society changes the way research is done. The distance to the moon is nowadays measured directly with lasers. These reflect on retroreflectors, which were put on the moon during three space missions. Space based observations deliver a incessant stream of data about the universe to earth. We create scenarios in laboratories, which would never occur naturally on our planet. Computers solve complex mathematical problems numerically faster than humans could with simplified analytical approaches.

A relatively new branch in the field of astrophysics is nuclear astrophysics, which is dedicated to the reconstruction of the solar element distribution as it is observed on earth. Numerous processes contribute to the galactic chemical evolution. Therefore, it is crucial to achieve a good understanding of every single nucleosynthesis site in order to draw conclusions about the entirety of these processes [Timmes et al. 1995, Goswami and Prantzos 2000, Travaglio et al. 2004, Kobayashi et al. 2006]. Stars are the fusion reactors in the universe, which contribute to altering the chemical abundance distribution. Stellar fusion and stellar neutron capture processes could in principle create all elements up to lead out of hydrogen [Pignatari et al. 2013]. Stellar

neutron capture processes do not occur in every star. First, the right initial conditions have to arise, which involve multiple generations of stars to lay the foundation.

The slow neutron capture process (*s* process) is one of the processes, which accounts to the creation of the abundances heavier than iron in the solar system. Since the discovery of the *s* process stellar models were tweaked to result in self consistent mechanisms, which create the *s*-process sites. Gallino et al. 1998 introduced a parametrised standard (ST) case, which was motivated by stellar simulations, but the parameters were fitted to the result. This ST case is still widely adapted, even though more consistent stellar models with less free parameters have been developed in the mean time [Herwig et al. 2007]. Furthermore the weak *s* process contributions from Raiteri et al. 1993, which are used in ongoing galactic chemical evolution discussions, show deviating conclusions from current simulations. In this thesis four state-of-the-art *s*-process scenarios, extracted from an up-to-date set of stellar models [Pignatari et al. 2013], were post-processed with nucleosynthesis networks of about 1100 isotopes and about 14 000 rates. Every single rate was checked for its influence on the final result of the *s* process. The purpose of this, is to give a guideline on refining the understanding of the *s* process with experimental data on nuclear reactions. Furthermore, the discussion about a possible *i* process (intermediate neutron capture process [Cowan and Rose 1977]) was revived by isotopic measurements of meteorite silicon carbide grains [Fujiya et al. 2013, Jadhav et al. 2013, Liu et al. 2014]. A proposed *i*-process scenario, the hydrogen combustion thermal pulse, introduced by Herwig et al. 2011 is examined with a comprehensive set of 124 000 simulations.

Previously impracticable experiments and measurements will be feasible in the future with new experimental setups, like the neutron source FRANZ [Reifarth et al. 2009] or the newly developed FAIR facility [Reifarth et al. 2013]. Therefore, regardless of the current feasibility of experiments, the set of systematic sensitivity studies presented here represents a useful compendium for the future of neutron capture astrophysics.

An ongoing debate, based on the results from Raiteri et al. 1993, about the production of Sr, Y, and Zr in an undefined scenario is puzzling the nuclear astrophysics community [Pignatari et al. 2010]. The so-called lighter element primary process (LEPP) should account as primary process to the production of these light isotopes in the solar system [Travaglio et al. 2004]. The sensitivity studies of all five scenarios of this thesis were evaluated additionally with a special focus on LEPP isotopes.

1.2 Nucleosynthesis

Nucleosynthesis is the hypernym for all processes that alter the composition of an atomic nucleus [Rolfs and Rodney 1988]. In this chapter, the signature of the main nucleosynthesis processes on the solar abundance distribution is presented.

1.2.1 Solar abundance distribution

In order to find a good reproduction of the abundance distribution in the solar system (figure 1.1), many efforts have been made to get a genuine picture out of different observations. The most important sources for the determination of the solar abundance distribution are data from the solar photospheric spectrum and analytical data of meteorites [Suess and Urey 1956, Bernatowicz et al. 1987, Anders and Zinner 1993, Lodders et al. 2009].

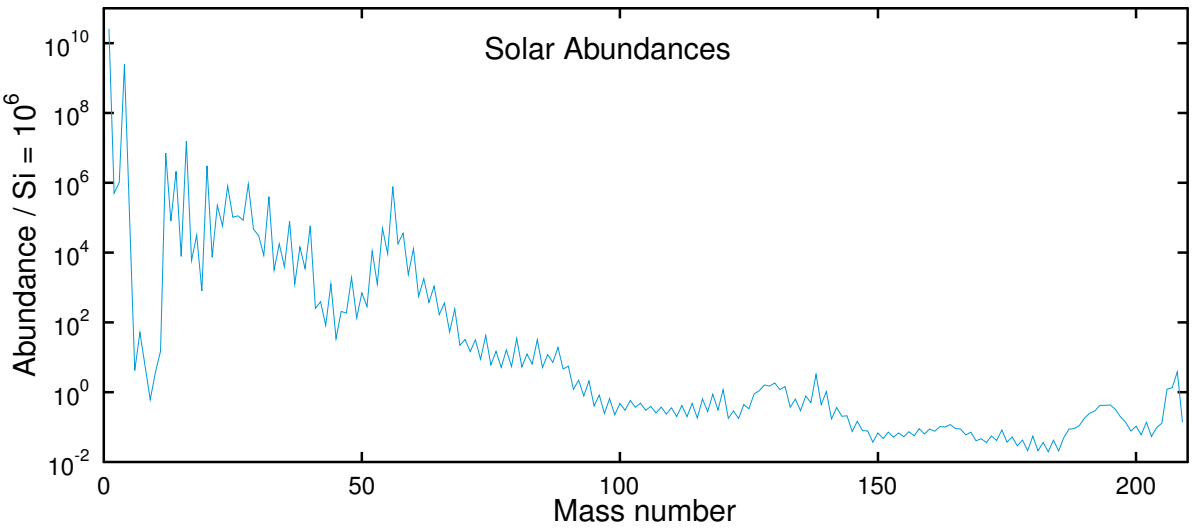

Figure 1.1: Solar abundance distribution normalised to Silicon at 10^6, adapted from Lodders 2003. The peaks in the distribution show the signatures of the different processes. The first peak around helium results from the primordial nucleosynthesis. The second peak around iron originates from nuclear statistical equilibrium and the following double peak structures from neutron capture processes.

The solar abundance distribution can roughly be decomposed in four main nucleosynthesis scenarios, namely the Big Bang nucleosynthesis, fusion reactions as well as slow and rapid neutron capture reactions. These account for the most obvious distinctive features of the solar abundance distribution. Residual abundances result from other processes, which have a minor impact on the overall distribution but can not be neglected in a detailed analysis of individual isotopes.

1.2.2 Primordial nucleosynthesis

After the formation of the universe from a singularity, expansion caused a dilution of the energy per unit volume. Knowing the baryon-to-photon ratio, which includes the baryon density and the expansion rate the primordial yields can be determined with three kinds of rates. The expansion rate, the weak interaction rates, which interconvert neutrons and protons, and the nuclear reaction rates, which build up the complex nuclei. Once the interconversion rate becomes less than the expansion rate, neutrons and protons freeze out at a ratio of about $1 : 6$. The universe has to expand even more until deuterium becomes stable against photodissociation, binding 99.99% of the neutrons into ^{4}He. At this time the free neutron decay dropped the $n : p$ ratio to about $1 : 7$, leading to an ^{4}He mass fraction of 25%. The increasing Coulomb barriers and a lack of stable nuclei at mass numbers 5 and 8 prohibit the Big Bang nucleosynthesis to effectively produce elements beyond ^{7}Li. During the first 20 minutes after the Big Bang, the fuel for the first stars was produced [Olive et al. 2000].

1.2.3 Fusion

The outcome of the primordial nucleosynthesis is the foundation for the next step in altering the composition of the atomic nuclei in the universe, namely fusion processes in stars. Stars formed out of large gas clouds containing approximately 75% hydrogen and 25% helium. Small disturbances in the density are the seed for gravitational collapsing structures in these clouds, forming the protostars. The potential energy released from the collapse heats up the protostar until the temperature in the center is high enough to facilitate fusion processes. In order to fuse two nuclei together the repulsing electromagnetic force has to be exceeded. The electromagnetic force is far reaching and the strong force is not perceptible as long as the particles are separated. Therefore fusion processes, as they exist in stars with temperatures much too low to overcome the Coulomb barrier kinetically, can not be described classically. Only quantum mechanical tunneling processes enable the fusion of two repulsing charged particles in stellar conditions [Rolfs and Rodney 1988, Rauscher 2010]. The Gamow window describes the energy range in which fusion processes of charged particles take place. It is the convolution of the particle energy distribution with the tunnel probability (figure 1.2).

Binding energy

The binding energy of a nucleus results from the mass defect of the sum of its components. The helium nucleus for instance consists of two protons and two neutrons, but its mass is lighter than the sum of those four particles. The missing bit of mass is in the binding energy of the particles

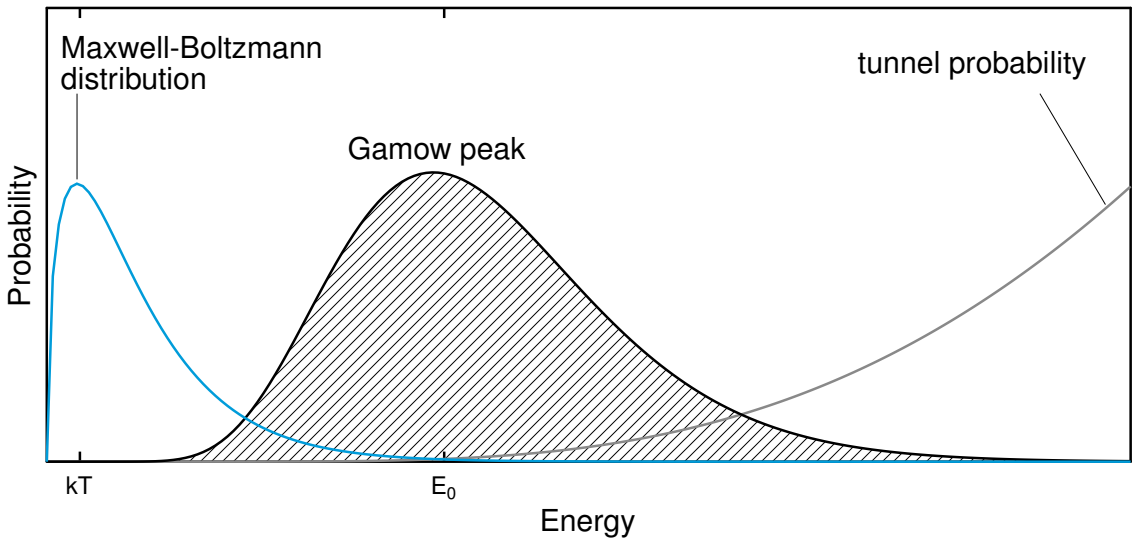

Figure 1.2: The Gamow window. Illustration of the energy range in which fusion processes occur in stars. The convolution of the energy distribution with the tunnel probability of the particles in concern gives the Gamow window.

and can be calculated via Einsteins formula $E = m \cdot c^2$. The general trend of the binding energy per nucleon with the mass number is increasing up to iron and nickel and then decreasing with higher mass numbers. Thus, energy can be released via fusion from hydrogen up to iron and afterwards via fission. Two exceptions in the binding energy trend are at mass numbers 5 and 8, which do not have a stable configuration. Since the ^{4}He nucleus is stronger bound than these nuclei, they decay almost instantly back to helium, producing a gap in the abundance pattern at these mass numbers. The change in the steepness of the binding energy curve, as illustrated in figure 1.3, from hydrogen to iron, results in different lifetimes of different burning processes in stars. Hydrogen fusion, which has the highest power output per nucleon, is the longest burning stage in a star while the later burning stages become increasingly shorter.

The p-p chain

The first major nuclear burning process, the hydrogen burning, starts at temperatures of about $4 \cdot 10^6$ K. Stars with masses between 0.07 and 1.4 $M_\odot$ (with $M_\odot$ being the solar mass) spend most of their time producing helium from hydrogen via the p-p chain. The p-p chain is a sequence of nuclear reactions transforming hydrogen to deuterium [Bethe and Critchfield 1938], which is altered to ^{3}He and finally produce ^{4}He.

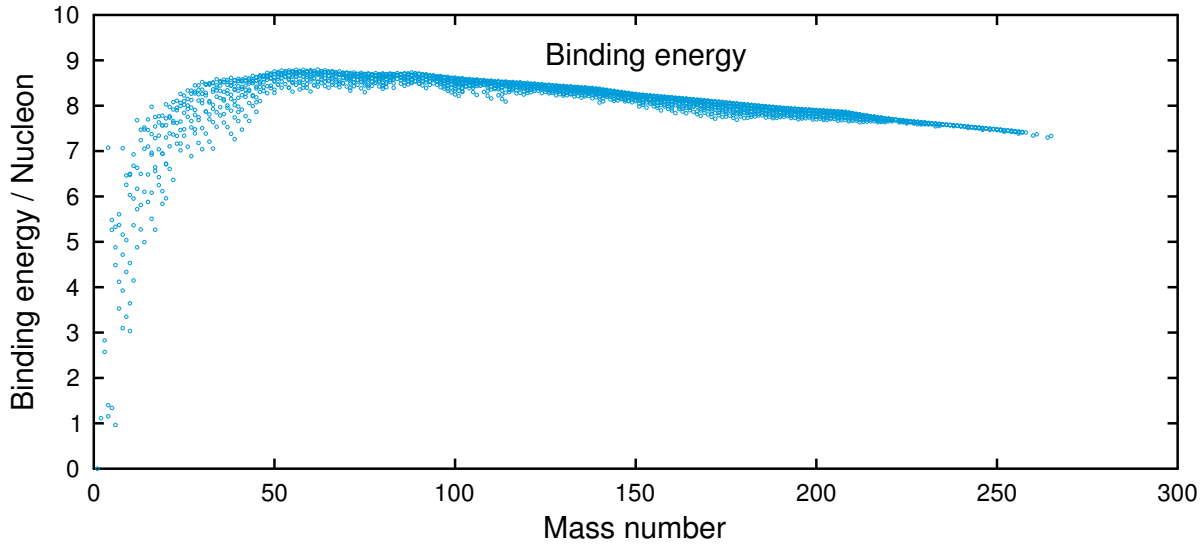

Figure 1.3: Maximum binding energy per nucleon as function of mass number. Especially stable configurations with a local maximum in the binding energy are ^{4}He, ^{12}C and ^{16}O. Data from Audi et al. 2003.

$$\begin{aligned} p + p &\rightarrow {}^{2}D + e^{+} + \nu \\ {}^{2}D + p &\rightarrow {}^{3}He + \gamma \\ {}^{3}He + {}^{3}He &\rightarrow {}^{4}He + 2p \end{aligned}$$

The energy per nucleon released in this process is 6.55 MeV. The p-p chain has its bottleneck in the first step of the proton-proton fusion, since it is the only step, which depends on the weak force to convert one proton into a neutron. The last step, which has a higher Coulomb barrier, by fusing two ^{3}He nuclei together, happens faster as the first step at the same temperature since it is not dependent on the weak force [Adelberger et al. 2011].

The CNO cycle

The CNO cycle, triggered around $15 \cdot 10^{6}$ K, competes with the p-p chain and dominates in stars with masses higher than 1.4 $M_{\odot}$. The CNO cycle produces also helium from hydrogen, only that it uses ^{12}C as catalyst. The CNO cycle is not competing with the weak force in any fusion step, thus, making it more temperature dependent than the p-p chain and the dominant process at higher temperatures, due to higher rates [Bethe 1939, Adelberger et al. 2011].

$$
\begin{aligned}
{}^{12}\mathrm{C} + {}^{1}\mathrm{H} &\rightarrow {}^{13}\mathrm{N} + \gamma \\
{}^{13}\mathrm{N} &\rightarrow {}^{13}\mathrm{C} + \mathrm{e}^{+} + \nu \\
{}^{13}\mathrm{C} + {}^{1}\mathrm{H} &\rightarrow {}^{14}\mathrm{N} + \gamma \\
{}^{14}\mathrm{N} + {}^{1}\mathrm{H} &\rightarrow {}^{15}\mathrm{O} + \gamma \\
{}^{15}\mathrm{O} &\rightarrow {}^{15}\mathrm{N} + \mathrm{e}^{+} + \nu \\
{}^{15}\mathrm{N} + {}^{1}\mathrm{H} &\rightarrow {}^{12}\mathrm{C} + {}^{4}\mathrm{He}
\end{aligned}
$$

The energy per nucleon released in this process is 6.25 MeV. The bottleneck during the CNO cycle is the proton capture on ^{14}N, resulting in an increased abundance of ^{14}N after the CNO cycle.

Helium burning

After the hydrogen in the center of the star is consumed and a helium core has formed, the core contracts until temperatures reach 10^8 K to facilitate helium burning. However stars with masses below 0.3 $M_\odot$ do not produce large enough helium cores to continue with further fusion processes. All the other stars proceed with hydrogen shell burning and helium core burning. In stars with masses below 7 $M_\odot$, helium burning is facilitated in electron degenerated matter, thus leading to explosive helium burning, which is referred to as helium flash. In stars above 7 $M_\odot$ helium burning is accommodated in non-degenerated matter. Because of the very short lifetime of ^{8}Be of $2.6 \cdot 10^{-16}$ s, helium burning can only work if three alpha particles collide almost coincidently. Therefore, helium burning is also referred to as triple alpha process. The tunnel barrier of two helium nuclei is already overcome in the p-p chain, but the simultaneous collision of three particles becomes only statistical likely at higher temperatures, densities and higher helium abundances.

$$
\begin{aligned}
{}^{4}\mathrm{He} + {}^{4}\mathrm{He} &\rightleftarrows {}^{8}\mathrm{Be} \\
{}^{8}\mathrm{Be} + {}^{4}\mathrm{He} &\rightarrow {}^{12}\mathrm{C}
\end{aligned}
$$

The energy per nucleon released in this process is 0.61 MeV. The resulting carbon can capture further alpha particles and create heavier alpha elements, which are elements with a nucleus consisting of a multiple of alpha particles.

$$
\begin{aligned}
^{12}\mathrm{C} + {}^{4}\mathrm{He} &\rightarrow {}^{16}\mathrm{O} \\
^{16}\mathrm{O} + {}^{4}\mathrm{He} &\rightarrow {}^{20}\mathrm{Ne} \\
^{20}\mathrm{Ne} + {}^{4}\mathrm{He} &\rightarrow {}^{24}\mathrm{Mg} \\
^{24}\mathrm{Mg} + {}^{4}\mathrm{He} &\rightarrow {}^{28}\mathrm{Si} \\
&\vdots
\end{aligned}
$$

The missing resonances and increasing coulomb barrier of the heavier alpha elements decreases the likelihood of further alpha captures [Prialnik 2009].

An important side branch of the helium burning takes place for example on the leftover from the CNO cycle. ^{14}N, the bottleneck of the CNO cycle, captures alpha particles, thus, enabling the following reactions:

$$
\begin{aligned}
^{14}\mathrm{N} + {}^{4}\mathrm{He} &\rightarrow {}^{18}\mathrm{O} \\
^{18}\mathrm{O} + {}^{4}\mathrm{He} &\rightarrow {}^{22}\mathrm{Ne} \\
^{22}\mathrm{Ne} + {}^{4}\mathrm{He} &\rightarrow {}^{25}\mathrm{Mg} + \mathrm{n}
\end{aligned}
$$

This is one of the neutron sources for the *s* process (compare chapter 2.2.1).

Carbon and oxygen burning

Carbon and oxygen burning are triggered at temperatures above $5 \cdot 10^8$ K and 10^9 K respectively. Both burnings produce an excited compound nucleus, which decays via various channels depending on the temperature.

$$
\begin{aligned}
^{12}\mathrm{C} + {}^{12}\mathrm{C} &\rightarrow {}^{24}\mathrm{Mg} + \gamma \\
&\rightarrow {}^{23}\mathrm{Mg} + \mathrm{n} \\
&\rightarrow {}^{23}\mathrm{Na} + \mathrm{p} \\
&\rightarrow {}^{20}\mathrm{Ne} + \alpha \\
&\rightarrow {}^{16}\mathrm{O} + 2\alpha
\end{aligned}
\qquad
\begin{aligned}
^{16}\mathrm{O} + {}^{16}\mathrm{O} &\rightarrow {}^{32}\mathrm{S} + \gamma \\
&\rightarrow {}^{31}\mathrm{S} + \mathrm{n} \\
&\rightarrow {}^{31}\mathrm{P} + \mathrm{p} \\
&\rightarrow {}^{28}\mathrm{Si} + \alpha \\
&\rightarrow {}^{24}\mathrm{Mg} + 2\alpha
\end{aligned}
$$

The average energy released per nucleon is around 0.54 MeV for the carbon burning and about 0.3 MeV for the oxygen burning. The major product from the oxygen burning is ^{28}Si [Prialnik 2009].

Silicon burning

Before stars can reach temperatures high enough to surpass the Coulomb barrier for direct Si-Si fusion, photodisintegration of the black body radiation at around $3 \cdot 10^9$ K occurs on silicon nuclei, producing lighter elements. These light nuclei can then be recaptured on other silicon nuclei thereby producing heavier nuclei. A network of nuclear reactions in which heavy nuclei exchange light particles is created. Although the reactions of production and depletion strive to a state of equilibrium, the so called nuclear statistical equilibrium (NSE) results in the production of the stable iron group (Fe, Co, Ni), which has the maximum binding energy per nucleon [Prialnik 2009].

Core collapse supernovae and primary processes

Stars, which are heavy enough to facilitate Si burning, seal their fate in a core collapse supernova. Surpassing the iron peak with further fusion processes would withdraw energy from the star, thus, silicon burning is the last stable burning stage in a star. The electron degenerated iron core ultimately overcomes the Chandrasekhar limit, surpassing the degenerated electron pressure. Thus, the core starts collapsing in almost free fall, while heating up. Blackbody radiation starts depleting iron via photodisintegration:

$$^{56}\mathrm{Fe} \rightarrow 13 \cdot {}^{4}\mathrm{He} + 4\mathrm{n},$$

absorbing about 2 MeV per nucleon. This energy absorption fuels the collapse even more, until the temperature becomes so high that the photons disintegrate helium:

$$^{4}\mathrm{He} \rightarrow 2\mathrm{p} + 2\mathrm{n}.$$

This reaction absorbs even more energy, about 6 MeV per nucleon. The core collapses even faster until the density becomes high enough and protons capture electrons and turn into neutrons. Finally the collapse comes to a halt when the neutron gas becomes dense enough in order

to degenerate, stabilizing the core with the neutron degeneration pressure. Even heavier stars can overcome the neutron degeneration pressure and collapse into a black hole [Bethe 1990]. All iron created from the silicon burning before the collapse of the massive star was photodisintegrated and vanished into a neutron star or black hole. The outer layers of the star, which contain the products of the earlier burning stages gets ejected during the supernova into the interstellar medium (ISM). In principle, there was no net production of iron if the supernova would not contribute to nucleosynthesis itself in the ejected outer layers. When the shock-wave of the collapse reaches the outer layers, temperatures raise up to $5 \cdot 10^9$ K building up ^{56}Ni via the NSE, which ultimately decays via ^{56}Co to ^{56}Fe. Iron, which enriches the interstellar medium is produced during the supernova nucleosynthesis in the shock front and does not originate from the iron core of the supernova progenitor [Prialnik 2009]. The iron production during the NSE in the shock front is independent of the seed nuclei. All isotopes, which scale strictly with the iron abundance, are considered to be produced in a primary process, whereas isotope enrichments, which depend on a certain metallicity originate from secondary processes.

Trans iron elements

Fusion cannot build up isotopes heavier than the iron peak, hence, another production channel must contribute to nucleosynthesis, as elements heavier than iron exist in the universe. The viable way to build up elements with higher mass numbers than iron is via neutron capture reactions. Uncharged neutrons are not repulsed by positively charged nuclei, therefore, an accumulation of neutrons on any nucleus is only limited by the stability of the resulting configuration. The discovery of the unstable technetium in the atmosphere of red giants by Merrill 1952 identified stars as production site for heavy elements.

1.2.4 Neutron capture reactions

Nuclear physics describes neutron capture processes with reaction probabilities. These reaction probabilities are expressed as energy dependent cross sections. Once a neutron is captured the future evolution of the freshly synthesised nucleus depends on the stability of the configuration. In the shell model, the nucleus is treated as a potential with different energy levels for protons and neutrons, which are populated according to the Pauli-principle. If a certain nuclear configuration is less stable than a neighboring one (one isotope has a smaller binding energy per nucleon than a neighboring isotope on the isobar), a β-decay occurs converting the nucleus to its more stable neighbor by the weak interaction.

Cross sections and reaction rate

The cross section σ for nuclear reactions describes the probability of a reaction to take place. This probability is used to calculate the number of reactions, which take place per unit volume and unit time. Classically, the cross section is a combined geometrical area of the projectile and target nucleus. The cross section is therefore expressed as unit area. Cross sections are of the order 10^{-24} cm^2, therefore, this area was defined as barn (b). A quantum mechanical treatment of the cross section results in an energy-dependent or, correspondingly, velocity-dependent cross section

$$\sigma = \sigma(v). \tag{1.1}$$

With v the relative velocity between the projectile and target nucleus.

The reaction rate r is the number of reactions per unit volume and per unit time. It is expressed as

$$r = N_{target} \cdot N_{projectile}\, v\, \sigma(v) \tag{1.2}$$

with N_{target} the target nuclei number density and $N_{projectile}$ the projectile nuclei number density. The reaction rate is expressed as number of reactions per second per cubic centimeter. With a thermal velocity distribution the convolution of $v\sigma(v)$ with the probability function $\Phi(v)$ gives an averaged reaction rate per particle pair $\langle\sigma v\rangle$

$$\int_0^\infty \Phi(v)dv = 1 \tag{1.3}$$

$$\langle\sigma v\rangle = \int_0^\infty \Phi(v) \cdot v\sigma(v)dv. \tag{1.4}$$

The total rate for non-identical particles can then be expressed as [Rolfs and Rodney 1988]

$$r = N_{target} \cdot N_{projectile}\, \langle\sigma v\rangle. \tag{1.5}$$

Nuclear shell model

The structure of a nucleus and the resulting effect on the neutron capture cross section can be calculated with the shell model. The stability of a nucleus depends on the population of the

nuclear energy levels for protons and neutrons. The nuclear shell model calculates a potential, resulting from the effect of all nucleons in a nuclei and solves the Schrödinger equation for this potential. The resulting energy levels can then be populated with each four particles, having two particle pairs, namely protons and neutrons and two spin configurations ($+1/2$ and $-1/2$). When calculating the binding energy for all isotopes one finds certain points, where adding one more nucleon (proton or neutron) to the nucleus results in a significantly lower binding energy compared to the previously added nucleon. These points, which represent closed proton or neutron shells are called magic numbers. The magic numbers are for protons and neutrons at 2, 8, 20, 28, 50, 82, 126. Nuclei, which have a closed shell of one particle species are called either proton- or neutron-magic and having both shells closed results in double-magic nuclei.

MACS AND SEF

In stars, free neutrons are thermalised via elastic scattering and their velocities are represented by a Maxwell-Boltzmann distribution. The convolution of the energy dependent cross section with an Maxwell-Boltzmann velocity distribution, gives an averaged cross section for stellar conditions. The most probable neutron energy is at $E = kT$, therefore, the Maxwellian-averaged cross section (MACS) $\langle\sigma\rangle$ should be close to σ_T, which is the cross section of the thermal energy at temperature T. A correlation of the MACS with the size of the nucleus, with local minima at closed neutron shells (figure 1.4) is observed.

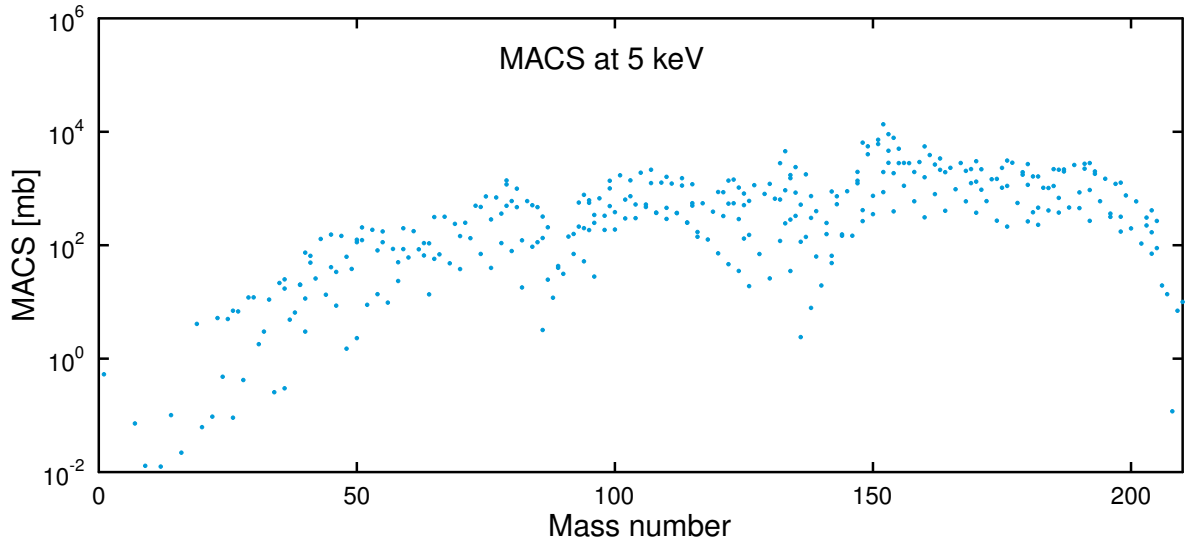

Figure 1.4: MACS at 5 keV as function of mass number, from Dillmann et al. 2006. A correlation to the mass of the nucleus can be observed. Closed neutron shells result in local minima.

The experimentally determined cross sections are measured with the target nucleus in ground

state. A correction for thermally populated exited states, as they exist in stellar conditions has to be performed on the MACS. This stellar enhancement factor (SEF) has to be calculated theoretically [Käppeler et al. 2011].

Stellar neutron captures

Looking at the solar trans-iron abundance distribution from figure 1.1 the double peak structures at and around neutron magic isotopes suggests the presence of two neutron capture processes at high and low neutron densities creating the heavy elements [Burbidge et al. 1957]. Neutron capture reactions can be neglected for the overall energy balance in stars. Thereby bearing the advantage that calculations of the stellar structure and neutron capture networks can be separated, decreasing the complexity of simulations. Figure 1.5 gives an overview of the main nucleosynthesis processes on the chart of nuclides.

Classical *s* process

The *s* process is the slow neutron capture process. Starting from ^{56}Fe, heavier elements are generated by neutron captures. In *s*-process conditions, the typical neutron capture time is much longer than the typical lifetime of a beta-unstable isotope. The *s* process starts by definition at ^{56}Fe, which is used as seed isotope for neutron captures. This makes the *s* process a secondary process and its boundary condition is supported by observations, which show a metallicity dependent ratio of *s* isotopes as function of iron (chapter 1.2.3).

s-process path

The *s* process is a series of neutron capture reactions on stable isotopes. The capture sequence proceeds until an unstable isotope is reached and a β-decay occurs. If the decay daughter is stable, it represents the starting point for the next sequence of neutron captures (figure 1.6).

The *s* process follows the valley of stability until its termination point ^{209}Bi is reached. A further neutron capture produces the α-unstable ^{210}Po, which decays back to ^{206}Pb (figure 1.7).

In *s*-process conditions, the time dependent change in abundance of an isotope A is expressed as:

$$\frac{dN_A(t)}{dt} = N_n(t)N_{A-1}(t)\langle\sigma v\rangle_{A-1} - N_n(t)N_A(t)\langle\sigma v\rangle_A \pm \lambda_\beta(t)N_A(t) \tag{1.6}$$

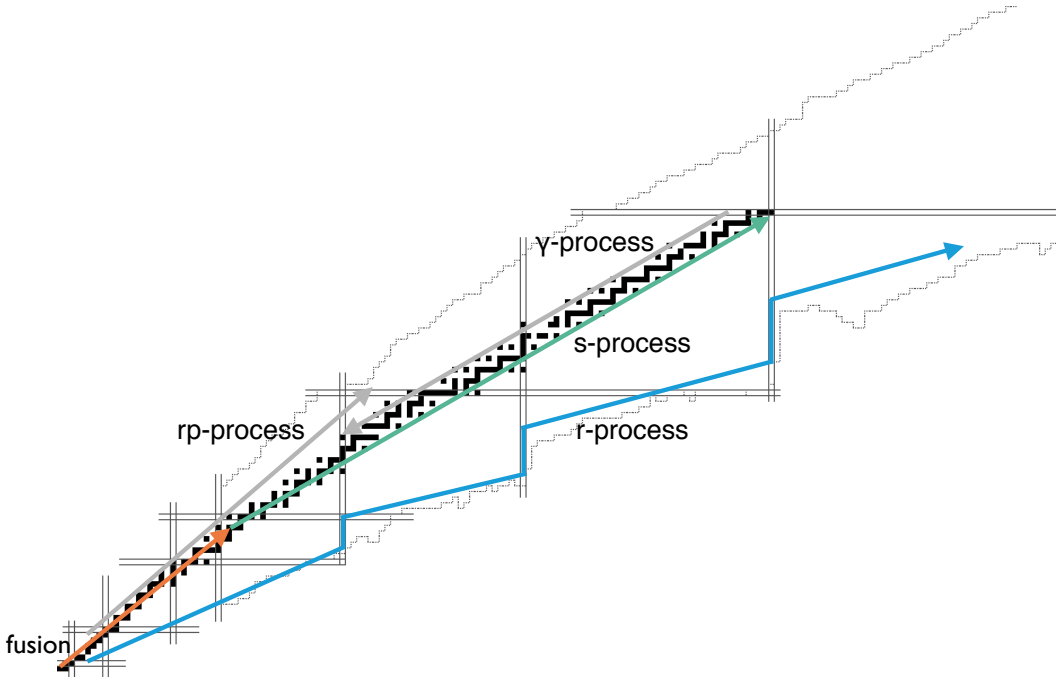

Figure 1.5: Overview of the main nucleosynthesis paths along the chart of nuclides. In orange the fusion contribution (chapter 1.2.3), in green the *s*-process path, in blue the *r*-process path (page 24) and in grey the *rp*- and γ processes (page 24). The *s* process and the γ process are secondary processes, which depend on certain seed isotopes, whereas fusion, the *r* process and the *rp* process are primary processes, which are not dependent on prior nucleosynthesis. Adapted from Glorius 2013.

with N_A the abundance of the isotope with mass-number A, N_n the neutron density and $\lambda_\beta(t)$ the β-decay rate, if the isotope A or a respective isobar is unstable. In the *s* process, the change in abundance depends on the production channel, which consists of neutron captures on the isotope with a mass number reduced by one and β-decays along the isobaric line and the destruction via neutron capture on the isotope in concern and possible β-decays of the isotope. For almost all unstable isotopes the assumption is justified, that the β-decay happens either instantly or on much slower compared to typical *s*-process timescales. Thus the equation (1.6) can be simplified to:

$$\frac{dN_A(t)}{dt} = v_T N_n(t)(\sigma_{A-1}N_{A-1} - \sigma_A N_A) \tag{1.7}$$

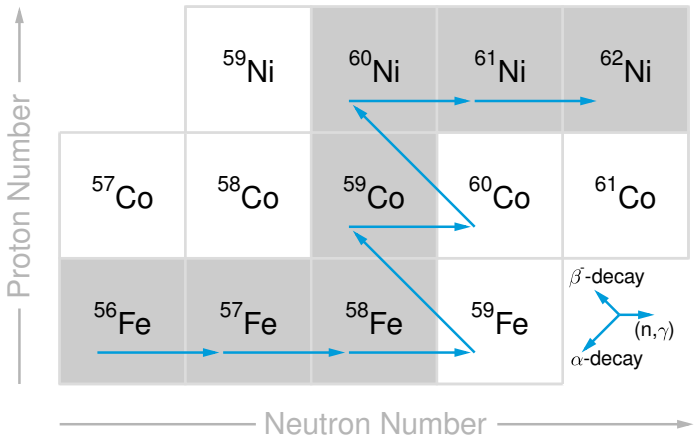

Figure 1.6: The *s*-process path. If a beta unstable isotope is reached, it decays back to the next stable isotope. Stable isotopes are marked grey, and unstable isotopes white.

with σ_A the MACS of isotope A, v_T the thermal velocity, and sequential mass-numbers represent following stable isotopes along the *s*-process path [Rolfs and Rodney 1988].

Neutron density

The *s* process predominantly takes place in steady conditions. The time dependent neutron density can be replaced by the integrated neutron flux τ:

$$\tau = v_T \int_0^t N_n(t)dt \ \frac{\text{neutrons}}{cm^2} \tag{1.8}$$

Thus, replacing the variable t in equation (1.7) with the new quantity τ gives:

$$dN_A(t)/d\tau = \sigma_{A-1}N_{A-1} - \sigma_A N_A. \tag{1.9}$$

The change in abundance is now in respect to the neutron exposure τ. Looking at the solar *s*-process abundances, the isotopes with mass number larger than 90 can almost be perfectly reproduced with the local equilibrium approximation, $dN_A(t)/d\tau = 0$, which means that the abundance of an *s*-only isotope builds up until the rate of destruction equals the rate of production:

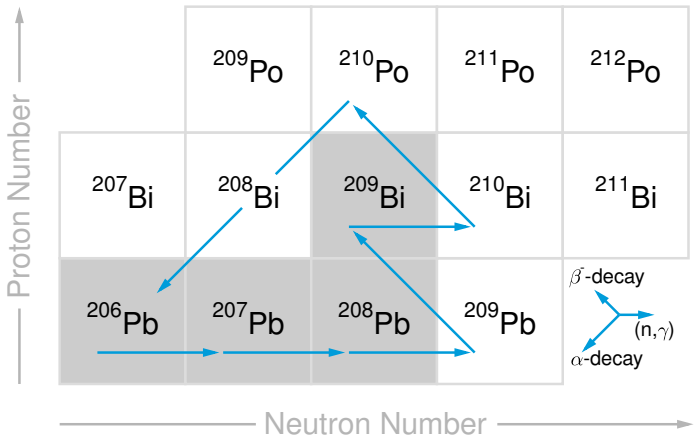

Figure 1.7: The termination point of the *s* process. A neutron capture on ^{209}Bi produces ^{210}Bi, which decays to ^{210}Po, which itself is alpha unstable and decays back to ^{206}Pb. Stable isotopes are marked grey, and unstable isotopes white.

$$\sigma_{A-1}N_{A-1} = \sigma_A N_A = constant. \tag{1.10}$$

Only closed neutron shells result in a drop of the following plateau of the $\sigma_A N_A$ curve (figure 1.8). In order to reproduce the entire $\sigma_A N_A$ curve for all *s*-isotopes, a superposition of different neutron irradiations has to be fitted to the data. As shown by Clayton et al. 1961 a single neutron irradiation of an iron seed can not reproduce the solar *s*-process abundances. A satisfying reproduction of *s*-element distribution was obtained with three different exponential neutron irradiations [Seeger et al. 1965]. These three neutron irradiations were assigned to three *s*-process components.

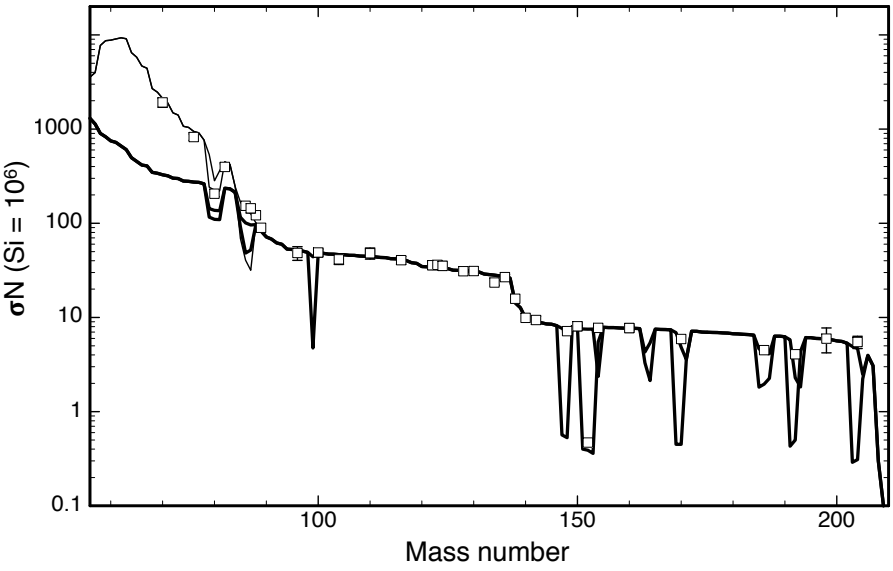

Figure 1.8: The σN curve. This curve is the characteristic product of the cross section times the *s*-process abundance plotted as a function of mass number. The thick solid line represents the main component obtained by means of the classical model, the thin line additionally takes into account the weak component in massive stars. Symbols denote the empirical products for the *s*-only nuclei. Some important branchings of the neutron capture chain are indicated by the splited line. Figure from Käppeler et al. 2011.

A main component, which is responsible for the production of the *s*-nuclei from mass number 90 up to lead. The strong component, which accounts for the production of the lead peak, and the weak component responsible for the production of the *s*-elements from the iron peak up to mass number 90 [Käppeler et al. 1982, Käppeler et al. 1989, Cui et al. 2007]. The neutron densities in *s*-process conditions are around $10^6 - 10^{10}$ cm^{-3}, thus, resulting in about one neutron capture every 10 years. The overall trend of the three components of the *s* process are illustrated in overabundance plots, as seen in figure 1.9. Overabundance factors are used to compare single observations or simulations to the solar abundance distribution. The overabundance factors compare isotopes, normalised to the solar abundances of one particular isotope. If a process is solely responsible for the creation of one isotope, the overabundance factor of this process and isotope is one. If multiple processes contribute to the creation, then the overabundance factor for each process is between zero and one.

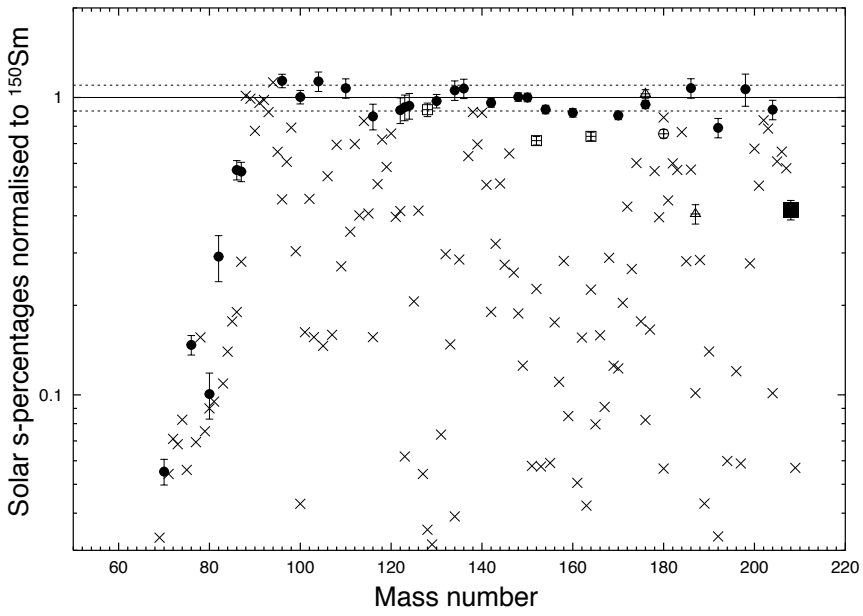

Figure 1.9: Overabundance factors of the main component. Solar *s*-percentage normalised to ^{150}Sm versus atomic mass for the solar main component (from Bisterzo et al. 2010). The reconstruction of the solar abundance distribution of *s*-only isotopes (black circles) with mass numbers larger than 90 is well matched, except for isotopes with strong *p*-process contributions (open symbols). Crosses symbolise isotopes, which are only partially produced in the *s* process and the black square represents the double magic isotope ^{208}Pb. The production of isotopes of mass numbers 60-to 90 is accounted for by the weak component, whereas the production of isotopes around mass numbers of 208 is caused by the strong component.

The production site for the main component is in thermally pulsing asymptotic giant branch stars with solar metallicity, as will be discussed in chapter 2.2.1. The sites for the weak component

are helium and carbon burning in massive stars, as will be described in chapter 1.3.2. The site for the strong component was identified as being identical to the main component only at lower metallicities, thus, resulting in a higher neutron per seed ratio accompanied by increased production of heavy elements. The stellar site for the main and strong component is described in chapter 2.2.3.

Branching points

Branching points are isotopes or isomers on the *s*-process path, which undergo a β-decay on the same timescale as a neutron capture. This leads to a branching in the *s*-process path where some of the mass flow follows the β-decay branch and the rest of the mass flow the neutron capture path (figure 1.10).

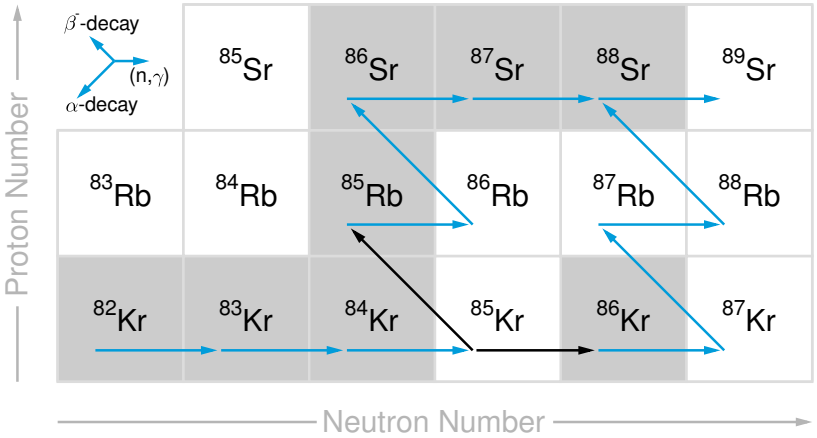

Figure 1.10: Branching point ^{85}Kr along the *s*-process path. ^{85}Kr has a half-life of about 10 years, which would make it an excellent probe for *s*-process conditions, if all reaction channels would be known to good precision. Stable isotopes are marked grey, and unstable isotopes white.

Branching points are very sensitive to the neutron density and a good way to verify the theoretical calculations with observations. The branching ratio R can be expressed as the ratio of the β-decay rate, λ_β, and the neutron capture rate, λ_n:

$$R = \frac{\lambda_\beta}{\lambda_n} = \frac{1}{\tau_\beta N_n \langle \sigma v \rangle_A} \,. \tag{1.11}$$

For known $\langle \sigma v \rangle_A$ and temperature independent β-decay lifetimes τ_β the observed branching ratio

can be used to constrain the neutron density N_n. If the β-decay is temperature dependent and the neutron density known, branching points can be used to constrain temperatures in *s*-process environments [Käppeler et al. 2009].

Waiting points during the *s* process

Waiting points are isotopes along the *s*-process path, which have a very small neutron capture cross section. They act as bottleneck for the production of the isotopes, which lie on the *s*-process path behind them. Neutron magic isotopes are such waiting points. The waiting points are responsible for the *s* process peaks in the solar abundance distribution as seen in figure 1.1.

The *s*-only isotopes

The *s*-only isotopes are isotopes, which are created almost solely by the *s* process and are shielded from other processes. These isotopes are often considered when comparing observations to simulations (figure 1.11).

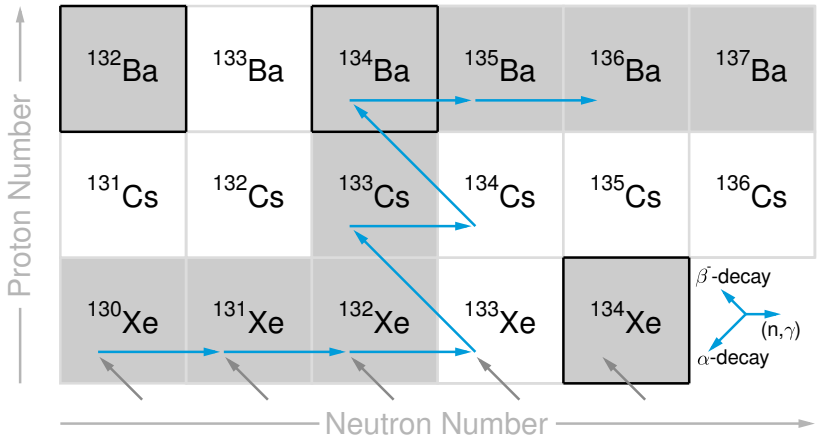

Figure 1.11: *s*-, *r*- and *p*-only isotopes. The *s*-only isotope ^{134}Ba is shielded from the *r* process (grey arrows) by the stable isotope ^{134}Xe. ^{134}Xe is on the other hand an *r*-only isotope (page 24), since the *s*-process path does not reach further than ^{133}Xe. ^{132}Ba is a *p*-only isotope (page 24), which is not produced by the *s* , nor *r* process. Stable isotopes are marked grey, and unstable isotopes white.

Table 1.1 lists all *s*-only isotopes and their solar abundances.

s-only isotopes	solar abundances	s-only isotopes	solar abundances
^{64}Zn	613	^{128}Xe	0.103
^{70}Ge	24.4	^{130}Xe	0.205
^{87}Rb	1.97	^{134}Ba	0.109
^{86}Sr	2.32	^{136}Ba	0.353
^{87}Sr	1.64	^{138}Ba	3.22
^{89}Y	4.64	^{142}Nd	0.225
^{90}Zr	5.87	^{148}Sm	0.0292
^{91}Zr	1.28	^{150}Sm	0.0191
^{92}Zr	1.96	^{154}Gd	0.00719
^{94}Zr	1.98	^{160}Dy	0.00922
^{93}Nb	0.698	^{170}Yb	0.00756
^{96}Mo	0.425	^{176}Lu	0.000951
^{100}Ru	0.234	^{176}Hf	0.00802
^{104}Pd	0.155	^{186}Os	0.0107
^{110}Cd	0.201	^{187}Os	0.0108
^{122}Te	0.124	^{192}Pt	0.0105
^{123}Te	0.0428	^{198}Hg	0.0339
^{124}Te	0.229	^{204}Pb	0.0611

Table 1.1: s-only isotopes and their respective solar abundances normalised to Si = 10^6 [Anders and Grevesse 1989]. The only two exceptions in this table are ^{64}Zn and ^{70}Ge. ^{64}Zn results from explosive nucleosynthesis and NSE, but acts as seed for the *s* process and ^{70}Ge has still a small NSE contribution.

THE *r*-PROCESS SIGNATURE

The double peak structure in the solar abundance distribution hints to a second process with higher neutron densities. The *r* process is the rapid neutron capture process, which is a short neutron irradiation with neutron densities higher than 10^{20} cm^{-3}. During the *r* process the neutron capture times are much faster than the β-decay times of the isotopes leading it away from the valley of stability in the chart of nuclides. The site for the *r* process is still not identified to date [Thielemann et al. 2011].

THE *r*-PROCESS PATH

The *r* process is a short time period where multiple neutron captures occur on shorter timescales than the respective β-decays. Thus leading the evolution of isotopes away from the valley of stability right up to the neutron drip line (figure 1.5), where the nucleus undergoes immediate decay and emit the freshly added neutron. After the irradiation, the neutron-rich isotopes perform a series of β-decays, until they become stable again [Kratz et al. 1993]. The waiting points for the *r* process are the neutron magic isotopes. Those isotopes act as bottlenecks during the neutron irradiation, thus piling up unstable neutron magic isotopes. After the neutron exposure, these isotopes decay on their isobaric lines and produce a peak in the *r*-process abundance distribution, at lower mass numbers than the *s*-process peak (figure 1.12). This is the reason for the double peak structure in the solar abundance distribution (figure 1.1).

R-ONLY ISOTOPES

The *r*-only isotopes are isotopes, which cannot be synthesised by other processes. These isotopes are stable isotopes on the neutron-rich side of the chart of nuclides, which are separated from the *s*-process path by β-unstable isotopes. Those isotopes are often paired with one isobaric *s*-only isotope (figure 1.11).

THE *p* PROCESS

The *p* process is a collective term for all processes, that produce the so called *p*-nuclei. The *p*-nuclei are stable isotopes on the proton-rich side of the chart of nuclides, which cannot be reached via the *s* or *r*-process path (figure 1.11). Different processes can build up these *p*-only nuclei. Namely the *rp* process, the *νp* process and the γ process. The γ process is a photodisintegration process on neutron-rich isotopes [Arnould and Goriely 2003] in the oxygen-neon layer of core

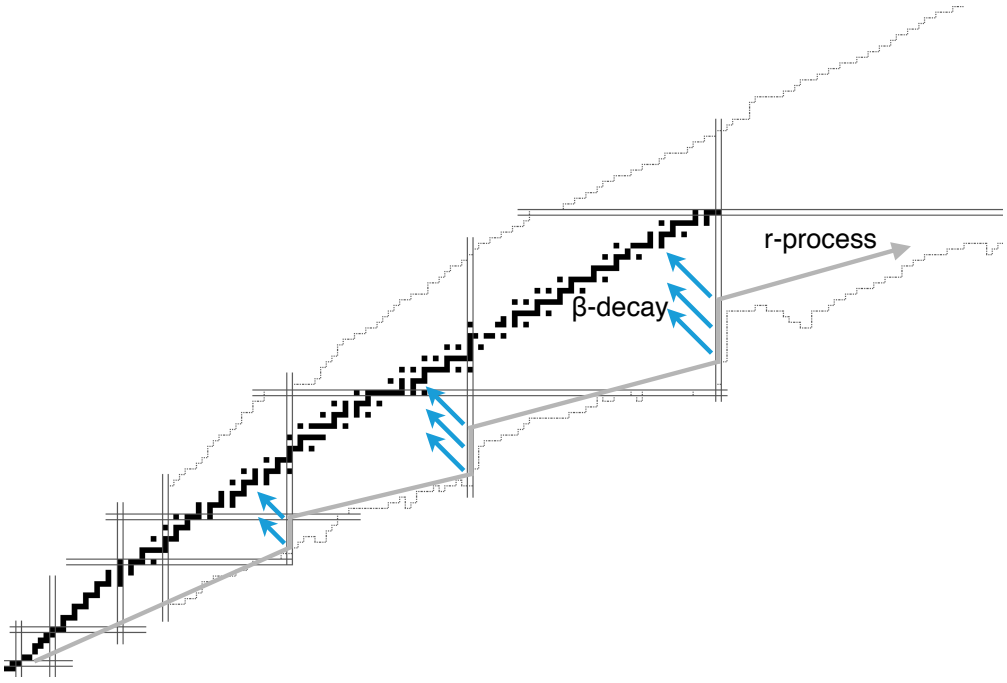

Figure 1.12: The *r*-process peaks. The *r* process consists of a short, strong neutron irradiation (grey) followed by a chain of β-decays (blue arrows). Thus leading to a production of stable isotopes on the neutron-rich side of the isobaric lines, with the typical peak structure on the isobaric stable elements of the neutron magic waiting points. Further β-decays are as well occurring between the neutron magic numbers, which are not indicated in this plot.

collapse supernovae. The *rp* process is the rapid proton capture in neutrino driven winds during explosive scenarios (figure 1.5) [Schatz et al. 1998]. Parallel to the *rp* process, which has to overcome the waiting points, ^{64}Ge, ^{68}Se, ^{72}Kr, the *vp* process results from neutrinos captured on the protons and produce a tiny amount of free neutrons, which induce the (n,p) reaction on these waiting points [Fröhlich et al. 2006, Wanajo et al. 2011].

LEPP

An unaccounted enhancement in the solar abundances of the light *s*-isotopes, Sr, Y and Zr, which is also observed in *r*-process-rich stars [Travaglio et al. 2004, Serminato et al. 2009, Zhang et al. 2006], suggest an additional process, which produces these light *s*-isotopes [Bennett 2011]. The

observed enrichment is also of primary nature as a constant or slightly decreasing ratio of these isotopes as function of Ba is observed with increasing metallicities. Travaglio et al. 2004 defined the Lighter Element Primary Process (LEPP) in order to account for the missing 8% of solar Sr and 18% of the solar Y and Zr abundances, after subtracting the r, s and weak *s* processes from the solar abundances [Bisterzo et al. 2012]. Table 1.2 lists the isotopic *s*-process contributions from the galactical chemical evolution (GCE) model used from Travaglio et al. 2004. It can be seen, that the neutron-poor isotopes of an element are the most deficient in this analysis.

Isotope	*s*-process contribution (GCE)
^{86}Sr	52%
^{87}Sr	53%
^{88}Sr	75%
^{89}Y	68%
^{90}Zr	56%
^{91}Zr	88%
^{92}Zr	82%
^{94}Zr	84%
^{96}Zr	101%

Table 1.2: Isotopic *s*-process contribution to solar abundances at the epoch of the solar system formation. GCE data from Travaglio et al. 2004. The contribution of neutron-poor isotopes is lower than the contribution of the neutron-rich isotopes. The GCE model overproduces ^{96}Zr.

THE *i* PROCESS

Looking at the solar abundance distribution, figure 1.1, and the double peak structures of the *s* and *r* process suggest no presence of a dominant neutron capture process, with neutron densities between the *s* and *r* process. Nevertheless such a process was discussed in the past, see e.g. Cowan and Rose 1977, and revived more recently by Herwig et al. 2011 in order to account for peculiar isotopic ratios, which are for instance observed in pre-solar meteoritic grains [Fujiya et al. 2013, Jadhav et al. 2013, Liu et al. 2014]. This process was introduced as intermediate neutron capture process (i-process) with neutron densities around 10^{15} cm^{-2}. Such neutron densities results in a network flux, parallel to the valley of stability [Bertolli et al. 2013].

1.3 Stellar evolution

In this section the evolution of a 3 $M_\odot$ and a 25 $M_\odot$ (with $M_\odot$ representing the solar mass) star is presented.

1.3.1 Stellar evolution of a 3 solar-mass star

The stellar evolution of a 3 $M_\odot$ star at solar metallicity up to the formation of a white dwarf is discussed in this section.

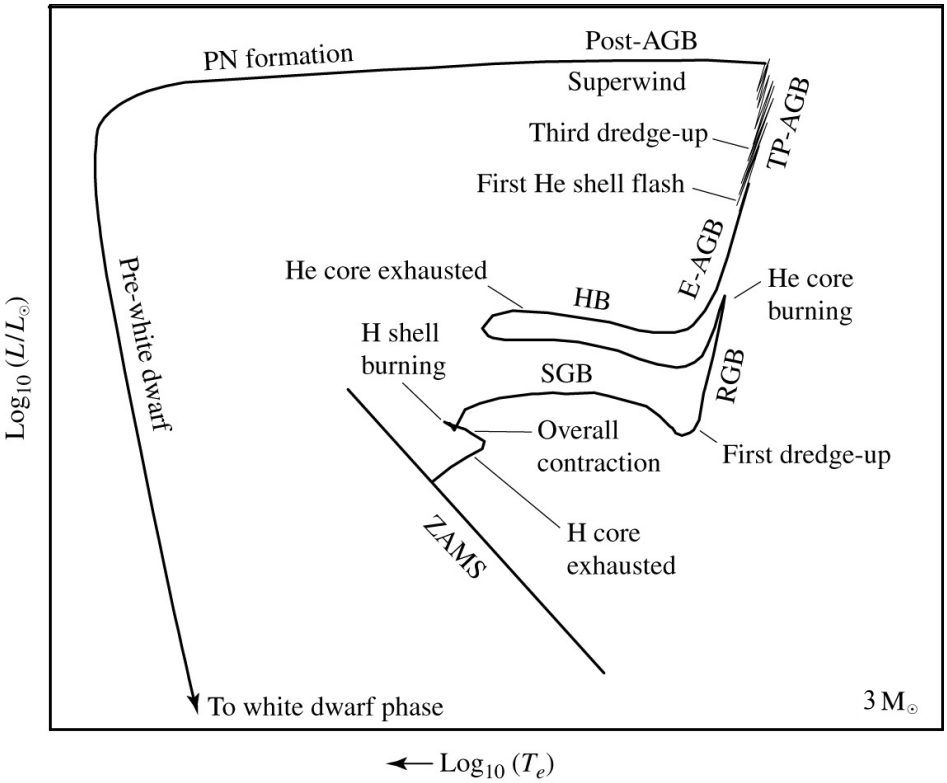

Figure 1.13: Schematic Hertzsprung-Russel diagram of a 3 $M_\odot$ star. The evolutionary phases for the 3 $M_\odot$ star are labeled as follows: Zero-Age-Main-Sequence (ZAMS), Sub-Giant Branch (SGB), Red Giant Branch (RGB), Horizontal Branch (HB), Early Asymptotic Giant Branch (E-AGB), Thermal Pulse Asymptotic Giant Branch (TP-AGB), Post Asymptotic Giant Branch (Post-AGB), Planetary Nebula formation (PN formation), and Pre-white dwarf phase leading to white dwarf phase. Adapted from Carroll and Ostlie 2007.

During the core hydrogen burning the star is located on the main sequence of the Hertzsprung-Russel diagram (HRD), as seen in figure 1.13. The HRD plots the absolute magnitude of a star

on the vertical axis versus the spectral type of a star on the horizontal axis, thereby inferring the size of the star (stars of the same temperature with different luminosities must have different sizes). Hydrogen is transformed to helium via the CNO cycle. After the exhaustion of hydrogen in the center of the star, hydrogen burning continues in the shell around the core accompanied by the contraction of the helium core. The core contraction increases the temperature, thus, increasing the CNO cycle burning rate of the shell burning. The increasing energy production forces the star to expand its envelope and cool down, thus increasing its opacity. The energy form the shell hydrogen-burning can only be transported sufficiently via convection at this point, which means, that the hot gas rises along the radial coordinating, transporting matter and energy together (radiation is only effective for energy transportation if the mean free path of a photon is large, which is the case if the opacity is low. Heat conduction is only effective if the mean free path of an electron is large. This is the case in electron degenerated matter). The star is on the sub-giant branch on the HRD at this stage. The convective envelope reaches layers in the star, where previously hydrogen burning took place mixing the ashes from that burning into the envelope. This is referred to as the first dredge-up. When the helium core has grown large enough and temperature in the center reaches about 10^8 K helium burning starts. The central part of the helium core is convective because of the high temperature sensitivity of the helium burning $\sim T^{40}$. Building up a uniform carbon-oxygen core surrounded by a helium layer beneath the hydrogen burning shell. The carbon-oxygen core contracts and heats up after the exhaustion of helium burning material in the center, expanding and cooling the outer envelope up to the exhaustion of the shell hydrogen-burning. (Stars of 4 to 8 solar masses would at this point experience a second dredge up, as the inner boundary of the convective envelope enters the helium layer while mixing mainly helium and nitrogen throughout it.) The contraction of the core continues until the density reaches the point where electrons become degenerate, forming a steady, isothermal core. After stopping the core contraction due to electron degeneration, the envelope stops expanding and the star has become an AGB-star on the HRD. Alternating explosive shell helium burning (thermal pulse, TP) and stable shell hydrogen burning sets in, hosting the *s* process and enabling the third dredge-up event bringing freshly synthesized heavy isotopes to the surface of the star, accompanied by strong stellar winds (figure 1.14).

This phase of stellar evolution accommodating the main component of the *s* process is discussed in more detail in chapter 2.2.1. During the TP-AGB (thermally pulsing asymptotic giant branch) phase, the star ejects the largest part of its envelope, so that, after the last thermal pulse, the star is surrounded by an almost spherical, dense nebula. As the gravitational pressure in the star decreases after ejecting most of the envelope, the core expands slightly, causing the remaining hydrogen envelope to contract and heat up, facilitating the last hydrogen shell burning. Having only a small envelope left, the surface temperature is sufficient to produce high energetic photons. These photons ionize the previous ejected envelope causing it to glow via fluorescence. At this state the ejecta has become a planetary nebula. After exhaustion of the hydrogen-shell

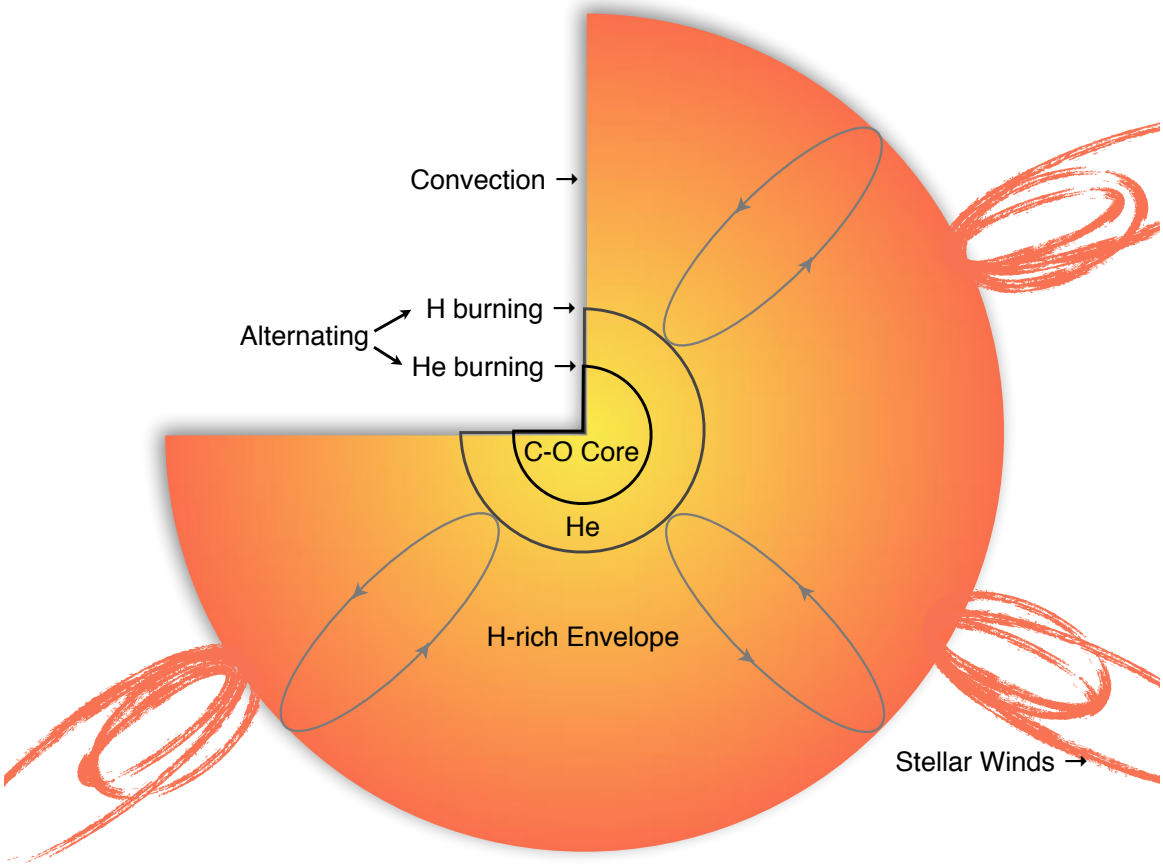

Figure 1.14: Schematic picture of a TP-AGB star, with an electron degenerated C-O core, a helium intershell and a convective hydrogen envelope. The mass loss during the TP-AGB phase and is indicated by the stellar wind ejecta. The radii are not to scale. For details, see text.

burning material, the star cools down and the luminous nebular fades away. The leftover nucleus, consisting of a degenerated carbon-oxygen core, a helium shell and a possible hydrogen layer, keeps cooling down as a white dwarf [Iben and Renzini 1983, Herwig 2006, Karakas and Lattanzio 2007, Prialnik 2009].

1.3.2 Stellar evolution of a 25 solar-mass star

Massive stars (10 $M_\odot$ < M < 30 $M_\odot$) pass all burning phases introduced in chapter 1.2.3 up to the formation of iron. The gravitational potential in massive stars is sufficient to trigger all burning phases as soon as there is enough burning material. This happens without degeneration or thermal pulses. Unlike the intermediate mass stars, an onion-like shell burning structure is formed, while going through different burning stages. After the exhaustion of the core-hydrogen burning material, shell-hydrogen burning occurs simultaneously to core-helium burning. Fol-

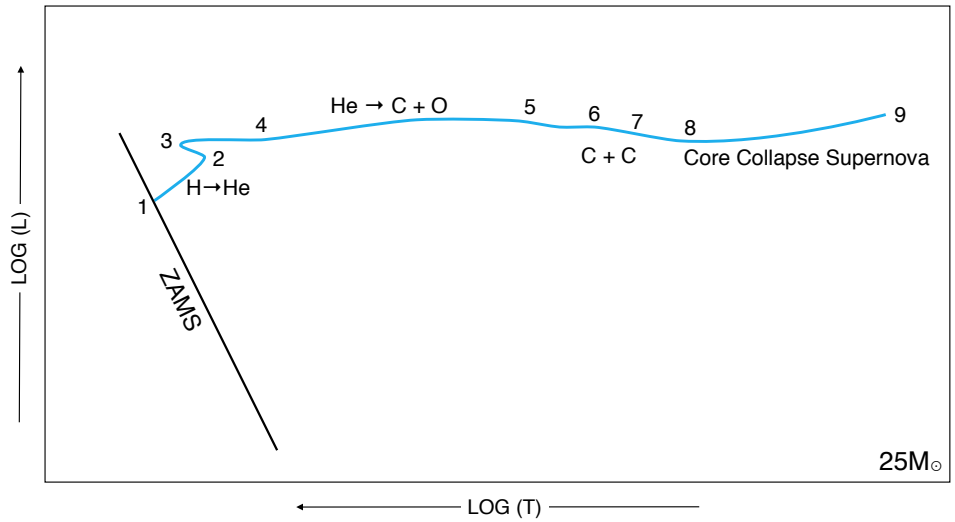

Figure 1.15: Schematic Hertzsprung-Russel diagram of the evolution of a 25 $M_\odot$ star from zero-age main sequence (ZAMS) to the supernova explosion. The evolutionary course for the 25 $M_\odot$ star is: 1-2, main sequence; 2-3, overall contraction; 4-5, helium burning; 6-7, carbon burning; 8-9, core collapse supernova. Adapted from Iben 1985 and Prialnik 2009.

lowed by core-carbon burning with co-occuring shell-helium and shell-hydrogen burning. This continues until the degenerated iron core, surrounded by shell-silicon, -oxygen, -carbon, -helium and -hydrogen burning (figure 1.16), grows large enough in mass to surpass the electron degeneration and collapses in a violent scenario, known as core collapse supernova (page 11). During the core-helium and later the shell-carbon burning, free neutrons are released via the ^{22}Ne(α,n) reaction as well as the ^{12}C(^{12}C,n)^{23}Mg reaction during the shell-carbon burning to accommodate the weak component of the *s* process [Arcoragi et al. 1991, Pignatari et al. 2006]. The shell of the star, which gets ejected into the interstellar medium during the supernova explosion contains the freshly synthesized *s*-process material [Käppeler 2012]. On the HRD the luminosity does not change much over the stellar lifetime, since it is close to the Eddington critical limit during all burning stages (figure 1.15). The Eddington critical limit is the maximum luminosity that a star can have while remaining in hydrostatic equilibrium. Exceeding this limit results in mass loss, driven by radiation pressure [Carroll and Ostlie 2007].

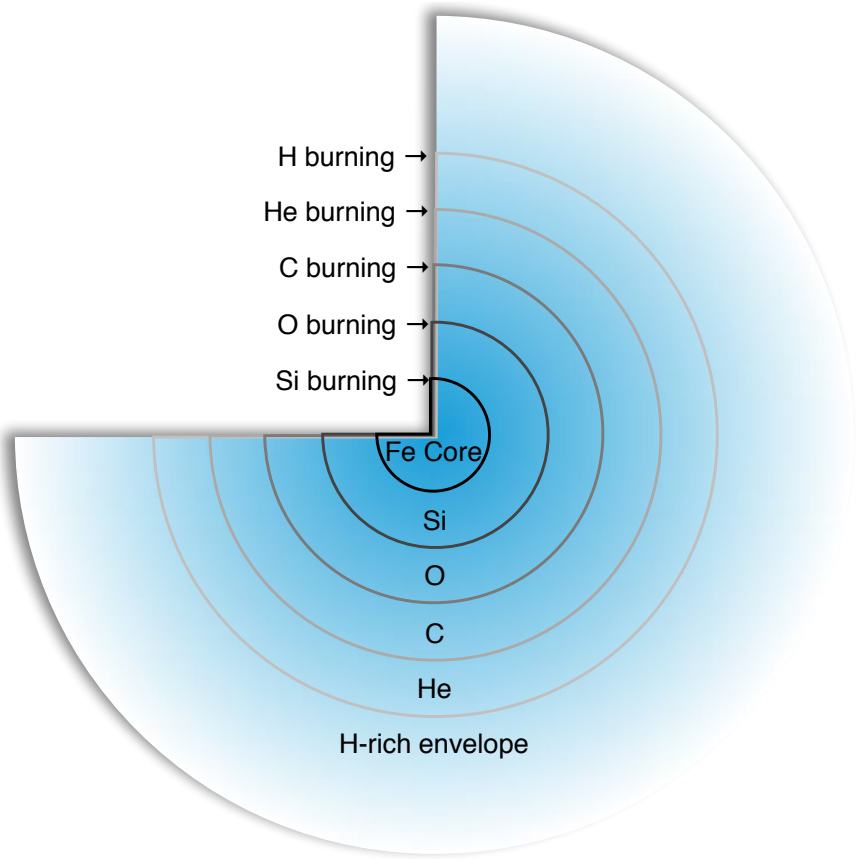

Figure 1.16: Schematic onion shell burning structure of a 25 $M_\odot$ star, before the core collapse supernova. The radii are not to scale. For details, see text.

2 Simulation & analysis tools

The simulation tools of the NuGrid collaboration [http://www.nugridstars.org/], which were used to calculate the stellar evolution and nucleosynthesis for this work are described in this chapter. Afterwards the extraction of the stellar parameters for the main *s*-process site is presented. The astrophysical sites for the weak *s* process and *i* process are described of, which pre-existing trajectories were used for the sensitivity studies.

2.1 Simulation codes

The stellar models, which were used for this thesis were taken from the NuGrid set 1 [Pignatari et al. 2013]. These 3 $M_\odot$ and 25 $M_\odot$ models at solar metallicity were simulated with the MESA framework and post processed with MPPNP. PPN was used to post process single zone trajectories.

2.1.1 Stellar evolution calculation

One dimensional stellar evolution calculations can be performed with the MESA (Modules for Experiments in Stellar Astrophysics) star module. MESA star solves fully coupled structure and composition equations simultaneously. In order to increase the speed of simulations, only a small energy providing network of nuclear rates (describing the fusion processes) is considered. Larger networks for *s* or *r*-process simulations can be post processed with the MPPNP tool, since their impact on the overall energy balance can be neglected. The here used MESA star models were supplied from the NuGrid collaboration. A detailed description of the MESA tools is provided by Paxton et al. 2011 and Paxton et al. 2013.

2.1.2 Post processing

The goal of post processing is to reconstruct the function describing the abundances of all isotopes over time. The results from the stellar simulations are used as input for the complete nuclear network calculations. This simplifies computation greatly, as the energy generation of the network was already considered. Temperature, density and mixing coefficients (describing convection) are input parameters to the network calculations. Thus, the functional dependence of the abundances is calculated with a set of initial abundances and a full set of temperature and density dependent rates. In general the change in abundance N of an isotope i can be described as

$$\frac{dN_i}{dt} = \sum \Phi_{i,production} - \sum \Phi_{i,destruction} \tag{2.1}$$

with $\sum \Phi_{i,production}$ representing all rates producing isotope i and $\sum \Phi_{i,destruction}$ summing all rates destroying isotope i. At s-process conditions, only a few channels for production and destruction have to be considered, and the simplified equations (1.6) or (1.7) can be used.

Post Processing Network – PPN

The Post Processing Network (PPN) from the NuGrid collaboration is a single zone simulation tool, evolving nuclear networks over time with thermodynamical input. Any set of initial abundances can be post processed with a trajectory, which is a set of temperatures and densities over time, or in static conditions. The trajectories for PPN are mostly extracted from a stellar model. Single zone post processing of a one dimensional stellar model means that the nucleosynthesis at only one radial coordinate is calculated. Thus, no convection between different zones along the stellar radius is considered. For some scenarios a convective environment can be represented with a "mean" single zone simulation, where the zone is chosen or the parameters are tweaked accordingly. This was done for the weak s-process simulations (chapter 3.2.1 and 3.2.2).

The equation (2.1) can be written for all isotopes in the following matrix form:

$$\left(\frac{d\vec{X}}{dt}\right)_{burn} = \hat{F} \cdot \vec{X} \tag{2.2}$$

with $\vec{X}$ the vector containing all abundances and $\hat{F}$ the rate matrix with all functional dependences of the reaction rates on the state variables. The matrix $\hat{F}$ is almost diagonal for s-process conditions. PPN consists of a physics package, with the network data taken from a broad range

of single rates and widely used reaction compilations. The charged particle-induced reactions on stable isotopes in the mass range A = 1-28, are taken from the NACRE compilation [Angulo et al. 1999]. Rates from the most recent compilation by Iliadis et al. 2001 of proton capture rates in the mass range 20-40 are also included. Neutron capture reaction rates are used from the KADoNiS project [Dillmann et al. 2006], which combines the rates from earlier compilations of e.g. Bao et al. 2000. Beta-decay rates for unstable isotopes are taken from Oda et al. 1994 and Fuller et al. 1985. Further rates are taken from the Basel REACLIB compilation [Thielemann et al. 1987]. The solver package of PPN is based on a Newton-Raphson solver [Herwig et al. 2008]. The number of iterations for the solver can be chosen before a sub-time stepping is applied. By calculating the change in abundance at every time step starting at given initial abundances, the function describing the abundances over time can be reconstructed numerically.

Multi-zone Post Processing Network Parallel – MPPNP

The multi-zone driver of PPN is MPPNP. A one-dimensional multi-zone nuclear network is computed over time by calculating each zone for one time step individually followed by a mixing step afterwards. A one dimensional stellar model with convection can be computed this way. After all zones along the stellar radius are evolved by one time step similar to PPN (equation (2.2)), a second order partial differential equation is set up for each isotope and a mixing is applied to the abundances in the different zones in order to obtain the initial abundances for the next time step. The diffusion equation can be written as

$$\left(\frac{dX_i}{dt}\right)_{mix} = \frac{\delta}{\delta m}\left[(4\pi r^2\rho)^2 D\frac{\delta X_i}{\delta m}\right] \tag{2.3}$$

with X_i the abundance of isotope i, ρ the density, r the radius, m the mass coordinate and D the diffusion coefficient. A detailed description of mixing in convectively unstable regions can be found in Langer et al. 1985, Freytag et al. 1996 and Herwig et al. 1997 and a detailed code description of MPPNP in Herwig 2001.

2.2 Stellar simulations

In this section the stellar models, which were provided from the NuGrid collaboration are introduced and the location and extraction of the ^{13}C-pocket and thermal pulse for the main *s*-process site are described. For the weak *s* process and *i* process existing trajectories from the NuGrid collaboration were utilized for the sensitivity studies.

2.2.1 3 Solar-mass stellar model

The MESA 3 $M_\odot$ stellar model used in this work was provided by the NuGrid collaboration from paper 1 [Pignatari et al. 2013]. For the post processing a trajectory of a ^{13}C-pocket had to be extracted and for the convective thermal pulse different efforts have been made to find a representative single zone trajectory, which was in the end discarded and post processed in MPPNP.

The **Kippenhahn diagram** (figure 2.6) is a very useful tool to analyze the stellar evolution. It plots the mass coordinate, which corresponds to the expansion invariant radius, of a star against the time. The mass distribution describes how much mass M is within a concentrical sphere at radius r in a star with the density ρ.

$$\frac{dM}{dr} = 4\pi r^2 \rho. \tag{2.4}$$

At radius $r = 0$ the mass is zero and at the stellar radius the mass equals the stellar mass at the zero age main sequence. The mass coordinate integrates the mass along the radius normalized to the solar mass $M/M_\odot$. Convection zones and thresholds for certain isotopic abundances are incorporated as contours in this depiction. Thus enabling the identification of e.g. different burning stages, the respective energy transport, and the mass loss of the star over time.

The TK-plot (figure 2.2) is an extension of the Kippenhahn diagram with an additional dimension. TK stands for the initials of the last names of Benedikt Thomas and Alexander Koloczek [Thomas 2013]. All parameters of the Kippenhahn diagram are plotted on top of a 3 dimensional contour plot where the amplitude of the parameter in concern is represented by the color. The colormap can be taken either from the stellar model or the post processing. For example, the abundance of a certain isotope is plotted this way or the temperature of the star. This extra dimension, which shows the full spectrum of the parameter in concern enables a more detailed examination compared to the contours in the basic Kippenhahn diagram.

TP-AGB phase

The TP-AGB phase is responsible for the main component of the *s* process. Two alternating production sites exist in this phase, the TP and the ^{13}C-pocket [Busso et al. 1999]. In the ^{13}C-pocket, the *s* process occurs almost in equilibrium, which means that the abundance of one isotope is increased up to the point where the production and destruction rates of this isotope are equal. Due to the convective nature of the TP, the material receives an exponential neutron irradiation, which is too short for any equilibrium state to adjust.

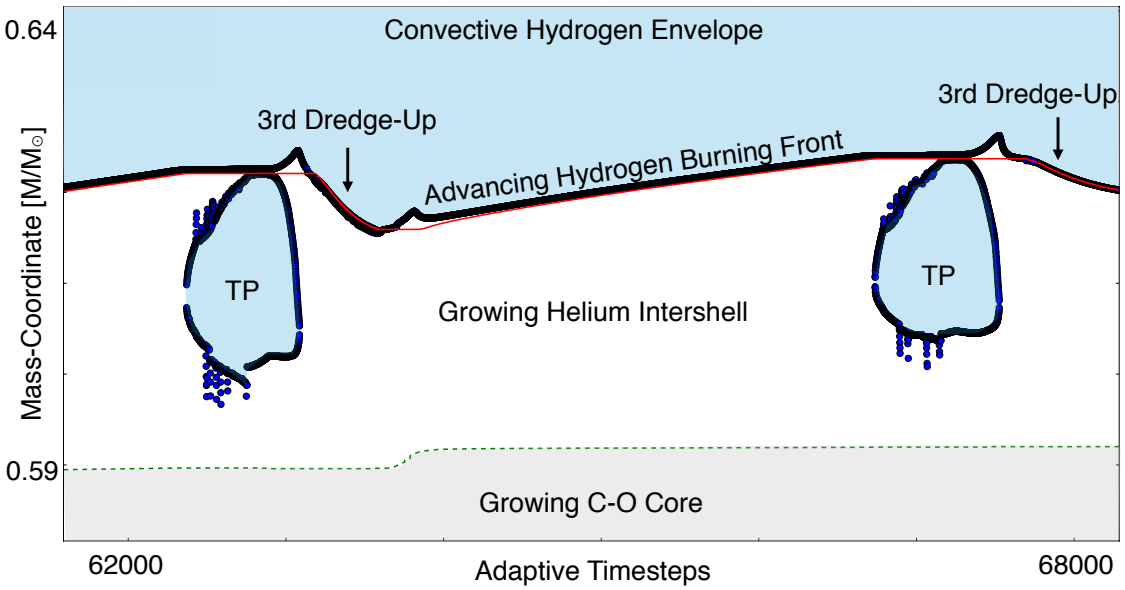

Figure 2.1: Kippenhahn diagram of the helium intershell of a 3 $M_\odot$ stellar model during the TP-AGB phase. The stellar mass relative to the solar mass is plotted as expansion independent radial coordinate. The time steps are not of equal size and allow a detailed inspection during short burning periods. The Kippenhahn diagram depicts a zoom into the helium intershell during the TP-AGB phase. Two subsequent TPs with a timespan of around 100 years per TP are illustrated, while the interpulse phase lasts around 10^5 years. Convection zones are filled in light blue, the convective boundaries are dark blue, the helium intershell is white and the degenerated carbon-oxygen core is light grey. The red line signifies the hydrogen boundary and the green dotted line the helium boundary, at, which either of the abundances fall below a certain value.

THERMAL PULSE

The TP represents the helium shell-burning ignition. Due to its explosive burning and high power output, the TP can be identified as reoccurring convection zones in the helium intershell with lifetimes of ~100 years (figure 2.1). During the convective TP, free neutrons are generated and the material in the convection zone receives an exponential neutron irradiation.

During the shell hydrogen burning, the helium intershell grows in mass and contracts. If the tem-

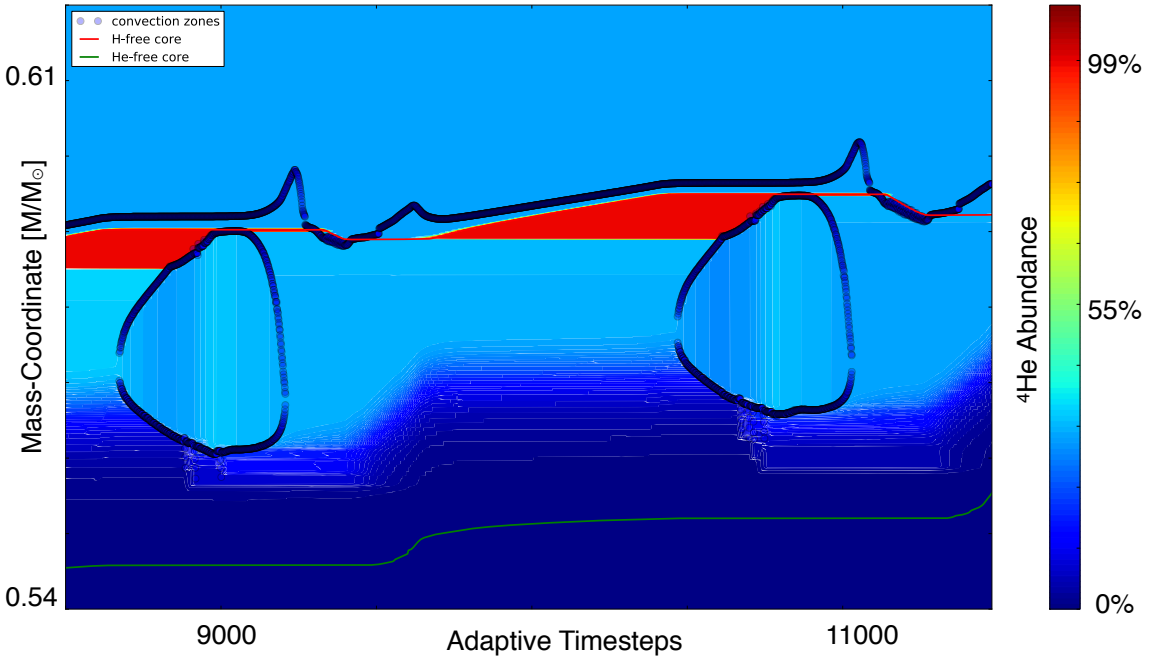

Figure 2.2: TK-plot of the ^{4}He abundance in the helium intershell of a 3 $M_\odot$ stellar model during the TP-AGB phase. The TK depicts the same scenarios as figure 2.1 only with two early occurring TPs at lower mass coordinates. The reoccurring ignition of the helium burning in the thermal pulses (deformed circles) and the following feeding the C-O core is depicted (blue slopes shortly after the TPs). The alternating hydrogen burning, which produces almost exclusively helium feeds the helium intershell for the next TP (increasing red area). The convective boundaries are the blue dotted lines, the red line signifies the hydrogen boundary and the green dotted line the helium boundary. The green line is below the visible boundary, which results from the TK-plot. This is due to a overestimated hard coded helium abundance value in the Kippenhahn diagram.

perature at the bottom of the helium intershell surpasses 10^8 K, helium burning ignites. Since the helium intershell is thin [Schwarzschild and Härm 1965], no stable helium burning occurs, but a thermonuclear runaway. This thin shell instability results from the lacking ability of the helium shell to lift the hydrogen envelope by a significant amount, which would decrease hydrostatic pressure and stabilize the burning. To the contrary, since the helium shell is thin compared to the overall size of the star, an expansion to double or more its size does not decrease the hydrostatic pressure of the envelope noticeably, but decrease the particle density significantly in the helium shell. This increases the temperature due to the law of ideal gases. This feedback

results in a thermonuclear runaway consuming most of the helium in a short period of about 100 years, producing luminosities around 10^8 $L_\odot$. The energy produced in the explosive burning is in turn absorbed by the hydrogen envelope leading to expansion and finally adjusting the hydrostatic pressure. The helium burning becomes stable, while at the same time the hydrogen burning extincts. As the remaining helium is not abundant enough to produce enough power to keep the star in the stable configuration, the envelope contracts again. During that contraction the convective hydrogen envelope enters into the helium intershell, thus, mixing freshly synthesized helium-burning material into the hydrogen envelope. This mixing, which is also referred to as the third dredge-up, comes to halt when the hydrogen burning re-ignites, due to the increasing temperature resulting from the contraction. The now present energy source from the hydrogen shell-burning stabilizes the star and the stable helium burning is quenched with ceasing burning material. A new cycle of the hydrogen shell burning followed by a TP starts [Straniero et al. 2006].

During the TP, the reaction ^{22}Ne(α,n) generates free neutrons for the *s* process, with neutron densities of around 10^{10-12} cm^{-3}. At the peak of the thermal pulse, when temperatures reach their maximum, the reaction chain ^{14}N(α,γ)^{18}F(β^+)^{18}O(α,γ)^{22}Ne creates fresh ^{22}Ne, which drives the *s* process in the ongoing as well as in the next TP until the above reaction chain is initiated again (figure 2.3).

^{13}C-POCKET

The ^{13}C-pocket represents the reoccurring formation of a ^{13}C-rich layer during the third dredge up event between two thermal pulses. With the stable shell-hydrogen burning on top of this layer, this ^{13}C-pocket produces free neutrons in a radiative environment. This inter-pulse period last two to three orders of magnitude longer ($\sim$ 10^4-10^5 years) than the TP, promoting the *s*-process nucleosynthesis in the mass region between 90 and 209.

During the third dredge-up event, protons from the hydrogen-rich envelope get ingested into the helium intershell. These protons are captured by the abundant ^{12}C, the product of the helium burning, and ^{13}C is formed via the reaction chain ^{12}C(p,γ)^{13}N(β^+)^{13}C. A ^{13}C-rich layer is generated, which is called the ^{13}C-pocket (figure 2.4). At larger mass coordinates of the helium intershell, where the ingestion of hydrogen is even stronger, the generated ^{13}C captures another proton producing ^{14}N. This layer is the ^{14}N-pocket [Gallino et al. 1988, Herwig 2005].

During the hydrogen shell burning the reaction ^{13}C(α,n) creates free neutrons for the *s* process. The neutron densities in this ^{13}C-pocket are around 10^{6-7} cm^{-3}. Since the ^{14}N(n,p) reaction acts as neutron poison for the *s* process the exact location where the *s* process efficiently occurs is where the difference of the ^{13}C abundance and the ^{14}N abundance has its maximum.

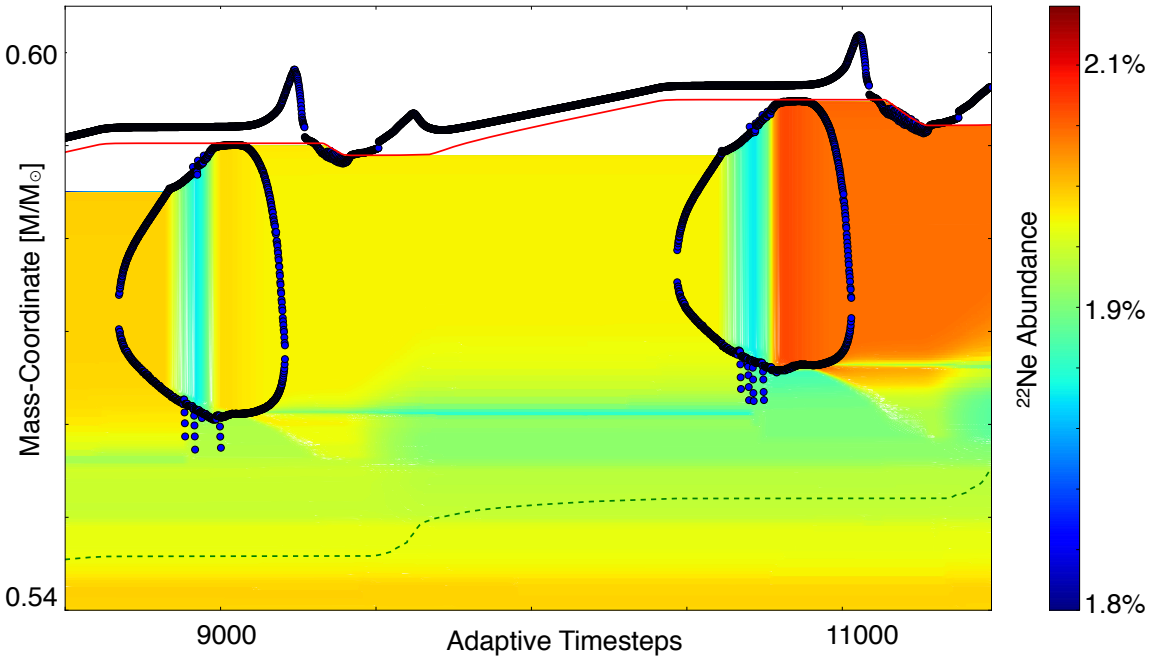

Figure 2.3: TK-plot of the ^{22}Ne abundance in the helium intershell of a 3 $M_\odot$ stellar model during the TP-AGB phase. The production and depletion of ^{22}Ne during the TP can be seen where the convective zone of the TP has its maximum size along the radius, the ^{22}Ne abundance first increases and then decreases slightly. The strong decrease of the ^{22}Ne abundance during the increasing convection zone is the result dilution. The colormap represents the ^{22}Ne abundance, which peaks at $\sim$ 2.1% during the second TP in the plot. Abundances below 1.8% are not shown.

^{13}C-POCKET AND TP FINDER

For the analysis of the 3 $M_\odot$ stellar model, a tool was developed to identify ^{13}C-pockets and the main site of *s*-process production during TP (figure 2.5). In order to locate the start coordinate of a ^{13}C-pocket, the mass and time coordinate at, which the difference of the ^{13}C and the ^{14}N abundance has a local maximum (in this specific case surpassed a threshold of 0.01 in the number abundance) serves as a good indicator for the beginning of a ^{13}C-pocket. The end of the ^{13}C-pocket is identified by the sudden decrease of the constantly increasing neutron magic ^{138}Ba isotope. This happens when the TP convection zone dilutes the ^{13}C-pocket material. In figure 2.4 could be seen, that the ^{13}C-pocket reaches up to the convection zone of the TP. The main production site of the TP is identified by searching the maximum ^{138}Ba abundance (which is as

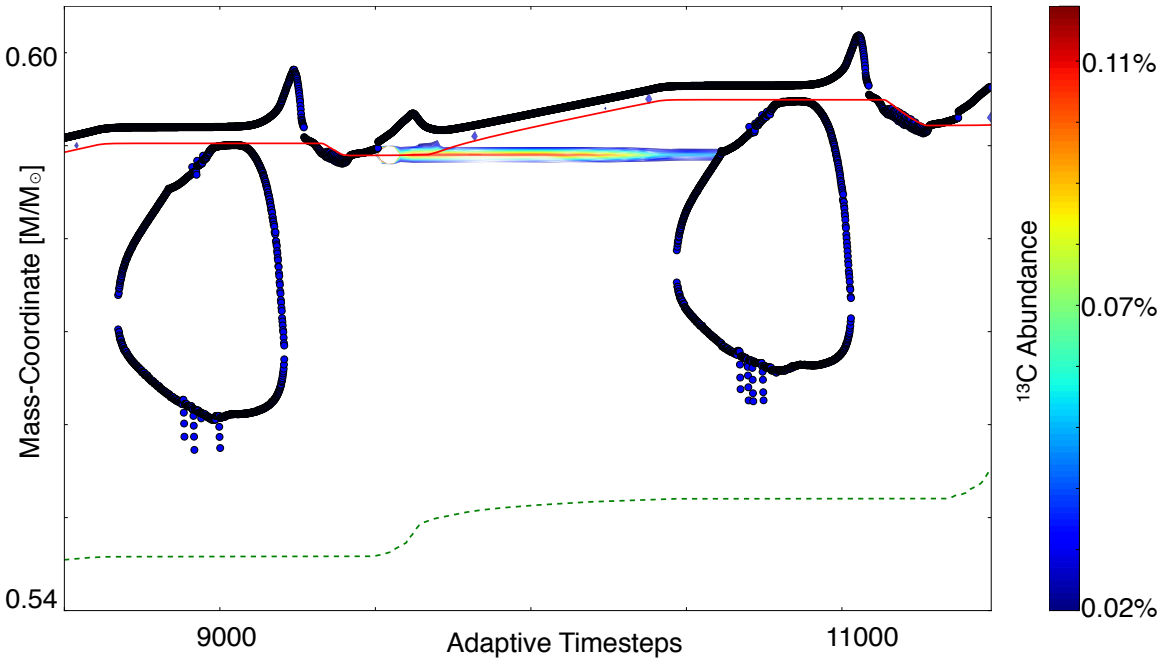

Figure 2.4: TK-plot of the ^{13}C abundance in the helium intershell of a 3 $M_\odot$ stellar model during the TP-AGB phase. The ^{13}C-pocket after the third dredge up event between the two TPs is observed at the lowest point of the hydrogen boundary. The colormap represents the ^{13}C abundance, which is thresholded above $\sim 0.11\%$ (this value is surpassed at the point of the formation) and below 0.02%.

well produced in the TP) at the time coordinate of the start of the ^{13}C-pocket. Since the intershell is only convective during the TP and not afterwards, the beginning of the ^{13}C-pocket is a safe indicator for the extinct TP. At this time the *s* process in the ^{13}C-pocket did not start yet and a clear separation between *s*-process production in the ^{13}C-pocket and the TP is achieved. A start coordinate of the TPs is not necessary for sensitivity studies, since only the end points of the production sites are compared between different post processed models.

2.2.2 25 Solar-mass stellar model

The NuGrid collaboration provided a MESA 25 $M_\odot$ stellar model (figure 2.6) and two different single zone trajectory for the weak *s*-process component.

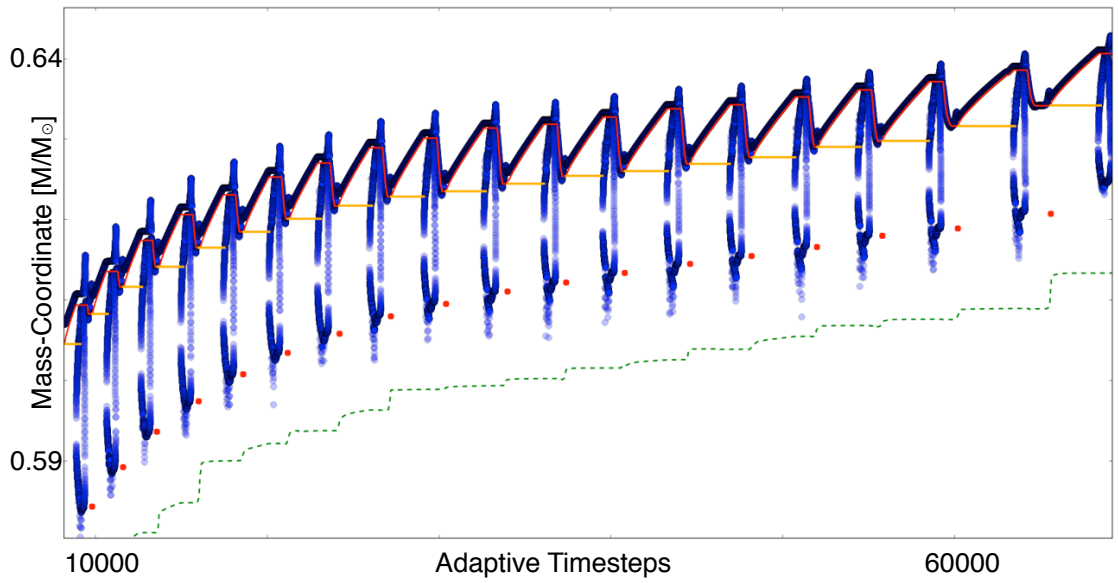

Figure 2.5: ^{13}C-pockets and TP peak abundances located by the finder routine. The ^{13}C-pockets are marked as orange lines and the red dots indicate the main site of *s*-process production after the TPs.

A weak *s*-process single zone trajectory extracted from Frischknecht 2007 and Hirschi et al. 2008 was utilized for the sensitivity studies in this work. The trajectory represents the weak *s* process in different burning stages in massive stars, namely the core-helium burning with the ^{22}Ne(α,n)^{25}Mg neutron source and the shell-carbon burning with the ^{12}C(^{12}C,n)^{23}Mg neutron source [Arnett and Truran 1969, Reifarth et al. 2014]. A second weak *s*-process single zone trajectory from Pignatari et al. 2013, which is extracted from the convective shell carbon burning, was used as well in order to disentangle the impact of the two burning zones from the weak *s*-process trajectory.

2.2.3 Low metallicity stars

With advancing age of the universe, the inter stellar medium (ISM) receives enrichment with more and more metals from stellar nucleosynthesis. In astronomy, all elements and isotopes

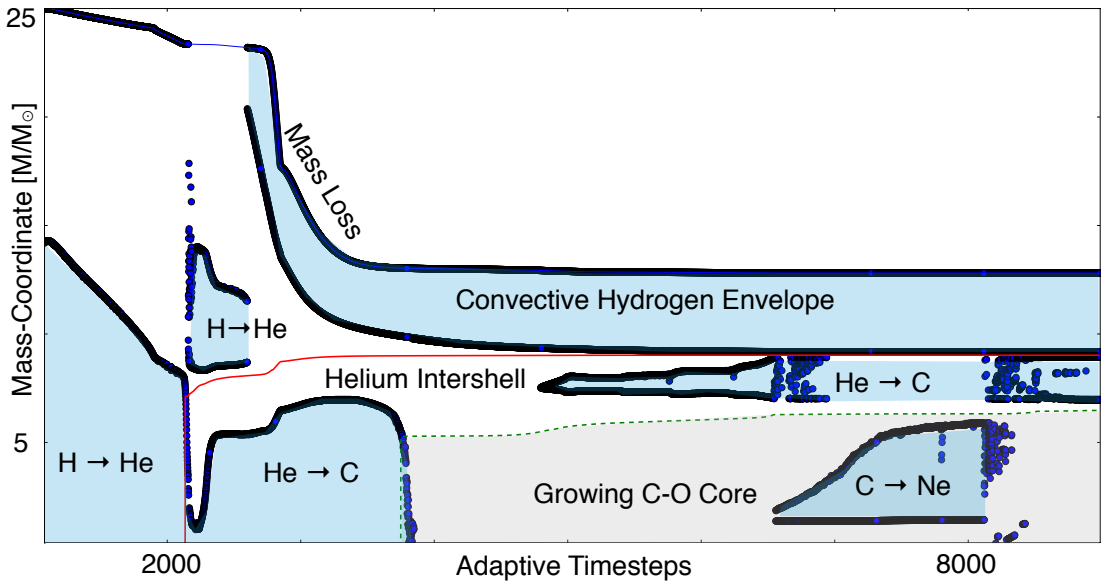

Figure 2.6: Kippenhahn diagram of the first three central burning phases of a 25 $M_\odot$ stellar model. The Kippenhahn diagram depicts the core-hydrogen burning, the core-helium burning with shell-hydrogen burning, and core-carbon burning with shell-helium and shell-hydrogen burning. Convection zones are filled in light blue, the convective boundaries are dark blue, the helium intershell is white and the degenerated carbon-oxygen core is light grey. The red line signifies the underlying hydrogen free core and the green dotted line the helium free core. As the MESA model only saves four convective boundaries, three convection zones on top of each are not depicted properly with convective boundaries in the Kippenhahn diagram.

heavier than helium are considered as metals. Iron is mostly compared to hydrogen in order to determine the metal enrichment of a star, which gives the epoch of the universe in which the star was formed. The first stars should have had almost no metal content at all and from there on with each generation increasing metal content up to solar metal content, which is around two percent. Therefore, the metal content is one chronometer of the universe. The metal content is compared to the solar metal content and defined as metallicity:

$$[\mathrm{Fe/H}] = \log_{10}(\mathrm{Fe/H}) - \log_{10}(\mathrm{Fe/H})_\odot \tag{2.5}$$

which gives for solar metallicities [Fe/H] = 0 and negative values for stars with metallicities below the sun [Carroll and Ostlie 2007].

The main component of the *s* process is produced at a metallicity starting at [Fe/H] ~ -0.66 [Cui et al. 2007], which corresponds to the time interval $t > 2.6$ Gyr. Going to even lower metallicities or further back in time, gives insight to an undiluted view on other processes. At lower metallicities, from [Fe/H] ~ -1.16 to [Fe/H] ~ -0.66 [Cui et al. 2007], the site for the strong component of the *s* process was identified. At even lower metallicities, before the *s* process sets in, the LEPP is believed to occur somewhere in stars. Simulations of very late thermal pulses of metal poor stars revived the *i* process discussion (chapter 2.2.4), which could contribute to the LEPP.

STRONG COMPONENT

The strong component of the *s* process is hosted in the same stellar sites as the main component (chapter 2.2.1) only at lower metallicities, from [Fe/H] ~ -1.16 to [Fe/H] ~ -0.66. The lower metallicity yields a higher neutron per seed ratio, thus propagating the *s* process further to the lead region on the chart of nuclides [Gallino et al. 1998]. The neutron per seed ratio is a measure of how many neutrons are captured per ^{56}Fe seed isotope. The higher the value the more heavy isotopes are produced. The neutron per seed ratio can either be increased by a larger integrated neutron flux or a reduced amount of seed isotopes. As the overall contribution from the strong component can be neglected except for the lead peak [Travaglio et al. 2001], the impacting rates (chapter 2.3.1) of the main component, should apply for this component as well. The higher neutron per seed value depletes lighter isotopes compared to the ones found in the lead peak. Thus, only the rates affecting the overall neutron budget of the main component (tables 3.2, 3.3, 3.4 and 3.5) should attribute to the final outcome of the strong component. Therefore, no dedicated post processing sensitivity study has to be performed for the strong component.

2.2.4 THE *i* PROCESS

After the AGB phase of low and intermediate mass stars (chapter 1.3.1), the star is descending on the white dwarf cooling track on the HRD (figure 1.13). Some of these stars can undergo a final helium shell flash [Asplund 1999], or very late thermal pulse (VLTP), triggered by the compressional heating of the stellar interior, bringing the star back to supergiant dimensions. These stars are referred to as ”born-again” giants, before they descent a second time and this time definitely on the white dwarf cooling track [Asplund et al. 1999]. Observations of abundances in Sakurais object (V4334 Sagittarii) [Asplund et al. 1998], a born again post-AGB star, show highly non so-

lar abundances [Herwig et al. 2006]. Herwig et al. 2011 proposed a possible scenario, where an intermediate neutron capture process (i-process [Cowan and Rose 1977]) with neutron densities around 10^{15} cm^{-3} could be added to the s and *r* process (see also page 26).

The *i*-process mechanism

As three dimensional hydrodynamic simulation showed, there could be an overlap in the convective zone of the VLTP in low mass AGB stars with the hydrogen envelope [Herwig et al. 2011]. This overlap results in a hydrogen ingestion into the VLTP, where the protons are captured on ^{12}C forming ^{13}N. The convective timescale in this scenario is approximately the same as the beta decay timescale of ^{13}N. Freshly synthesized ^{13}C reaches the bottom of the convective VLTP. There the reaction ^{13}C(α,n) occurs at much higher temperatures than in the ^{13}C-pocket, producing neutron densities around 10^{15} cm^{-3}. A single zone trajectory reproducing this scenario was obtained from the NuGrid collaboration [Bertolli et al. 2013], which generates the neutron source of the ^{13}C-pocket with the stellar parameters of a TP.

LEPP

The LEPP is of unknown origin [Pignatari et al. 2010] (see also page 25). The here studied *s* process (main and weak) and *i* process are examined with a particular focus on the impact of nuclear rates on the LEPP isotopes, Sr, Y and Zr (chapter 3.4).

2.3 Sensitivity

Sensitivity studies are needed in order to identify the impact of single parameters on the outcome of complex systems. Sensitivity studies focus on a single change at a time. This way correlations between the parameter in concern and the final outcome can be determined.

2.3.1 Definition

The sensitivity s gives the amplitude and algebraic sign of the coupling between the change of a parameter p and the change in the final outcome O.

$$s = \frac{\Delta O/O}{\Delta p/p} \tag{2.6}$$

For this particular work, the impact of nuclear rates on the final abundance during different stellar scenarios was examined, particularizing the equation to:

$$s_{ij} = \frac{\Delta N_j/N_j}{\Delta r_i/r_i} \ . \tag{2.7}$$

The sensitivity s_{ij} is the ratio of the relative change in abundance $\Delta N_j/N_j$ of isotope j and the relative change of the rate $\Delta r_i/r_i$. In order to extract the sensitivity of a certain rate, simulations with a change in this rate are compared with the default simulation, where the network consists of the default rates selected by PPN or MPPNP.

Global sensitivities

Rates with global sensitivities are in the following considered to be rates, which impact the overall development of the nucleosynthesis during the specific scenario. For neutron capture nucleosynthesis, these are mostly rates, which impact the overall neutron density or neutron per seed ratio during the scenario. For the *s* process, e.g., the influence of a rate on all *s*-only isotopes from table 1.1 was checked. If a trend or impact is seen over a large range of mass numbers, then the sensitivity of the range is considered to be global. The criteria of how many isotopes have to be affected in order to consider the rate as global, has to be adapted on the scenario as e.g. the weak component affects less isotopes than the main component, or convection dilutes the impact of rates compared to radiative scenarios. A further discrimination is applied in neutron donators, neutron poisons, competing captures and bottlenecks. Neutron donators are rates, which increase

the overall neutron density during the scenario. Neutron poisons lower the neutron per seed ratio. Competing captures are usually rates, which are neutron captures on seed isotopes of the *s*-process path, increasing the amount of participating seed isotopes and lowering the neutron per seed ratio. Bottleneck isotopes are mostly neutron magic isotopes, which rise or lower the entire σN curve (figure 1.8) of the succeeding isotopes.

Local sensitivities

Rates of local sensitivity are considered to be rates only affecting isotopes, which are in the direct neighborhood on the chart of nuclides. If the (n, γ) rate on isotope X only affects isotope X and the neighboring isotope X+1 then this rate has a local impact. Branching points are one example for important local sensitive rates. They can be used to probe different parameters during the *s* process (page 21), but do not affect the overall *s* process.

Systematic studies

For this work, systematic sensitivity studies of nuclear rates for the *s* and *i* process were performed. For the *s* process, a post processing reaction network of about 14 000 rates was examined on the impact of single rates. The *i*-process network consisted of about 56 000 rates. For each scenario, all branching points, all global sensitive rates and the three largest local sensitive rates for each isotope were determined.

2.3.2 Sensitivity plots

For the analysis of the simulation data, sensitivity plots are used to illustrate global sensitivities. All rates with a maximum sensitivity below 0.1 were not considered. For the **main component**, all sensitivities of one rate for all *s*-only isotopes as well as ^{64}Zn and ^{70}Ge are plotted. The *s*-only isotopes of the weak component are plotted in front of a blue color gradient. Neutron magic isotopes are highlighted with dotted vertical lines in grey color, as seen in figure 2.7. On a few plots, the reaction and s-process path is plotted on a section of the chart of nuclides, on top of the sensitivity plot, which helps to visualize the described behavior. This addition serves as a conceptional aid. The neutron magic isotopes ^{87}Rb, ^{89}Y and ^{90}Zr are referred to as first *s*-process peak or first neutron magic peak. ^{138}Ba and ^{142}Nd are referred to as second *s*-process or neutron magic peak. The last neutron magic peak at ^{208}Pb is not on the *s*-only sensitivity plots but is referred to as lead, third or last *s*-process peak. As can be seen in figure 2.7, an increased neutron

capture rate on ^{89}Y promotes the the mass flux pass the first neutron magic peak, which reduces the depletion of lighter seed isotopes and promotes the production of heavy isotopes.

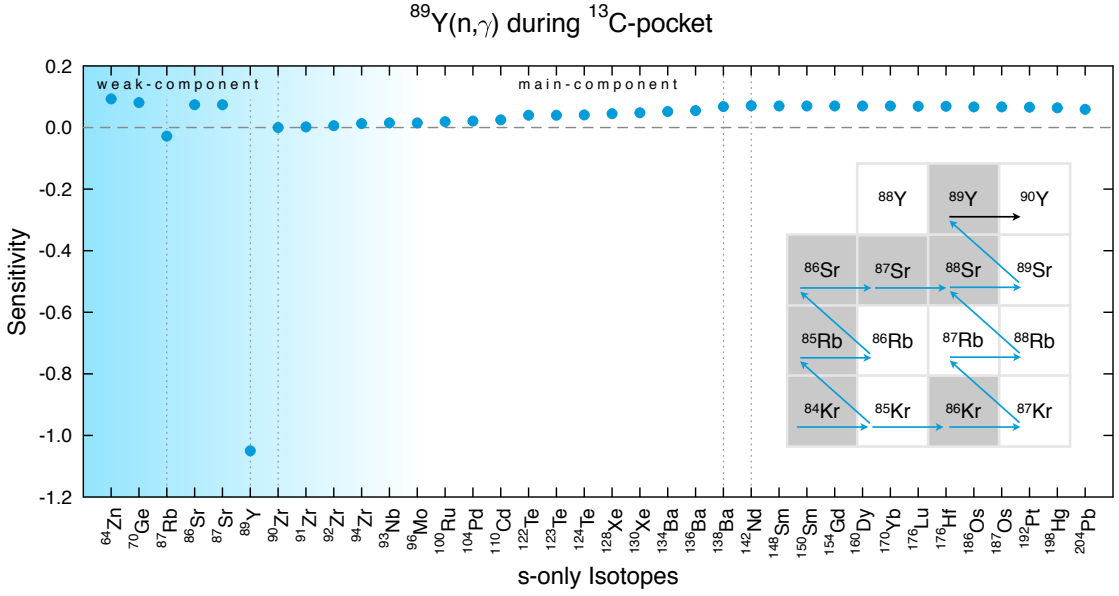

Figure 2.7: Bottleneck reaction ^{89}Y(n,γ) during the ^{13}C-pocket (table 3.5). The bottleneck rates from the first *s*-process peak compete directly with the iron peak seed isotopes. Thus, a general increase of all other isotopes is observed. An increased neutron capture rate on the neutron magic isotope ^{89}Y decreases the ^{89}Y abundance. ^{87}Rb is sensitive to the branching point ^{85}Kr. The neutron capture on ^{89}Y competes with the neutron capture on ^{85}Kr, which is the channel to produce ^{87}Rb. The blue color gradient marks the weak *s*-process region. The vertical grey dotted lines are plotted on neutron magic isotopes. The section of the chart of nuclides, provides the s-process path (blue arrows) and indicates the ^{89}Y(n,γ) reaction (black arrow).

For the **weak component**, the concept of the plot is the same except that no heavier isotopes than ^{142}Nd are considered. No net production occurs on heavier isotopes as discussed in chapter 3.2.1.

For the ***i* process**, which proceeds in between the *s* and *r*-process paths, the sensitivities of the *r*-only isotopes are plotted. Five additional isotopes are of interest in the *i* process: ^{28}Si, which is one of the *i*-process seed isotopes, ^{48}Ca, which is a double magic isotope, ^{64}Ni, which is the heaviest, stable, proton magic isotope of the iron peak, ^{132}Xe, which is the stable isobaric counterpart of the double magic nuclei ^{132}Sn and ^{208}Pb, which is also double magic. The three double magic nucleus (^{132}Xe substituting ^{132}Sn) are marked in the sensitivity plot with the vertical, grey dotted lines, as seen in figure 2.8. The *i*-process simulations generate a two plateau structure, which lies between the three double magic isotopes. A neutron poison like ^{16}O reduces the mass flux pass the double magic isotope ^{48}Ca, which lowers the following plateau. This reduces the

depletion of the second plateau (between ^{132}Sn and ^{208}Pb).

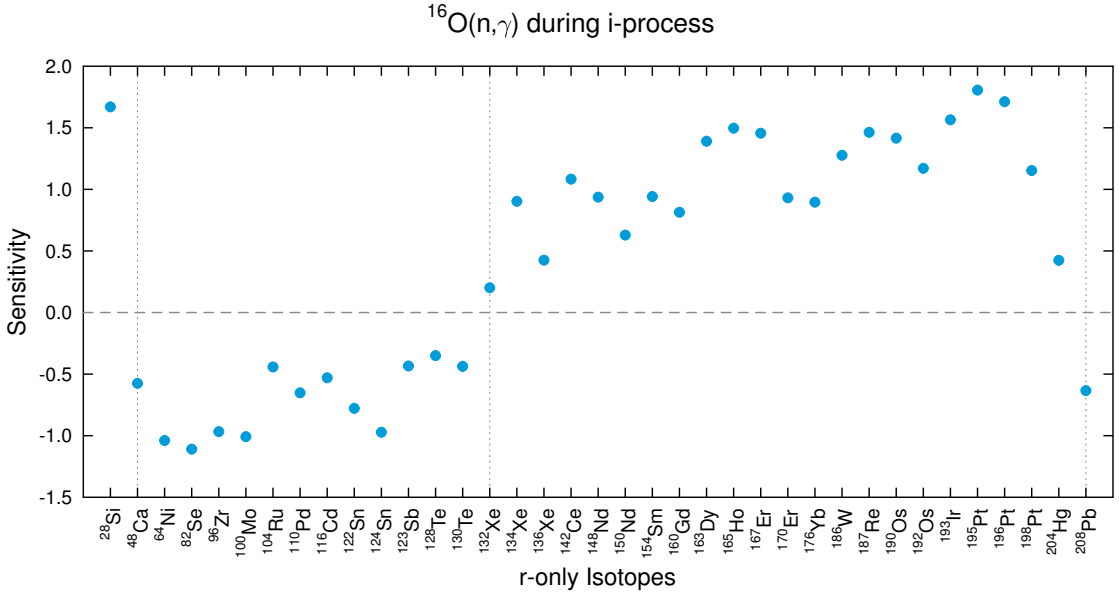

Figure 2.8: Neutron poison ^{16}O(n,γ) during the *i* process (table 3.25). The reduced neutron per seed value, results in negative sensitivities in the first *i*-process plateau between ^{48}Ca and ^{132}Sn, which depends on the waiting point ^{48}Ca. The second plateau between ^{132}Sn and ^{208}Pb has a positive sensitivity since neutron captures usually deplete this plateau in order to produce lead. ^{28}Si, which is representative for the *i*-process seed isotopes is less depleted with a lower neutron density.

Branching points, which affect isotopes from the global sensitivity plots are plotted in the same way only with both competing reactions. Plotted branching point reactions are not excluded from the local sensitivity tables (chapter 2.3.3).

2.3.3 Sensitivity tables

The local sensitivity tables show for each stable isotope in each scenario up to three rates with sensitivities larger than 0.1, which are not globally sensitive rates. For the main component of the *s* process, these tables show the sensitivities of the isotopes from ^{56}Fe up to ^{209}Bi. For the weak component the sensitivity tables go from ^{56}Fe up to ^{142}Nd. For the *i* process, all isotopes from ^{20}Ne up to ^{209}Bi were considered. If an isotope is only impacted by its own neutron capture rate and is not sensitive to any other local channels, than it is not listed in the tables.

3 Results

The following sections are thought as reference work for the sensitivity studies. The results of more than 250 000 simulations, which are extracted from over 400 TB of raw data are ordered in the following way. The *s* process is divided into the main and weak component. The main component is subdivided into the ^{13}C-pocket and the TP. The weak component is subdivided into the weak *s* process and the convective carbon shell burning. The *i* process consists of one scenario. For each scenario, i.e., ^{13}C-pocket, TP, weak *s* process, convective carbon shell burning and the *i* process, the trajectory is introduced and the impact on the overall abundance distribution is presented. Afterwards, all branching points for the scenario of concern are listed in a table and a single representative branching point plot is shown. The remaining plots of the other branching points are listed in the appendix. Subsequently, the globally sensitive rates for each scenario are listed. These are subdivided into neutron donators, neutron poisons, competing captures, bottlenecks and, in some cases, in recycled neutron poisons and light neutron poisons. For each of these categories all containing rates are listed in a table and a single representative sensitivity plot is shown. Additional sensitivity plots as well as the local sensitivity tables are listed in the appendix. Thus, every globally sensitive rate in each scenario is plotted in this work. The tables in chapter 2.2.4 are used to structure these plots.

The LEPP analysis is subdivided into the five aforementioned scenarios. A table with all globally impacting rates on the LEPP isotopes is listed and all locally sensitive rates, which can be found in the sensitivity tables, are listed in the text. If possible at all, a single representative sensitivity plot is shown for each scenario. Additional plots are listed in the appendix.

3.1 Main component

The main component is analyzed as two components because of the different nature of the ^{13}C-pocket and the TP.

3.1.1 ^{13}C-pocket

For this work, a single zone ^{13}C-pocket trajectory (figure 3.1) was extracted from the 3 $M_\odot$ stellar model and the consistency was validated with the other ^{13}C-pockets from the ^{13}C-pocket and TP finder (page 40). The ^{13}C-pocket trajectory was re-simulated in PPN about 56000 times. Every simulation changed one rate at a time by ±5% and ±20%. Since the sensitivity of each rate turned out to be constant for all four simulations, all further sensitivity studies were performed with a change of ±10%.

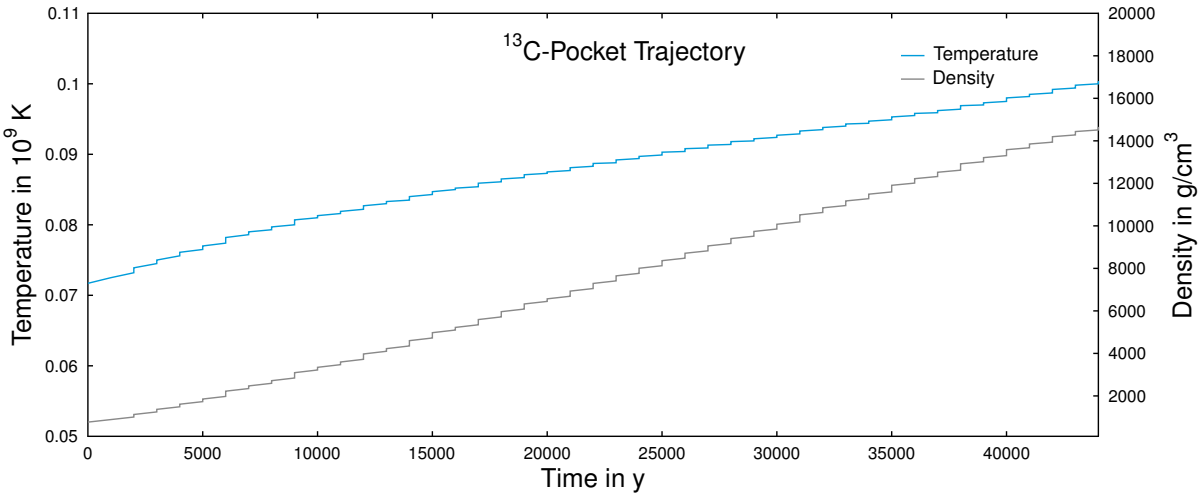

Figure 3.1: Trajectory of ^{13}C-pocket used in PPN. Temperature and density are plotted as function time. The initial abundances for this trajectory are listed in table A.2.

The ^{13}C-pocket has low neutron densities but is not convective and lasts for around $5 \cdot 10^4$ years. In these conditions sensitive rates can easily impact the whole abundance distribution with a global trend. The global trend of the ^{13}C-pocket is illustrated in figure 3.2.

A strong increase in *s*-isotopes during the neutron irradiation of the radiative ^{13}C-pocket is observed. The nucleosynthesis during the ^{13}C-pocket reproduces the main component characteristics very well. The behavior of the nucleosynthesis during the ^{13}C-pocket is a shift in the abundances from lower mass numbers (iron peak) to higher mass numbers (trans iron *s*-isotopes).

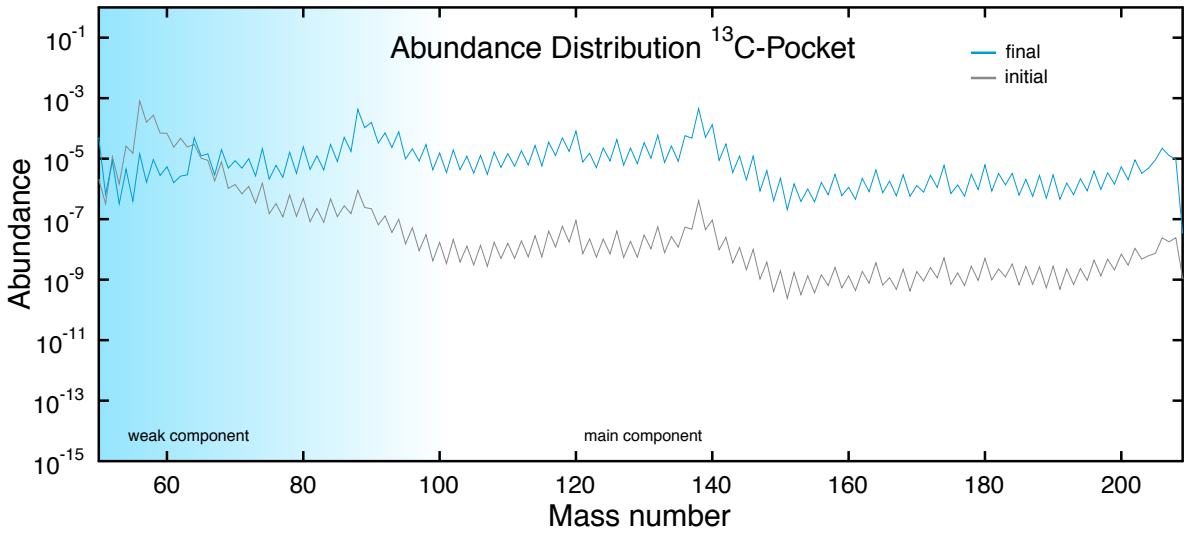

Figure 3.2: Abundance distribution before and after a single ^{13}C-pocket. The depletion of the iron peak, which is used as seed for the main component, is observed. An increase in the abundances of about one to two orders of magnitude above mass number 90 shows the impact of the *s*-process nucleosynthesis of the ^{13}C-pocket. The trajectory is from the last ^{13}C-pocket of the 3 $M_\odot$ stellar model with solar metallicities, thus, the *r*-process peaks are already depleted during previous *s*-process nucleosynthesis.

Branching points during the ^{13}C-pocket

During the ^{13}C-pocket, three isotopes in the global sensitivity plots are branching points. These branching points are labeled with their respective figure number in table 3.1. In the local sensitivity table, 24 additional branching points were detected. These branching points are labeled with the local sensitivity table. The complete list is shown in table 3.1. Using the example of ^{64}Cu, a globally impacting branching point is illustrated in figure 3.3.

Branching point	competing reactions	figure / table
^{64}Cu	^{64}Cu(β^-), ^{64}Cu(β^+)	figure 3.3
^{70}Ga	^{70}Ga(β^-), ^{70}Ga(β^+)	table A.1
^{76}As	^{76}As(β^-), ^{76}As(β^+)	table A.1
^{79}Se	^{79}Se(β^-), ^{79}Se(n,γ)	table A.1
^{81}Se	^{81}Se(β^-), ^{81}Se(n,γ)	table A.1
^{85}Kr	^{85}Kr(β^-), ^{85}Kr(n,γ)	figure A.1
^{93}Zr	^{93}Zr(β^-), ^{93}Zr(n,γ)	figure A.2
^{95}Zr	^{95}Zr(β^-), ^{95}Zr(n,γ)	table A.1
^{99}Tc	^{99}Tc(β^-), ^{99}Tc(n,γ)	table A.1
^{104}Rh	^{104}Rh(β^-), ^{104}Rh(β^+)	table A.1
^{107}Pd	^{107}Pd(β^-), ^{107}Pd(n,γ)	table A.1
^{110}Ag	^{110}Ag(β^-), ^{110}Ag(β^+)	table A.1
^{115}Cd	^{115}Cd(β^-), ^{115}Cd(n,γ)	table A.1
^{122}Sb	^{122}Sb(β^-), ^{122}Sb(β^+)	table A.1
^{128}I	^{128}I(β^-), ^{128}I(β^+)	table A.1
^{134}Cs	^{134}Cs(β^-), ^{134}Cs(β^+)	table A.1
^{136}Cs	^{136}Cs(β^-), ^{136}Cs(β^+)	table A.1
^{147}Nd	^{147}Nd(β^-), ^{147}Nd(n,γ)	table A.1
^{151}Sm	^{151}Sm(β^-), ^{151}Sm(n,γ)	table A.1
^{154}Eu	^{154}Eu(β^-), ^{154}Eu(β^+)	table A.1
^{157}Gd	^{157}Gd(β^-), ^{157}Gd(n,γ)	table A.1
^{159}Gd	^{159}Gd(β^-), ^{159}Gd(n,γ)	table A.1
^{170}Tm	^{170}Tm(β^-), ^{170}Tm(β^+)	table A.1
^{175}Yb	^{175}Yb(β^-), ^{175}Yb(n,γ)	table A.1
^{186}Re	^{186}Re(β^-), ^{186}Re(β^+)	table A.1
^{198}Au	^{198}Au(β^-), ^{198}Au(β^+)	table A.1
^{204}Tl	^{204}Tl(β^-), ^{204}Tl(β^+)	table A.1

Table 3.1: Branching point isotopes and reactions during ^{13}C-pocket.

Global sensitivities during the ^{13}C-pocket

In the following section, all global sensitivities during the ^{13}C-pocket are listed and classified between neutron donators (table 3.2), neutron poisons (table 3.3), competing captures (table 3.4) and bottlenecks (table 3.5).

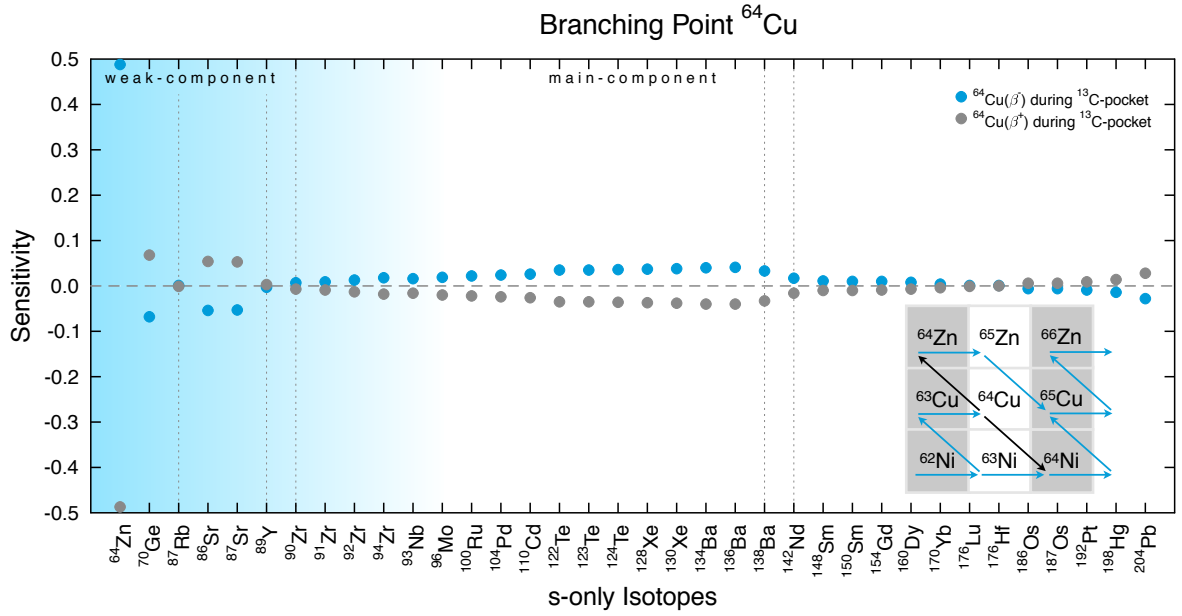

Figure 3.3: Branching point ^{64}Cu during the ^{13}C-pocket (table 3.1). The increased β^+-decay rate reduces the neutron per seed ratio, because ^{64}Zn has a larger neutron capture cross section than ^{64}Ni. Thus, ^{64}Ni acts as a "bottleneck" in the case of an increased β^+-decay rate. The section of the chart of nuclides, provides the s-process path (blue arrows) and indicates the branching reactions (black arrows).

Neutron donators

The overall impact of a neutron donator on the *s* process during the ^{13}C-pocket can be seen e.g. in figure 3.4. In the case of ^{12}C(p,γ), isotopes with lower mass numbers than about 120 are depleted as they capture more neutrons and build up heavier isotopes. The sensitivities of the *s*-isotopes with mass numbers below about 120 are negative and above about 120 positive. The location of the turning point from negative to positive sensitivities, is depending on the integrated neutron flux. An exception in the general trend is the neutron magic isotope ^{87}Rb, which is dependent on the branching point ^{85}Kr (figure 1.10). If more neutrons are released from a neutron donator, then the branching favors the path via ^{86}Kr and ^{87}Rb, resulting in a positive sensitivity of ^{87}Rb to neutron donators. An interesting isotope, which shows complicated behaviors during all *s*-process conditions is ^{93}Nb. ^{93}Nb is dependent on the temperature-dependent β-decay of ^{93}Zr, which has a half life time of about $1.6 \cdot 10^6$ years. Thus, in ^{13}C-pocket conditions it has a delayed sensitivity to changes of the ^{93}Zr abundance, while in hot *s*-process conditions it is directly branching sensitive to ^{93}Zr.

Rate	Figure	Features
^{12}C(p,γ)	figure 3.4	representative
^{13}C(α,n)	figure A.3	high ^{93}Nb sensitivity

Table 3.2: Globally sensitive neutron donator reactions during ^{13}C-pocket. The ^{12}C(p,γ) rate is representative for a neutron donator rate and the ^{13}C(α,n) rate is similar except to the ^{93}Nb sensitivity.

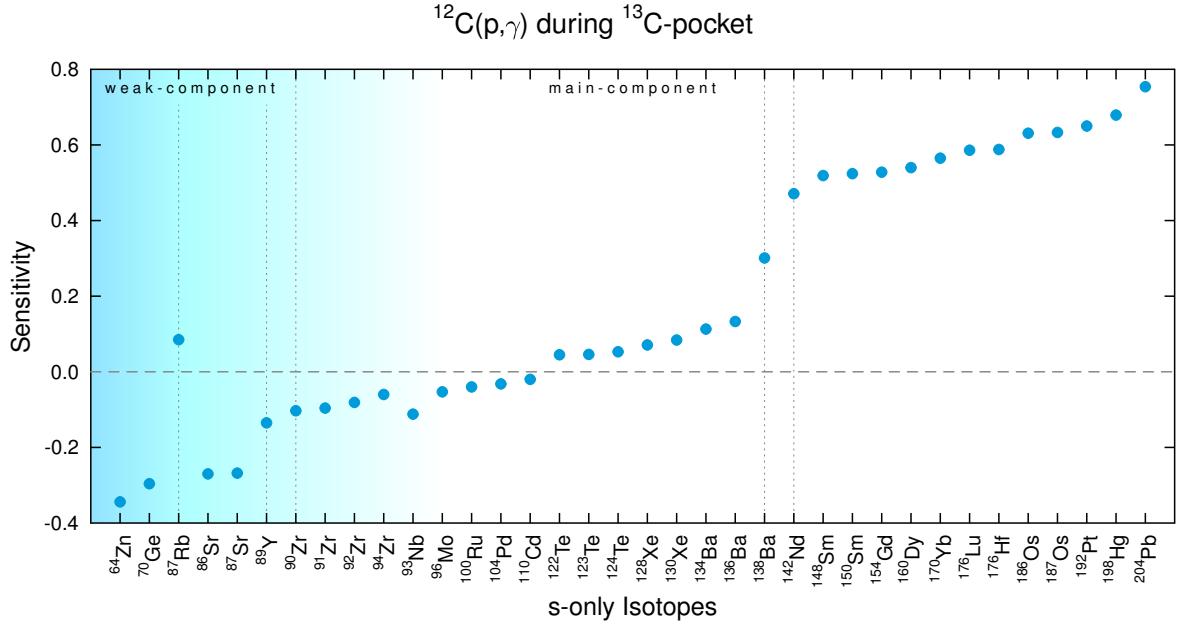

Figure 3.4: Neutron donator reaction ^{12}C(p,γ) during the ^{13}C-pocket (table 3.2). The produced ^{13}N from this reaction decays to ^{13}C, which creates free neutrons with the reaction ^{13}C(α,n).

Neutron poisons

The overall impact of neutron poisons during the ^{13}C-pocket is opposite to the trend of the neutron donators, as seen on the example of ^{14}N(n,p) in figure 3.5. Lighter *s*-isotopes show a positive sensitivity whereas heavier *s*-isotopes show a negative sensitivity. The lowered neutron irradiation results in a lower depletion of lighter *s*-isotopes and lower production of heavier *s*-isotopes. ^{87}Rb is less produced with increased neutron poison reactions, as the path around the branching point ^{85}Kr follows more the β-decay over ^{85}Rb (figure 1.10). Neutron poisons deplete the mass fractions of either neutrons directly or α-particles or ^{13}C to hinder the ^{13}C(α,n) reaction. The turning point from positive to negative sensitivities, is for all the neutron poisons around mass number 120.

Rate	Figure	Features
^{14}N(n,p)	figure 3.5	representative
^{13}C(p, γ)	figure A.4	representative
^{16}O(n, γ)	figure A.6	representative
^{22}Ne(n, γ)	figure A.7	representative
^{14}C(α, γ)	figure A.5	low sensitivites, ^{93}Nb
^{14}C(β^-)	figure A.8	low sensitivites, ^{93}Nb

Table 3.3: Globally sensitive neutron poison reactions during ^{13}C-pocket. The feature distinguishes between representative neutron poison rates and rates, which have low sensitivities but have a similar pattern to the representative ones. The rates labeled with ^{93}Nb show a peculiar ^{93}Nb sensitivity.

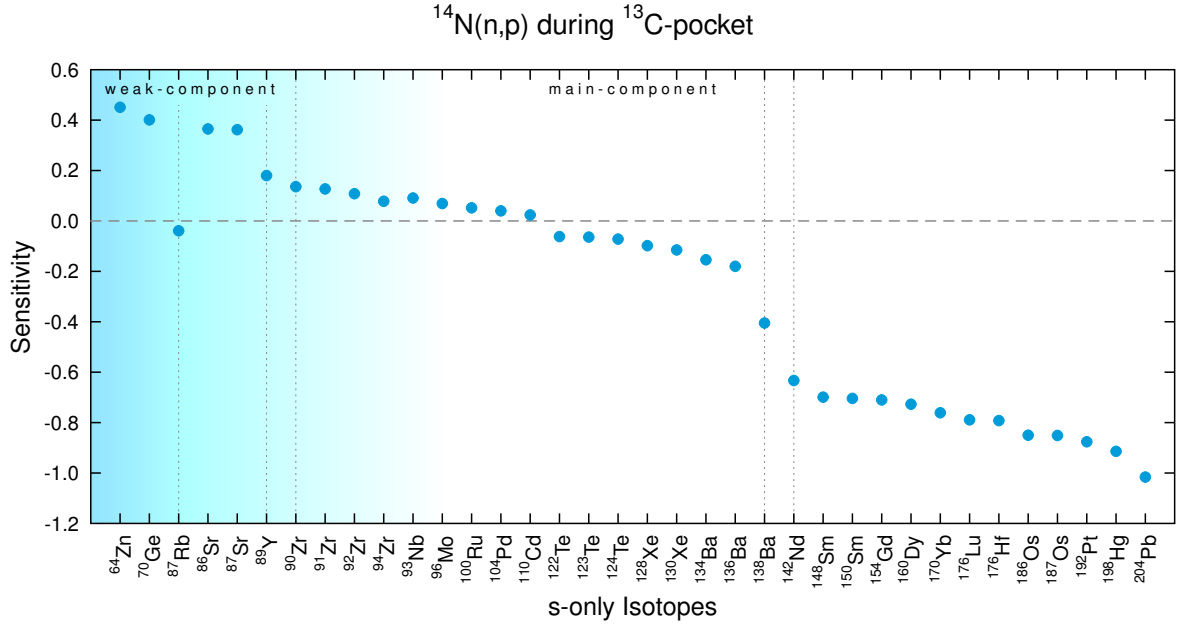

Figure 3.5: Neutron poison reaction ^{14}N(n,p) during the ^{13}C-pocket (table 3.3). The reaction ^{14}N(n,p) withdraws neutrons from the overall neutron household and produces protons, which then compete with the neutron source reaction ^{13}C(α,n) via the proton capture reaction ^{13}C(p, γ), producing even more of the neutron poison isotope ^{14}N (figure A.4).

Competing captures

Competing captures are usually reactions on *s*-process seed isotopes like ^{56}Fe (figure 3.6). They do not lower the neutron density, but decrease the neutron per seed ratio, as more seed isotopes participate in the *s* process. The general trend is similar to the trend of neutron poisons, only that more seed isotopes are depleted, and not spared through a lower neutron density. The general trend with an increased competing capture rate gives a negative sensitivity of the seed isotopes, a positive sensitivity of the plateau between the first (A $\sim$ 90) and second (A $\sim$ 140) *s*-process peak and a negative sensitivity again after the second *s*-process peak. Basically, more material

is passed through the first neutron magic barrier, relative to the second. Thus, ^{87}Rb is increased as well as the other neutron magic isotopes from the first *s*-process peak. The only exception is ^{120}Sn(n, γ), which is a competing capture reaction far away from the NSE peak. ^{120}Sn acts as seed isotope for the heavier (following) isotopes along the *s*-process path. As it competes with iron as seed, an increased neutron capture rate of ^{120}Sn reduces the depletion of the lighter *s*-isotopes. The increased production of heavy isotopes, with their respective higher neutron capture cross sections, decreases the overall neutron density, which is indicated by the branching sensitive isotope ^{87}Rb. For neutron poisons and neutron donators, ^{120}Sn also acts as turning point for the sensitivities.

Rate	Figure	Features	Rate	Figure	Features
^{56}Fe(n,γ)	figure 3.6	representative	^{58}Fe(n,γ)	figure A.11	representative
^{64}Ni(n,γ)	figure A.9	representative	^{120}Sn(n,γ)	figure A.10	different

Table 3.4: Globally sensitive competing capture reactions during ^{13}C-pocket. The feature distinguishes between representative competing capture rates and a rate that produces a different sensitivity pattern.

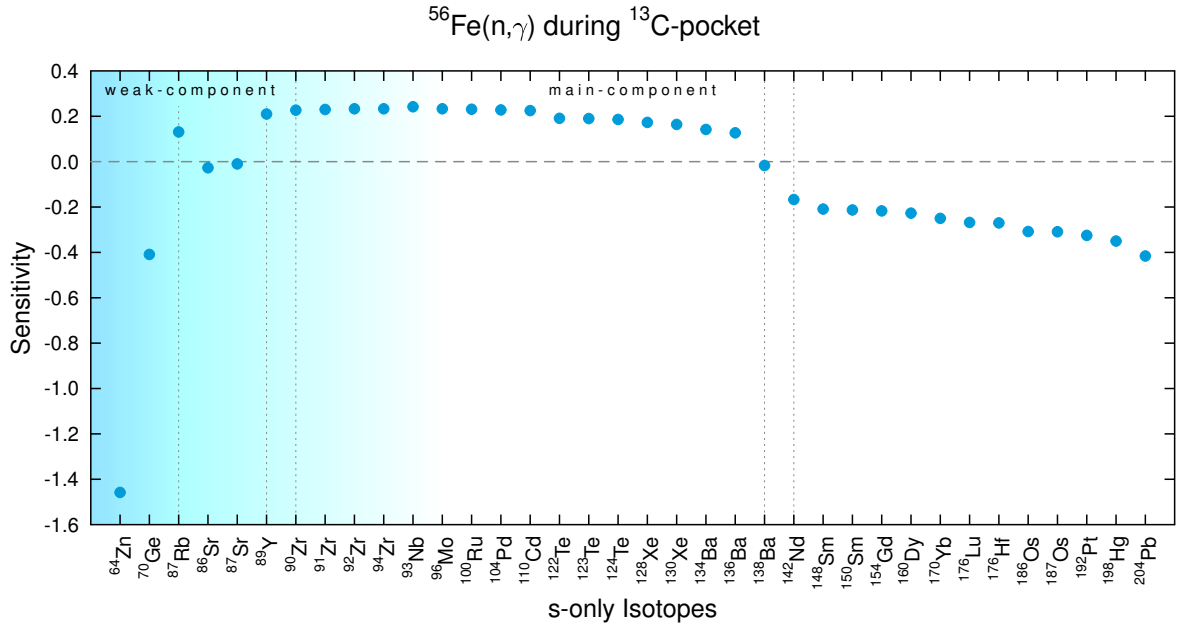

Figure 3.6: Competing capture ^{56}Fe(n,γ) during the ^{13}C-pocket (table 3.4). A strong depletion of seed isotopes can be seen, resulting in a neutron poison like effect on the main component.

Bottleneck

Bottlenecks are neutron magic isotopes with small neutron capture cross sections, which affect the following plateaus of the *s*-only isotopes in the σN curve. The trend in sensitivity of an increased neutron capture rate is an increased production of all following isotopes, whereas the isotope itself gets more depleted and the previous isotopes are almost not affected. Bottleneck rates in the first *s*-process peak (A $\sim$ 90) compete with the depletion of NSE peak seed isotopes, whereas the bottleneck rates in the second *s*-process peak (A $\sim$ 140) almost exclusively affect the production of following isotopes. ^{88}Sr is the strongest (highest sensitivities) bottleneck isotope in the first *s*-process peak (figure 3.7). Its increased neutron capture rate reduces the neutron per seed ratio, as more isotopes participate during the *s* process. But it also acts as a new starting point for the *s* process, competing with the NSE peak isotopes. Thus, the reduced neutron per seed ratio is compensated by the heavier starting point. Only the lead peak suffers in production.

Rate	Figure	Feature	Rate	Figure	Feature
^{88}Sr(n,γ)	figure 3.7	high sensitivities	^{139}La(n,γ)	figure A.14	rep. 2. peak
^{89}Y(n,γ)	figure 2.7	rep. 1. peak	^{140}Ce(n,γ)	figure A.15	rep. 2. peak
^{90}Zr(n,γ)	figure A.13	rep. 1. peak	^{142}Nd(n,γ)	figure A.16	rep. 2. peak
^{138}Ba(n,γ)	figure A.12	rep. 2. peak			

Table 3.5: Globally sensitive bottleneck reactions during ^{13}C-pocket. The feature distinguishes between Bottleneck isotopes in the first *s*-process peak (rep. 1. peak), in the second *s*-process peak (rep. 2. peak), and a bottleneck reaction with high sensitivities, which is unlike the representative rates.

Local sensitivities

For the local sensitivities a different approach in the analysis was chosen. For each isotope, the three most sensitive rates, which are not global sensitivities are listed with descending impact. If one isotope is of special interest, because it can be measured in meteorites or spectral lines, a list of all impacting rates (globally and locally) is presented for this isotope. Branching points for example do not affect the global trend, but locally impact the isotopic ratios. Branching points, which are of great interest for testing the *s*-process models, can be detected for each scenario with the local sensitivities.

The table A.1 in the appendix A.1.1 lists the local sensitivities of all isotopes for the ^{13}C-pocket. In table 3.1, all detected branching points during the ^{13}C-pocket are listed.

In the local sensitivities, ^{23}Na(n,γ) acts as neutron poison around the lead peak. This happens, as it is to weak to count as global neutron poison and only at mass numbers over 200 the accu-

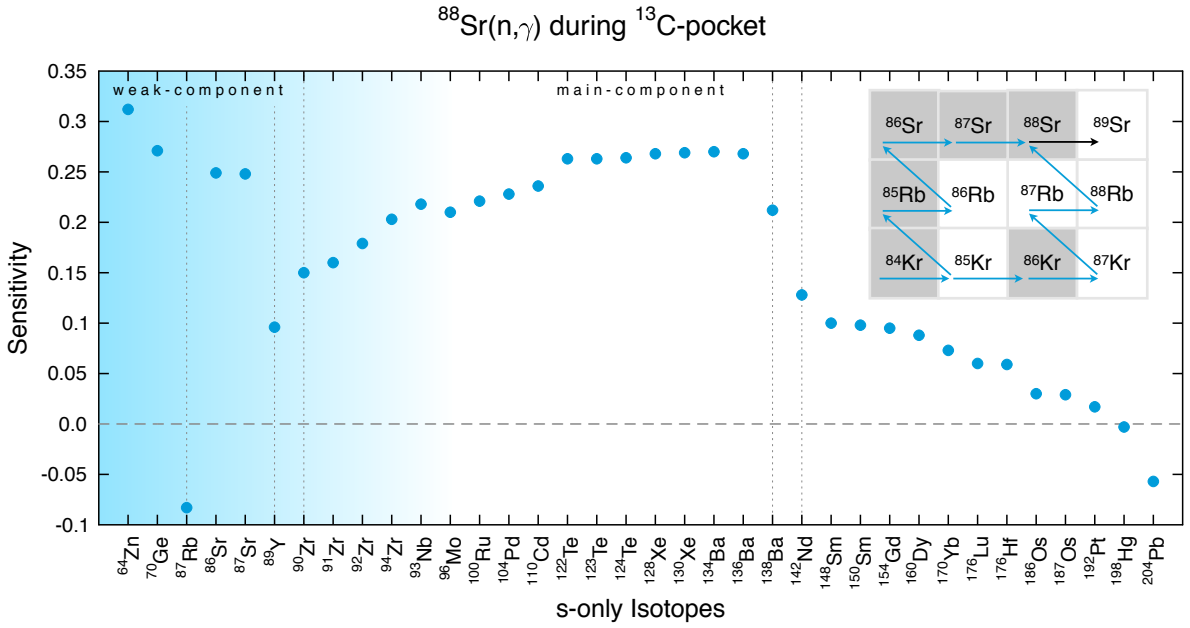

Figure 3.7: Bottleneck reaction ^{88}Sr(n,γ) during the ^{13}C-pocket (table 3.5). ^{88}Sr(n,γ), which is the bottleneck reaction with the highest sensitivies in the first *s*-process peak. It increases the production of the following isotopes, except for the lead peak. The neutron capture on ^{88}Sr competes directly with the NSE peak seed isotope reactions and has therefore a positive sensitivity to those. As more material passes the first *s*-process peak, the neutron per seed ratio is lowered, but as the seed is shifted from ^{56}Fe to ^{88}Sr only the lead peak suffers from a decreased production. With the presence of more heavy isotopes and their higher neutron capture cross sections, the overall neutron density is lowered as seen on ^{87}Rb.

mulated effect surpasses the 0.1 sensitivity threshold. The proton-rich isotope ^{58}Ni, which is not produced by the *s* process reaches sensitivities $\ll -1$ on its own depletion via neutron capture. This occurs as well with *p*-nuclei, which are in the initial seed. These nuclei act only as seed nuclei during the *s* process. An increased depletion channel is not compensated by any feeding, which results in these high sensitivity values.

3.1.2 Thermal pulse

The stellar model during the convective TP has about 1200 zones. No full network sensitivity study in MPPNP could be performed within the scope of this work, as the simulations for the TP would have taken longer than 3 years to perform. Due to the convective nature of the TP, the scenario could not be simplified to full satisfaction with one PPN trajectory, therefore, a preselection of rates for the sensitivity study had to be conducted. A PPN trajectory through the bottom coordinate of the TP was selected and the network of 14000 rates checked for sensitivi-

ties. All rates showing a sensitivity were re-simulated in MPPNP. The temperature and density for the 1D models of the TP are plotted in TK-plots (see figures 3.8 and A.17). The TP has a peak temperature of about $3 \cdot 10^8$ K and ignites when densities reach almost 50000 g/cm^3.

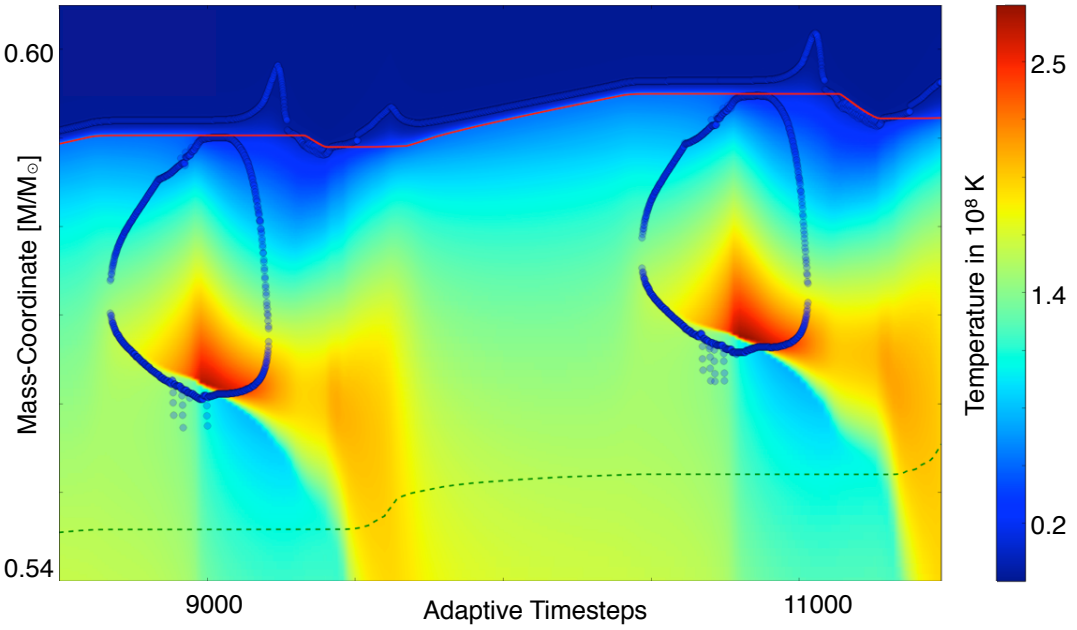

Figure 3.8: TK-plot of the temperature in the helium intershell of a 3 $M_\odot$ stellar model during the TP-AGB phase. The reoccurring ignition of helium burning in the thermal pulses with their tails of hot burning ashes feeding the C-O core is depicted. This can be seen, where temperatures reach the local maxima in the convective zones, followed by a tail outside of the convection zone going down in the mass coordinate. The colormap represents the temperature, which peaks at almost $3 \cdot 10^8$ K during the TP. The convective boundaries are the blue dotted lines, the red line signifies the hydrogen boundary and the green dotted line the helium boundary.

The TP has a higher neutron density than the ^{13}C-pocket, but is convective and only lasts for around 100 years. In these conditions sensitive rates can mostly impact a tail of following isotopes on the chart of nuclides, except for the neutron donators and poisons. The global trend of the TP is illustrated in figure 3.9.

A slight increase in lighter (mass number 60 to 90) and heavy (mass number > 200) *s*-isotopes during the neutron irradiation of the convective TP is observed. The general trend can be explained as a superposition of production tails (see bottleneck reactions, page 67 and following)

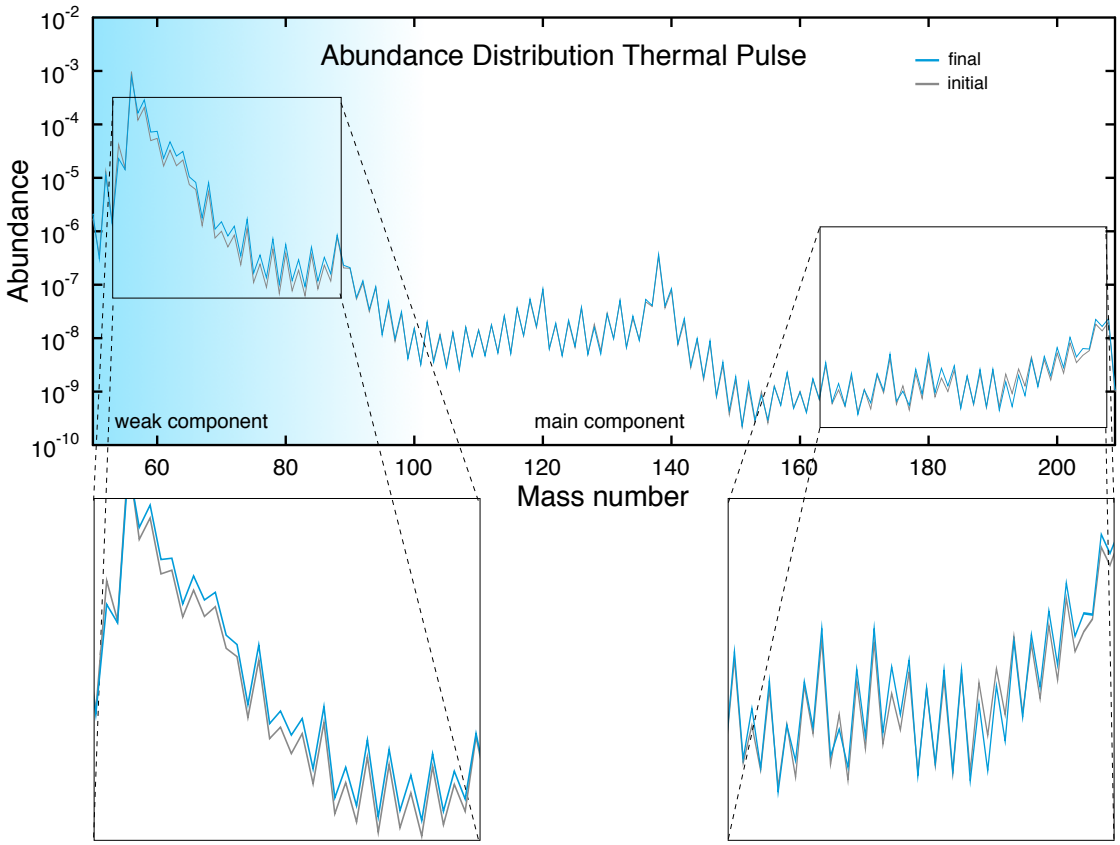

Figure 3.9: Abundance distribution before and after a single thermal pulse. The TP has almost no impact on the overall abundance distribution. A small increase in the abundances of the weak component (left enlargement) is observed as well as as shift from mass number about 190 to the lead peak (right enlargement).

from different seed isotopes throughout the entire mass regime.

Branching points during the TP

Within the global sensitivity analysis, seven branching points were detected during the TP. These branching points are labeled with their respective figure number in table 3.6. In the local sensitivity table A.3, a additional 24 branching points showed an impact on the abundances of single isotopes. These branching points are labeled with the local sensitivity table. The complete list is shown in table 3.6. Using the example of ^{85}Kr, a locally impacting branching point is illustrated in figure 3.10. If the neutron capture on ^{85}Kr is increased the isotopes on the β-decay path show a negative sensitivity and vice versa.

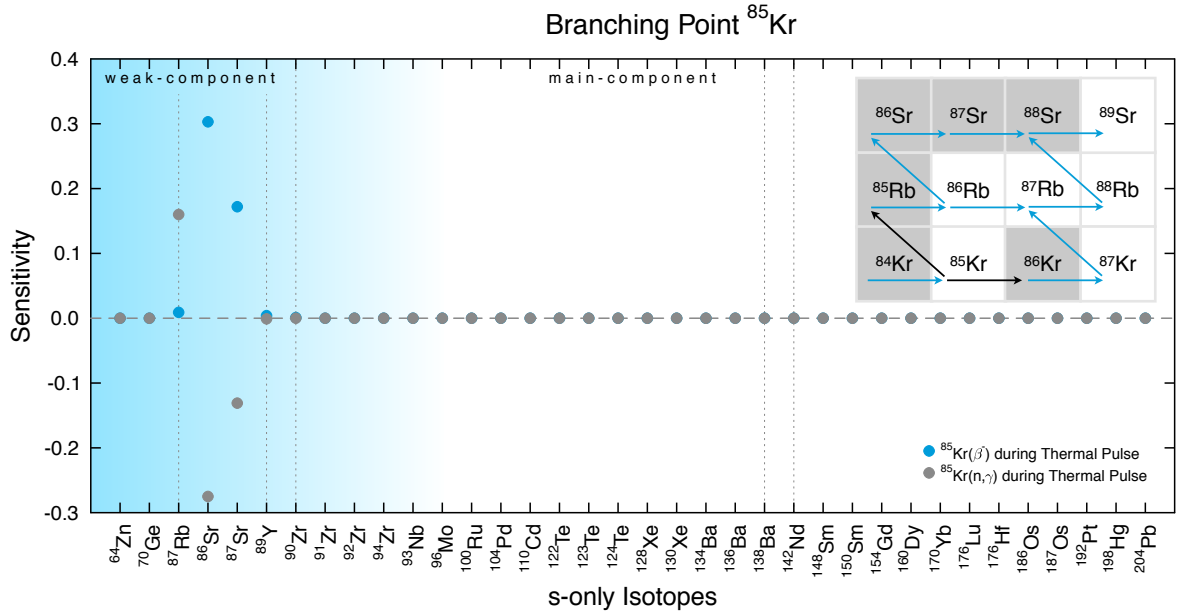

Figure 3.10: Branching point ^{85}Kr during the TP (table 3.6). The sensitivities of both rates are not exactly "mirrored". An increased β-decay rate of ^{85}Kr feeds the branching point ^{86}Rb, which produces ^{87}Rb in TP conditions, with the higher neutron densities compared to the ^{13}C-pocket. Therefore, the influence of the β-decay rate on the abundance of ^{87}Rb is close to zero. An increased neutron capture rate on ^{85}Kr produces more isotopes along the neutron capture path around the branching point and less along the β-decay path.

Branching point	competing reactions	figure / table
^{63}Ni	^{63}Ni(β^-), ^{63}Ni(n,γ)	figure A.18
^{64}Cu	^{64}Cu(β^-), ^{64}Cu(β^+)	figure A.19
^{79}Se	^{79}Se(β^-), ^{79}Se(n,γ)	table A.3
^{85}Kr	^{85}Kr(β^-), ^{85}Kr(n,γ)	figure 3.10
^{86}Rb	^{86}Rb(β^-), ^{86}Rb(n,γ)	figure A.20
^{93}Zr	^{93}Zr(β^-), ^{93}Zr(n,γ)	figure A.21
^{95}Zr	^{95}Zr(β^-), ^{95}Zr(n,γ)	figure A.22
^{99}Mo	^{99}Mo(β^-), ^{99}Mo(n,γ)	table A.3
^{99}Tc	^{99}Tc(β^-), ^{99}Tc(n,γ)	table A.3
^{103}Ru	^{103}Ru(β^-), ^{103}Ru(n,γ)	table A.3
^{107}Pd	^{107}Pd(β^-), ^{107}Pd(n,γ)	table A.3
^{109}Pd	^{109}Pd(β^-), ^{109}Pd(n,γ)	table A.3
^{115}Cd	^{115}Cd(β^-), ^{115}Cd(n,γ)	table A.3
^{121}Sn	^{121}Sn(β^-), ^{121}Sn(n,γ)	table A.3
^{128}I	^{128}I(β^-), ^{128}I(β^+)	table A.3
^{133}Xe	^{133}Xe(β^-), ^{133}Xe(n,γ)	table A.3
^{141}Ce	^{141}Ce(β^-), ^{141}Ce(n,γ)	table A.3
^{147}Nd	^{147}Nd(β^-), ^{147}Nd(n,γ)	table A.3
^{151}Sm	^{151}Sm(β^-), ^{151}Sm(n,γ)	table A.3
^{153}Sm	^{153}Sm(β^-), ^{153}Sm(n,γ)	table A.3
^{157}Gd	^{157}Gd(β^-), ^{157}Gd(n,γ)	table A.3
^{159}Gd	^{159}Gd(β^-), ^{159}Gd(n,γ)	table A.3
^{169}Er	^{169}Er(β^-), ^{169}Er(n,γ)	table A.3
^{175}Yb	^{175}Yb(β^-), ^{175}Yb(n,γ)	table A.3
^{179}Hf	^{179}Hf(β^-), ^{179}Hf(n,γ)	table A.3
^{185}W	^{185}W(β^-), ^{185}W(n,γ)	table A.3
^{191}Os	^{191}Os(β^-), ^{191}Os(n,γ)	table A.3
^{192}Ir	^{192}Ir(β^-), ^{192}Ir(n,γ)	figure A.23
^{197}Pt	^{197}Pt(β^-), ^{197}Pt(n,γ)	table A.3
^{204}Tl	^{204}Tl(β^-), ^{204}Tl(β^+)	table A.3
^{205}Pb	^{205}Pb(β^+), ^{205}Pb(n,γ)	table A.3

Table 3.6: Branching point isotopes and reactions during the thermal pulse.

Global sensitivities during the TP

In the following section, all global sensitivities during the TP are listed and classified between neutron donators (table 3.7), neutron poisons (table 3.8), competing captures (table 3.9) and

bottlenecks (table 3.10).

NEUTRON DONATORS

The general effect of the neutron donator reaction ^{22}Ne(α,n) during the TP (figure 3.11) is an increase in the overall TP production trend as seen in figure 3.9. This is mainly a production of isotopes in the weak component regime and a peak at Hg and Pb. Changes in the abundance in between the weak region and the lead peak is the result of production tails on seed isotopes, which act as local start points for neutron capture nucleosynthesis along the *s*-process path. An important example for such a seed isotope is ^{110}Cd, which is stronger depleted with higher neutron densities. The highest sensitivities of the *s* process during the TP occur for the weak *s*-process component isotopes (mass number 60 - 90), which are the main product of the TP. ^{93}Nb is sensitive to the branching point ^{93}Zr.

Rate	Figure
^{22}Ne(α,n)	figure 3.11

Table 3.7: Globally sensitive neutron donator during the thermal pulse.

NEUTRON POISONS

Neutron poisons show the opposite trend of the neutron donators during the TP, therefore, the weak *s*-process isotopes and the isotopes of the lead peak have the highest negative sensitivity values. TP seed isotopes show a positive sensitivity and all other a negative sensitivity. ^{93}Nb, which is dependent on the β-decay of the branching point ^{93}Zr, is produced more with reduced neutron densities along with ^{110}Cd, which is depleted less as seed isotope. ^{25}Mg(n,γ) is the neutron poison with the highest sensitivities during the TP (figure 3.12). The neutron capture on ^{22}Ne competes with the α capture of ^{22}Ne. This results in the absorption of free neutrons from the *s* process as well in the destruction of the neutron source isotope ^{22}Ne for the reaction ^{22}Ne(α,n).

Rate	Figure	Feature
^{25}Mg(n,γ)	figure 3.12	representative
^{22}Ne(n,γ)	figure A.24	low sensitivities

Table 3.8: Globally sensitive neutron poisons during the thermal pulse. The ^{25}Mg(n,γ) rate is representative for the neutron poisons and the ^{22}Ne(n,γ) rate is alike only with lower sensitivity values.

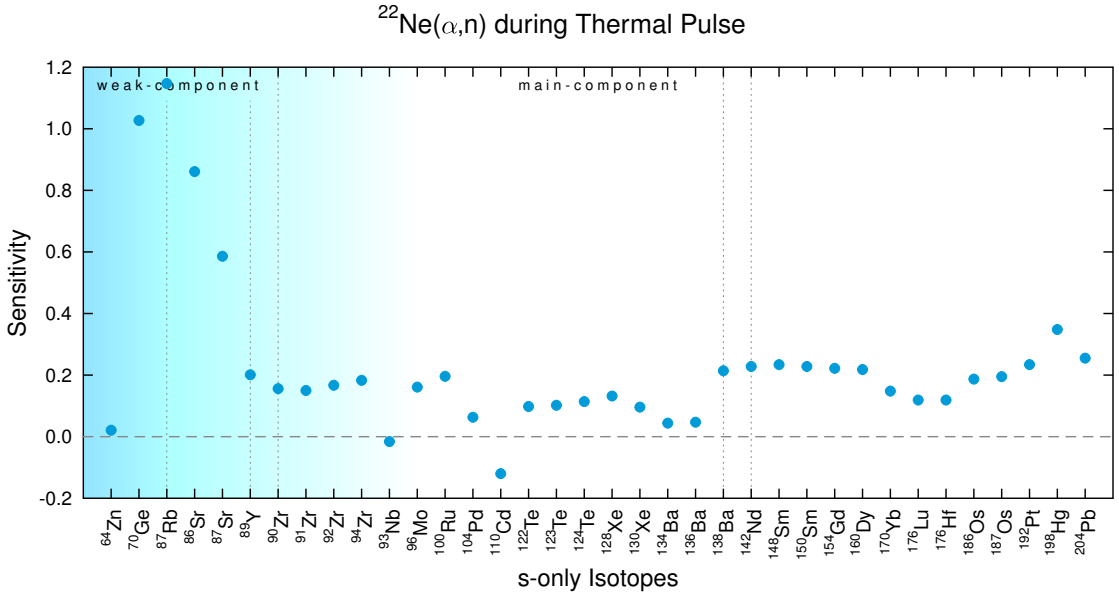

Figure 3.11: Neutron source ^{22}Ne(α,n) during the thermal pulse (table 3.7). This reaction is the only neutron donator during the TP. The sensitivity of the neutron donator reaction ^{22}Ne(α,n) shows the overall *s*-process trend during the TP, which is mainly producing isotopes in the weak component regime and a peak at Hg and Pb. The partial plateau structure, which is obtained for up to 6 *s*-only isotopes is the result of a superposition of different production tails on seed isotopes along the *s*-process path. These seed isotopes produce locally confined production tails. ^{110}Cd is such a seed isotope, which gets more depleted with increased neutron densities. ^{93}Nb is sensitive to the branching point ^{93}Zr and is less produced with higher neutron densities.

Competing captures

Competing captures during the TP have the same effect as neutron poisons, since the TP has a low neutron per seed ratio. If the neutron capture rate on ^{56}Fe is increased (figure 3.13), neutrons are taken from the entire system, but the production peak of isotopes resulting from the neutron capture reactions on iron does not reach further than ^{64}Zn. The impact of a competing capture during the TP is almost the same as a neutron poison.

Rate	Figure
^{56}Fe(n,γ)	figure 3.13

Table 3.9: Globally sensitive competing capture reaction during the thermal pulse.

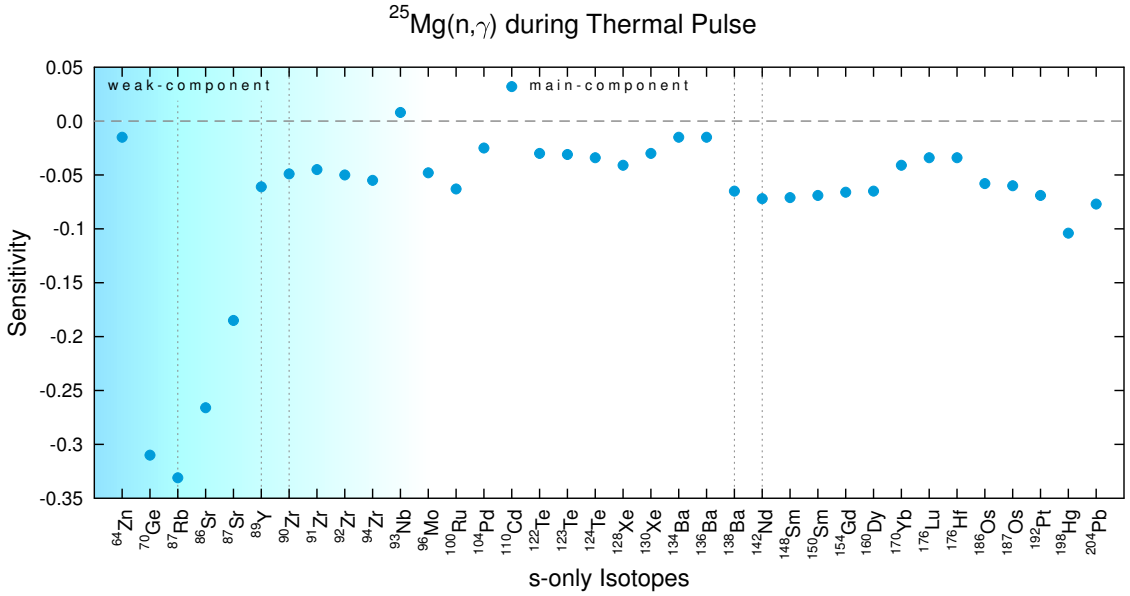

Figure 3.12: Neutron poison rate ^{25}Mg(n,γ) during the thermal pulse (table 3.8). ^{25}Mg, which is the result from the neutron source reaction ^{22}Ne(α,n) is very abundant during the TP. An increased neutron capture rate on ^{25}Mg withdraws neutrons from the *s* process during the TP. In TP conditions where no equilibrium occurs, this results in a net effect.

Bottleneck

Bottleneck reactions during the TP are the before mentioned seed isotopes for the neutron captures along the *s*-process path. The seed isotope is depleted and a peak in production of *s*-only isotopes in the subsequent 1 to 30 mass numbers can be seen. The tail of the peak can span over 50 mass numbers in some cases. An example for a direct following peak with a tail of 20 mass numbers is illustrated in figure 3.14 with the neutron capture reaction on ^{90}Zr. In general, the larger the distance of the peak to the isotope with changed rate, the bigger the impact of the initial abundance of the seed isotope, since it gets depleted and the peak supports itself as seed for the *s* process during the TP. The larger the tail of the sensitivity, the more global the impact of the rate. All reactions between the first and second *s*-process peak have a maximum tail span of 20 mass numbers whereas between the second and third *s*-process peak the impacting tails span between 24 and 50 mass numbers. This effect results from the larger impact of the *s* process during the TP on the heavy isotopes. This can be seen, e.g., in the sensitivity plot of the neutron donator (figure 3.11), which has higher sensitivities between the second and third *s*-process peaks. Bottlenecks, which have large abundances, like neutron magic isotopes, have the peak impact only few mass numbers behind the isotope with changed rate.

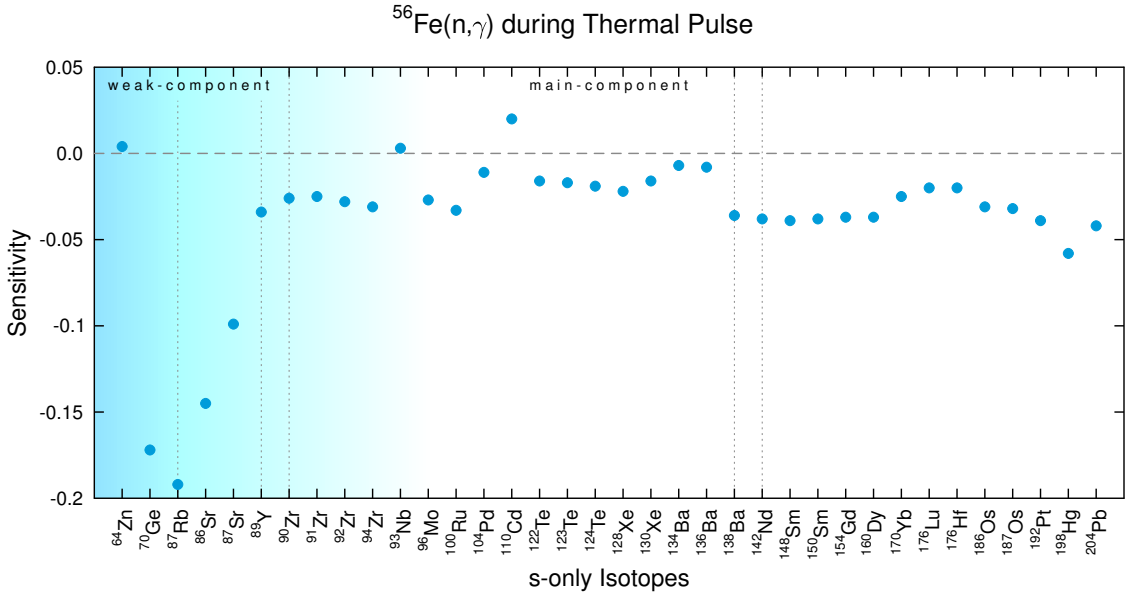

Figure 3.13: Competing capture ^{56}Fe(n,γ) during the thermal pulse (table 3.9). Like a neutron poison the competing capture ^{56}Fe(n,γ) withdraws neutrons from the system, because of the low neutron per seed isotope value.

Rate	Figure	Feature	Rate	Figure	Feature
^{90}Zr(n,γ)	figure 3.14	rep. 1. peak	^{140}Ce(n,γ)	figure A.36	rep. 2. peak
^{91}Zr(n,γ)	figure A.27	rep. 1. plateau	^{141}Pr(n,γ)	figure A.37	rep. 2. peak
^{92}Zr(n,γ)	figure A.28	rep. 1. plateau	^{142}Nd(n,γ)	figure A.38	rep. 2. peak
^{94}Zr(n,γ)	figure A.29	rep. 1. plateau	^{144}Nd(n,γ)	figure A.39	rep. 2. plateau
^{96}Mo(n,γ)	figure A.25	low sens.	^{146}Nd(n,γ)	figure A.26	rep. 2. plateau
^{110}Cd(n,γ)	figure A.30	low sens.	^{148}Sm(n,γ)	figure A.40	low sens.
^{114}Cd(n,γ)	figure A.31	low sens.	^{150}Sm(n,γ)	figure A.41	low sens.
^{116}Sn(n,γ)	figure A.32	low sens.	^{158}Gd(n,γ)	figure A.42	low sens.
^{118}Sn(n,γ)	figure A.33	rep. 1. plateau	^{164}Dy(n,γ)	figure A.43	low sens.
^{120}Sn(n,γ)	figure A.34	rep. 1. plateau	^{174}Yb(n,γ)	figure A.44	low sens.
^{139}La(n,γ)	figure A.35	rep. 2. peak	^{180}Hf(n,γ)	figure A.45	low sens.

Table 3.10: Globally sensitive bottlenecks during the thermal pulse. The feature distinguishes between representative Bottleneck isotopes wich are in first neutron magic peak (rep. 1. peak), representative bottleneck rates in between the first and second *s*-process peak (rep. 1. plateau), rates, which are like the representative ones only with low sensitivities (low sens.), representative neutron magic bottleneck isotopes of the secnod *s*-process peak (rep. 2. peak), and representative bottleneck rates in between the second and third *s*-process peak (rep. 2. plateau).

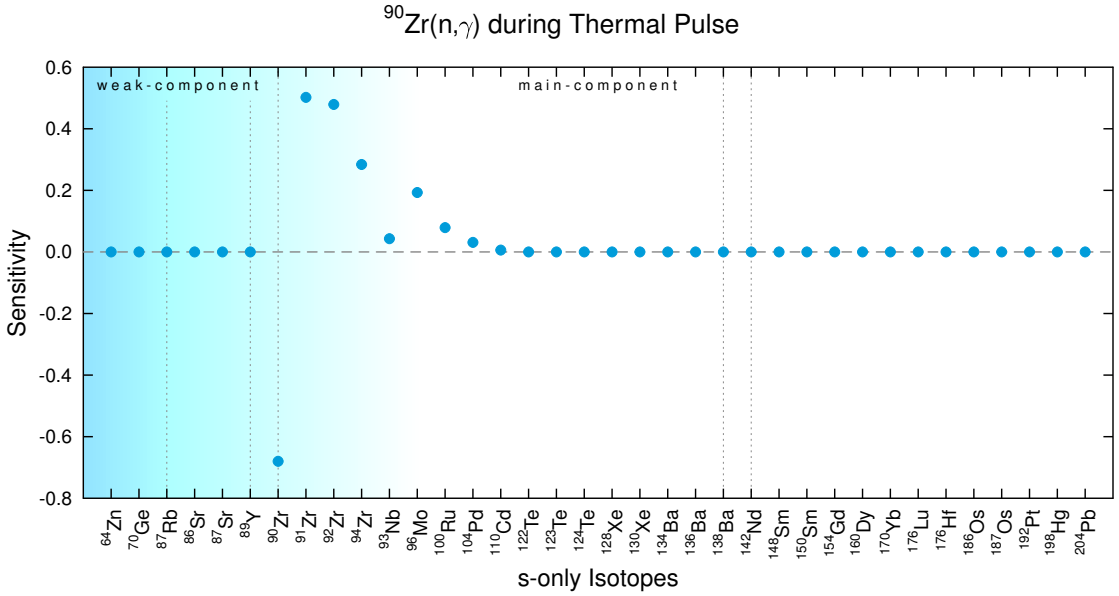

Figure 3.14: Bottleneck reaction ^{90}Zr(n,γ) during the thermal pulse (table 3.10). The neutron capture on the magic isotope ^{90}Zr has an impact tail of up to 20 mass numbers of *s*-only isotopes.

Local sensitivities

The table A.3 with the local sensitivities of all isotopes during the TP is listed in appendix A.1.2. The branching points from the local sensitivity table are already listed in table 3.6. ^{93}Nb is sensitive to the β^--decay and neutron capture rates of ^{93}Zr. This sensitivity agrees with the global sensitivity plots during the TP.

3.2 Weak component

The weak component of the *s* process consists of two components, the helium core burning and the carbon shell burning. The weak *s*-process simulation, which treats both components of the weak *s* process in a single zone trajectory produces in some cases “complicated” sensitivity trends. Therefore a second sensitivity study, which contains only the convective carbon shell burning was performed. The “complicated” sensitivity trends could then be assigned to light neutron poisons and recycled neutron poisons and the assumption that these trends result from a unintuitive superposition of sensitivities of both burning zones could be ruled out. These second simulations show, that the convective carbon shell burning has its main impact on branching points and almost no impact on the overall abundance distribution.

3.2.1 Weak *s* process

The weak *s*-process trajectory (figure 3.15) received a full network sensitivity study with ±10% in PPN.

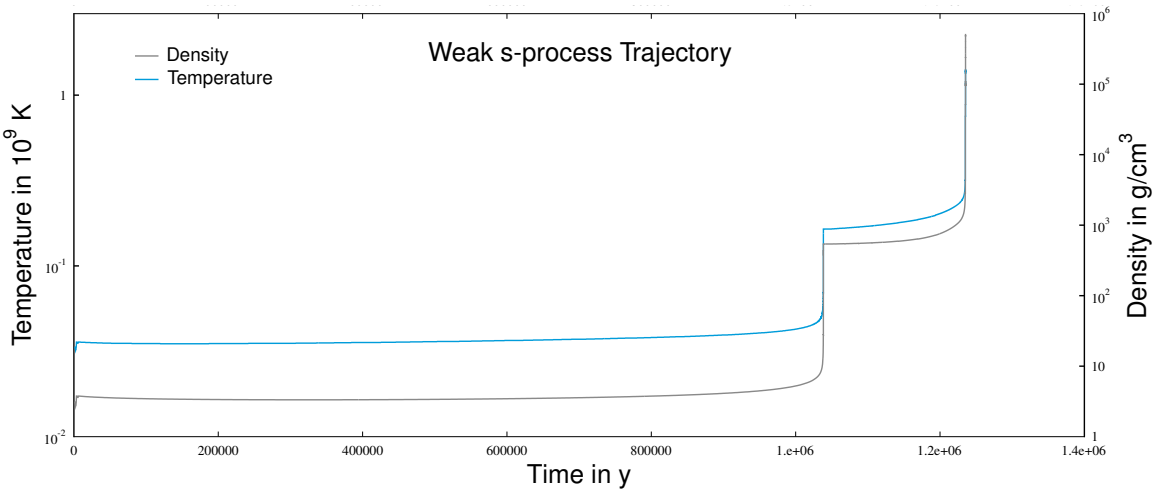

Figure 3.15: PPN trajectory of weak component. Temperature and density are plotted as function of time. The initial abundances for this trajectory are listed in table A.5. The different burning phases, central helium burning and shell carbon burning, are represented by the two different plateaus in the temperature and density. The helium core burning lasts $\sim$ 1 My and the shell carbon burning $\sim$ 200000 y. These timescales were stretched manually from Frischknecht 2007 in order to reproduce the multi zone model with a single zone trajectory.

The weak *s*-process trajectory is a single zone trajectory, going through two different burning stages of the star. This can be done, since there are only two sites for the weak *s* process, namely the helium core and carbon shell burning, and these burning sites are convective. The weak component is produced in this trajectory, as shown in figure 3.16, where a strong abundance increase in the mass regime 60-90 is observed.

The weak component has a lower neutron per seed ratio, than the main component. This prohibits the mass flux from surpassing mass number about 100 (figure 3.16). Only depletion on heavier isotopes, which are in the initial seed can be seen. For heavier isotopes, behind the second *s*-process peak at mass numbers higher than about 140, this becomes even more obvious. The initial abundance pattern gets depleted, but no effective feeding from lower mass numbers, which would have to surpass the neutron magic isotopes, occurs. Thus the jagged abundance pattern with decreases of up to 3 orders of magnitude results in this area. Since the depletion of the isotopes in that mass regime is depending only on the initial seed and is not the result from a net production in this regime, any influence of the weak *s* process on mass numbers higher than 142

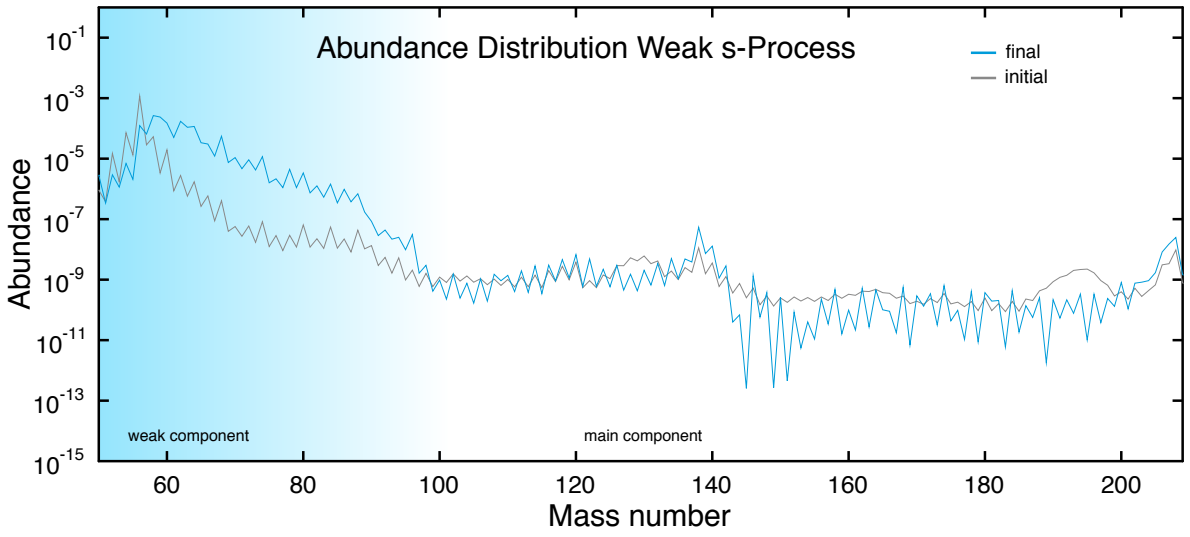

Figure 3.16: Abundance distribution before and after the weak component. A strong abundance increase in the weak *s*-process mass regime, 60-90, is observed. The depletion of the *r*-process peaks with a increase of the following *s*-process peaks is as well visible. The mass flux of the weak component does not surpass the second *s*-process peak at mass number $\sim$ 140. This results in a depletion of the initial seed material at mass numbers higher than $\sim$ 140, without any feeding from lower mass numbers.

are disregarded in the analysis.

Branching points during the weak component

In the simulations eleven branching points were detected in the global sensitivities. An additional 16 branching points were located in the local sensitivity tables. The branching point ^{64}Cu is illustrated in figure 3.17. The β^--decay path leads the mass flux to the isotope ^{64}Zn, which has a higher MACS than ^{64}Ni, the isotope reached by the β^+-decay path. Therefore, the *s* process is promoted with a increased β^--decay rate or suppressed with a increased β^+-decay rate.

Branching point	competing reactions	figure / table
^{63}Ni	^{63}Ni(β^-), ^{63}Ni(n,γ)	figure A.46
^{64}Cu	^{64}Cu(β^-), ^{64}Cu(β^+)	figure 3.17
^{69}Zn	^{69}Zn(β^-), ^{69}Zn(n,γ)	table A.4
^{74}As	^{74}As(β^-), ^{74}As(n,γ)	table A.4
^{75}Ge	^{75}Ge(β^-), ^{75}Ge(n,γ)	table A.4
^{79}Se	^{79}Se(β^-), ^{79}Se(n,γ)	table A.4
^{81}Se	^{81}Se(β^-), ^{81}Se(n,γ)	table A.4
^{85}Kr	^{85}Kr(β^-), ^{85}Kr(n,γ)	figure A.47
^{86}Rb	^{86}Rb(β^-), ^{86}Rb(n,γ)	figure A.48
^{89}Sr	^{89}Sr(β^-), ^{89}Sr(n,γ)	figure A.49
^{90}Y	^{90}Y(β^-), ^{90}Y(n,γ)	figure A.50
^{91}Y	^{91}Y(β^-), ^{91}Y(n,γ)	figure A.51
^{92}Nb	^{92}Nb(β^-), ^{92}Nb(β^+)	table A.4
^{93}Zr	^{93}Zr(β^-), ^{93}Zr(n,γ)	figure A.52
^{95}Zr	^{95}Zr(β^-), ^{95}Zr(n,γ)	figure A.53
^{99}Mo	^{99}Mo(β^-), ^{99}Mo(n,γ)	table A.4
^{99}Tc	^{99}Tc(β^-), ^{99}Tc(n,γ)	table A.4
^{107}Pd	^{107}Pd(β^-), ^{107}Pd(n,γ)	table A.4
^{109}Pd	^{109}Pd(β^-), ^{109}Pd(n,γ)	table A.4
^{115}Cd	^{115}Cd(β^-), ^{115}Cd(n,γ)	table A.4
^{115}In	^{115}In(β^-), ^{115}In(n,γ)	table A.4
^{121}Sn	^{121}Sn(β^-), ^{121}Sn(n,γ)	figure A.54
^{123}Sn	^{123}Sn(β^-), ^{123}Sn(n,γ)	table A.4
^{127}Te	^{127}Te(β^-), ^{127}Te(n,γ)	table A.4
^{129}Te	^{129}Te(β^-), ^{129}Te(n,γ)	table A.4
^{133}Xe	^{133}Xe(β^-), ^{133}Xe(n,γ)	figure A.55
^{141}Ce	^{141}Ce(β^-), ^{141}Ce(n,γ)	table A.4

Table 3.11: Branching point isotopes and reactions during the weak *s* process.

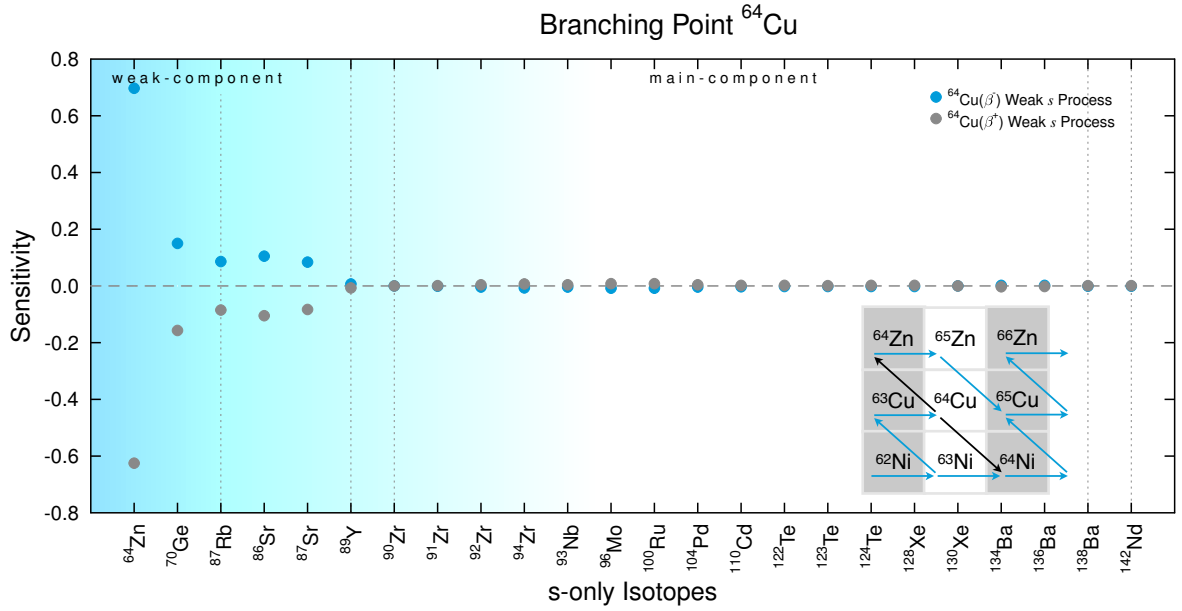

Figure 3.17: Branching point ^{64}Cu during the weak *s* process (table 3.11). The β^--decay path leads the mass flux to the isotope ^{64}Zn with its higher MACS compared to ^{64}Ni, promotes the *s* process of the weak component.

GLOBAL SENSITIVITIES DURING THE WEAK COMPONENT

In the following section, all global sensitivities during the weak component are listed and classified between neutron donators (table 3.12), recycled neutron poisons (table 3.13), neutron poisons (table 3.14), light neutron poisons (table 3.15), competing captures (table 3.16) and bottle necks (table 3.17).

NEUTRON DONATORS

The overall impact of a neutron donator on the abundances during the weak *s* process is a positive sensitivity for all isotopes except for the depletion of different seed isotopes like ^{64}Zn, ^{110}Cd, ^{130}Xe, ^{134}Ba, and ^{136}Ba. The strongest impact is on the first neutron magic peak around ^{87}Rb. An enhanced mass flow pass this peak results in different production peaks around ^{96}Mo, ^{124}Te and ^{142}Nd. ^{110}Cd and Ba are seed isotopes, which are more depleted with an increased neutron density. The weak *s* process is very sensitive to the initial seed distribution, like any *s*-process scenario, which is not in equilibrium, therefore, a superposition of neutron capture rates on the different seed isotopes, produces the sensitivity pattern (see table 3.17). ^{22}Ne(α,n) is the most effective neutron source (figure 3.18). It is the only neutron donator reaction where ^{64}Zn has a

positive sensitivity. This results from from an enhanced mass flux of lighter seed isotopes like ^{56}Fe. The two reactions ^{12}C(p,γ) and ^{13}N(β^+), which produce both ^{13}C are listed as neutron donators but the reaction ^{13}C(α,n) does not show strong sensitivities. This results from the high temperatures during the weak *s*-process conditions, which instantly consume all ^{13}C isotopes via the ^{13}C(α,n) reaction.. Therefore an increased ^{13}C(α,n) reaction, does not affect the neutron household, but an increased ^{13}C production.

Rate	Figure	Feature
^{22}Ne(α,n)	figure 3.18	high sensitivity
^{17}O(α,n)	figure A.56	representative

Rate	Figure	Feature
^{12}C(p,γ)	figure A.57	representative
^{13}N(β^+)	figure A.58	low sensitivites

Table 3.12: Globally sensitive neutron donator reactions during the weak component. The feature distinguishes between representative neutron donator reactions and neutron donators with high and low sensitivities.

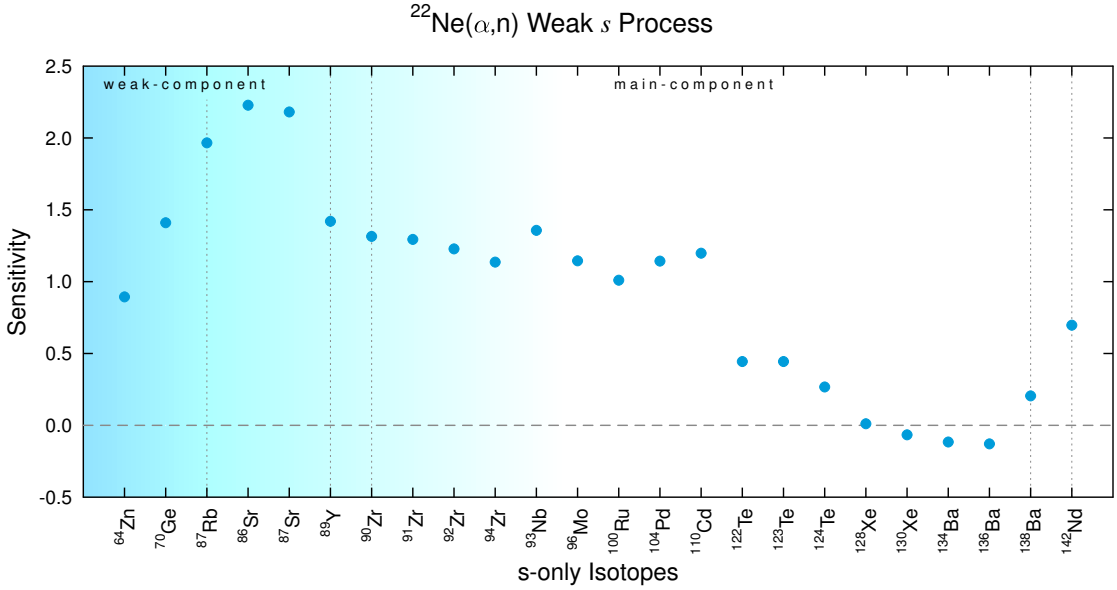

Figure 3.18: Neutron donator reaction ^{22}Ne(α,n) during the weak *s* process (table 3.12). A strong increase of weak component isotopes is observed, which reaches up to ^{110}Cd. The high sensitivity of this rate, which peaks at almost 2.5, promotes even the production of Te. Xe and Ba is used as seed for the production of the isotopes in the second *s*-process peak.

RECYCLED NEUTRON POISONS

Recycled neutron poisons [Travaglio et al. 1996] are neutron donators, which do not show a clear trend in the weak *s* process. These rates recycle light neutron poisons and release the previously absorbed neutron or alpha particle. A neutron donator like shape of sensitivities occurs, but the overall trend stays around sensitivity equal to zero. ^{20}Ne(γ,α) is for instance such a recycled neutron poison (figure 3.19), which releases α-particles for the neutron donator reactions in table 3.12.

Rate	Figure	Rate	Figure
^{20}Ne(γ,α)	figure 3.19	^{12}C$(^{12}C,\alpha)$	figure A.61
^{23}Na(p,α)	figure A.59	^{25}Mg(α,n)	figure A.62
^{26}Mg(α,n)	figure A.60	^{21}Ne(α,n)	figure A.63

Table 3.13: Globally sensitive recycled neutron poison reactions during the weak component. A representative rate for the recycled neutron poisons cannot be selected. Each sensitivity pattern is too unique.

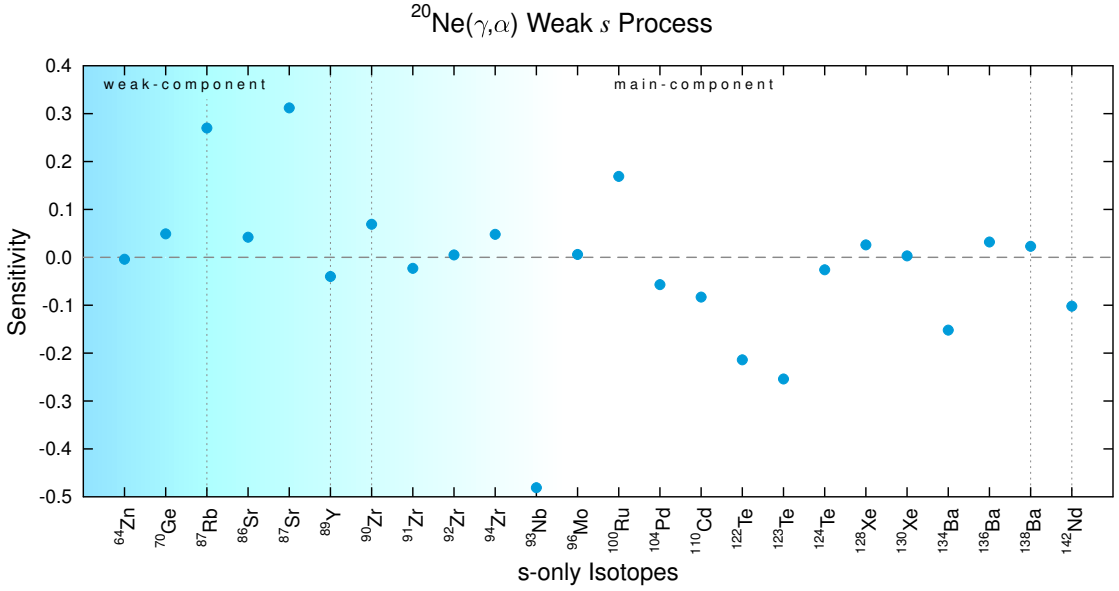

Figure 3.19: Recycled neutron poison reaction ^{20}Ne(γ,α) during the weak *s* process (table 3.13). No clear trend is visible. An α-particle is released via the ^{20}Ne(γ,α) reaction, which is the inverse reaction of the neutron poison reaction ^{16}O(α,γ).

Neutron poisons

The overall trend of sensitivities with increased neutron poison rates is opposite to the trend of the neutron donators. All isotopes show a negative sensitivity except for the Xe and Ba, which are seed isotopes, and less depleted with lower neutron densities. The neutron poison reaction $^{12}C(\alpha,\gamma)$, which withdraws α-particles from the neutron donator reactions (table 3.12) is shown in figure 3.20. This reaction produces as well the next neutron poison ^{16}O. The neutron poison reactions with the highest sensitivities are the ones, which capture α-particles. The triple-α reactions, which consumes three α-particles has the highest sensitivity with all isotopic sensitivities below zero. Neutron poison reactions, which capture neutrons have lower sensitivities.

Rate	Figure	Feature	Rate	Figure	Feature
$^{12}C(\alpha,\gamma)$	figure 3.20	representative	$^{16}O(n,\gamma)$	figure A.68	representative
Triple-α	figure A.64	high sens.	$^{32}S(n,\gamma)$	figure A.69	low sens.
$^{22}Ne(\alpha,\gamma)$	figure A.65	representative	$^{22}Ne(n,\gamma)$	figure A.70	low sens.
$^{16}O(\alpha,\gamma)$	figure A.66	representative	$^{13}N(\gamma,p)$	figure A.71	low sens.
$^{25}Mg(n,\gamma)$	figure A.67	representative	$^{28}Si(n,\gamma)$	figure A.72	low sens.

Table 3.14: Globally sensitive neutron poison reactions during the weak component. The feature distinguishes between rates, which produce high sensitivities (high sens.), rates, which are representative for neutron poisons and rates, which are as well representative but have low sensitivities (low sens.).

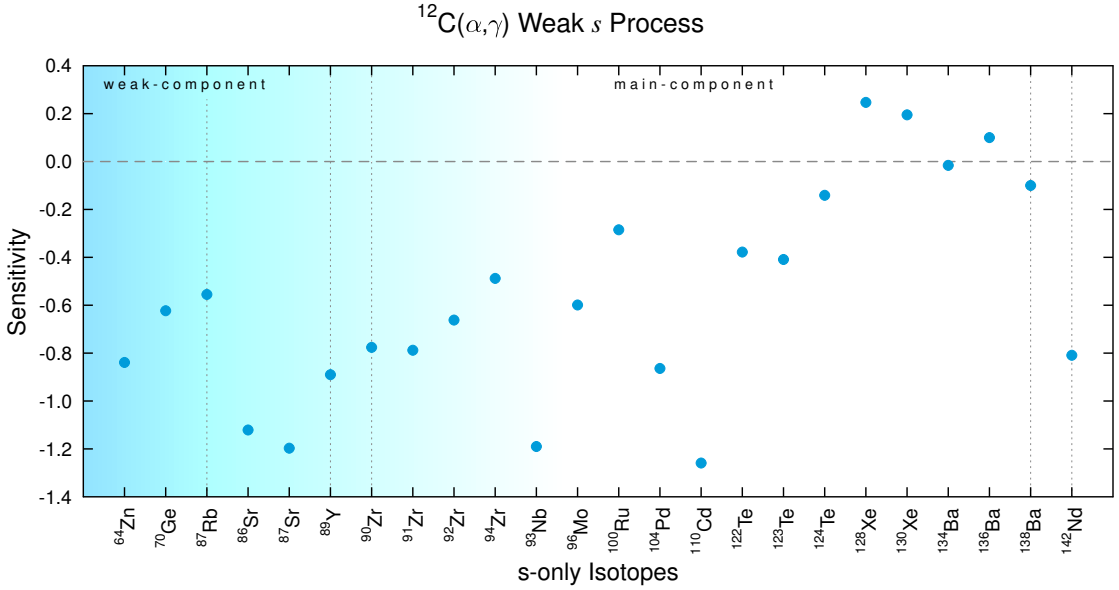

Figure 3.20: Neutron poison reaction $^{12}C(\alpha,\gamma)$ during the weak s process (table 3.14). The $^{12}C(\alpha,\gamma)$ withdraws α-particles for the neutron source reactions (table 3.12).

LIGHT NEUTRON POISON

Light neutron poisons [Limongi et al. 2000] do not show the same clear trend in the weak *s* process as neutron poisons. Their effect is comparable to a neutron poison, but no permanent reduction of the neutron density occurs. ^{24}Mg(n,γ) is for instance such a light neutron poison. The neutron is first absorbed, but will eventually be recycled via the ^{25}Mg(α,n) reaction. The increase in the (n,γ) rate, produces a neutron poison like sensitivity (figure 3.21).

Rate	Figure	Rate	Figure
^{24}Mg(n,γ)	figure 3.21	^{23}Na(n,γ)	figure A.76
^{20}Ne(α, γ)	figure A.73	^{26}Mg(p,γ)	figure A.77
^{12}C(^{12}C,p)	figure A.74	^{22}Ne(p,γ)	figure A.78
^{20}Ne(n,γ)	figure A.75	^{27}Al(n,γ)	figure A.79

Table 3.15: Globally sensitive light neutron poison reactions during the weak component. Like the recycled neutron poisons the effect in the sensitivity plot is too different in order to sub-categorize the light neutron poison reactions.

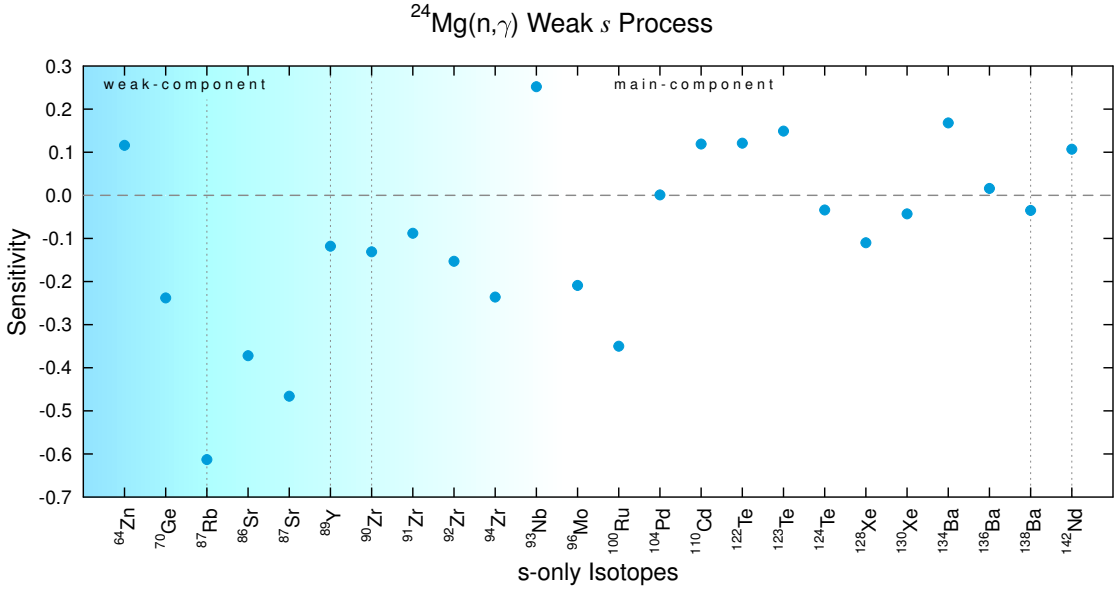

Figure 3.21: Light neutron poison ^{24}Mg(n,γ) during the weak *s* process (table 3.15). The negative sensitivities for the weak component *s*-isotopes resemble to a neutron poison, but the global trend is not as strong.

Competing captures

Competing capture reactions are usually on *s*-process seed isotopes like ^{56}Fe (figure 3.22). The increased material, which participates to the *s* process with the increased competing capture rates results in an accumulation of material before and at the first *s*-process peak. All succeeding isotopes show negative sensitivities except for the Ba seed isotopes, which are less depleted because of the reduced neutron per seed ratio (table 3.16). If the mass number of the competing capture isotope surpasses 60 then the isotopes in the first *s*-process peak start to show positive sensitivities. If the mass number of the competing capture isotope is below 60 then the first *s*-process peak has throughout negative sensitivities. This effect occurs because the competing capture isotope with increased neutron capture rate acts as new starting point (seed) isotope for the *s* process. Therefore, heavier starting points promote the *s* process further in mass numbers than starting points at lower mass numbers.

Rate	Figure	Feature	Rate	Figure	Feature
^{56}Fe(n,γ)	figure 3.22	rep. < 60	^{63}Cu(n,γ)	figure A.84	rep. ≥ 60
^{58}Fe(n,γ)	figure A.82	rep. < 60	^{59}Co(n,γ)	figure A.81	rep. < 60
^{57}Fe(n,γ)	figure A.83	rep. < 60	^{60}Ni(n,γ)	figure A.85	rep. ≥ 60
^{62}Ni(n,γ)	figure A.80	rep. ≥ 60	^{61}Ni(n,γ)	figure A.86	rep. ≥ 60

Table 3.16: Globally sensitive competing capture rates during the weak component. Two kind of representative rates are distinguished. The ones, which are neutron captures on an isotope at mass number below 60 (rep. < 60) and the ones, which are neutron captures on isotopes with mass number 60 and above (rep. ≥ 60).

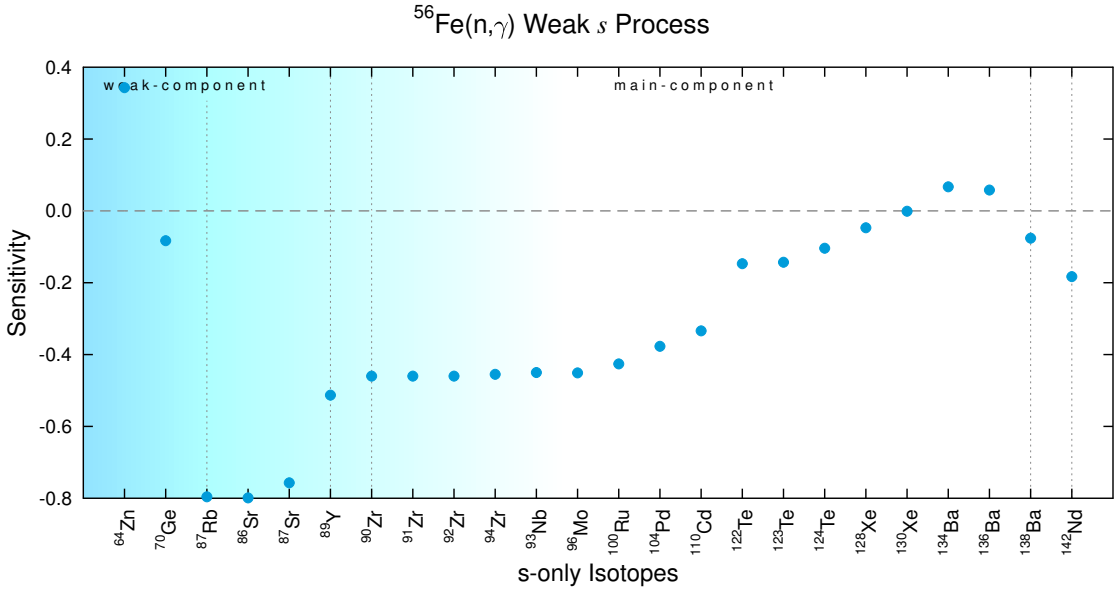

Figure 3.22: Competing capture ^{56}Fe(n,γ) during the weak *s* process (table 3.16). The effect results from a decreased neutron per seed ratio, which hinders the mass flux of surpassing the first *s*-process peak.

Bottleneck

Bottleneck reactinss are neutron capture rates on neutron magic or local seed isotopes, like ^{88}Sr (figure 3.23), which affect the production of the succeeding isotopes. An increased neutron capture rate on a bottleneck isotope results in a production tail of following isotopes along the *s*-process path. During the weak *s* process many isotopes show an impact as bottleneck isotope, which indicates, that a high sensitivity to the initial abundances impacts the overall abundance distribution because local equilibrium is not reached. The ^{93}Nb sensitivity lies for all bottleneck reactions between the sensitivity of ^{92}Zr and ^{94}Zr. The ^{93}Nb sensitivity is not the result of the neutron density sensitive branching of ^{93}Zr, but the result of an enhanced ^{93}Zr production and thereby ^{93}Nb production. The trend in sensitivities of the bottleneck rates seems to jump between ^{110}Cd and ^{122}Te, this is an effect of the sampling. The *s*-only isotopes between the first *s*-process peak and the second *s*-process peak are distributed with a maximum difference in mass numbers of six. Only between ^{110}Cd and ^{122}Te the gap spans over twelve mass numbers. Therefore, the sensitivities seem to behave differently.

Rate	Figure	Feature	Rate	Figure	Feature
^{88}Sr(n,γ)	figure 3.23	rep.	^{70}Ge(n,γ)	figure A.102	1. peak
^{89}Y(n,γ)	figure A.87	rep.	^{65}Cu(n,γ)	figure A.103	1. peak
^{92}Zr(n,γ)	figure A.88	rep.	^{64}Zn(n,γ)	figure A.104	only 1. peak
^{84}Kr(n,γ)	figure A.89	1. peak	^{67}Zn(n,γ)	figure A.105	low sens.
^{86}Sr(n,γ)	figure A.90	rep.	^{71}Ga(n,γ)	figure A.106	low sens.
^{90}Zr(n,γ)	figure A.91	rep.	^{69}Ga(n,γ)	figure A.107	low sens.
^{94}Zr(n,γ)	figure A.92	rep.	^{73}Ge(n,γ)	figure A.108	low sens.
^{74}Ge(n,γ)	figure A.93	1. peak	^{76}Se(n,γ)	figure A.109	low sens.
^{78}Se(n,γ)	figure A.94	1. peak	^{80}Se(n,γ)	figure A.110	1. peak
^{82}Kr(n,γ)	figure A.95	low sens.	^{85}Rb(n,γ)	figure A.111	1. peak
^{87}Sr(n,γ)	figure A.96	low sens.	^{96}Mo(n,γ)	figure A.112	low sens.
^{91}Zr(n,γ)	figure A.97	low sens.	^{122}Sn(n,γ)	figure A.113	short range
^{68}Zn(n,γ)	figure A.98	1. peak	^{90}Sr(n,γ)	figure A.114	low sens.
^{72}Ge(n,γ)	figure A.99	1. peak	^{95}Mo(n,γ)	figure A.115	low sens.
^{84}Kr(n,γ)	figure A.100	low sens.	^{98}Mo(n,γ)	figure A.116	low sens.
^{66}Zn(n,γ)	figure A.101	1. peak	^{126}Te(n,γ)	figure A.117	low sens.

Table 3.17: Globally sensitive bottleneck reactions during the weak component. The feature distinguishes between representative bottleneck rates (rep.), which have the highest sensitivities at larger mass numbers than the first *s*-process peak, rates, which have the highest sensitivities at the first *s*-process peak followed by lower sensitivities at higher mass numbers than 90 (1. peak), a rate, which has sensitivities only before and at the first *s*-process peak (only 1. peak), a rate on an isotope, which belongs to the main component and has only a short sensitivity range (short range) and rates, which have low sensitivities (low sens.).

Local sensitivities

The table A.4 in appendix A.2.1 lists the local sensitivities of all isotopes for the weak component. The branching points are already listed in table 3.11. ^{93}Nb is sensitive to the abundance of ^{93}Zr and delayed on the branching point reactions of ^{93}Zr.

3.2.2 Convective carbon shell burning

The convective carbon shell burning trajectory received like before a full network sensitivity study with ±10% in PPN. The trajectory is different from the carbon shell burning of the weak *s*-process trajectory. The trajectory is not stretched and covers a very short period of the stellar evolution ($\sim$ 0.1 y) as seen in figure 3.24. It is extracted from a stellar model right after the carbon burning ignition in the shell. The peaks in the trajectory results from re-adjustments of

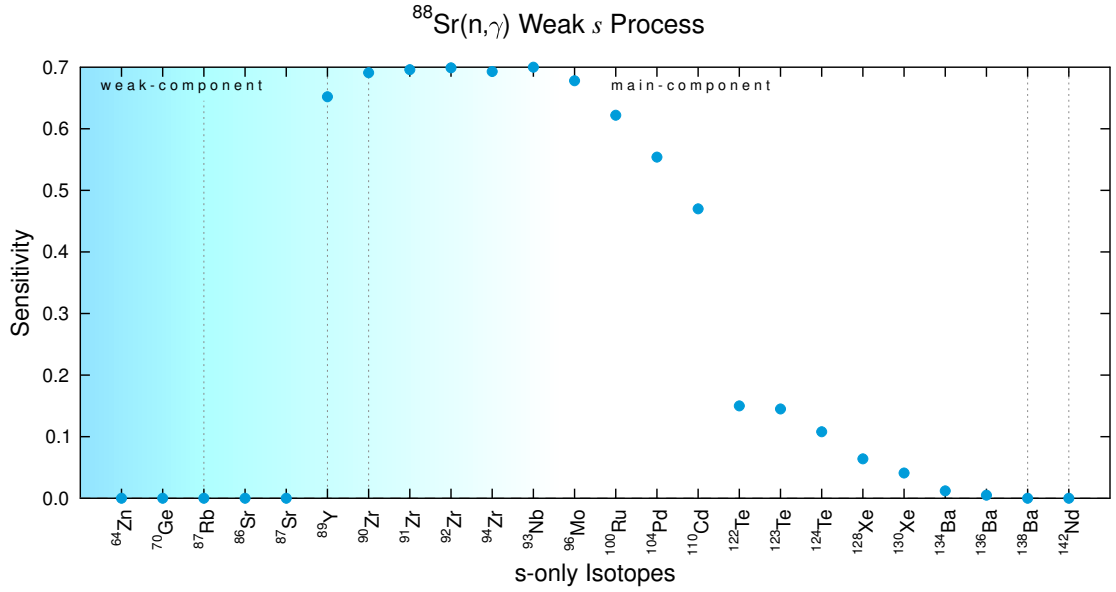

Figure 3.23: Bottleneck reaction ^{88}Sr(n,γ) during the weak *s* process (table 3.17). An increased neutron capture rate on this bottleneck isotope, produces a large impact on succeeding isotopes.

the stellar structure due to short burnings in other shells below the carbon shell. The overall impact on the abundance distribution of this particular trajectory is minor as seen in figure 3.25.

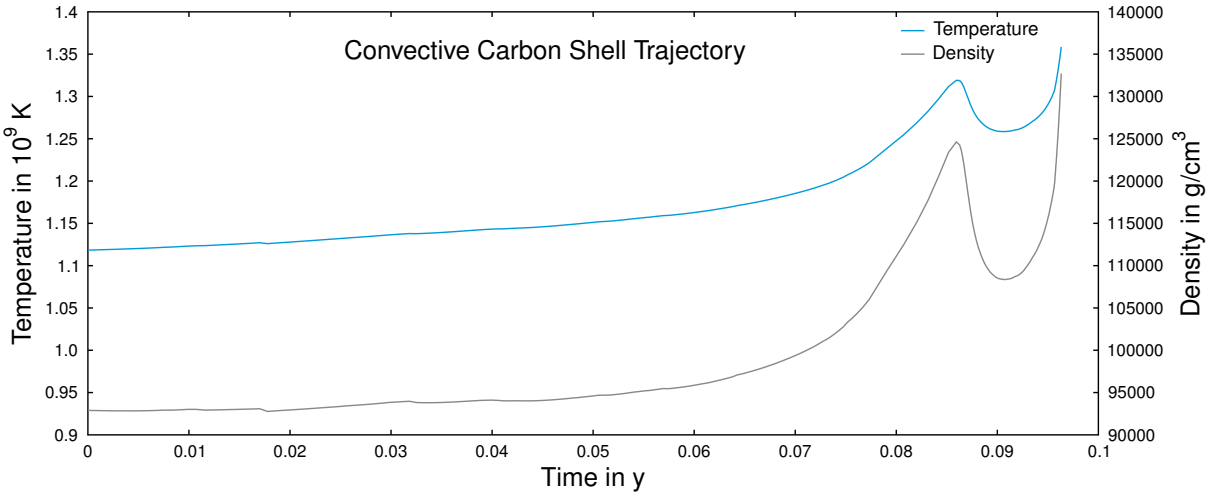

Figure 3.24: PPN trajectory of convective carbon shell burning. Temperature and density are plotted as function of time. The initial abundances for this trajectory are extracted at the start time- and mass-coordinate of this trajectory from the stellar model and listed in table A.7. The trajectory starts after the ignition of the carbon shell burning and has peaks due to re-adjustments in the stellar structure triggered by other shell burnings. The trajectory is not stretched in time.

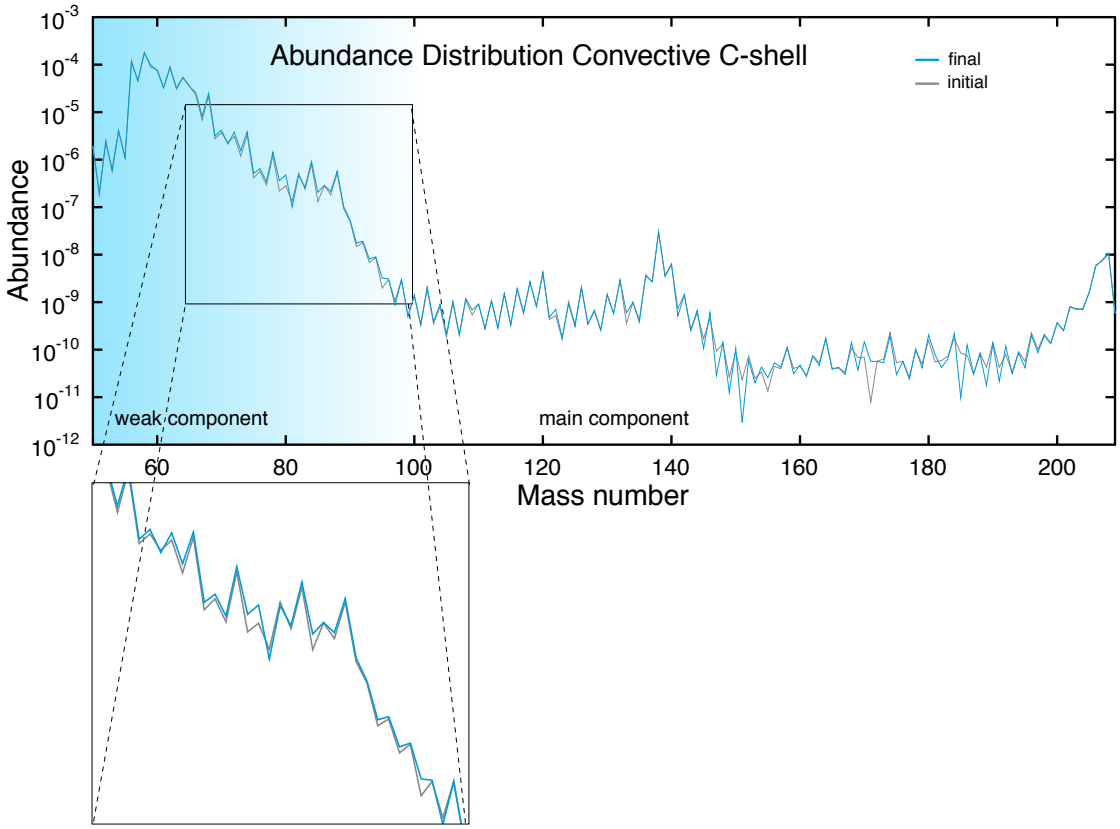

Figure 3.25: Abundance distribution before and after the convective carbon shell burning. Almost no impact of the convective carbon shell burning on the overall abundance distribution can be seen. The observed effect between the second and third *s*-process peak, results from the depletion of seed isotopes in that mass region. The initial abundances are different from the ones used for the weak *s* process, because the two trajectories start at a completely different evolutionary stages and the initial abundances are usually extracted at the starting mass- and time-coordinate of the trajectory.

Branching points during the convective carbon shell burning

In the simulations, four branching point reactions showed an impact on the final abundances of the *s*-only isotopes. These are labeled with their respective figure number in table 3.18. In the local sensitivity table, another 16 branching points were detected during the carbon shell burning, labeled with the local sensitivity table. ^{64}Cu is a branching point, which has very local impact (figure 3.26). The example of ^{64}Cu is representative for all branching points of the convective carbon shell burning, which were detected in the global sensitivity plots. These branching points only impact isotopes along the branching paths, up to the point where the paths rejoin.

Branching point	competing reactions	figure / table
^{64}Cu	^{64}Cu(β^-), ^{64}Cu(β^+)	figure 3.26
^{69}Zn	^{69}Zn(β^-), ^{69}Zn(n,γ)	table A.6
^{71}Ge	^{71}Ge(β^+), ^{71}Ge(n,γ)	table A.6
^{75}Ge	^{75}Ge(β^-), ^{75}Ge(n,γ)	table A.6
^{79}Se	^{79}Se(β^-), ^{79}Se(n,γ)	table A.6
^{85}Kr	^{85}Kr(β^-), ^{85}Kr(n,γ)	table A.6
^{86}Rb	^{86}Rb(β^-), ^{86}Rb(n,γ)	figure A.119
^{92}Nb	^{92}Nb(β^-), ^{92}Nb(β^+)	table A.6
^{95}Zr	^{95}Zr(β^-), ^{95}Zr(n,γ)	table A.6
^{99}Mo	^{99}Mo(β^-), ^{99}Mo(n,γ)	table A.6
^{99}Tc	^{99}Tc(β^-), ^{99}Tc(n,γ)	table A.6
^{103}Ru	^{103}Ru(β^-), ^{103}Ru(n,γ)	table A.6
^{107}Pd	^{107}Pd(β^-), ^{107}Pd(n,γ)	table A.6
^{109}Pd	^{109}Pd(β^-), ^{109}Pd(n,γ)	table A.6
^{115}Cd	^{115}Cd(β^-), ^{115}Cd(n,γ)	table A.6
^{115}In	^{115}In(β^-), ^{115}In(n,γ)	table A.6
^{121}Sn	^{121}Sn(β^-), ^{121}Sn(n,γ)	figure A.120
^{127}Te	^{127}Te(β^-), ^{127}Te(n,γ)	table A.6
^{133}Xe	^{133}Xe(β^-), ^{133}Xe(n,γ)	figure A.118
^{141}Ce	^{141}Ce(β^-), ^{141}Ce(n,γ)	table A.6

Table 3.18: Branching point isotopes and reactions during the convective carbon shell burning.

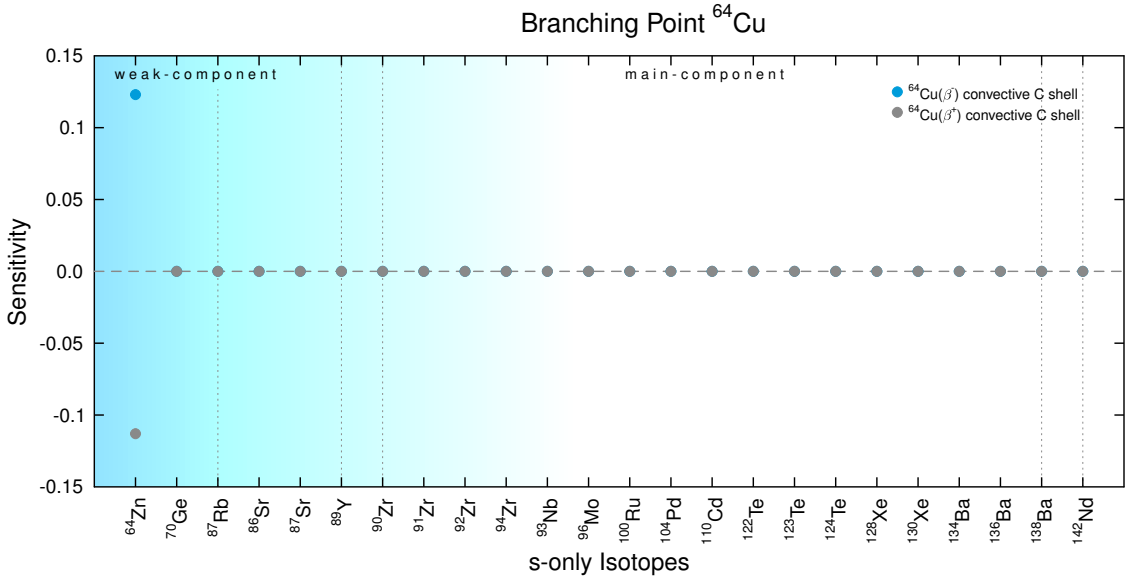

Figure 3.26: Branching point ^{64}Cu during the carbon shell burning (table 3.18). The sensitivities show a classical branching point behavior, which affects only the isotopes on the branching path.

GLOBAL SENSITIVITIES DURING THE CONVECTIVE CARBON SHELL BURNING

In the following section, all global sensitivities during the convective carbon shell burning are listed and classified between neutron donators (table 3.19), neutron poisons (table 3.20). Other interesting cases, which do not show the sensitivity toe would expect are listed in table 3.21 and 3.22 and discussed in the corresponding section.

NEUTRON DONATORS

The general impact of a neutron donator on the *s* process during the convective carbon shell burning is an increased ^{87}Rb production and a decreased ^{93}Nb production. This behavior cannot be explained with the branching points ^{85}Kr for ^{87}Rb or ^{93}Zr for ^{93}Nb, since they do not show any sensitivity in the local sensitivity tables. ^{85}Kr only impacts ^{85}Rb and ^{93}Zr is in this scenario no branching point at all. ^{93}Zr is therefore treated in the interesting cases. Other isotopes do not show strong sensitivities. The overall impact of the here utilized carbon shell burning trajectory is negligible and shows only the mentioned distinct peaks. One example for this behavior is the main neutron source ^{21}Ne(α,n) in figure 3.27.

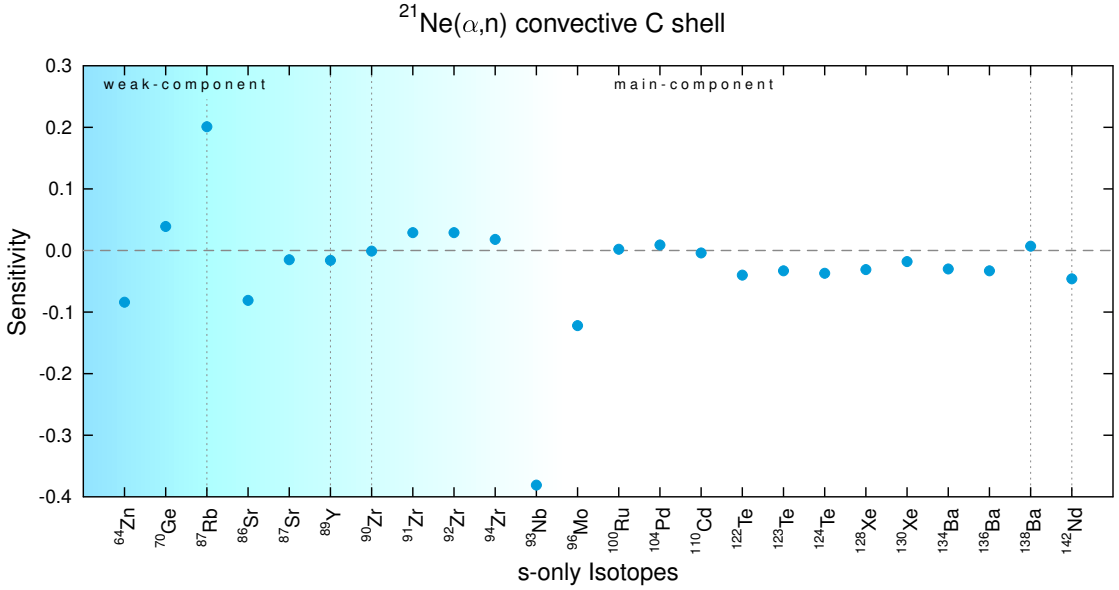

Figure 3.27: Neutron donator ^{21}Ne(α,n) during the convective carbon shell burning (table 3.19). The strongest impact is on the two isotopes ^{87}Rb and ^{93}Nb, which is not the result of branchings.

Rate	Figure	Feature
^{21}Ne(α,n)	figure 3.27	representative
^{22}Ne(α,n)	figure A.121	low sensitivities
^{25}Mg(α,n)	figure A.122	low sensitivities

Table 3.19: Globally sensitive neutron donator reactions during the convective carbon shell burning.

NEUTRON POISONS

The neutron density sensitive isotopes ^{93}Nb and ^{87}Rb show their expected behavior for neutron poisons. ^{93}Nb has a positive sensitivity and ^{87}Rb a negative sensitivity if a neutron poison rate is increased. This sensitivity is not the result of a branching. An representative example for all neutron poison reactions during the convective carbon shell burning is the ^{16}O(α,γ) in figure 3.28.

Rate	Figure	Rate	Figure
^{16}O(α,γ)	figure 3.28	^{20}Ne(α,γ)	figure A.125
^{20}Ne(n,γ)	figure A.124	^{25}Mg(n,γ)	figure A.123

Table 3.20: Globally sensitive neutron poison reactions during the convective carbon shell burning. The sensitivity trend for all listed neutron poison reactions is comparable.

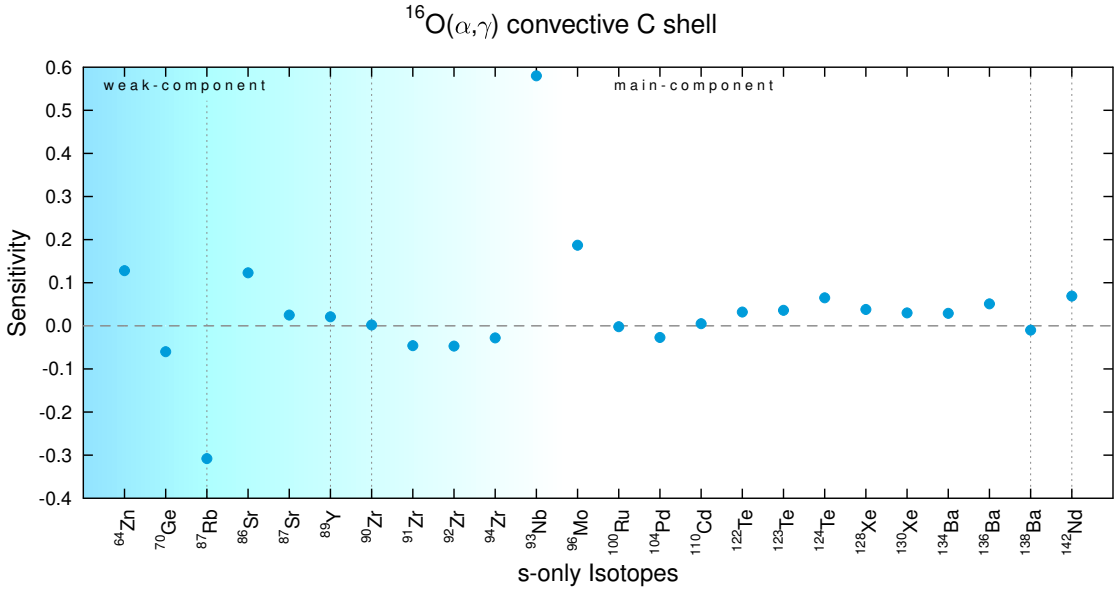

Figure 3.28: Neutron poison reaction ^{16}O(α, γ) during the convective carbon shell burning (table 3.20). The ^{16}O(α, γ) reaction withdraws α-particles from the neutron sources. The biggest impact of this rate is on the neutron density sensitive isotopes ^{87}Rb and ^{93}Nb.

Interesting cases

The convective carbon shell burning has a very little impact on the overall nucleosynthesis. Therefore, no bottlenecks or competing captures produce an influence over more than one or two succeeding *s*-only isotopes. It is also apparent, that the neutron source during the C shell burning is not as expected the ^{12}C(^{12}C,n) reaction (figure 3.29), but the sources listed in table 3.19. In the following the sensitivities of the carbon-carbon reactions are shown, which are negligible for this trajectory. Furthermore, the sensitivities of the reactions around ^{93}Nb with the ^{93}Zr branching are shown (figure 3.30). The branching turns out to be negligible as well, even though ^{93}Nb behaves with neutron donators/poisons as one would expect from a classical branching point. Thus, the sensitivity to the neutron density results solely from the depletion of the initial ^{93}Nb via neutron captures. If the neutron density is increased, ^{93}Nb is more depleted and has therefore a negative sensitivity and if the neutron density is decreased, more of the initial ^{93}Nb remains, producing positive sensitivities.

Rate	Figure
^{12}C(^{12}C,p)	figure A.126
^{12}C(^{12}C,α)	figure A.127
^{12}C(^{12}C,n)	figure 3.29

Table 3.21: Carbon-carbon reactions during the convective carbon shell burning. All reactions have low sensitivities.

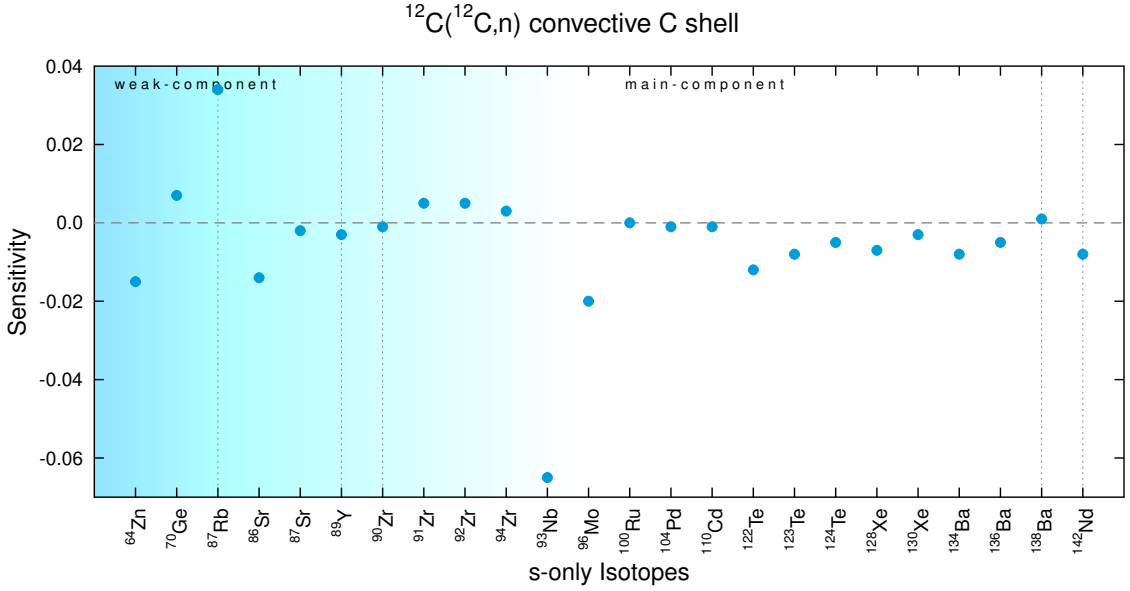

Figure 3.29: Expected neutron source ^{12}C(^{12}C,n) during the convective carbon shell burning (table 3.21). A minimal impact as neutron donator can be recorded, but much less, than one would expect from a dominant neutron source.

Rate	Figure
^{93}Zr(β^-)	figure 3.30
^{93}Zr(n,γ)	figure A.128
^{93}Nb(n,γ)	figure A.129

Table 3.22: Reactions around ^{93}Nb during the convective carbon shell burning. The ^{93}Nb sensitivities are negligible on the reactions of ^{93}Zr. Only the neutron capture on ^{93}Nb itself has an impact on the ^{93}Nb abundance.

Local sensitivities

The table A.6 in appendix A.2.2 lists the local sensitivities of all isotopes for the convective carbon shell burning. The branching points are already listed in table 3.18. ^{87}Rb and ^{93}Nb are

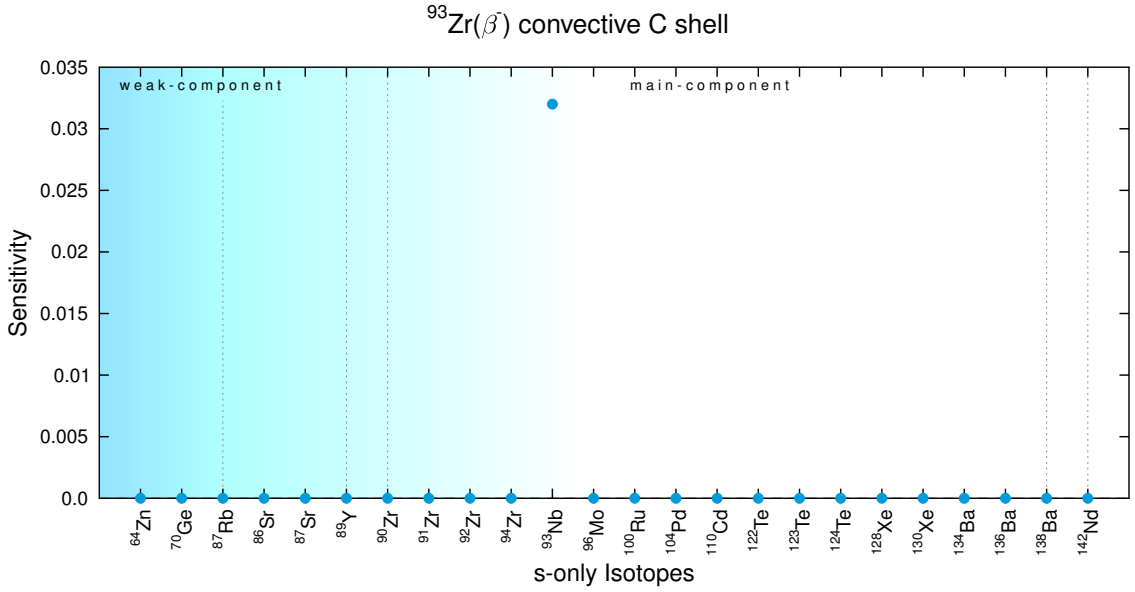

Figure 3.30: Expected branching path ^{93}Zr(β^-) during the convective carbon shell burning (table 3.22). The influence of the β-decay is below the usual 0.1 threshold and therefore negligible.

both sensitive to the reaction ^{24}Mg(n,γ), which is a neutron poison, but does not show in the global sensitivity plots. ^{24}Mg(n,γ) impacts mostly isotopes, which are not *s*-only isotopes.

3.3 THE *i* PROCESS

For the *i*-process simulations a large reaction network of about 62000 rates was used. The ad hoc trajectory from the NuGrid collaboration [www.nugridstars.org] consists of a constant temperature of $2 \cdot 10^8$ K, a constant density of $1 \cdot 10^4$ g/cm^3 and a lifetime of about four days. The change in abundance is plotted in figure 3.31 and the initial abundances are in table A.9.

The *i* process proceeds one to six mass numbers away from the valley of stability, on the neutron-rich side (figure 3.32). The analysis of global trends considers therefore the *r*-only isotopes, which are involved in the *i*-process nucleosynthesis.

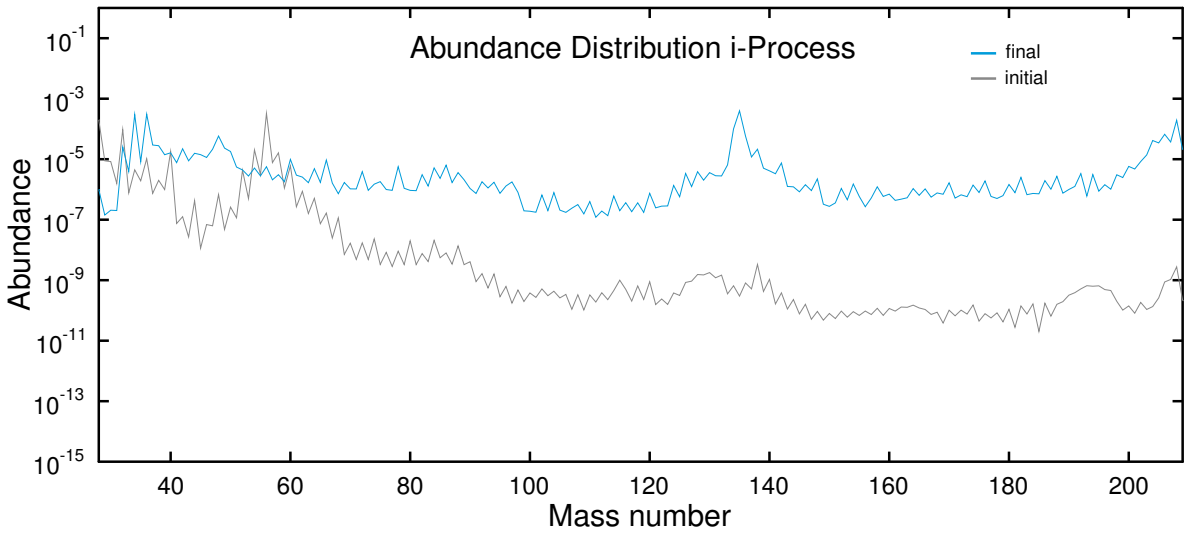

Figure 3.31: Abundance distribution before and after the *i* process. The depletion of the iron NSE peak and a strong increase in succeeding isotopes is observed. The peak, which is equivalent to the neutron magic waiting point *r* and *s*-process peaks, lies in between the *r*- and *s*-peaks. As this peak, which is the most prominent feature of the *i* process, is not visible in the solar abundance distribution (figure 1.1), the *i* process can play only a minor role on the solar abundance distribution, if any.

Branching points during the *i* process

During the *i* process, one seed isotope (^{34}P, figure 3.33) showed a globally sensitive branching on the *r*-only isotopes. ^{34}P affects the mass flow over the neutron magic barrier at neutron number 20. The increased neutron capture rate on ^{34}P competes with the depletion of other seed isotopes. As the *i* process proceeds along β-unstable isotopes, more or less every isotope is impacted by a "branching", which occurs on the isobaric line of each isotope, where a β-decay competes with a neutron capture. Therefore all local branchings can be looked up in table A.8 in the appendix and are not listed in table 3.23. The only local branching points, which are listed in table 3.23, are branching points, which do not have the same mass number as the isotope they affect.

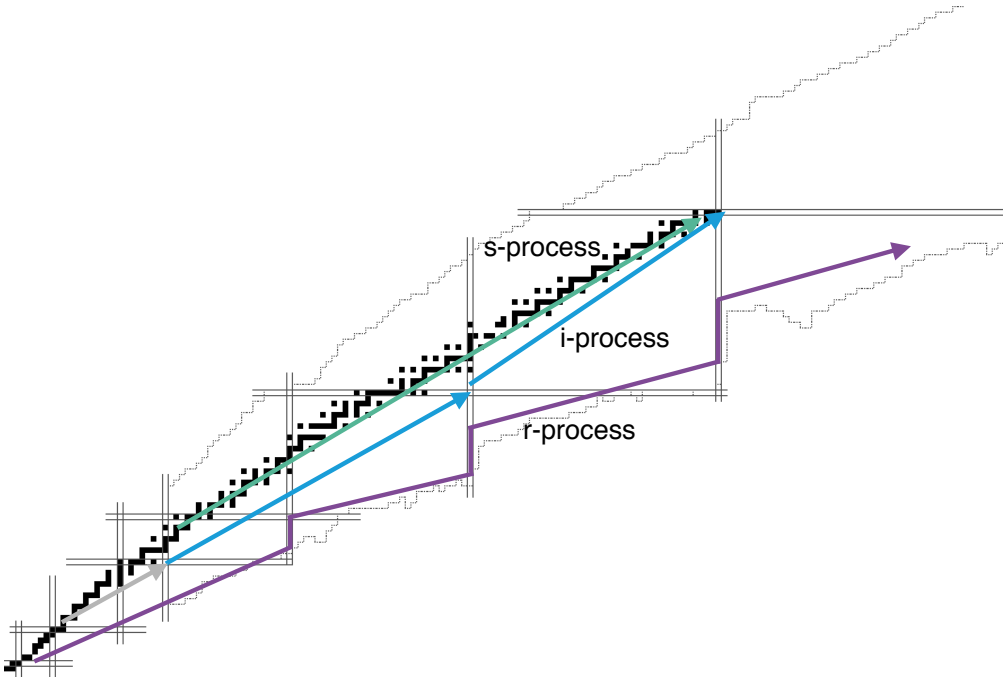

Figure 3.32: Schematic path of the *i* process. The seed isotopes lie between mass number 20 and 47 (grey arrow). Two plateaus form between the three double magic nuclei ^{48}Ca, ^{132}Sn (lower blue arrow) and ^{208}Pb (upper blue arrow). The *s*-process path (green arrow) and *r*-process path (purple arrow) are indicated as well.

Branching point	competing reactions	figure / table
^{34}P	^{34}P(β^-), ^{34}P(n,γ)	figure 3.33
^{66}Cu	^{66}Cu(β^-), ^{66}Cu(n,γ)	table A.8
^{75}Ga	^{75}Ga(β^-), ^{75}Ga(n,γ)	table A.8
^{75}Ge	^{75}Ge(β^-), ^{75}Ge(n,γ)	table A.8
^{103}Tc	^{103}Tc(β^-), ^{103}Tc(n,γ)	table A.8
^{114}Ag	^{114}Ag(β^-), ^{114}Ag(n,γ)	table A.8
^{115}Cd	^{115}Cd(β^-), ^{115}Cd(n,γ)	table A.8
^{195}Os	^{195}Os(β^-), ^{195}Os(n,γ)	table A.8
^{201}Pt	^{201}Pt(β^-), ^{201}Pt(n,γ)	table A.8

Table 3.23: Branching point isotopes and reactions during *i* process.

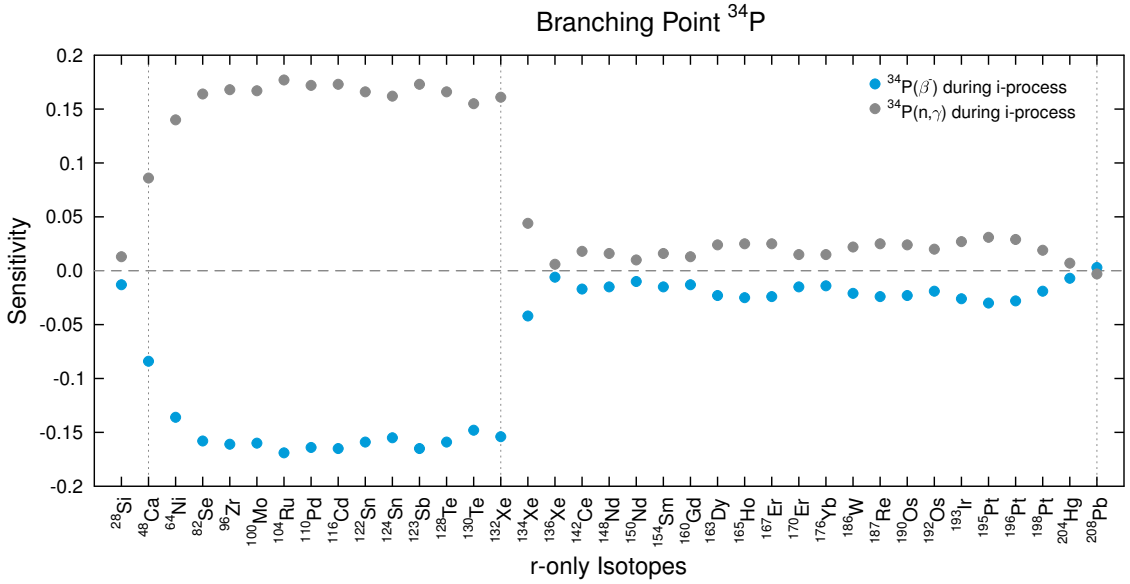

Figure 3.33: Branching point ^{34}P during the weak *s* process (table 3.23). The branching point ^{34}P is in the seed isotope region and affects the mass flow over the neutron magic barrier at neutron number 20 (see discussion on page 94). The increased neutron capture rate on ^{34}P competes with the depletion of other seed isotopes, like ^{28}Si, which has therefore a positive sensitivity.

Global sensitivities during the *i* process

In the following section, all global sensitivities during the *i* process are listed and classified between neutron donators (table 3.24), neutron poisons (table 3.25), competing captures (table 3.26) and bottle necks (table 3.27).

Neutron donators

With an increased neutron density during the *i* process more material surpasses the first double magic bottleneck ^{48}Ca, increasing the following plateau and lowering the abundance of seed isotopes. The second double magic bottleneck isotope ^{132}Sn is not sufficiently feeding its following plateau, and therefore the second plateau is depleted from the increased neutron density, resulting in a enhanced production of ^{208}Pb. The reaction producing neutrons is ^{13}C(α,n), which has the largest impact on the abundance distribution (figure 3.34). The ^{13}N(β^+) has a different sensitivity trend on the second plateau. The depletion of the second plateau does not propagate further than mass number 136, which results in an enhanced production of the following isotopes.

Rate	Figure	Feature
^{13}C(α,n)	figure 3.34	representative
^{15}O(β^+)	figure A.130	representative
^{13}N(β^+)	figure A.131	2. plateau

Table 3.24: Globally sensitive neutron donator reactions during *i* process. The reaction ^{13}N(β^+) has positive sensitivities of the second plateau except for ^{134}Xe and ^{136}Xe.

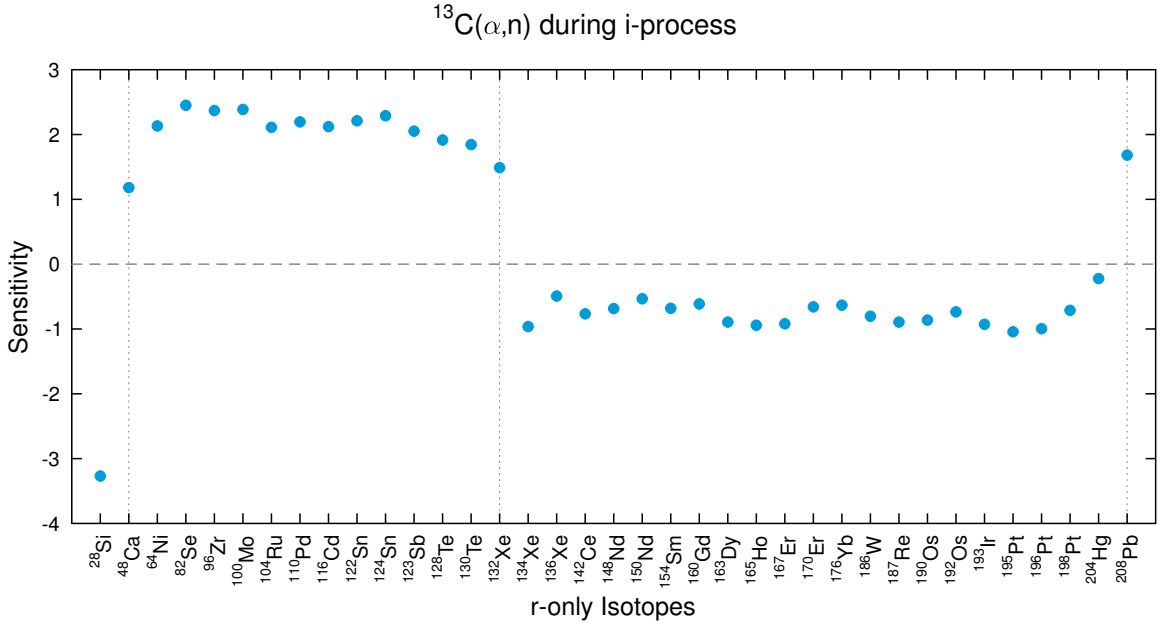

Figure 3.34: Neutron donator reaction ^{13}C(α,n) during the *i* process (table 3.24). ^{13}C(α,n) is the main neutron source during the *i* process, which has the highest sensitivities.

Neutron poisons

With enhanced neutron poison reactions the first plateau has negative sensitivities, whereas the second plateau is less depleted and has positive sensitivities. ^{208}Pb is less produced and the seed isotopes are less depleted. The ^{13}C(n,γ) reaction competes directly with the neutron source ^{13}C(α,n), which has therefore the highest sensitivities (figure 3.35).

Rate	Figure	Feature	Rate	Figure	Feature
^{13}C(n,γ)	figure 3.35	representative	^{13}C(p,γ)	figure A.132	low sensitivities
^{16}O(n,γ)	figure 2.8	representative	^{13}N(p,γ)	figure A.135	low sensitivities
^{12}C(n,γ)	figure A.134	representative	^{15}N(n,γ)	figure A.133	low sensitivities

Table 3.25: Globally sensitive neutron poison reactions during *i* process.

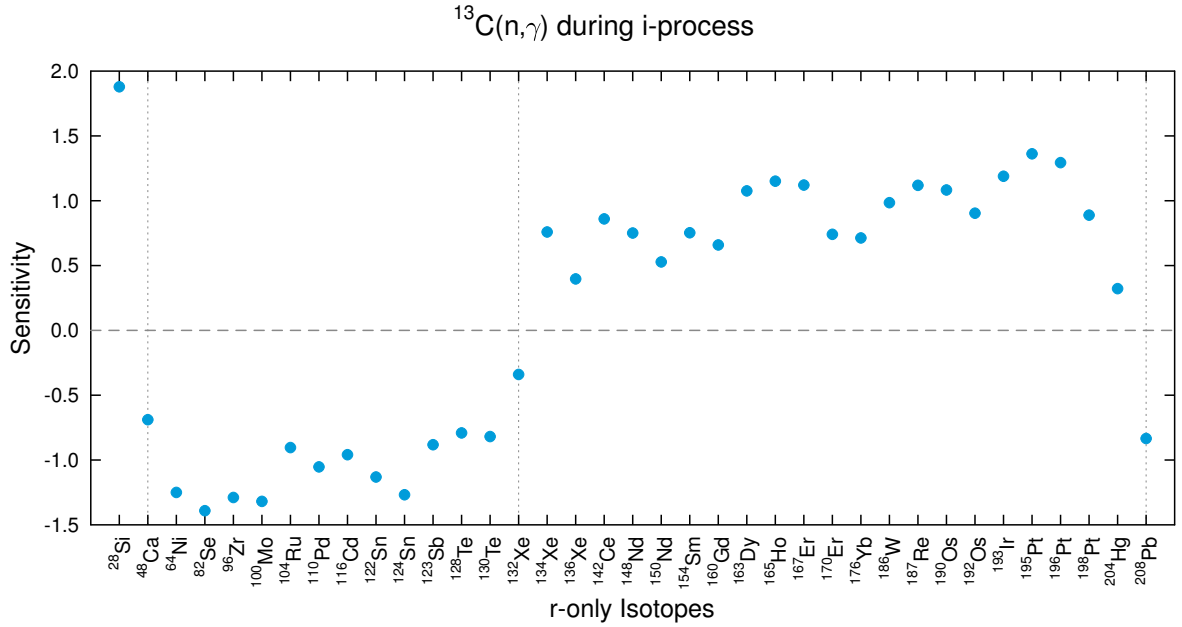

Figure 3.35: Neutron poison ^{13}C(n,γ) during the *i* process (table 3.25). The neutron capture on ^{13}C withdraws neutrons from the *i* process and depletes the neutron source ^{13}C itself.

Competing captures

Competing capture reactions during the *i* process are reactions on seed isotopes. An increased seed reaction increases in general all isotopes except for ^{208}Pb, which suffers from the decreased neutron per seed ratio. The necessity of seed isotopes shows that the *i* process is not primary. It could occur before the *s* process in a chemical evolution point of view as it only needs seed isotopes in the mass region between 20 and 47. The general impact of a seed isotope is an increased overcoming of the first double magic waiting point ^{48}Ca, with an increased first plateau, and a slightly increased second plateau, due to the lower neutron per seed ratio. ^{36}S(n,γ) is an example for such a seed isotope (figure 3.36).

Rate	Figure	Feature	Rate	Figure	Feature
^{36}S(n,γ)	figure 3.36	rep.	^{33}P(n,γ)	figure A.143	low sens.
^{34}S(n,γ)	figure A.138	rep.	^{37}Cl(n,γ)	figure A.144	low sens.
^{32}Si(n,γ)	figure A.139	rep.	^{42}Ar(n,γ)	figure A.145	low sens.
^{28}Si(p,γ)	figure A.136	low sens.	^{20}Ne(p,γ)	figure A.137	low sens.
^{30}Si(n,γ)	figure A.140	low sens.	^{31}Si(n,γ)	figure A.146	low sens.
^{37}S(β^-)	figure A.141	low sens.	^{39}Cl(n,γ)	figure A.147	low sens.
^{38}S(n,γ)	figure A.142	low sens.	^{47}Ca(n,γ)	figure A.148	low sens.

Table 3.26: Globally sensitive competing capture reactions during *i* process. All reactions show the same trend in the sensitivity. Three reactions reach sensitivity values above 0.4 and the remaining reactions, labeled with low sens., below 0.2.

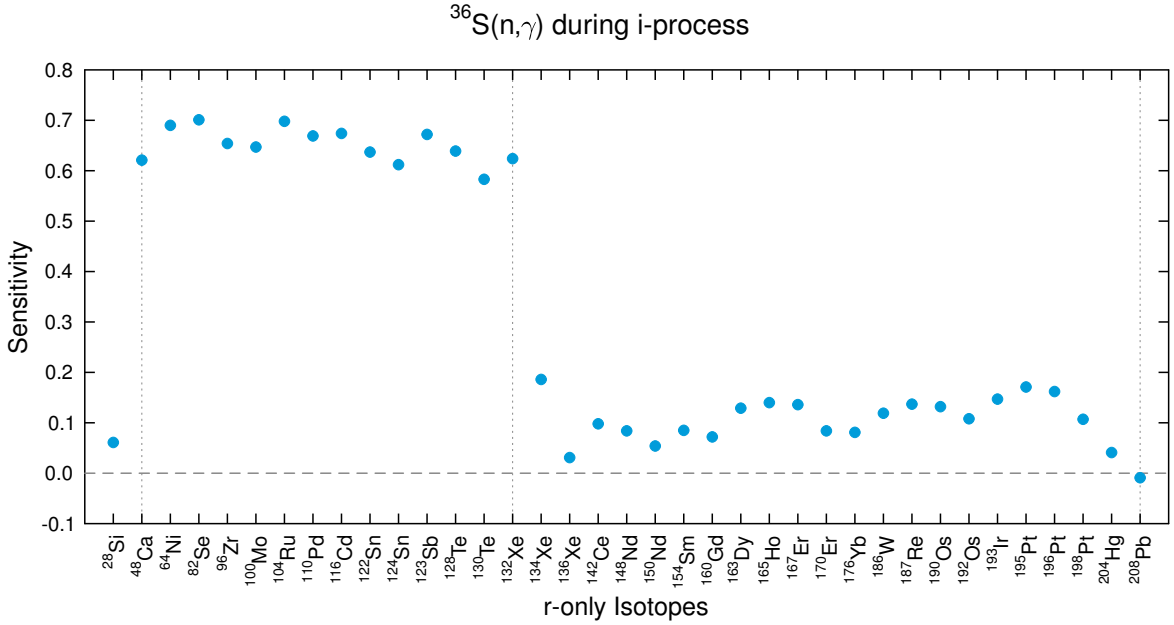

Figure 3.36: Competing capture ^{36}S(n,γ) during the *i* process (table 3.26). An increased neutron capture on the seed isotope ^{36}S results in a decreased depletion of ^{28}Si.

Bottleneck

Bottlenecks reactions during the *i* process are reactions responsible to overcome one of the two double magic isotope waiting points. Three reactions were identified to impact the overall evolution of the *i* process. ^{135}I(n,γ) is mainly responsible for the surpassing of the double magic nucleus ^{132}Sn (figure 3.37).

Rate	Figure	Feature
^{135}I(n,γ)	figure 3.37	2nd double magic
^{134}Te(β^-)	figure A.149	2nd double magic
^{48}Ca(n,γ)	figure A.150	1st double magic

Table 3.27: Globally sensitive bottleneck reactions during the *i* process. Two rates impact the surpassing of the second double magic isotope ^{132}Sn. The surpassing of the first double magic isotope ^{48}Ca is only impacted by its own neutron capture rate.

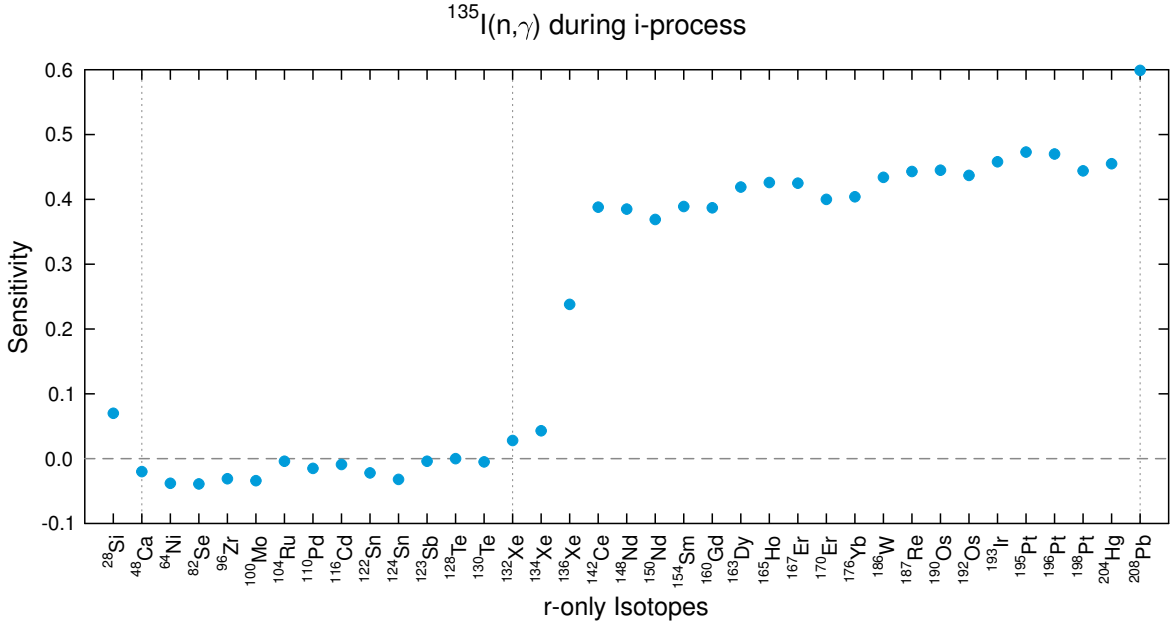

Figure 3.37: Bottleneck reaction ^{135}I(n,γ) during the *i* process (table 3.27). The neutron capture on ^{135}I is crucial for the entire evolution of the second plateau of the *i* process. An increased mass flux pass the second double magic isotope ^{132}Sn, competes with the mass flux pass the first double magic isotope ^{48}Ca.

Local sensitivities

The table A.8 in the appendix A.3 lists the local sensitivities of all isotopes for the *i* process. Almost every isotope is sensitive to a competing β-decay and neutron capture on an unstable isotope. This happens as the *i* process occurs away from the valley of stability and all stable isotopes are fed via β-decays. Each β-unstable isotope on the isobaric line is a potential "branching point" for a stable isotope.

3.4 Lighter element primary process – LEPP

The impact of the five scenarios on the LEPP isotopes was checked. A stricter ±0.5 sensitivity threshold was applied in order to list only the strongest sensitivities of LEPP isotopes.

LEPP isotopes during ^{13}C-pocket

During the ^{13}C-pocket no rate impacted the LEPP region globally. The following local rates only impacted one isotope at the time with a sensitivity above the threshold: ^{86}Sr(n,γ), ^{87}Sr(n,γ), ^{88}Sr(n,γ), ^{89}Y(n,γ), ^{90}Zr(n,γ), ^{91}Zr(n,γ), ^{92}Zr(n,γ), ^{94}Zr(n,γ), ^{95}Zr(n,γ), ^{95}Zr(β^-), ^{96}Zr(n,γ). The neutron capture rates of ^{86}Sr up to ^{94}Zr impact only the isotope, which captures the neutron (sensitivity around -1). The branching on ^{95}Zr and the neutron capture on ^{96}Zr impact the ^{96}Zr abundance.

LEPP isotopes during the TP

During the thermal pulse the global ^{22}Ne(α,n) rate has an impact on the LEPP isotopes (figure 3.38). The neutron source reaction ^{22}Ne(α,n) produces high sensitivity values of ^{86}Sr, ^{87}Sr and the maximum sensitivity of ^{96}Zr. Travaglio et al. 2004 showed that the the most deficient LEPP isotopes are the neutron-poor isotopes and that ^{96}Zr is sufficiently reproduced by GCE models. Therefore, an increased neutron density during the TP does not reproduce the LEPP characteristics. Furthermore, the same eleven locally sensitive rates from the ^{13}C-pocket showed an impact on different isotopes above the threshold (table A.3). The TP is not in equilibrium and therefore the neutron capture rates have a negative sensitivity to the isotope, which captures the neutron and a positive sensitivity to succeeding isotopes along the *s*-process path.

LEPP isotopes during the weak *s* process

During the weak *s* process eight globally sensitive rates impact the LEPP isotopes (table 3.28). Two of these rates, ^{22}Ne(α,n) (figure 3.39) and ^{68}Zn(n,γ) (figure A.157), produce sensitivity patterns, which would enhance mostly those LEPP isotopes, which are the most deficient. Therefore an increased ^{22}Ne(α,n) or ^{68}Zn(n,γ) rate during the weak *s* process is a good candidate for the LEPP. The other six globally sensitive rates produce sensitivities in the LEPP isotope region, but not in a way, which would reproduce the LEPP characteristics. Locally six rates (table A.4) surpass the sensitivity threshold: ^{87}Sr(n,γ), ^{89}Y(n,γ), ^{90}Zr(n,γ), ^{91}Zr(n,γ), ^{92}Zr(n,γ), ^{94}Zr(n,γ).

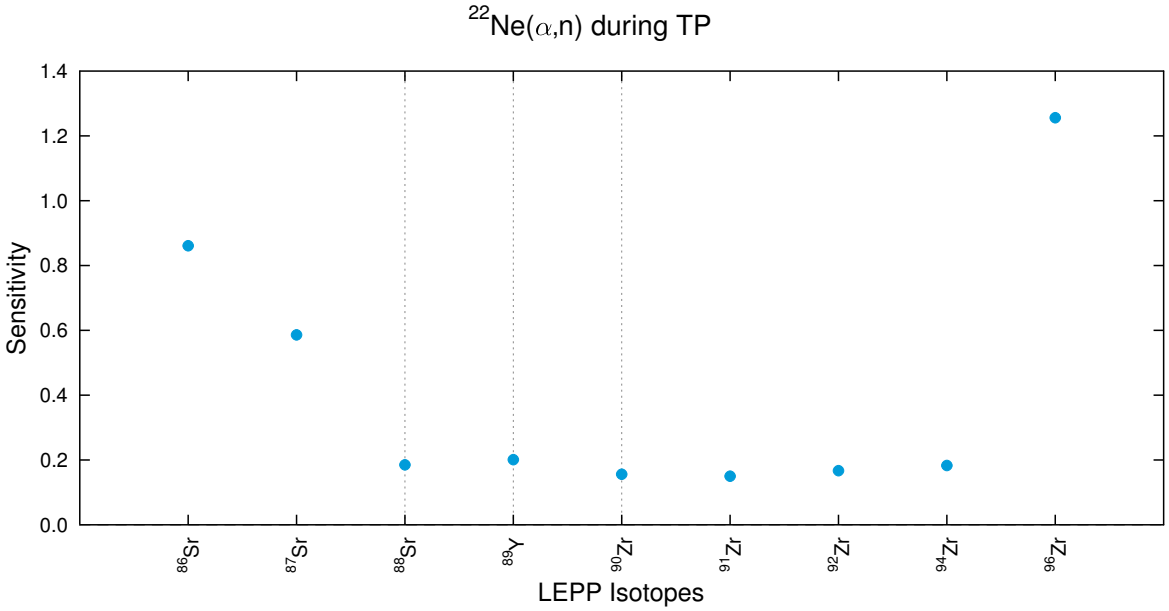

Figure 3.38: Impact of the neutron source reaction ^{22}Ne(α,n) during the TP on LEPP isotopes. The sensitivities of the LEPP isotopes are plotted. The reaction produces high sensitivities of ^{86}Sr, ^{87}Sr and the maximum sensitivity of ^{96}Zr. Therefore, an increased neutron density during the TP does not reproduce the LEPP characteristics. The vertical dotted grey lines symbolize neutron magic nuclei.

Rate	Figure	Feature	Rate	Figure	Feature
^{22}Ne(α,n)	figure 3.39	LEPP-like	^{25}Mg(n,γ)	figure A.155	different
Triple-α process	figure A.151	different	^{56}Fe(n,γ)	figure A.156	different
^{12}C(α,γ)	figure A.152	different	^{68}Zn(n,γ)	figure A.157	LEPP-like
^{22}Ne(α,γ)	figure A.153	different	^{16}O(α,γ)	figure A.158	different
^{88}Sr(n,γ)	figure A.154	different			

Table 3.28: Globally sensitive rates on LEPP isotopes during weak *s* process. Two rates produce "LEPP-like" sensitivities, which is an increased sensitivity of the neutron-poor LEPP isotopes, and the remaining rates produce different sensitivities, which would not exclusively enhance the deficient LEPP isotope production.

LEPP ISOTOPES DURING THE CONVECTIVE CARBON SHELL BURNING

During the convective carbon burning, only the ^{95}Zr(n,γ) reaction affects the ^{96}Zr abundance above the threshold (table A.6).

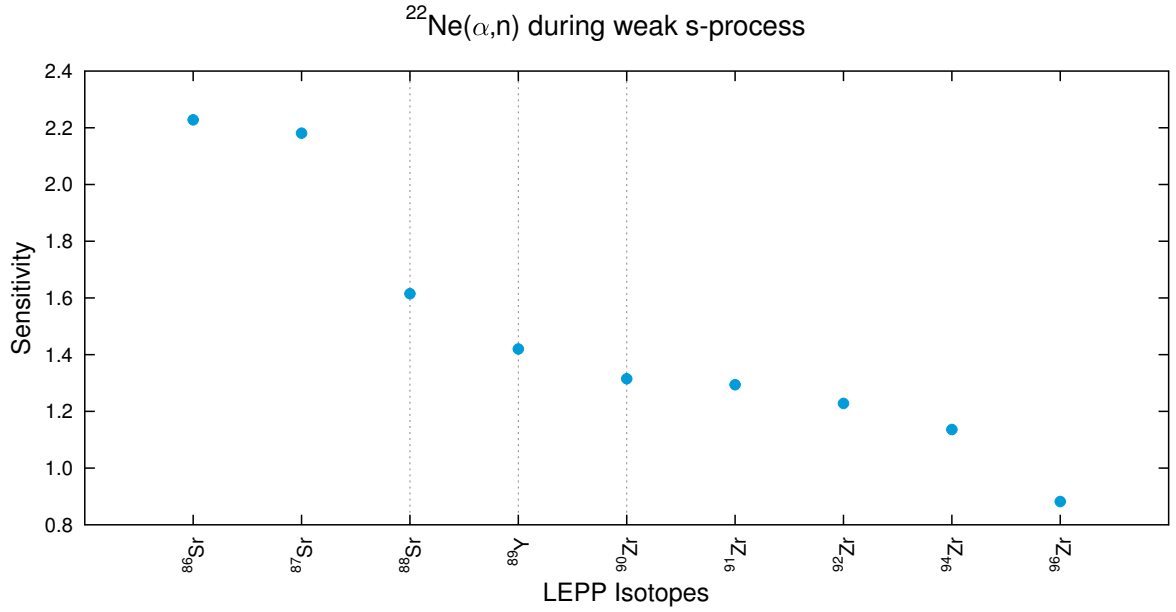

Figure 3.39: Impact of the neutron source reaction ^{22}Ne(α,n) during the weak *s* process on LEPP isotopes (table 3.28). The sensitivities of the LEPP isotopes are plotted. This rate produces a sensitivity pattern, which matches the LEPP characteristics and is therefore, a candidate for the LEPP. The vertical dotted grey lines symbolize neutron magic nuclei.

LEPP ISOTOPES DURING THE *i* PROCESS

During the *i* process, only five isotopes of the LEPP region are involved in nucleosynthesis: ^{88}Sr, ^{89}Y, ^{92}Zr, ^{94}Zr, ^{96}Zr. These isotopes are affected globally by six different rates (table 3.29). Among these isotopes, the neutron donator reaction ^{13}C(α,n) (figure 3.40) exhibits the most significant influence. Due to the high neutron densities compared to the *s* process, 23 local rates (table A.8) affect the evolution of always one LEPP isotope. These are the (n,γ)-rates of: ^{88}Kr, ^{89}Kr, ^{88}Rb, ^{89}Rb, ^{88}Sr, ^{89}Sr, ^{92}Sr, ^{89}Y, ^{92}Y, ^{94}Y, ^{96}Y, ^{92}Zr, ^{94}Zr, ^{96}Zr and the β^--decay rates of: ^{88}Kr, ^{89}Kr, ^{88}Rb, ^{89}Rb, ^{89}Sr, ^{92}Sr, ^{92}Y, ^{94}Y, ^{96}Y. The *i* process can be ruled out as LEPP candidate, because it depletes the neutron-poor LEPP isotopes completely and only produces neutron-rich LEPP isotopes. Which is the opposite nucleosynthesis effect of what is needed in order to account for the LEPP.

Rate	Figure	Rate	Figure
^{13}C(α,n)	figure 3.40	^{36}S(n,γ)	figure A.161
^{13}C(n,γ)	figure A.159	^{16}O(n,γ)	figure A.162
^{13}N(β^+)	figure A.160	^{34}S(n,γ)	figure A.163

Table 3.29: Globally sensitive rates on LEPP isotopes during *i* process. All rates impact only the neutron-rich LEPP isotopes and neutron-poor LEPP isotopes are not produced in the *i* process. Therefore these rates can be ruled out as LEPP candidate.

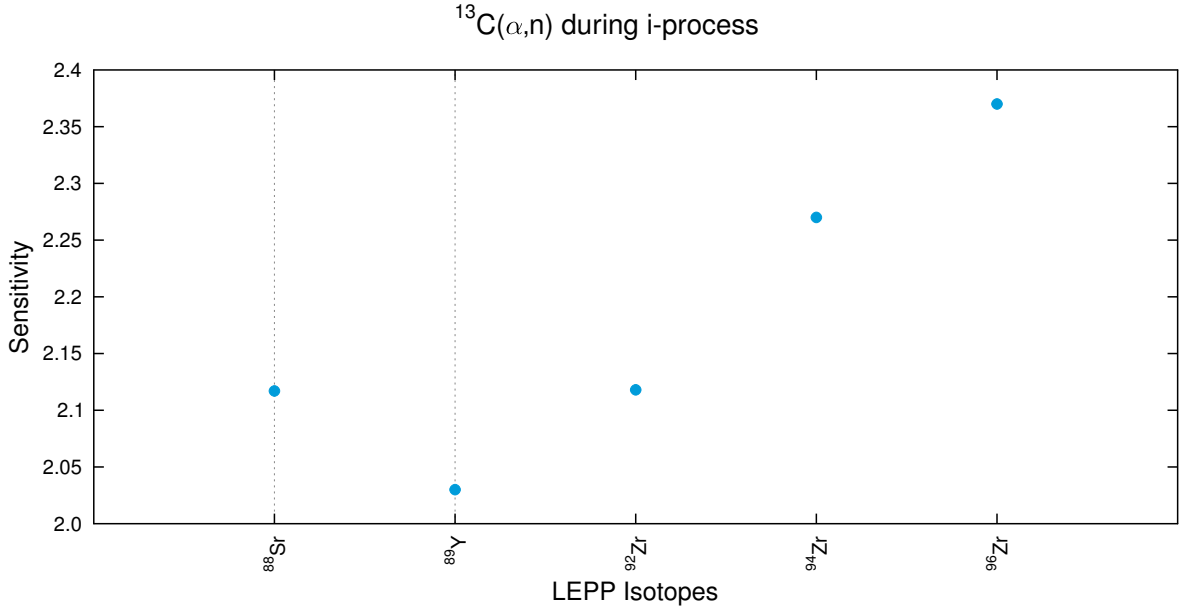

Figure 3.40: Impact of the neutron source reaction ^{13}C(α,n) during the *i* process on LEPP isotopes. (table 3.29). The sensitivities of the LEPP isotopes are plotted. The neutron-poor LEPP isotopes are not involved in the *i*-process nucleosynthesis and only the neutron-rich LEPP isotopes are produced. Therefore, this rate can be ruled out as LEPP candidate. The vertical dotted grey lines symbolize neutron magic nuclei.

4 Conclusion and outlook

4.1 Conclusion

Full network sensitivity studies for the main and weak component of the *s* process and the *i* process have been performed. All neutron sources and poisons have been identified as well as branching points, seed isotopes and bottleneck isotopes for each scenario. Furthermore, a list with up to three locally affecting rates on the stable isotopes is provided for each scenario. The four studied scenarios for the *s* process, namely the ^{13}C-pocket, thermal pulse, weak *s* process and convective carbon shell burning, were all extracted from stellar models and post processed with the tools from the NuGrid collaboration. The classical use of the parametrized standard case from Gallino et al. 1998, which is still widely adopted, should, therefore, be replaced by these state-of-the-art sensitivity studies. The new set of simulations uses thermodynamical input from stellar models and is therfore more consistent.

The *s* process is one of the processes responsible for the formation of elements heavier than iron. Via neutron captures and β-decays, the mass flux of the *s* process follows the valley of stability on the chart of nuclides up to the endpoint of the *s* process ^{209}Bi. The *s* process is divided into three components. The weak component, which is responsible for the production of isotopes in the mass region of 60 to 90, the main component of the *s* process produces of isotopes from mass number 90 up to lead, and the strong component, which accounts for the production of the lead peak.

The **main component** of the *s* process occurs during the thermally-pulsing asymptotic giant-branch phase of low-mass stars. In this phase two alternating *s*-process sites exist. The ^{13}C-pocket, which is a ^{13}C-rich layer, results from the ingestion of hydrogen into the helium shell after the thermal pulse, producing ^{13}C via the reaction chain ^{12}C(p,γ)^{13}N(β^+)^{13}C. The reaction

^{13}C(α,n) then generates free neutrons for the *s* process. This happens during the hydrogen shell burning. The hydrogen burning feeds the helium shell up to a point where helium burning ignites, resulting in a thermonuclear runaway. This thermal pulse opens the neutron source ^{22}Ne(α,n), which is available due to the reaction chain ^{14}N(α,γ)^{18}F(β^+)^{18}O(α,γ)^{22}Ne. The high power output from the convective thermal pulse forces the star to expand, while interrupting the hydrogen burning. After the extinction of the thermal pulse, the star contracts again, generating the next ^{13}C-pocket and allowing hydrogen shell burning to proceed.

The simulations conducted in the framework of this thesis show that the *s*-process nucleosynthesis in the **^{13}C-pocket** is driven by the neutron source ^{13}C(α,n). Twenty-seven branching points could be detected, whereas only three of these were impacting *s*-only isotopes. These three branching points, ^{64}Cu, ^{85}Kr and ^{93}Zr, are either isotopes from the iron peak, the weak component or the transition area from the weak to the main component. The neutron magic and branching sensitive isotope ^{87}Rb turned out to be a good indicator of the neutron density during the ^{13}C-pocket. ^{93}Nb is produced via the β^--decay of ^{93}Zr, which results with its long half-lives in a delayed production of ^{93}Nb. The second production channel for ^{93}Nb, the ^{93}Mo(β^+) reaction, which is fed from the *p*-nucleus ^{92}Mo (figure 4.1) turned out to be negligible for the overall ^{93}Nb production. The proton magic isotope ^{120}Sn acts as seed nucleus for succeeding isotopes along the *s*-process path. Bottlenecks are neutron-magic isotopes from the first and second *s*-process peak.

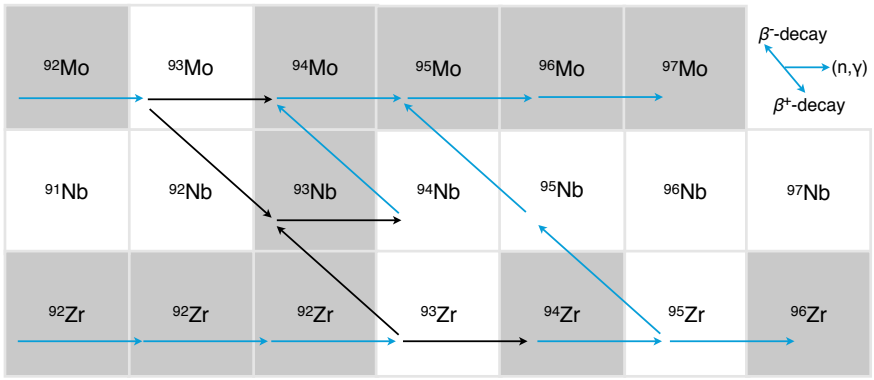

Figure 4.1: Possible production and destruction channels of ^{93}Nb. The β^--decay of ^{93}Zr and the β^+-decay of ^{93}Mo are possible production channels for ^{93}Nb. These two production channels compete with their respective neutron captures. ^{93}Nb is depleted by neutron captures.

The **thermal pulse** (TP) consists of a short and stronger neutron irradiation than the ^{13}C-pocket driven by the ^{22}Ne(α,n) reaction, which has been seen in the simulations. A superposition of production tails on different seed isotopes along all mass regimes produces the TP nucleosynthesis pattern, with the main production peaks in the weak *s*-process region and on the lead peak. During the thermal pulse, 31 branching points were detected, of, which seven could be identified in

the global sensitivity plots. The branching sensitive ^{93}Nb behaves as expected on neutron donators with a negative sensitivity and on neutron poisons with a positive sensitivity. ^{110}Cd indicates the neutron densities as well and behaves as if it was sensitive to the branching point ^{109}Pd. But in the local sensitivity table, ^{110}Cd does not show a sensitivity above the 0.1 threshold on ^{109}Pd. So ^{110}Cd is more likely a seed isotope for heavier nuclei. The *s* process during the thermal pulse is strongly dependent on the initial seed distribution, but has a minor overall impact on the main component. Branching points, which are not active during the ^{13}C-pocket, like ^{185}W, could act as indicators for the TP, if the affected isotopes (^{186}W and ^{187}Re) can be measured in grains.

The **weak component** of the s-process occurs in massive stars during the helium core burning and the carbon shell burning. The neutrons for the *s* process in massive stars result primarily from the ^{22}Ne(α,n) reaction.

The simulations show that the **weak *s* process**, consisting of the helium core burning and carbon shell burning, contributes to mass numbers between 60 and almost 100. Heavier isotopes are only involved because they act as seed. The mass flux does not pass the second neutron magic peak at neutron number 82. Twenty-seven branching points were identified during the weak *s* process in the mass region from 56 to 142, with eleven branching points showing an impact on the global abundance distribution. The higher neutron densities during the weak *s* process enable branchings at isotopes like ^{90}Y and ^{91}Y, which affect the ^{90}Zr to ^{92}Zr ratio and ^{91}Zr to ^{92}Zr ratio respectively. Four reactions affect the production of neutrons, either directly or indirectly. The two direct reactions are ^{22}Ne(α,n) and ^{17}O(α,n) and the other two (^{12}C(p,γ) and ^{13}N(β^+)) impact the ^{13}C(α,n) source, which itself is not sensitive since the bottleneck of this neutron source are the production channels of ^{13}C. Six additional recycled neutron poisons supply previously absorbed neutrons or α-particles but do not show a clear trend in the sensitivity. The reaction ^{12}C(^{12}C,n)^{23}Mg [Arnett and Truran 1969] was not important.

The **convective carbon shell burning** affects only isotopic ratios in the weak component, which has been seen in the simulations. The overall impact on the abundance distribution is negligible and only branchings affect the overall distribution. Twenty branching points were detected, four of, which can be recognized in the global sensitivity plots. The neutron density is indicated by ^{87}Rb and ^{93}Nb. ^{93}Nb is not sensitive to the branching reactions of ^{93}Zr, but of its own depletion via neutron captures. The three neutron sources during the convective carbon shell burning are ^{21}Ne, ^{22}Ne, and ^{25}Mg with their respective (α, n) reactions. The ^{12}C(^{12}C,n)^{23}Mg reaction is not an important neutron source.

The ***i* process** is believed to occur in very late thermal pulses, as a result of hydrogen ingestion into the thermal pulse, which generates the neutron source of the ^{13}C-pocket at thermodynamical conditions of the thermal pulse. The simulations show that the *i* process is driven by the neutron source ^{13}C(α,n). Two double magic nuclei, ^{48}Ca and ^{132}Sn, determine the nucleosynthesis of suc-

ceeding isotopes. Three reactions around these two isotopes are of special importance, namely ^{48}Ca(n,γ), ^{134}Te(β^-), and ^{135}I(n,γ). Seed isotopes for the *i* process lie in the mass region 20 to 47. Nine branching points affected other isotopes than their isobars. One branching point, ^{34}P, lies in the seed isotope region and affects the overall evolution.

The **LEPP** isotopes, Sr, Y and Zr, are not globally affected during the ^{13}C-pocket or the convective carbon shell burning. The convective carbon shell burning only impacts the branching at ^{95}Zr. In the TP the sensitivity to the neutron source ^{22}Ne(α,n) for production of three (^{86}Sr, ^{87}Sr and ^{96}Zr) LEPP isotopes is above the ±0.5 threshold. The two particularly interesting scenarios for the LEPP isotopes, which have strong impact are the weak *s* process and the *i* process. In these two scenarios the respective neutron sources (^{22}Ne(α,n) and ^{13}C(α,n)) show sensitivites in excess of two. Furthermore, these two scenarios can be tested against each other, since the weak *s* process affects all nine stable Sr, Y and Zr isotopes and the *i* process only affects five neutron-rich isotopes because of the high neutron densities. Travaglio et al. 2004 show that especially the neutron-poor LEPP isotopes are deficient (table 1.2), thus, the *i* process can be ruled out for the LEPP isotope production in favor of the weak *s* process. Travaglio et al. 2004 use the weak *s*-process contribution from Raiteri et al. 1993, which differs strongly from the weak *s*-process trajectory from Frischknecht 2007. Raiteri et al. 1993 account for the Sr isotopes a mean weak *s*-process contribution of 9% for Y = 5% and for Zr a mean contribution of 2%. The reported effect from Travaglio et al. 2004, i.e., that the weak *s*-process mass flux stops at the neutron magic ^{88}Sr, is in contrast to the results of the simulations performed in this thesis as seen in figure 3.16.

4.2 Outlook

The foundation of systematic sensitivity studies with the simulation tools of the NuGrid collaboration was developed within this work and should be applied to other scenarios like the *p* or *r* process.

Some scenarios, like the weak *s* process, turned out to be very sensitive to the initial abundance distribution. The sensitivity studies could as well be extended to initial abundances. This should be faster than the network sensitivity studies as less simulations have to be performed. During the weak *s* process, almost every isotope acts as a bottleneck and branching points affect these isotopes, which then combine their effects on the sensitivity.

^{93}Nb is produced by the temperature-dependent β^--decay rate of ^{93}Zr [Takahashi and Yokoi 1987]. During the ^{13}C-pocket and the helium burning of the weak *s* process, the long half-lives of the β^--decay result in a delayed production of ^{93}Nb. A final time step could be added to the simulations that waits for the remaining β-decays to occur. ^{85}Kr indicates the neutron

densities properly, but has not yet been measured experimentally and the predicted MACS have uncertainties of ~ 80 % [Dillmann et al. 2006].

The *i* process should be refined with a trajectory extract from a stellar model, if more evidence for such a process is found. Sensitivity studies could be reduced to the rates identified in this thesis, if the neutron densities and life times of the trajectories are of the same order of magnitude.

The LEPP discussion should reconsider the weak *s* process as a possible origin. Processes with higher neutron densities, like the *i* process, affect only neutron-rich LEPP isotopes, whereas the neutron poor are deficient (table 1.2). The main component to the *s* process produces LEPP isotopes but has no globally impacting rate in that region. The weak *s* process seems to match the LEPP signature. The neutron source ^{22}Ne(α,n) has a strong impact, in particular to the neutron-poor LEPP isotopes, and a production of these isotopes, which was ruled out by Travaglio et al. 2004 could be observed in the simulations. A state-of-the-art multi zone model with convection should be used to perform a sensitivity study of the nine identified rates with global impact (table 3.28) on the LEPP isotopes.

The sensitivity studies performed in this work can be used as a compendium for refining nuclear astrophysics experiments in the future. Currently, different facilities are under construction, which will enable previously unfeasible experiments. The n_TOF EAR-2 project [Guerrero et al. 2013] is expected to start operation in 2014 [Reifarth et al. 2014]. FRANZ is currently under development and will be the strongest neutron source in the astrophysically interesting energy region in the world [Reifarth et al. 2009]. FAIR will enable experiments with radioactive isotopes, even far away from the valley of stability [Reifarth et al. 2013], enabling experiments concerning the *i* process.

5 Zusammenfassung

Die vorliegende Arbeit untersucht den Einfluss einzelner Raten auf Netzwerkrechnung in verschiedenen *s*-Prozess- und *i*-Prozess-Szenarien. Für diese Sensitivitätsstudien wurden mehr als 250 000 Simulationen durchgeführt und ausgewertet. Die Simulationen basieren auf modernen *s*-Prozess-Modellen, mit Bedingungen für den *s*-Prozess aus aktuellen Sternmodellen [Pignatari et al. 2013].

Der *s*-Prozess wird zusammen mit anderen Prozessen für die Erzeugung von Elementen schwerer als Eisen im Sonnensystem verantwortlich gemacht. Durch Neutroneneinfänge und β-Zerfälle entwickelt sich der *s*-Prozess Massenfluß am Tal der Stabilität bis zum letzten stabilen Element ^{209}Bi (Abbildungen 1.5, 1.6 und 1.7). Dies geschieht in fortgeschrittenen Brennphasen von sowohl leichten als auch massereichen Sternen. Der *s*-Prozess wird in drei Komponenten eingeteilt, die jeweils einen anderen Einfluss auf die Häufigkeitsverteilung haben [Clayton et al. 1961, Seeger et al. 1965]. Die schwache Komponente ist für die Erzeugung der Isotope mit Massenzahl zwischen ~ 60 und ~ 90, die Hauptkomponente für Isotope mit Massenzahl größer ~ 90 und die starke Komponente für die Häufigkeiten von und um Blei verantwortlich (Abbildungen 1.8 und 1.9) [Käppeler et al. 1982, Käppeler et al. 1989, Cui et al. 2007].

Die schwache Komponente des *s*-Prozesses findet in schweren Sternen während des zentralen Heliumbrennes und anschließend während des Kohlenstoffschalenbrennens statt [Arcoragi et al. 1991, Pignatari et al. 2006]. Die Reaktionen, die dafür Neutronen freisetzen, sind ^{22}Ne(α,n)^{25}Mg und ^{12}C(^{12}C,n)^{23}Mg [Arnett und Truran 1969, Reifarth et al. 2014]. Für die Simulationen der schwachen Komponente wurden zwei verschiedene Trajektorien verwendet. Eine Trajektorie simuliert die vollständige schwache Komponente durch beide relevanten Brennphasen (Abbildungen 3.15 und 3.16) [Frischknecht 2007, Hirschi et al. 2008], während die andere Trajektorie nur das Kohlenstoffschalenbrennen betrachtet (Abbildungen 3.24 und 3.25) [Pignatari et al. 2013].

Die Hauptkomponente des *s*-Prozesses wird der thermisch-pulsierenden asymptotischer Riesenast (TP-AGB) Phase von leichten Sternen zugeschrieben (Abbildung 1.13) [Busso et al. 1999]. In dieser Phase füttert das Wasserstoffschalenbrennen die Heliumschale über dem degenerierten Kohlenstoff-Sauerstoff Kern (Abbildungen 1.14, 2.1 und 2.2) bis diese genug Masse erlangt, um explosionsartig einen Großteil des Heliums zu verbrennen (thermischer Puls) [Schwarzschild und Härm 1965]. Durch die hohe Energiefreisetzung während dieses thermischen Pulses kommt das Wasserstoffschalenbrennen nach Expansion des Sterns zum erliegen [Straniero et al. 2006]. Die Reaktion ^{14}N(α,γ)^{18}F(β^+)^{18}O(α,γ)^{22}Ne, welche am übrigen ^{14}N des CNO-Zyklus stattfindet (Kapitel 1.2.3), erzeugt das nötige ^{22}Ne, welches mit einem weiteren α-Einfang freie Neutronen während des thermischen Pulses über den Kanal ^{22}Ne(α,n)^{25}Mg abgibt (Abbildung 2.3). Dies erzeugt Neutronendichten von 10^{10-12} cm^{-3} bei Temperaturen von $\sim 3 \cdot 10^8$ K. Die Dauer des konvektiven thermischen Pulses beträgt ca. 100 Jahre.
Nach dem Erlöschen des thermischen Pulses kontrahiert der Stern wieder, was ein Eindringen von Protonen aus der Wasserstoffhülle in die Heliumschale zur Folge hat. Die Protonen werden an ^{12}C, dem Produkt des vorangegangenen Heliumbrennens, eingefangen und erzeugen über die Reaktion ^{12}C(p,γ)^{13}N(β^+)^{13}C die Neutronenquelle ^{13}C, welche ebenfalls über einen α-Einfang freie Neutronen über die Reaktion ^{13}C(α,n) bereitstellt. Dies passiert nachdem die Kontraktion des Sterns zum Erliegen gekommen ist und das Wasserstoffschalenbrennen wieder eingesetzt hat (Abbildung 2.4) [Gallino et al. 1988, Herwig 2005].
Für die Simulation der Hauptkomponente wurde eine Trajektorie für die ^{13}C(α,n)-Phase zwischen dem vorletzten und letzten thermischen Pulses eines 3 Sonnenmassen Sterns mit solarer Metallizität extrahiert (Abbildungen 3.1 und 3.2). Für den thermischen Puls wurden erst sensitive Raten mit einer Trajektorie durch den tiefsten Punkt des letzten thermischen Pulses gesucht und diese dann mit einem Multizonen-Modell simuliert (Abbildungen 3.8, A.17 und 3.9).

Die starke Komponente des *s*-Prozesses entspricht der Hauptkomponente bei Sternen niedriger Metallizität (Gleichung 2.5). Die Hauptkomponente startet bei Metallizitäten ab [Fe/H] ~ -0.66 und die starke Komponente wird Metallizitäten von [Fe/H] ~ -1.16 bis [Fe/H] ~ -0.66 zugeordnet [Cui et al. 2007]. Die niedrigere Metallizität resultiert in einem höheren Verhältnis von Neutronen zu Saatkernen, welches eine verstärkte Produktion der Isotope um Blei zur Folge hat [Gallino et al. 1998, Travaglio et al. 2001, Sneden et al. 2008]. Alle Raten die in der Hauptkomponente einen Einfluss auf die Neutronendichte haben, sind deshalb ebenfalls relevant für die starke Komponente, welche durch ihren geringen globalen Einfluss nicht in einer gesonderten Sensitivitätsstudie betrachtet wird.

Der *i*-Prozess [Cowan und Rose 1977] oder Neutroneneinfang mit mittleren Neutronendichten wurde als mögliche Erklärung für beobachtete Häufigkeitsverteilungen von Sakurais Objekt [Herwig et al. 2006, Herwig et al. 2011] und für gemessene Isotopenverhältnisse in prä-solarer Materie [Fujiya et al. 2013, Jadhav et al. 2013, Liu et al. 2014] postuliert. In dreidimensio-

nalen Hydrodynamik-Simulationen eines sehr späten thermischen Pulses von Sakurais Objekt [Asplund et al. 1998, Asplund et al. 1999, Asplund 1999] wurde von Herwig et al. 2011 ein Einschuss von Wasserstoff in den thermischen Puls beobachtet [Schwarzschild und Härm 1967]. Die Protonen werden vom Kohlenstoff über die Reaktion ^{12}C(p,γ)^{13}N eingefangen. Der β-Zerfall über die Reaktion ^{13}N(β^+)^{13}C passiert auf der gleichen Zeitskala wie die Konvektion zum tiefsten Punkt des thermischen Pulses. Dort werden durch einen α-Einfang freie Neutronen über die Neutronenquelle ^{13}C(α,n) bereitgestellt. Für die Simulationen wurde eine Ad-hoc-Trajektorie von der NuGrid-Kollaboration [http://www.nugridstars.org/] verwendet (Abbildungen 3.31 und 3.32). In dieser Trajektorie werden Neutronendichten von 10^{15} cm^{-3} bei Temperaturen von $2 \cdot 10^8$ K erreicht.

Der von Travaglio et al. 2004 angeregte primäre Prozess zur Erzeugung leichter Kerne (LEPP) bedarf noch genauerer Untersuchung [Pignatari et al. 2010]. Eine Überhäufigkeit von Sr, Y und Zr wird im Sonnensystem beobachtet, welche nicht durch galaktisch chemische Evolution von allen bisher bekannten Prozessen erklärt werden kann [Bisterzo et al. 2012]. Da diese Kerne sowohl im *s*-Prozess als auch im *i*-Prozess produziert werden, wurden die Sensitivitätsstudien zusätzlich für alle LEPP-Isotope gesondert ausgewertet (Kapitel 3.4).

Die umfangreichen Simulationen in dieser Arbeit decken alle Raten der jeweiligen Nukleosynthesenetzwerke ab. Reaktionen, die einen globalen Einfluss auf das jeweilige Szenario haben, sind in dieser Arbeit graphisch dargestellt (Kapitel 2.3.2). Alle Raten mit einem lokalen Einfluss sind in Sensitivitätstabellen (Kapitel 2.3.3) im Anhang gelistet. Verzweigungspunkte, die zur Einschränkung von Parametern dienen können (siehe Seite 21), wurden aus den Sensitivitätstabellen und Plots gesondert herausgesucht.

Für die ^{13}C(α,n)-Phase wurde keine weitere Neutronenquelle identifiziert. Der *s*-Prozess während der ^{13}C(α,n)-Phase wird von 19 Raten beeinflusst. Es wurden insgesamt 27 Verzweigungspunkte identifiziert. Besonders der Verzweigungspunkt ^{85}Kr reagiert sehr sensibel auf die Neutronendichte, welche über den neutronenmagischen Kern ^{87}Rb angezeigt wird (Abbildung A.1). Das protonenmagische Isotop ^{120}Sn dient als Saatkern für im *s*-Prozess folgende Isotope. Neutronenmagische Kerne erzeugen die lokalen Maxima in den solaren Häufigkeiten (Abbildung 1.1) und erweisen sich als Flaschenhals bei der Erzeugung nachfolgender Isotope.

Der thermische Puls ist eine kurze Zeitspanne mit höheren Neutronendichten als die ^{13}C(α,n)-Phase. Allein die Reaktion ^{22}Ne(α,n) liefert die freien Neutronen. Der generelle Verlauf des *s*-Prozesses während des thermischen Pulses wird von 26 Raten beeinflusst. Neutroneneinfänge an verschiedenen Saatkernen entlang aller Massenregionen erzeugt das Muster der Nukleosynthese im thermischen Puls. Interessanterweise findet die Hauptproduktion in der Massenregion der schwachen und starken Komponente statt (Abbildung 3.9). 31 Verzweigungspunkte wurden identifiziert, von denen diejenigen, die nicht während der ^{13}C(α,n)-Phase aktiv sind, als reiner

Indikator für den thermischen Puls dienen könnten. ^{110}Cd dient als Saatkern für schwerere Isotope. Generell ist der Einfluss des thermischen Pulses sehr abhängig von der Saatkernverteilung, aber vernachlässigbar gering im Vergleich zur ^{13}C(α,n)-Phase.

Die Simulationen der schwache Komponente zeigen Abweichungen im Vergleich zu der Beschreibung in der Literatur. Sowohl in der allgemeinen Simulation beider Brennphasen als auch in der Simulation des reinen Kohlenstoffschalenbrennens wurde die Neutronenquelle ^{12}C(^{12}C,n) nicht bestätigt (Abbildung 5.1). Diese hat eine zu geringe Sensitivität, als dass sie als Neutronenquelle bezeichnet werden könnte. Während der allgemeinen Simulation beider Brennphasen ist die Neutronenquelle ^{22}Ne(α,n) die dominante, neben ^{17}O(α,n) und zwei Reaktionen zur Produktion von ^{13}C. Sechs weitere Reaktionen liefern Neutronen oder α-Teilchen. Von diesen ist ^{12}C(^{12}C,α) die einzige Kohlenstoff-Kohlenstoff Reaktion mit signifikanten Einfluß auf die Endhäufigkeiten. Des weiteren ist die Produktion von Isotopen während der schwachen Komponente nicht auf Massenzahlen kleiner 90 begrenzt, sondern erreicht fast Massenzahl 100. In der Massenregion von 56 bis 142 wurden 27 Verzweigungspunkte identifiziert, wie z.B. ^{90}Y und ^{91}Y.

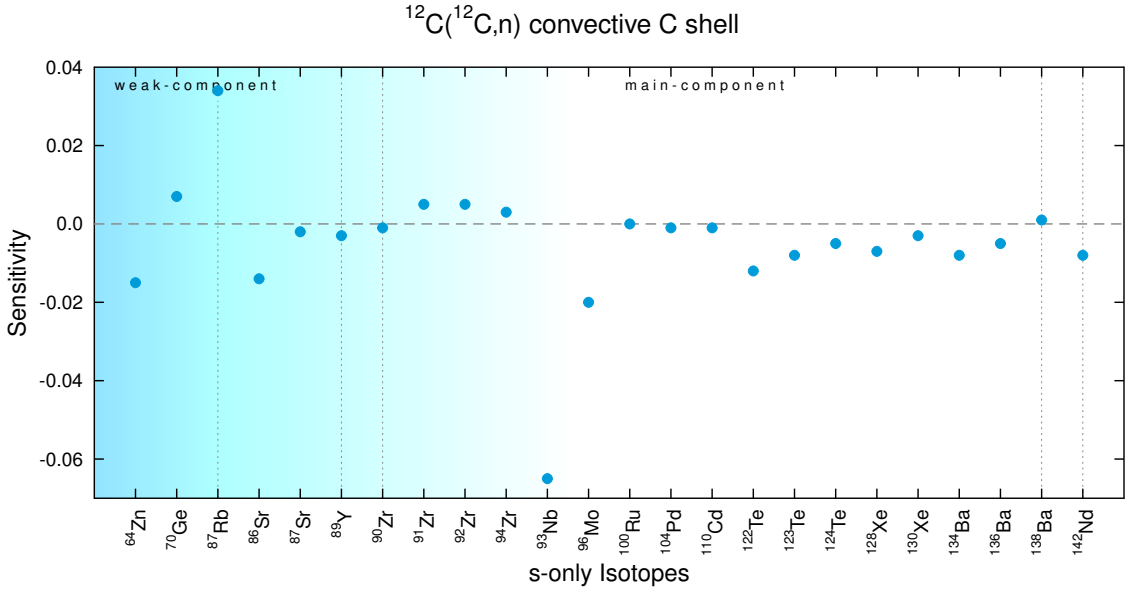

Abbildung 5.1: Sensitivität der erwarteten Neutronenquelle ^{12}C(^{12}C,n)^{23}Mg während des Kohlenstoffschalenbrennens. Die Sensitivitäten sind zu gering, um die Reaktion als dominante Neutronenquelle für die schwache Komponente zu bezeichnen. Die vertikalen, gestrichelten Linien symbolisieren neutronenmagische Kerne.

In den Simulationen des Kohlenstoffschalenbrennens wurde die Reaktion ^{21}Ne(α,n) als Hauptneutronenquelle identifiziert. ^{22}Ne(α,n) und ^{25}Mg(α,n) liefern ebenfalls einen Beitrag. Der generelle Einfluss des Kohlenstoffschalenbrennens auf die Häufigkeitsverteilung ist minimal. Einzig

Verzweigungspunkte erreichen Sensitivitäten, die die Schwelle von 0.1 überschreiten. 20 Verzweigungspunkte wurden während des Kohlenstoffschalenbrennens identifiziert.

Der *i*-Prozess nutzt als Neutronenquelle die ^{13}C(α,n) Reaktion. Durch die Protoneneinmischung in den sehr späten thermischen Puls mit hohen Temperaturen findet neben der Erzeugung von ^{13}C auch der CNO-Zyklus statt. Dieser liefert ebenfalls α-Teilchen für die Neutronenquelle. Die zwei doppelmagischen Kerne ^{48}Ca und ^{132}Sn bestimmen die *i*-Prozess-Nukleosynthese. Drei Reaktionen die zur Überwindung dieser Kerne dienen, sind deshalb besonders wichtig: ^{48}Ca(n,γ), ^{134}Te(β^-) und ^{135}I(n,γ). Saatkerne für den *i*-Prozess liegen zwischen Massenzahl 20 und 47. Durch den Massenfluss parallel zum Tal der Stabilität dient fast jeder β-instabile Kern als Verzweigungspunkt für einen stabilen Kern entlang der Isobaren. Neun Verzweigungspunkte beeinflussen Isotope, die nicht die gleiche Massenzahl haben. Die hier verwendete Trajektorie des *i*-Prozesses erzeugt zwei Plateaus. Das erste Plateau liegt zwischen ^{48}Ca und ^{132}Sn. Das zweite Plateau liegt zwischen ^{132}Sn und ^{208}Pb (Abbildung 5.2).

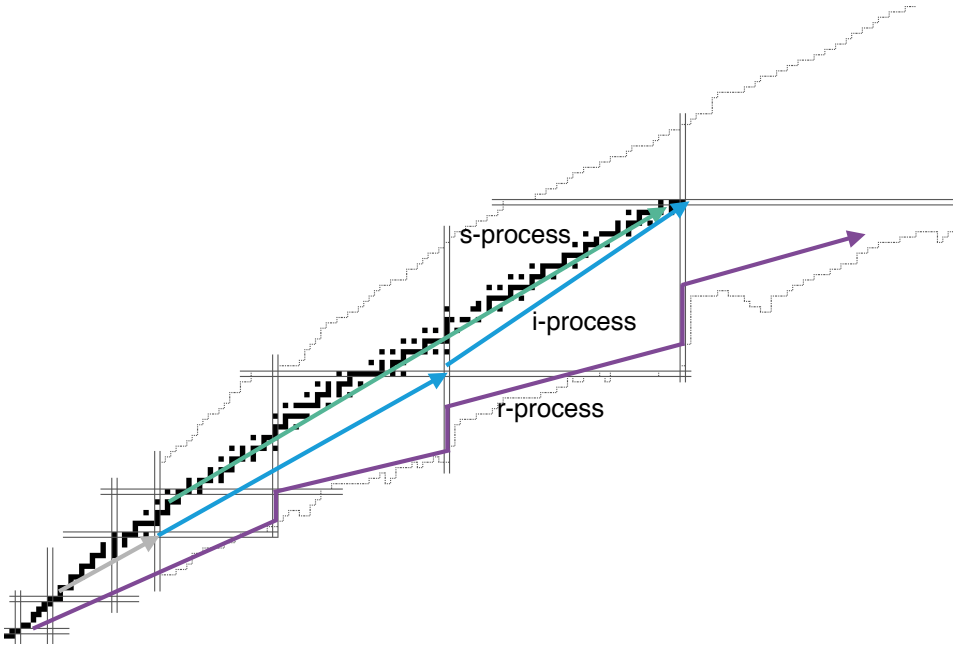

Abbildung 5.2: Schematischer *i*-Prozesspfad. Die Saatkerne, die der *i*-Prozess benötigt, liegen zwischen Massenzahl 20 und 47 (grauer Pfeil). Zwei Plateaus bilden sich zwischen den drei doppelmagischen Kernen ^{48}Ca, ^{132}Sn (unterer blauer Pfeil) und ^{208}Pb (oberer blauer Pfeil). Der *s*-Prozesspfad (grüner Pfeil) und *r*-Prozesspfad (lila Pfeil) sind ebenfalls eingezeichnet.

Die Analyse der LEPP-Isotope zeigt, dass von allen hier untersuchten Prozessen die schwache Komponente des *s*-Prozesses am besten auf den LEPP passt (Abbildung 5.3 und Tabelle 1.2). Da diese Komponente noch zusätzlich durch von der Literatur abweichendes Verhalten überrascht hat, sollte in diesem Fall die galaktisch chemische Evolution explizit mit neuen Modellen weiter untersucht werden.

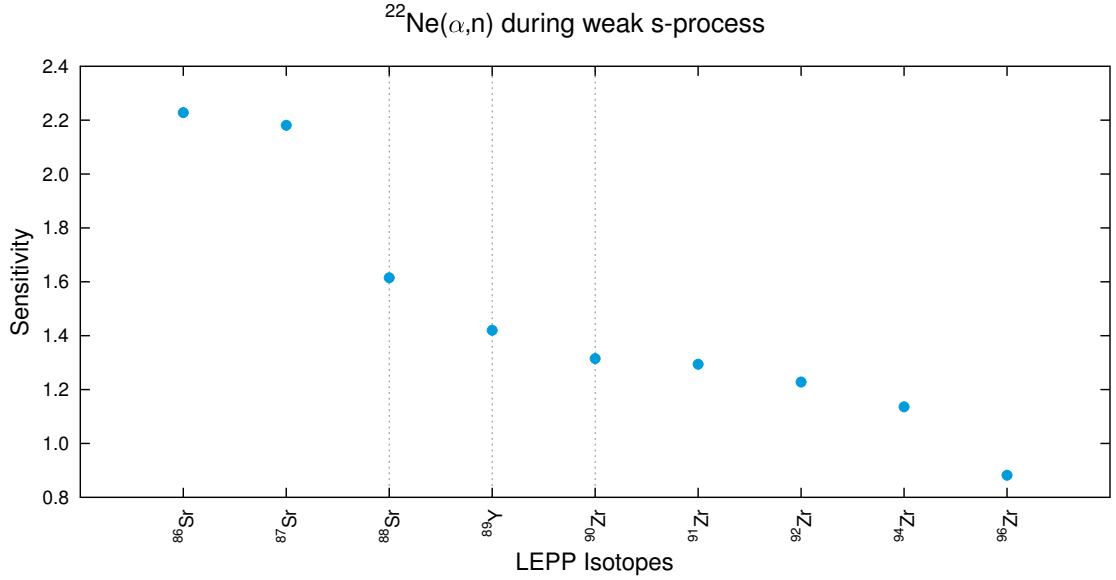

Abbildung 5.3: Sensitivität der Neutronenquelle ^{22}Ne(α,n) während der schwachen Komponente des *s*-Prozesses auf die LEPP-Isotope. Die Sensitivät der LEPP-Isotope ist graphisch dargestellt. Die ^{22}Ne(α,n) Rate produziert ein Sensitivitätsmuster, welches auf den LEPP passt (Tabelle 1.2). Die vertikalen, gestrichelten Linien symbolisieren neutronenmagische Kerne. Einen vergleichbaren Sensitivitätstrend zeigt die ^{68}Zn(n,γ) Rate (Abbildung A.157).

Bibliography

Adelberger, E. G., A. García, R. G. H. Robertson, K. A. Snover, A. B. Balantekin, K. Heeger, M. J. Ramsey-Musolf, D. Bemmerer, A. Junghans, C. A. Bertulani, J.-W. Chen, H. Costantini, P. Prati, M. Couder, E. Uberseder, et al. (2011). "Solar fusion cross sections. II. The pp chain and CNO cycles". In: *Reviews of Modern Physics* 83, pp. 195–246. DOI: 10.1103/RevModPhys.83.195. arXiv: 1004.2318 [nucl-ex].

Anders, E. and N. Grevesse (1989). "Abundances of the elements - Meteoritic and solar". In: *Geochimica Cosmochimica Acta* 53, pp. 197–214. DOI: 10.1016/0016-7037(89)90286-X.

Anders, E. and E. Zinner (1993). "Interstellar grains in primitive meteorites - Diamond, silicon carbide, and graphite". In: *Meteoritics* 28, pp. 490–514.

Angulo, C., M. Arnould, M. Rayet, P. Descouvemont, D. Baye, C. Leclercq-Willain, A. Coc, S. Barhoumi, P. Aguer, C. Rolfs, R. Kunz, J. Hammer, A. Mayer, T. Paradellis, S. Kossionides, et al. (1999). "A compilation of charged-particle induced thermonuclear reaction rates". In: *Nuclear Physics A* 656.1, pp. 3 –183. DOI: 10.1016/S0375-9474(99)00030-5.

Arcoragi, J.-P., N. Langer, and M. Arnould (1991). "Neutron capture nucleosynthesis and the evolution of 15 and 30 solar mass mass-losing stars. II - The core carbon-burning phase". In: *Astronomy and Astrophysics* 249, pp. 134–140.

Arnett, W. D. and J. W. Truran (1969). "Carbon-Burning Nucleosynthesis at Constant Temperature". In: *Astrophysical Journal* 157, p. 339. DOI: 10.1086/150072.

Arnould, M. and S. Goriely (2003). "The p-process of stellar nucleosynthesis: astrophysics and nuclear physics status". In: *Physics Reports* 384.1–2, pp. 1 –84. DOI: 10.1016/S0370-1573(03)00242-4.

Asplund, M. (1999). "Sakurai's object – stellar evolution in real time". In: *Asymptotic Giant Branch Stars*. Ed. by T. Le Bertre, A. Lebre, and C. Waelkens. Vol. 191. IAU Symposium, p. 481.

Asplund, M., B. Gustafsson, N. Kameswara Rao, and D. L. Lambert (1998). "Abundance similarities between the RCrB star V854Cen and the born-again Sakurai's object". In: *Astronomy and Astrophysics* 332, pp. 651–660. eprint: astro-ph/9801068.

Asplund, M., D. L. Lambert, T. Kipper, D. Pollacco, and M. D. Shetrone (1999). "The rapid evolution of the born-again giant Sakurai's object". In: *Astronomy and Astrophysics* 343, pp. 507–518. eprint: astro-ph/9811208.

Audi, G., O. Bersillon, J. Blachot, and A. Wapstra (2003). "The Nubase evaluation of nuclear and decay properties". In: *Nuclear Physics A* 729.1. The 2003 {NUBASE} and Atomic Mass Evaluations, pp. 3 –128. DOI: 10.1016/j.nuclphysa.2003.11.001.

Bao, Z., H. Beer, F. Kaeppler, F. Voss, K. Wisshak, and T. Rauscher (2000). "NEUTRON CROSS SECTIONS FOR NUCLEOSYNTHESIS STUDIES". In: *Atomic Data and Nuclear Data Tables* 76.1, pp. 70 –154. DOI: 10.1006/adnd.2000.0838.

Bennett, M. E. (2011). "Carbon burning and hydrodynamic mixing uncertainties in stellar models". PhD thesis. University of Keele.

Bernatowicz, T., G. Fraundorf, T. Ming, E. Anders, B. Wopenka, E. Zinner, and P. Fraundorf (1987). "Evidence for interstellar SiC in the Murray carbonaceous meteorite". In: *Nature* 330, pp. 728–730. DOI: 10.1038/330728a0.

Bertolli, M. G., F. Herwig, M. Pignatari, and T. Kawano (2013). "Systematic and correlated nuclear uncertainties in the i-process at the neutron shell closure N = 82". In: *ArXiv e-prints*. arXiv: 1310.4578 [astro-ph.SR].

Bethe, H. A. (1939). "Energy Production in Stars". In: *Physical Review* 55 (1), pp. 103–103. DOI: 10.1103/PhysRev.55.103.

Bethe, H. A. (1990). "Supernova mechanisms". In: *Reviews of Modern Physics* 62, pp. 801–866. DOI: 10.1103/RevModPhys.62.801.

Bethe, H. A. and C. L. Critchfield (1938). "The Formation of Deuterons by Proton Combination". In: *Physical Review* 54 (4), pp. 248–254. DOI: 10.1103/PhysRev.54.248.

Bisterzo, S., R. Gallino, O. Straniero, S. Cristallo, and F. Käppeler (2010). "s-Process in low-metallicity stars - I. Theoretical predictions". In: *Monthly Notices of the Royal Astronomy Society* 404, pp. 1529–1544. DOI: 10.1111/j.1365-2966.2010.16369.x. arXiv: 1001.5376 [astro-ph.SR].

Bisterzo, S., R. Gallino, O. Straniero, S. Cristallo, and F. Käppeler (2012). "The s-process in low-metallicity stars - III. Individual analysis of CEMP-s and CEMP-s/r with asymptotic giant branch models". In: *Monthly Notices of the Royal Astronomy Society* 422, pp. 849–884. DOI: 10.1111/j.1365-2966.2012.20670.x. arXiv: 1201.6198 [astro-ph.SR].

Burbidge, E. M., G. R. Burbidge, W. A. Fowler, and F. Hoyle (1957). "Synthesis of the Elements in Stars". In: *Reviews of Modern Physics* 29, pp. 547–650. DOI: 10.1103/RevModPhys.29.547.

Busso, M., R. Gallino, and G. J. Wasserburg (1999). "Nucleosynthesis in Asymptotic Giant Branch Stars: Relevance for Galactic Enrichment and Solar System Formation". In: *Annual*

Review of Astronomy and Astrophysics 37, pp. 239–309. DOI: 10.1146/annurev.astro.37.1.239.

Carroll, B. W. and D. A. Ostlie (2007). *An introduction to modern astrophysics*. San Francisco: Pearson Addison-Wesley.

Clayton, D. D., W. A. Fowler, T. E. Hull, and B. A. Zimmerman (1961). "Neutron capture chains in heavy element synthesis". In: *Annals of Physics* 12.3, pp. 331 –408. DOI: 10.1016/0003-4916(61)90067-7.

Cowan, J. J. and W. K. Rose (1977). "Production of C-14 and neutrons in red giants". In: *Astrophysical Journal* 212, pp. 149–158. DOI: 10.1086/155030.

Cui, W., W. Zhang, and B. Zhang (2007). "Evolution of the Distribution of Neutron Exposures in the Galaxy Disc: An Analytical Model". In: *Journal of Astrophysics and Astronomy* 28, pp. 55–66. DOI: 10.1007/s12036-007-0006-6.

Dillmann, I., M. Heil, F. Käppeler, R. Plag, T. Rauscher, and F.-K. Thielemann (2006). "KADoNiS-The Karlsruhe Astrophysical Database of Nucleosynthesis in Stars". In: *Capture Gamma-Ray Spectroscopy and Related Topics*. Ed. by A. Woehr and A. Aprahamian. Vol. 819. American Institute of Physics Conference Series, pp. 123–127. DOI: 10.1063/1.2187846.

Freytag, B., H.-G. Ludwig, and M. Steffen (1996). "Hydrodynamical models of stellar convection. The role of overshoot in DA white dwarfs, A-type stars, and the Sun." In: *Astronomy and Astrophysics* 313, pp. 497–516.

Frischknecht, U. (2007). "S-Process Nucleosynthesis in Massive Stars". MA thesis. University of Basel.

Fröhlich, C., G. Martínez-Pinedo, M. Liebendörfer, F.-K. Thielemann, E. Bravo, W. R. Hix, K. Langanke, and N. T. Zinner (2006). "Neutrino-Induced Nucleosynthesis of $A > 64$ Nuclei: The νp Process". In: *Phys. Rev. Lett.* 96 (14), p. 142502. DOI: 10.1103/PhysRevLett.96.142502.

Fujiya, W., P. Hoppe, E. Zinner, M. Pignatari, and F. Herwig (2013). "Evidence for Radiogenic Sulfur-32 in Type AB Presolar Silicon Carbide Grains?" In: *Astrophysical Journal, Letters* 776, L29, p. L29. DOI: 10.1088/2041-8205/776/2/L29. arXiv: 1310.0485 [astro-ph.SR].

Fuller, G. M., W. A. Fowler, and M. J. Newman (1985). "Stellar weak interaction rates for intermediate-mass nuclei. IV - Interpolation procedures for rapidly varying lepton capture rates using effective log (ft)-values". In: *Astrophysical Journal* 293, pp. 1–16. DOI: 10.1086/163208.

Gallino, R., M. Busso, G. Picchio, C. M. Raiteri, and A. Renzini (1988). "On the role of low-mass asymptotic giant branch stars in producing a solar system distribution of s-process isotopes". In: *Astrophysical Journal, Letters* 334, pp. L45–L49. DOI: 10.1086/185309.

Gallino, R., C. Arlandini, M. Busso, M. Lugaro, C. Travaglio, O. Straniero, A. Chieffi, and M. Limongi (1998). "Evolution and Nucleosynthesis in Low-Mass Asymptotic Giant Branch

Stars. II. Neutron Capture and the S-Process". In: *Astrophysical Journal* 497, pp. 388–403. DOI: 10.1086/305437.

Glorius, J. (2013). "Experimental studies of optical potentials for p-process nucleosynthesis". PhD thesis. Goethe-Universität Frankfurt.

Goswami, A. and N. Prantzos (2000). "Abundance evolution of intermediate mass elements (C to Zn) in the Milky Way halo and disk". In: *Astronomy and Astrophysics* 359, pp. 191–212. eprint: astro-ph/0005179.

Guerrero, C., A. Tsinganis, E. Berthoumieux, M. Barbagallo, F. Belloni, F. Gunsing, C. Weiß, E. Chiaveri, M. Calviani, V. Vlachoudis, S. Altstadt, S. Andriamonje, J. Andrzejewski, L. Audouin, V. Bécares, et al. (2013). "Performance of the neutron time-of-flight facility n_TOF at CERN". In: *The European Physical Journal A* 49.2, 27. URL: http://dx.doi.org/10.1140/epja/i2013-13027-6.

Herwig, F. (2001). "Internal mixing and surface abundance of [WC]-CSPN". In: *Astrophysics and Space Science* 275, pp. 15–26. eprint: astro-ph/9912353.

Herwig, F. (2006). "AGB stars evolution and nucleosynthesis". In: *International Symposium on Nuclear Astrophysics - Nuclei in the Cosmos*.

Herwig, F., T. Bloecker, D. Schoenberner, and M. El Eid (1997). "Stellar evolution of low and intermediate-mass stars. IV. Hydrodynamically-based overshoot and nucleosynthesis in AGB stars." In: *Astronomy and Astrophysics* 324, pp. L81–L84. eprint: astro-ph/9706122.

Herwig, F., B. Freytag, R. M. Hueckstaedt, and F. X. Timmes (2006). "Hydrodynamic Simulations of He Shell Flash Convection". In: *Astrophysical Journal* 642, pp. 1057–1074. DOI: 10.1086/501119. eprint: astro-ph/0601164.

Herwig, F., B. Freytag, T. Fuchs, J. P. Hansen, R. M. Hueckstaedt, D. H. Porter, F. X. Timmes, and P. R. Woodward (2007). "Convective and Non-Convective Mixing in AGB Stars". In: *Why Galaxies Care About AGB Stars: Their Importance as Actors and Probes*. Ed. by F. Kerschbaum, C. Charbonnel, and R. F. Wing. Vol. 378. Astronomical Society of the Pacific Conference Series, p. 43. arXiv: 0709.0197.

Herwig, F., S. Diehl, C. L. Fryer, R. Hirschi, A. Hungerford, G. Magkotsios, M. Pignatari, G. Rockefeller, F. X. Timmes, P. Young, and M. E. Bennet (2008). "Nucleosynthesis simulations for a wide range of nuclear production sites from NuGrid". In: *Nuclei in the Cosmos (NIC X)*. arXiv: 0811.4653.

Herwig, F., M. Pignatari, P. R. Woodward, D. H. Porter, G. Rockefeller, C. L. Fryer, M. Bennett, and R. Hirschi (2011). "Convective-reactive Proton-^{12}C Combustion in Sakurai's Object (V4334 Sagittarii) and Implications for the Evolution and Yields from the First Generations of Stars". In: *Astrophysical Journal* 727, 89, p. 89. DOI: 10.1088/0004-637X/727/2/89. arXiv: 1002.2241 [astro-ph.SR].

Herwig, F. (2005). "EVOLUTION OF ASYMPTOTIC GIANT BRANCH STARS". In: *Annual Review of Astronomy and Astrophysics* 43.1, pp. 435–479. DOI: 10.1146/annurev.astro.

43.072103.150600. eprint: http://dx.doi.org/10.1146/annurev.astro.43.072103.150600.

Hirschi, R., U. Frischknecht, M. Pignatari, F. K. Thielemann, M. E. Bennet, S. Diehl, C. L. Fryer, F. Herwig, A. Hungerford, G. Magkotsios, G. Rockefeller, F. X. Timmes, and P. Young (2008). "NuGrid: s process in massive stars". In: *Nuclei in the Cosmos (NIC X)*. arXiv: 0811.4654.

Iben Jr., I. (1985). "The life and times of an intermediate mass star - In isolation/in a close binary". In: *Quarterly Journal of the RAS* 26, pp. 1–39.

Iben Jr., I. and A. Renzini (1983). "Asymptotic giant branch evolution and beyond". In: *Annual Review of Astronomy and Astrophysics* 21, pp. 271–342. DOI: 10.1146/annurev.aa.21.090183.001415.

Iliadis, C., J. M. D'Auria, S. Starrfield, W. J. Thompson, and M. Wiescher (2001). "Proton-induced Thermonuclear Reaction Rates for A=20-40 Nuclei". In: *Astrophysical Journal, Supplement* 134, pp. 151–171. DOI: 10.1086/320364.

Jadhav, M., M. Pignatari, F. Herwig, E. Zinner, R. Gallino, and G. R. Huss (2013). "Relics of Ancient Post-AGB Stars in a Primitive Meteorite". In: *Astrophysical Journal, Letters* 777, L27, p. L27. DOI: 10.1088/2041-8205/777/2/L27. arXiv: 1310.2679 [astro-ph.EP].

Käppeler, F. (2012). "Stellar neutron capture rates and the s process". In: *European Physical Journal Web of Conferences*. Vol. 21. European Physical Journal Web of Conferences, p. 3006. DOI: 10.1051/epjconf/20122103006.

Käppeler, F., H. Beer, K. Wisshak, D. D. Clayton, R. L. Macklin, and R. A. Ward (1982). "S-process studies in the light of new experimental cross sections - Distribution of neutron fluences and r-process residuals". In: *Astrophysical Journal* 257, pp. 821–846. DOI: 10.1086/160033.

Käppeler, F., H. Beer, and K. Wisshak (1989). "s-process nucleosynthesis-nuclear physics and the classical model". In: *Reports on Progress in Physics* 52, pp. 945–1013. DOI: 10.1088/0034-4885/52/8/002.

Käppeler, F., S. Bisterzo, R. Gallino, M. Heil, M. Pignatari, R. Reifarth, O. Straniero, S. Walter, N. Winckler, and K. Wisshak (2009). "Time-Scales of the s Process: from Minutes to Ages". In: *Publications of the Astronomical Society of Australia* 26, pp. 209–216. DOI: 10.1071/AS08052. arXiv: 0912.0098 [astro-ph.SR].

Käppeler, F., R. Gallino, S. Bisterzo, and W. Aoki (2011). "The s process: Nuclear physics, stellar models, and observations". In: *Reviews of Modern Physics* 83, pp. 157–194. DOI: 10.1103/RevModPhys.83.157. arXiv: 1012.5218 [astro-ph.SR].

Karakas, A. and J. C. Lattanzio (2007). "Stellar Models and Yields of Asymptotic Giant Branch Stars". In: *Publications of the Astronomical Society of Australia* 24, pp. 103–117. DOI: 10.1071/AS07021. arXiv: 0708.4385.

Kobayashi, C., H. Umeda, K. Nomoto, N. Tominaga, and T. Ohkubo (2006). "Galactic Chemical Evolution: Carbon through Zinc". In: *Astrophysical Journal* 653, pp. 1145–1171. DOI: 10.1086/508914. eprint: astro-ph/0608688.

Kratz, K.-L., J.-P. Bitouzet, F.-K. Thielemann, P. Moeller, and B. Pfeiffer (1993). "Isotopic r-process abundances and nuclear structure far from stability - Implications for the r-process mechanism". In: *Astrophysical Journal* 403, pp. 216–238. DOI: 10.1086/172196.

Langer, N., M. F. El Eid, and K. J. Fricke (1985). "Evolution of massive stars with semiconvective diffusion". In: *Astronomy and Astrophysics* 145, pp. 179–191.

Limongi, M., O. Straniero, and A. Chieffi (2000). "Massive Stars in the Range 13-25 M_{solar}: Evolution and Nucleosynthesis. II. The Solar Metallicity Models". In: *Astrophysical Journal, Supplement* 129, pp. 625–664. DOI: 10.1086/313424. eprint: astro-ph/0003401.

Liu, N., M. R. Savina, A. M. Davis, R. Gallino, O. Straniero, F. Gyngard, M. J. Pellin, D. G. Willingham, N. Dauphas, M. Pignatari, S. Bisterzo, S. Cristallo, and F. Herwig (2014). "Barium Isotopic Composition of Mainstream Silicon Carbides from Murchison: Constraints for s-process Nucleosynthesis in Asymptotic Giant Branch Stars". In: *Astrophysical Journal* 786, 66, p. 66. DOI: 10.1088/0004-637X/786/1/66. arXiv: 1403.4336 [astro-ph.SR].

Lodders, K. (2003). "Solar System Abundances and Condensation Temperatures of the Elements". In: *Astrophysical Journal* 591, pp. 1220–1247. DOI: 10.1086/375492.

Lodders, K., H. Palme, and H.-P. Gail (2009). "Abundances of the Elements in the Solar System". In: *Landolt Börnstein*, p. 44. DOI: 10.1007/978-3-540-88055-4_34. arXiv: 0901.1149 [astro-ph.EP].

Merrill, P. W. (1952). "Spectroscopic Observations of Stars of Class". In: *Astrophysical Journal* 116, p. 21. DOI: 10.1086/145589.

Oda, T., M. Hino, K. Muto, M. Takahara, and K. Sato (1994). "Rate Tables for the Weak Processes of sd-Shell Nuclei in Stellar Matter". In: *Atomic Data and Nuclear Data Tables* 56, pp. 231–403. DOI: 10.1006/adnd.1994.1007.

Olive, K. A., G. Steigman, and T. P. Walker (2000). "Primordial nucleosynthesis: theory and observations". In: *Physics Reports* 333, pp. 389–407. DOI: 10.1016/S0370-1573(00)00031-4. eprint: astro-ph/9905320.

Paxton, B., L. Bildsten, A. Dotter, F. Herwig, P. Lesaffre, and F. Timmes (2011). "Modules for Experiments in Stellar Astrophysics (MESA)". In: *Astrophysical Journal, Supplement* 192, 3, p. 3. DOI: 10.1088/0067-0049/192/1/3. arXiv: 1009.1622 [astro-ph.SR].

Paxton, B., M. Cantiello, P. Arras, L. Bildsten, E. F. Brown, A. Dotter, C. Mankovich, M. H. Montgomery, D. Stello, F. X. Timmes, and R. Townsend (2013). "Modules for Experiments in Stellar Astrophysics (MESA): Planets, Oscillations, Rotation, and Massive Stars". In: *Astrophysical Journal, Supplement* 208, 4, p. 4. DOI: 10.1088/0067-0049/208/1/4. arXiv: 1301.0319 [astro-ph.SR].

Pignatari, M., R. Gallino, C. Baldovin, M. Wiescher, F. Herwig, A. Heger, M. Heil, and F. Käppeler (2006). "The s-process in massive stars: the Shell C-burning contribution". In: *International Symposium on Nuclear Astrophysics - Nuclei in the Cosmos*.

Pignatari, M., R. Gallino, M. Heil, M. Wiescher, F. Käppeler, F. Herwig, and S. Bisterzo (2010). "The Weak s-Process in Massive Stars and its Dependence on the Neutron Capture Cross

Sections". In: *The Astrophysical Journal* 710.2, p. 1557. URL: http://stacks.iop.org/0004-637X/710/i=2/a=1557.

Pignatari, M., F. Herwig, R. Hirschi, M. Bennett, G. Rockefeller, C. Fryer, F. X. Timmes, A. Heger, S. Jones, U. Battino, C. Ritter, A. Dotter, R. Trappitsch, S. Diehl, U. Frischknecht, et al. (2013). "NuGrid stellar data set. I. Stellar yields from H to Bi for stars with metallicities Z = 0.02 and Z = 0.01". In: *ArXiv e-prints*. arXiv: 1307.6961 [astro-ph.SR].

Prialnik, D. (2009). *An Introduction to the Theory of Stellar Structure and Evolution*. Cambridge University Press.

Raiteri, C. M., R. Gallino, M. Busso, D. Neuberger, and F. Käppeler (1993). "The Weak s-Component and Nucleosynthesis in Massive Stars". In: *Astrophysical Journal* 419, p. 207. DOI: 10.1086/173476.

Rauscher, T. (2010). "Relevant energy ranges for astrophysical reaction rates". In: *Physical Review C* 81.4, 045807, p. 045807. DOI: 10.1103/PhysRevC.81.045807. arXiv: 1003.2802 [astro-ph.SR].

Reifarth, R., L. P. Chau, M. Heil, F. Käppeler, O. Meusel, R. Plag, U. Ratzinger, A. Schempp, and K. Volk (2009). "Opportunities for Nuclear Astrophysics at FRANZ". In: *Publications of the Astronomical Society of Australia* 26, pp. 255–258. DOI: 10.1071/AS08061. arXiv: 0909.5279 [astro-ph.IM].

Reifarth, R., L. P. Chau, M. Heil, F. Käppeler, O. Meusel, R. Plag, U. Ratzinger, A. Schempp, and K. Volk (2009). "Opportunities for Nuclear Astrophysics at FRANZ". In: *PASA - Publications of the Astronomical Society of Australia* 26 (03), pp. 255–258. DOI: 10.1071/AS08061.

Reifarth, R., S. Altstadt, K. Göbel, T. Heftrich, M. Heil, A. Koloczek, C. Langer, R. Plag, M. Pohl, K. Sonnabend, and et al. (2013). "Nuclear astrophysics with radioactive ions at FAIR". In: *ArXiv e-prints*. arXiv: 1310.1632 [astro-ph.IM].

Reifarth, R, C Lederer, and F Käppeler (2014). "Neutron reactions in astrophysics". In: *Journal of Physics G: Nuclear and Particle Physics* 41.5, p. 053101. URL: http://stacks.iop.org/0954-3899/41/i=5/a=053101.

Rolfs, C. E. and W. S. Rodney (1988). *Cauldrons in the cosmos: Nuclear astrophysics*.

Schatz, H., A. Aprahamian, J. Görres, M. Wiescher, T. Rauscher, J. Rembges, F.-K. Thielemann, B. Pfeiffer, P. Möller, K.-L. Kratz, H. Herndl, B. Brown, and H. Rebel (1998). "rp-process nucleosynthesis at extreme temperature and density conditions". In: *Physics Reports* 294.4, pp. 167 –263. DOI: 10.1016/S0370-1573(97)00048-3.

Schwarzschild, M. and R. Härm (1965). "Thermal Instability in Non-Degenerate Stars." In: *Astrophysical Journal* 142, p. 855. DOI: 10.1086/148358.

Schwarzschild, M. and R. Härm (1967). "Hydrogen Mixing by Helium-Shell Flashes". In: *Astrophysical Journal* 150, p. 961. DOI: 10.1086/149396.

Seeger, P. A., W. A. Fowler, and D. D. Clayton (1965). "Nucleosynthesis of Heavy Elements by Neutron Capture." In: *Astrophysical Journal, Supplement* 11, p. 121. DOI: 10.1086/190111.

Serminato, A., R. Gallino, C. Travaglio, S. Bisterzo, and O. Straniero (2009). "Galactic Chemical Evolution of the s Process from AGB Stars". In: *Publications of the Astronomical Society of Australia* 26, pp. 153–160. DOI: 10.1071/AS08053. arXiv: 0909.5570 [astro-ph.SR].

Sneden, C., J. J. Cowan, and R. Gallino (2008). "Neutron-Capture Elements in the Early Galaxy". In: *Annual Review of Astronomy and Astrophysics* 46, pp. 241–288. DOI: 10.1146/annurev.astro.46.060407.145207.

Straniero, O., R. Gallino, and S. Cristallo (2006). "s process in low-mass asymptotic giant branch stars". In: *Nuclear Physics A* 777, pp. 311–339. DOI: 10.1016/j.nuclphysa.2005.01.011. eprint: astro-ph/0501405.

Suess, H. E. and H. C. Urey (1956). "Abundances of the Elements". In: *Rev. Mod. Phys.* 28 (1), pp. 53–74. DOI: 10.1103/RevModPhys.28.53.

Takahashi, K. and K. Yokoi (1987). "Beta-decay rates of highly ionized heavy atoms in stellar interiors". In: *Atomic Data and Nuclear Data Tables* 36.3, pp. 375 –409. DOI: 10.1016/0092-640X(87)90010-6.

Thielemann, F.-K., M. Arnould, and J. W. Truran (1987). "Reaclib data tables of nuclear reaction rate". In: *Advances in Nuclear Astrophysics (Gif-sur-Yvette)*, p. 525.

Thielemann, F.-K., A. Arcones, R. Käppeli, M. Liebendörfer, T. Rauscher, C. Winteler, C. Fröhlich, I. Dillmann, T. Fischer, G. Martinez-Pinedo, K. Langanke, K. Farouqi, K.-L. Kratz, I. Panov, and I. Korneev (2011). "What are the astrophysical sites for the -process and the production of heavy elements?" In: *Progress in Particle and Nuclear Physics* 66.2. Particle and Nuclear Astrophysics International Workshop on Nuclear Physics, 32nd Course, pp. 346 –353. DOI: 10.1016/j.ppnp.2011.01.032.

Thomas, B. (2013). "Isomere im s-Prozess". MA thesis. Goethe-Universität Frankfurt.

Timmes, F. X., S. E. Woosley, and T. A. Weaver (1995). "Galactic chemical evolution: Hydrogen through zinc". In: *Astrophysical Journal, Supplement* 98, pp. 617–658. DOI: 10.1086/192172. eprint: astro-ph/9411003.

Travaglio, C., R. Gallino, C. Arlandini, and M. Busso (1996). "On the neutron recycling by ^{12}C and ^{16}O in AGB and massive stars". In: *Mem. Societa Astronomica Italiana* 67, p. 831.

Travaglio, C., R. Gallino, M. Busso, and R. Gratton (2001). "Lead: Asymptotic Giant Branch Production and Galactic Chemical Evolution". In: *Astrophysical Journal* 549, pp. 346–352. DOI: 10.1086/319087. eprint: astro-ph/0011050.

Travaglio, C., R. Gallino, E. Arnone, J. Cowan, F. Jordan, and C. Sneden (2004). "Galactic Evolution of Sr, Y, And Zr: A Multiplicity of Nucleosynthetic Processes". In: *Astrophysical Journal* 601, pp. 864–884. DOI: 10.1086/380507. eprint: astro-ph/0310189.

Wanajo, S., H.-T. Janka, and S. Kubono (2011). "Uncertainties in the νp-process: Supernova Dynamics Versus Nuclear Physics". In: *Astrophysical Journal* 729, 46, p. 46. DOI: 10.1088/0004-637X/729/1/46. arXiv: 1004.4487 [astro-ph.SR].

Zhang, B., K. Ma, and G. Zhou (2006). “Neutron-Capture Elements in the s- and r-Process-rich Stars: Constraints on Neutron-Capture Nucleosynthesis Processes”. In: *Astrophysical Journal* 642, pp. 1075–1081. DOI: 10.1086/501421. eprint: astro-ph/0605340.

List of Figures

1.1 Solar abundance distribution normalised to Silicon at 10^6. 5

1.2 The Gamow window. 7

1.3 Maximum binding energy per nucleon as function of mass number. 8

1.4 MACS at 5 keV. 14

1.5 Overview of the main nucleosynthesis paths along the chart of nuclides. 16

1.6 The *s*-process path. 17

1.7 The termination point of the *s* process. 18

1.8 The σN curve. 19

1.9 Overabundance factors of the main component. 20

1.10 Branching point ^{85}Kr along the *s*-process path. 21

1.11 *s*-, *r*- and *p*-only isotopes 22

1.12 The *r*-process peaks. 25

1.13 Schematic Hertzsprung-Russel diagram of a 3 $M_\odot$ star. 27

1.14 Schematic picture of a TP-AGB star. 29

1.15 Schematic Hertzsprung-Russel diagram of a 25 $M_\odot$ star. 30

1.16 Schematic onion-like shell burning structure of a 25 $M_\odot$ star, shortly before its death in a core collapse supernova. 31

2.1 Kippenhahn diagram of the helium intershell of a 3 $M_\odot$ stellar model during the TP-AGB phase. 37

2.2 TK-plot of the ^{4}He abundance in the helium intershell of a 3 $M_\odot$ stellar model during the TP-AGB phase. 38

2.3 TK-plot of the ^{22}Ne abundance in the helium intershell of a 3 $M_\odot$ stellar model during the TP-AGB phase. 40

2.4 TK-plot of the ^{13}C abundance in the helium intershell of a 3 $M_\odot$ stellar model during the TP-AGB phase. 41

2.5 ^{13}C-pockets and TP peak abundances located by the finder routine introduced on page 40. 42

2.6 Kippenhahn diagram of the first three central burning phases of a 25 $M_\odot$ stellar model. 43

2.7 Bottleneck reaction ^{89}Y(n,γ) during the ^{13}C-pocket (table 3.5). 48

2.8 Neutron poison ^{16}O(n,γ) during the *i* process (table 3.25). 49

3.1 Trajectory of ^{13}C-pocketused in PPN. 52

3.2 Abundance distribution before and after the ^{13}C-pocket. 53

3.3 Branching point ^{64}Cu during the ^{13}C-pocket (table 3.1). 55

3.4 Neutron donator reaction ^{12}C(p,γ) during the ^{13}C-pocket (table 3.2). 56

3.5 Neutron poison reaction ^{14}N(n,p) during the ^{13}C-pocket (table 3.3). 57

3.6 Competing capture ^{56}Fe(n,γ) during the ^{13}C-pocket (table 3.4). 58

3.7 Bottleneck reaction ^{88}Sr(n,γ) during the ^{13}C-pocket (table 3.5). 60

3.8 TK-plot of the temperature in the helium intershell of a 3 $M_\odot$ stellar model during the TP-AGB phase. 61

3.9 Abundance distribution before and after the thermal pulse. 62

3.10 Branching point ^{85}Kr during the TP (table 3.6). 63

3.11 Neutron source ^{22}Ne(α,n) during the thermal pulse (table 3.7). 66

3.12 Neutron poison rate ^{25}Mg(n,γ) during the thermal pulse (table 3.8). 67

3.13 Competing capture ^{56}Fe(n,γ) during the thermal pulse (table 3.9). 68

3.14 Bottleneck reaction ^{90}Zr(n,γ) during the thermal pulse (table 3.10). 69

3.15 PPN trajectory of weak component. 70

3.16 Abundance distribution before and after the weak component. 71

3.17 Branching point ^{64}Cu during the weak *s* process (table 3.11). 73

3.18 Neutron donator reaction ^{22}Ne(α,n) during the weak *s* process (table 3.12). . . . 74

3.19 Recycled neutron poison reaction ^{20}Ne(γ, α) during the weak *s* process (table 3.13). 75

3.20 Neutron poison reaction ^{12}C(α, γ) during the weak *s* process (table 3.14). 76

3.21 Light neutron poison ^{24}Mg(n,γ) during the weak *s* process (table 3.15). 77

3.22 Competing capture ^{56}Fe(n,γ) during the weak *s* process (table 3.16). 79

3.23 Bottleneck reaction ^{88}Sr(n,γ) during the weak *s* process (table 3.17). 81

3.24 PPN trajectory of convective carbon shell burning. 81

3.25 Abundance distribution before and after the convective carbon shell burning. . . 82

3.26 Branching point ^{64}Cu during the carbon shell burning (table 3.18). 84

3.27 Neutron donator ^{21}Ne(α,n) during the convective carbon shell burning (table 3.19). 85

3.28 Neutron poison reaction ^{16}O(α, γ) during the convective carbon shell burning (table 3.20). 87

3.29 Expected neutron source ^{12}C(^{12}C,n) during the convective carbon shell burning (table 3.21). 88

3.30 Expected branching path ^{93}Zr(β^-) during the convective carbon shell burning (table 3.22). 89

3.31 Abundance distribution before and after the *i* process. 90

3.32 Schematic path of the *i* process. 91

3.33 Branching point ^{34}P during the weak *s* process (table 3.23). 92

3.34 Neutron donator reaction ^{13}C(α,n) during the *i* process (table 3.24). 93

3.35 Neutron poison ^{13}C(n,γ) during the *i* process (table 3.25). 94

3.36 Competing capture ^{36}S(n,γ) during the *i* process (table 3.26). 95

3.37 Bottleneck reaction ^{135}I(n,γ) during the *i* process (table 3.27). 96

3.38 Impact of the neutron source reaction ^{22}Ne(α,n) during the TP on LEPP isotopes. 98

3.39 Impact of the neutron source reaction ^{22}Ne(α,n) during the weak *s* process on LEPP isotopes. (table 3.28). 99

3.40 Impact of the neutron source reaction ^{13}C(α,n) during the *i* process on LEPP isotopes. (table 3.29). 100

4.1 Possible production and destruction channels of ^{93}Nb. 102

5.1 Sensitivität der erwarteten Neutronenquelle ^{12}C(^{12}C,n)^{23}Mg wähnend der Kohlenstoffschalenbrennens. 110

5.2 Schematischer *i*-Prozesspfad. 111

5.3 Sensitivität der Neutronenquelle ^{22}Ne(α,n) während der schwachen Komponente des *s*-Prozesses auf die LEPP-Isotope. 112

A.1 Branching point ^{85}Kr during the ^{13}C-pocket (table 3.1). 146

A.2 Branching point ^{93}Zr during the ^{13}C-pocket (table 3.1). 146

A.3 Neutron donator reaction ^{13}C(α,n) during the ^{13}C-pocket (table 3.2). 147

A.4 Neutron poison reaction ^{13}C(p,γ) during the ^{13}C-pocket (table 3.3). 147

A.5 Neutron poison reaction ^{14}C(α,γ) during the ^{13}C-pocket (table 3.3). 148

A.6 Neutron poison reaction ^{16}O(n,γ) during the ^{13}C-pocket (table 3.3). 148

A.7 Neutron poison reaction ^{22}Ne(n,γ) during the ^{13}C-pocket (table 3.3). 149

A.8 Neutron poison reaction ^{14}C(β^-) during the ^{13}C-pocket (table 3.3). 149

A.9 Competing capture reaction ^{64}Ni(n,γ) during the ^{13}C-pocket (table 3.4). 150

A.10 Competing capture reaction ^{120}Sn(n,γ) during the ^{13}C-pocket (table 3.4). 150

A.11 Competing capture reaction ^{58}Fe(n,γ) during the ^{13}C-pocket (table 3.4). 151

A.12 Bottleneck reaction ^{138}Ba(n,γ) during the ^{13}C-pocket (table 3.5). 151

A.13 Bottleneck reaction ^{90}Zr(n,γ) during the ^{13}C-pocket (table 3.5). 152

A.14 Bottleneck reaction ^{139}La(n,γ) during the ^{13}C-pocket (table 3.5). 152

A.15 Bottleneck reaction ^{140}Ce(n,γ) during the ^{13}C-pocket (table 3.5). 153

A.16 Bottleneck reaction ^{142}Nd(n,γ) during the ^{13}C-pocket (table 3.5). 153

A.17 TK-plot of the density in the helium intershell of a 3 $M_\odot$ stellar model during the TP-AGB phase. 158

A.18 Branching point ^{63}Ni during the TP (table 3.6). 159

A.19 Branching point ^{64}Cu during the TP (table 3.6). 159

A.20 Branching point ^{86}Rb during the TP (table 3.6). 160

A.21 Branching point ^{93}Zr during the TP (table 3.6). 160

A.22 Branching point ^{95}Zr during the TP (table 3.6). 161

A.23 Branching point ^{192}Ir during the TP (table 3.6). 161

A.24 Neutron poison reaction ^{22}Ne(n,γ) during the thermal pulse (table 3.8). 162

A.25 Bottleneck reaction ^{96}Mo(n,γ) during the thermal pulse (table 3.10). 162

A.26 Bottleneck reaction ^{146}Nd(n,γ) during the thermal pulse (table 3.10). 163

A.27 Bottleneck reaction ^{91}Zr(n,γ) during the thermal pulse (table 3.10). 163

A.28 Bottleneck reaction ^{92}Zr(n,γ) during the thermal pulse (table 3.10). 164

A.29 Bottleneck reaction ^{94}Zr(n,γ) during the thermal pulse (table 3.10). 164

A.30 Bottleneck reaction ^{110}Cd(n,γ) during the thermal pulse (table 3.10). 165

A.31 Bottleneck reaction ^{114}Cd(n,γ) during the thermal pulse (table 3.10). 165

A.32 Bottleneck reaction ^{116}Sn(n,γ) during the thermal pulse (table 3.10). 166

A.33 Bottleneck reaction ^{118}Sn(n,γ) during the thermal pulse (table 3.10). 166

A.34 Bottleneck reaction ^{120}Sn(n,γ) during the thermal pulse (table 3.10). 167

A.35 Bottleneck reaction ^{139}La(n,γ) during the thermal pulse (table 3.10). 167

A.36 Bottleneck reaction ^{140}Ce(n,γ) during the thermal pulse (table 3.10). 168

A.37 Bottleneck reaction ^{141}Pr(n,γ) during the thermal pulse (table 3.10). 169

A.38 Bottleneck reaction ^{142}Nd(n,γ) during the thermal pulse (table 3.10). 169

A.39 Bottleneck reaction ^{144}Nd(n,γ) during the thermal pulse (table 3.10). 170

A.40 Bottleneck reaction ^{148}Sm(n,γ) during the thermal pulse (table 3.10). 170

A.41 Bottleneck reaction ^{150}Sm(n,γ) during the thermal pulse (table 3.10). 171

A.42 Bottleneck reaction ^{158}Gd(n,γ) during the thermal pulse (table 3.10). 171

A.43 Bottleneck reaction ^{164}Dy(n,γ) during the thermal pulse (table 3.10). 172

A.44 Bottleneck reaction ^{174}Yb(n,γ) during the thermal pulse (table 3.10). 172

A.45 Bottleneck reaction ^{180}Hf(n,γ) during the thermal pulse (table 3.10). 173

A.46 Branching point ^{63}Ni during the weak *s* process (table 3.11). 180

A.47 Branching point ^{85}Kr during the weak *s* process (table 3.11). 181

A.48 Branching point ^{86}Rb during the weak *s* process (table 3.11). 181

A.49 Branching point ^{89}Sr during the weak *s* process (table 3.11). 182

A.50 Branching point ^{90}Y during the weak *s* process (table 3.11). 182

A.51 Branching point ^{91}Y during the weak *s* process (table 3.11). 183

A.52 Branching point ^{93}Zr during the weak *s* process (table 3.11). 183

A.53 Branching point ^{95}Zr during the weak *s* process (table 3.11). 184

A.54 Branching point ^{121}Sn during the weak *s* process (table 3.11). 184

A.55 Branching point ^{133}Xe during the weak *s* process (table 3.11). 185

A.56 Neutron donator reaction ^{17}O(α, n) during the weak *s* process (table 3.12). . . . 185

A.57 Neutron donator reaction ^{12}C(p, γ) during the weak *s* process (table 3.12). . . . 186

A.58 Neutron donator reaction ^{13}N(β^+) during the weak *s* process (table 3.12). 186

A.59 Recycled neutron poison reaction ^{23}Na(p, α) during the weak *s* process (table 3.13). 187

A.60 Recycled neutron poison reaction ^{26}Mg(α, n) during the weak *s* process (table 3.13). 187

A.61 Recycled neutron poison reaction ^{12}C$(^{12}C, \alpha)$ during the weak *s* process (table 3.13). 188

A.62 Recycled neutron poison reaction ^{25}Mg(α, n) during the weak *s* process (table 3.13). 188

A.63 Recycled neutron poison reaction ^{21}Ne(α, n) during the weak *s* process (table 3.13). 189

A.64 Neutron poison reaction Triple-α during the weak *s* process (table 3.14). 189

A.65 Neutron poison reaction ^{22}Ne(α, γ) during the weak *s* process (table 3.14). . . . 190

A.66 Neutron poison reaction ^{16}O(α, γ) during the weak *s* process (table 3.14). 190

A.67 Neutron poison reaction ^{25}Mg(n, γ) during the weak *s* process (table 3.14). . . . 191

A.68 Neutron poison reaction ^{16}O(n, γ) during the weak *s* process (table 3.14). 191

A.69 Neutron poison reaction ^{32}S(n, γ) during the weak *s* process (table 3.14). 192

A.70 Neutron poison reaction ^{22}Ne(n, γ) during the weak *s* process (table 3.14). . . . 192

A.71 Neutron poison reaction ^{13}N$(\gamma$,p) during the weak *s* process (table 3.14). 193

A.72 Neutron poison reaction ^{28}Si(n, γ) during the weak *s* process (table 3.14). . . . 193

A.73 Light neutron poison reaction ^{20}Ne(α, γ) during the weak *s* process (table 3.15). 194

A.74 Light neutron poison reaction ^{12}C$(^{12}C, p)$ during the weak *s* process (table 3.15). 194

A.75 Light neutron poison reaction ^{20}Ne(n,γ) during the weak *s* process (table 3.15). 195

A.76 Light neutron poison reaction ^{23}Na(n,γ) during the weak *s* process (table 3.15). 195

A.77 Light neutron poison reaction ^{26}Mg(p,γ) during the weak *s* process (table 3.15). 196

A.78 Light neutron poison reaction ^{22}Ne(p,γ) during the weak *s* process (table 3.15). 196

A.79 Light neutron poison reaction ^{27}Al(n,γ) during the weak *s* process (table 3.15). 197

A.80 Competing capture reaction ^{62}Ni(n,γ) during the weak *s* process (table 3.16). . 197

A.81 Competing capture reaction ^{59}Co(n,γ) during the weak *s* process (table 3.16). . 198

A.82 Competing capture reaction ^{58}Fe(n,γ) during the weak *s* process (table 3.16). . 198

A.83 Competing capture reaction ^{57}Fe(n,γ) during the weak *s* process (table 3.16). . 199

A.84 Competing capture reaction ^{63}Cu(n,γ) during the weak *s* process (table 3.16). . 199

A.85 Competing capture reaction ^{60}Ni(n,γ) during the weak *s* process (table 3.16). . 200

A.86 Competing capture reaction ^{61}Ni(n,γ) during the weak *s* process (table 3.16). . 200

A.87 Bottleneck reaction ^{89}Y(n,γ) during the weak *s* process (table 3.17). 201

A.88 Bottleneck reaction ^{92}Zr(n,γ) during the weak *s* process (table 3.17). 201

A.89 Bottleneck reaction ^{84}Kr(n,γ) during the weak *s* process (table 3.17). 202

A.90 Bottleneck reaction ^{86}Sr(n,γ) during the weak *s* process (table 3.17). 202

A.91 Bottleneck reaction ^{90}Zr(n,γ) during the weak *s* process (table 3.17). 203

A.92 Bottleneck reaction ^{94}Zr(n,γ) during the weak *s* process (table 3.17). 203

A.93 Bottleneck reaction ^{74}Ge(n,γ) during the weak *s* process (table 3.17). 204

A.94 Bottleneck reaction ^{78}Se(n,γ) during the weak *s* process (table 3.17). 204

A.95 Bottleneck reaction ^{82}Kr(n,γ) during the weak *s* process (table 3.17). 205

A.96 Bottleneck reaction ^{87}Sr(n,γ) during the weak *s* process (table 3.17). 205

A.97 Bottleneck reaction ^{91}Zr(n,γ) during the weak *s* process (table 3.17). 206

A.98 Bottleneck reaction ^{68}Zn(n,γ) during the weak *s* process (table 3.17). 206

A.99 Bottleneck reaction ^{72}Ge(n,γ) during the weak *s* process (table 3.17). 207

A.100 Bottleneck reaction ^{84}Kr(n,γ) during the weak *s* process (table 3.17). 207

A.101 Bottleneck reaction ^{66}Zn(n,γ) during the weak *s* process (table 3.17). 208

A.102 Bottleneck reaction ^{70}Ge(n,γ) during the weak *s* process (table 3.17). 208

A.103 Bottleneck reaction ^{65}Cu(n,γ) during the weak *s* process (table 3.17). 209

A.104 Bottleneck reaction ^{64}Zn(n,γ) during the weak *s* process (table 3.17). 209

A.105 Bottleneck reaction ^{67}Zn(n,γ) during the weak *s* process (table 3.17). 210

A.106 Bottleneck reaction ^{71}Ga(n,γ) during the weak *s* process (table 3.17). 210

A.107 Bottleneck reaction ^{69}Ga(n,γ) during the weak *s* process (table 3.17). 211

A.108 Bottleneck reaction ^{73}Ge(n,γ) during the weak *s* process (table 3.17). 211

A.109 Bottleneck reaction ^{76}Se(n,γ) during the weak *s* process (table 3.17). 212

A.110 Bottleneck reaction ^{80}Se(n,γ) during the weak *s* process (table 3.17). 212

A.111 Bottleneck reaction ^{85}Rb(n,γ) during the weak *s* process (table 3.17). 213

A.112 Bottleneck reaction ^{96}Mo(n,γ) during the weak *s* process (table 3.17). 213

A.113 Bottleneck reaction ^{122}Sn(n,γ) during the weak *s* process (table 3.17). 214

A.114 Bottleneck reaction ^{90}Sr(n,γ) during the weak *s* process (table 3.17). 214

A.115 Bottleneck reaction ^{95}Mo(n,γ) during the weak *s* process (table 3.17). 215

A.116 Bottleneck reaction ^{98}Mo(n,γ) during the weak *s* process (table 3.17). 215

A.117 Bottleneck reaction ^{126}Te(n,γ) during the weak *s* process (table 3.17). 216

A.118 Branching point ^{133}Xe during the carbon shell burning (table 3.18). 224

A.119 Branching point ^{86}Rb during the carbon shell burning (table 3.18). 224

A.120 Branching point ^{121}Sn during the carbon shell burning (table 3.18). 225

A.121 Neutron donator reaction ^{22}Ne(α,n) during the convective carbon shell burning (table 3.19). 225

A.122 Neutron donator reaction $^{25}Mg(\alpha, n)$ during the convective carbon shell burning (table 3.19). 226

A.123 Neutron poison reaction $^{25}Mg(n, \gamma)$ during the convective carbon shell burning (table 3.20). 226

A.124 Neutron poison reaction $^{20}Ne(n, \gamma)$ during the convective carbon shell burning (table 3.20). 227

A.125 Neutron poison reaction $^{20}Ne(\alpha, \gamma)$ during the convective carbon shell burning (table 3.20). 227

A.126 Expected neutron poison reaction $^{12}C(^{12}C, p)$ during the convective carbon shell burning (table 3.21). 228

A.127 Expected neutron poison reaction $^{12}C(^{12}C, \alpha)$ during the convective carbon shell burning (table 3.21). 228

A.128 Expected branching path $^{93}Zr(n, \gamma)$ during the convective carbon shell burning (table 3.22). 229

A.129 Destruction path $^{93}Nb(n, \gamma)$ during the convective carbon shell burning (table 3.22). 229

A.130 Neutron donator reaction $^{15}O(\beta^+)$ during the *i* process (table 3.24). 238

A.131 Neutron donator reaction $^{13}N(\beta^+)$ during the *i* process (table 3.24). 239

A.132 Neutron poison reaction $^{13}C(p, \gamma)$ during the *i* process (table 3.25). 239

A.133 Neutron poison reaction $^{15}N(n, \gamma)$ during the *i* process (table 3.25). 240

A.134 Neutron poison reaction $^{12}C(n, \gamma)$ during the *i* process (table 3.25). 240

A.135 Neutron poison reaction $^{13}N(p, \gamma)$ during the *i* process (table 3.25). 241

A.136 Competing capture reaction $^{28}Si(p, \gamma)$ during the *i* process (table 3.26). 241

A.137 Competing capture reaction $^{20}Ne(p, \gamma)$ during the *i* process (table 3.26). 242

A.138 Competing capture reaction $^{34}S(n, \gamma)$ during the *i* process (table 3.26). 242

A.139 Competing capture reaction $^{32}Si(n, \gamma)$ during the *i* process (table 3.26). 243

A.140 Competing capture reaction $^{30}Si(n, \gamma)$ during the *i* process (table 3.26). 243

A.141 Competing capture reaction $^{37}S(\beta^-)$ during the *i* process (table 3.26). 244

A.142 Competing capture reaction $^{38}S(n,\gamma)$ during the *i* process (table 3.26). 244

A.143 Competing capture reaction $^{33}P(n,\gamma)$ during the *i* process (table 3.26). 245

A.144 Competing capture reaction $^{37}Cl(n,\gamma)$ during the *i* process (table 3.26). 245

A.145 Competing capture reaction $^{42}Ar(n,\gamma)$ during the *i* process (table 3.26). 246

A.146 Competing capture reaction $^{31}Si(n,\gamma)$ during the *i* process (table 3.26). 246

A.147 Competing capture reaction $^{39}Cl(n,\gamma)$ during the *i* process (table 3.26). 247

A.148 Competing capture reaction $^{47}Ca(n,\gamma)$ during the *i* process (table 3.26). 248

A.149 Bottleneck reaction $^{134}Te(\beta^-)$ during the *i* process (table 3.27). 248

A.150 Bottleneck reaction $^{48}Ca(n,\gamma)$ during the *i* process (table 3.27). 249

A.151 Triple-α process during the weak *s* process on LEPP isotopes. (table 3.28). . . . 250

A.152 $^{12}C(\alpha,\gamma)$ during the weak *s* process on LEPP isotopes. (table 3.28). 251

A.153 $^{22}Ne(\alpha,\gamma)$ during the weak *s* process on LEPP isotopes. (table 3.28). 251

A.154 Bottleneck reaction $^{88}Sr(n,\gamma)$ during the weak *s* process on LEPP isotopes. (table 3.28). 252

A.155 Neutron poison reaction $^{25}Mg(n,\gamma)$ during the weak *s* process on LEPP isotopes. (table 3.28). 252

A.156 Competing capture reaction $^{56}Fe(n,\gamma)$ during the weak *s* process on LEPP isotopes. (table 3.28). 253

A.157 $^{68}Zn(n,\gamma)$ impact during the weak *s* process on LEPP isotopes. (table 3.28). . . 253

A.158 $^{16}O(\alpha,\gamma)$ during the weak *s* process on LEPP isotopes. (table 3.28). 254

A.159 Neutron poison reaction $^{13}C(n,\gamma)$ during the *i* process on LEPP isotopes. (table 3.29). 255

A.160 $^{13}N(\beta^+)$ during the *i* process on LEPP isotopes. (table 3.29). 255

A.161 Seed reaction $^{36}S(n,\gamma)$ during the *i* process on LEPP isotopes. (table 3.29). . . . 256

A.162 Neutron poison reaction $^{16}O(n,\gamma)$ during the *i* process on LEPP isotopes. (table 3.29). 256

A.163 Seed reaction $^{34}S(n,\gamma)$ during the *i* process on LEPP isotopes. (table 3.29). . . . 257

List of Tables

1.1 s-only isotopes and their respective solar abundances normalised to Si = 10^6. . . . 23

1.2 Isotopic *s*-process contribution to solar abundances. 26

3.1 Branching point isotopes and reactions during ^{13}C-pocket. 54

3.2 Globally sensitive neutron donator reactions during ^{13}C-pocket. 56

3.3 Globally sensitive neutron poison reactions during ^{13}C-pocket. 57

3.4 Globally sensitive competing capture reactions during ^{13}C-pocket. 58

3.5 Globally sensitive bottleneck reactions during ^{13}C-pocket. 59

3.6 Branching point isotopes and reactions during the thermal pulse. 64

3.7 Globally sensitive neutron donator during the thermal pulse. 65

3.8 Globally sensitive neutron poisons during the thermal pulse. 65

3.9 Globally sensitive competing capture reaction during the thermal pulse. 66

3.10 Globally sensitive bottlenecks during the thermal pulse. 68

3.11 Branching point isotopes and reactions during the weak *s* process. 72

3.12 Globally sensitive neutron donator reactions during the weak component. 74

3.13 Globally sensitive recycled neutron poison reactions during the weak component. 75

3.14 Globally sensitive neutron poison reactions during the weak component. 76

3.15 Globally sensitive light neutron poison reactions during the weak component. . . 77

3.16 Globally sensitive competing capture rates during the weak component. 78

3.17 Globally sensitive bottleneck reactions during the weak component. 80

3.18 Branching point isotopes and reactions during the convective carbon shell burning. 83

3.19 Globally sensitive neutron donator reactions during the convective carbon shell burning. 86

3.20 Globally sensitive neutron poison reactions during the convective carbon shell burning. 86

3.21 Carbon-carbon reactions during the convective carbon shell burning. 88

3.22 Reactions around ^{93}Nb during the convective carbon shell burning. 88

3.23 Branching point isotopes and reactions during *i* process. 91

3.24 Globally sensitive neutron donator reactions during *i* process. 93

3.25 Globally sensitive neutron poison reactions during *i* process. 94

3.26 Globally sensitive competing capture reactions during *i* process. 95

3.27 Globally sensitive bottleneck reactions during the *i* process. 96

3.28 Globally sensitive rates on LEPP isotopes during weak *s* process. 98

3.29 Globally sensitive rates on LEPP isotopes during *i* process. 100

A.1 Reactions with strongest local sensitivities in the ^{13}C-pocket for each isotope. . . 140

A.2 Initial abundances for the ^{13}C-pocket simulations. 142

A.3 Reactions with strongest local sensitivities in the thermal pulse for each isotope . 154

A.4 Reactions with strongest local sensitivities during the weak *s* process. 174

A.5 Initial abundances for the weak *s* process simulations. 177

A.6 Reactions with strongest local sensitivities during the convective carbon shell burning. 216

A.7 Initial abundances for the convective C shell simulations. 220

A.8 Reactions with strongest local sensitivities during the *i* process. 230

A.9 Initial abundances for the *i* process simulations. 235

A

Appendix

A.1 MAIN COMPONENT

In this part of the appendix the local sensitivity tables, initial abundances for the ^{13}C-pocket trajectory and remaining global sensitivity plots are listed for the ^{13}C-pocket and thermal pulse.

A.1.1 ^{13}C-POCKET

LOCAL SENSITIVITIES DURING THE ^{13}C-POCKET

Table A.1: Reactions with strongest local sensitivities in the ^{13}C-pocket for each isotope. Filter criteria in chapter 2.3.3 on page 49.

Isotope	Most important reactions with respective sensitivities					
^{56}Fe	^{50}Ti(n,γ)	0.198	-		-	
^{57}Fe	^{57}Fe(n,γ)	-1.096	^{50}Ti(n,γ)	0.176	-	
^{58}Fe	^{50}Ti(n,γ)	0.100	-		-	
^{58}Ni	^{58}Ni(n,γ)	-53.355	^{60}Ni(n,γ)	0.321	^{68}Zn(n,γ)	0.320
^{64}Ni	^{64}Cu(β^-)	-0.278	^{64}Cu(β^+)	0.278	^{63}Ni(β^-)	-0.179
^{64}Zn	^{64}Zn(n,γ)	-1.056	^{64}Cu(β^-)	0.488	^{64}Cu(β^+)	-0.487
^{70}Zn	^{70}Zn(n,γ)	-1.261	^{70}Ga(β^-)	-1.039	^{70}Ga(β^+)	0.998
^{76}Ge	^{76}Ge(n,γ)	-1.245	^{76}As(β^-)	-1.038	^{76}As(β^+)	0.997
^{82}Se	^{82}Se(n,γ)	-2.224	^{81}Se(β^-)	-0.853	^{81}Se(n,γ)	0.819
^{79}Br	^{79}Se(n,γ)	-0.899	^{79}Se(β^-)	0.480	^{79}Br(n,γ)	-0.219
^{80}Kr	^{79}Se(n,γ)	-0.946	^{79}Se(β^-)	0.828	^{80}Kr(n,γ)	-0.548
^{86}Kr	^{85}Kr(β^-)	-0.982	^{85}Kr(n,γ)	0.946	^{86}Kr(n,γ)	-0.652
^{87}Rb	^{87}Rb(n,γ)	-1.033	^{85}Kr(β^-)	-0.970	^{85}Kr(n,γ)	0.934
^{96}Zr	^{96}Zr(n,γ)	-1.481	^{95}Zr(β^-)	-1.041	^{95}Zr(n,γ)	0.999
^{93}Nb	^{93}Zr(n,γ)	-1.041	^{93}Zr(β^-)	0.998	^{93}Nb(n,γ)	-0.175
^{94}Mo	^{93}Zr(n,γ)	-1.041	^{93}Zr(β^-)	0.999	^{94}Mo(n,γ)	-0.517
^{100}Mo	^{100}Mo(n,γ)	-1.571	^{99}Mo(β^-)	-0.643	^{99}Mo(n,γ)	0.617
^{99}Ru	^{99}Tc(n,γ)	-1.035	^{99}Tc(β^-)	0.973	^{99}Ru(n,γ)	-0.162
^{104}Ru	^{104}Ru(n,γ)	-1.047	^{104}Rh(β^-)	-1.034	^{104}Rh(β^+)	0.993
^{110}Pd	^{110}Pd(n,γ)	-1.044	^{110}Ag(β^-)	-1.036	^{110}Ag(β^+)	0.995
^{107}Ag	^{107}Pd(n,γ)	-1.042	^{107}Pd(β^-)	0.999	^{107}Ag(n,γ)	-0.171

Isotope	Most important reactions with respective sensitivities					
^{108}Cd	^{107}Pd(n,γ)	-1.042	^{107}Pd(β^-)	1.000	^{108}Cd(n,γ)	-0.484
^{116}Cd	^{116}Cd(n,γ)	-1.680	^{115}Cd(β^-)	-0.809	^{115}Cd(n,γ)	0.776
^{122}Sn	^{122}Sb(β^-)	-1.013	^{122}Sn(n,γ)	-0.981	^{122}Sb(β^+)	0.974
^{124}Sn	^{124}Sn(n,γ)	-1.580	^{123}Sn(β^-)	-1.026	^{122}Sb(β^-)	-1.011
^{123}Sb	^{123}Sb(n,γ)	-1.040	^{122}Sb(β^-)	-1.013	^{122}Sb(β^+)	0.973
^{128}Te	^{128}Te(n,γ)	-0.997	^{128}I (β^-)	-0.964	^{128}I (β^+)	0.931
^{130}Te	^{130}Te(n,γ)	-1.318	^{128}I (β^-)	-0.963	^{128}I (β^+)	0.930
^{134}Xe	^{134}Cs(β^-)	-0.987	^{134}Cs(β^+)	0.967	^{134}Xe(n,γ)	-0.882
^{136}Xe	^{136}Cs(β^-)	-0.984	^{136}Cs(β^+)	0.945	^{134}Cs(β^-)	-0.929
^{138}La	^{138}La(n,γ)	-1.014	^{141}Pr(n,γ)	-1.005	^{141}Pr(n,α)	1.000
^{142}Ce	^{142}Ce(n,γ)	-1.132	^{141}Ce(β^-)	-0.517	^{142}Pr(β^-)	-0.506
^{148}Nd	^{148}Nd(n,γ)	-1.829	^{147}Nd(β^-)	-0.991	^{147}Nd(n,γ)	0.951
^{152}Sm	^{152}Sm(n,γ)	-1.314	^{151}Sm(β^-)	-0.347	^{151}Sm(n,γ)	0.309
^{154}Sm	^{154}Sm(n,γ)	-1.075	^{154}Eu(β^-)	-0.925	^{154}Eu(β^+)	0.904
^{152}Gd	^{152}Gd(n,γ)	-0.866	^{151}Sm(n,γ)	-0.225	^{152}Eu(β^-)	0.203
^{160}Gd	^{160}Gd(n,γ)	-1.801	^{159}Gd(β^-)	-0.999	^{159}Gd(n,γ)	0.959
^{158}Dy	^{157}Gd(n,γ)	-1.034	^{157}Gd(β^-)	1.000	^{157}Tb(β^+)	-0.908
^{170}Er	^{170}Er(n,γ)	-1.048	^{170}Tm(β^-)	-0.984	^{170}Tm(β^+)	0.948
^{176}Yb	^{176}Yb(n,γ)	-1.778	^{175}Yb(β^-)	-1.041	^{175}Yb(n,γ)	1.000
^{176}Lu	^{176}Lu(n,γ)	-1.037	^{175}Lu(n,γ)	0.871	-	
^{176}Hf	^{176}Hf(n,γ)	-1.030	^{175}Lu(n,γ)	-0.129	-	
^{186}W	^{186}W(n,γ)	-1.012	^{186}Re(β^-)	-0.960	^{186}Re(β^+)	0.927
^{187}Re	^{187}Re(n,γ)	-1.035	^{186}Re(β^-)	-0.959	^{186}Re(β^+)	0.925
^{192}Os	^{192}Os(n,γ)	-0.992	^{192}Ir(β^-)	-0.983	^{192}Ir(β^+)	0.949
^{198}Pt	^{198}Pt(n,γ)	-1.004	^{198}Au(β^-)	-0.927	^{198}Au(β^+)	0.890
^{202}Hg	^{202}Hg(n,γ)	-0.911	^{23}Na(n,γ)	-0.102	-	
^{204}Hg	^{204}Tl(β^-)	-0.999	^{204}Tl(β^+)	0.976	^{204}Hg(n,γ)	-0.830
^{203}Tl	^{203}Tl(n,γ)	-0.990	^{202}Hg(n,γ)	0.123	^{23}Na(n,γ)	-0.104
^{205}Tl	^{205}Tl(n,γ)	-0.860	^{202}Hg(n,γ)	0.129	^{23}Na(n,γ)	-0.110
^{204}Pb	^{204}Pb(n,γ)	-0.948	^{202}Hg(n,γ)	0.125	^{23}Na(n,γ)	-0.106
^{206}Pb	^{206}Pb(n,γ)	-0.503	^{205}Tl(n,γ)	0.177	^{202}Hg(n,γ)	0.138

Isotope	Most important reactions with respective sensitivities					
^{207}Pb	^{206}Pb(n,γ)	0.515	^{207}Pb(n,γ)	-0.416	^{205}Tl(n,γ)	0.182
^{208}Pb	^{207}Pb(n,γ)	0.559	^{206}Pb(n,γ)	0.486	^{205}Tl(n,γ)	0.170
^{209}Bi	^{208}Pb(n,γ)	0.994	^{207}Pb(n,γ)	0.523	^{206}Pb(n,γ)	0.450

INITIAL ABUNDANCES FOR THE ^{13}C-POCKET

Table A.2: Initial abundances for the ^{13}C-pocket simulations. Added abundances give unity.

isotope	initial abundance	isotope	initial abundance	isotope	initial abundance
Protons	$8.81281 \cdot 10^{-14}$	^{4}He	$4.15832 \cdot 10^{-01}$	^{11}B	$2.85589 \cdot 10^{-09}$
^{12}C	$2.98007 \cdot 10^{-01}$	^{13}C	$3.23601 \cdot 10^{-02}$	^{13}N	$1.39994 \cdot 10^{-14}$
^{14}N	$1.00924 \cdot 10^{-02}$	^{14}C	$9.34548 \cdot 10^{-07}$	^{15}N	$2.22316 \cdot 10^{-07}$
^{16}O	$1.79600 \cdot 10^{-01}$	^{17}O	$2.09270 \cdot 10^{-05}$	^{18}O	$2.17151 \cdot 10^{-07}$
^{18}F	$2.01223 \cdot 10^{-19}$	^{19}F	$9.57564 \cdot 10^{-05}$	^{20}Ne	$2.47000 \cdot 10^{-03}$
^{21}Ne	$2.05217 \cdot 10^{-05}$	^{22}Ne	$5.01649 \cdot 10^{-02}$	^{23}Na	$7.70855 \cdot 10^{-04}$
^{24}Mg	$9.85231 \cdot 10^{-04}$	^{25}Mg	$1.85571 \cdot 10^{-03}$	^{26}Mg	$4.54377 \cdot 10^{-03}$
^{26}Al	$4.61834 \cdot 10^{-07}$	^{27}Al	$1.16728 \cdot 10^{-04}$	^{28}Si	$7.22893 \cdot 10^{-04}$
^{29}Si	$6.19509 \cdot 10^{-05}$	^{30}Si	$1.09170 \cdot 10^{-04}$	^{31}P	$2.02420 \cdot 10^{-05}$
^{32}S	$3.25147 \cdot 10^{-04}$	^{33}S	$8.42161 \cdot 10^{-06}$	^{34}S	$3.29317 \cdot 10^{-05}$
^{35}S	$1.54084 \cdot 10^{-13}$	^{36}S	$2.64515 \cdot 10^{-06}$	^{35}Cl	$4.13104 \cdot 10^{-06}$
^{36}Cl	$3.44863 \cdot 10^{-07}$	^{37}Cl	$2.31113 \cdot 10^{-05}$	^{36}Ar	$4.90230 \cdot 10^{-05}$
^{37}Ar	$5.15324 \cdot 10^{-11}$	^{38}Ar	$2.81785 \cdot 10^{-05}$	^{39}Ar	$1.39171 \cdot 10^{-09}$
^{40}Ar	$6.92000 \cdot 10^{-07}$	^{39}K	$5.50973 \cdot 10^{-06}$	^{40}K	$6.23870 \cdot 10^{-07}$
^{41}K	$1.38308 \cdot 10^{-06}$	^{40}Ca	$5.07949 \cdot 10^{-05}$	^{41}Ca	$1.45343 \cdot 10^{-06}$
^{42}Ca	$2.94137 \cdot 10^{-06}$	^{43}Ca	$6.77221 \cdot 10^{-07}$	^{44}Ca	$2.64114 \cdot 10^{-06}$
^{45}Ca	$3.52841 \cdot 10^{-13}$	^{46}Ca	$7.40488 \cdot 10^{-08}$	^{47}Ca	$1.75454 \cdot 10^{-16}$
^{48}Ca	$1.57970 \cdot 10^{-07}$	^{44}Sc	$1.00000 \cdot 10^{-99}$	^{45}Sc	$4.02680 \cdot 10^{-07}$
^{46}Sc	$3.81200 \cdot 10^{-13}$	^{47}Sc	$1.31016 \cdot 10^{-16}$	^{44}Ti	$3.80621 \cdot 10^{-24}$
^{45}Ti	$1.00000 \cdot 10^{-99}$	^{46}Ti	$5.51847 \cdot 10^{-07}$	^{47}Ti	$2.29458 \cdot 10^{-07}$
^{48}Ti	$1.11906 \cdot 10^{-06}$	^{49}Ti	$1.37211 \cdot 10^{-06}$	^{50}Ti	$1.90355 \cdot 10^{-06}$
^{49}V	$2.03799 \cdot 10^{-27}$	^{50}V	$1.63117 \cdot 10^{-10}$	^{51}V	$3.21807 \cdot 10^{-07}$
^{50}Cr	$1.29776 \cdot 10^{-07}$	^{51}Cr	$1.99617 \cdot 10^{-12}$	^{52}Cr	$1.15108 \cdot 10^{-05}$
^{53}Cr	$1.47119 \cdot 10^{-06}$	^{54}Cr	$5.26915 \cdot 10^{-06}$	^{53}Mn	$1.61388 \cdot 10^{-16}$
^{54}Mn	$4.07101 \cdot 10^{-20}$	^{55}Mn	$1.50992 \cdot 10^{-05}$	^{56}Mn	$8.96040 \cdot 10^{-15}$
^{54}Fe	$2.07223 \cdot 10^{-05}$	^{55}Fe	$6.39146 \cdot 10^{-09}$	^{56}Fe	$8.07565 \cdot 10^{-04}$

isotope	initial abundance	isotope	initial abundance	isotope	initial abundance
^{57}Fe	$1.60263 \cdot 10^{-04}$	^{58}Fe	$2.59610 \cdot 10^{-04}$	^{59}Fe	$2.21451 \cdot 10^{-11}$
^{60}Fe	$5.18759 \cdot 10^{-06}$	^{56}Co	$1.24491 \cdot 10^{-19}$	^{57}Co	$1.78069 \cdot 10^{-23}$
^{58}Co	$3.24102 \cdot 10^{-19}$	^{59}Co	$6.55132 \cdot 10^{-05}$	^{60}Co	$6.96451 \cdot 10^{-10}$
^{58}Ni	$1.37418 \cdot 10^{-05}$	^{59}Ni	$4.68569 \cdot 10^{-06}$	^{60}Ni	$6.37291 \cdot 10^{-05}$
^{61}Ni	$2.38751 \cdot 10^{-05}$	^{62}Ni	$4.71316 \cdot 10^{-05}$	^{63}Ni	$1.08700 \cdot 10^{-08}$
^{64}Ni	$2.42188 \cdot 10^{-05}$	^{63}Cu	$2.41233 \cdot 10^{-05}$	^{64}Cu	$2.40471 \cdot 10^{-13}$
^{65}Cu	$1.03981 \cdot 10^{-05}$	^{64}Zn	$5.58463 \cdot 10^{-06}$	^{65}Zn	$4.85689 \cdot 10^{-11}$
^{66}Zn	$8.77751 \cdot 10^{-06}$	^{67}Zn	$1.83143 \cdot 10^{-06}$	^{68}Zn	$7.79236 \cdot 10^{-06}$
^{69}Zn	$1.85306 \cdot 10^{-15}$	^{70}Zn	$1.20226 \cdot 10^{-08}$	^{69}Ga	$1.03231 \cdot 10^{-06}$
^{70}Ga	$3.46423 \cdot 10^{-16}$	^{71}Ga	$6.87294 \cdot 10^{-07}$	^{70}Ge	$1.38132 \cdot 10^{-06}$
^{71}Ge	$7.50738 \cdot 10^{-13}$	^{72}Ge	$1.20716 \cdot 10^{-06}$	^{73}Ge	$3.39778 \cdot 10^{-07}$
^{74}Ge	$1.55200 \cdot 10^{-06}$	^{75}Ge	$6.41016 \cdot 10^{-16}$	^{76}Ge	$1.09821 \cdot 10^{-08}$
^{75}As	$1.51582 \cdot 10^{-07}$	^{74}Se	$1.42548 \cdot 10^{-11}$	^{76}Se	$3.14170 \cdot 10^{-07}$
^{77}Se	$1.19301 \cdot 10^{-07}$	^{78}Se	$6.34923 \cdot 10^{-07}$	^{79}Se	$8.04393 \cdot 10^{-08}$
^{80}Se	$4.70175 \cdot 10^{-07}$	^{81}Se	$4.78289 \cdot 10^{-17}$	^{82}Se	$8.10225 \cdot 10^{-09}$
^{79}Br	$4.42479 \cdot 10^{-08}$	^{80}Br	$6.48273 \cdot 10^{-17}$	^{81}Br	$7.73356 \cdot 10^{-08}$
^{78}Kr	$4.02790 \cdot 10^{-12}$	^{79}Kr	$3.02855 \cdot 10^{-19}$	^{80}Kr	$1.58165 \cdot 10^{-08}$
^{81}Kr	$5.76859 \cdot 10^{-09}$	^{82}Kr	$2.16857 \cdot 10^{-07}$	^{83}Kr	$7.87992 \cdot 10^{-08}$
^{84}Kr	$4.69764 \cdot 10^{-07}$	^{85}Kr	$9.35212 \cdot 10^{-12}$	^{86}Kr	$1.56776 \cdot 10^{-07}$
^{85}Rb	$1.20214 \cdot 10^{-07}$	^{86}Rb	$6.69244 \cdot 10^{-14}$	^{87}Rb	$8.06675 \cdot 10^{-08}$
^{84}Sr	$2.55612 \cdot 10^{-12}$	^{85}Sr	$1.86393 \cdot 10^{-17}$	^{86}Sr	$1.20718 \cdot 10^{-07}$
^{87}Sr	$7.21014 \cdot 10^{-08}$	^{88}Sr	$8.91555 \cdot 10^{-07}$	^{89}Sr	$3.70843 \cdot 10^{-14}$
^{90}Sr	$2.08520 \cdot 10^{-18}$	^{89}Y	$2.43245 \cdot 10^{-07}$	^{90}Y	$2.94273 \cdot 10^{-15}$
^{90}Zr	$2.20459 \cdot 10^{-07}$	^{91}Zr	$6.49623 \cdot 10^{-08}$	^{92}Zr	$1.27550 \cdot 10^{-07}$
^{93}Zr	$3.59160 \cdot 10^{-08}$	^{94}Zr	$9.73772 \cdot 10^{-08}$	^{95}Zr	$4.25622 \cdot 10^{-14}$
^{96}Zr	$2.52505 \cdot 10^{-08}$	^{93}Nb	$3.51862 \cdot 10^{-10}$	^{94}Nb	$2.92808 \cdot 10^{-14}$
^{95}Nb	$2.32302 \cdot 10^{-14}$	^{92}Mo	$1.06655 \cdot 10^{-10}$	^{93}Mo	$4.27014 \cdot 10^{-12}$
^{94}Mo	$4.75566 \cdot 10^{-10}$	^{95}Mo	$1.52557 \cdot 10^{-08}$	^{96}Mo	$2.67996 \cdot 10^{-08}$
^{97}Mo	$9.01596 \cdot 10^{-09}$	^{98}Mo	$3.06969 \cdot 10^{-08}$	^{99}Mo	$1.68457 \cdot 10^{-15}$
^{100}Mo	$2.43101 \cdot 10^{-09}$	^{99}Tc	$3.79632 \cdot 10^{-09}$	^{96}Ru	$5.41944 \cdot 10^{-12}$
^{97}Ru	$7.94019 \cdot 10^{-19}$	^{98}Ru	$1.02709 \cdot 10^{-11}$	^{99}Ru	$3.80906 \cdot 10^{-10}$
^{100}Ru	$1.45640 \cdot 10^{-08}$	^{101}Ru	$3.38856 \cdot 10^{-09}$	^{102}Ru	$2.12889 \cdot 10^{-08}$
^{103}Ru	$1.02991 \cdot 10^{-15}$	^{104}Ru	$1.79933 \cdot 10^{-09}$	^{103}Rh	$3.84695 \cdot 10^{-09}$
^{102}Pd	$3.31812 \cdot 10^{-13}$	^{103}Pd	$4.91246 \cdot 10^{-19}$	^{104}Pd	$1.09748 \cdot 10^{-08}$
^{105}Pd	$3.06684 \cdot 10^{-09}$	^{106}Pd	$1.36607 \cdot 10^{-08}$	^{107}Pd	$2.72121 \cdot 10^{-09}$
^{108}Pd	$1.71428 \cdot 10^{-08}$	^{109}Pd	$3.62016 \cdot 10^{-16}$	^{110}Pd	$1.77928 \cdot 10^{-09}$
^{107}Ag	$1.33214 \cdot 10^{-11}$	^{108}Ag	$2.38440 \cdot 10^{-21}$	^{109}Ag	$5.03450 \cdot 10^{-09}$
^{106}Cd	$6.29754 \cdot 10^{-13}$	^{107}Cd	$1.01562 \cdot 10^{-20}$	^{108}Cd	$3.44935 \cdot 10^{-11}$

isotope	initial abundance	isotope	initial abundance	isotope	initial abundance
^{109}Cd	$7.13089 \cdot 10^{-16}$	^{110}Cd	$1.41198 \cdot 10^{-08}$	^{111}Cd	$5.04531 \cdot 10^{-09}$
^{112}Cd	$1.91879 \cdot 10^{-08}$	^{113}Cd	$5.66183 \cdot 10^{-09}$	^{114}Cd	$2.83811 \cdot 10^{-08}$
^{115}Cd	$2.74707 \cdot 10^{-14}$	^{116}Cd	$4.88638 \cdot 10^{-09}$	^{113}In	$6.72958 \cdot 10^{-13}$
^{114}In	$8.84347 \cdot 10^{-23}$	^{115}In	$5.69767 \cdot 10^{-09}$	^{112}Sn	$2.23515 \cdot 10^{-12}$
^{113}Sn	$1.00847 \cdot 10^{-17}$	^{114}Sn	$1.30212 \cdot 10^{-11}$	^{115}Sn	$7.14004 \cdot 10^{-12}$
^{116}Sn	$3.52606 \cdot 10^{-08}$	^{117}Sn	$1.19995 \cdot 10^{-08}$	^{118}Sn	$5.80835 \cdot 10^{-08}$
^{119}Sn	$1.76234 \cdot 10^{-08}$	^{120}Sn	$9.00875 \cdot 10^{-08}$	^{121}Sn	$1.81708 \cdot 10^{-15}$
^{122}Sn	$1.14757 \cdot 10^{-08}$	^{123}Sn	$2.38346 \cdot 10^{-16}$	^{124}Sn	$5.07378 \cdot 10^{-10}$
^{121}Sb	$7.19502 \cdot 10^{-09}$	^{122}Sb	$1.71084 \cdot 10^{-15}$	^{123}Sb	$1.74176 \cdot 10^{-09}$
^{120}Te	$1.02729 \cdot 10^{-13}$	^{121}Te	$1.72960 \cdot 10^{-19}$	^{122}Te	$1.09002 \cdot 10^{-08}$
^{123}Te	$3.75004 \cdot 10^{-09}$	^{124}Te	$2.14681 \cdot 10^{-08}$	^{125}Te	$7.11974 \cdot 10^{-09}$
^{126}Te	$4.04159 \cdot 10^{-08}$	^{127}Te	$2.61801 \cdot 10^{-16}$	^{128}Te	$5.83171 \cdot 10^{-09}$
^{129}Te	$1.76429 \cdot 10^{-18}$	^{130}Te	$3.02504 \cdot 10^{-09}$	^{127}I	$5.37723 \cdot 10^{-09}$
^{128}I	$1.07299 \cdot 10^{-17}$	^{129}I	$3.75470 \cdot 10^{-13}$	^{124}Xe	$1.30734 \cdot 10^{-13}$
^{125}Xe	$1.52869 \cdot 10^{-20}$	^{126}Xe	$2.29615 \cdot 10^{-13}$	^{127}Xe	$5.88586 \cdot 10^{-19}$
^{128}Xe	$1.25475 \cdot 10^{-08}$	^{129}Xe	$5.52609 \cdot 10^{-09}$	^{130}Xe	$2.70031 \cdot 10^{-08}$
^{131}Xe	$1.05136 \cdot 10^{-08}$	^{132}Xe	$5.57666 \cdot 10^{-08}$	^{134}Xe	$9.02231 \cdot 10^{-09}$
^{135}Xe	$1.11358 \cdot 10^{-17}$	^{136}Xe	$1.45057 \cdot 10^{-09}$	^{133}Cs	$7.84092 \cdot 10^{-09}$
^{134}Cs	$3.92757 \cdot 10^{-13}$	^{135}Cs	$6.40245 \cdot 10^{-09}$	^{130}Ba	$1.05438 \cdot 10^{-13}$
^{131}Ba	$1.82963 \cdot 10^{-19}$	^{132}Ba	$1.72620 \cdot 10^{-13}$	^{133}Ba	$3.49007 \cdot 10^{-19}$
^{134}Ba	$1.73610 \cdot 10^{-08}$	^{135}Ba	$5.60801 \cdot 10^{-09}$	^{136}Ba	$5.31417 \cdot 10^{-08}$
^{137}Ba	$4.65953 \cdot 10^{-08}$	^{138}Ba	$4.07551 \cdot 10^{-07}$	^{138}La	$2.72174 \cdot 10^{-14}$
^{139}La	$4.44572 \cdot 10^{-08}$	^{136}Ce	$8.46445 \cdot 10^{-14}$	^{137}Ce	$2.09845 \cdot 10^{-21}$
^{138}Ce	$3.62709 \cdot 10^{-13}$	^{139}Ce	$1.75362 \cdot 10^{-18}$	^{140}Ce	$9.35947 \cdot 10^{-08}$
^{141}Ce	$4.92482 \cdot 10^{-15}$	^{142}Ce	$3.81970 \cdot 10^{-09}$	^{141}Pr	$9.78599 \cdot 10^{-09}$
^{142}Nd	$2.11373 \cdot 10^{-08}$	^{143}Nd	$3.58723 \cdot 10^{-09}$	^{144}Nd	$1.15432 \cdot 10^{-08}$
^{145}Nd	$2.13613 \cdot 10^{-09}$	^{146}Nd	$9.93144 \cdot 10^{-09}$	^{147}Nd	$1.47019 \cdot 10^{-15}$
^{148}Nd	$1.56569 \cdot 10^{-09}$	^{149}Nd	$3.13835 \cdot 10^{-18}$	^{150}Nd	$2.59802 \cdot 10^{-11}$
^{147}Pm	$1.11367 \cdot 10^{-13}$	^{144}Sm	$2.93120 \cdot 10^{-12}$	^{147}Sm	$1.06693 \cdot 10^{-09}$
^{148}Sm	$2.21902 \cdot 10^{-09}$	^{149}Sm	$4.11702 \cdot 10^{-10}$	^{150}Sm	$1.92429 \cdot 10^{-09}$
^{151}Sm	$2.84972 \cdot 10^{-12}$	^{152}Sm	$1.62590 \cdot 10^{-09}$	^{153}Sm	$2.44443 \cdot 10^{-16}$
^{154}Sm	$6.30174 \cdot 10^{-10}$	^{151}Eu	$2.47307 \cdot 10^{-10}$	^{152}Eu	$2.61859 \cdot 10^{-13}$
^{153}Eu	$3.18340 \cdot 10^{-10}$	^{152}Gd	$9.17695 \cdot 10^{-11}$	^{153}Gd	$5.38311 \cdot 10^{-15}$
^{154}Gd	$7.12475 \cdot 10^{-10}$	^{155}Gd	$3.69955 \cdot 10^{-10}$	^{156}Gd	$1.44397 \cdot 10^{-09}$
^{157}Gd	$6.47581 \cdot 10^{-10}$	^{158}Gd	$2.51765 \cdot 10^{-09}$	^{159}Gd	$1.11665 \cdot 10^{-16}$
^{160}Gd	$4.67231 \cdot 10^{-10}$	^{159}Tb	$5.38308 \cdot 10^{-10}$	^{156}Dy	$5.44250 \cdot 10^{-15}$
^{157}Dy	$5.60479 \cdot 10^{-22}$	^{158}Dy	$1.96363 \cdot 10^{-13}$	^{159}Dy	$6.23912 \cdot 10^{-18}$
^{160}Dy	$8.61066 \cdot 10^{-10}$	^{161}Dy	$4.40730 \cdot 10^{-10}$	^{162}Dy	$1.84740 \cdot 10^{-09}$

isotope	initial abundance	isotope	initial abundance	isotope	initial abundance
^{163}Dy	$7.73941 \cdot 10^{-10}$	^{164}Dy	$3.60583 \cdot 10^{-09}$	^{165}Ho	$6.63760 \cdot 10^{-10}$
^{162}Er	$8.65107 \cdot 10^{-15}$	^{163}Er	$1.44211 \cdot 10^{-22}$	^{164}Er	$1.06562 \cdot 10^{-13}$
^{165}Er	$1.08567 \cdot 10^{-20}$	^{166}Er	$1.14958 \cdot 10^{-09}$	^{167}Er	$4.84240 \cdot 10^{-10}$
^{168}Er	$2.19140 \cdot 10^{-09}$	^{169}Er	$9.78335 \cdot 10^{-16}$	^{170}Er	$1.14296 \cdot 10^{-09}$
^{169}Tm	$4.23344 \cdot 10^{-10}$	^{168}Yb	$8.81077 \cdot 10^{-15}$	^{169}Yb	$6.03672 \cdot 10^{-20}$
^{170}Yb	$7.12985 \cdot 10^{-10}$	^{171}Yb	$9.14050 \cdot 10^{-10}$	^{172}Yb	$2.48619 \cdot 10^{-09}$
^{173}Yb	$1.15639 \cdot 10^{-09}$	^{174}Yb	$5.17967 \cdot 10^{-09}$	^{175}Yb	$4.57608 \cdot 10^{-16}$
^{176}Yb	$9.11970 \cdot 10^{-10}$	^{175}Lu	$7.04472 \cdot 10^{-10}$	^{176}Lu	$3.21475 \cdot 10^{-10}$
^{174}Hf	$6.94324 \cdot 10^{-15}$	^{175}Hf	$8.65989 \cdot 10^{-20}$	^{176}Hf	$4.44787 \cdot 10^{-10}$
^{177}Hf	$6.34632 \cdot 10^{-10}$	^{178}Hf	$2.77252 \cdot 10^{-09}$	^{179}Hf	$9.48508 \cdot 10^{-10}$
^{180}Hf	$5.01535 \cdot 10^{-09}$	^{181}Hf	$3.93979 \cdot 10^{-15}$	^{182}Hf	$2.63973 \cdot 10^{-10}$
^{180}Ta	$3.34284 \cdot 10^{-16}$	^{181}Ta	$9.96811 \cdot 10^{-10}$	^{180}W	$3.45437 \cdot 10^{-13}$
^{181}W	$6.46476 \cdot 10^{-18}$	^{182}W	$1.97474 \cdot 10^{-09}$	^{183}W	$1.24433 \cdot 10^{-09}$
^{184}W	$3.30055 \cdot 10^{-09}$	^{185}W	$1.01340 \cdot 10^{-14}$	^{186}W	$1.44109 \cdot 10^{-09}$
^{185}Re	$6.76055 \cdot 10^{-10}$	^{186}Re	$5.68888 \cdot 10^{-16}$	^{187}Re	$3.64617 \cdot 10^{-10}$
^{184}Os	$4.27443 \cdot 10^{-15}$	^{185}Os	$5.07957 \cdot 10^{-20}$	^{186}Os	$1.28037 \cdot 10^{-09}$
^{187}Os	$3.42760 \cdot 10^{-10}$	^{188}Os	$2.66003 \cdot 10^{-09}$	^{189}Os	$5.43250 \cdot 10^{-10}$
^{190}Os	$2.76853 \cdot 10^{-09}$	^{191}Os	$1.28804 \cdot 10^{-15}$	^{192}Os	$1.52614 \cdot 10^{-09}$
^{191}Ir	$4.87742 \cdot 10^{-10}$	^{192}Ir	$1.07653 \cdot 10^{-14}$	^{193}Ir	$6.94494 \cdot 10^{-10}$
^{190}Pt	$6.43980 \cdot 10^{-15}$	^{191}Pt	$2.46671 \cdot 10^{-21}$	^{192}Pt	$7.23041 \cdot 10^{-10}$
^{193}Pt	$1.56083 \cdot 10^{-12}$	^{194}Pt	$2.33027 \cdot 10^{-09}$	^{195}Pt	$9.52095 \cdot 10^{-10}$
^{196}Pt	$4.39619 \cdot 10^{-09}$	^{197}Pt	$1.08675 \cdot 10^{-16}$	^{198}Pt	$4.56203 \cdot 10^{-10}$
^{197}Au	$1.35177 \cdot 10^{-09}$	^{198}Au	$4.83370 \cdot 10^{-16}$	^{199}Au	$2.55596 \cdot 10^{-17}$
^{196}Hg	$5.74750 \cdot 10^{-14}$	^{197}Hg	$6.29544 \cdot 10^{-21}$	^{198}Hg	$4.29664 \cdot 10^{-09}$
^{199}Hg	$2.08891 \cdot 10^{-09}$	^{200}Hg	$7.00192 \cdot 10^{-09}$	^{201}Hg	$3.02503 \cdot 10^{-09}$
^{202}Hg	$1.08052 \cdot 10^{-08}$	^{203}Hg	$1.87098 \cdot 10^{-16}$	^{204}Hg	$3.38882 \cdot 10^{-10}$
^{203}Tl	$4.79708 \cdot 10^{-09}$	^{204}Tl	$1.60743 \cdot 10^{-13}$	^{205}Tl	$7.36825 \cdot 10^{-09}$
^{204}Pb	$5.83764 \cdot 10^{-09}$	^{205}Pb	$2.78630 \cdot 10^{-13}$	^{206}Pb	$2.41561 \cdot 10^{-08}$
^{207}Pb	$1.78277 \cdot 10^{-08}$	^{208}Pb	$2.43652 \cdot 10^{-08}$	^{209}Bi	$1.10186 \cdot 10^{-09}$

BRANCHING POINTS DURING THE ^{13}C-POCKET

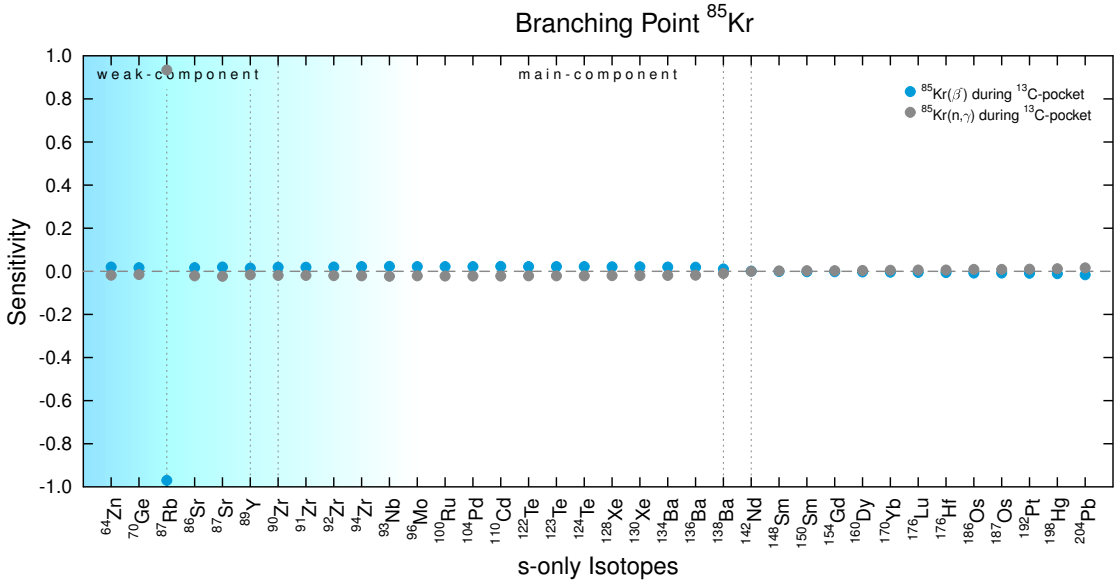

Figure A.1: Branching point ^{85}Kr during the ^{13}C-pocket (table 3.1). ^{87}Rb lies on the neutron capture branch of the branching point ^{85}Kr.

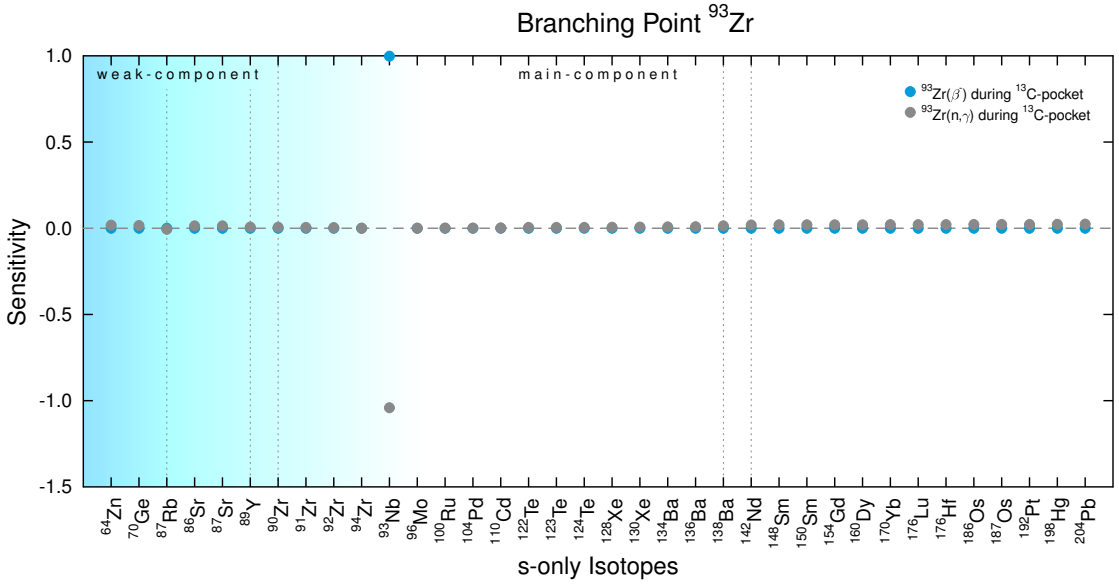

Figure A.2: Branching point ^{93}Zr during the ^{13}C-pocket (table 3.1). The β-decay of the branching point ^{93}Zr is the only channel to produce ^{93}Nb.

GLOBAL SENSITIVITIES DURING THE ^{13}C-POCKET

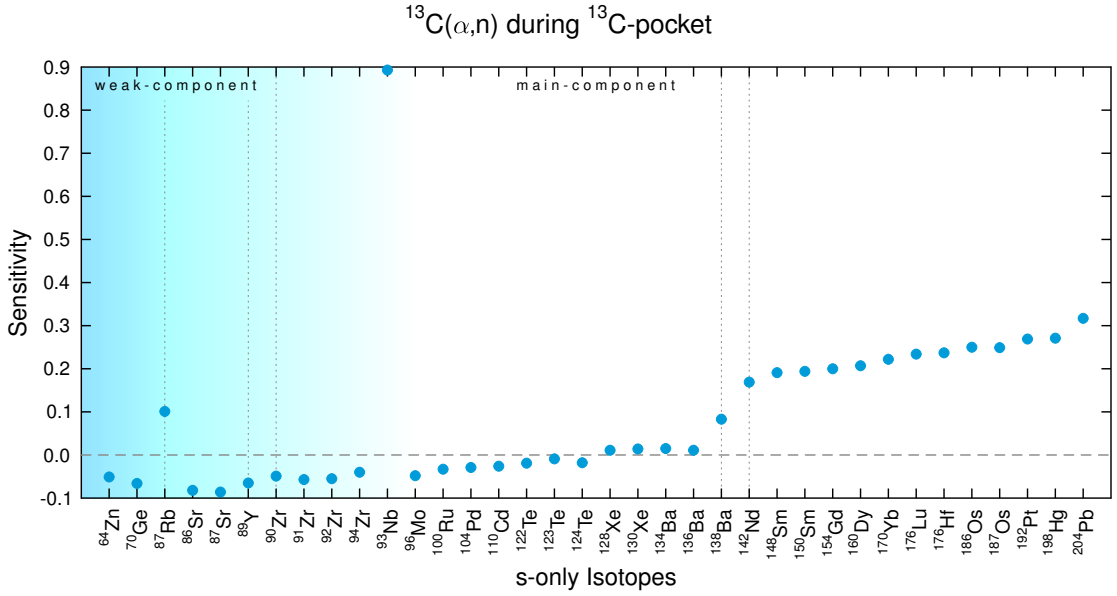

Figure A.3: Neutron donator reaction ^{13}C(α,n) during the ^{13}C-pocket (table 3.2). An increased α-capture efficiency increases the overall neutron abundance, resulting in an increased production of heavy isotopes.

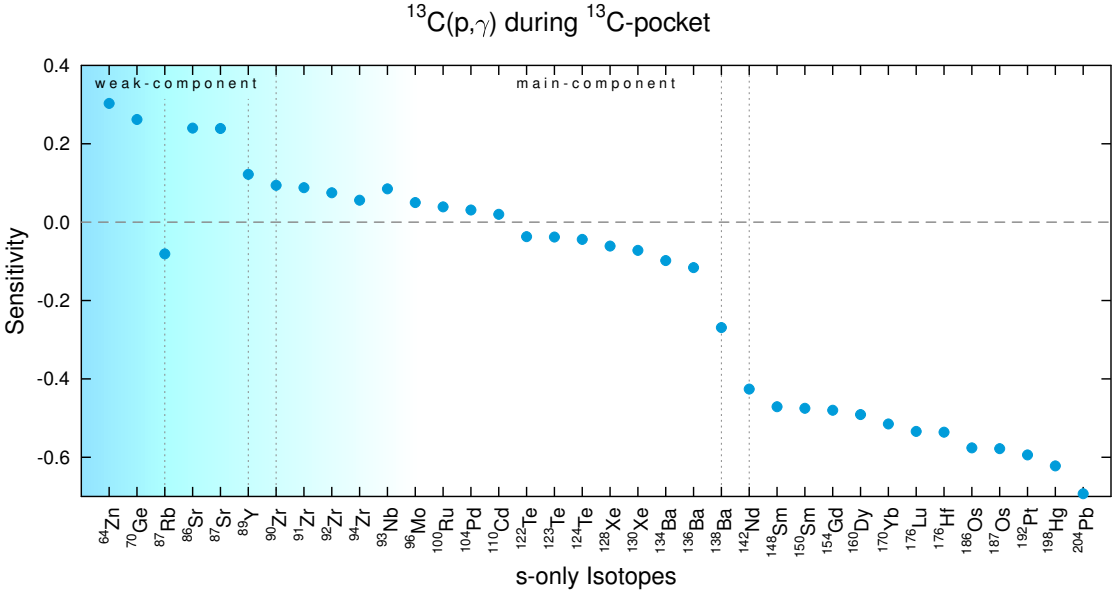

Figure A.4: Neutron poison reaction ^{13}C(p,γ) during the ^{13}C-pocket (table 3.3). The proton capture competes directly with the α-capture, resulting in a lower yield of the neutron source ^{13}C(α,n) and an increased production of the neutron poison reaction ^{14}N (figure 3.5).

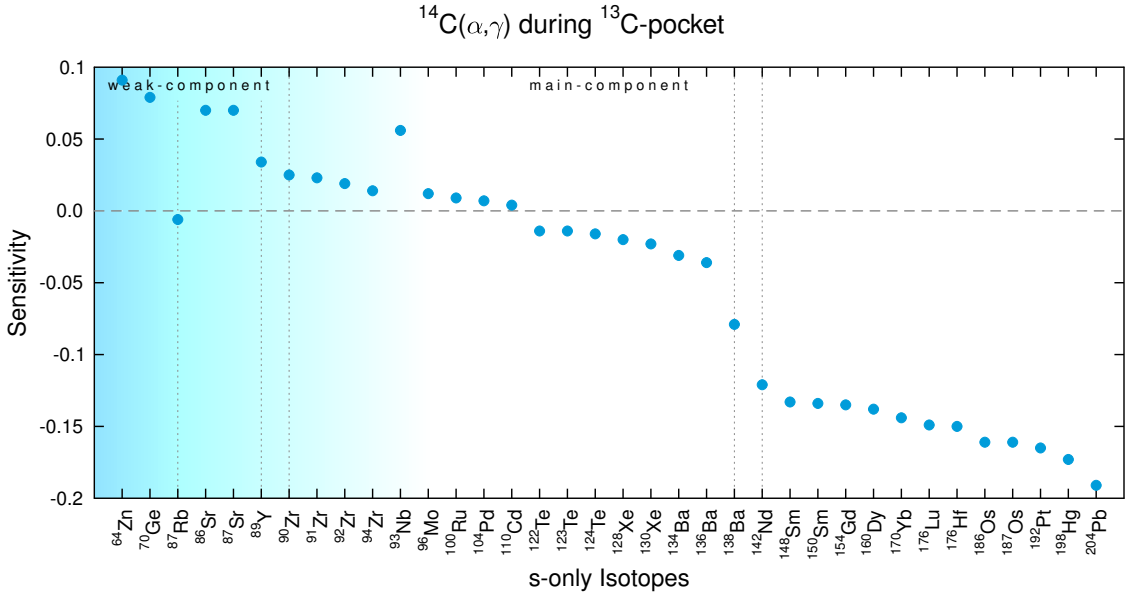

Figure A.5: Neutron poison reaction ^{14}C(α,γ) during the ^{13}C-pocket (table 3.3). The α-capture on ^{14}C, competes on the alphas with the neutron source ^{13}C(α,n), thereby reducing the overall produced neutrons.

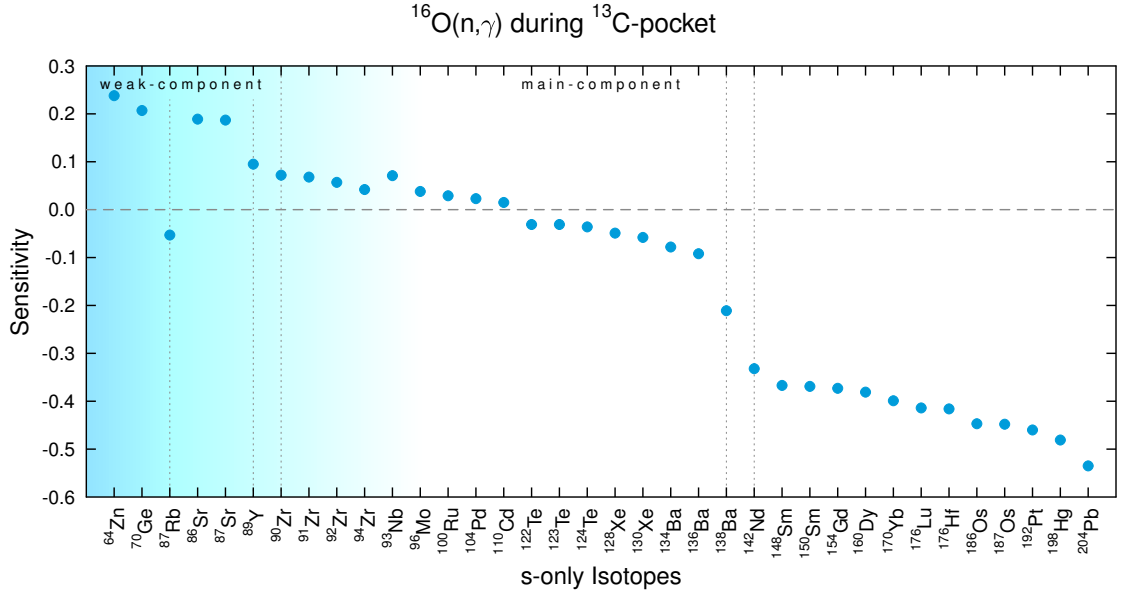

Figure A.6: Neutron poison reaction ^{16}O(n,γ) during the ^{13}C-pocket (table 3.3). The neutron capture on ^{16}O, steals neutrons from the *s* process, since this reaction does not participate to the *s* process.

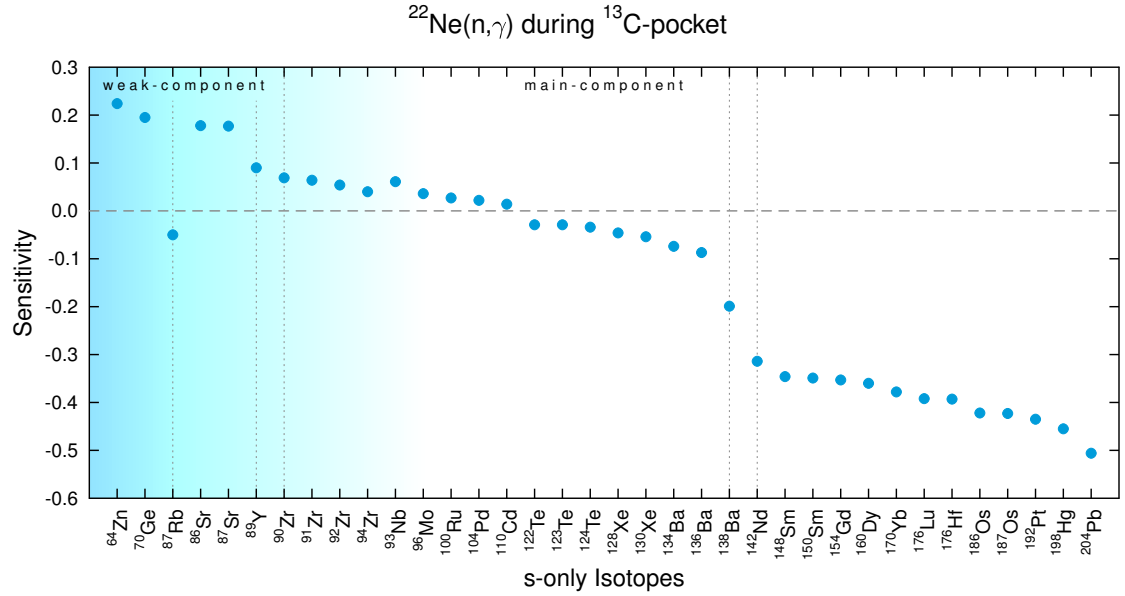

Figure A.7: Neutron poison reaction ^{22}Ne(n,γ) during the ^{13}C-pocket (table 3.3). The neutron capture on ^{22}Ne, steals neutrons from the *s* process, since this reaction does not participate to the *s* process.

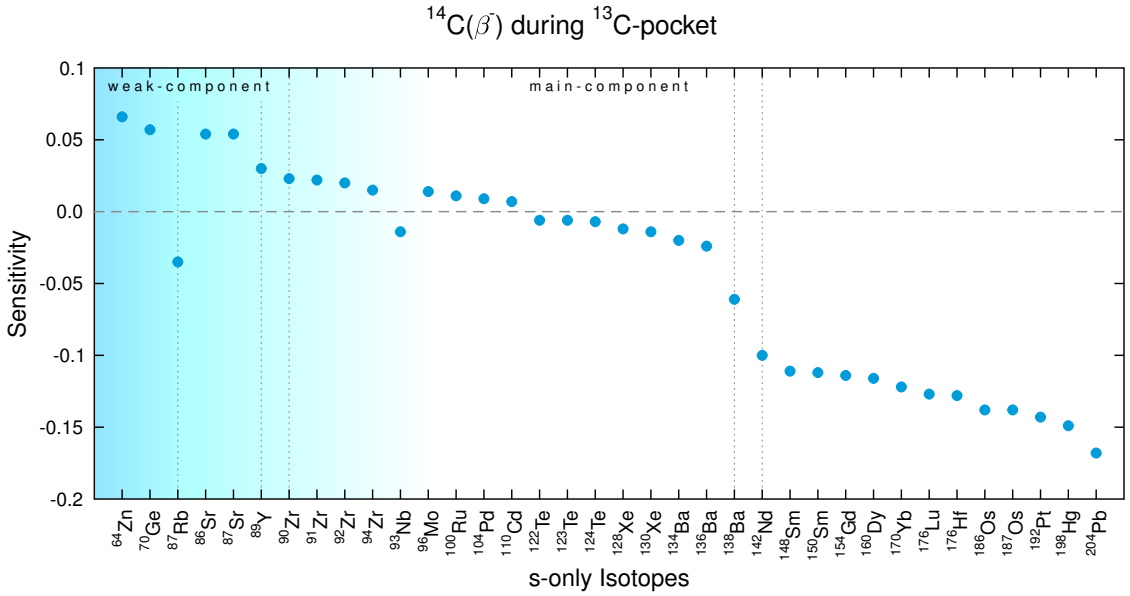

Figure A.8: Neutron poison reaction ^{14}C(β^-) during the ^{13}C-pocket (table 3.3). The β^--decay of ^{14}C produces the neutron poison reaction ^{14}N (figure 3.5).

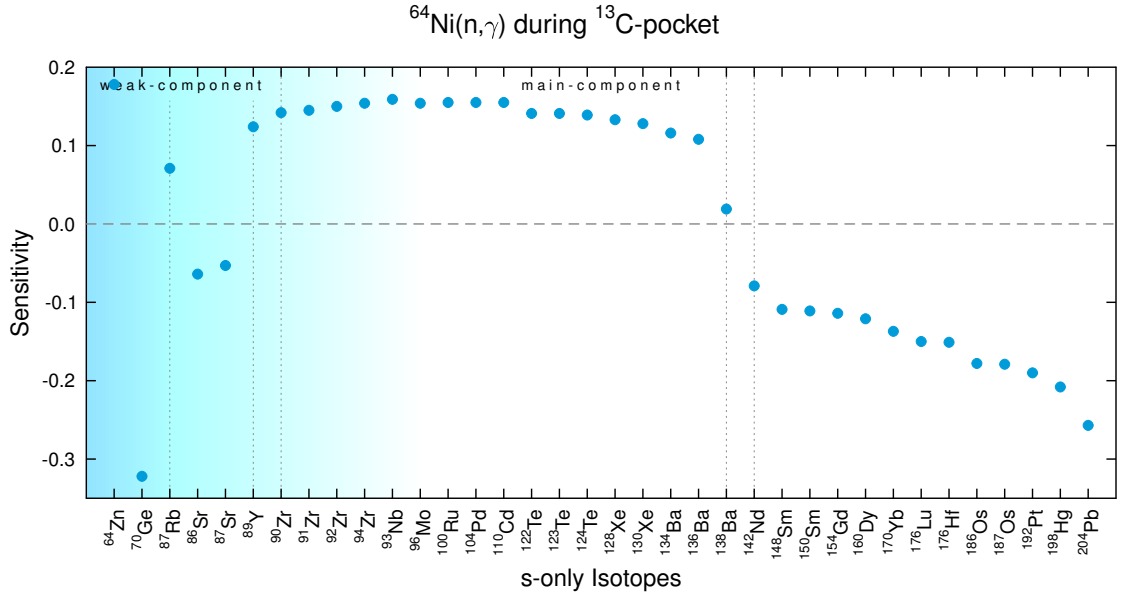

Figure A.9: Competing capture reaction ^{64}Ni(n,γ) during the ^{13}C-pocket (table 3.4). ^{64}Ni competes with ^{64}Zn as seed isotope. The increased neutron capture rate results in a positive ^{64}Zn sensitivity.

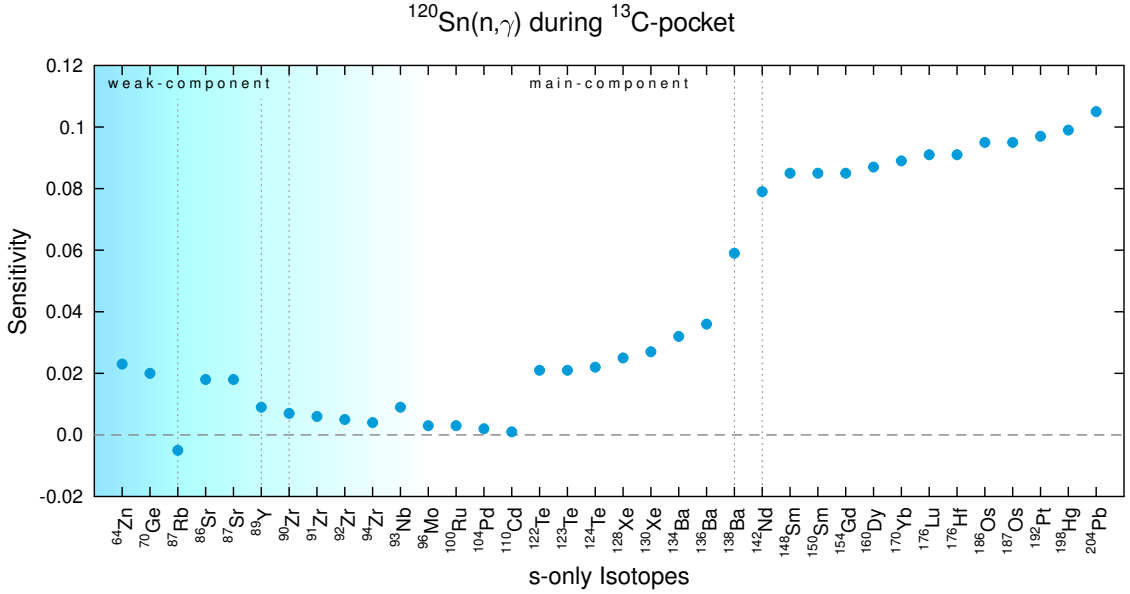

Figure A.10: Competing capture reaction ^{120}Sn(n,γ) during the ^{13}C-pocket (table 3.4). ^{120}Sn acts as seed isotope for the heavier (following) isotopes along the *s* process path. As it competes with iron as seed, an increased neutron capture rate of ^{120}Sn reduces the depletion of the lighter *s*-isotopes. The increased production of heavy isotopes, with their respective higher neutron capture cross sections, decreases the overall neutron density, which is indicated by the branching sensitive isotope ^{87}Rb.

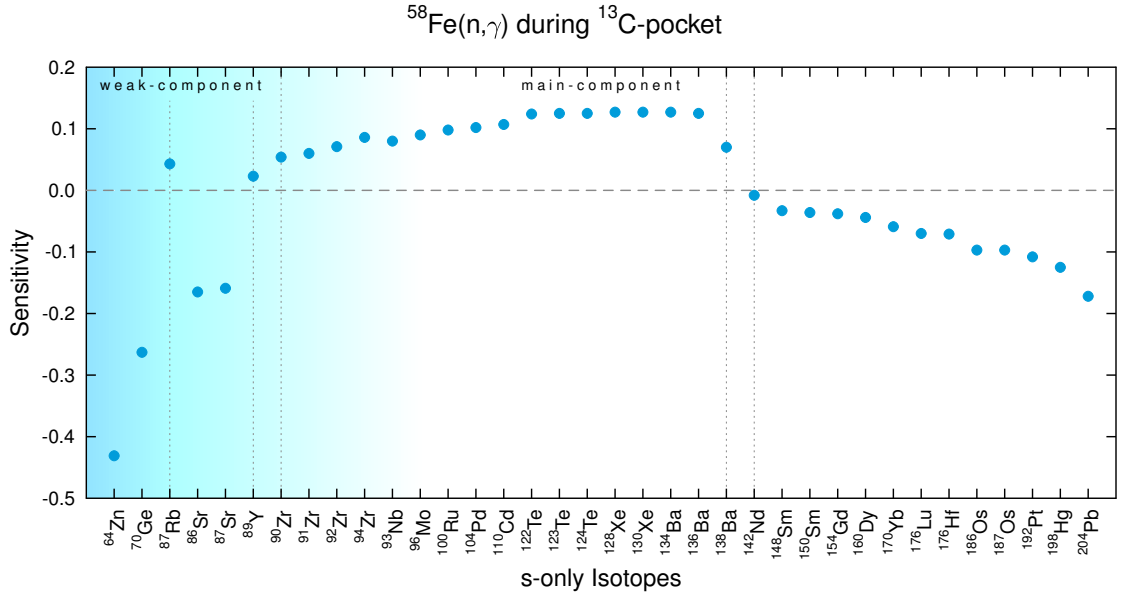

Figure A.11: Competing capture reaction ^{58}Fe(n,γ) during the ^{13}C-pocket (table 3.4). Similar to ^{56}Fe, an increased neutron capture on ^{58}Fe promotes the depletion of seed isotopes and a neutron poison reaction like shape for the main component. As ^{56}Fe is still the main seed isotope, the ^{58}Fe(n,γ) produces lower sensitivities.

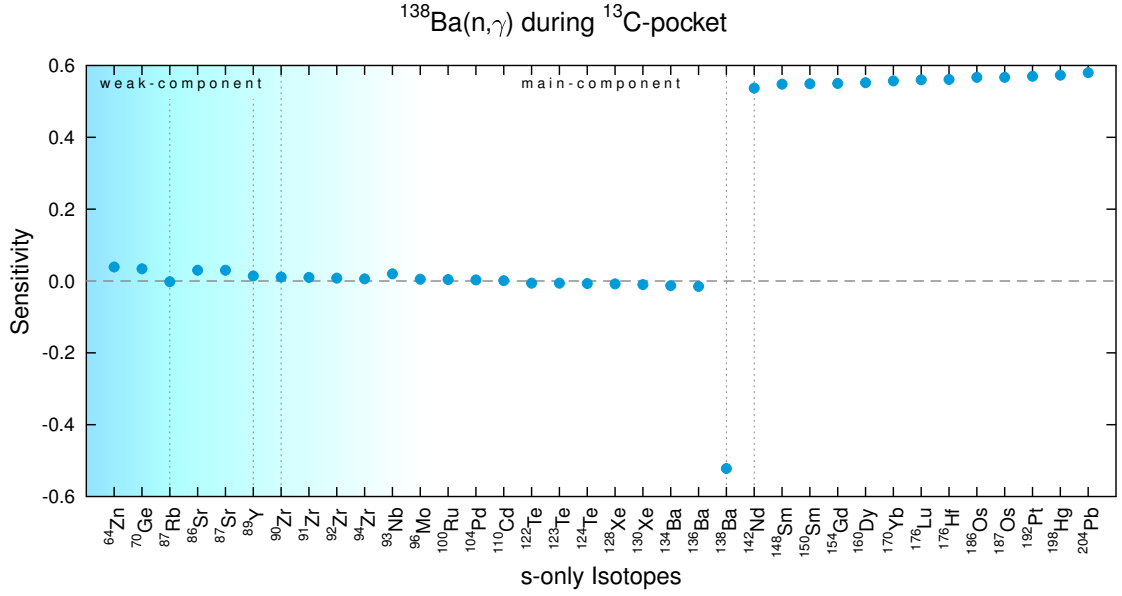

Figure A.12: Bottleneck reaction ^{138}Ba(n,γ) during the ^{13}C-pocket (table 3.5). The increased ^{138}Ba(n,γ) rate increases the production of the following isotopes as described in the general discussion.

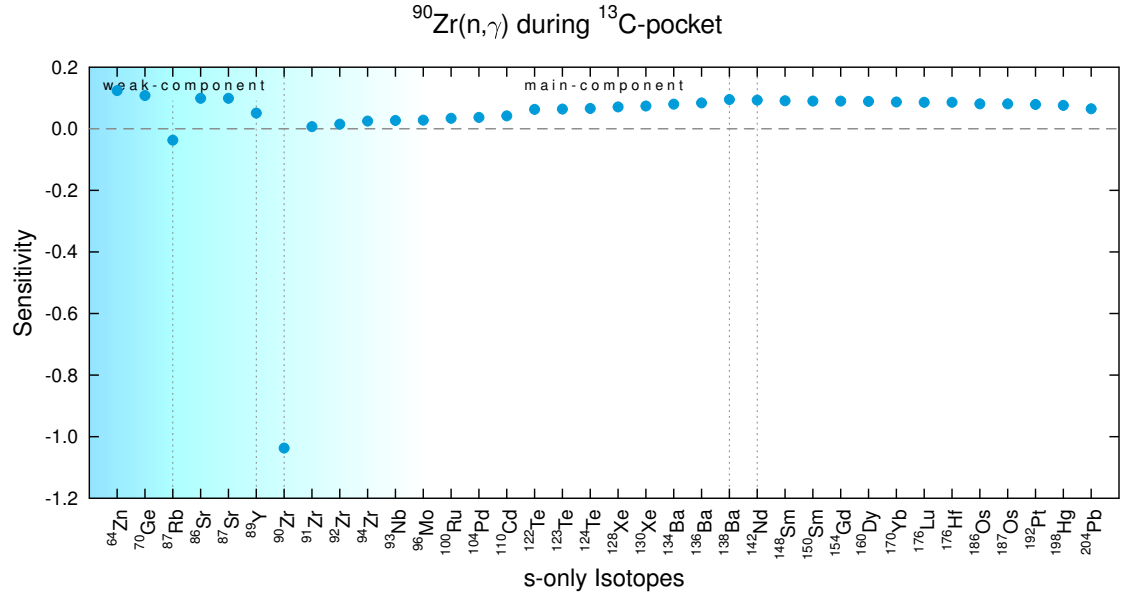

Figure A.13: Bottleneck reaction ^{90}Zr(n,γ) during the ^{13}C-pocket (table 3.5). The bottleneck reaction rates from the first *s* process peak compete directly with the NSE peak seed isotopes. Thus a general increase of all other isotopes is observed.

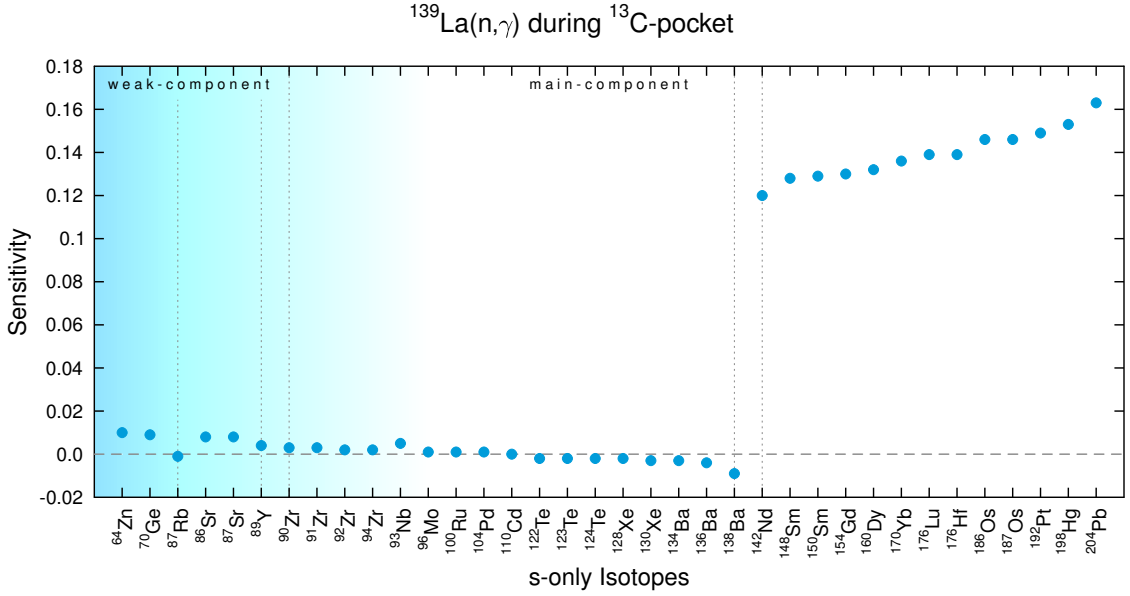

Figure A.14: Bottleneck reaction ^{139}La(n,γ) during the ^{13}C-pocket (table 3.5). The increased ^{139}La(n,γ) rate increases the production of the following isotopes as described in the general discussion.

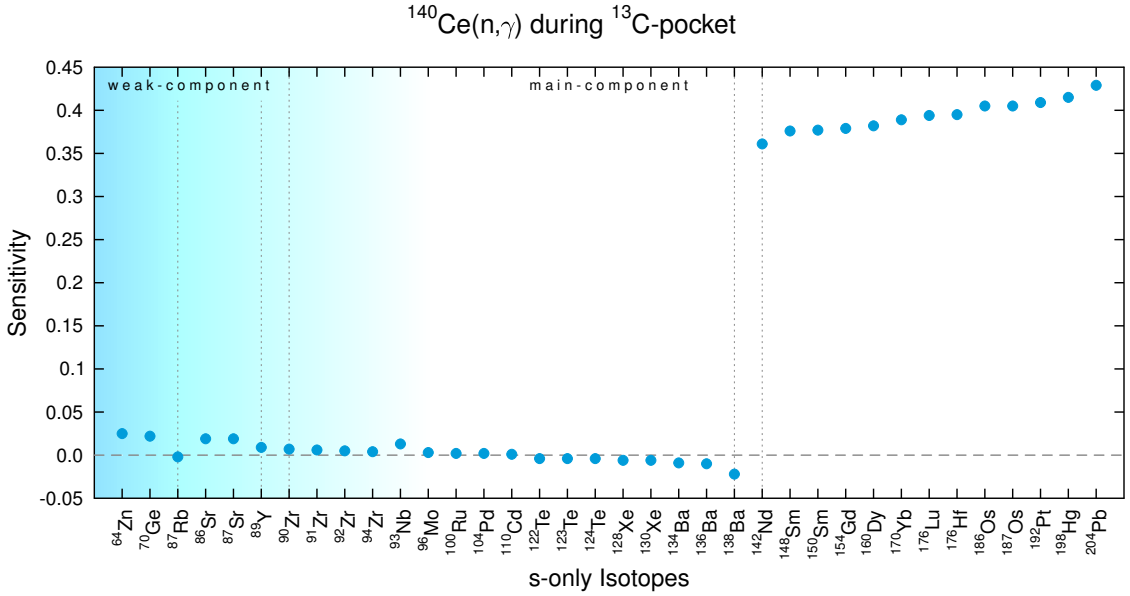

Figure A.15: Bottleneck reaction ^{140}Ce(n,γ) during the ^{13}C-pocket (table 3.5). The increased ^{140}Ce(n,γ) rate increases the production of the following isotopes as described in the general discussion.

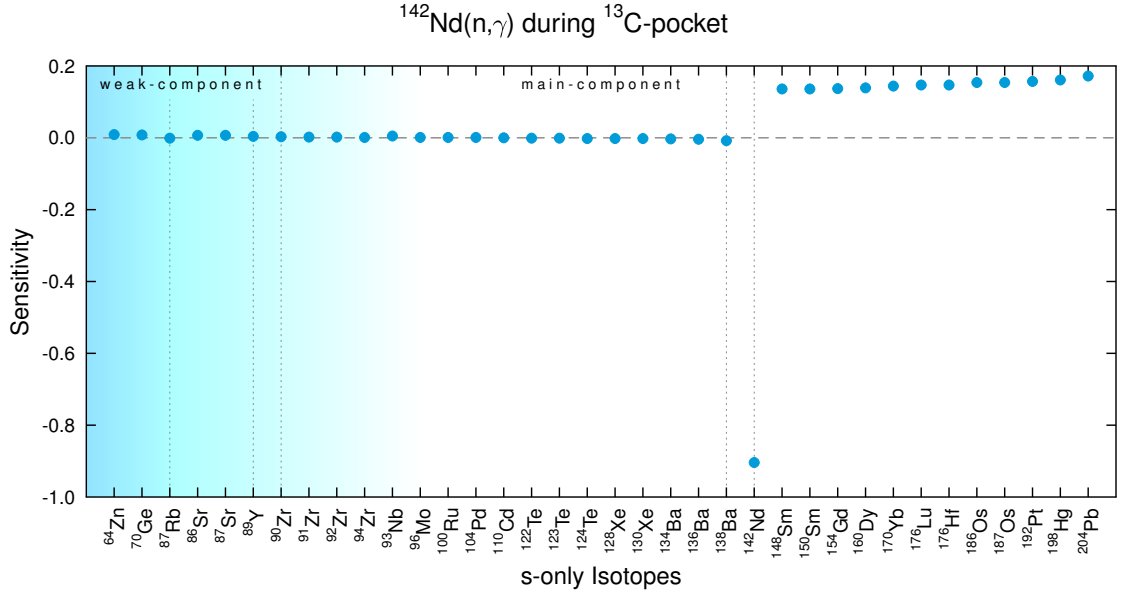

Figure A.16: Bottleneck reaction ^{142}Nd(n,γ) during the ^{13}C-pocket (table 3.5). The increased ^{142}Nd(n,γ) rate increases the production of the following isotopes as described in the general discussion.

A.1.2 THERMAL PULSE

LOCAL SENSITIVITIES DURING THE TP

Table A.3: Reactions with strongest local sensitivities in the thermal pulse for each isotope. Filter criteria in chapter 2.3.3 on page 49.

Isotope	Most important reactions with respective sensitivities					
^{58}Fe	^{58}Fe(n,γ)	-0.612	^{57}Fe(n,γ)	0.302	-	
^{59}Co	^{59}Co(n,γ)	-1.127	^{58}Fe(n,γ)	0.901	^{57}Fe(n,γ)	0.353
^{60}Ni	^{60}Ni(n,γ)	-0.924	^{58}Fe(n,γ)	0.702	^{59}Co(n,γ)	0.423
^{61}Ni	^{61}Ni(n,γ)	-1.349	^{58}Fe(n,γ)	0.618	^{60}Ni(n,γ)	0.530
^{62}Ni	^{62}Ni(n,γ)	-1.038	^{60}Ni(n,γ)	0.521	^{59}Co(n,γ)	0.379
^{64}Ni	^{62}Ni(n,γ)	0.834	^{63}Ni(n,γ)	0.798	^{64}Ni(n,γ)	-0.493
^{63}Cu	^{63}Ni(β^-)	0.894	^{63}Ni(n,γ)	-0.646	^{62}Ni(n,γ)	0.585
^{65}Cu	^{65}Cu(n,γ)	-0.766	^{64}Ni(n,γ)	0.661	^{62}Ni(n,γ)	0.317
^{64}Zn	^{64}Zn(n,γ)	-0.620	^{63}Ni(β^-)	0.413	^{62}Ni(n,γ)	0.248
^{66}Zn	^{66}Zn(n,γ)	-1.017	^{64}Ni(n,γ)	0.383	^{65}Cu(n,γ)	0.380
^{67}Zn	^{67}Zn(n,γ)	-1.301	^{65}Cu(n,γ)	0.386	^{64}Ni(n,γ)	0.340
^{68}Zn	^{68}Zn(n,γ)	-0.829	^{66}Zn(n,γ)	0.560	^{65}Cu(n,γ)	0.351
^{69}Ga	^{69}Ga(n,γ)	-1.489	^{68}Zn(n,γ)	0.820	^{66}Zn(n,γ)	0.600
^{71}Ga	^{71}Ga(n,γ)	-1.146	^{68}Zn(n,γ)	0.968	^{66}Zn(n,γ)	0.583
^{70}Ge	^{70}Ge(n,γ)	-1.435	^{68}Zn(n,γ)	0.937	^{66}Zn(n,γ)	0.617
^{72}Ge	^{72}Ge(n,γ)	-1.473	^{68}Zn(n,γ)	1.015	^{66}Zn(n,γ)	0.500
^{73}Ge	^{73}Ge(n,γ)	-1.678	^{68}Zn(n,γ)	1.023	^{66}Zn(n,γ)	0.467
^{74}Ge	^{74}Ge(n,γ)	-1.199	^{68}Zn(n,γ)	0.808	^{70}Ge(n,γ)	0.408
^{75}As	^{75}As(n,γ)	-1.738	^{68}Zn(n,γ)	0.776	^{74}Ge(n,γ)	0.604
^{76}Se	^{76}Se(n,γ)	-1.651	^{68}Zn(n,γ)	0.683	^{74}Ge(n,γ)	0.647
^{77}Se	^{77}Se(n,γ)	-1.745	^{74}Ge(n,γ)	0.662	^{68}Zn(n,γ)	0.639
^{78}Se	^{78}Se(n,γ)	-1.399	^{74}Ge(n,γ)	0.774	^{72}Ge(n,γ)	0.500
^{80}Se	^{80}Se(n,γ)	-1.527	^{74}Ge(n,γ)	0.856	^{78}Se(n,γ)	0.592
^{79}Br	^{79}Br(n,γ)	-1.156	^{79}Se(n,γ)	-0.864	^{74}Ge(n,γ)	0.725
^{81}Br	^{81}Br(n,γ)	-1.957	^{74}Ge(n,γ)	0.848	^{78}Se(n,γ)	0.614
^{80}Kr	^{79}Se(n,γ)	-1.062	^{80}Kr(n,γ)	-1.021	^{79}Se(β^-)	0.830

Isotope	Most important reactions with respective sensitivities					
^{82}Kr	^{82}Kr(n,γ)	-1.426	^{74}Ge(n,γ)	0.746	^{78}Se(n,γ)	0.590
^{83}Kr	^{83}Kr(n,γ)	-1.675	^{74}Ge(n,γ)	0.693	^{78}Se(n,γ)	0.606
^{84}Kr	^{84}Kr(n,γ)	-0.607	^{80}Se(n,γ)	0.548	^{78}Se(n,γ)	0.472
^{86}Kr	^{84}Kr(n,γ)	1.408	^{85}Kr(n,γ)	0.840	^{82}Kr(n,γ)	0.386
^{85}Rb	^{85}Rb(n,γ)	-0.945	^{85}Kr(n,γ)	-0.631	^{80}Se(n,γ)	0.503
^{86}Sr	^{86}Sr(n,γ)	-0.883	^{80}Se(n,γ)	0.368	^{85}Kr(β^-)	0.303
^{87}Sr	^{87}Sr(n,γ)	-0.985	^{80}Se(n,γ)	0.265	^{86}Sr(n,γ)	0.255
^{88}Sr	^{88}Sr(n,γ)	-0.326	^{86}Sr(n,γ)	0.109	-	
^{89}Y	^{88}Sr(n,γ)	0.711	^{89}Y(n,γ)	-0.692	-	
^{90}Zr	^{89}Y (n,γ)	0.445	^{88}Sr(n,γ)	0.370	-	
^{91}Zr	^{89}Y (n,γ)	0.387	^{88}Sr(n,γ)	0.270	-	
^{92}Zr	^{89}Y (n,γ)	0.242	^{88}Sr(n,γ)	0.125	-	
^{96}Zr	^{95}Zr(n,γ)	0.855	^{95}Zr(β^-)	-0.831	^{96}Zr(n,γ)	-0.496
^{93}Nb	^{93}Zr(β^-)	0.108	^{93}Zr(n,γ)	-0.105	-	
^{95}Mo	^{95}Mo(n,γ)	-1.063	^{93}Zr(n,γ)	0.108	-	
^{97}Mo	^{97}Mo(n,γ)	-1.092	^{93}Zr(n,γ)	0.141	-	
^{98}Mo	^{98}Mo(n,γ)	-1.031	^{93}Zr(n,γ)	0.159	^{95}Zr(n,γ)	-0.105
^{100}Mo	^{100}Mo(n,γ)	-0.449	^{99}Mo(β^-)	-0.201	^{99}Mo(n,γ)	0.199
^{99}Ru	^{99}Tc(n,γ)	-0.812	^{99}Tc(β^-)	0.778	^{99}Ru(n,γ)	-0.532
^{100}Ru	^{100}Ru(n,γ)	-1.077	^{93}Zr(n,γ)	0.163	^{95}Zr(n,γ)	-0.126
^{101}Ru	^{101}Ru(n,γ)	-1.078	^{93}Zr(n,γ)	0.158	^{95}Zr(n,γ)	-0.125
^{102}Ru	^{102}Ru(n,γ)	-1.015	^{93}Zr(n,γ)	0.144	^{95}Zr(β^-)	0.130
^{104}Ru	^{104}Ru(n,γ)	-0.415	^{103}Ru(β^-)	-0.170	^{103}Ru(n,γ)	0.168
^{103}Rh	^{103}Rh(n,γ)	-1.027	^{93}Zr(n,γ)	0.141	^{95}Zr(β^-)	0.134
^{104}Pd	^{104}Pd(n,γ)	-1.010	^{95}Zr(β^-)	0.144	^{93}Zr(n,γ)	0.131
^{105}Pd	^{105}Pd(n,γ)	-0.996	^{95}Zr(β^-)	0.143	^{93}Zr(n,γ)	0.126
^{106}Pd	^{106}Pd(n,γ)	-0.981	^{95}Zr(β^-)	0.144	^{93}Zr(n,γ)	0.111
^{108}Pd	^{108}Pd(n,γ)	-0.982	^{95}Zr(β^-)	0.136	-	
^{110}Pd	^{110}Pd(n,γ)	-0.328	^{109}Pd(β^-)	-0.132	^{109}Pd(n,γ)	0.130
^{107}Ag	^{107}Pd(n,γ)	-0.780	^{107}Pd(β^-)	0.775	^{107}Ag(n,γ)	-0.479
^{109}Ag	^{109}Ag(n,γ)	-0.988	^{95}Zr(β^-)	0.133	^{98}Mo(n,γ)	0.103

Isotope	Most important reactions with respective sensitivities					
^{108}Cd	^{107}Pd(n,γ)	-0.312	^{107}Pd(β^-)	0.310	^{108}Cd(n,γ)	-0.165
^{110}Cd	^{98}Mo(n,γ)	0.133	^{95}Zr(β^-)	0.119	-	
^{111}Cd	^{111}Cd(n,γ)	-0.970	^{98}Mo(n,γ)	0.140	^{95}Zr(β^-)	0.111
^{112}Cd	^{112}Cd(n,γ)	-0.993	^{98}Mo(n,γ)	0.178	-	
^{113}Cd	^{113}Cd(n,γ)	-0.983	^{98}Mo(n,γ)	0.188	-	
^{116}Cd	^{116}Cd(n,γ)	-0.455	^{115}Cd(β^-)	-0.196	^{115}Cd(n,γ)	0.194
^{115}In	^{115}In(n,γ)	-1.006	^{98}Mo(n,γ)	0.214	-	
^{116}Sn	^{98}Mo(n,γ)	0.186	^{102}Ru(n,γ)	0.133	^{100}Ru(n,γ)	0.103
^{117}Sn	^{117}Sn(n,γ)	-1.026	^{98}Mo(n,γ)	0.164	^{102}Ru(n,γ)	0.138
^{119}Sn	^{119}Sn(n,γ)	-1.073	^{102}Ru(n,γ)	0.102	-	
^{122}Sn	^{122}Sn(n,γ)	-0.568	^{121}Sn(β^-)	-0.257	^{121}Sn(n,γ)	0.256
^{123}Sb	^{123}Sb(n,γ)	-0.661	^{121}Sn(β^-)	-0.231	^{121}Sn(n,γ)	0.229
^{128}Te	^{128}Te(n,γ)	-0.560	^{128}I (β^-)	-0.146	^{128}I (β^+)	0.144
^{132}Xe	^{132}Xe(n,γ)	-1.025	^{126}Te(n,γ)	0.162	^{124}Te(n,γ)	0.109
^{134}Xe	^{134}Xe(n,γ)	-0.513	^{133}Xe(β^-)	-0.235	^{133}Xe(n,γ)	0.233
^{133}Cs	^{133}Cs(n,γ)	-1.060	^{126}Te(n,γ)	0.172	^{124}Te(n,γ)	0.114
^{134}Ba	^{134}Ba(n,γ)	-1.033	^{126}Te(n,γ)	0.203	^{124}Te(n,γ)	0.123
^{135}Ba	^{135}Ba(n,γ)	-1.088	^{126}Te(n,γ)	0.217	^{124}Te(n,γ)	0.127
^{136}Ba	^{136}Ba(n,γ)	-1.048	^{126}Te(n,γ)	0.205	^{132}Xe(n,γ)	0.172
^{137}Ba	^{137}Ba(n,γ)	-1.069	^{132}Xe(n,γ)	0.244	^{126}Te(n,γ)	0.159
^{138}Ba	^{138}Ba(n,γ)	-0.214	^{136}Ba(n,γ)	0.117	^{137}Ba(n,γ)	0.100
^{142}Ce	^{142}Ce(n,γ)	-0.938	^{141}Ce(β^-)	-0.660	^{141}Ce(n,γ)	0.652
^{143}Nd	^{143}Nd(n,γ)	-1.185	^{138}Ba(n,γ)	0.161	-	
^{148}Nd	^{148}Nd(n,γ)	-1.130	^{147}Nd(β^-)	-0.484	^{147}Nd(n,γ)	0.475
^{152}Sm	^{152}Sm(n,γ)	-1.260	^{151}Sm(β^-)	-0.170	^{151}Sm(n,γ)	0.147
^{154}Sm	^{154}Sm(n,γ)	-0.739	^{153}Sm(β^-)	-0.318	^{153}Sm(n,γ)	0.315
^{151}Eu	^{151}Eu(n,γ)	-0.704	^{151}Sm(n,γ)	-0.605	^{151}Sm(β^-)	0.557
^{152}Gd	^{151}Sm(n,γ)	-0.685	^{151}Sm(β^-)	0.652	^{152}Gd(n,γ)	-0.564
^{160}Gd	^{160}Gd(n,γ)	-0.440	^{159}Gd(β^-)	-0.190	^{159}Gd(n,γ)	0.188
^{158}Dy	^{157}Gd(n,γ)	-0.653	^{157}Gd(β^-)	0.647	^{158}Tb(β^-)	0.385
^{170}Er	^{170}Er(n,γ)	-1.104	^{169}Er(β^-)	-0.461	^{169}Er(n,γ)	0.453

Isotope	Most important reactions with respective sensitivities					
^{170}Yb	^{170}Yb(n,γ)	-0.948	^{170}Tm(n,γ)	-0.181	-	
^{171}Yb	^{171}Yb(n,γ)	-1.105	^{170}Yb(n,γ)	0.121	-	
^{176}Yb	^{176}Yb(n,γ)	-0.519	^{175}Yb(β^-)	-0.228	^{175}Yb(n,γ)	0.225
^{176}Hf	^{176}Hf(n,γ)	-1.105	^{175}Lu(n,γ)	-0.740	-	
^{180}W	^{179}Hf(n,γ)	-1.154	^{179}Hf(β^-)	1.142	^{180}W(n,γ)	-0.883
^{183}W	^{183}W(n,γ)	-1.210	^{182}W(n,γ)	0.114	-	
^{184}W	^{184}W(n,γ)	-1.256	^{182}W(n,γ)	0.116	-	
^{186}W	^{186}W(n,γ)	-2.311	^{185}W(β^-)	-0.882	^{185}W(n,γ)	0.823
^{185}Re	^{185}Re(n,γ)	-1.263	^{182}W(n,γ)	0.115	-	
^{187}Re	^{187}Re(n,γ)	-1.504	^{185}W(β^-)	-0.881	^{186}W(n,γ)	-0.851
^{186}Os	^{186}Os(n,γ)	-1.203	^{182}W(n,γ)	0.111	^{158}Gd(n,γ)	0.101
^{187}Os	^{187}Os(n,γ)	-1.285	^{185}W(n,γ)	-0.115	^{182}W(n,γ)	0.110
^{188}Os	^{188}Os(n,γ)	-1.270	^{186}W(n,γ)	-0.106	^{158}Gd(n,γ)	0.100
^{189}Os	^{189}Os(n,γ)	-1.311	^{186}W(n,γ)	-0.105	^{158}Gd(n,γ)	0.100
^{192}Os	^{192}Os(n,γ)	-0.895	^{191}Os(β^-)	-0.335	^{191}Os(n,γ)	0.330
^{193}Ir	^{193}Ir(n,γ)	-1.378	^{192}Ir(β^-)	-0.589	^{192}Ir(n,γ)	0.483
^{192}Pt	^{192}Pt(n,γ)	-1.132	^{192}Ir(n,γ)	-0.161	^{192}Ir(β^-)	0.153
^{194}Pt	^{194}Pt(n,γ)	-1.221	^{192}Pt(n,γ)	0.116	-	
^{195}Pt	^{195}Pt(n,γ)	-1.219	^{192}Pt(n,γ)	0.105	-	
^{198}Pt	^{198}Pt(n,γ)	-0.307	^{197}Pt(β^-)	-0.105	^{197}Pt(n,γ)	0.104
^{200}Hg	^{200}Hg(n,γ)	-1.037	^{184}W(n,γ)	0.109	-	
^{201}Hg	^{201}Hg(n,γ)	-1.070	^{184}W(n,γ)	0.118	-	
^{202}Hg	^{202}Hg(n,γ)	-1.087	^{184}W(n,γ)	0.103	-	
^{204}Hg	^{204}Hg(n,γ)	-0.615	^{204}Tl(β^+)	0.371	^{204}Tl(β^-)	-0.355
^{203}Tl	^{203}Tl(n,γ)	-1.232	^{202}Hg(n,γ)	0.138	^{196}Pt(n,γ)	0.107
^{205}Tl	^{205}Tl(n,γ)	-0.520	^{205}Pb(n,γ)	-0.446	^{205}Pb(β^+)	0.413
^{204}Pb	^{204}Pb(n,γ)	-1.219	^{202}Hg(n,γ)	0.258	^{200}Hg(n,γ)	0.192
^{206}Pb	^{206}Pb(n,γ)	-0.596	^{202}Hg(n,γ)	0.258	^{204}Pb(n,γ)	0.203
^{207}Pb	^{206}Pb(n,γ)	0.618	^{207}Pb(n,γ)	-0.468	^{204}Pb(n,γ)	0.106
^{208}Pb	^{207}Pb(n,γ)	0.331	^{206}Pb(n,γ)	0.136	-	
^{209}Bi	^{208}Pb(n,γ)	0.300	^{209}Bi(n,γ)	-0.146	-	

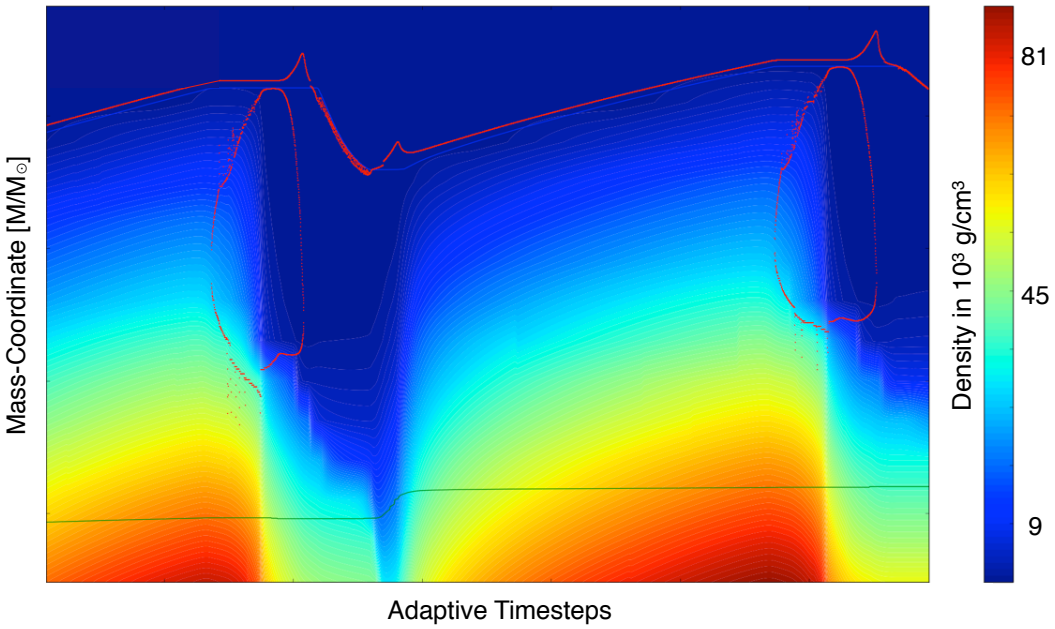

Figure A.17: TK-plot of the density in the helium intershell of a 3 $M_\odot$ stellar model during the TP-AGB phase. The reoccurring expansion of the helium intershell during the thermal pulses is depicted. The colormap represents the density, which reaches almost 50000 g/cm^3 in the helium intershell before the helium burning ignites. The convective boundaries are the red dotted lines, the blue line signifies the hydrogen boundary and the green dotted line the helium boundary.

GLOBAL SENSITIVITIES AND BRANCHING POINTS DURING THE TP

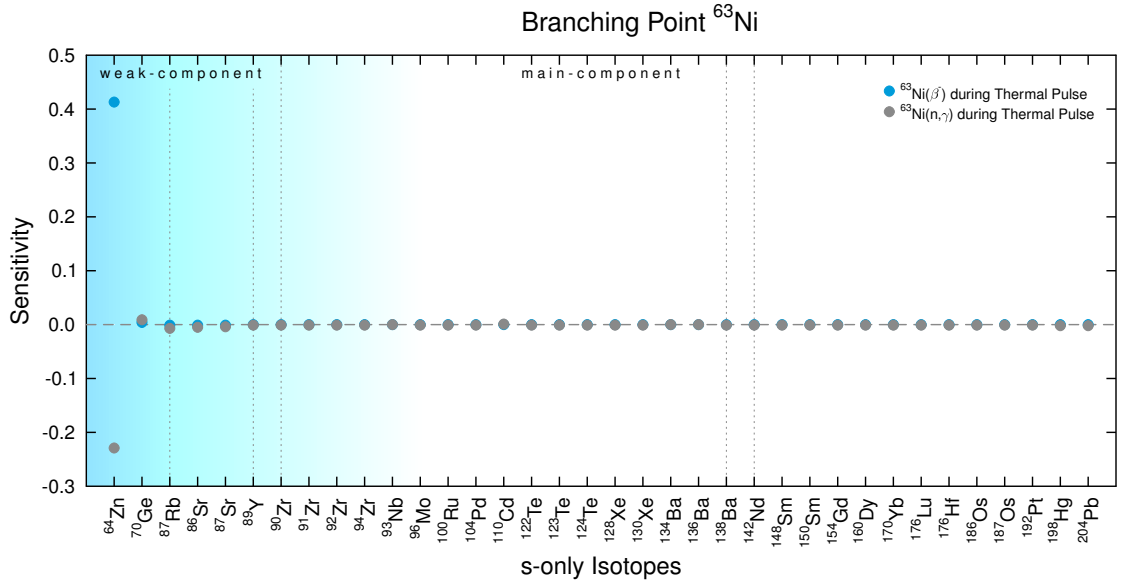

Figure A.18: Branching point ^{63}Ni during the TP (table 3.6). The β-decay of ^{63}Ni is responsible for the production of ^{64}Zn, but the neutron capture on ^{63}Ni also competes with the depletion of ^{64}Zn.

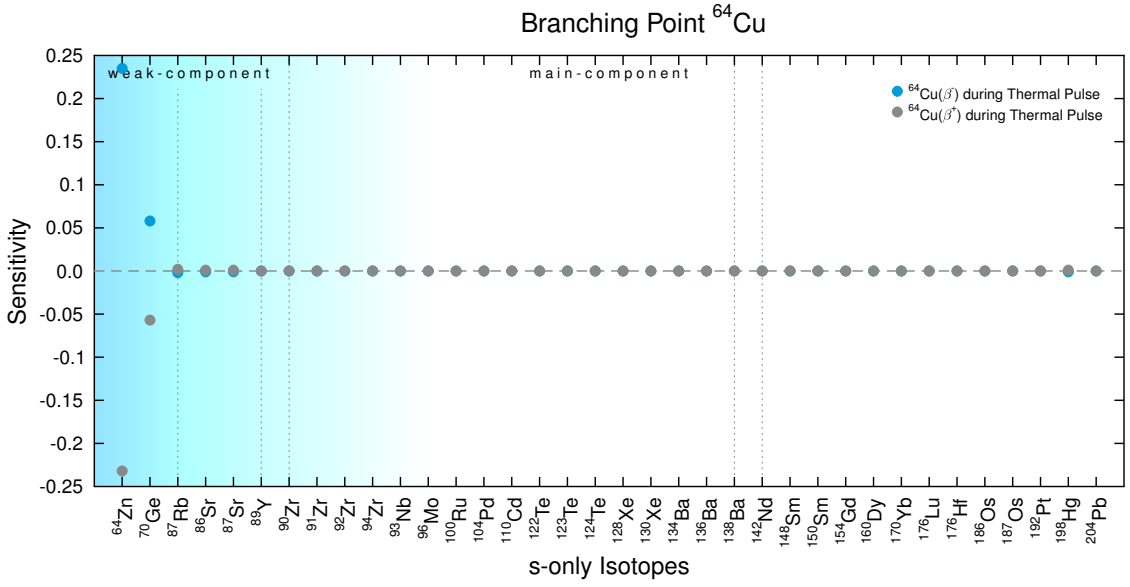

Figure A.19: Branching point ^{64}Cu during the TP (table 3.6). As ^{64}Zn has a higher neutron capture cross-section than ^{64}Ni, the branching over ^{64}Zn increases the *s* process on following isotopes, which can be seen on ^{70}Ge.

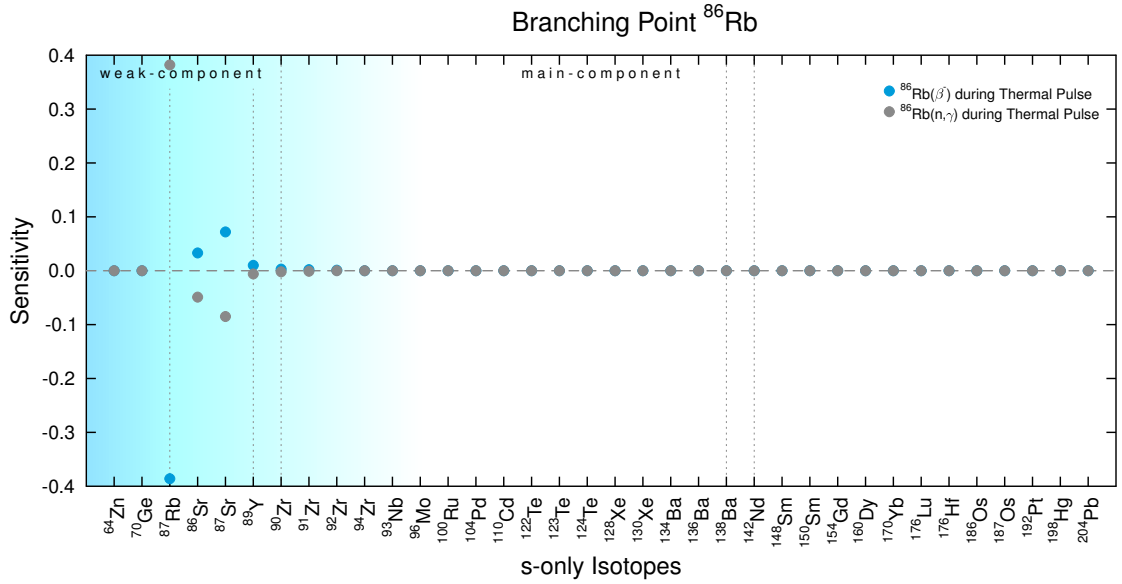

Figure A.20: Branching point ^{86}Rb during the TP (table 3.6). ^{86}Rb acts as classical branching point in TP conditions.

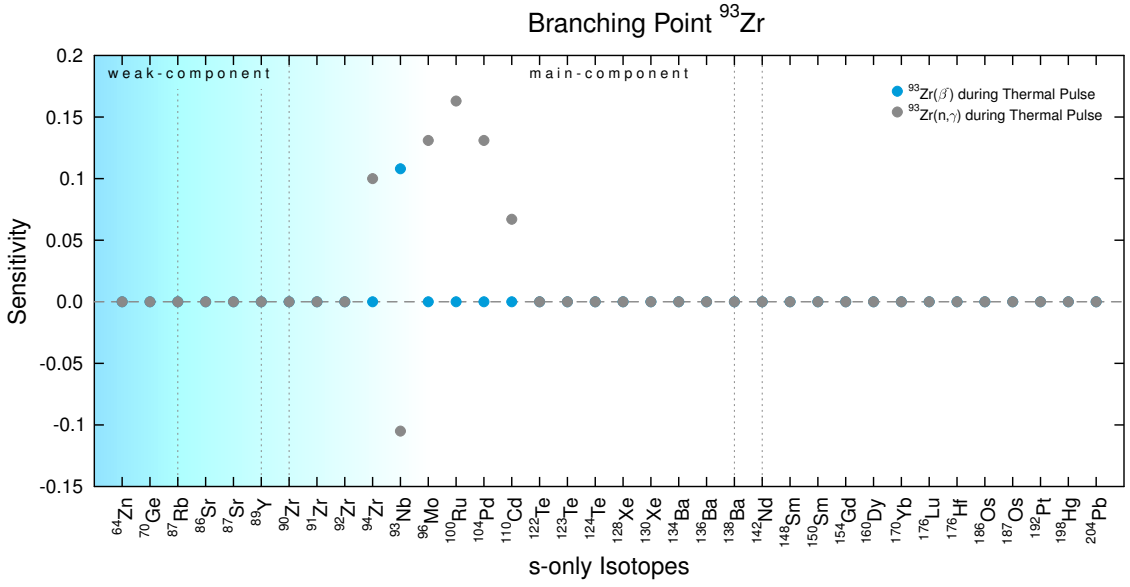

Figure A.21: Branching point ^{93}Zr during the TP (table 3.6). The β-decay path of ^{93}Zr goes over ^{93}Nb and ^{94}Nb, where it rejoins the β-decay path of ^{95}Zr. Whereas the neutron capture on ^{93}Zr acts as seed isotope and impacts succeeding isotopes along the *s* process path.

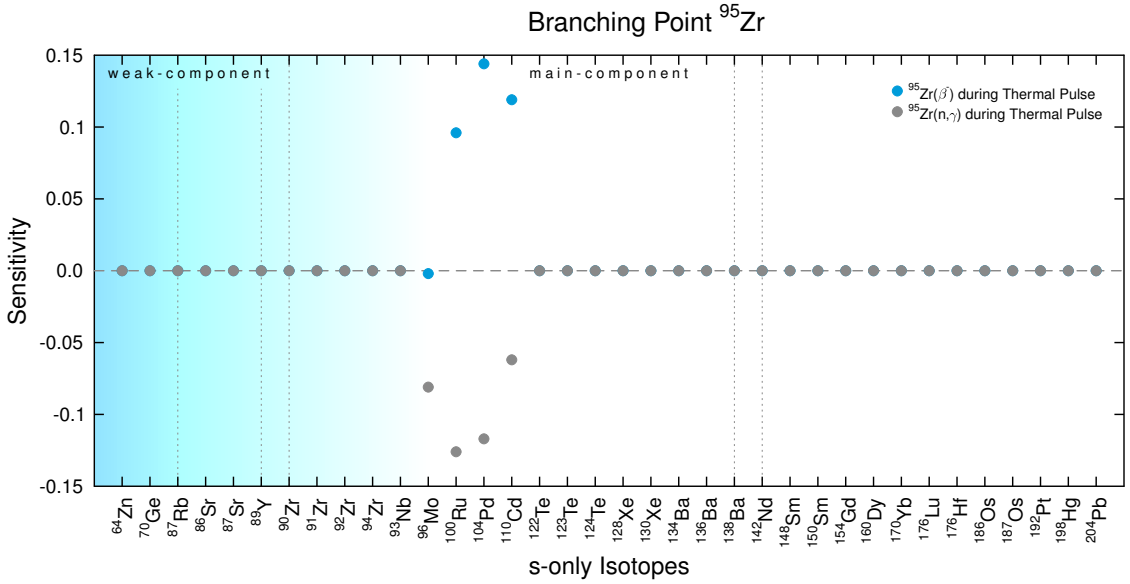

Figure A.22: Branching point ^{95}Zr during the TP (table 3.6). The neutron capture on ^{95}Zr only feeds ^{96}Zr, which withdraws material from the *s* process for the succeeding isotopes. The increased β-decay results in a faster feeding of succeeding seed isotopes, which increases the depletion (not visible in the plot) of these isotopes with a turning point around ^{96}Mo.

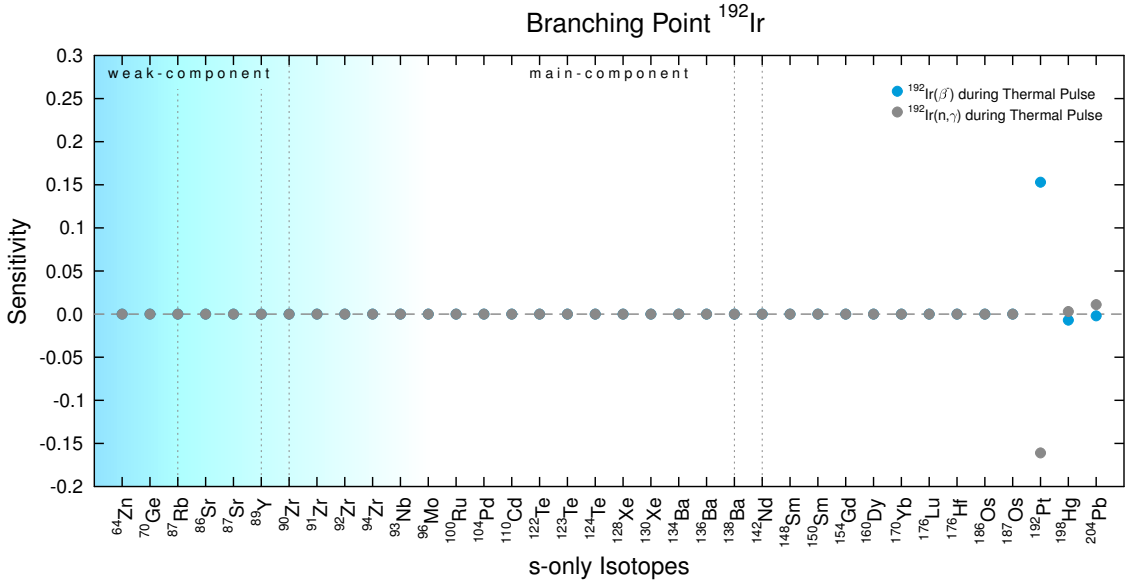

Figure A.23: Branching point ^{192}Ir during the TP (table 3.6). ^{192}Ir acts as classical branching point, which produces two competing seed isotopes for the succeeding *s* process nucleosynthesis.

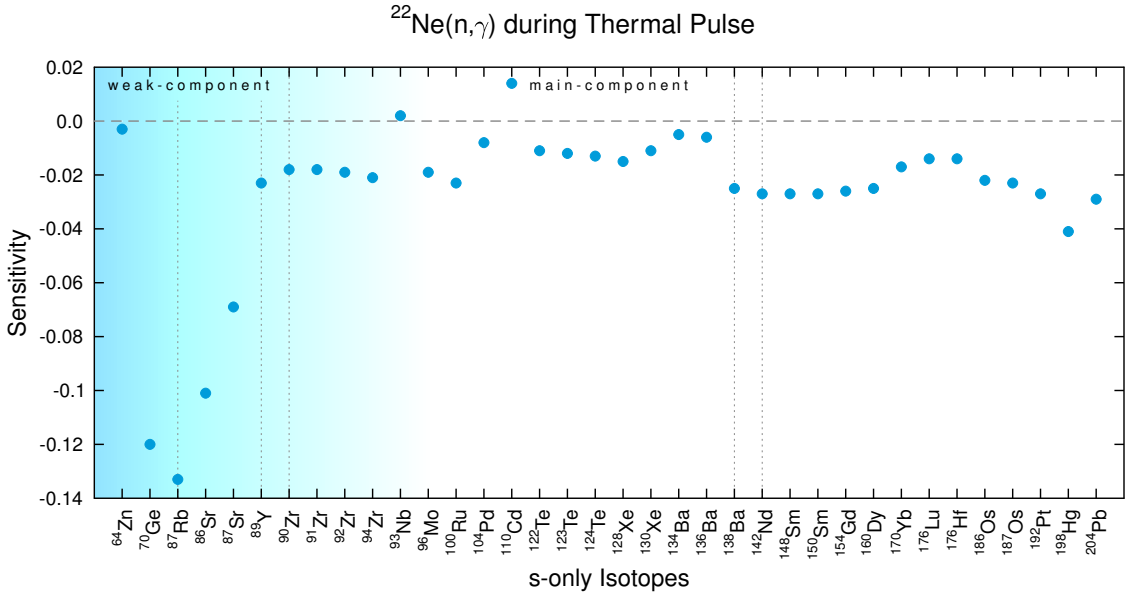

Figure A.24: Neutron poison reaction $^{22}\mathrm{Ne}(n,\gamma)$ during the thermal pulse (table 3.8). The neutron capture on ^{22}Ne competes with the α capture of ^{22}Ne. This results in the absorption of free neutrons from the *s* process as well in the destruction of ^{22}Ne for the neutron source reaction $^{22}\mathrm{Ne}(\alpha,n)$.

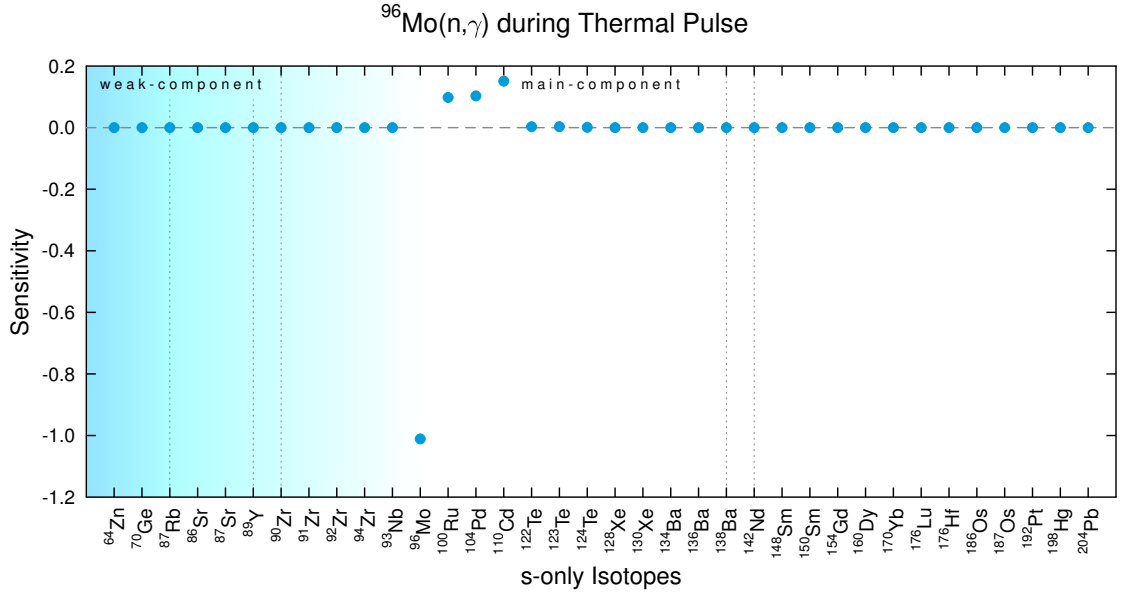

Figure A.25: Bottleneck reaction $^{96}\mathrm{Mo}(n,\gamma)$ during the thermal pulse (table 3.10). This reaction has its impact peak and tail 14 mass numbers above.

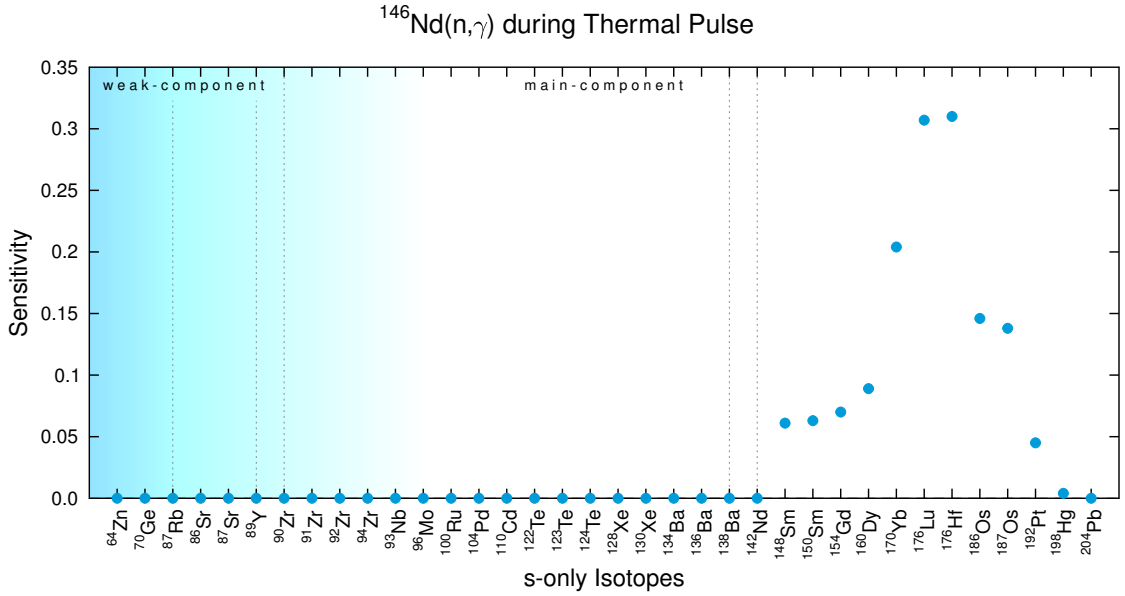

Figure A.26: Bottleneck reaction ^{146}Nd(n,γ) during the thermal pulse (table 3.10). The sensitivity of the ^{146}Nd(n,γ) rate has its peak impact 30 mass numbers later and an overall impact span of 46 mass numbers.

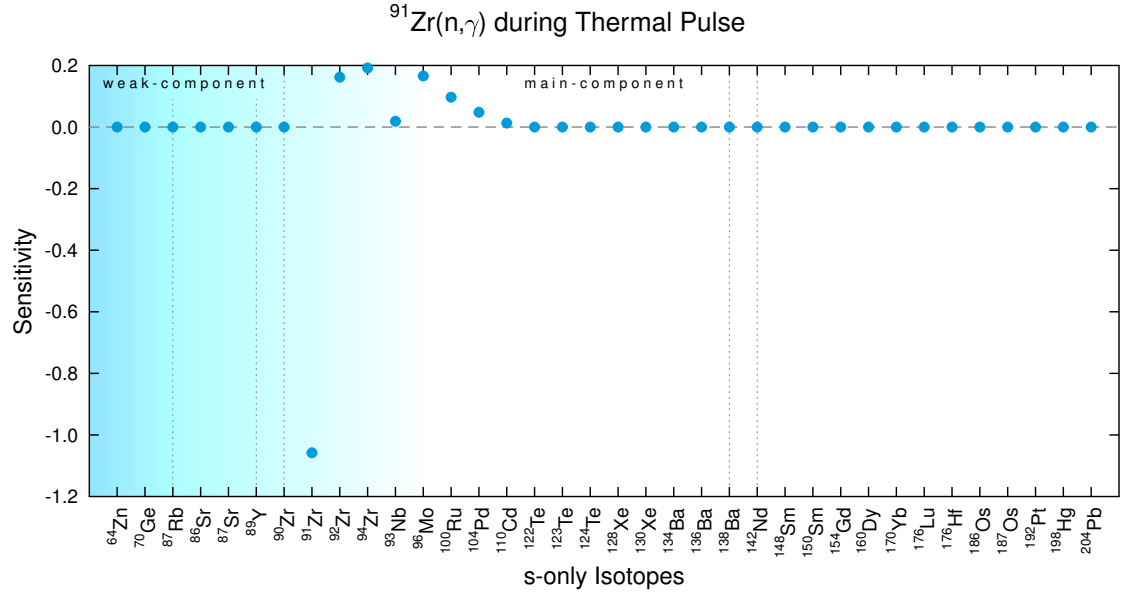

Figure A.27: Bottleneck reaction ^{91}Zr(n,γ) during the thermal pulse (table 3.10).

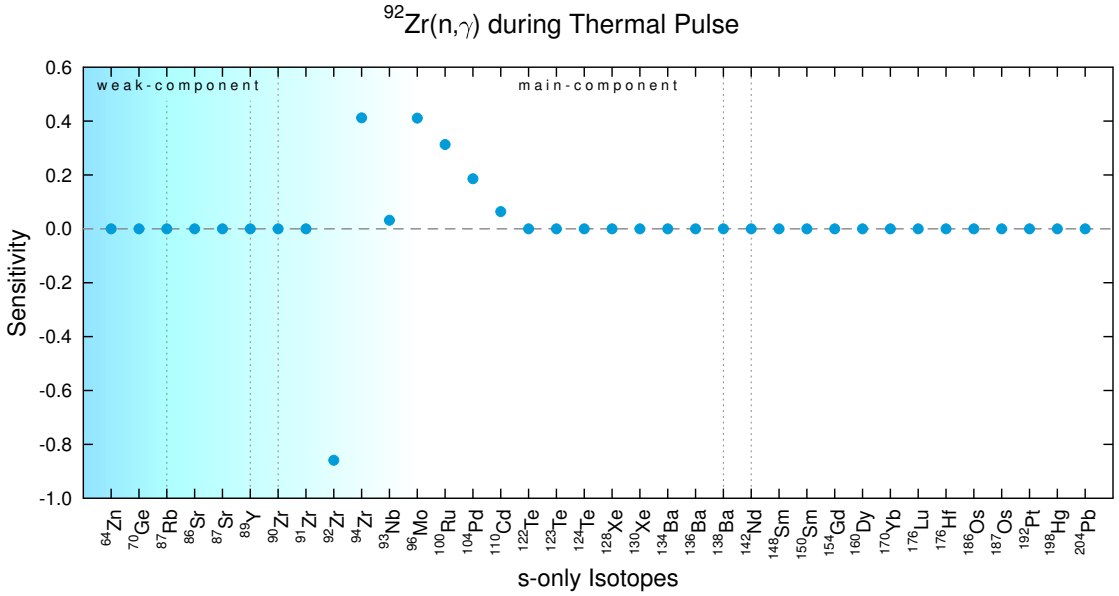

Figure A.28: Bottleneck reaction ^{92}Zr(n,γ) during the thermal pulse (table 3.10).

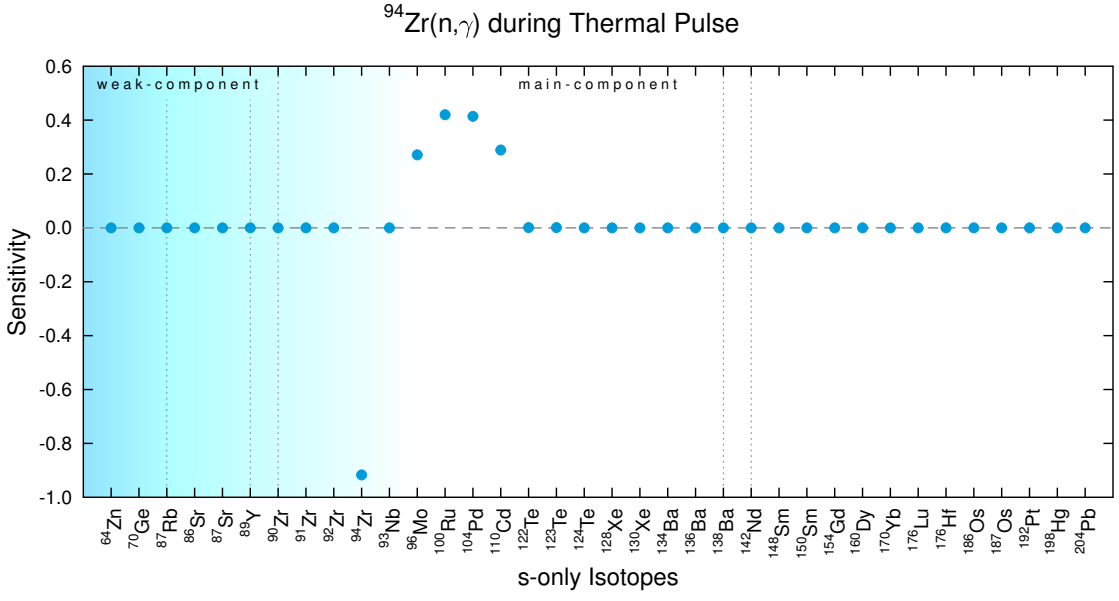

Figure A.29: Bottleneck reaction ^{94}Zr(n,γ) during the thermal pulse (table 3.10).

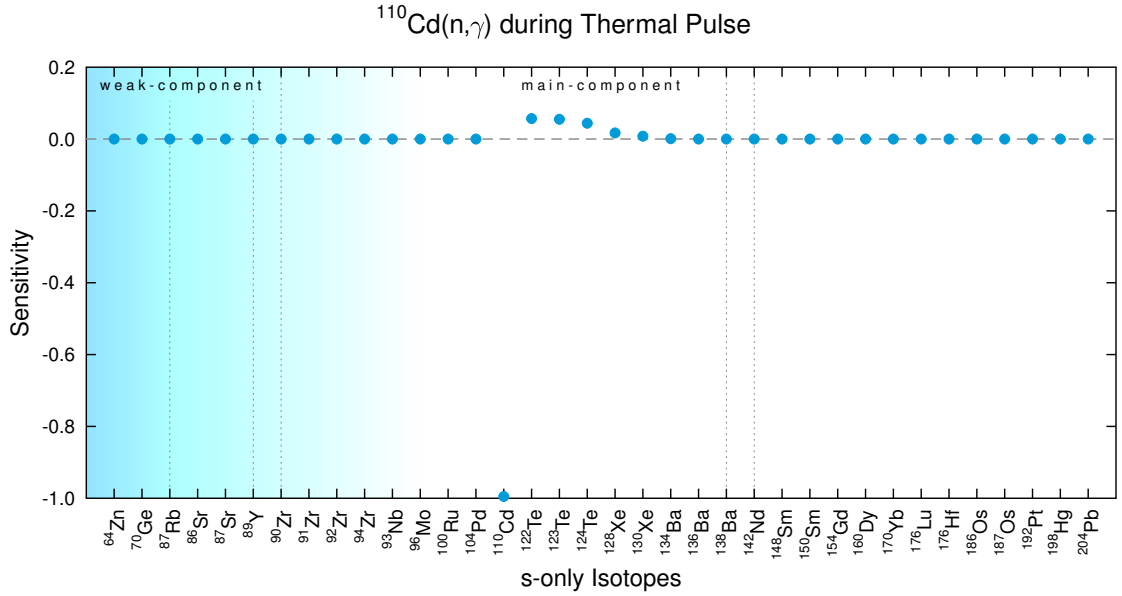

Figure A.30: Bottleneck reaction ^{110}Cd(n,γ) during the thermal pulse (table 3.10).

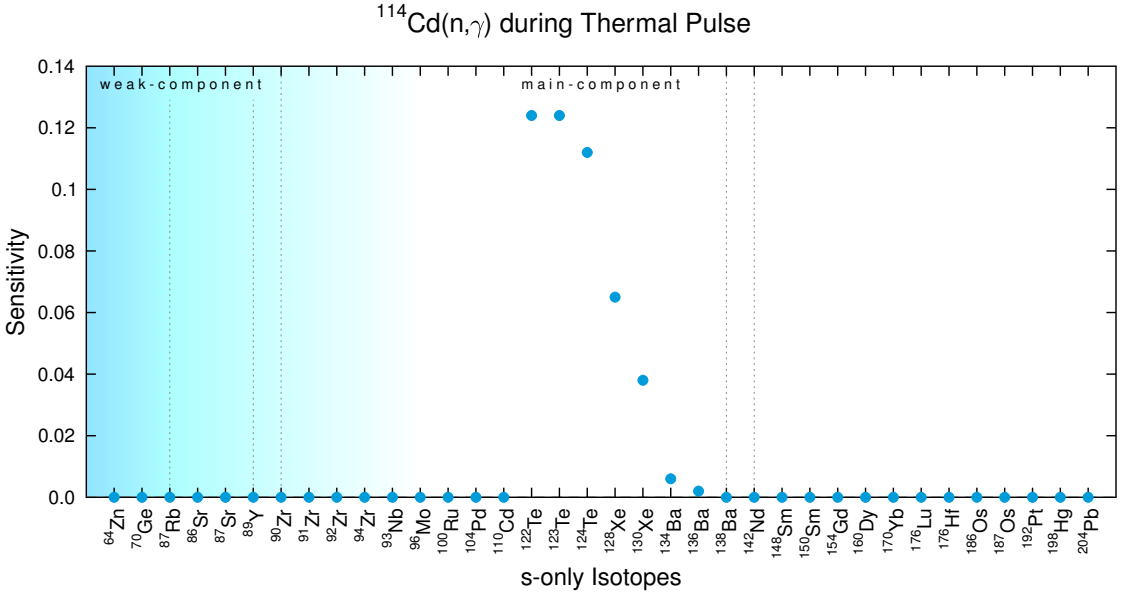

Figure A.31: Bottleneck reaction ^{114}Cd(n,γ) during the thermal pulse (table 3.10).

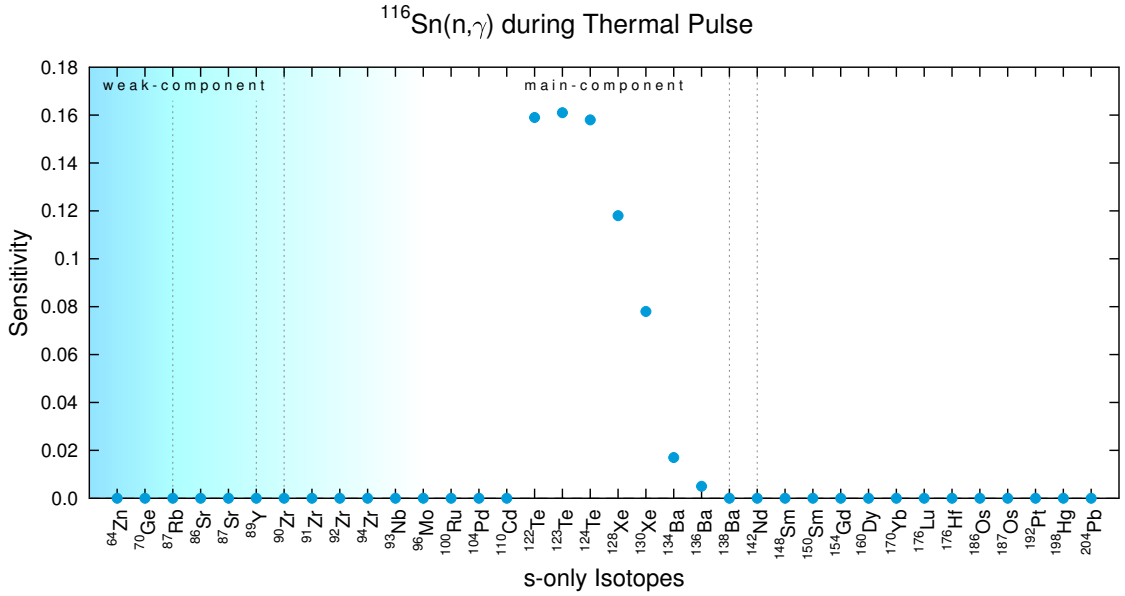

Figure A.32: Bottleneck reaction $^{116}\mathrm{Sn}(n,\gamma)$ during the thermal pulse (table 3.10).

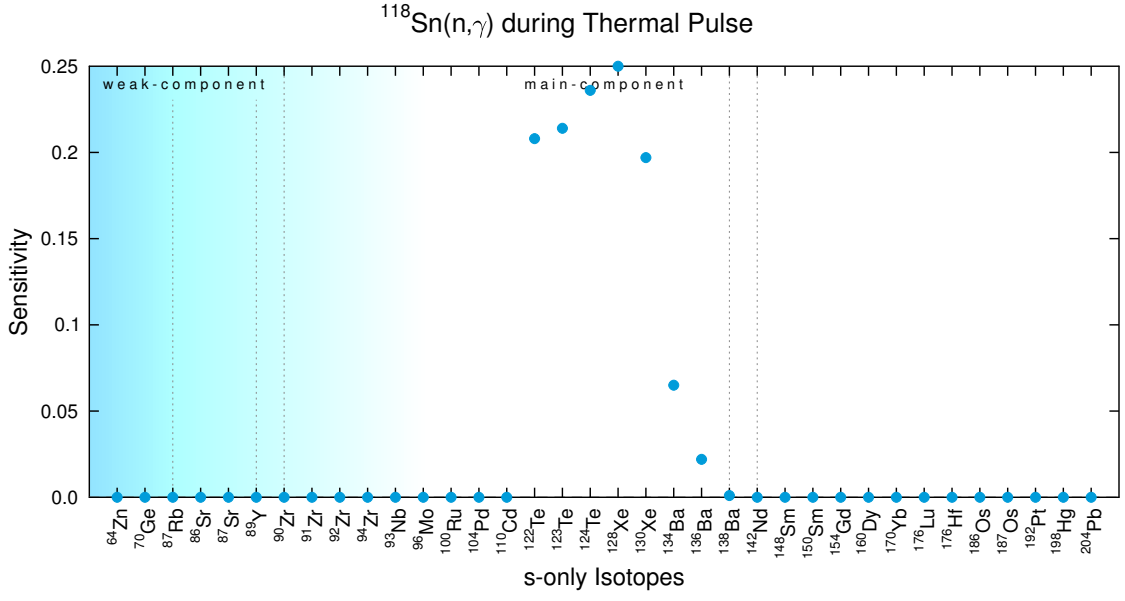

Figure A.33: Bottleneck reaction $^{118}\mathrm{Sn}(n,\gamma)$ during the thermal pulse (table 3.10).

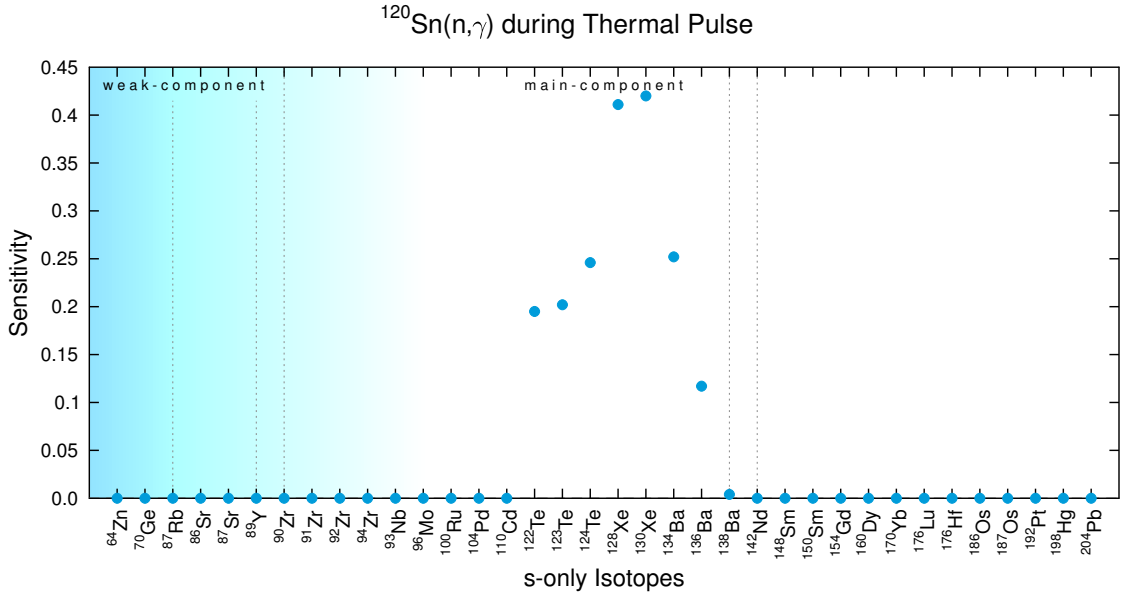

Figure A.34: Bottleneck reaction $^{120}\mathrm{Sn}(n,\gamma)$ during the thermal pulse (table 3.10).

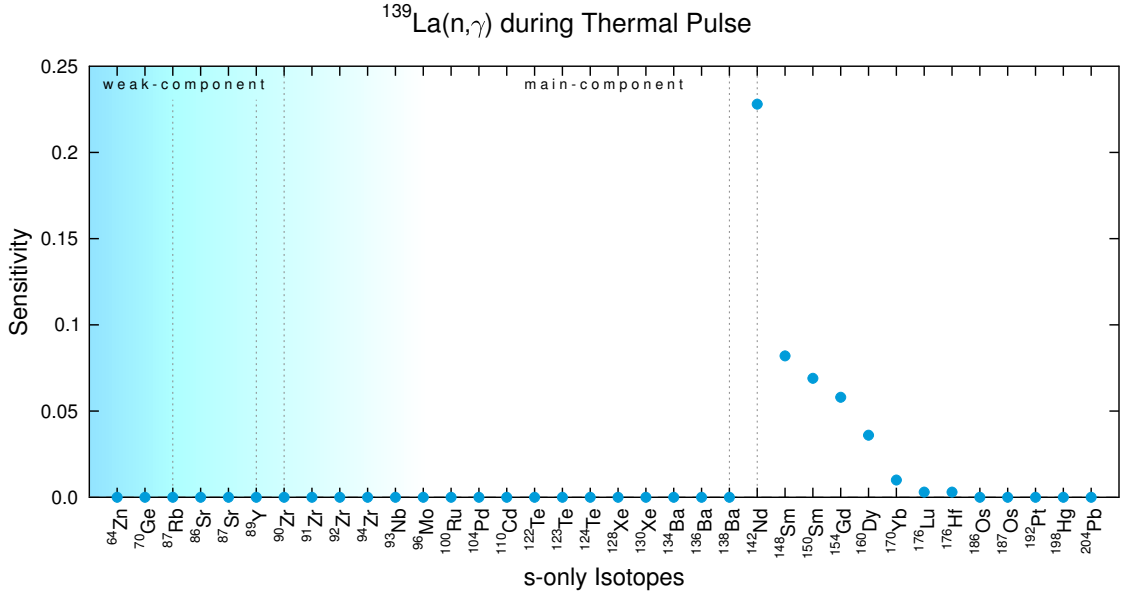

Figure A.35: Bottleneck reaction $^{139}\mathrm{La}(n,\gamma)$ during the thermal pulse (table 3.10).

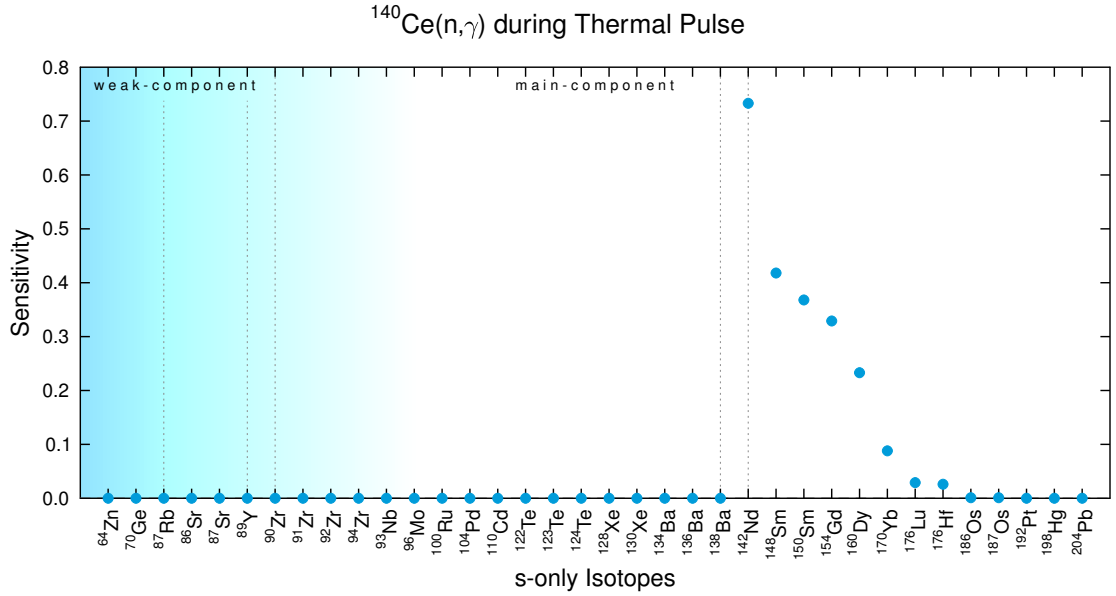

Figure A.36: Bottleneck reaction ^{140}Ce(n,γ) during the thermal pulse (table 3.10).

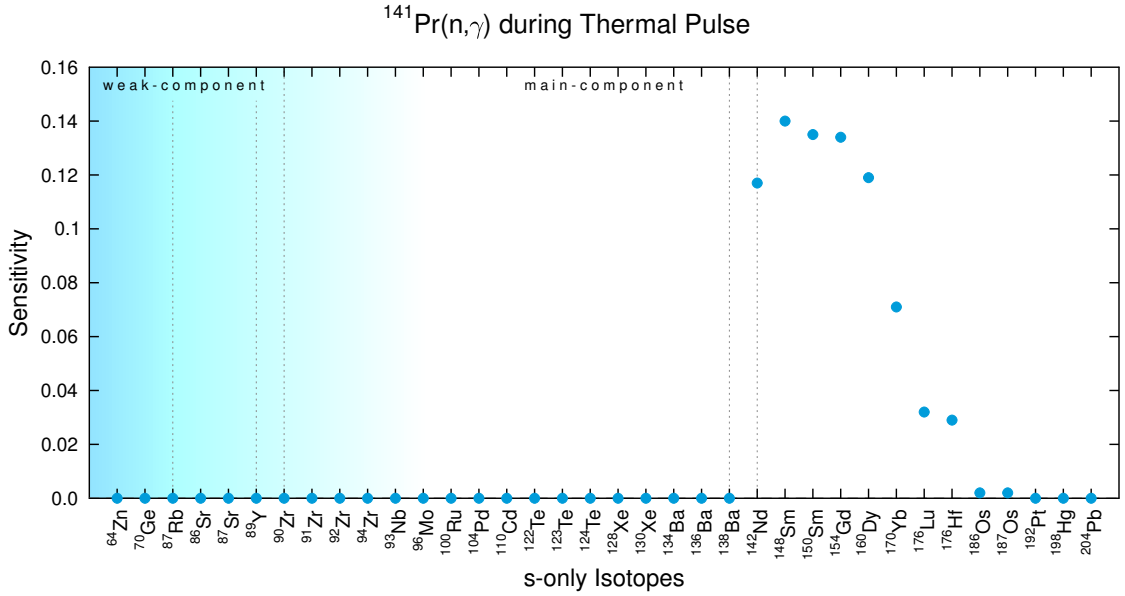

Figure A.37: Bottleneck reaction $^{141}\mathrm{Pr}(n,\gamma)$ during the thermal pulse (table 3.10).

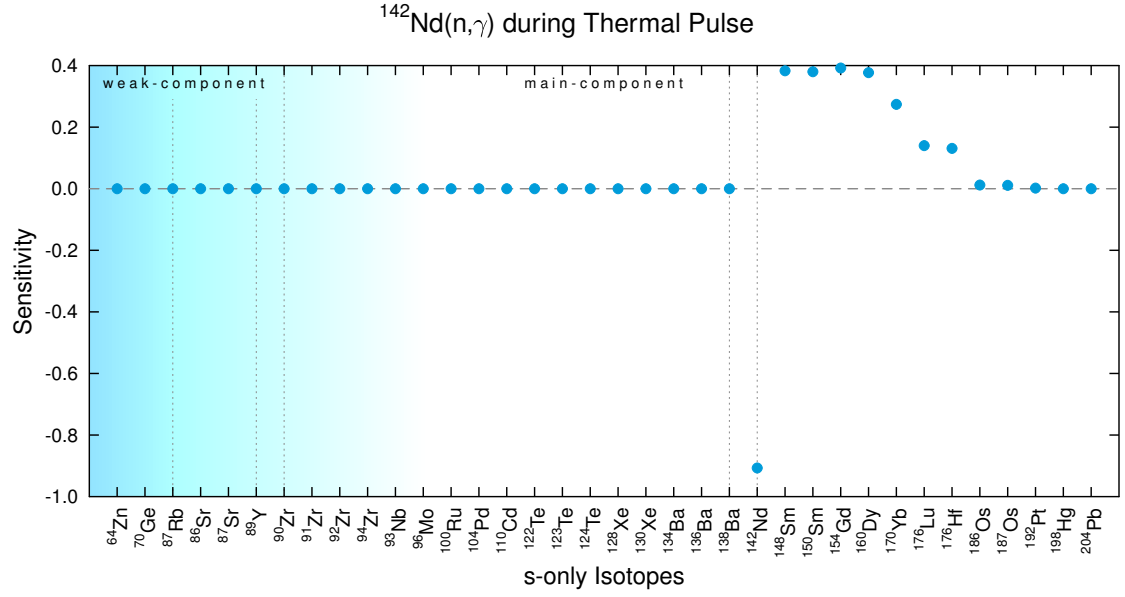

Figure A.38: Bottleneck reaction $^{142}\mathrm{Nd}(n,\gamma)$ during the thermal pulse (table 3.10).

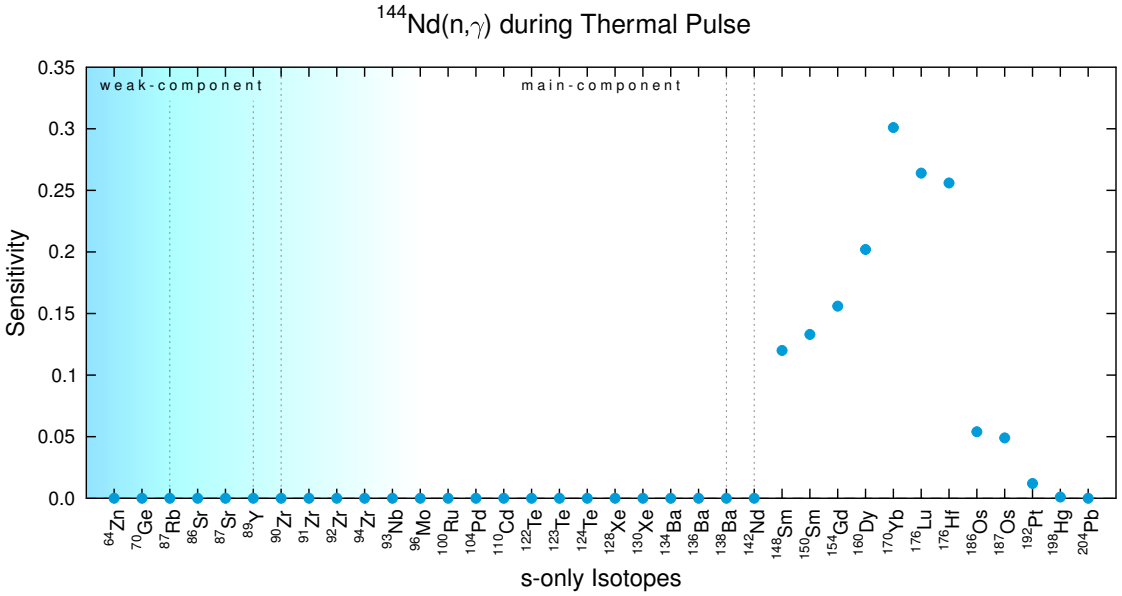

Figure A.39: Bottleneck reaction $^{144}\mathrm{Nd}(n,\gamma)$ during the thermal pulse (table 3.10).

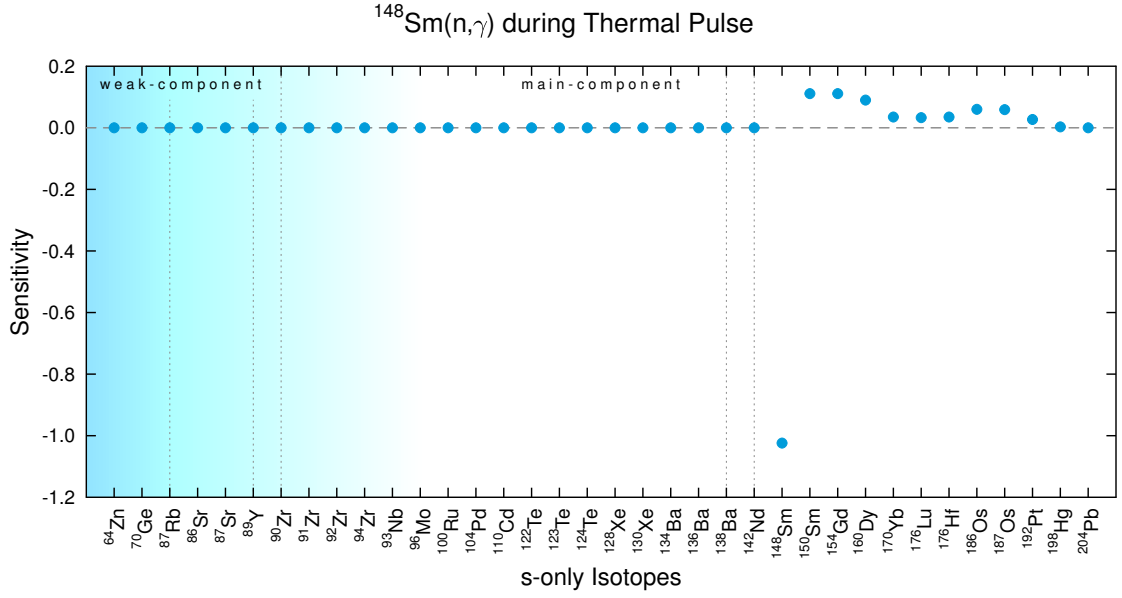

Figure A.40: Bottleneck reaction $^{148}\mathrm{Sm}(n,\gamma)$ during the thermal pulse (table 3.10).

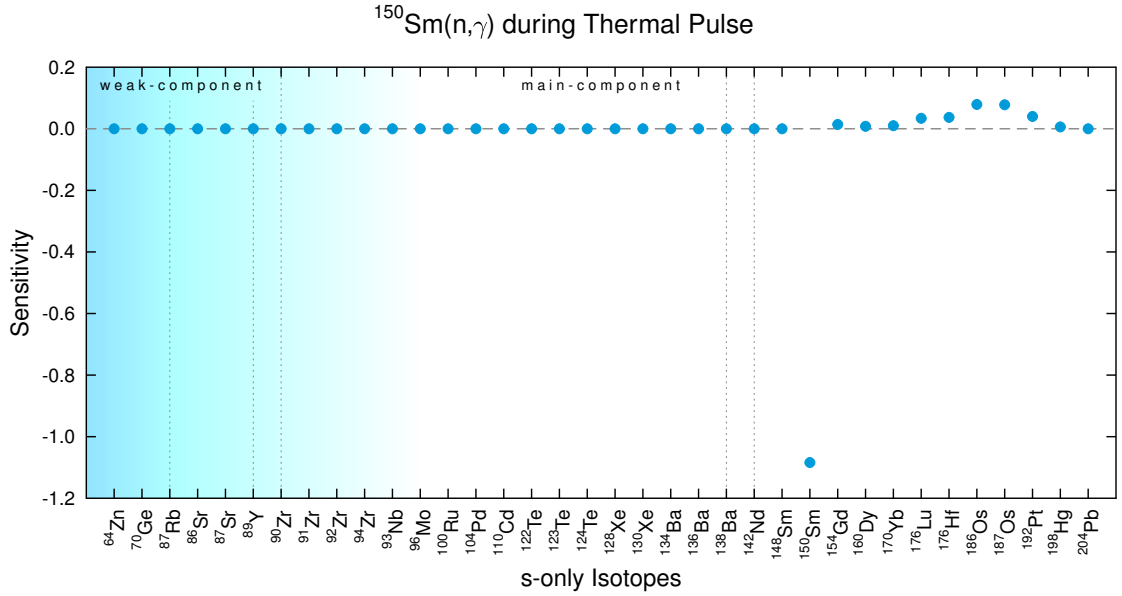

Figure A.41: Bottleneck reaction ^{150}Sm(n,γ) during the thermal pulse (table 3.10).

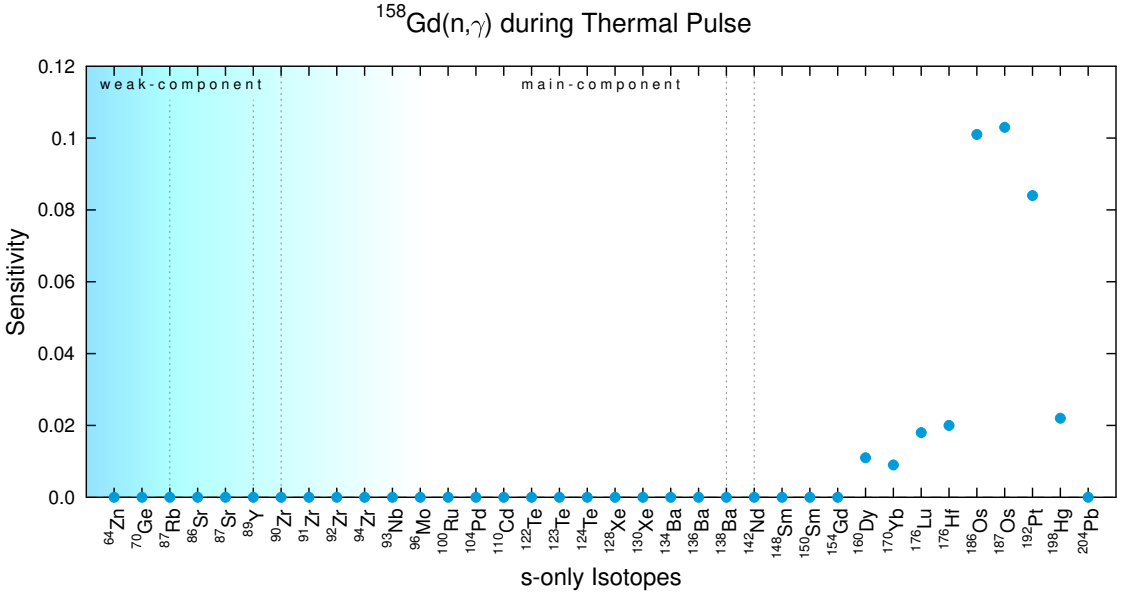

Figure A.42: Bottleneck reaction ^{158}Gd(n,γ) during the thermal pulse (table 3.10).

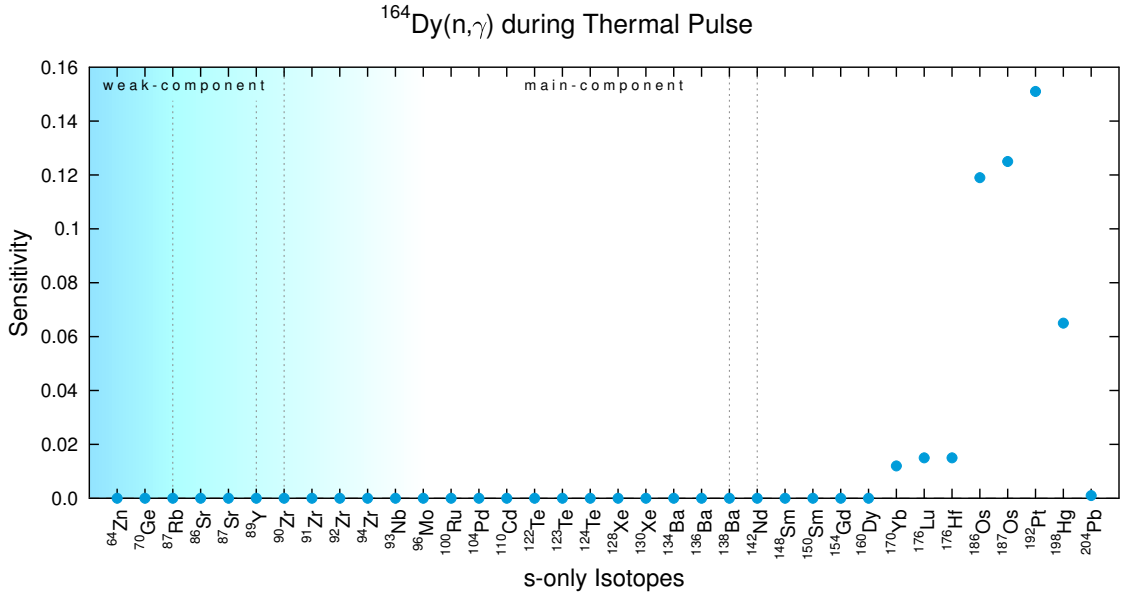

Figure A.43: Bottleneck reaction $^{164}\mathrm{Dy}(n,\gamma)$ during the thermal pulse (table 3.10).

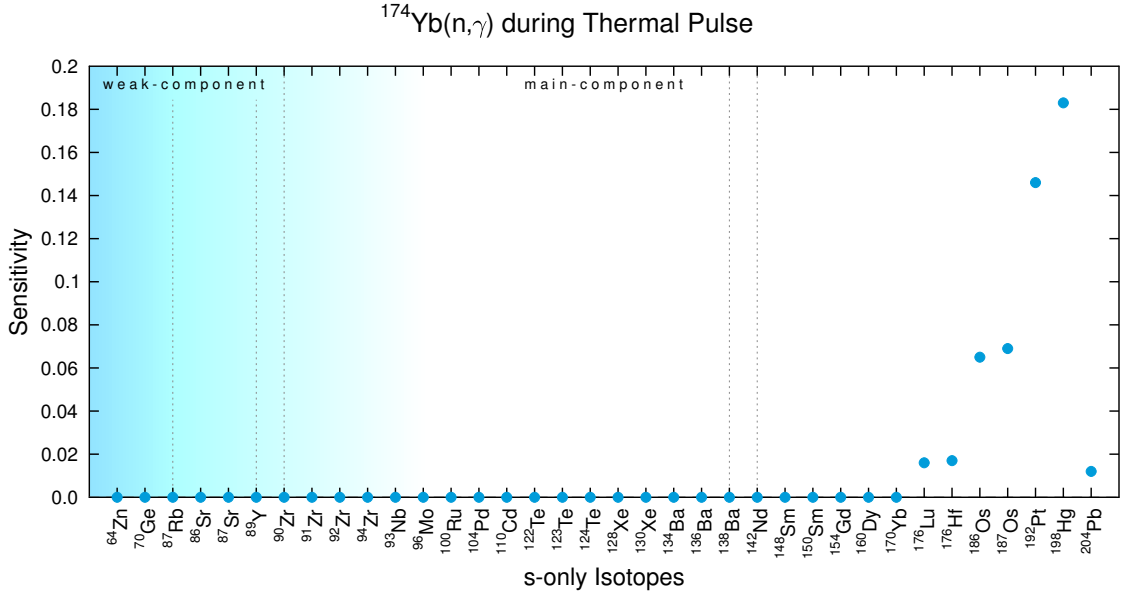

Figure A.44: Bottleneck reaction $^{174}\mathrm{Yb}(n,\gamma)$ during the thermal pulse (table 3.10).

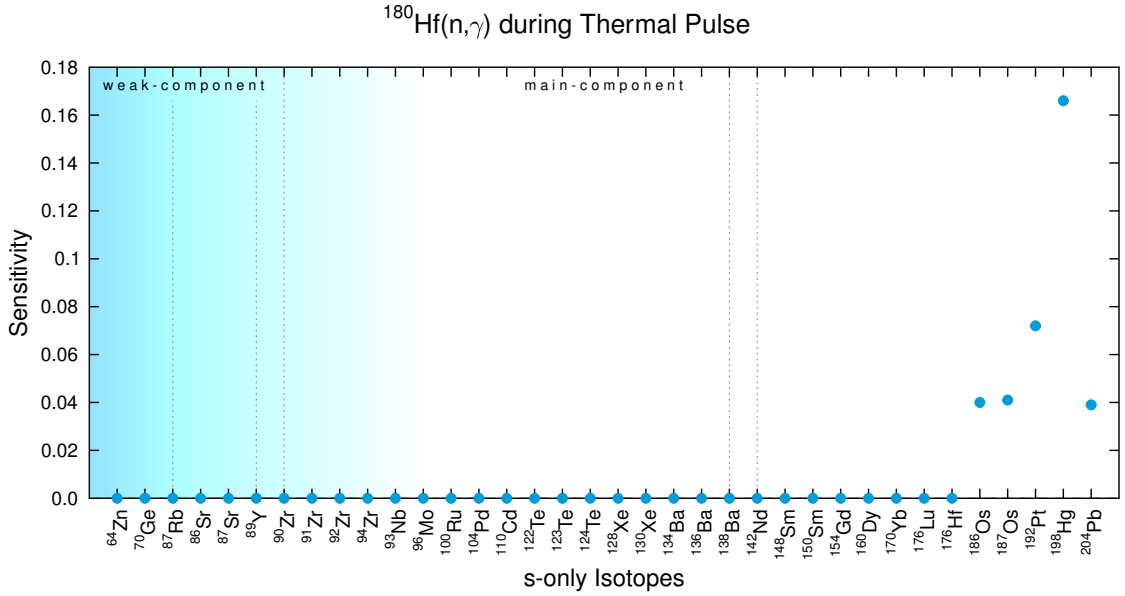

Figure A.45: Bottleneck reaction ^{180}Hf(n,γ) during the thermal pulse (table 3.10).

A.2 WEAK COMPONENT

In this part of the appendix the local sensitivity tables, initial abundances for the trajectories and remaining global sensitivity plots are listed for the weak component trajectory and convective C shell burning.

A.2.1 WEAK *S* PROCESS

LOCAL SENSITIVITIES DURING THE WEAK *S* PROCESS

Table A.4: Reactions with strongest local sensitivities during the weak *s* process. Filter criteria in chapter 2.3.3 on page 49.

Isotope	Most important reactions with respective sensitivities					
^{58}Ni	^{58}Ni(n,γ)	-8.932	^{17}O (p,α)	0.161	^{17}O (n,α)	0.156
^{64}Ni	^{64}Ni(n,γ)	-0.367	^{63}Ni(n,γ)	0.353	^{64}Cu(β^+)	0.206
^{63}Cu	^{63}Ni(β^-)	0.798	^{63}Ni(n,γ)	-0.407	-	
^{65}Cu	^{64}Ni(n,γ)	0.417	^{63}Ni(n,γ)	0.174	-	
^{64}Zn	^{64}Cu(β^-)	0.697	^{64}Cu(β^+)	-0.625	^{63}Ni(β^-)	0.447
^{68}Zn	^{64}Ni(n,γ)	0.160	^{64}Cu(β^+)	-0.143	^{64}Cu(β^-)	0.131
^{70}Zn	^{69}Zn(β^-)	-0.943	^{69}Zn(n,γ)	0.940	^{70}Zn(n,γ)	-0.839
^{69}Ga	^{64}Cu(β^+)	-0.150	^{64}Ni(n,γ)	0.150	^{64}Cu(β^-)	0.140
^{71}Ga	^{71}Ge(n,γ)	-0.729	^{71}Ge(β^+)	0.712	^{64}Cu(β^+)	-0.162
^{70}Ge	^{64}Cu(β^+)	-0.157	^{64}Cu(β^-)	0.150	^{64}Ni(n,γ)	0.137
^{72}Ge	^{64}Cu(β^+)	-0.163	^{64}Cu(β^-)	0.158	^{64}Ni(n,γ)	0.123
^{73}Ge	^{64}Cu(β^+)	-0.164	^{64}Cu(β^-)	0.160	^{64}Ni(n,γ)	0.119
^{74}Ge	^{64}Cu(β^+)	-0.163	^{64}Cu(β^-)	0.162	^{64}Ni(n,γ)	0.110
^{76}Ge	^{75}Ge(n,γ)	0.962	^{75}Ge(β^-)	-0.952	^{76}Ge(n,γ)	-0.780
^{75}As	^{75}As(n,γ)	-0.937	^{64}Cu(β^+)	-0.163	^{64}Cu(β^-)	0.162
^{74}Se	^{74}As(β^-)	0.929	^{74}Se(n,γ)	-0.912	^{74}As(n,γ)	-0.713
^{76}Se	^{64}Cu(β^+)	-0.163	^{64}Cu(β^-)	0.162	^{71}Ge(n,γ)	0.107
^{77}Se	^{77}Se(n,γ)	-0.947	^{64}Cu(β^-)	0.162	^{64}Cu(β^+)	-0.162
^{78}Se	^{64}Cu(β^-)	0.160	^{64}Cu(β^+)	-0.160	^{71}Ge(n,γ)	0.104
^{80}Se	^{79}Se(n,γ)	0.234	^{64}Cu(β^-)	0.154	^{64}Cu(β^+)	-0.153

Isotope	Most important reactions with respective sensitivities					
^{82}Se	^{81}Se(β^-)	-0.841	^{81}Se(n,γ)	0.837	^{82}Se(n,γ)	-0.562
^{79}Br	^{79}Br(n,γ)	-1.003	^{79}Se(β^-)	0.666	^{79}Se(n,γ)	-0.638
^{81}Br	^{81}Br(n,γ)	-0.899	^{79}Se(n,γ)	0.202	^{64}Cu(β^-)	0.152
^{80}Kr	^{80}Kr(n,γ)	-0.789	^{79}Se(n,γ)	-0.711	^{79}Se(β^-)	0.679
^{82}Kr	^{79}Se(β^-)	0.165	^{64}Cu(β^-)	0.151	^{64}Cu(β^+)	-0.150
^{83}Kr	^{83}Kr(n,γ)	-0.797	^{64}Cu(β^-)	0.148	^{64}Cu(β^+)	-0.147
^{84}Kr	^{83}Kr(n,γ)	0.143	^{64}Cu(β^-)	0.131	^{64}Cu(β^+)	-0.130
^{86}Kr	^{85}Kr(n,γ)	0.525	^{85}Kr(β^-)	-0.214	^{86}Kr(n,γ)	-0.173
^{85}Rb	^{85}Kr(n,γ)	-0.350	^{17}O (p,α)	-0.124	^{64}Cu(β^-)	0.118
^{87}Rb	^{86}Rb(n,γ)	0.352	^{87}Rb(n,γ)	-0.311	^{85}Kr(β^-)	0.272
^{86}Sr	^{85}Kr(n,γ)	-0.469	^{86}Rb(β^-)	0.365	^{85}Kr(β^-)	0.299
^{87}Sr	^{85}Kr(n,γ)	-0.375	^{85}Kr(β^-)	0.372	^{86}Rb(β^-)	0.330
^{89}Y	^{89}Sr(β^-)	0.285	^{89}Sr(n,γ)	-0.212	-	
^{90}Zr	^{90}Y (n,γ)	-0.197	^{89}Sr(β^-)	0.173	^{90}Y (β^-)	0.161
^{91}Zr	^{91}Y (n,γ)	-0.283	^{91}Y (β^-)	0.184	^{89}Sr(n,γ)	0.122
^{94}Zr	^{93}Zr(n,γ)	0.199	^{91}Y (n,γ)	0.108	-	
^{96}Zr	^{95}Zr(n,γ)	0.422	^{93}Zr(n,γ)	0.226	^{95}Zr(β^-)	-0.145
^{93}Nb	^{93}Zr(β^-)	0.986	^{93}Zr(n,γ)	-0.825	^{93}Nb(n,γ)	-0.812
^{92}Mo	^{92}Mo(n,γ)	-1.304	^{92}Nb(β^-)	0.882	^{92}Nb(β^+)	-0.824
^{94}Mo	^{94}Mo(n,γ)	-1.638	^{93}Zr(β^-)	0.753	^{93}Zr(n,γ)	-0.571
^{95}Mo	^{95}Zr(n,γ)	-0.596	^{95}Nb(β^-)	0.536	^{95}Zr(β^-)	0.510
^{96}Mo	^{95}Zr(n,γ)	-0.611	^{95}Zr(β^-)	0.569	^{96}Mo(n,γ)	-0.495
^{97}Mo	^{97}Mo(n,γ)	-0.756	^{95}Zr(β^-)	0.581	^{95}Zr(n,γ)	-0.562
^{98}Mo	^{95}Zr(β^-)	0.497	^{95}Zr(n,γ)	-0.326	^{96}Mo(n,γ)	0.238
^{100}Mo	^{100}Mo(n,γ)	-2.130	^{99}Mo(n,γ)	0.976	^{99}Mo(β^-)	-0.970
^{98}Ru	^{99}Ru(γ,n)	0.997	^{99}Ru(n,γ)	-0.953	^{99}Tc(n,γ)	-0.803
^{99}Ru	^{99}Ru(n,γ)	-0.939	^{99}Tc(β^-)	0.825	^{99}Tc(n,γ)	-0.780
^{100}Ru	^{100}Ru(n,γ)	-0.928	^{95}Zr(β^-)	0.391	^{96}Zr(n,γ)	0.303
^{101}Ru	^{101}Ru(n,γ)	-0.977	^{95}Zr(β^-)	0.371	^{96}Zr(n,γ)	0.311
^{102}Ru	^{102}Ru(n,γ)	-1.019	^{96}Zr(n,γ)	0.264	^{95}Zr(β^-)	0.251
^{104}Ru	^{104}Ru(n,γ)	-2.060	^{103}Ru(β^-)	-0.746	^{103}Ru(n,γ)	0.745

Isotope	Most important reactions with respective sensitivities					
^{103}Rh	^{103}Rh(n,γ)	-1.017	^{96}Zr(n,γ)	0.253	^{95}Zr(β^-)	0.230
^{104}Pd	^{104}Pd(n,γ)	-1.044	^{96}Zr(n,γ)	0.219	^{96}Mo(n,γ)	-0.212
^{105}Pd	^{105}Pd(n,γ)	-1.031	^{96}Mo(n,γ)	-0.214	^{96}Zr(n,γ)	0.200
^{106}Pd	^{106}Pd(n,γ)	-1.073	^{96}Mo(n,γ)	-0.210	^{96}Zr(n,γ)	0.148
^{108}Pd	^{108}Pd(n,γ)	-1.056	^{96}Mo(n,γ)	-0.172	^{104}Ru(n,γ)	-0.110
^{110}Pd	^{110}Pd(n,γ)	-1.924	^{109}Pd(n,γ)	0.811	^{109}Pd(β^-)	-0.803
^{107}Ag	^{107}Ag(n,γ)	-1.055	^{107}Pd(β^-)	0.979	^{107}Pd(n,γ)	-0.957
^{109}Ag	^{109}Ag(n,γ)	-1.064	^{96}Mo(n,γ)	-0.146	-	
^{108}Cd	^{107}Pd(n,γ)	-0.979	^{107}Pd(β^-)	0.969	^{108}Cd(n,γ)	-0.807
^{110}Cd	^{110}Cd(n,γ)	-1.023	^{96}Mo(n,γ)	-0.113	-	
^{111}Cd	^{111}Cd(n,γ)	-1.025	^{96}Mo(n,γ)	-0.100	-	
^{112}Cd	^{112}Cd(n,γ)	-0.916	^{113}Cd(n,γ)	-0.142	^{113}Cd(γ,n)	0.135
^{113}Cd	^{113}Cd(n,γ)	-0.866	^{113}Cd(γ,n)	-0.152	-	
^{114}Cd	^{114}Cd(n,γ)	-0.848	^{115}Cd(γ,n)	0.125	^{115}Cd(β^-)	-0.107
^{116}Cd	^{116}Cd(n,γ)	-1.551	^{115}Cd(n,γ)	0.608	^{115}Cd(β^-)	-0.591
^{115}In	^{115}In(n,γ)	-0.937	^{115}Cd(β^-)	0.331	^{115}Cd(γ,n)	-0.281
^{114}Sn	^{115}Sn(γ,n)	0.998	^{115}In(n,γ)	-0.974	^{115}In(β^-)	0.928
^{115}Sn	^{115}Sn(n,γ)	-1.005	^{115}In(n,γ)	-0.949	^{115}In(β^-)	0.935
^{116}Sn	^{116}Sn(n,γ)	-0.904	^{115}Cd(β^-)	0.200	^{115}Cd(n,γ)	-0.176
^{117}Sn	^{117}Sn(n,γ)	-1.034	^{116}Sn(n,γ)	0.127	-	
^{119}Sn	^{119}Sn(n,γ)	-0.929	^{119}Sn(γ,n)	-0.122	-	
^{122}Sn	^{121}Sn(n,γ)	0.425	^{121}Sn(β^-)	-0.367	-	
^{124}Sn	^{124}Sn(n,γ)	-1.178	^{123}Sn(n,γ)	0.604	^{123}Sn(β^-)	-0.593
^{121}Sb	^{121}Sb(n,γ)	-1.051	^{121}Sn(β^-)	0.147	^{121}Sn(γ,n)	-0.140
^{123}Sb	^{123}Sb(n,γ)	-1.075	^{121}Sn(n,γ)	0.377	^{121}Sn(β^-)	-0.328
^{122}Te	^{122}Te(n,γ)	-1.034	^{121}Sn(n,γ)	-0.168	-	
^{123}Te	^{123}Te(n,γ)	-1.035	^{121}Sn(n,γ)	-0.192	-	
^{124}Te	^{124}Te(n,γ)	-0.843	^{121}Sn(n,γ)	-0.119	-	
^{125}Te	^{125}Te(n,γ)	-0.895	^{124}Te(n,γ)	0.168	^{121}Sn(n,γ)	-0.137
^{126}Te	^{121}Sn(n,γ)	-0.176	^{121}Sn(β^-)	0.146	^{124}Te(n,γ)	0.119
^{128}Te	^{128}Te(n,γ)	-1.530	^{127}Te(β^-)	-0.564	^{127}Te(n,γ)	0.563

Isotope	Most important reactions with respective sensitivities					
^{130}Te	^{130}Te(n,γ)	-2.445	^{129}Te(n,γ)	0.296	^{129}Te(β^-)	-0.293
^{127}I	^{127}I (n,γ)	-0.976	^{121}Sn(n,γ)	-0.181	^{121}Sn(β^-)	0.166
^{128}Xe	^{128}Xe(n,γ)	-0.933	^{121}Sn(β^-)	0.185	^{121}Sn(n,γ)	-0.181
^{129}Xe	^{129}Xe(n,γ)	-0.985	^{121}Sn(β^-)	0.188	^{121}Sn(n,γ)	-0.174
^{130}Xe	^{130}Xe(n,γ)	-0.888	^{121}Sn(β^-)	0.166	^{121}Sn(n,γ)	-0.125
^{131}Xe	^{131}Xe(n,γ)	-0.918	^{121}Sn(β^-)	0.156	^{121}Sn(n,γ)	-0.109
^{134}Xe	^{134}Xe(n,γ)	-0.731	^{133}Xe(n,γ)	0.437	^{133}Xe(β^-)	-0.380
^{136}Xe	^{136}Xe(n,γ)	-0.171	^{135}Xe(n,γ)	0.109	^{135}Xe(β^-)	-0.101
^{133}Cs	^{133}Cs(n,γ)	-1.043	^{133}Xe(n,γ)	-0.108	-	
^{134}Ba	^{134}Ba(n,γ)	-0.945	^{133}Xe(n,γ)	-0.207	^{132}Xe(n,γ)	-0.103
^{135}Ba	^{135}Ba(n,γ)	-0.997	^{133}Xe(n,γ)	-0.184	^{135}Cs(n,γ)	-0.114
^{136}Ba	^{136}Ba(n,γ)	-0.799	^{133}Xe(n,γ)	-0.191	^{134}Xe(n,γ)	0.128
^{137}Ba	^{137}Ba(n,γ)	-0.889	^{134}Xe(n,γ)	0.206	^{133}Xe(β^-)	0.118
^{138}Ba	^{138}Ba(n,γ)	-0.393	^{120}Sn(n,γ)	0.110	-	
^{139}La	^{139}La(n,γ)	-0.830	^{138}Ba(n,γ)	0.636	^{120}Sn(n,γ)	0.104
^{140}Ce	^{138}Ba(n,γ)	0.690	^{140}Ce(n,γ)	-0.491	^{139}La(n,γ)	0.206
^{142}Ce	^{138}Ba(n,γ)	0.701	^{142}Ce(n,γ)	-0.543	^{142}Ce(γ,α)	-0.472
^{141}Pr	^{141}Ce(n,γ)	-0.737	^{138}Ba(n,γ)	0.693	^{141}Ce(β^-)	0.502
^{142}Nd	^{142}Nd(n,γ)	-0.895	^{138}Ba(n,γ)	0.684	^{143}Nd(n,γ)	-0.302

INITIAL ABUNDANCES FOR THE WEAK *S* PROCESS

Table A.5: Initial abundances for the weak *s* process simulations. Added abundances give unity.

isotope	initial abundance	isotope	initial abundance	isotope	initial abundance
Protons	$7.05725 \cdot 10^{-01}$	^{2}H	$4.80117 \cdot 10^{-05}$	^{3}He	$2.92911 \cdot 10^{-05}$
^{4}He	$2.75210 \cdot 10^{-01}$	^{7}Li	$9.35334 \cdot 10^{-09}$	^{11}B	$4.72517 \cdot 10^{-09}$
^{12}C	$3.03211 \cdot 10^{-03}$	^{13}C	$3.65013 \cdot 10^{-05}$	^{14}N	$1.10504 \cdot 10^{-03}$
^{15}N	$4.36316 \cdot 10^{-06}$	^{16}O	$9.59235 \cdot 10^{-03}$	^{17}O	$3.88714 \cdot 10^{-06}$
^{18}O	$2.16708 \cdot 10^{-05}$	^{19}F	$4.05115 \cdot 10^{-07}$	^{20}Ne	$1.61906 \cdot 10^{-03}$
^{21}Ne	$4.12715 \cdot 10^{-06}$	^{22}Ne	$1.30205 \cdot 10^{-04}$	^{23}Na	$3.33912 \cdot 10^{-05}$

isotope	initial abundance	isotope	initial abundance	isotope	initial abundance
^{24}Mg	$5.14819 \cdot 10^{-04}$	^{25}Mg	$6.76624 \cdot 10^{-05}$	^{26}Mg	$7.76028 \cdot 10^{-05}$
^{27}Al	$5.79821 \cdot 10^{-05}$	^{28}Si	$6.53024 \cdot 10^{-04}$	^{29}Si	$3.42612 \cdot 10^{-05}$
^{30}Si	$2.35208 \cdot 10^{-05}$	^{31}P	$8.15529 \cdot 10^{-06}$	^{32}S	$3.95814 \cdot 10^{-04}$
^{33}S	$3.22212 \cdot 10^{-06}$	^{34}S	$1.86607 \cdot 10^{-05}$	^{36}S	$9.37934 \cdot 10^{-08}$
^{35}Cl	$2.53209 \cdot 10^{-06}$	^{37}Cl	$8.54531 \cdot 10^{-07}$	^{36}Ar	$7.74028 \cdot 10^{-05}$
^{38}Ar	$1.53806 \cdot 10^{-05}$	^{40}Ar	$2.52909 \cdot 10^{-08}$	^{39}K	$3.46913 \cdot 10^{-06}$
^{40}K	$5.54520 \cdot 10^{-09}$	^{41}K	$2.63109 \cdot 10^{-07}$	^{40}Ca	$5.99022 \cdot 10^{-05}$
^{42}Ca	$4.19615 \cdot 10^{-07}$	^{43}Ca	$8.97332 \cdot 10^{-08}$	^{44}Ca	$1.41905 \cdot 10^{-06}$
^{46}Ca	$2.79310 \cdot 10^{-09}$	^{48}Ca	$1.38405 \cdot 10^{-07}$	^{45}Sc	$3.89314 \cdot 10^{-08}$
^{46}Ti	$2.23408 \cdot 10^{-07}$	^{47}Ti	$2.08108 \cdot 10^{-07}$	^{48}Ti	$2.15008 \cdot 10^{-06}$
^{49}Ti	$1.63606 \cdot 10^{-07}$	^{50}Ti	$1.64406 \cdot 10^{-07}$	^{50}V	$9.25833 \cdot 10^{-10}$
^{51}V	$3.76714 \cdot 10^{-07}$	^{50}Cr	$7.42427 \cdot 10^{-07}$	^{52}Cr	$1.48805 \cdot 10^{-05}$
^{53}Cr	$1.72006 \cdot 10^{-06}$	^{54}Cr	$4.35716 \cdot 10^{-07}$	^{55}Mn	$1.32905 \cdot 10^{-05}$
^{54}Fe	$7.13026 \cdot 10^{-05}$	^{56}Fe	$1.16904 \cdot 10^{-03}$	^{57}Fe	$2.85510 \cdot 10^{-05}$
^{58}Fe	$3.69713 \cdot 10^{-06}$	^{59}Co	$3.35812 \cdot 10^{-06}$	^{58}Ni	$4.94418 \cdot 10^{-05}$
^{60}Ni	$1.95807 \cdot 10^{-05}$	^{61}Ni	$8.59431 \cdot 10^{-07}$	^{62}Ni	$2.77610 \cdot 10^{-06}$
^{64}Ni	$7.26926 \cdot 10^{-07}$	^{63}Cu	$5.75321 \cdot 10^{-07}$	^{65}Cu	$2.64710 \cdot 10^{-07}$
^{64}Zn	$9.92436 \cdot 10^{-07}$	^{66}Zn	$5.87721 \cdot 10^{-07}$	^{67}Zn	$8.76232 \cdot 10^{-08}$
^{68}Zn	$4.05915 \cdot 10^{-07}$	^{70}Zn	$1.38105 \cdot 10^{-08}$	^{69}Ga	$3.96214 \cdot 10^{-08}$
^{71}Ga	$2.71210 \cdot 10^{-08}$	^{70}Ge	$4.32016 \cdot 10^{-08}$	^{72}Ge	$5.93721 \cdot 10^{-08}$
^{73}Ge	$1.71406 \cdot 10^{-08}$	^{74}Ge	$8.12429 \cdot 10^{-08}$	^{76}Ge	$1.78406 \cdot 10^{-08}$
^{75}As	$1.24504 \cdot 10^{-08}$	^{74}Se	$1.03004 \cdot 10^{-09}$	^{76}Se	$1.07704 \cdot 10^{-08}$
^{77}Se	$9.15433 \cdot 10^{-09}$	^{78}Se	$2.90010 \cdot 10^{-08}$	^{80}Se	$6.25323 \cdot 10^{-08}$
^{82}Se	$1.18204 \cdot 10^{-08}$	^{79}Br	$1.19504 \cdot 10^{-08}$	^{81}Br	$1.19204 \cdot 10^{-08}$
^{78}Kr	$3.01911 \cdot 10^{-10}$	^{80}Kr	$2.02207 \cdot 10^{-09}$	^{82}Kr	$1.06804 \cdot 10^{-08}$
^{83}Kr	$1.08304 \cdot 10^{-08}$	^{84}Kr	$5.46120 \cdot 10^{-08}$	^{86}Kr	$1.70506 \cdot 10^{-08}$
^{85}Rb	$1.10104 \cdot 10^{-08}$	^{87}Rb	$4.64317 \cdot 10^{-09}$	^{84}Sr	$2.80510 \cdot 10^{-10}$
^{86}Sr	$5.04718 \cdot 10^{-09}$	^{87}Sr	$3.56913 \cdot 10^{-09}$	^{88}Sr	$4.32116 \cdot 10^{-08}$
^{89}Y	$1.04504 \cdot 10^{-08}$	^{90}Zr	$1.33605 \cdot 10^{-08}$	^{91}Zr	$2.94611 \cdot 10^{-09}$
^{92}Zr	$4.56116 \cdot 10^{-09}$	^{94}Zr	$4.70817 \cdot 10^{-09}$	^{96}Zr	$7.77128 \cdot 10^{-10}$
^{93}Nb	$1.64206 \cdot 10^{-09}$	^{92}Mo	$8.79732 \cdot 10^{-10}$	^{94}Mo	$5.61120 \cdot 10^{-10}$
^{95}Mo	$9.75635 \cdot 10^{-10}$	^{96}Mo	$1.03204 \cdot 10^{-09}$	^{97}Mo	$5.98722 \cdot 10^{-10}$
^{98}Mo	$1.52506 \cdot 10^{-09}$	^{100}Mo	$6.22322 \cdot 10^{-10}$	^{96}Ru	$2.50109 \cdot 10^{-10}$
^{98}Ru	$8.67631 \cdot 10^{-11}$	^{99}Ru	$5.91021 \cdot 10^{-10}$	^{100}Ru	$5.91921 \cdot 10^{-10}$
^{101}Ru	$8.07329 \cdot 10^{-10}$	^{102}Ru	$1.51705 \cdot 10^{-09}$	^{104}Ru	$9.15533 \cdot 10^{-10}$
^{103}Rh	$8.96232 \cdot 10^{-10}$	^{102}Pd	$3.66413 \cdot 10^{-11}$	^{104}Pd	$4.07815 \cdot 10^{-10}$
^{105}Pd	$8.23330 \cdot 10^{-10}$	^{106}Pd	$1.01904 \cdot 10^{-09}$	^{108}Pd	$1.00504 \cdot 10^{-09}$
^{110}Pd	$4.53516 \cdot 10^{-10}$	^{107}Ag	$6.82125 \cdot 10^{-10}$	^{109}Ag	$6.45223 \cdot 10^{-10}$

isotope	initial abundance	isotope	initial abundance	isotope	initial abundance
^{106}Cd	$5.38919 \cdot 10^{-11}$	^{108}Cd	$3.90714 \cdot 10^{-11}$	^{110}Cd	$5.59320 \cdot 10^{-10}$
^{111}Cd	$5.78421 \cdot 10^{-10}$	^{112}Cd	$1.09904 \cdot 10^{-09}$	^{113}Cd	$5.63120 \cdot 10^{-10}$
^{114}Cd	$1.33505 \cdot 10^{-09}$	^{116}Cd	$3.55013 \cdot 10^{-10}$	^{113}In	$2.25808 \cdot 10^{-11}$
^{115}In	$5.12018 \cdot 10^{-10}$	^{112}Sn	$1.05404 \cdot 10^{-10}$	^{114}Sn	$7.26726 \cdot 10^{-11}$
^{115}Sn	$3.75214 \cdot 10^{-11}$	^{116}Sn	$1.62806 \cdot 10^{-09}$	^{117}Sn	$8.67131 \cdot 10^{-10}$
^{118}Sn	$2.76110 \cdot 10^{-09}$	^{119}Sn	$9.87336 \cdot 10^{-10}$	^{120}Sn	$3.77914 \cdot 10^{-09}$
^{122}Sn	$5.46220 \cdot 10^{-10}$	^{124}Sn	$6.93225 \cdot 10^{-10}$	^{121}Sb	$5.41720 \cdot 10^{-10}$
^{123}Sb	$4.10715 \cdot 10^{-10}$	^{120}Te	$1.30505 \cdot 10^{-11}$	^{122}Te	$3.82714 \cdot 10^{-10}$
^{123}Te	$1.33205 \cdot 10^{-10}$	^{124}Te	$7.18326 \cdot 10^{-10}$	^{125}Te	$1.08104 \cdot 10^{-09}$
^{126}Te	$2.89710 \cdot 10^{-09}$	^{128}Te	$4.94118 \cdot 10^{-09}$	^{130}Te	$5.37319 \cdot 10^{-09}$
^{127}I	$2.89110 \cdot 10^{-09}$	^{124}Xe	$1.79106 \cdot 10^{-11}$	^{126}Xe	$1.62206 \cdot 10^{-11}$
^{128}Xe	$3.33512 \cdot 10^{-10}$	^{129}Xe	$4.17715 \cdot 10^{-09}$	^{130}Xe	$6.74124 \cdot 10^{-10}$
^{131}Xe	$3.38012 \cdot 10^{-09}$	^{132}Xe	$4.14015 \cdot 10^{-09}$	^{134}Xe	$1.55606 \cdot 10^{-09}$
^{136}Xe	$1.28305 \cdot 10^{-09}$	^{133}Cs	$1.25105 \cdot 10^{-09}$	^{130}Ba	$1.56506 \cdot 10^{-11}$
^{132}Ba	$1.51305 \cdot 10^{-11}$	^{134}Ba	$3.69513 \cdot 10^{-10}$	^{135}Ba	$1.01104 \cdot 10^{-09}$
^{136}Ba	$1.21404 \cdot 10^{-09}$	^{137}Ba	$1.74706 \cdot 10^{-09}$	^{138}Ba	$1.12404 \cdot 10^{-08}$
^{138}La	$1.42805 \cdot 10^{-12}$	^{139}La	$1.56806 \cdot 10^{-09}$	^{136}Ce	$7.43127 \cdot 10^{-12}$
^{138}Ce	$9.87936 \cdot 10^{-12}$	^{140}Ce	$3.55913 \cdot 10^{-09}$	^{142}Ce	$4.52616 \cdot 10^{-10}$
^{141}Pr	$5.95622 \cdot 10^{-10}$	^{142}Nd	$8.08229 \cdot 10^{-10}$	^{143}Nd	$3.61713 \cdot 10^{-10}$
^{144}Nd	$7.17626 \cdot 10^{-10}$	^{145}Nd	$2.52009 \cdot 10^{-10}$	^{146}Nd	$5.24419 \cdot 10^{-10}$
^{148}Nd	$1.78606 \cdot 10^{-10}$	^{150}Nd	$1.77206 \cdot 10^{-10}$	^{144}Sm	$2.91411 \cdot 10^{-11}$
^{147}Sm	$1.48405 \cdot 10^{-10}$	^{148}Sm	$1.09304 \cdot 10^{-10}$	^{149}Sm	$1.34205 \cdot 10^{-10}$
^{150}Sm	$7.24726 \cdot 10^{-11}$	^{152}Sm	$2.64910 \cdot 10^{-10}$	^{154}Sm	$2.28308 \cdot 10^{-10}$
^{151}Eu	$1.77606 \cdot 10^{-10}$	^{153}Eu	$1.96607 \cdot 10^{-10}$	^{152}Gd	$2.53809 \cdot 10^{-12}$
^{154}Gd	$2.80110 \cdot 10^{-11}$	^{155}Gd	$1.91307 \cdot 10^{-10}$	^{156}Gd	$2.66710 \cdot 10^{-10}$
^{157}Gd	$2.04907 \cdot 10^{-10}$	^{158}Gd	$3.27712 \cdot 10^{-10}$	^{160}Gd	$2.91811 \cdot 10^{-10}$
^{159}Tb	$2.42509 \cdot 10^{-10}$	^{156}Dy	$8.72131 \cdot 10^{-13}$	^{158}Dy	$1.51105 \cdot 10^{-12}$
^{160}Dy	$3.73213 \cdot 10^{-11}$	^{161}Dy	$3.03411 \cdot 10^{-10}$	^{162}Dy	$4.13915 \cdot 10^{-10}$
^{163}Dy	$4.04915 \cdot 10^{-10}$	^{164}Dy	$4.60517 \cdot 10^{-10}$	^{165}Ho	$3.71013 \cdot 10^{-10}$
^{162}Er	$1.43805 \cdot 10^{-12}$	^{164}Er	$1.67606 \cdot 10^{-11}$	^{166}Er	$3.54013 \cdot 10^{-10}$
^{167}Er	$2.43309 \cdot 10^{-10}$	^{168}Er	$2.85610 \cdot 10^{-10}$	^{170}Er	$1.60806 \cdot 10^{-10}$
^{169}Tm	$1.61606 \cdot 10^{-10}$	^{168}Yb	$1.36805 \cdot 10^{-12}$	^{170}Yb	$3.25112 \cdot 10^{-11}$
^{171}Yb	$1.53106 \cdot 10^{-10}$	^{172}Yb	$2.36209 \cdot 10^{-10}$	^{173}Yb	$1.75006 \cdot 10^{-10}$
^{174}Yb	$3.46813 \cdot 10^{-10}$	^{176}Yb	$1.40205 \cdot 10^{-10}$	^{175}Lu	$1.58006 \cdot 10^{-10}$
^{176}Lu	$4.60817 \cdot 10^{-12}$	^{174}Hf	$1.09604 \cdot 10^{-12}$	^{176}Hf	$3.53013 \cdot 10^{-11}$
^{177}Hf	$1.28505 \cdot 10^{-10}$	^{178}Hf	$1.89107 \cdot 10^{-10}$	^{179}Hf	$9.50834 \cdot 10^{-11}$
^{180}Hf	$2.46309 \cdot 10^{-10}$	^{180}Ta	$1.12904 \cdot 10^{-14}$	^{181}Ta	$9.47734 \cdot 10^{-11}$
^{180}W	$7.87728 \cdot 10^{-13}$	^{182}W	$1.61106 \cdot 10^{-10}$	^{183}W	$8.79532 \cdot 10^{-11}$

isotope	initial abundance	isotope	initial abundance	isotope	initial abundance
^{184}W	$1.89907 \cdot 10^{-10}$	^{186}W	$1.78806 \cdot 10^{-10}$	^{185}Re	$9.03233 \cdot 10^{-11}$
^{187}Re	$1.66006 \cdot 10^{-10}$	^{184}Os	$5.67820 \cdot 10^{-13}$	^{186}Os	$5.03418 \cdot 10^{-11}$
^{187}Os	$3.81714 \cdot 10^{-11}$	^{188}Os	$4.27015 \cdot 10^{-10}$	^{189}Os	$5.21119 \cdot 10^{-10}$
^{190}Os	$8.55531 \cdot 10^{-10}$	^{192}Os	$1.34505 \cdot 10^{-09}$	^{191}Ir	$1.19304 \cdot 10^{-09}$
^{193}Ir	$2.02107 \cdot 10^{-09}$	^{190}Pt	$8.17029 \cdot 10^{-13}$	^{192}Pt	$5.09918 \cdot 10^{-11}$
^{194}Pt	$2.16408 \cdot 10^{-09}$	^{195}Pt	$2.23408 \cdot 10^{-09}$	^{196}Pt	$1.67606 \cdot 10^{-09}$
^{198}Pt	$4.82317 \cdot 10^{-10}$	^{197}Au	$9.31834 \cdot 10^{-10}$	^{196}Hg	$2.57809 \cdot 10^{-12}$
^{198}Hg	$1.69806 \cdot 10^{-10}$	^{199}Hg	$2.88910 \cdot 10^{-10}$	^{200}Hg	$3.97114 \cdot 10^{-10}$
^{201}Hg	$2.27808 \cdot 10^{-10}$	^{202}Hg	$5.18619 \cdot 10^{-10}$	^{204}Hg	$1.20204 \cdot 10^{-10}$
^{203}Tl	$2.78810 \cdot 10^{-10}$	^{205}Tl	$6.72624 \cdot 10^{-10}$	^{204}Pb	$3.15311 \cdot 10^{-10}$
^{206}Pb	$3.09011 \cdot 10^{-09}$	^{207}Pb	$3.37212 \cdot 10^{-09}$	^{208}Pb	$9.61835 \cdot 10^{-09}$
^{209}Bi	$7.61327 \cdot 10^{-10}$				

GLOBAL SENSITIVITIES DURING THE WEAK *S* PROCESS

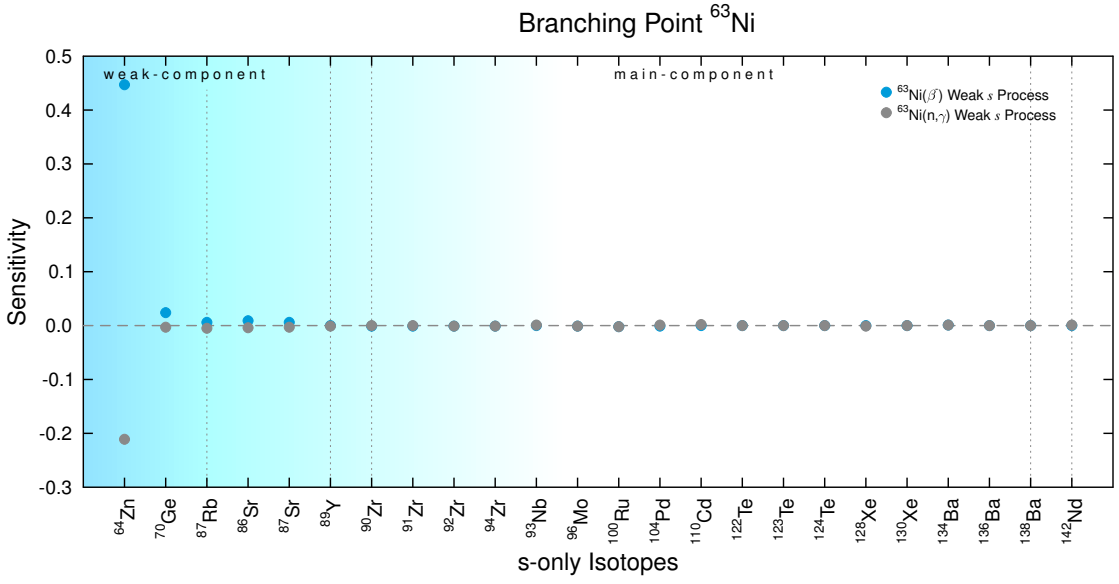

Figure A.46: Branching point ^{63}Ni during the weak *s* process (table 3.11).

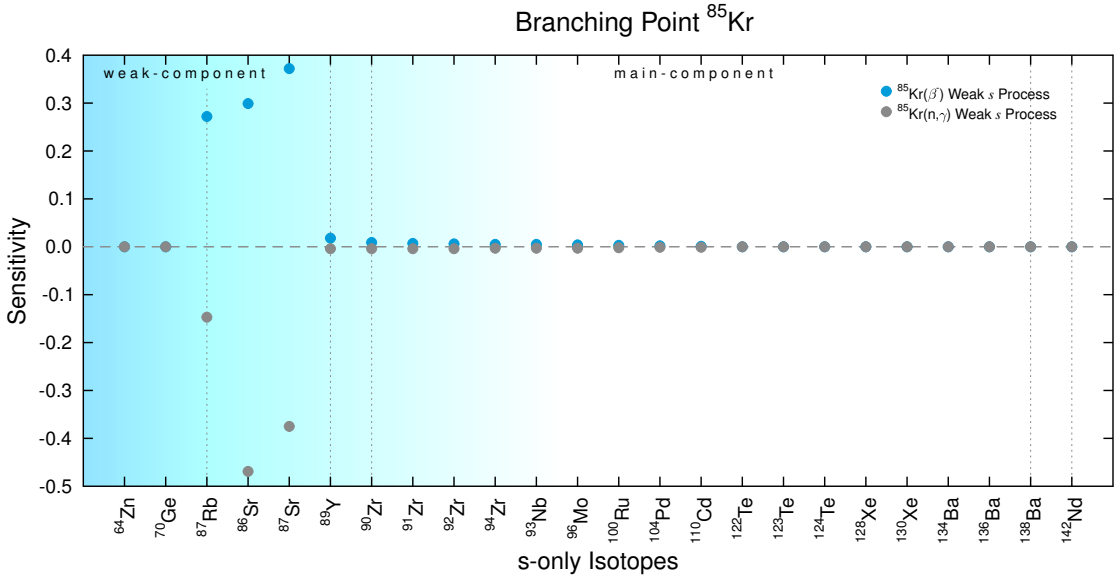

Figure A.47: Branching point ^{85}Kr during the weak *s* process (table 3.11).

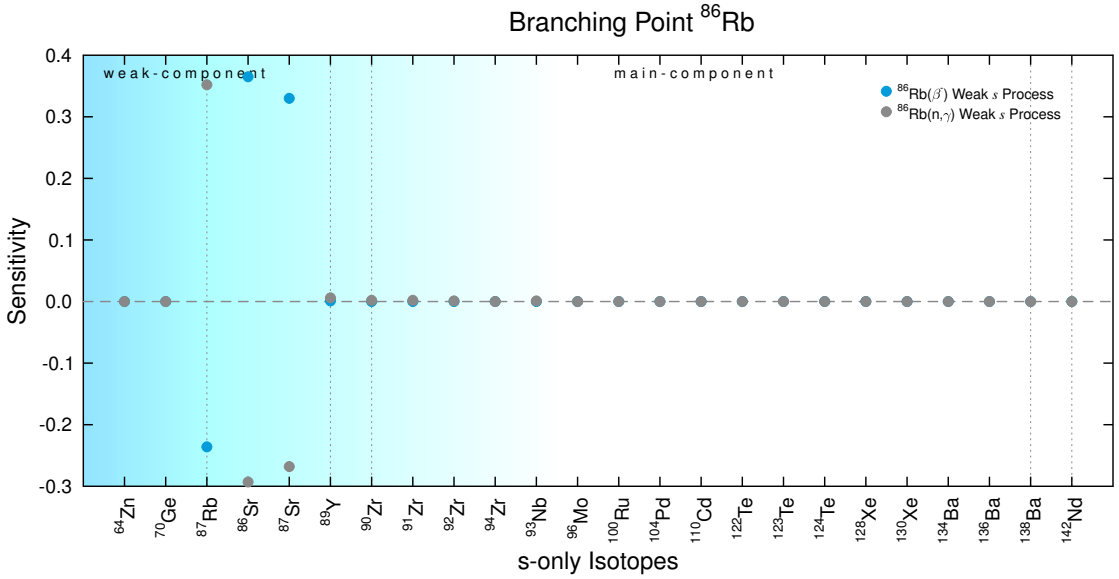

Figure A.48: Branching point ^{86}Rb during the weak *s* process (table 3.11).

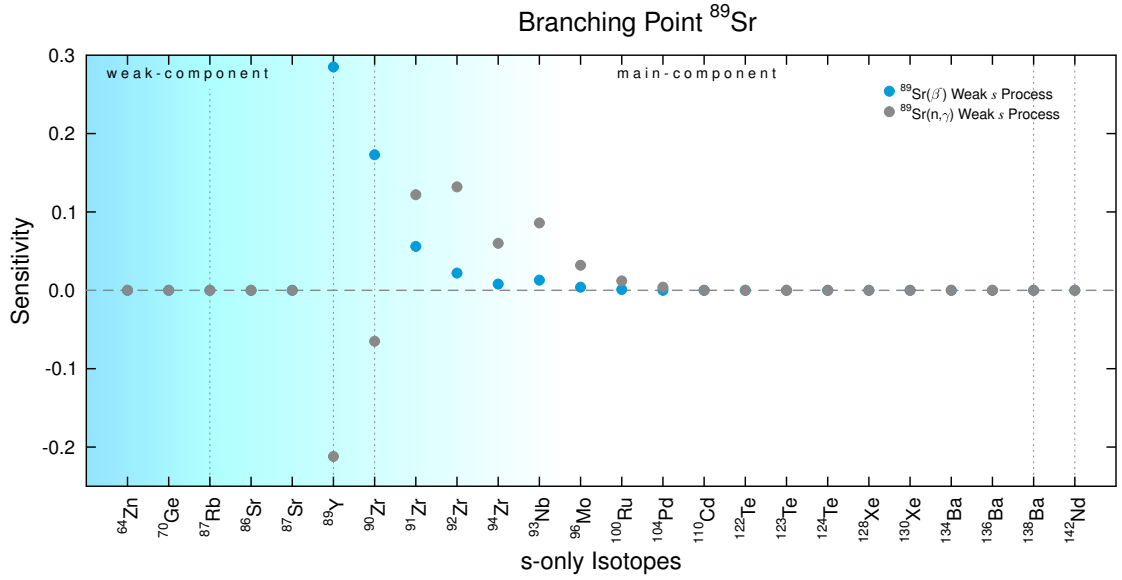

Figure A.49: Branching point ^{89}Sr during the weak *s* process (table 3.11).

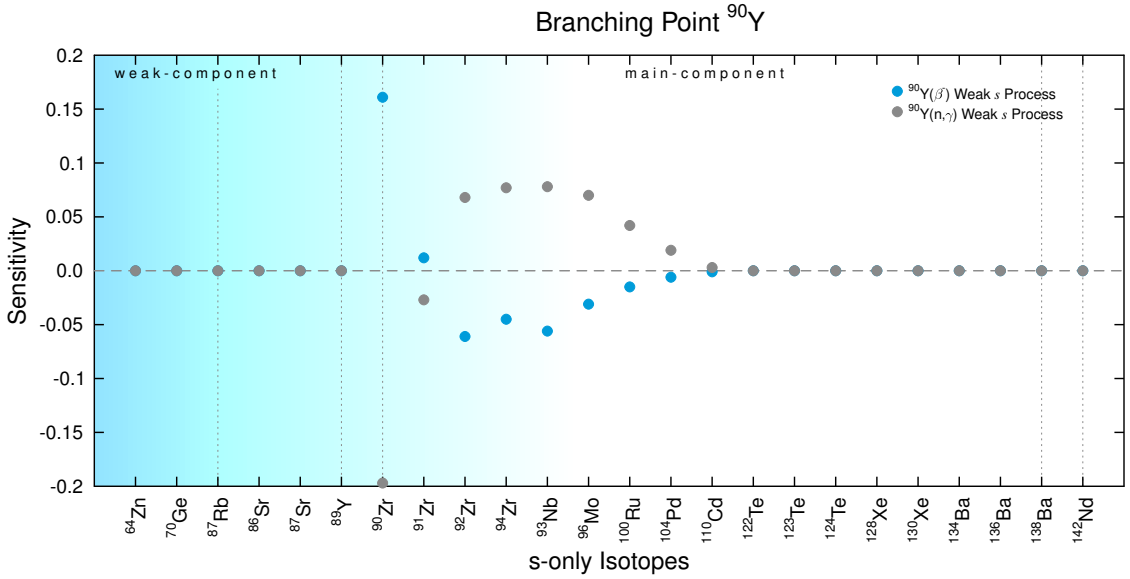

Figure A.50: Branching point ^{90}Y during the weak *s* process (table 3.11).

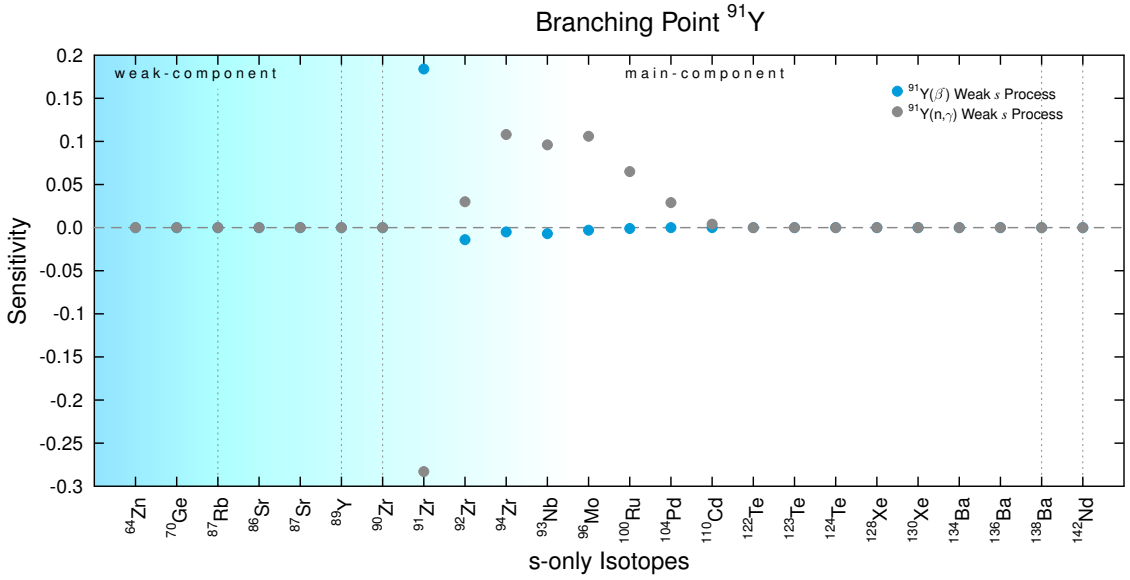

Figure A.51: Branching point ^{91}Y during the weak *s* process (table 3.11).

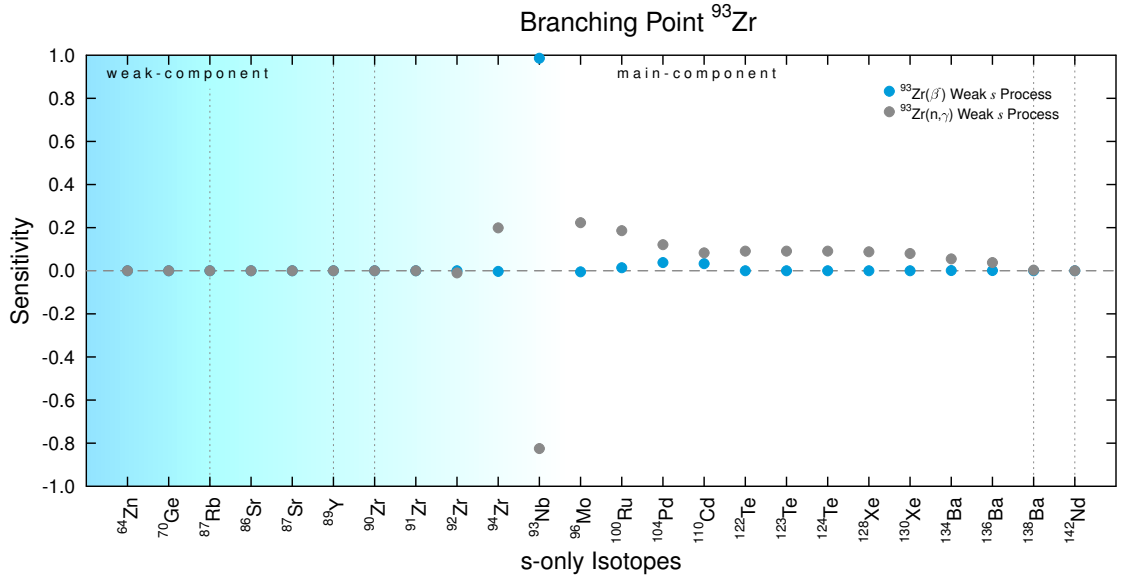

Figure A.52: Branching point ^{93}Zr during the weak *s* process (table 3.11).

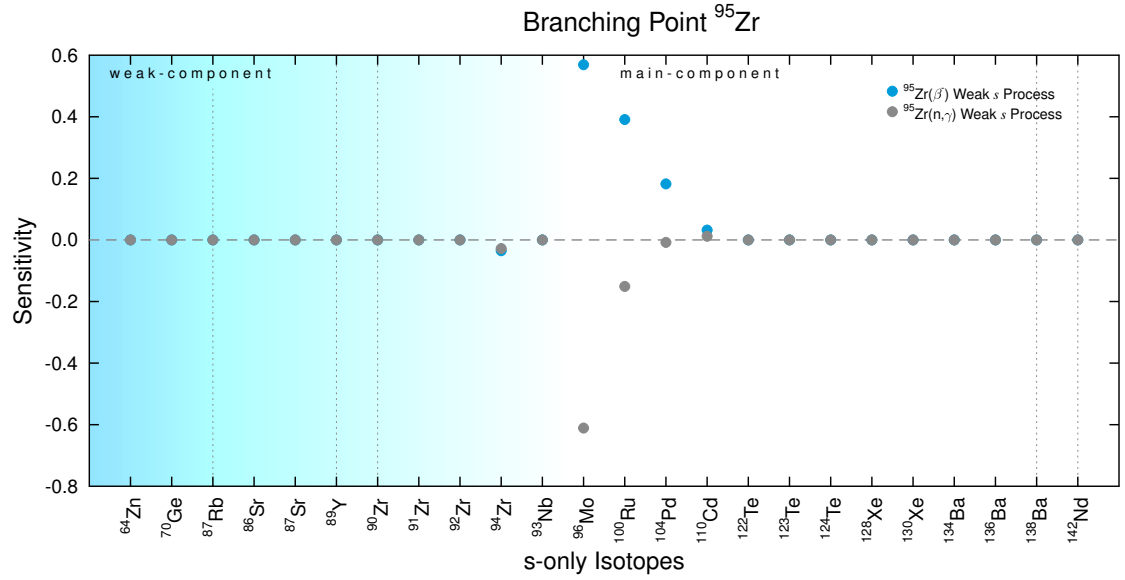

Figure A.53: Branching point ^{95}Zr during the weak *s* process (table 3.11).

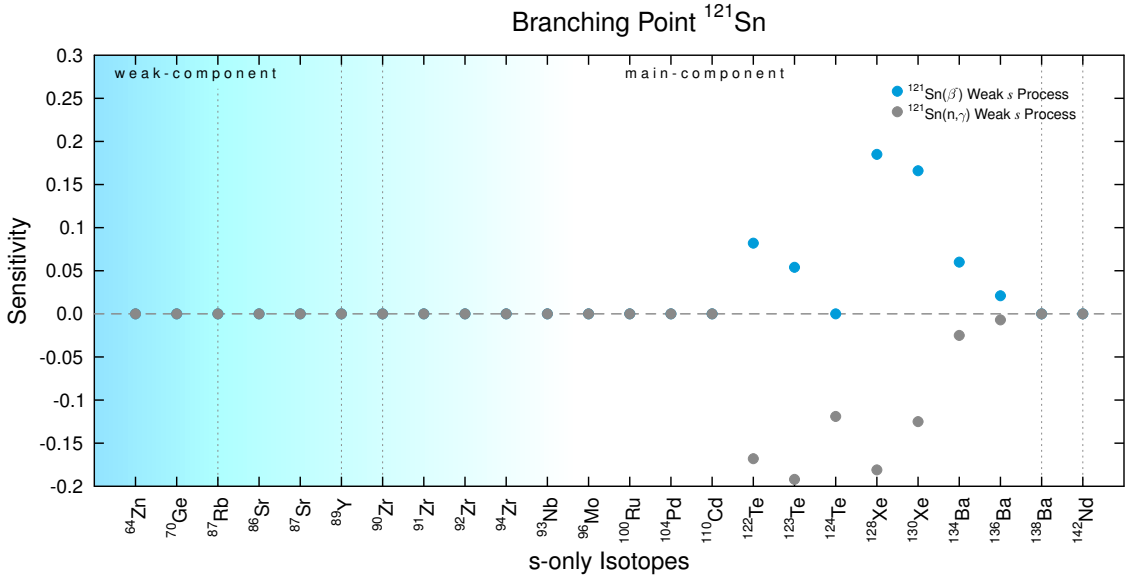

Figure A.54: Branching point ^{121}Sn during the weak *s* process (table 3.11).

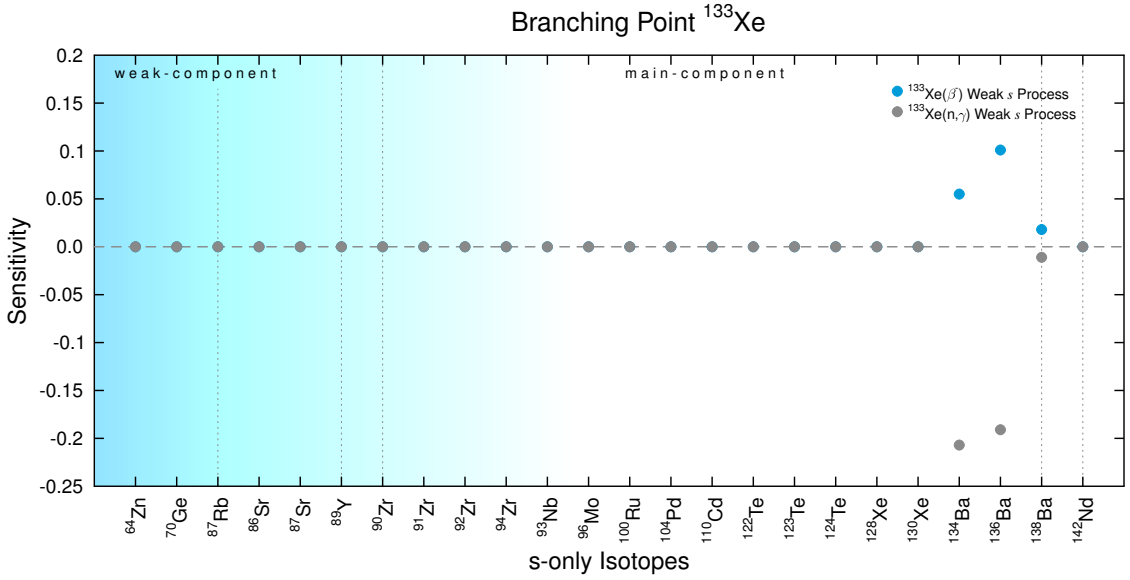

Figure A.55: Branching point ^{133}Xe during the weak *s* process (table 3.11).

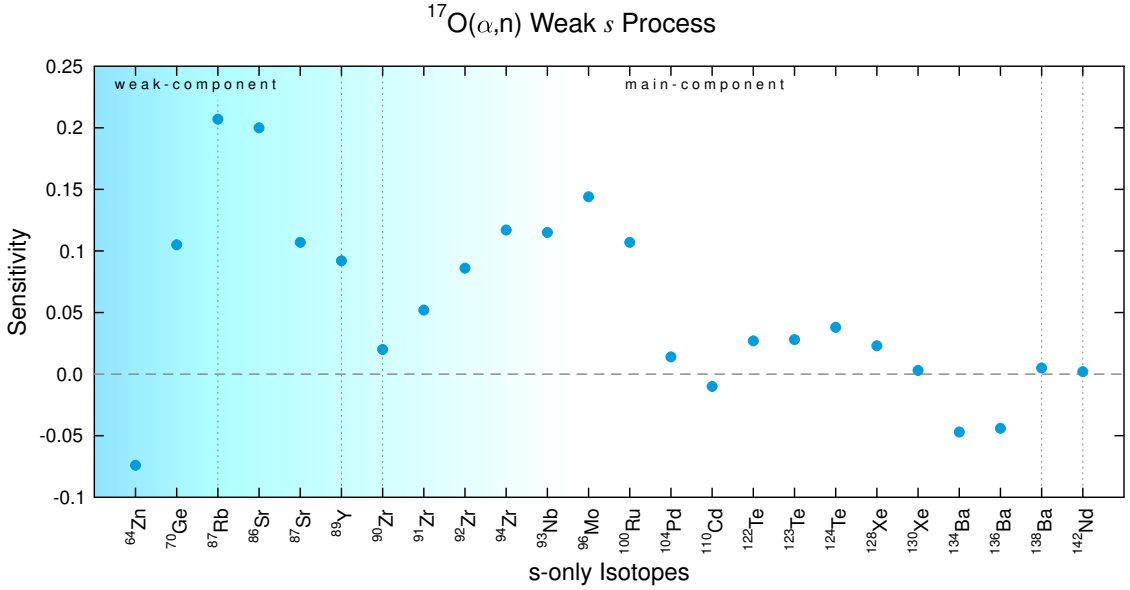

Figure A.56: Neutron donator reaction ^{17}O(α, n) during the weak *s* process (table 3.12).

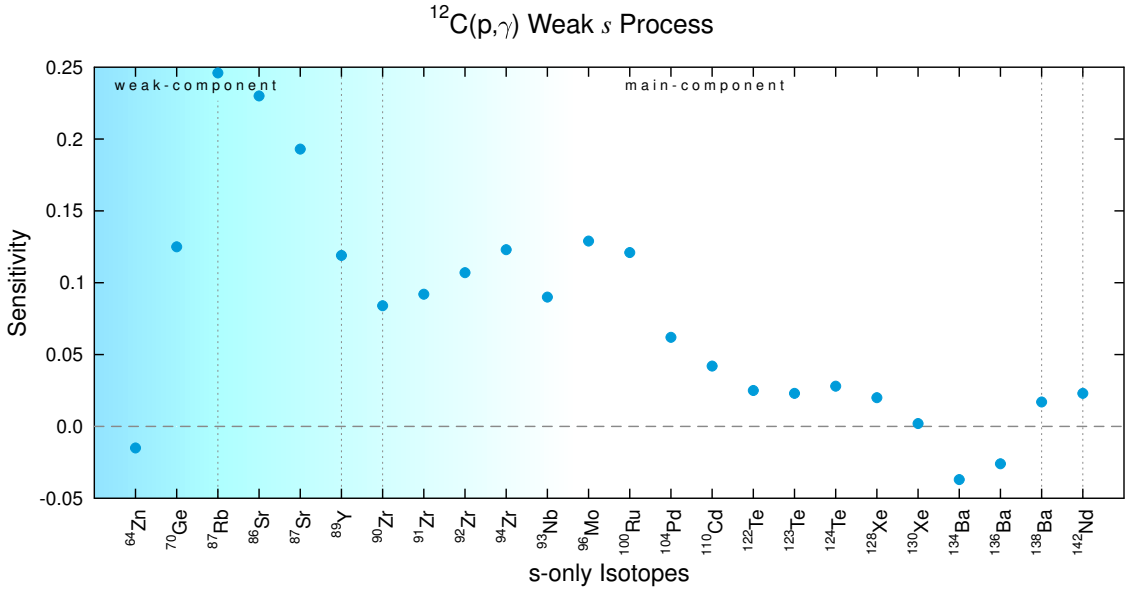

Figure A.57: Neutron donator reaction ^{12}C(p,γ) during the weak s process (table 3.12).

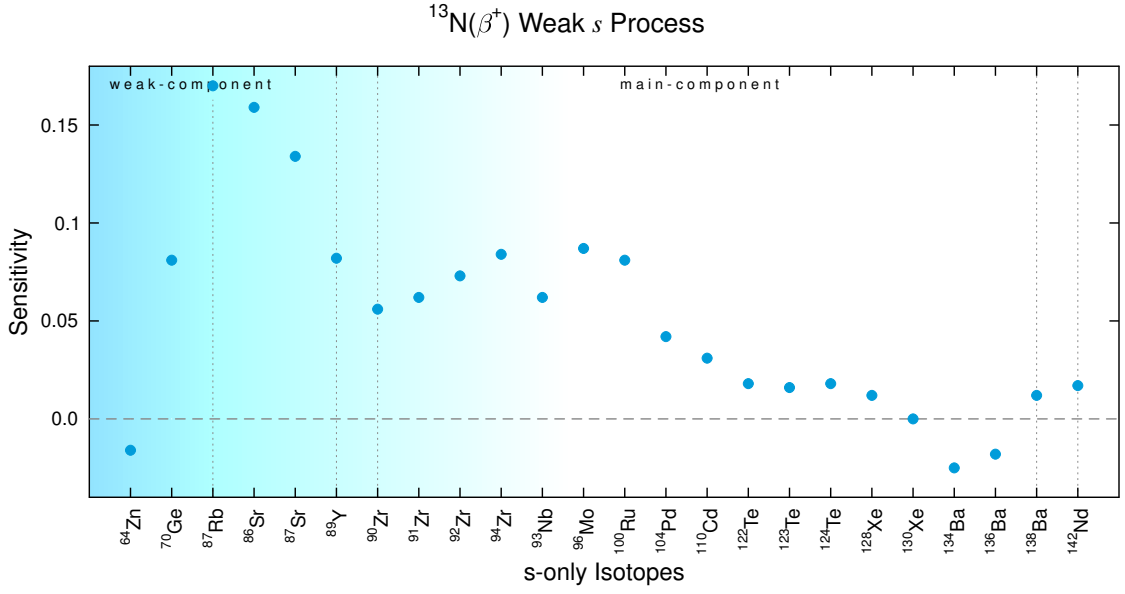

Figure A.58: Neutron donator reaction ^{13}N(β^+) during the weak s process (table 3.12).

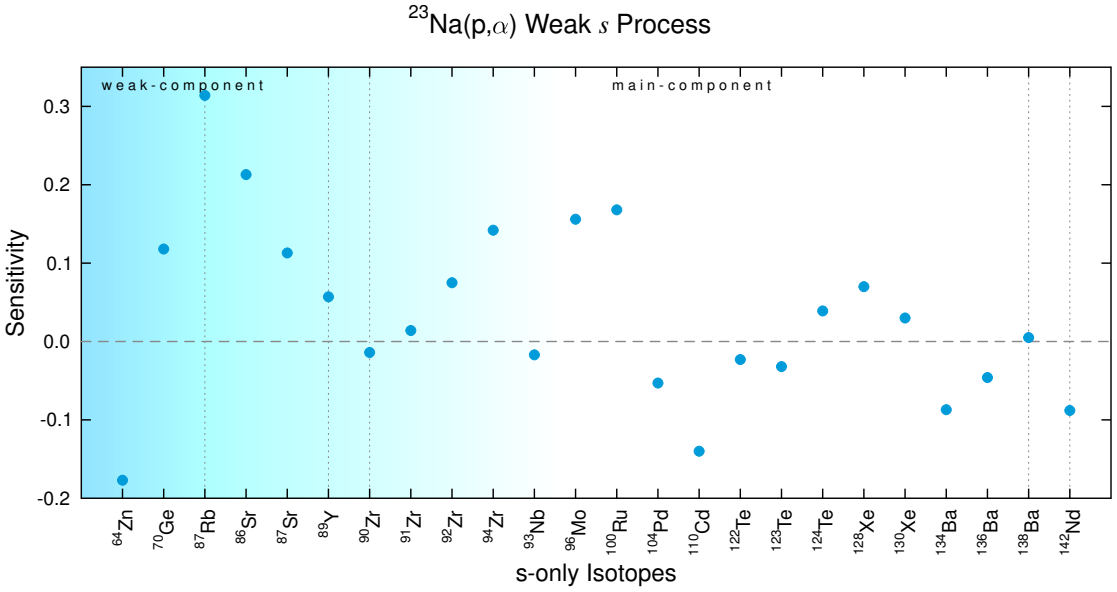

Figure A.59: Recycled neutron poison reaction ^{23}Na(p,α) during the weak s process (table 3.13).

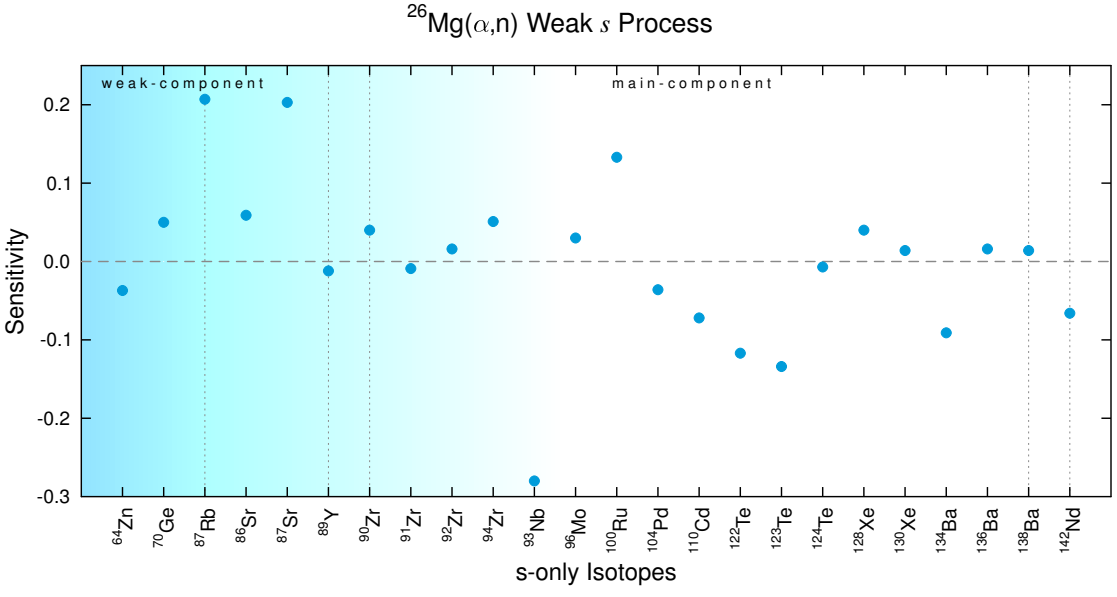

Figure A.60: Recycled neutron poison reaction ^{26}Mg(α,n) during the weak s process (table 3.13).

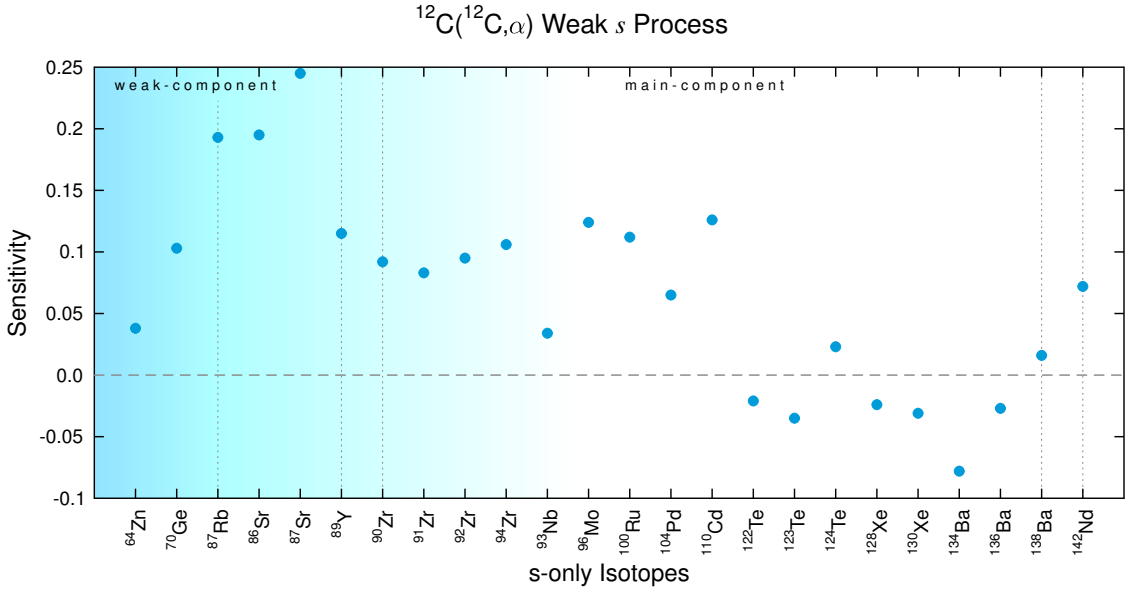

Figure A.61: Recycled neutron poison reaction ^{12}C($^{12}C, \alpha$) during the weak s process (table 3.13).

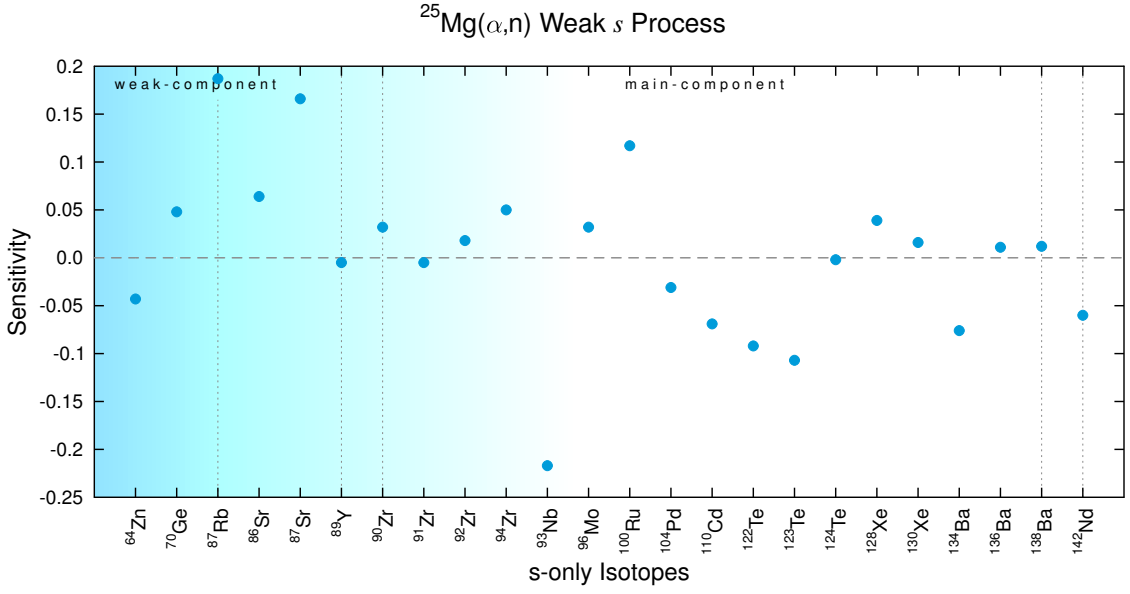

Figure A.62: Recycled neutron poison reaction ^{25}Mg(α, n) during the weak s process (table 3.13).

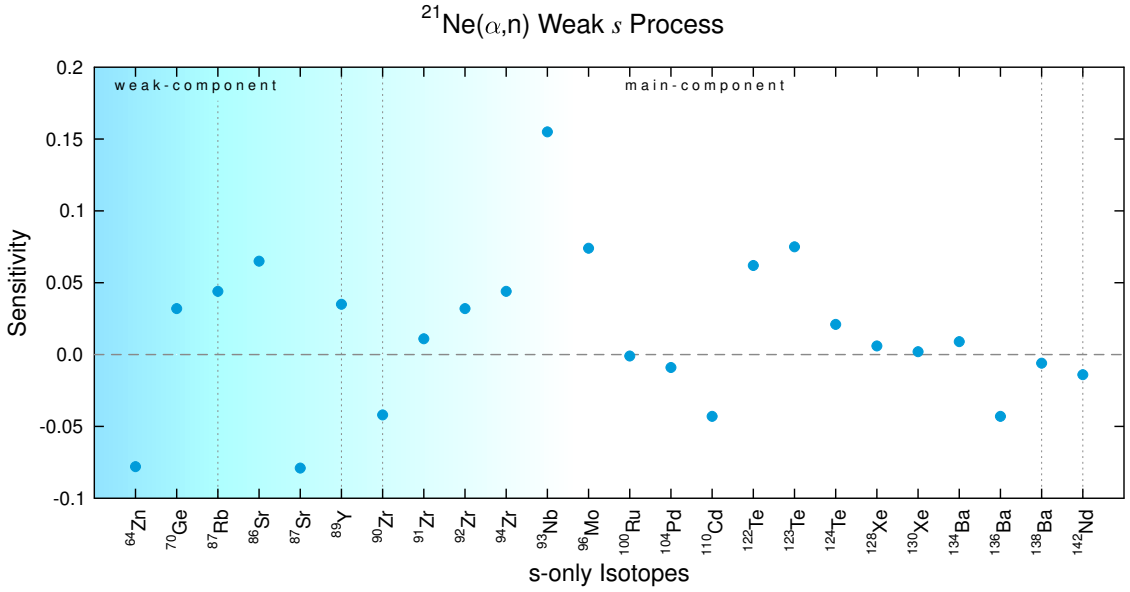

Figure A.63: Recycled neutron poison reaction ^{21}Ne(α, n) during the weak s process (table 3.13).

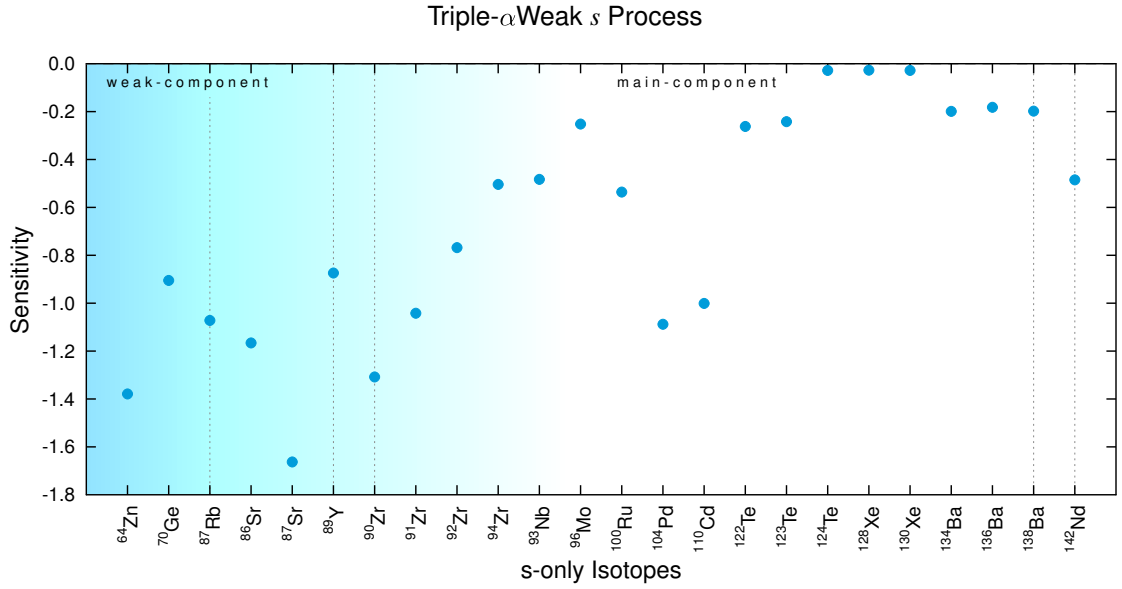

Figure A.64: Neutron poison reaction Triple-α during the weak s process (table 3.14). The triple-α reaction steals α-particles, which demonstrates the dominance of the α-capture neutron sources.

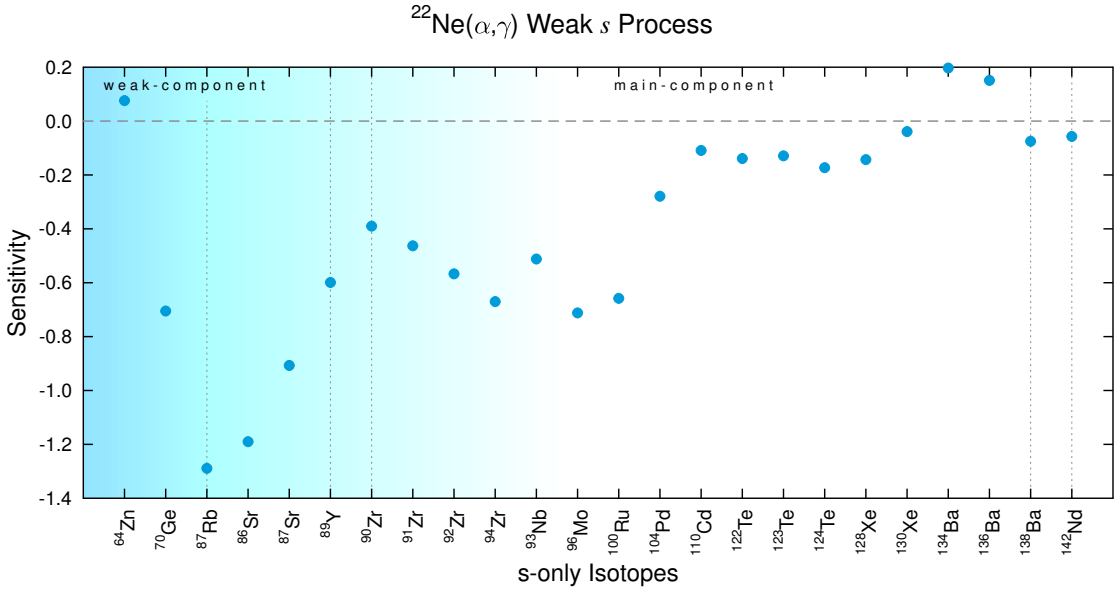

Figure A.65: Neutron poison reaction ^{22}Ne(α,γ) during the weak s process (table 3.14). The ^{22}Ne(α,γ) competes with the ^{22}Ne(α,n) reaction.

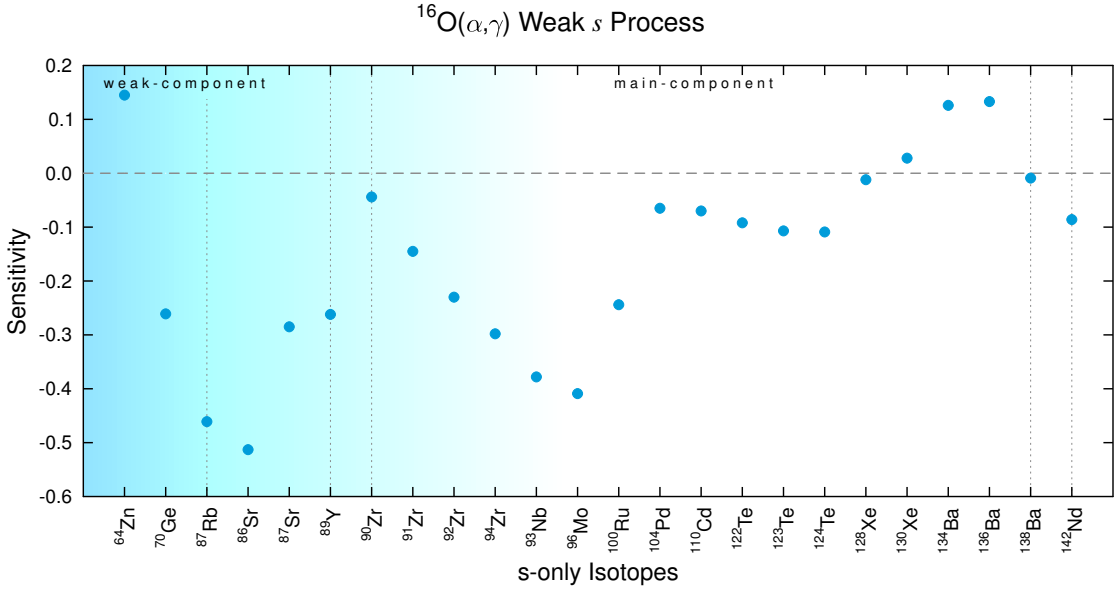

Figure A.66: Neutron poison reaction ^{16}O(α,γ) during the weak s process (table 3.14).

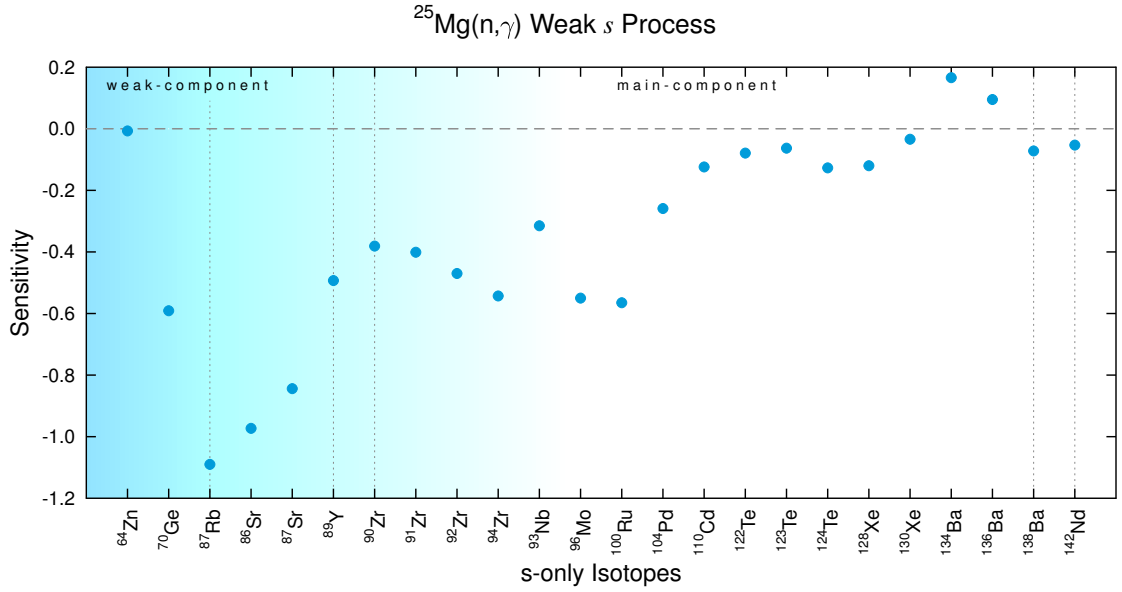

Figure A.67: Neutron poison reaction $^{25}\mathrm{Mg}(n,\gamma)$ during the weak *s* process (table 3.14).

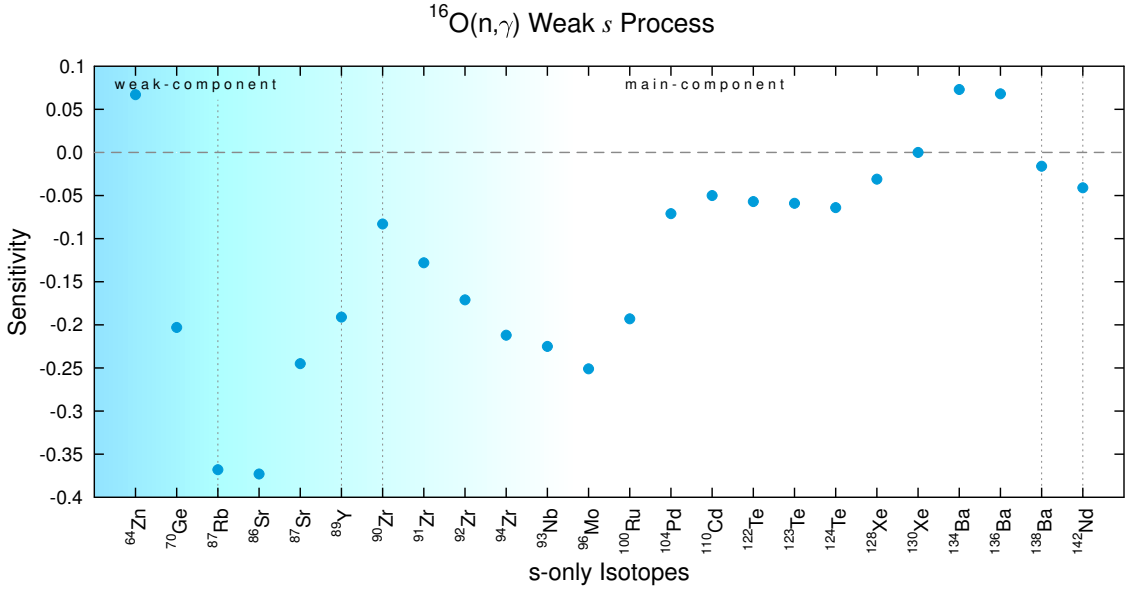

Figure A.68: Neutron poison reaction $^{16}\mathrm{O}(n,\gamma)$ during the weak *s* process (table 3.14).

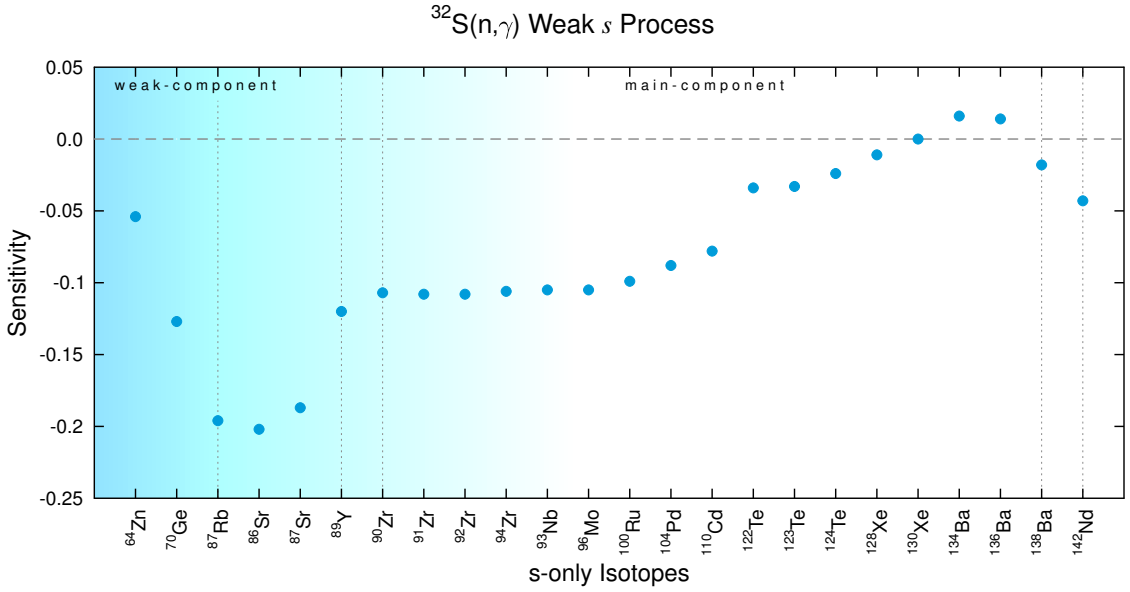

Figure A.69: Neutron poison reaction $^{32}\mathrm{S}(n,\gamma)$ during the weak *s* process (table 3.14).

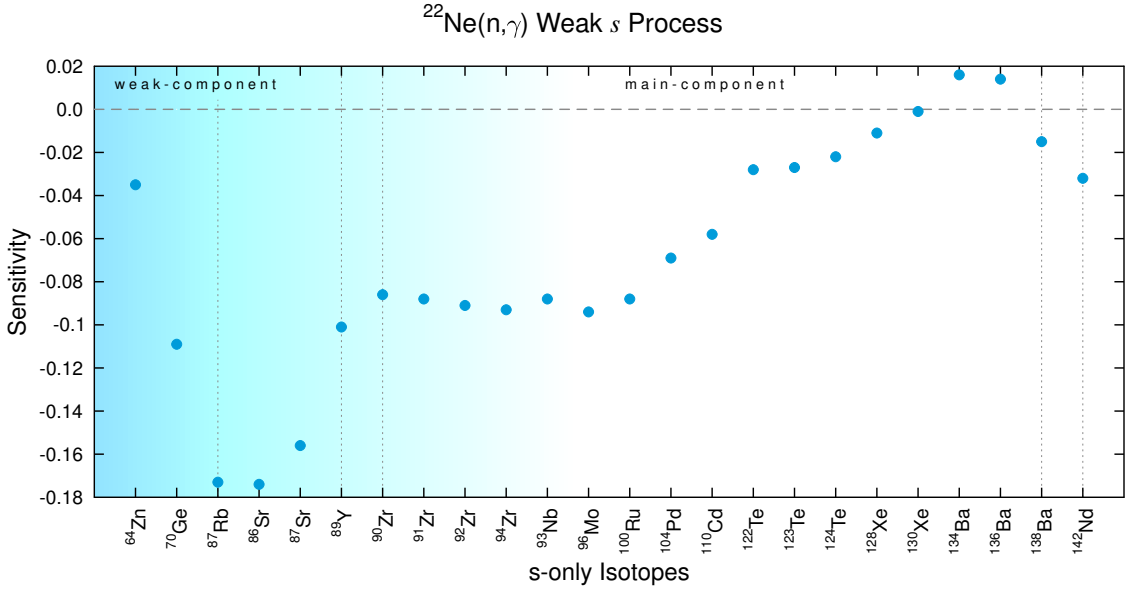

Figure A.70: Neutron poison reaction $^{22}\mathrm{Ne}(n,\gamma)$ during the weak *s* process (table 3.14).

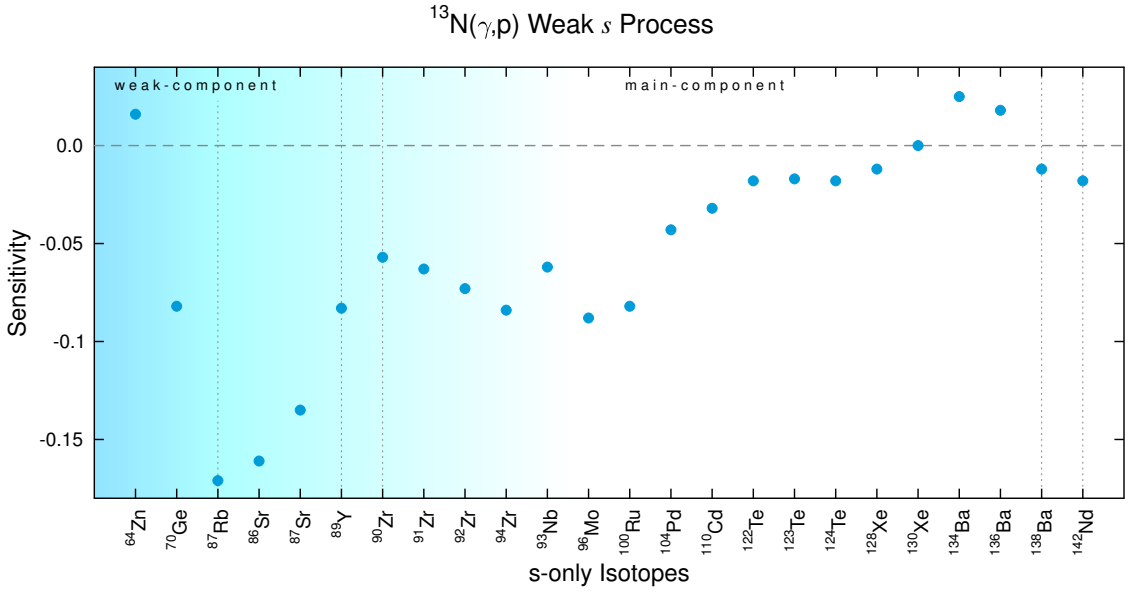

Figure A.71: Neutron poison reaction ^{13}N(γ,p) during the weak s process (table 3.14).

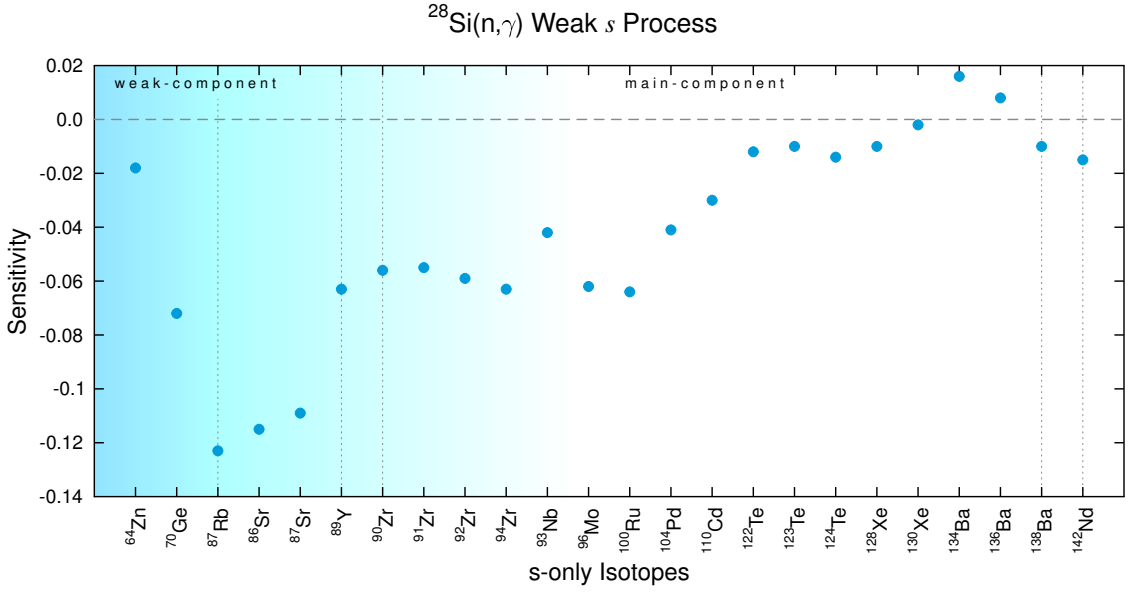

Figure A.72: Neutron poison reaction ^{28}Si(n,γ) during the weak s process (table 3.14).

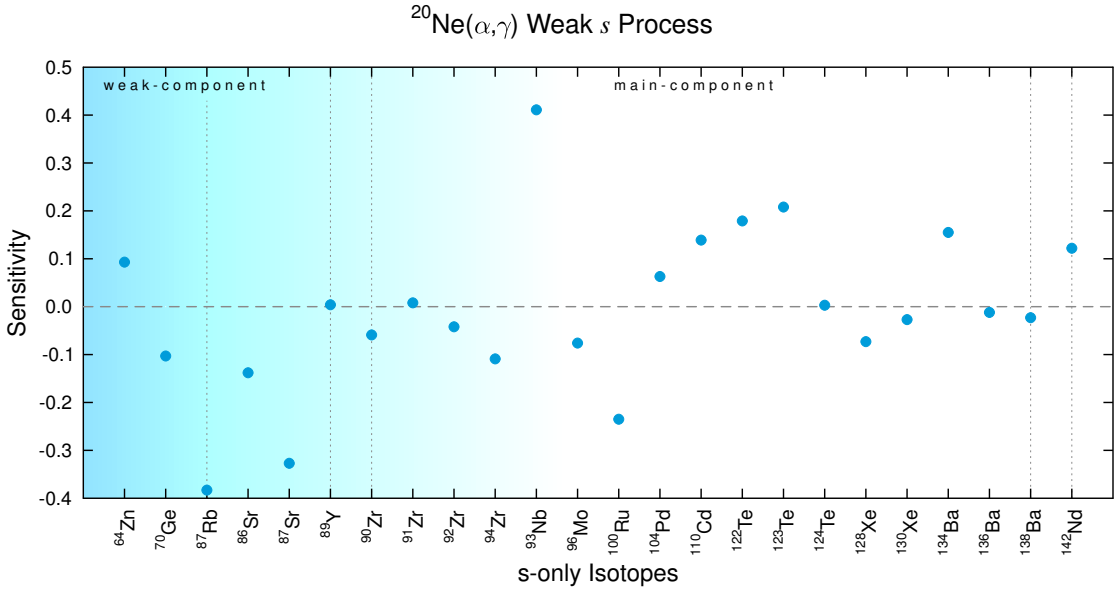

Figure A.73: Light neutron poison reaction ^{20}Ne(α, γ) during the weak s process (table 3.15).

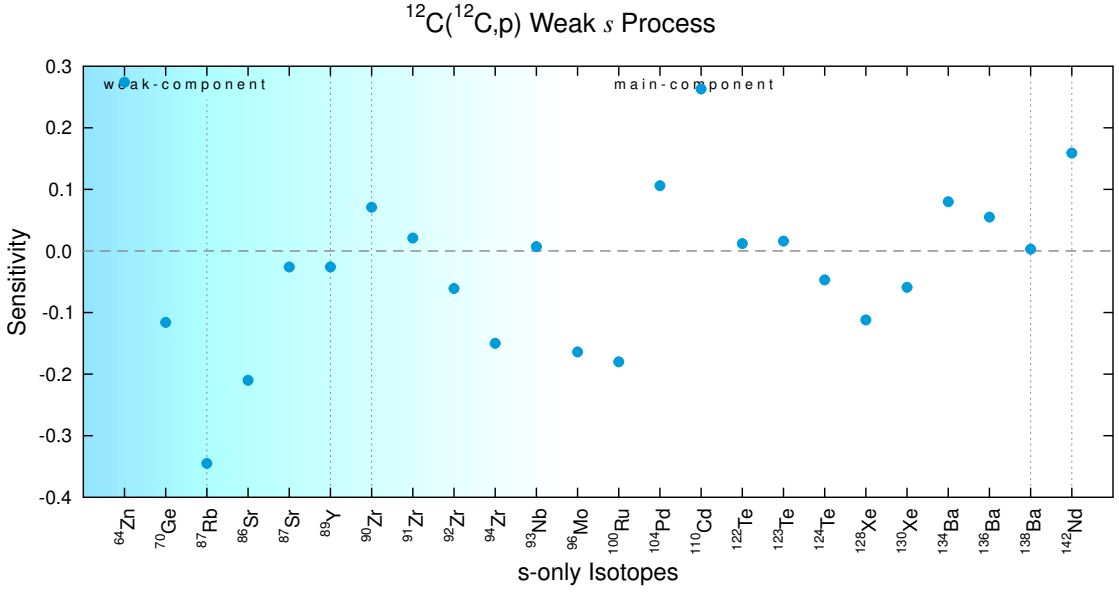

Figure A.74: Light neutron poison reaction ^{12}C(^{12}C, p) during the weak s process (table 3.15).

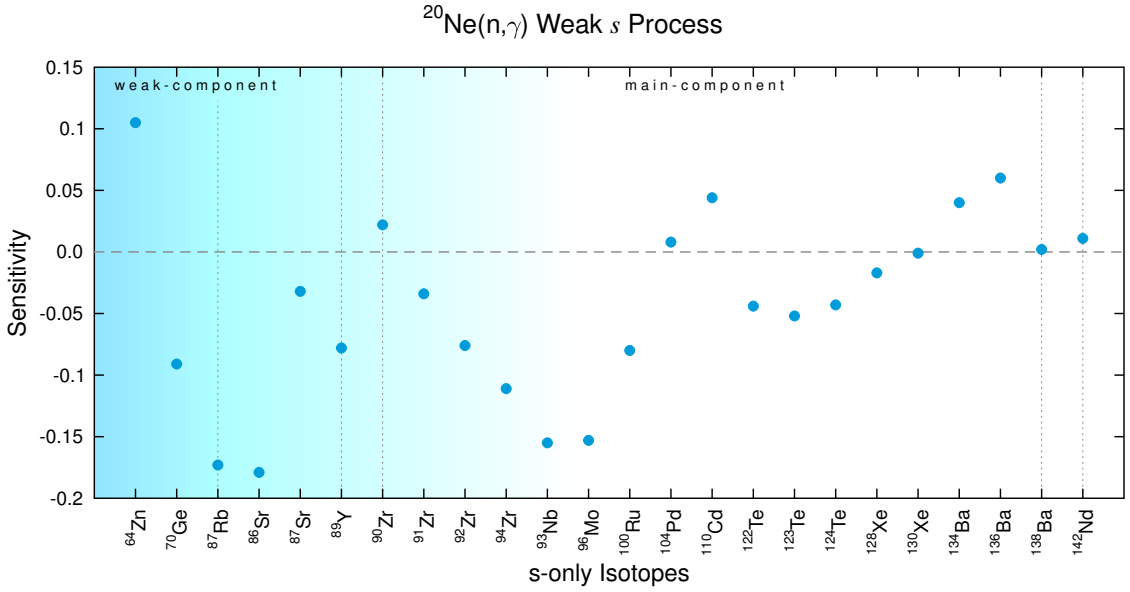

Figure A.75: Light neutron poison reaction ^{20}Ne(n,γ) during the weak s process (table 3.15).

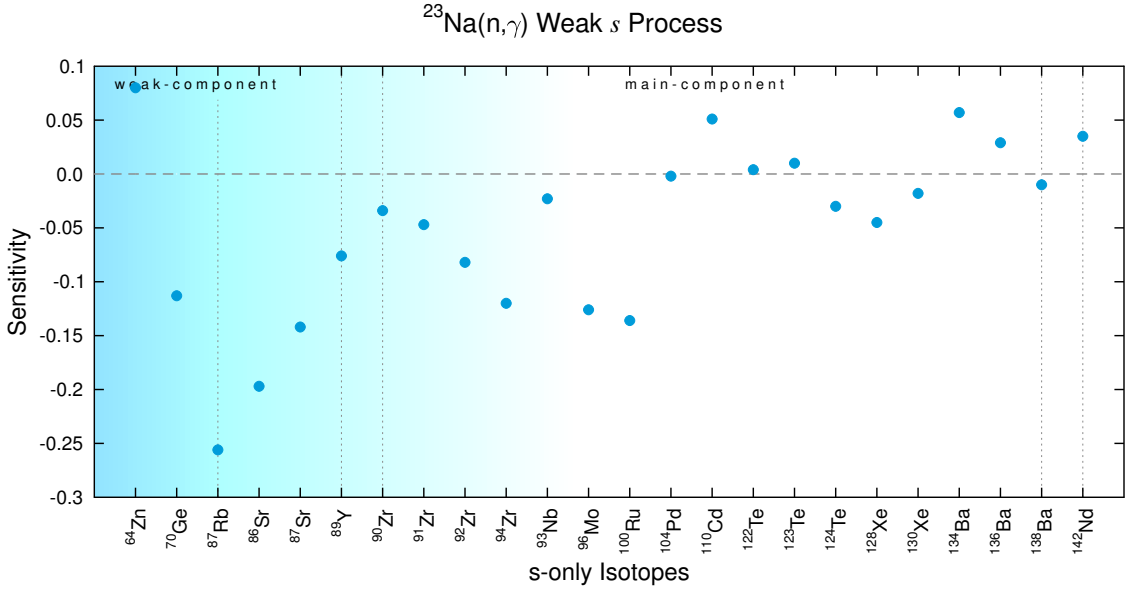

Figure A.76: Light neutron poison reaction ^{23}Na(n,γ) during the weak s process (table 3.15).

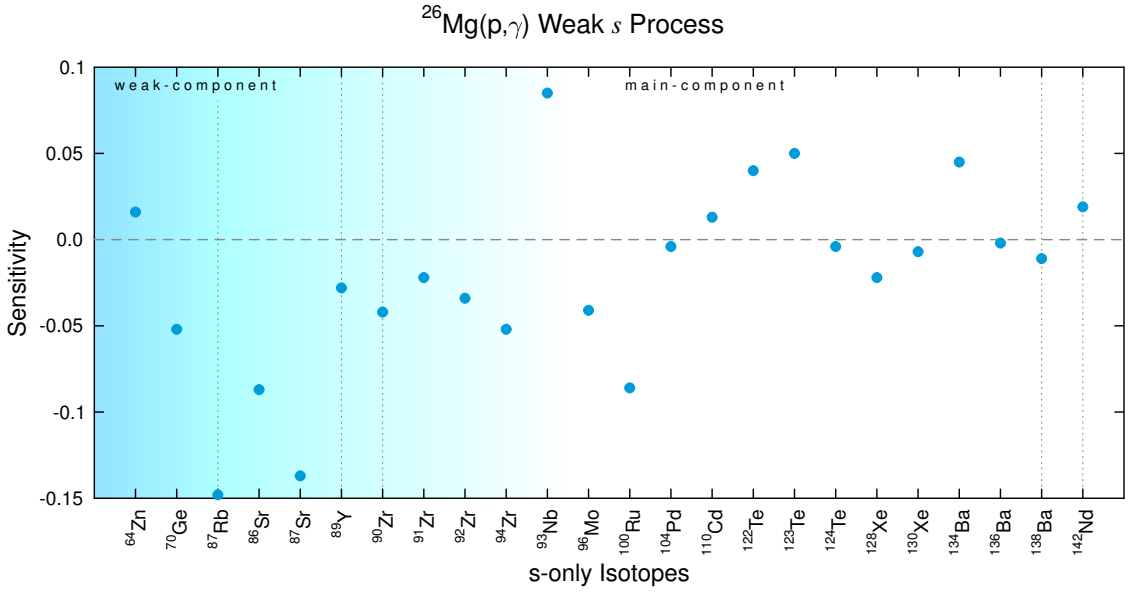

Figure A.77: Light neutron poison reaction ^{26}Mg(p,γ) during the weak s process (table 3.15).

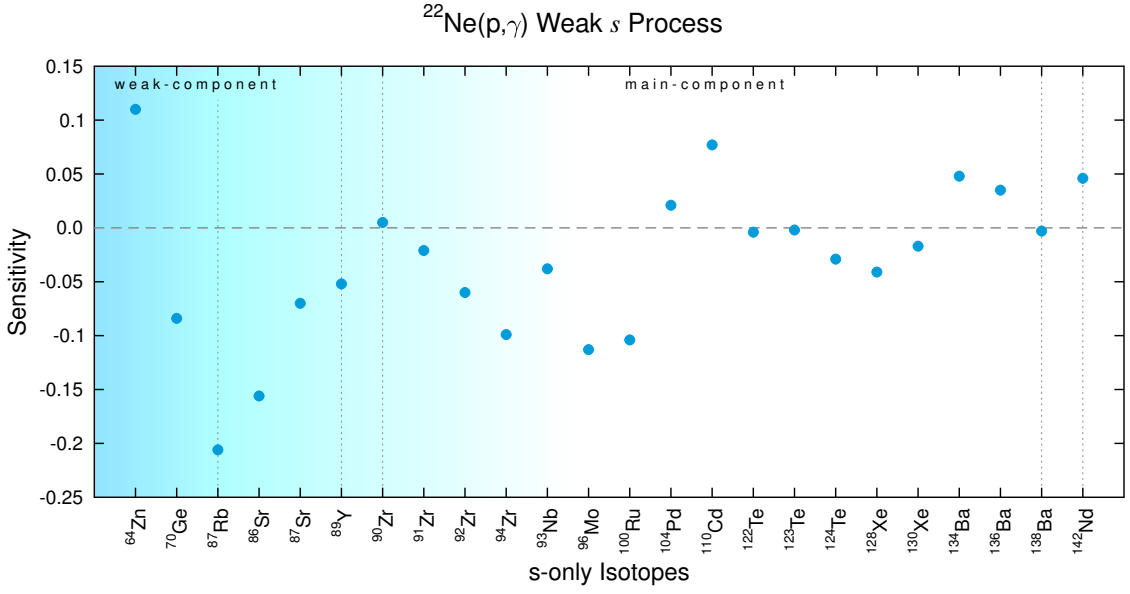

Figure A.78: Light neutron poison reaction ^{22}Ne(p,γ) during the weak s process (table 3.15).

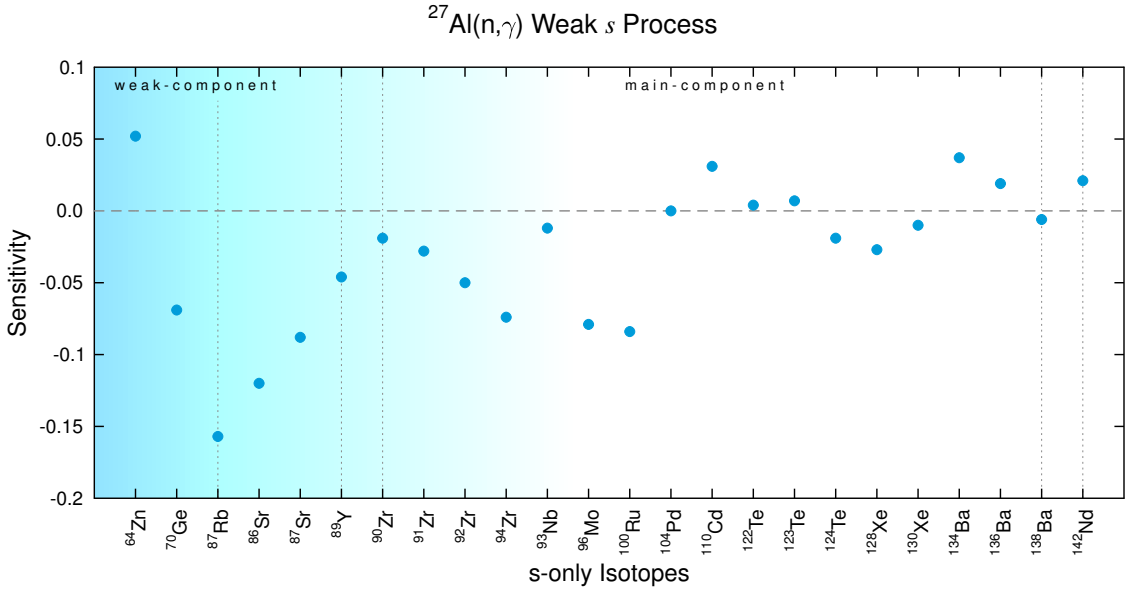

Figure A.79: Light neutron poison reaction ^{27}Al(n,γ) during the weak s process (table 3.15).

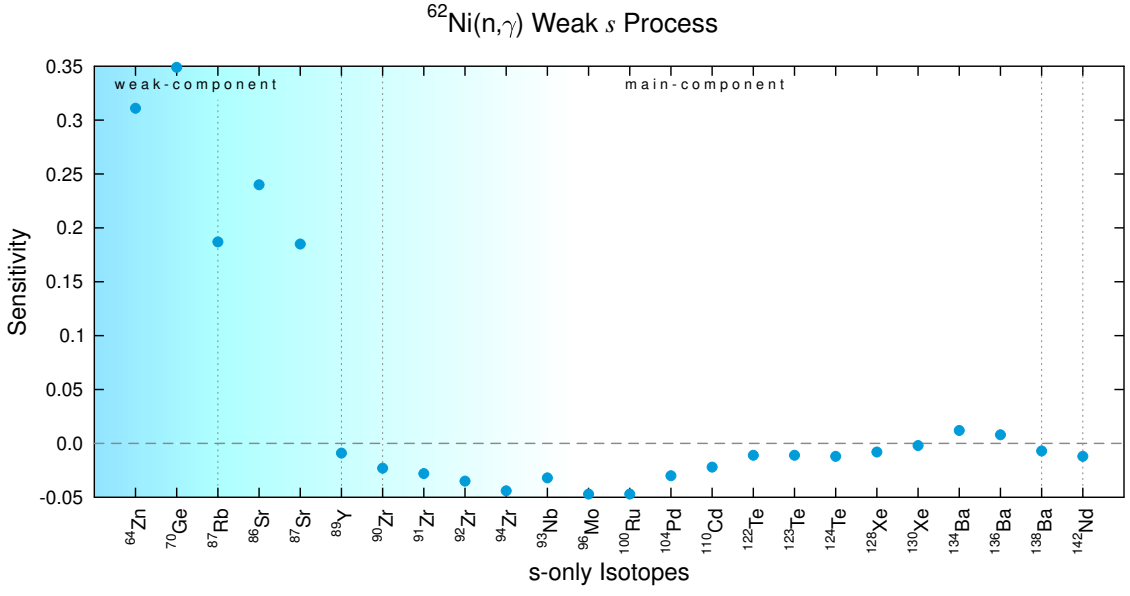

Figure A.80: Competing capture reaction ^{62}Ni(n,γ) during the weak s process (table 3.16).

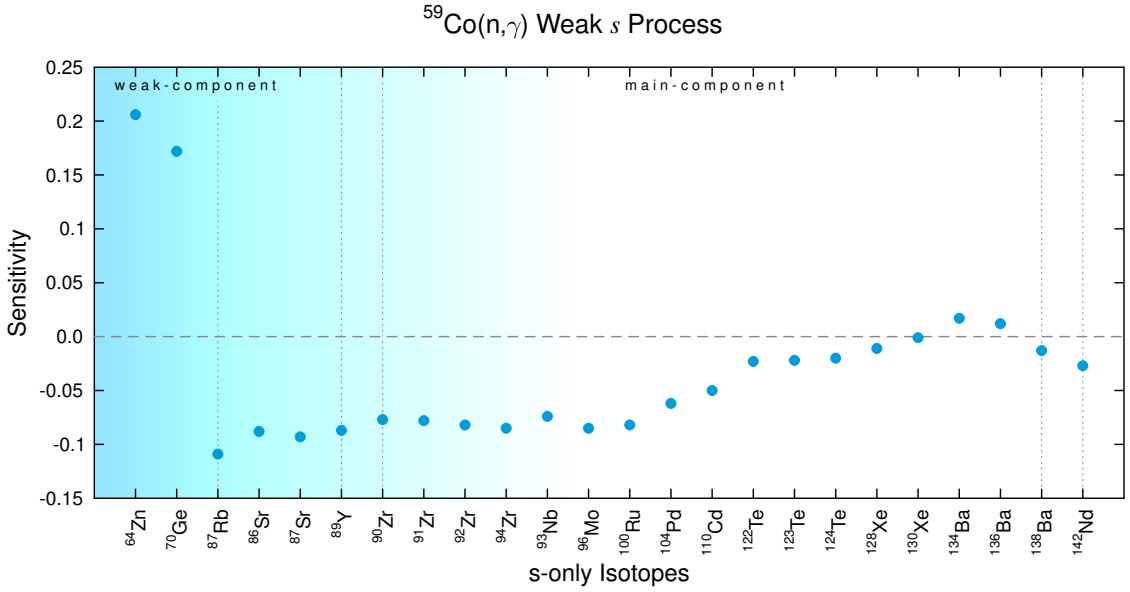

Figure A.81: Competing capture reaction ^{59}Co(n,γ) during the weak *s* process (table 3.16).

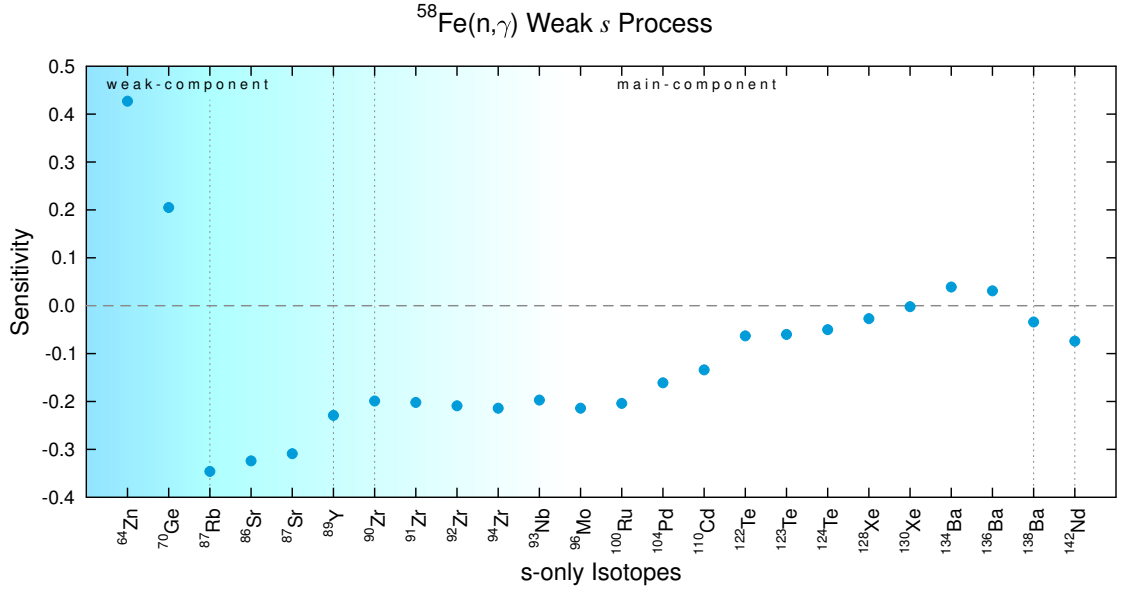

Figure A.82: Competing capture reaction ^{58}Fe(n,γ) during the weak *s* process (table 3.16).

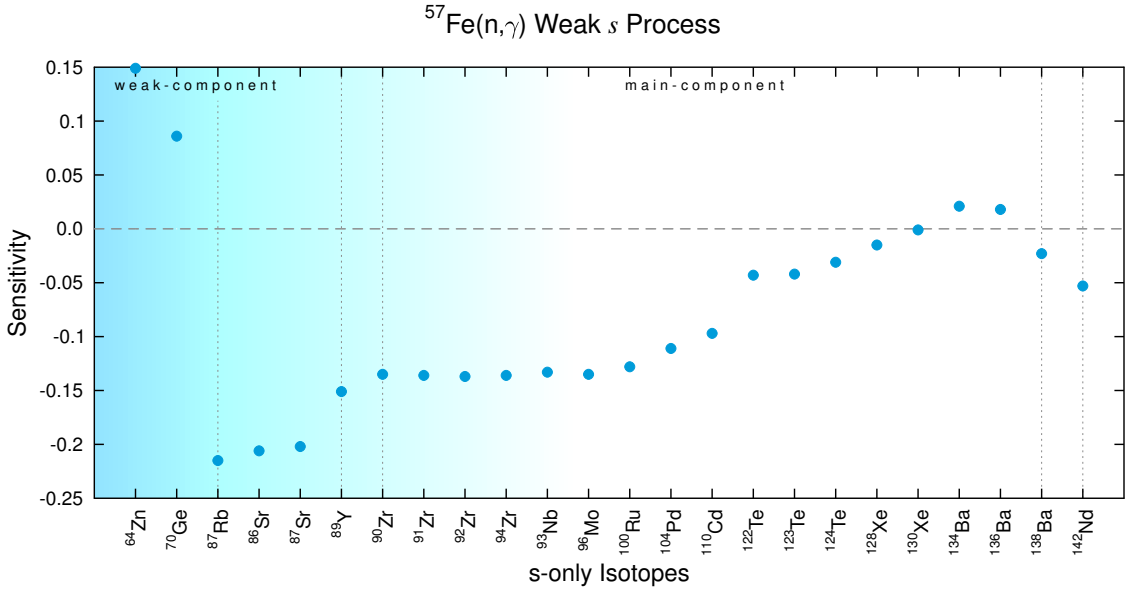

Figure A.83: Competing capture reaction ^{57}Fe(n,γ) during the weak *s* process (table 3.16).

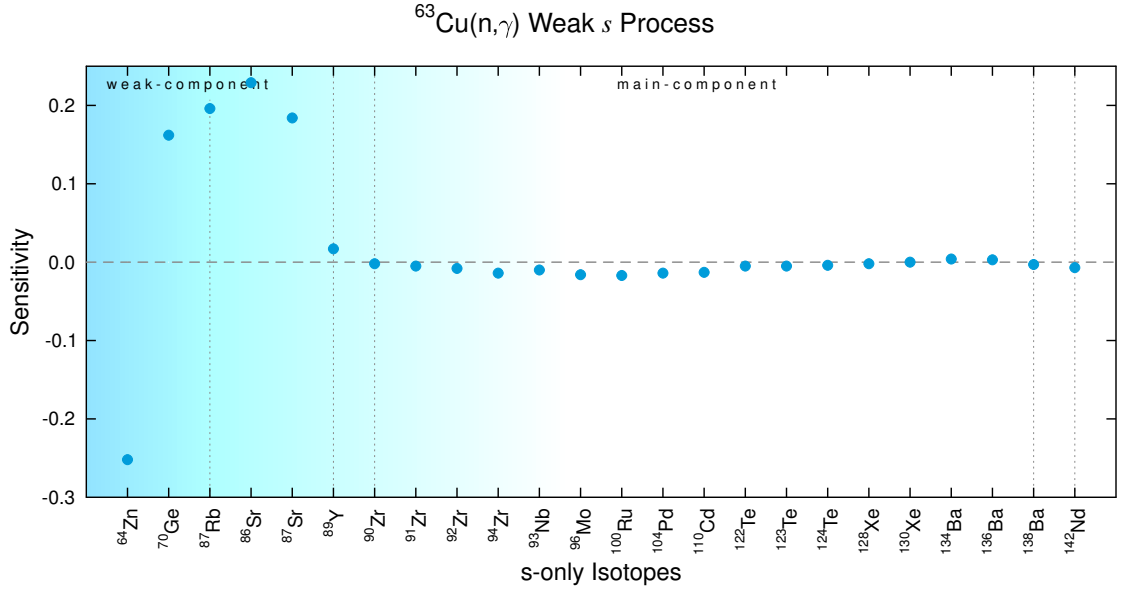

Figure A.84: Competing capture reaction ^{63}Cu(n,γ) during the weak *s* process (table 3.16).

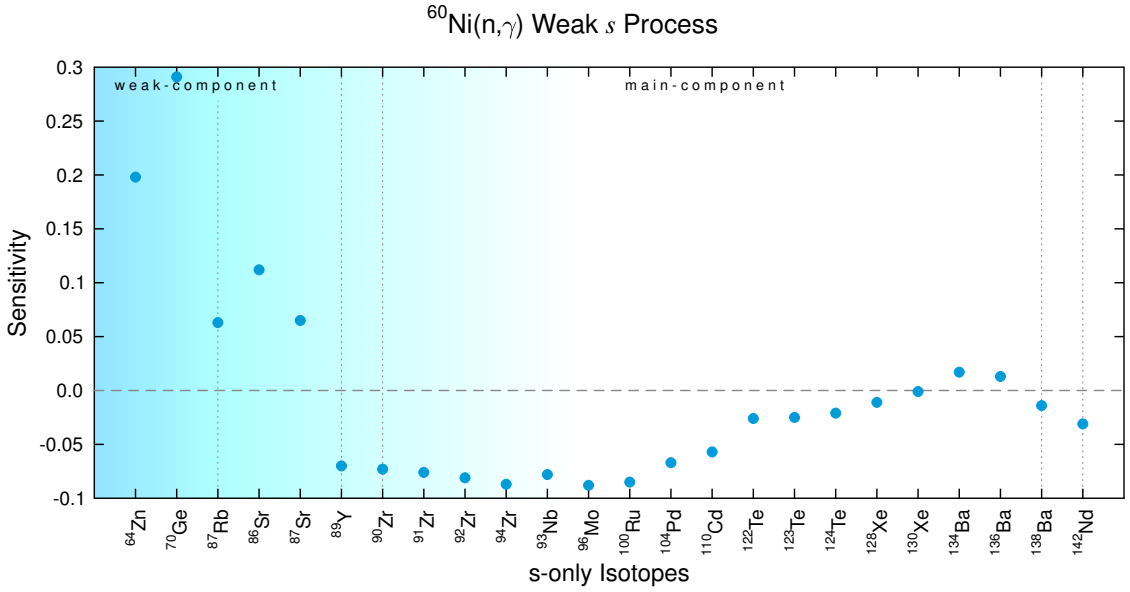

Figure A.85: Competing capture reaction ^{60}Ni(n,γ) during the weak *s* process (table 3.16).

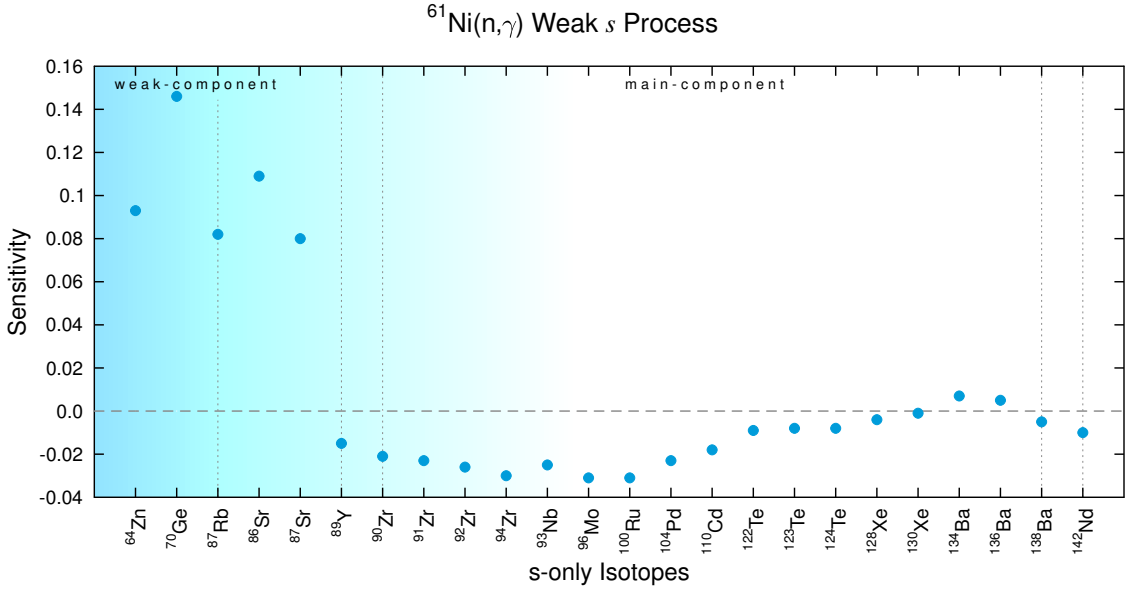

Figure A.86: Competing capture reaction ^{61}Ni(n,γ) during the weak *s* process (table 3.16).

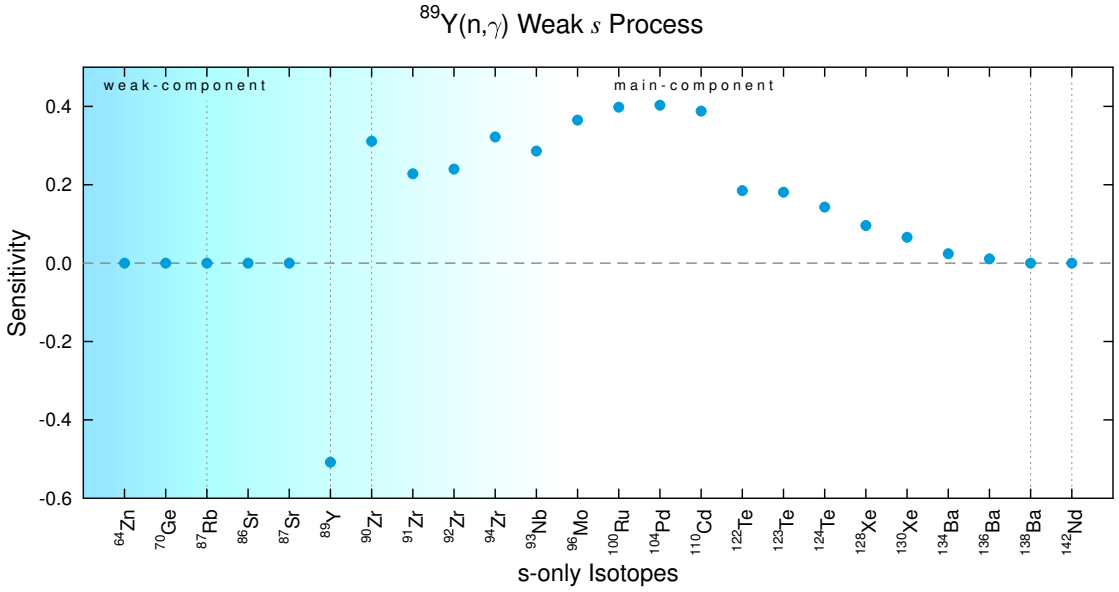

Figure A.87: Bottleneck reaction ^{89}Y(n,γ) during the weak *s* process (table 3.17).

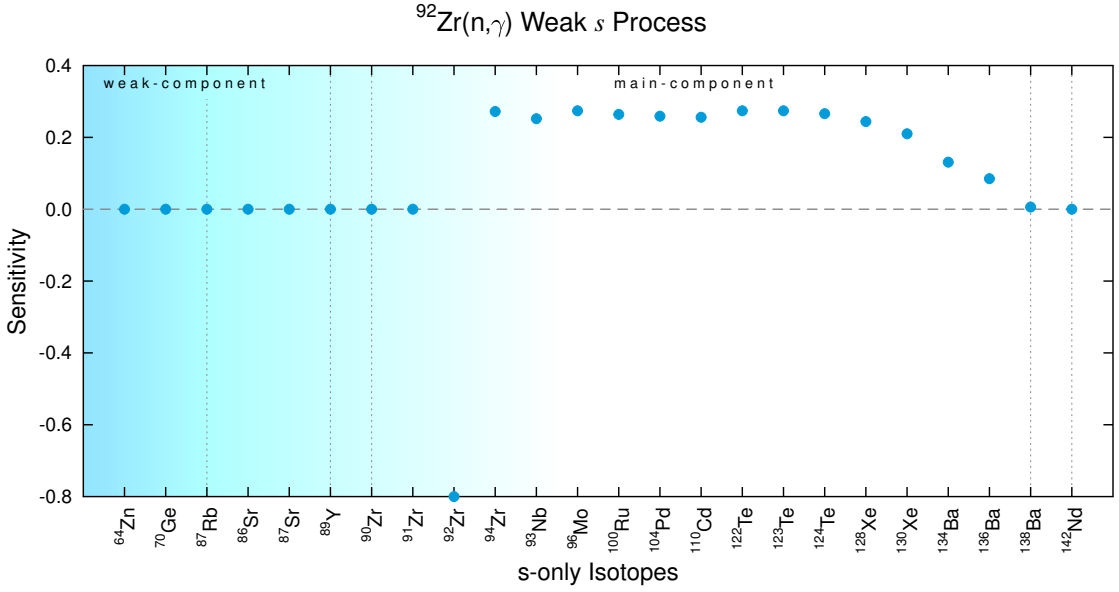

Figure A.88: Bottleneck reaction ^{92}Zr(n,γ) during the weak *s* process (table 3.17).

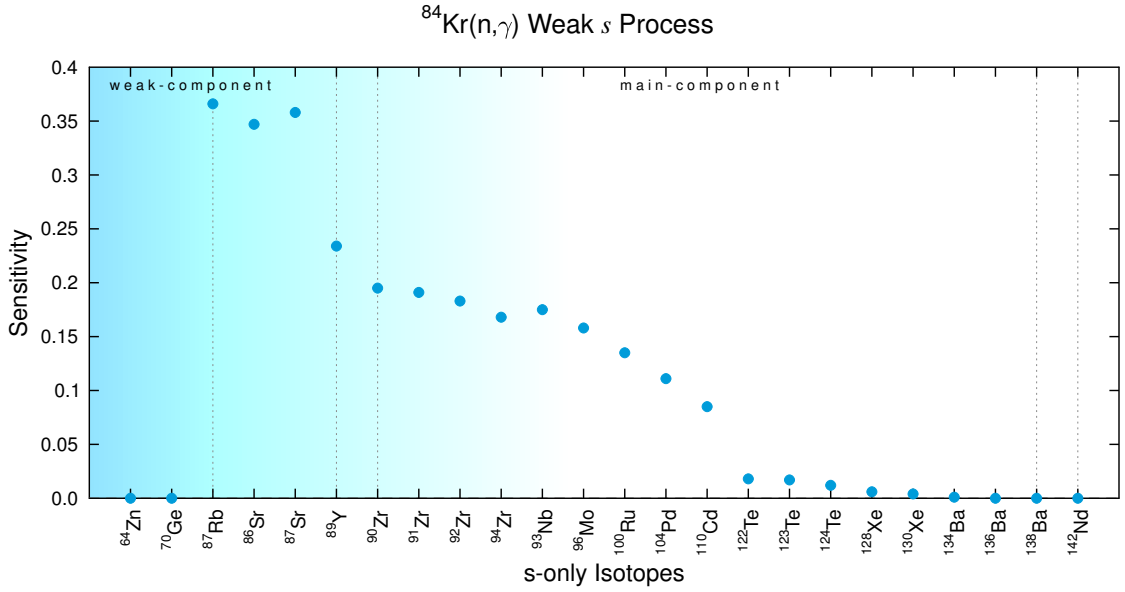

Figure A.89: Bottleneck reaction ^{84}Kr(n,γ) during the weak *s* process (table 3.17).

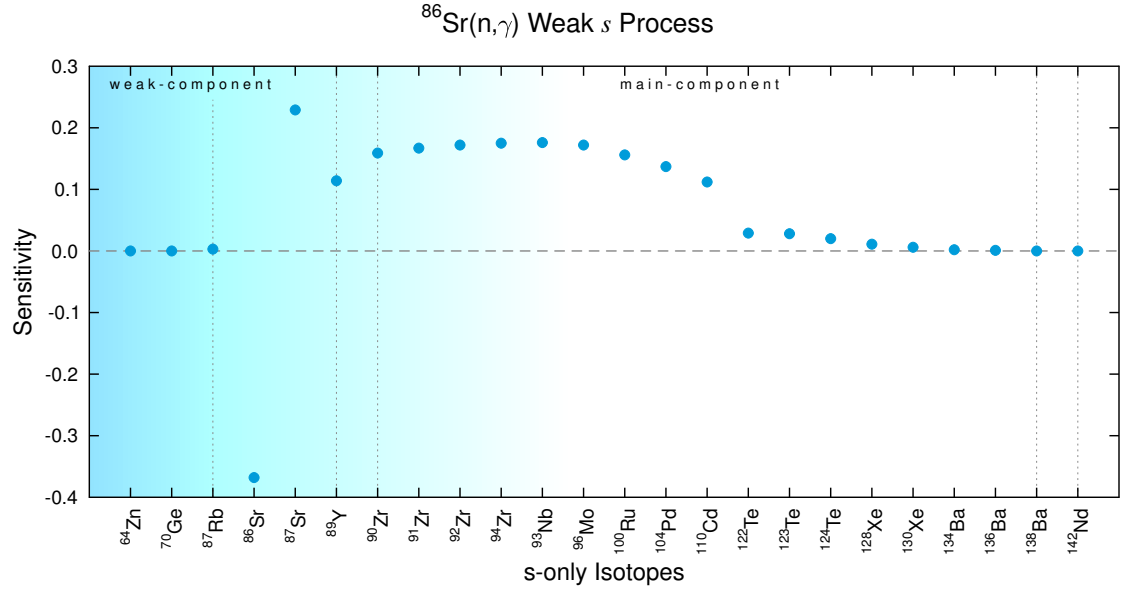

Figure A.90: Bottleneck reaction ^{86}Sr(n,γ) during the weak *s* process (table 3.17).

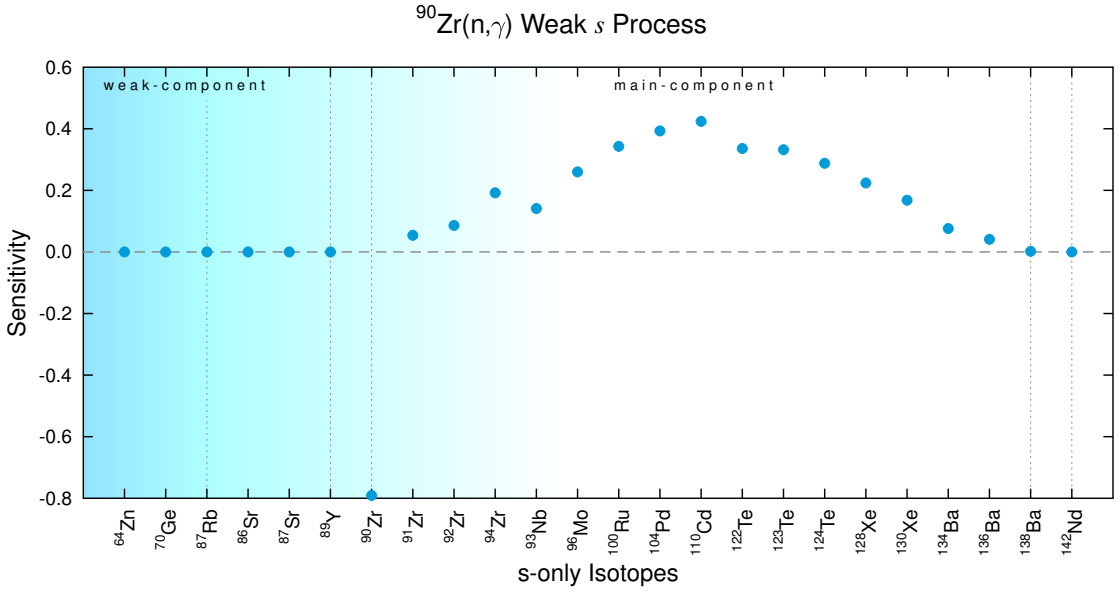

Figure A.91: Bottleneck reaction ^{90}Zr(n,γ) during the weak *s* process (table 3.17).

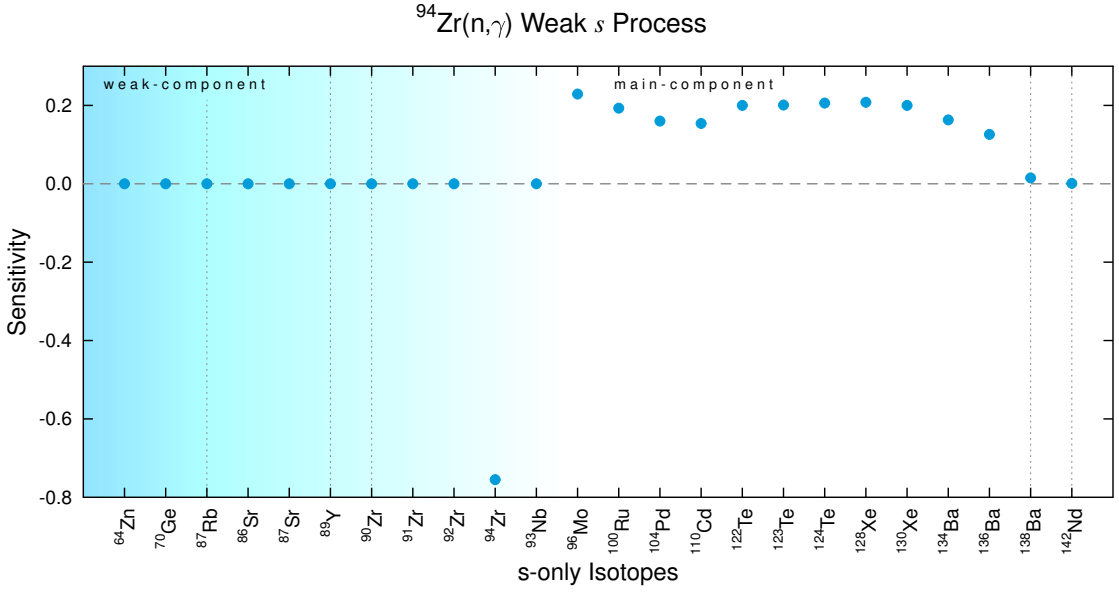

Figure A.92: Bottleneck reaction ^{94}Zr(n,γ) during the weak *s* process (table 3.17).

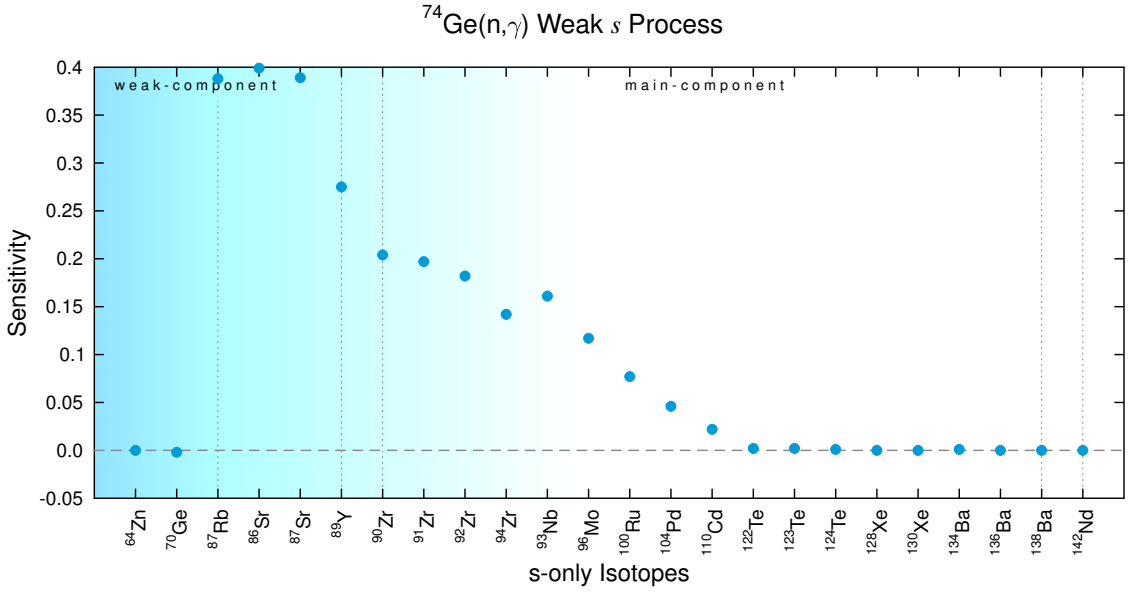

Figure A.93: Bottleneck reaction ^{74}Ge(n,γ) during the weak s process (table 3.17).

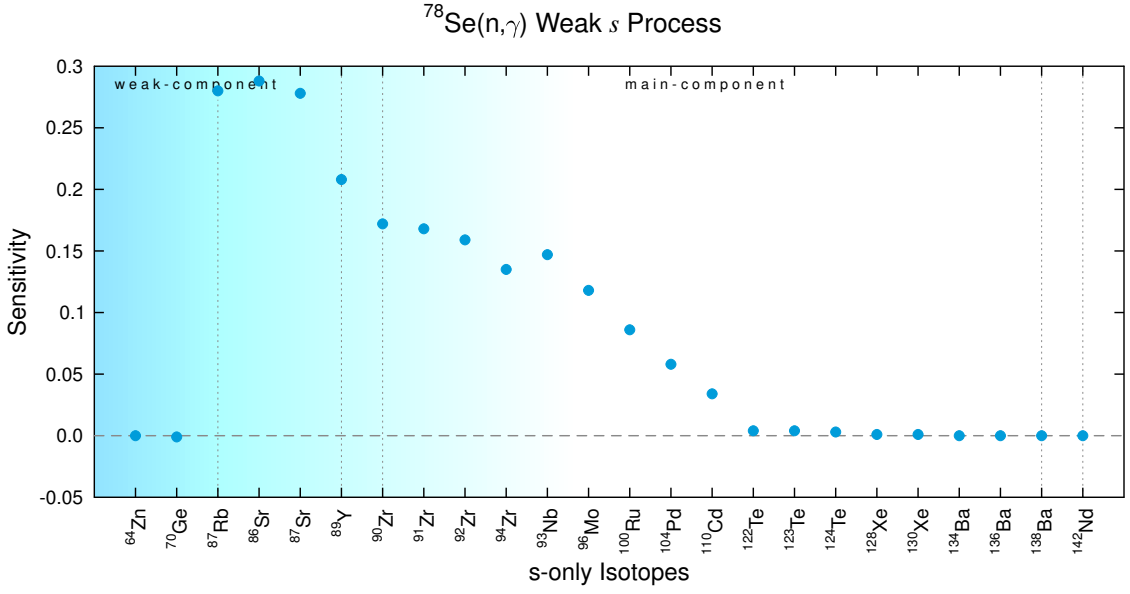

Figure A.94: Bottleneck reaction ^{78}Se(n,γ) during the weak s process (table 3.17).

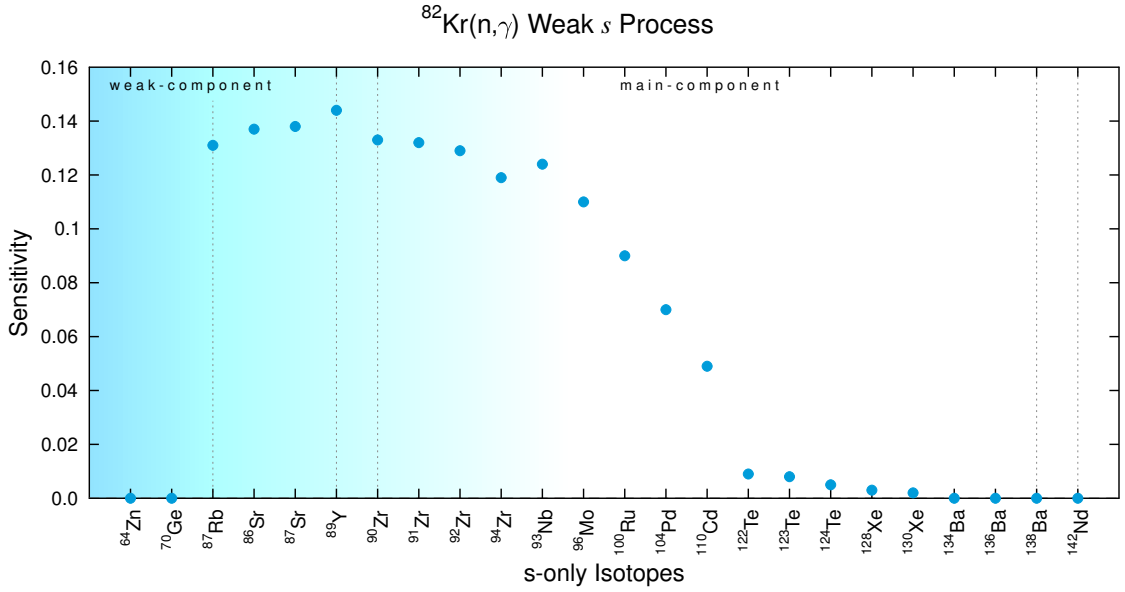

Figure A.95: Bottleneck reaction ^{82}Kr(n,γ) during the weak *s* process (table 3.17).

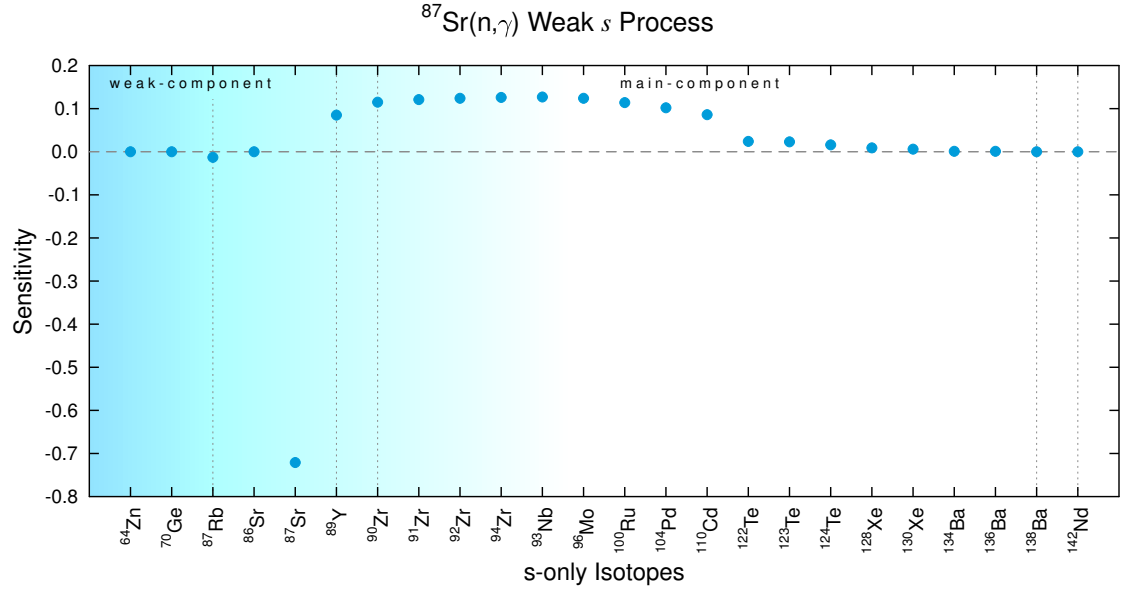

Figure A.96: Bottleneck reaction ^{87}Sr(n,γ) during the weak *s* process (table 3.17).

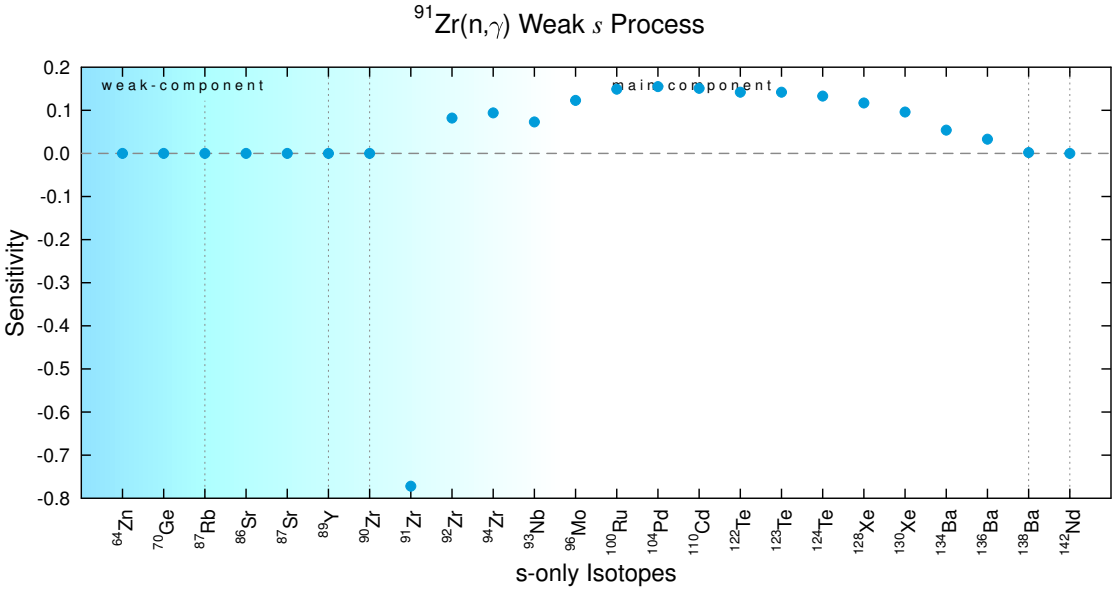

Figure A.97: Bottleneck reaction $^{91}\mathrm{Zr}(n,\gamma)$ during the weak *s* process (table 3.17).

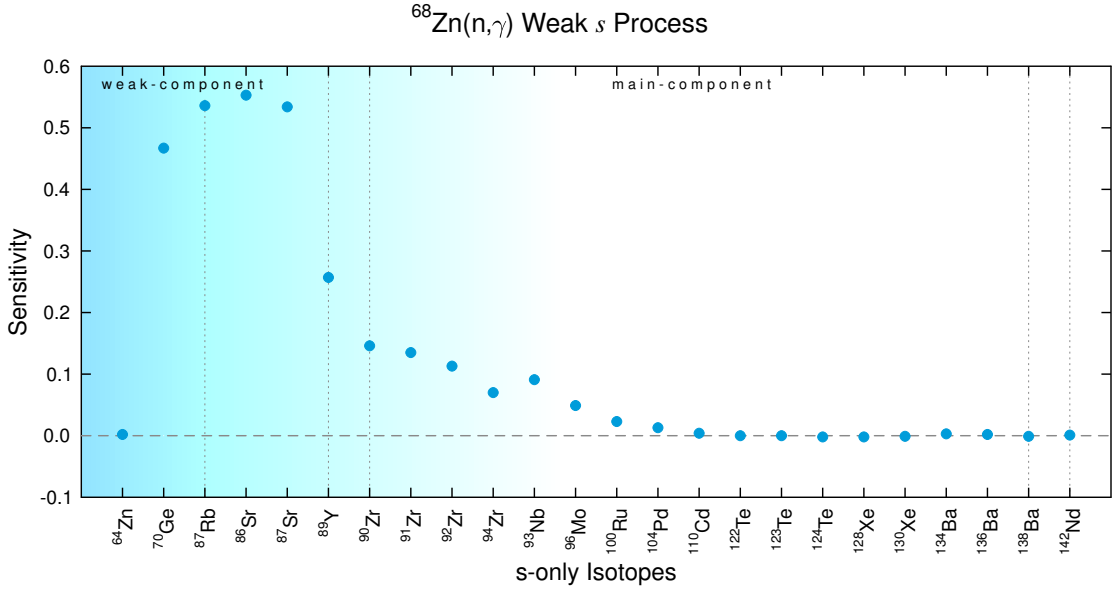

Figure A.98: Bottleneck reaction $^{68}\mathrm{Zn}(n,\gamma)$ during the weak *s* process (table 3.17).

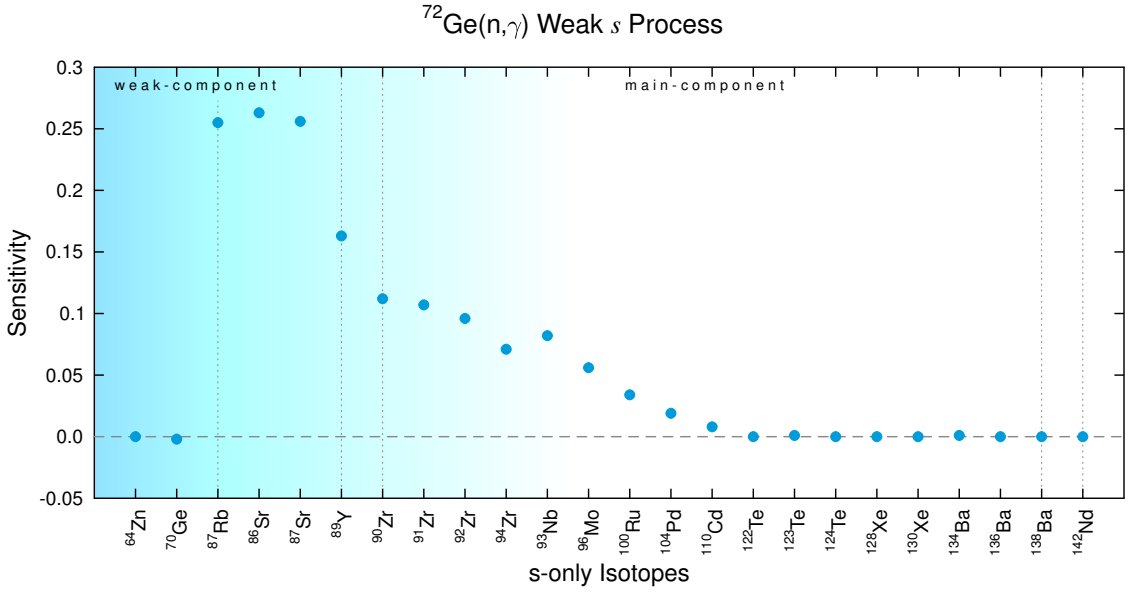

Figure A.99: Bottleneck reaction ^{72}Ge(n,γ) during the weak s process (table 3.17).

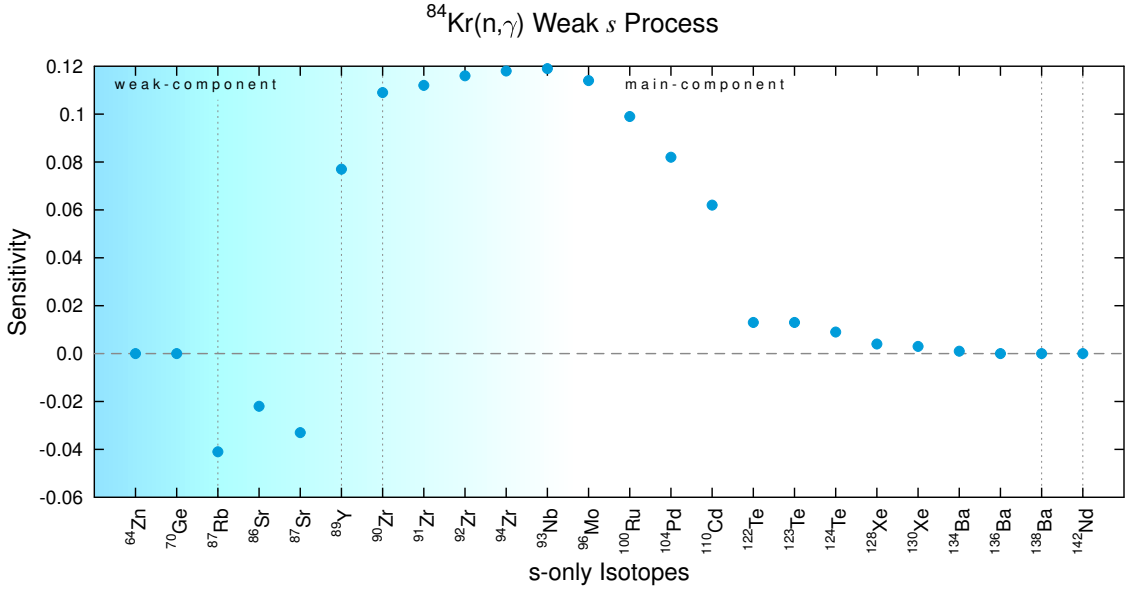

Figure A.100: Bottleneck reaction ^{84}Kr(n,γ) during the weak s process (table 3.17).

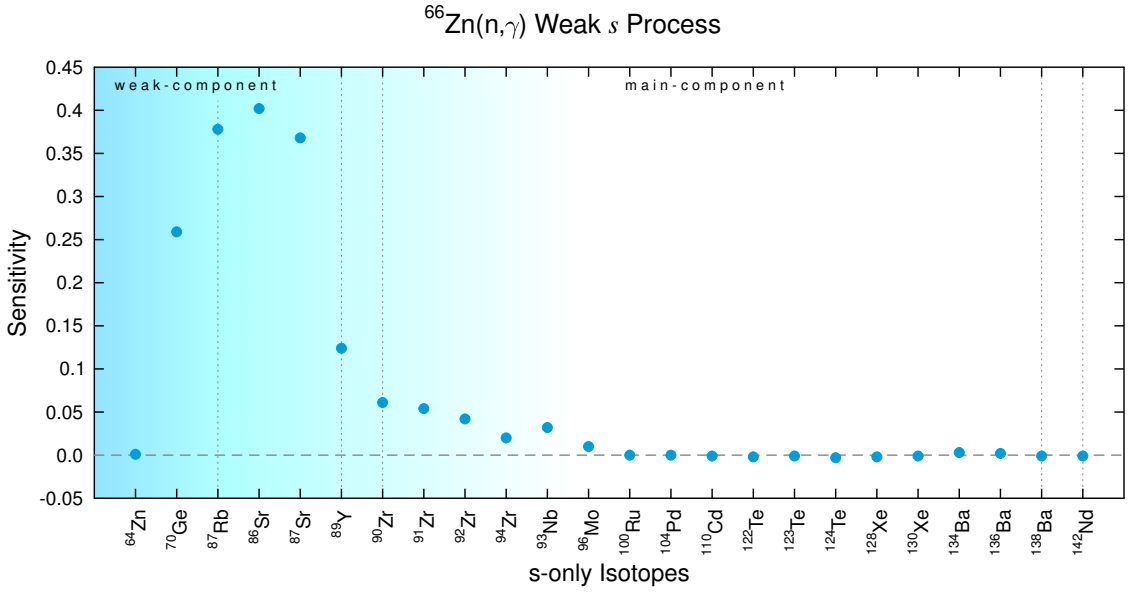

Figure A.101: Bottleneck reaction ^{66}Zn(n,γ) during the weak *s* process (table 3.17).

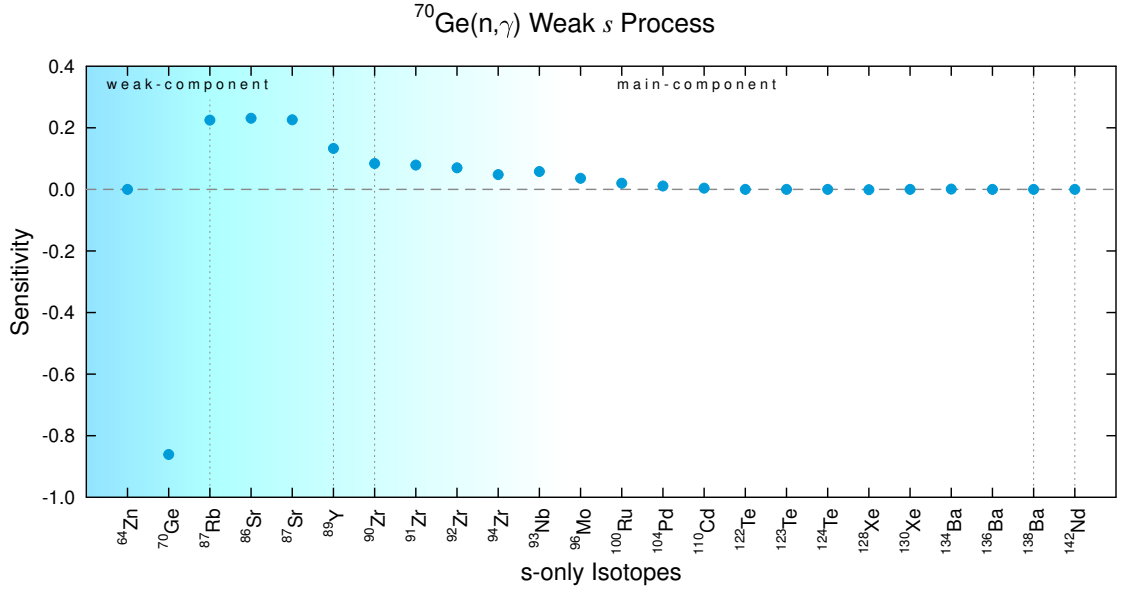

Figure A.102: Bottleneck reaction ^{70}Ge(n,γ) during the weak *s* process (table 3.17).

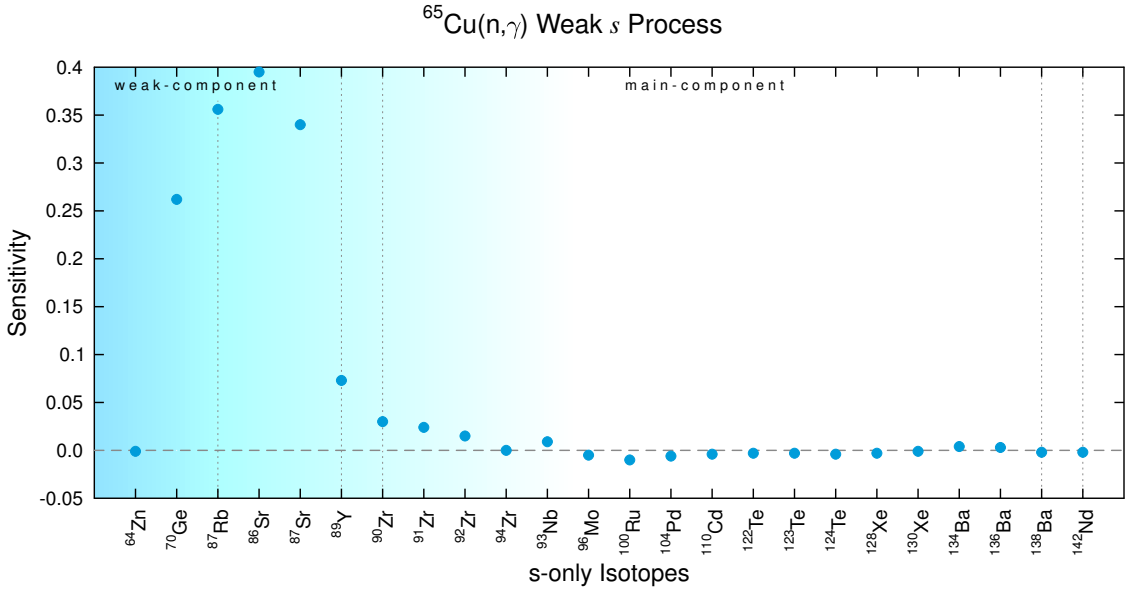

Figure A.103: Bottleneck reaction ^{65}Cu(n,γ) during the weak s process (table 3.17).

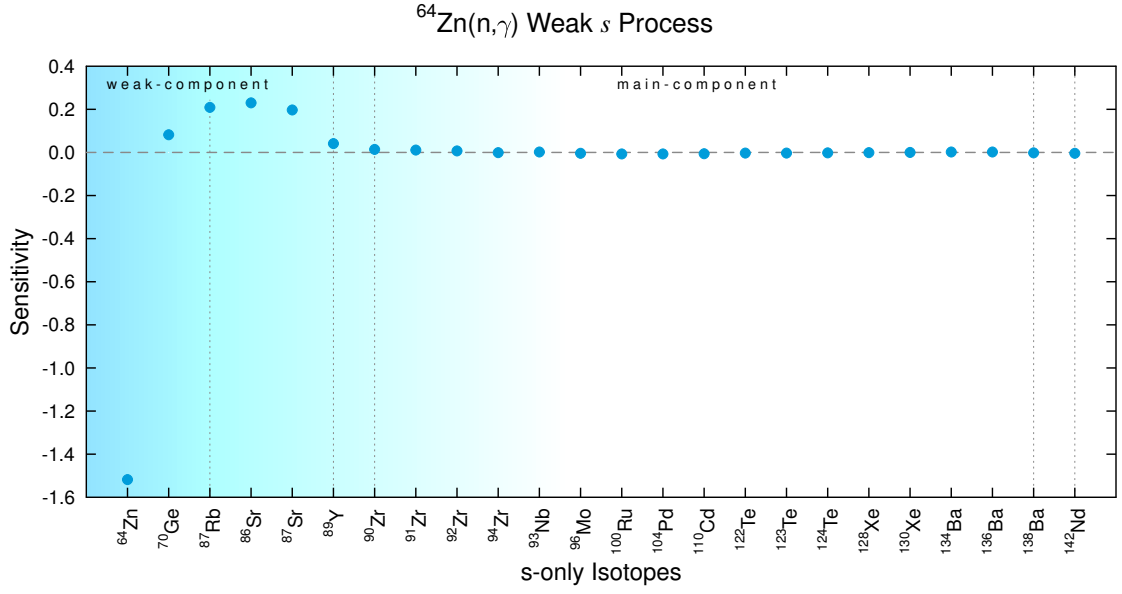

Figure A.104: Bottleneck reaction ^{64}Zn(n,γ) during the weak s process (table 3.17).

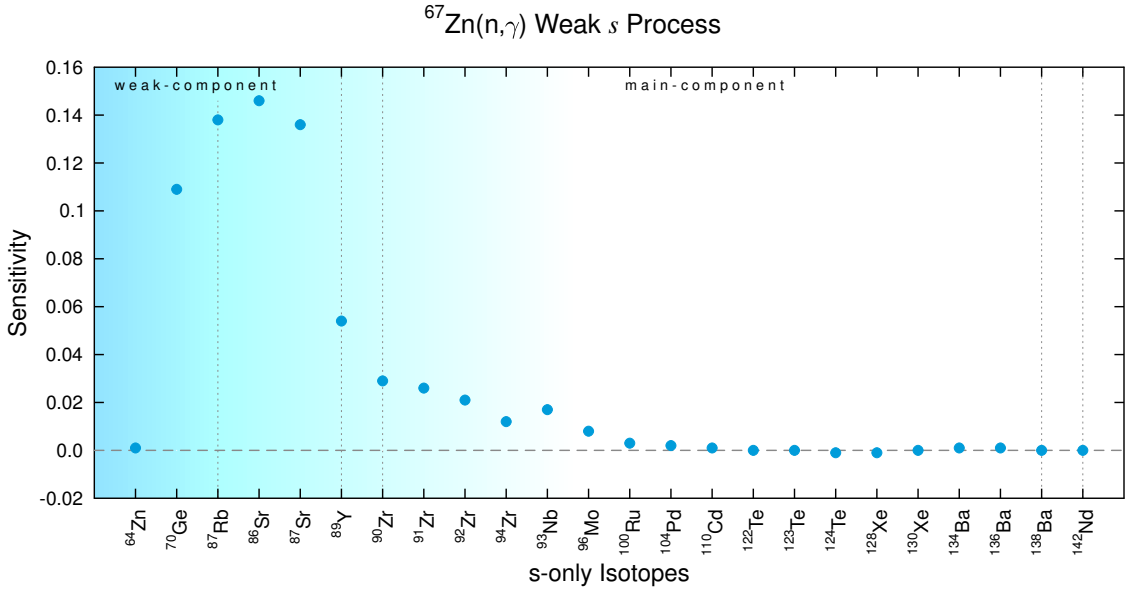

Figure A.105: Bottleneck reaction ^{67}Zn(n,γ) during the weak *s* process (table 3.17).

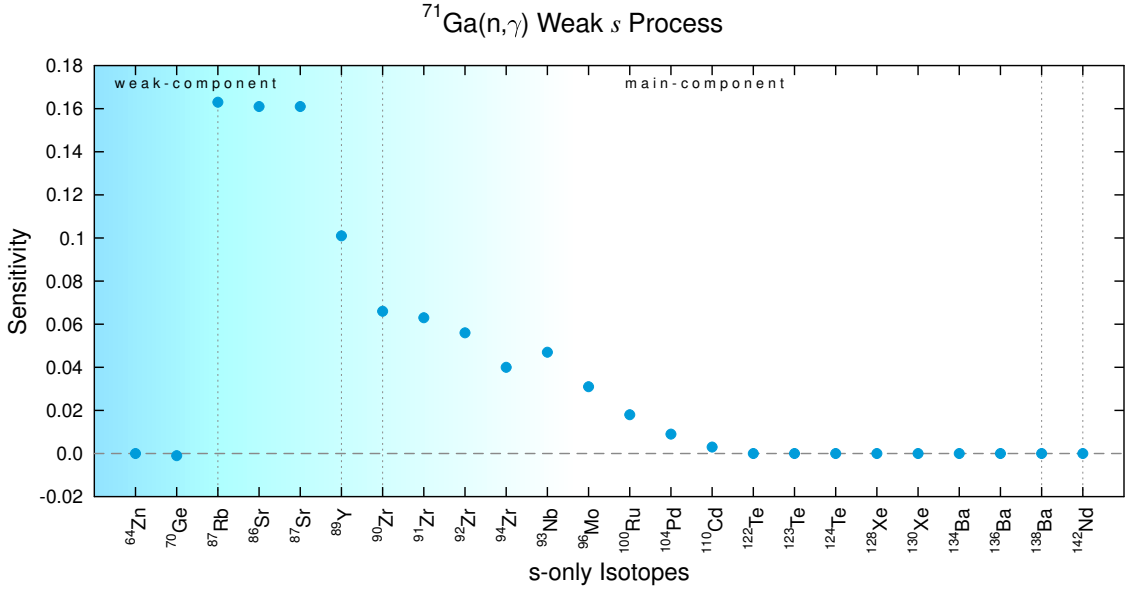

Figure A.106: Bottleneck reaction ^{71}Ga(n,γ) during the weak *s* process (table 3.17).

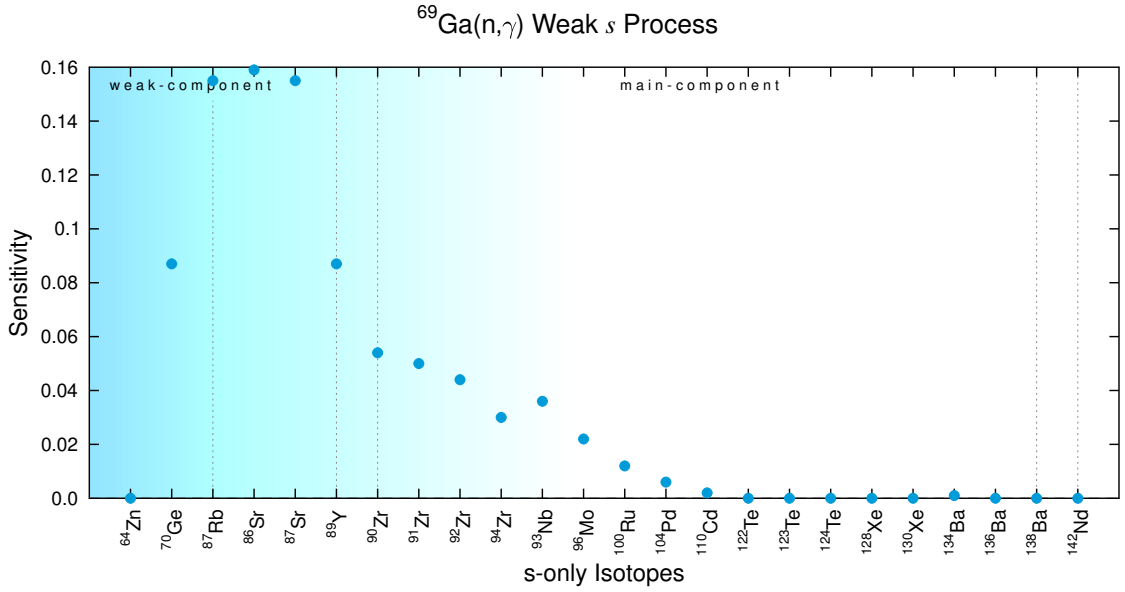

Figure A.107: Bottleneck reaction ^{69}Ga(n,γ) during the weak *s* process (table 3.17).

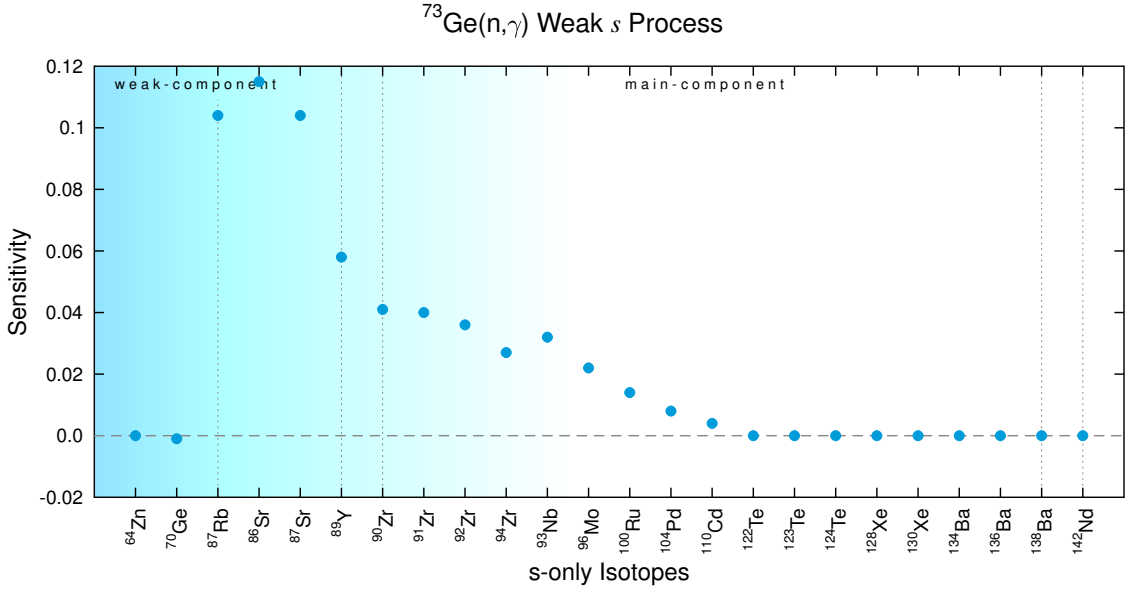

Figure A.108: Bottleneck reaction ^{73}Ge(n,γ) during the weak *s* process (table 3.17).

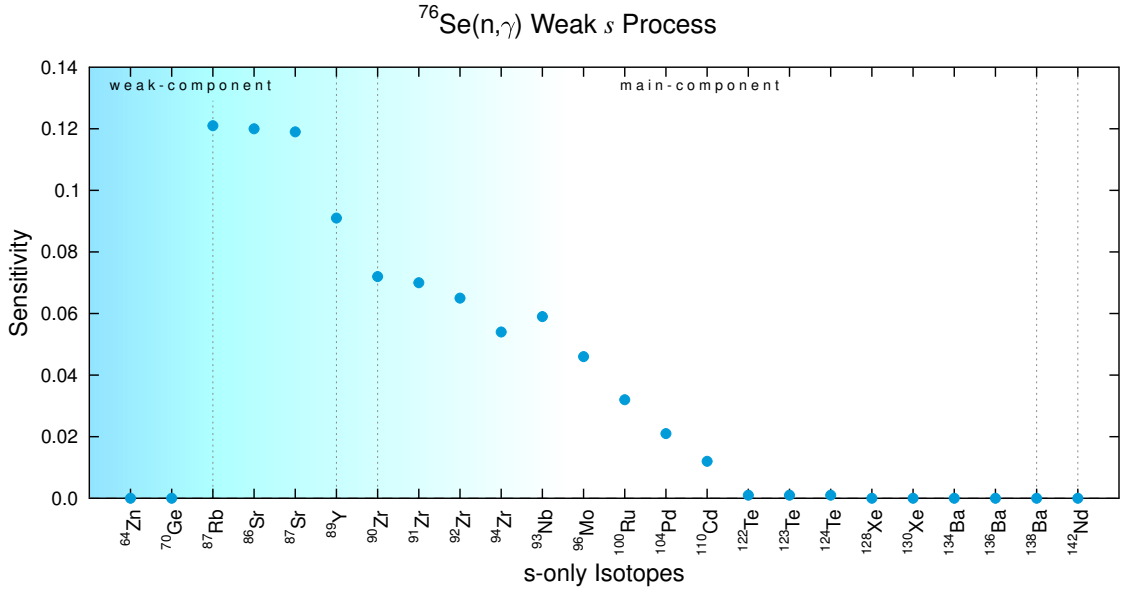

Figure A.109: Bottleneck reaction ^{76}Se(n,γ) during the weak s process (table 3.17).

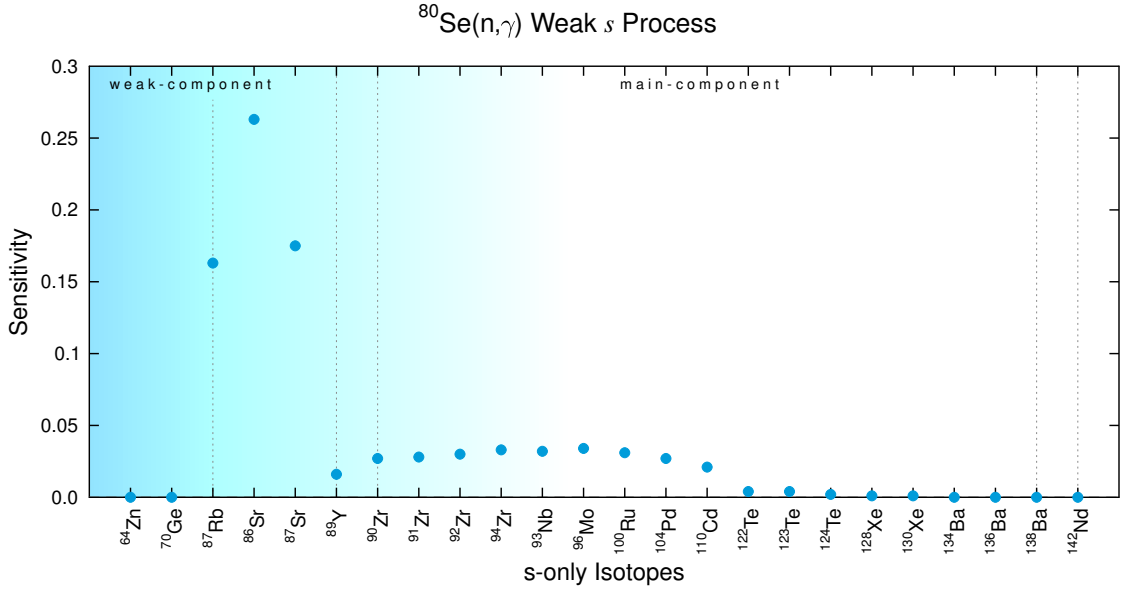

Figure A.110: Bottleneck reaction ^{80}Se(n,γ) during the weak s process (table 3.17).

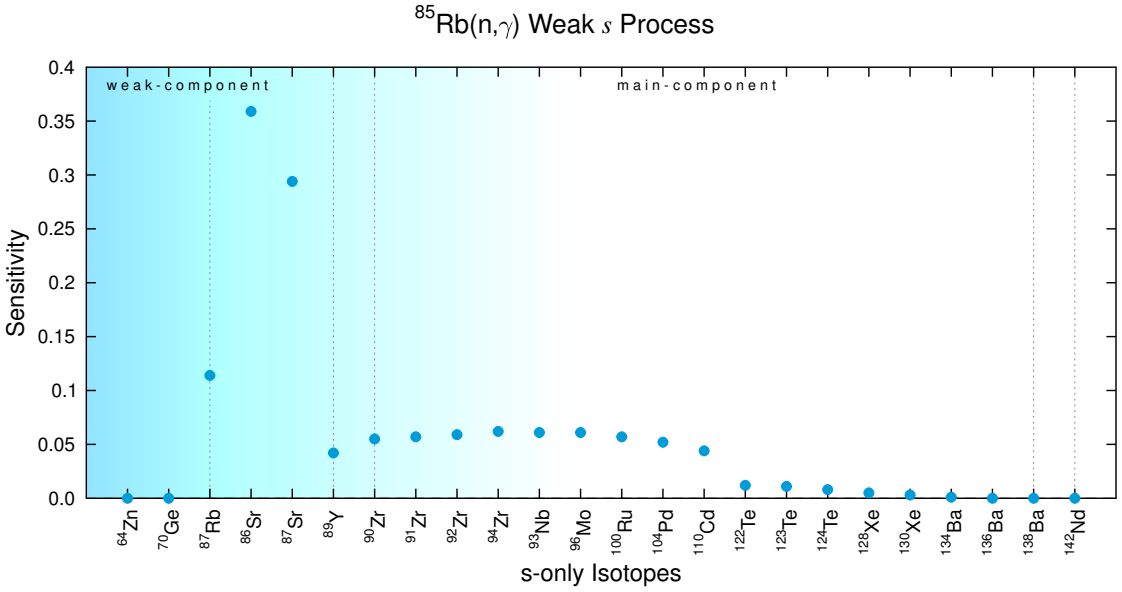

Figure A.111: Bottleneck reaction ^{85}Rb(n,γ) during the weak *s* process (table 3.17).

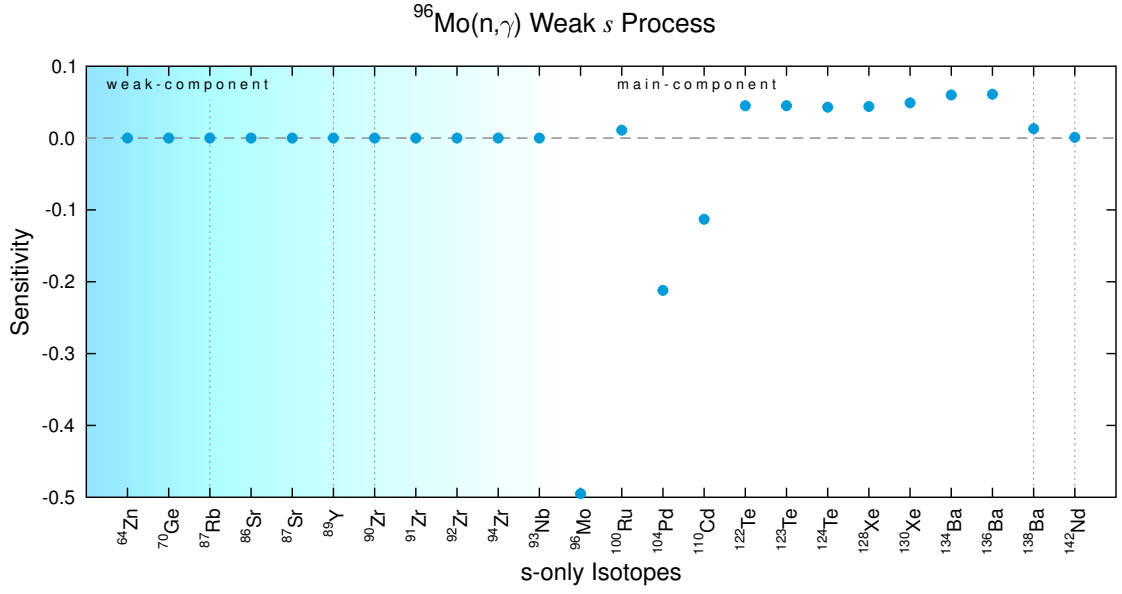

Figure A.112: Bottleneck reaction ^{96}Mo(n,γ) during the weak *s* process (table 3.17).

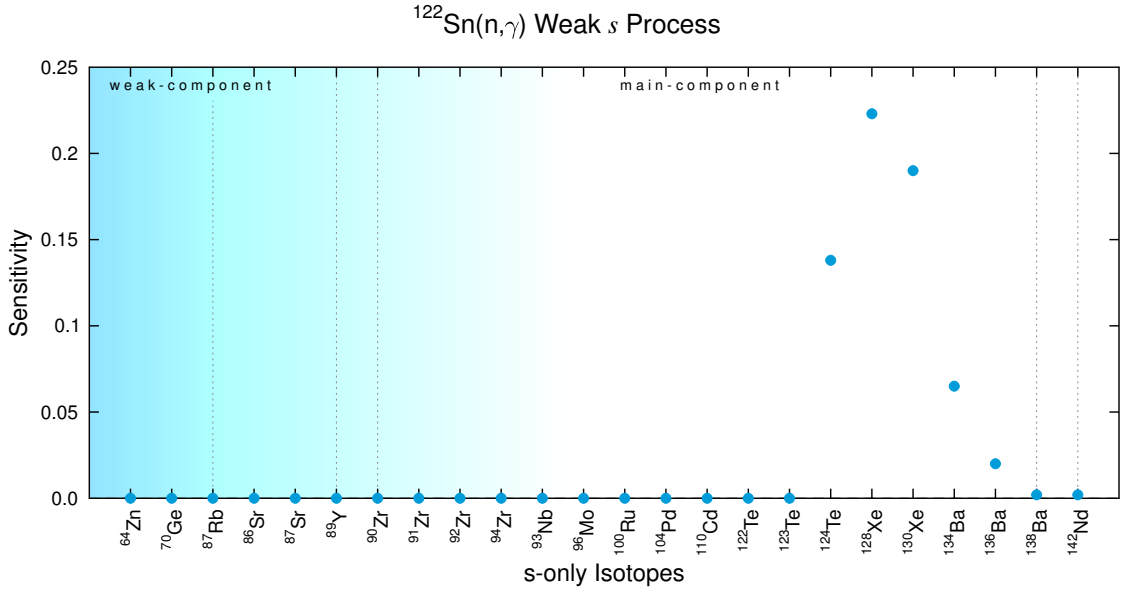

Figure A.113: Bottleneck reaction $^{122}\mathrm{Sn}(n,\gamma)$ during the weak *s* process (table 3.17).

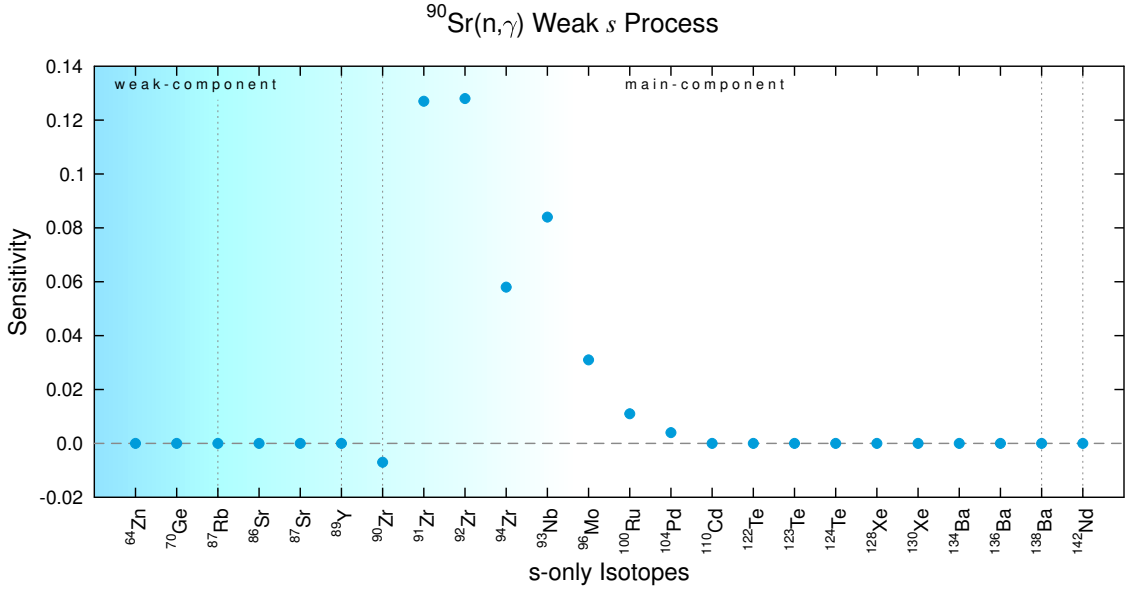

Figure A.114: Bottleneck reaction $^{90}\mathrm{Sr}(n,\gamma)$ during the weak *s* process (table 3.17).

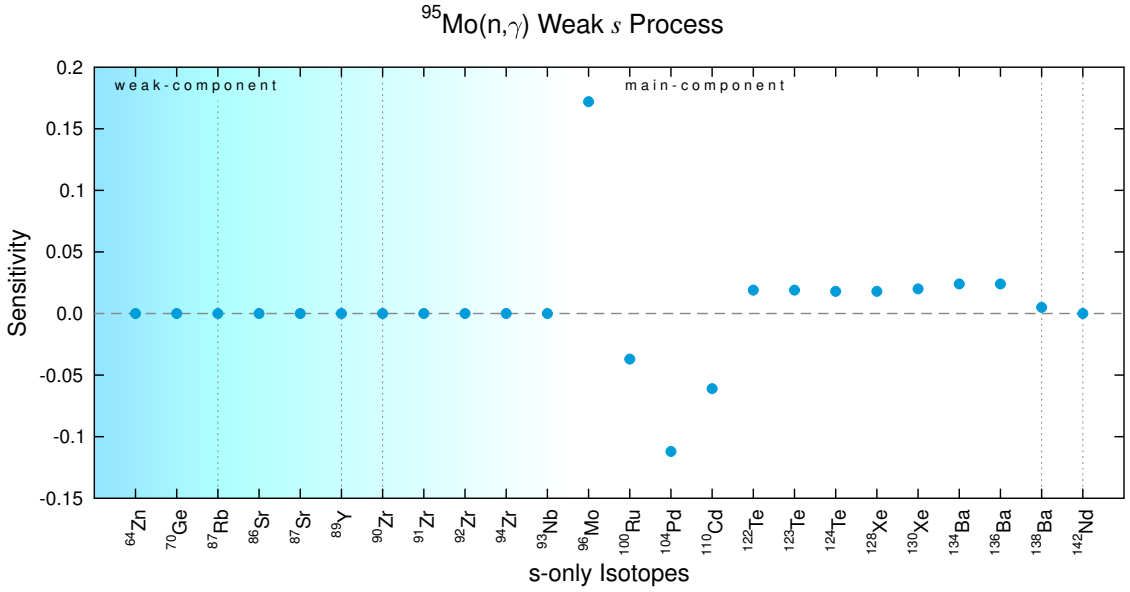

Figure A.115: Bottleneck reaction ^{95}Mo(n,γ) during the weak *s* process (table 3.17).

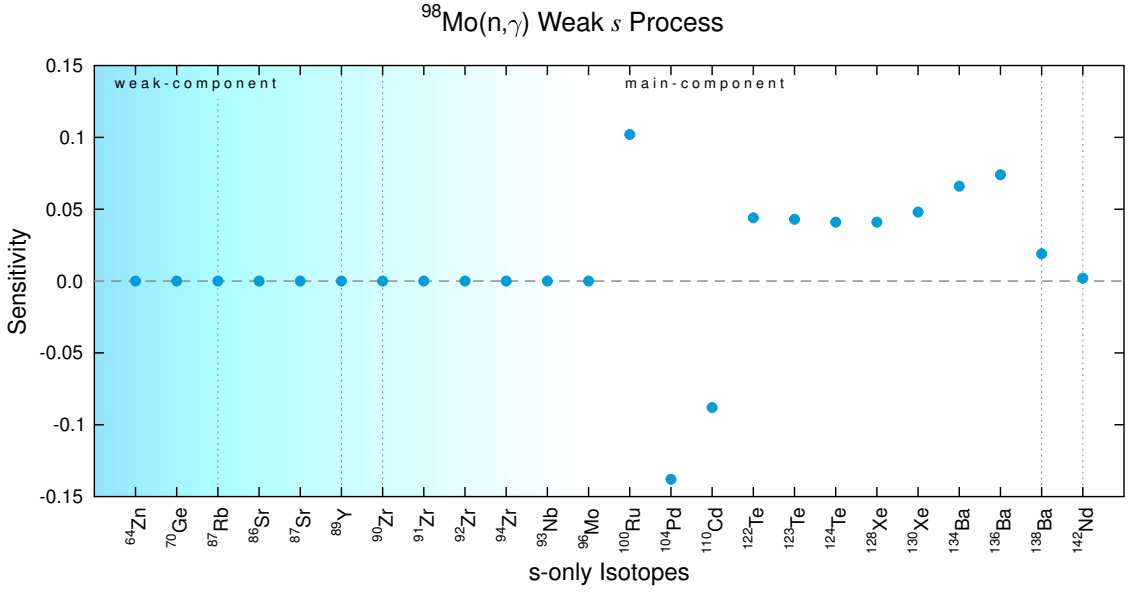

Figure A.116: Bottleneck reaction ^{98}Mo(n,γ) during the weak *s* process (table 3.17).

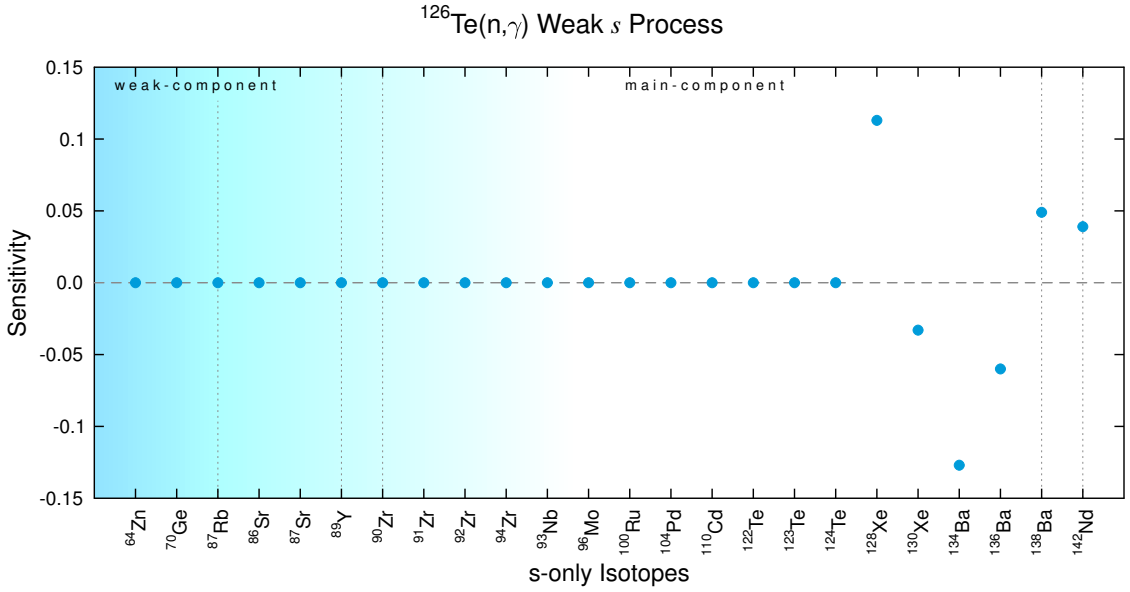

Figure A.117: Bottleneck reaction ^{126}Te(n,γ) during the weak s process (table 3.17).

A.2.2 CONVECTIVE C SHELL BURNING

LOCAL SENSITIVITIES DURING THE CONVECTIVE C SHELL BURNING

Table A.6: Reactions with strongest local sensitivities during the convective carbon shell burning. Filter criteria in chapter 2.3.3 on page 49.

Isotope	Most important reactions with respective sensitivities					
^{57}Fe	^{57}Fe(n,γ)	-0.223	^{56}Fe(n,γ)	0.201	-	
^{58}Ni	^{58}Ni(n,γ)	-0.298	^{24}Mg(n,γ)	0.107	-	
^{60}Ni	^{60}Ni(n,γ)	-0.169	^{59}Co(n,γ)	0.108	-	
^{61}Ni	^{61}Ni(n,γ)	-0.361	^{60}Ni(n,γ)	0.315	-	
^{62}Ni	^{61}Ni(n,γ)	0.123	^{62}Ni(n,γ)	-0.119	-	
^{63}Cu	^{63}Cu(n,γ)	-0.408	^{24}Mg(n,γ)	0.141	-	
^{64}Zn	^{64}Zn(n,γ)	-0.417	^{63}Cu(n,γ)	0.148	^{64}Cu(β^-)	0.123
^{66}Zn	^{66}Zn(n,γ)	-0.242	^{65}Cu(n,γ)	0.218	-	
^{67}Zn	^{66}Zn(n,γ)	0.528	^{67}Zn(n,γ)	-0.500	-	
^{68}Zn	^{67}Zn(n,γ)	0.156	^{68}Zn(n,γ)	-0.119	-	
^{70}Zn	^{68}Zn(n,γ)	0.354	^{69}Zn(β^-)	-0.347	^{69}Zn(n,γ)	0.346

Isotope	Most important reactions with respective sensitivities					
^{69}Ga	^{68}Zn(n,γ)	0.610	^{69}Ga(n,γ)	-0.585	-	
^{71}Ga	^{71}Ga(n,γ)	-0.613	^{71}Ge(β^+)	0.211	^{24}Mg(n,γ)	0.200
^{70}Ge	^{70}Ge(n,γ)	-0.425	^{69}Ga(n,γ)	0.322	^{68}Zn(n,γ)	0.210
^{72}Ge	^{72}Ge(n,γ)	-0.376	^{70}Ge(n,γ)	0.201	^{71}Ge(n,γ)	0.170
^{73}Ge	^{73}Ge(n,γ)	-0.592	^{72}Ge(n,γ)	0.554	-	
^{74}Ge	^{74}Ge(n,γ)	-0.219	^{73}Ge(n,γ)	0.209	^{72}Ge(n,γ)	0.137
^{76}Ge	^{75}Ge(n,γ)	0.578	^{75}Ge(β^-)	-0.573	^{74}Ge(n,γ)	0.507
^{75}As	^{75}As(n,γ)	-0.791	^{74}Ge(n,γ)	0.743	^{73}Ge(n,γ)	0.140
^{74}Se	^{74}Se(n,γ)	-0.879	^{23}Na(p,α)	-0.724	^{12}C(^{12}C,p)	0.575
^{76}Se	^{76}Se(n,γ)	-0.695	^{74}Ge(n,γ)	0.464	^{75}As(n,γ)	0.299
^{77}Se	^{77}Se(n,γ)	-0.861	^{76}Se(n,γ)	0.414	^{74}Ge(n,γ)	0.287
^{78}Se	^{78}Se(n,γ)	-0.325	^{76}Se(n,γ)	0.183	^{77}Se(n,γ)	0.161
^{80}Se	^{79}Se(n,γ)	0.462	^{78}Se(n,γ)	0.420	^{24}Mg(n,γ)	-0.293
^{79}Br	^{79}Br(n,γ)	-0.875	^{79}Se(β^-)	0.841	^{78}Se(n,γ)	0.637
^{81}Br	^{80}Se(n,γ)	0.683	^{81}Br(n,γ)	-0.615	^{79}Se(n,γ)	0.320
^{80}Kr	^{80}Kr(n,γ)	-1.010	^{79}Se(β^-)	0.477	^{78}Se(n,γ)	0.313
^{83}Kr	^{83}Kr(n,γ)	-0.687	^{82}Kr(n,γ)	0.491	-	
^{84}Kr	^{84}Kr(n,γ)	-0.185	^{83}Kr(n,γ)	0.176	^{82}Kr(n,γ)	0.114
^{86}Kr	^{85}Kr(n,γ)	0.535	^{84}Kr(n,γ)	0.314	^{24}Mg(n,γ)	-0.303
^{85}Rb	^{85}Rb(n,γ)	-0.617	^{85}Kr(β^-)	0.558	^{84}Kr(n,γ)	0.507
^{87}Rb	^{86}Rb(n,γ)	0.403	^{24}Mg(n,γ)	-0.237	^{85}Rb(n,γ)	0.231
^{86}Sr	^{86}Sr(n,γ)	-0.317	^{86}Rb(β^-)	0.111	-	
^{87}Sr	^{87}Sr(n,γ)	-0.371	^{86}Sr(n,γ)	0.318	-	
^{90}Zr	^{89}Y (n,γ)	0.134	^{90}Zr(n,γ)	-0.123	-	
^{91}Zr	^{90}Zr(n,γ)	0.325	^{91}Zr(n,γ)	-0.276	-	
^{92}Zr	^{91}Zr(n,γ)	0.211	^{92}Zr(n,γ)	-0.210	-	
^{94}Zr	^{94}Zr(n,γ)	-0.284	^{93}Zr(n,γ)	0.253	-	
^{96}Zr	^{95}Zr(n,γ)	0.602	^{94}Zr(n,γ)	0.359	^{24}Mg(n,γ)	-0.354
^{93}Nb	^{93}Nb(n,γ)	-1.257	^{24}Mg(n,γ)	0.448	^{12}C(^{12}C,p)	0.129
^{92}Mo	^{92}Nb(β^-)	0.443	^{92}Nb(β^+)	-0.406	^{23}Na(p,α)	-0.377
^{94}Mo	^{94}Mo(n,γ)	-0.700	^{24}Mg(n,γ)	0.243	^{93}Nb(n,γ)	0.118

Isotope	Most important reactions with respective sensitivities					
^{95}Mo	^{95}Mo(n,γ)	-1.076	^{24}Mg(n,γ)	0.397	^{95}Nb(β^-)	0.334
^{96}Mo	^{96}Mo(n,γ)	-0.615	^{24}Mg(n,γ)	0.141	^{95}Zr(β^-)	0.133
^{97}Mo	^{97}Mo(n,γ)	-0.940	^{96}Mo(n,γ)	0.474	^{24}Mg(n,γ)	0.104
^{98}Mo	^{98}Mo(n,γ)	-0.488	^{96}Mo(n,γ)	0.197	^{97}Mo(n,γ)	0.177
^{100}Mo	^{100}Mo(n,γ)	-0.592	^{99}Mo(β^-)	-0.568	^{99}Mo(n,γ)	0.566
^{99}Ru	^{99}Ru(n,γ)	-1.022	^{99}Tc(β^-)	0.825	^{99}Tc(n,γ)	-0.761
^{100}Ru	^{100}Ru(n,γ)	-0.756	^{98}Mo(n,γ)	0.471	^{99}Tc(n,γ)	0.114
^{101}Ru	^{101}Ru(n,γ)	-1.000	^{98}Mo(n,γ)	0.419	^{100}Ru(n,γ)	0.321
^{102}Ru	^{102}Ru(n,γ)	-0.561	^{100}Ru(n,γ)	0.301	^{98}Mo(n,γ)	0.145
^{104}Ru	^{103}Ru(n,γ)	0.737	^{103}Ru(β^-)	-0.671	^{104}Ru(n,γ)	-0.519
^{103}Rh	^{103}Rh(n,γ)	-0.867	^{102}Ru(n,γ)	0.518	^{100}Ru(n,γ)	0.275
^{104}Pd	^{104}Pd(n,γ)	-0.847	^{102}Ru(n,γ)	0.517	^{100}Ru(n,γ)	0.156
^{105}Pd	^{105}Pd(n,γ)	-0.991	^{102}Ru(n,γ)	0.499	^{104}Pd(n,γ)	0.193
^{106}Pd	^{106}Pd(n,γ)	-0.764	^{104}Pd(n,γ)	0.285	^{102}Ru(n,γ)	0.270
^{108}Pd	^{108}Pd(n,γ)	-0.665	^{106}Pd(n,γ)	0.354	^{104}Pd(n,γ)	0.176
^{110}Pd	^{109}Pd(n,γ)	0.743	^{109}Pd(β^-)	-0.711	^{110}Pd(n,γ)	-0.475
^{107}Ag	^{107}Pd(β^-)	0.979	^{107}Pd(n,γ)	-0.970	^{107}Ag(n,γ)	-0.969
^{109}Ag	^{109}Ag(n,γ)	-0.753	^{108}Pd(n,γ)	0.440	^{106}Pd(n,γ)	0.281
^{108}Cd	^{108}Cd(n,γ)	-1.306	^{24}Mg(n,γ)	0.466	^{12}C(^{12}C,p)	0.135
^{110}Cd	^{110}Cd(n,γ)	-0.795	^{108}Pd(n,γ)	0.280	^{109}Ag(n,γ)	0.253
^{111}Cd	^{111}Cd(n,γ)	-1.000	^{110}Cd(n,γ)	0.285	^{109}Ag(n,γ)	0.244
^{112}Cd	^{112}Cd(n,γ)	-0.725	^{110}Cd(n,γ)	0.308	^{109}Ag(n,γ)	0.131
^{113}Cd	^{113}Cd(n,γ)	-0.998	^{112}Cd(n,γ)	0.366	^{110}Cd(n,γ)	0.286
^{114}Cd	^{114}Cd(n,γ)	-0.586	^{112}Cd(n,γ)	0.295	^{110}Cd(n,γ)	0.102
^{116}Cd	^{115}Cd(n,γ)	0.653	^{115}Cd(β^-)	-0.581	^{114}Cd(n,γ)	0.446
^{115}In	^{115}In(n,γ)	-0.872	^{114}Cd(n,γ)	0.505	^{112}Cd(n,γ)	0.256
^{115}Sn	^{115}Sn(n,γ)	-1.085	^{115}In(β^-)	0.728	^{115}In(n,γ)	-0.682
^{116}Sn	^{116}Sn(n,γ)	-0.498	^{114}Cd(n,γ)	0.275	-	
^{117}Sn	^{117}Sn(n,γ)	-0.866	^{116}Sn(n,γ)	0.535	^{114}Cd(n,γ)	0.178
^{118}Sn	^{118}Sn(n,γ)	-0.357	^{116}Sn(n,γ)	0.173	^{117}Sn(n,γ)	0.148
^{119}Sn	^{119}Sn(n,γ)	-0.764	^{118}Sn(n,γ)	0.593	-	

Isotope	Most important reactions with respective sensitivities					
^{120}Sn	^{120}Sn(n,γ)	-0.243	^{119}Sn(n,γ)	0.126	^{118}Sn(n,γ)	0.106
^{122}Sn	^{121}Sn(n,γ)	0.563	^{120}Sn(n,γ)	0.466	^{121}Sn(β^-)	-0.423
^{121}Sb	^{121}Sb(n,γ)	-0.920	^{120}Sn(n,γ)	0.781	^{121}Sn(β^-)	0.194
^{123}Sb	^{123}Sb(n,γ)	-0.686	^{120}Sn(n,γ)	0.451	^{122}Sn(n,γ)	0.441
^{122}Te	^{122}Te(n,γ)	-0.871	^{120}Sn(n,γ)	0.594	^{121}Sn(β^-)	0.181
^{123}Te	^{123}Te(n,γ)	-0.992	^{120}Sn(n,γ)	0.513	^{121}Sb(n,γ)	0.210
^{124}Te	^{124}Te(n,γ)	-0.709	^{122}Te(n,γ)	0.221	^{120}Sn(n,γ)	0.163
^{125}Te	^{125}Te(n,γ)	-0.998	^{124}Te(n,γ)	0.405	^{122}Te(n,γ)	0.190
^{126}Te	^{126}Te(n,γ)	-0.450	^{124}Te(n,γ)	0.194	-	
^{128}Te	^{127}Te(n,γ)	0.585	^{127}Te(β^-)	-0.531	^{126}Te(n,γ)	0.472
^{127}I	^{127}I (n,γ)	-0.916	^{126}Te(n,γ)	0.636	^{124}Te(n,γ)	0.145
^{128}Xe	^{128}Xe(n,γ)	-0.881	^{126}Te(n,γ)	0.542	^{127}I (n,γ)	0.127
^{129}Xe	^{129}Xe(n,γ)	-1.003	^{126}Te(n,γ)	0.460	^{128}Xe(n,γ)	0.217
^{130}Xe	^{130}Xe(n,γ)	-0.650	^{128}Xe(n,γ)	0.219	^{126}Te(n,γ)	0.146
^{131}Xe	^{131}Xe(n,γ)	-0.901	^{130}Xe(n,γ)	0.452	^{128}Xe(n,γ)	0.155
^{132}Xe	^{132}Xe(n,γ)	-0.370	^{130}Xe(n,γ)	0.152	^{131}Xe(n,γ)	0.133
^{134}Xe	^{133}Xe(n,γ)	0.533	^{132}Xe(n,γ)	0.491	^{133}Xe(β^-)	-0.403
^{133}Cs	^{133}Cs(n,γ)	-0.847	^{132}Xe(n,γ)	0.720	^{133}Xe(β^-)	0.204
^{134}Ba	^{134}Ba(n,γ)	-0.745	^{132}Xe(n,γ)	0.430	^{133}Cs(n,γ)	0.202
^{135}Ba	^{135}Ba(n,γ)	-0.997	^{134}Ba(n,γ)	0.366	^{132}Xe(n,γ)	0.277
^{136}Ba	^{136}Ba(n,γ)	-0.373	^{134}Ba(n,γ)	0.125	-	
^{137}Ba	^{137}Ba(n,γ)	-0.401	^{136}Ba(n,γ)	0.315	-	
^{139}La	^{138}Ba(n,γ)	0.164	^{139}La(n,γ)	-0.114	-	
^{142}Ce	^{141}Ce(n,γ)	0.681	^{140}Ce(n,γ)	0.430	^{24}Mg(n,γ)	-0.370
^{141}Pr	^{141}Pr(n,γ)	-0.432	^{141}Ce(β^-)	0.259	^{140}Ce(n,γ)	0.200
^{142}Nd	^{142}Nd(n,γ)	-0.234	^{141}Pr(n,γ)	0.100	-	

INITIAL ABUNDANCES FOR THE CONVECTIVE C SHELL BURNING

Table A.7: Initial abundances for the convective C shell simulations. Added abundances give unity.

isotope	initial abundance	isotope	initial abundance	isotope	initial abundance
Protons	$2.22159 \cdot 10^{-15}$	^{4}He	$4.41221 \cdot 10^{-10}$	^{11}B	$1.42796 \cdot \cdot 10^{-09}$
^{12}C	$7.64245 \cdot 10^{-02}$	^{13}C	$1.27021 \cdot 10^{-08}$	^{13}N	$2.09331 \cdot 10^{-12}$
^{14}N	$3.63127 \cdot 10^{-05}$	^{14}C	$3.11207 \cdot 10^{-06}$	^{15}N	$8.38017 \cdot 10^{-08}$
^{16}O	$6.00483 \cdot 10^{-01}$	^{17}O	$1.51468 \cdot 10^{-05}$	^{18}O	$4.61673 \cdot 10^{-07}$
^{18}F	$1.79250 \cdot 10^{-07}$	^{19}F	$7.23729 \cdot 10^{-08}$	^{20}Ne	$2.77973 \cdot 10^{-01}$
^{21}Ne	$5.83218 \cdot 10^{-04}$	^{22}Ne	$6.87297 \cdot 10^{-04}$	^{23}Na	$1.00156 \cdot 10^{-02}$
^{24}Mg	$1.86463 \cdot 10^{-02}$	^{25}Mg	$5.72302 \cdot 10^{-03}$	^{26}Mg	$4.77511 \cdot 10^{-03}$
^{26}Al	$7.02351 \cdot 10^{-07}$	^{27}Al	$2.15703 \cdot 10^{-03}$	^{28}Si	$1.12300 \cdot 10^{-03}$
^{29}Si	$1.22003 \cdot 10^{-04}$	^{30}Si	$1.24593 \cdot 10^{-04}$	^{31}P	$4.41357 \cdot 10^{-05}$
^{32}S	$1.09002 \cdot 10^{-04}$	^{33}S	$4.36983 \cdot 10^{-06}$	^{34}S	$1.52037 \cdot 10^{-05}$
^{35}S	$5.62065 \cdot 10^{-08}$	^{36}S	$2.52227 \cdot 10^{-06}$	^{35}Cl	$1.65637 \cdot 10^{-06}$
^{36}Cl	$7.01781 \cdot 10^{-08}$	^{37}Cl	$2.72704 \cdot 10^{-05}$	^{36}Ar	$7.70753 \cdot 10^{-06}$
^{37}Ar	$7.34576 \cdot 10^{-08}$	^{38}Ar	$2.53168 \cdot 10^{-05}$	^{39}Ar	$1.26961 \cdot 10^{-06}$
^{40}Ar	$8.61045 \cdot 10^{-07}$	^{39}K	$4.55414 \cdot 10^{-06}$	^{40}K	$6.60469 \cdot 10^{-07}$
^{41}K	$9.96428 \cdot 10^{-07}$	^{40}Ca	$1.19029 \cdot 10^{-05}$	^{41}Ca	$3.94521 \cdot 10^{-07}$
^{42}Ca	$2.16214 \cdot 10^{-06}$	^{43}Ca	$7.47656 \cdot 10^{-07}$	^{44}Ca	$2.58477 \cdot 10^{-06}$
^{45}Ca	$5.89852 \cdot 10^{-08}$	^{46}Ca	$3.29153 \cdot 10^{-09}$	^{47}Ca	$1.33450 \cdot 10^{-11}$
^{48}Ca	$7.06874 \cdot 10^{-08}$	^{44}Sc	$5.57616 \cdot 10^{-11}$	^{45}Sc	$3.98850 \cdot 10^{-07}$
^{46}Sc	$5.97932 \cdot 10^{-09}$	^{47}Sc	$2.57243 \cdot 10^{-10}$	^{44}Ti	$1.06445 \cdot 10^{-13}$
^{45}Ti	$2.34830 \cdot 10^{-15}$	^{46}Ti	$6.39735 \cdot 10^{-07}$	^{47}Ti	$3.13582 \cdot 10^{-07}$
^{48}Ti	$4.67951 \cdot 10^{-07}$	^{49}Ti	$4.95568 \cdot 10^{-07}$	^{50}Ti	$1.89134 \cdot 10^{-06}$
^{49}V	$2.94486 \cdot 10^{-10}$	^{50}V	$7.45819 \cdot 10^{-10}$	^{51}V	$1.82011 \cdot 10^{-07}$
^{50}Cr	$4.95357 \cdot 10^{-11}$	^{51}Cr	$7.62407 \cdot 10^{-12}$	^{52}Cr	$2.49459 \cdot 10^{-06}$
^{53}Cr	$5.60557 \cdot 10^{-07}$	^{54}Cr	$3.99335 \cdot 10^{-06}$	^{53}Mn	$5.52641 \cdot 10^{-10}$
^{54}Mn	$1.60387 \cdot 10^{-10}$	^{55}Mn	$1.08246 \cdot 10^{-06}$	^{56}Mn	$1.01272 \cdot 10^{-10}$
^{54}Fe	$1.00448 \cdot 10^{-07}$	^{55}Fe	$1.14153 \cdot 10^{-08}$	^{56}Fe	$1.22450 \cdot 10^{-04}$
^{57}Fe	$4.59935 \cdot 10^{-05}$	^{58}Fe	$1.81399 \cdot 10^{-04}$	^{59}Fe	$8.09679 \cdot 10^{-06}$
^{60}Fe	$2.99857 \cdot 10^{-07}$	^{56}Co	$6.96821 \cdot 10^{-14}$	^{57}Co	$5.34131 \cdot 10^{-09}$
^{58}Co	$2.34010 \cdot 10^{-09}$	^{59}Co	$8.01691 \cdot 10^{-05}$	^{60}Co	$4.35384 \cdot 10^{-07}$
^{58}Ni	$5.07718 \cdot 10^{-08}$	^{59}Ni	$6.39435 \cdot 10^{-09}$	^{60}Ni	$7.83280 \cdot 10^{-05}$
^{61}Ni	$3.26273 \cdot 10^{-05}$	^{62}Ni	$8.55574 \cdot 10^{-05}$	^{63}Ni	$5.79528 \cdot 10^{-06}$
^{64}Ni	$3.60568 \cdot 10^{-05}$	^{63}Cu	$2.45735 \cdot 10^{-05}$	^{64}Cu	$4.87344 \cdot 10^{-07}$
^{65}Cu	$3.28482 \cdot 10^{-05}$	^{64}Zn	$1.71598 \cdot 10^{-05}$	^{65}Zn	$2.82331 \cdot 10^{-06}$
^{66}Zn	$2.31201 \cdot 10^{-05}$	^{67}Zn	$6.78559 \cdot 10^{-06}$	^{68}Zn	$2.19853 \cdot 10^{-05}$

isotope	initial abundance	isotope	initial abundance	isotope	initial abundance
^{69}Zn	$1.00077 \cdot 10^{-08}$	^{70}Zn	$5.56822 \cdot 10^{-09}$	^{69}Ga	$2.76192 \cdot 10^{-06}$
^{70}Ga	$4.62439 \cdot 10^{-09}$	^{71}Ga	$1.59349 \cdot 10^{-06}$	^{70}Ge	$3.64103 \cdot 10^{-06}$
^{71}Ge	$6.90573 \cdot 10^{-07}$	^{72}Ge	$3.05955 \cdot 10^{-06}$	^{73}Ge	$1.19029 \cdot 10^{-06}$
^{74}Ge	$3.31762 \cdot 10^{-06}$	^{75}Ge	$5.77346 \cdot 10^{-09}$	^{76}Ge	$1.89400 \cdot 10^{-09}$
^{75}As	$4.06001 \cdot 10^{-07}$	^{74}Se	$1.53917 \cdot 10^{-14}$	^{76}Se	$5.64625 \cdot 10^{-07}$
^{77}Se	$2.90980 \cdot 10^{-07}$	^{78}Se	$1.23175 \cdot 10^{-06}$	^{79}Se	$1.87696 \cdot 10^{-07}$
^{80}Se	$1.36915 \cdot 10^{-07}$	^{81}Se	$9.56918 \cdot 10^{-11}$	^{82}Se	$1.22429 \cdot 10^{-09}$
^{79}Br	$2.78635 \cdot 10^{-08}$	^{80}Br	$3.75833 \cdot 10^{-10}$	^{81}Br	$4.50152 \cdot 10^{-08}$
^{78}Kr	$2.96942 \cdot 10^{-17}$	^{79}Kr	$5.23355 \cdot 10^{-17}$	^{80}Kr	$1.43663 \cdot 10^{-07}$
^{81}Kr	$8.91483 \cdot 10^{-08}$	^{82}Kr	$5.15170 \cdot 10^{-07}$	^{83}Kr	$2.38817 \cdot 10^{-07}$
^{84}Kr	$7.91766 \cdot 10^{-07}$	^{85}Kr	$7.96238 \cdot 10^{-08}$	^{86}Kr	$2.48031 \cdot 10^{-08}$
^{85}Rb	$5.08261 \cdot 10^{-08}$	^{86}Rb	$2.65345 \cdot 10^{-08}$	^{87}Rb	$2.55993 \cdot 10^{-08}$
^{84}Sr	$1.77300 \cdot 10^{-16}$	^{85}Sr	$6.48091 \cdot 10^{-16}$	^{86}Sr	$2.32435 \cdot 10^{-07}$
^{87}Sr	$1.55079 \cdot 10^{-07}$	^{88}Sr	$5.15292 \cdot 10^{-07}$	^{89}Sr	$9.68203 \cdot 10^{-09}$
^{90}Sr	$3.20764 \cdot 10^{-10}$	^{89}Y	$8.29713 \cdot 10^{-08}$	^{90}Y	$1.22553 \cdot 10^{-09}$
^{90}Zr	$4.89581 \cdot 10^{-08}$	^{91}Zr	$1.47423 \cdot 10^{-08}$	^{92}Zr	$1.79644 \cdot 10^{-08}$
^{93}Zr	$6.74978 \cdot 10^{-09}$	^{94}Zr	$8.62419 \cdot 10^{-09}$	^{95}Zr	$1.25001 \cdot 10^{-09}$
^{96}Zr	$3.63224 \cdot 10^{-10}$	^{93}Nb	$2.68831 \cdot 10^{-11}$	^{94}Nb	$5.88846 \cdot 10^{-12}$
^{95}Nb	$8.10024 \cdot 10^{-11}$	^{92}Mo	$2.87070 \cdot 10^{-15}$	^{93}Mo	$7.33419 \cdot 10^{-16}$
^{94}Mo	$5.50421 \cdot 10^{-11}$	^{95}Mo	$6.29547 \cdot 10^{-10}$	^{96}Mo	$2.62958 \cdot 10^{-09}$
^{97}Mo	$1.05995 \cdot 10^{-09}$	^{98}Mo	$2.98330 \cdot 10^{-09}$	^{99}Mo	$9.13495 \cdot 10^{-12}$
^{100}Mo	$5.45936 \cdot 10^{-12}$	^{99}Tc	$3.80989 \cdot 10^{-10}$	^{96}Ru	$1.08524 \cdot 10^{-19}$
^{97}Ru	$2.29179 \cdot 10^{-20}$	^{98}Ru	$8.70047 \cdot 10^{-18}$	^{99}Ru	$1.31007 \cdot 10^{-10}$
^{100}Ru	$1.33004 \cdot 10^{-09}$	^{101}Ru	$3.16310 \cdot 10^{-10}$	^{102}Ru	$1.84319 \cdot 10^{-09}$
^{103}Ru	$8.35525 \cdot 10^{-11}$	^{104}Ru	$5.84147 \cdot 10^{-11}$	^{103}Rh	$2.62783 \cdot 10^{-10}$
^{102}Pd	$1.21394 \cdot 10^{-21}$	^{103}Pd	$6.40014 \cdot 10^{-19}$	^{104}Pd	$7.33641 \cdot 10^{-10}$
^{105}Pd	$1.83899 \cdot 10^{-10}$	^{106}Pd	$9.72351 \cdot 10^{-10}$	^{107}Pd	$1.86033 \cdot 10^{-10}$
^{108}Pd	$8.46086 \cdot 10^{-10}$	^{109}Pd	$2.76821 \cdot 10^{-11}$	^{110}Pd	$2.91723 \cdot 10^{-11}$
^{107}Ag	$1.29422 \cdot 10^{-11}$	^{108}Ag	$7.83431 \cdot 10^{-14}$	^{109}Ag	$4.48259 \cdot 10^{-10}$
^{106}Cd	$7.07336 \cdot 10^{-22}$	^{107}Cd	$2.29778 \cdot 10^{-22}$	^{108}Cd	$2.82643 \cdot 10^{-10}$
^{109}Cd	$5.87654 \cdot 10^{-11}$	^{110}Cd	$8.76720 \cdot 10^{-10}$	^{111}Cd	$2.76517 \cdot 10^{-10}$
^{112}Cd	$1.05953 \cdot 10^{-09}$	^{113}Cd	$2.83722 \cdot 10^{-10}$	^{114}Cd	$1.47430 \cdot 10^{-09}$
^{115}Cd	$8.78326 \cdot 10^{-11}$	^{116}Cd	$7.70114 \cdot 10^{-11}$	^{113}In	$5.24149 \cdot 10^{-19}$
^{114}In	$5.15324 \cdot 10^{-22}$	^{115}In	$2.16335 \cdot 10^{-10}$	^{112}Sn	$7.23253 \cdot 10^{-23}$
^{113}Sn	$8.67951 \cdot 10^{-24}$	^{114}Sn	$7.69753 \cdot 10^{-19}$	^{115}Sn	$3.37931 \cdot 10^{-11}$
^{116}Sn	$1.73699 \cdot 10^{-09}$	^{117}Sn	$5.77584 \cdot 10^{-10}$	^{118}Sn	$2.62700 \cdot 10^{-09}$
^{119}Sn	$7.91315 \cdot 10^{-10}$	^{120}Sn	$4.17096 \cdot 10^{-09}$	^{121}Sn	$1.96583 \cdot 10^{-10}$
^{122}Sn	$1.06397 \cdot 10^{-10}$	^{123}Sn	$1.20361 \cdot 10^{-13}$	^{124}Sn	$3.68005 \cdot 10^{-11}$

isotope	initial abundance	isotope	initial abundance	isotope	initial abundance
^{121}Sb	$2.33175 \cdot 10^{-10}$	^{122}Sb	$6.65854 \cdot 10^{-12}$	^{123}Sb	$1.64273 \cdot 10^{-11}$
^{120}Te	$8.87661 \cdot 10^{-24}$	^{121}Te	$1.16835 \cdot 10^{-21}$	^{122}Te	$4.09677 \cdot 10^{-10}$
^{123}Te	$1.50165 \cdot 10^{-10}$	^{124}Te	$9.97217 \cdot 10^{-10}$	^{125}Te	$3.39219 \cdot 10^{-10}$
^{126}Te	$2.08986 \cdot 10^{-09}$	^{127}Te	$4.57900 \cdot 10^{-11}$	^{128}Te	$6.43320 \cdot 10^{-11}$
^{129}Te	$1.29883 \cdot 10^{-13}$	^{130}Te	$2.27833 \cdot 10^{-10}$	^{127}I	$2.94355 \cdot 10^{-10}$
^{128}I	$4.51377 \cdot 10^{-12}$	^{129}I	$1.31820 \cdot 10^{-11}$	^{126}Xe	$4.44016 \cdot 10^{-20}$
^{127}Xe	$1.52334 \cdot 10^{-20}$	^{128}Xe	$5.63205 \cdot 10^{-10}$	^{129}Xe	$2.44667 \cdot 10^{-10}$
^{130}Xe	$1.26676 \cdot 10^{-09}$	^{131}Xe	$5.77840 \cdot 10^{-10}$	^{132}Xe	$2.91284 \cdot 10^{-09}$
^{134}Xe	$1.07085 \cdot 10^{-10}$	^{135}Xe	$3.13997 \cdot 10^{-13}$	^{136}Xe	$6.15959 \cdot 10^{-10}$
^{133}Cs	$3.52178 \cdot 10^{-10}$	^{134}Cs	$1.93348 \cdot 10^{-11}$	^{135}Cs	$3.25836 \cdot 10^{-11}$
^{132}Ba	$2.54596 \cdot 10^{-22}$	^{133}Ba	$2.89620 \cdot 10^{-21}$	^{134}Ba	$8.71745 \cdot 10^{-10}$
^{135}Ba	$3.91698 \cdot 10^{-10}$	^{136}Ba	$3.15065 \cdot 10^{-09}$	^{137}Ba	$2.66667 \cdot 10^{-09}$
^{138}Ba	$2.92443 \cdot 10^{-08}$	^{138}La	$1.17336 \cdot 10^{-18}$	^{139}La	$3.46524 \cdot 10^{-09}$
^{136}Ce	$2.80153 \cdot 10^{-27}$	^{138}Ce	$4.55444 \cdot 10^{-23}$	^{139}Ce	$1.52070 \cdot 10^{-17}$
^{140}Ce	$6.10041 \cdot 10^{-09}$	^{141}Ce	$2.02779 \cdot 10^{-10}$	^{142}Ce	$3.58369 \cdot 10^{-11}$
^{141}Pr	$5.29134 \cdot 10^{-10}$	^{142}Nd	$1.39934 \cdot 10^{-09}$	^{143}Nd	$2.47691 \cdot 10^{-10}$
^{144}Nd	$6.00837 \cdot 10^{-10}$	^{145}Nd	$1.70377 \cdot 10^{-10}$	^{146}Nd	$4.55036 \cdot 10^{-10}$
^{147}Nd	$6.38690 \cdot 10^{-11}$	^{148}Nd	$4.86623 \cdot 10^{-11}$	^{149}Nd	$3.26271 \cdot 10^{-13}$
^{150}Nd	$1.65703 \cdot 10^{-13}$	^{147}Pm	$2.35936 \cdot 10^{-11}$	^{144}Sm	$9.30902 \cdot 10^{-18}$
^{147}Sm	$4.34238 \cdot 10^{-12}$	^{148}Sm	$8.68834 \cdot 10^{-11}$	^{149}Sm	$2.61396 \cdot 10^{-11}$
^{150}Sm	$9.04274 \cdot 10^{-11}$	^{151}Sm	$2.32553 \cdot 10^{-11}$	^{152}Sm	$7.08819 \cdot 10^{-11}$
^{153}Sm	$8.12118 \cdot 10^{-12}$	^{154}Sm	$1.43506 \cdot 10^{-11}$	^{151}Eu	$1.37319 \cdot 10^{-13}$
^{152}Eu	$1.85459 \cdot 10^{-14}$	^{153}Eu	$1.57844 \cdot 10^{-11}$	^{152}Gd	$1.76002 \cdot 10^{-12}$
^{153}Gd	$8.05475 \cdot 10^{-13}$	^{154}Gd	$1.85829 \cdot 10^{-11}$	^{155}Gd	$1.29290 \cdot 10^{-11}$
^{156}Gd	$4.55943 \cdot 10^{-11}$	^{157}Gd	$4.00953 \cdot 10^{-11}$	^{158}Gd	$1.06617 \cdot 10^{-10}$
^{159}Gd	$1.31388 \cdot 10^{-11}$	^{160}Gd	$1.39040 \cdot 10^{-11}$	^{159}Tb	$2.68938 \cdot 10^{-11}$
^{158}Dy	$3.27647 \cdot 10^{-13}$	^{159}Dy	$2.95931 \cdot 10^{-13}$	^{160}Dy	$3.04402 \cdot 10^{-11}$
^{161}Dy	$2.87846 \cdot 10^{-11}$	^{162}Dy	$7.47643 \cdot 10^{-11}$	^{163}Dy	$5.29864 \cdot 10^{-11}$
^{164}Dy	$1.73841 \cdot 10^{-10}$	^{165}Ho	$4.02046 \cdot 10^{-11}$	^{164}Er	$1.98765 \cdot 10^{-23}$
^{165}Er	$1.43229 \cdot 10^{-23}$	^{166}Er	$3.98147 \cdot 10^{-11}$	^{167}Er	$3.44984 \cdot 10^{-11}$
^{168}Er	$1.08652 \cdot 10^{-10}$	^{169}Er	$6.13662 \cdot 10^{-11}$	^{170}Er	$6.31123 \cdot 10^{-11}$
^{169}Tm	$6.36456 \cdot 10^{-12}$	^{169}Yb	$9.90286 \cdot 10^{-26}$	^{170}Yb	$3.23389 \cdot 10^{-12}$
^{171}Yb	$6.54650 \cdot 10^{-12}$	^{172}Yb	$5.95499 \cdot 10^{-11}$	^{173}Yb	$6.45069 \cdot 10^{-11}$
^{174}Yb	$2.33348 \cdot 10^{-10}$	^{175}Yb	$1.66119 \cdot 10^{-11}$	^{176}Yb	$1.97793 \cdot 10^{-11}$
^{175}Lu	$3.67550 \cdot 10^{-11}$	^{176}Lu	$1.08531 \cdot 10^{-11}$	^{175}Hf	$1.55395 \cdot 10^{-24}$
^{176}Hf	$2.58073 \cdot 10^{-11}$	^{177}Hf	$2.59874 \cdot 10^{-11}$	^{178}Hf	$9.71277 \cdot 10^{-11}$
^{179}Hf	$5.03028 \cdot 10^{-11}$	^{180}Hf	$1.52677 \cdot 10^{-10}$	^{181}Hf	$6.31576 \cdot 10^{-12}$
^{182}Hf	$2.54853 \cdot 10^{-12}$	^{180}Ta	$1.43234 \cdot 10^{-12}$	^{181}Ta	$4.70262 \cdot 10^{-11}$

isotope	initial abundance	isotope	initial abundance	isotope	initial abundance
^{180}W	$2.74724 \cdot 10^{-12}$	^{181}W	$1.92934 \cdot 10^{-12}$	^{182}W	$5.50186 \cdot 10^{-11}$
^{183}W	$7.45783 \cdot 10^{-11}$	^{184}W	$1.74076 \cdot 10^{-10}$	^{185}W	$7.97817 \cdot 10^{-11}$
^{186}W	$5.64549 \cdot 10^{-11}$	^{185}Re	$3.92348 \cdot 10^{-12}$	^{186}Re	$2.39153 \cdot 10^{-12}$
^{187}Re	$1.54620 \cdot 10^{-11}$	^{185}Os	$5.34139 \cdot 10^{-25}$	^{186}Os	$1.60340 \cdot 10^{-11}$
^{187}Os	$1.47311 \cdot 10^{-11}$	^{188}Os	$8.70143 \cdot 10^{-11}$	^{189}Os	$4.28155 \cdot 10^{-11}$
^{190}Os	$1.42730 \cdot 10^{-10}$	^{191}Os	$2.42705 \cdot 10^{-11}$	^{192}Os	$5.99951 \cdot 10^{-11}$
^{191}Ir	$1.83223 \cdot 10^{-11}$	^{192}Ir	$1.15104 \cdot 10^{-11}$	^{193}Ir	$2.81792 \cdot 10^{-11}$
^{192}Pt	$6.78232 \cdot 10^{-12}$	^{193}Pt	$4.72024 \cdot 10^{-12}$	^{194}Pt	$9.13715 \cdot 10^{-11}$
^{195}Pt	$5.73229 \cdot 10^{-11}$	^{196}Pt	$2.27753 \cdot 10^{-10}$	^{197}Pt	$1.10927 \cdot 10^{-11}$
^{198}Pt	$6.52005 \cdot 10^{-12}$	^{197}Au	$9.01494 \cdot 10^{-11}$	^{198}Au	$4.68271 \cdot 10^{-12}$
^{199}Au	$1.51869 \cdot 10^{-12}$	^{196}Hg	$1.51736 \cdot 10^{-24}$	^{197}Hg	$6.83462 \cdot 10^{-25}$
^{198}Hg	$2.00374 \cdot 10^{-10}$	^{199}Hg	$1.35459 \cdot 10^{-10}$	^{200}Hg	$3.73529 \cdot 10^{-10}$
^{201}Hg	$2.48032 \cdot 10^{-10}$	^{202}Hg	$8.19616 \cdot 10^{-10}$	^{203}Hg	$9.83736 \cdot 10^{-12}$
^{204}Hg	$8.08787 \cdot 10^{-12}$	^{203}Tl	$6.75360 \cdot 10^{-10}$	^{204}Tl	$4.86800 \cdot 10^{-12}$
^{205}Tl	$1.44447 \cdot 10^{-09}$	^{204}Pb	$7.37046 \cdot 10^{-10}$	^{205}Pb	$1.96815 \cdot 10^{-10}$
^{206}Pb	$6.03390 \cdot 10^{-09}$	^{207}Pb	$7.33473 \cdot 10^{-09}$	^{208}Pb	$1.03465 \cdot 10^{-08}$
^{209}Bi	$5.87670 \cdot 10^{-10}$	^{210}Bi	$1.02329 \cdot 10^{-13}$	^{208}Pb	$1.03465 \cdot 10^{-08}$

GLOBAL SENSITIVITIES AND INTERESTING CASES DURING THE CONVECTIVE C SHELL BURNING

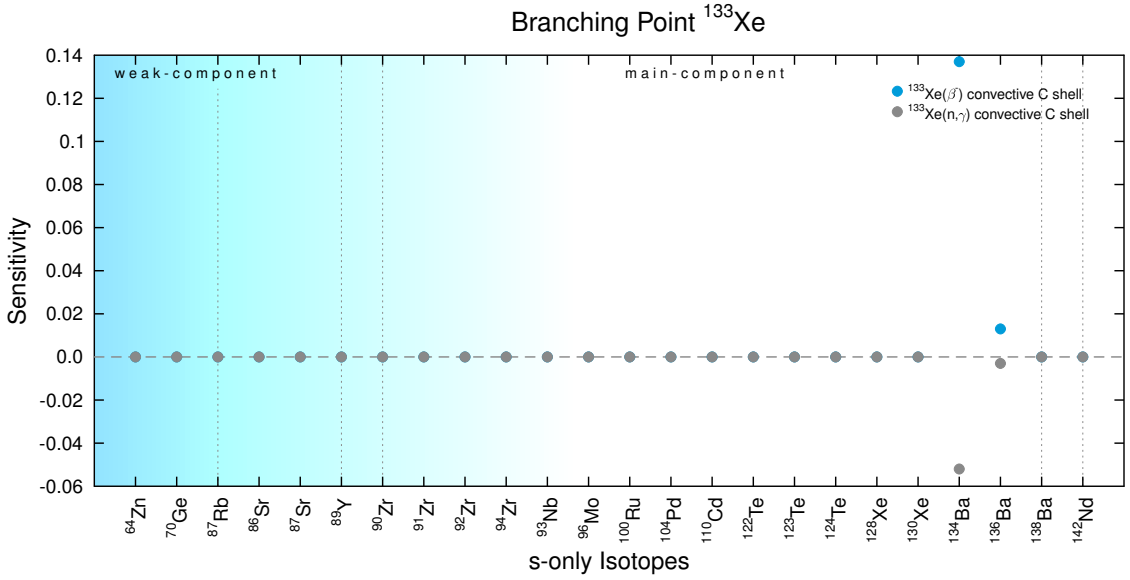

Figure A.118: Branching point ^{133}Xe during the carbon shell burning (table 3.18).

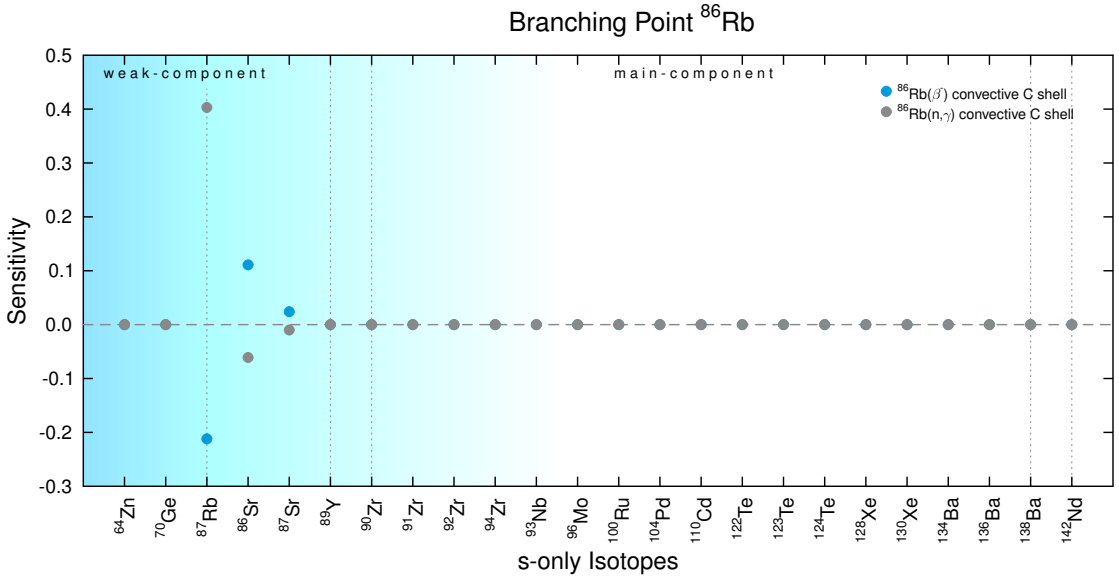

Figure A.119: Branching point ^{86}Rb during the carbon shell burning (table 3.18).

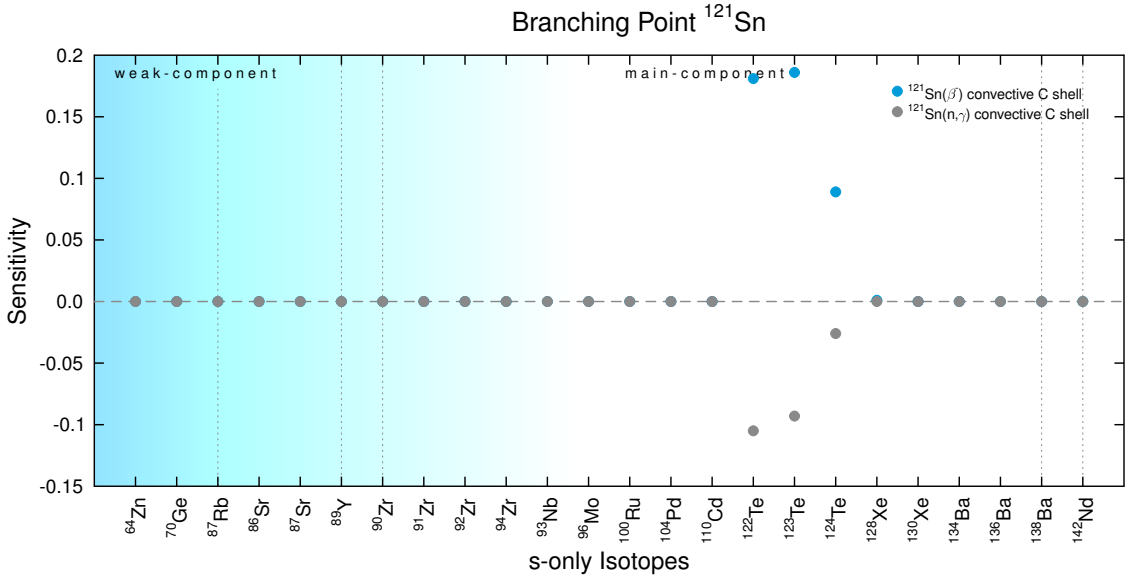

Figure A.120: Branching point ^{121}Sn during the carbon shell burning (table 3.18).

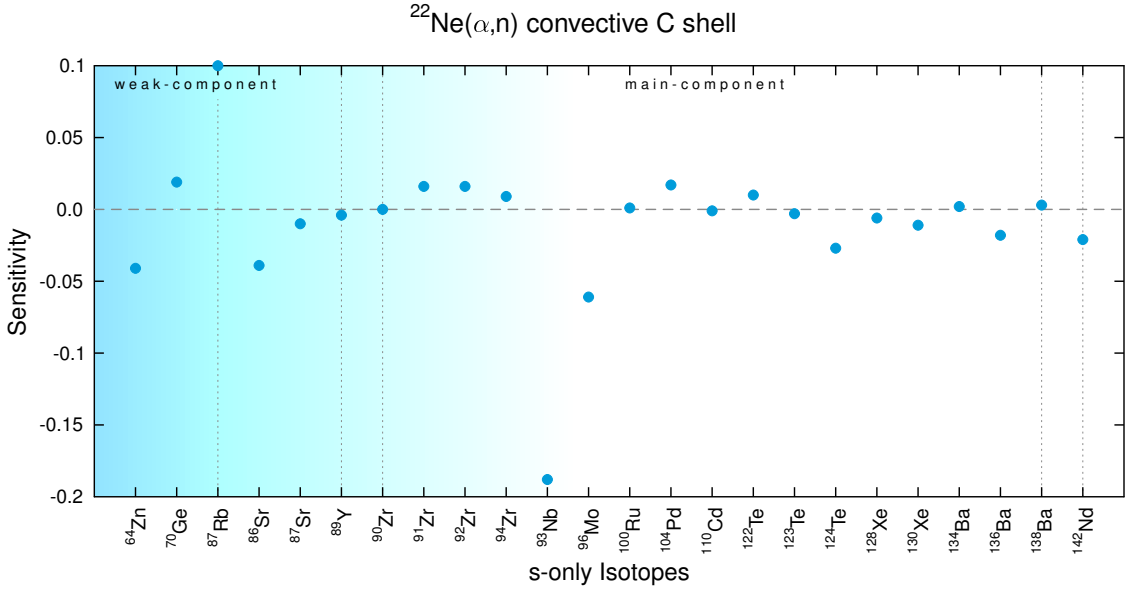

Figure A.121: Neutron donator reaction ^{22}Ne(α, n) during the convective carbon shell burning (table 3.19).

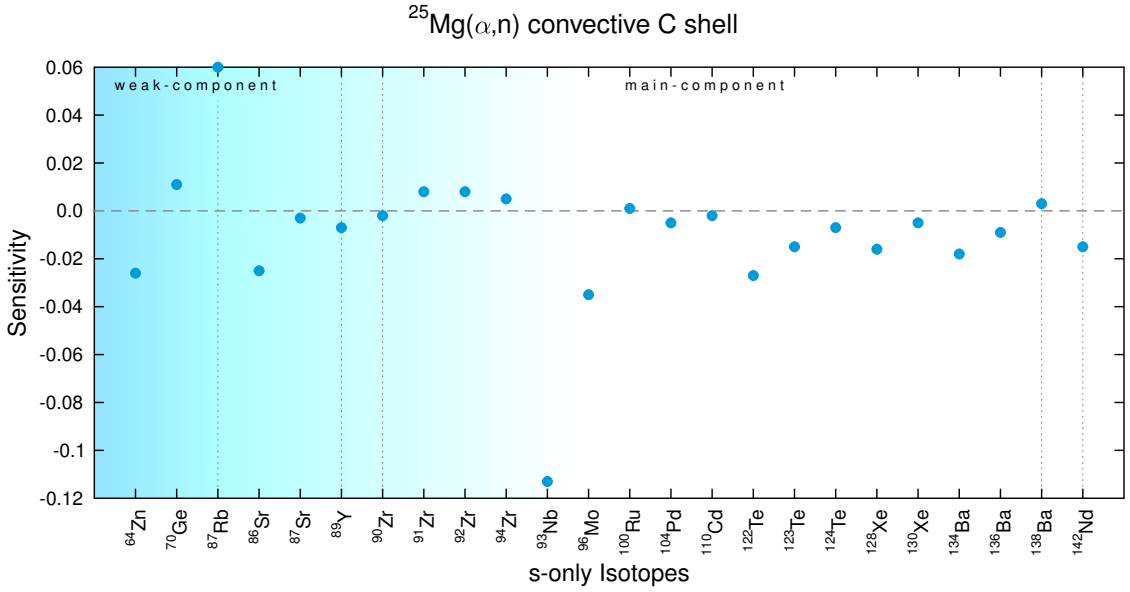

Figure A.122: Neutron donator reaction $^{25}\mathrm{Mg}(\alpha, n)$ during the convective carbon shell burning (table 3.19).

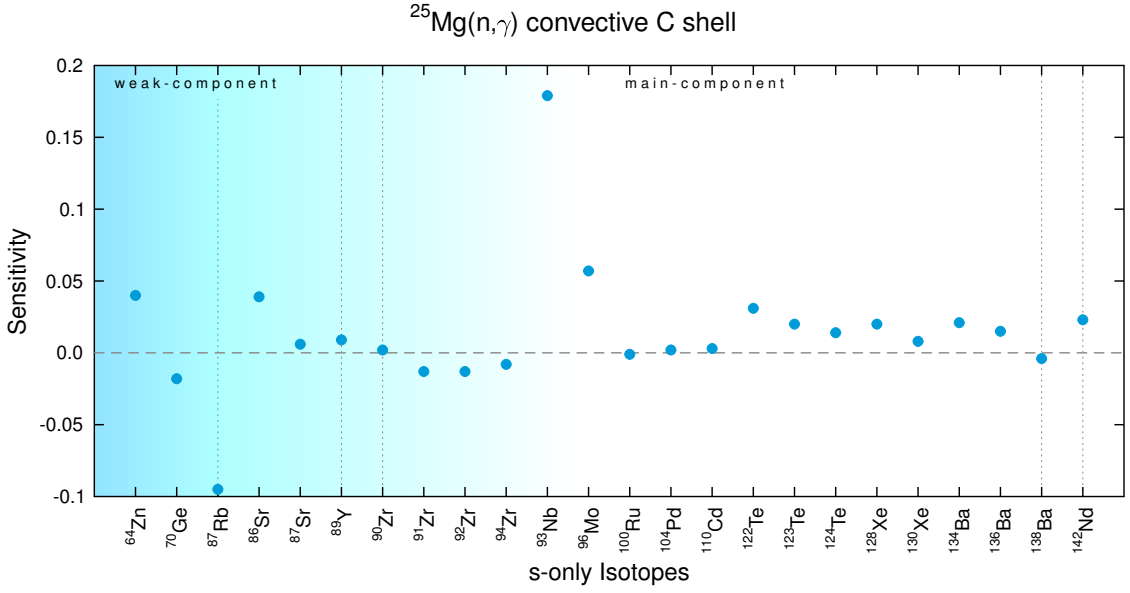

Figure A.123: Neutron poison reaction $^{25}\mathrm{Mg}(n, \gamma)$ during the convective carbon shell burning (table 3.20).

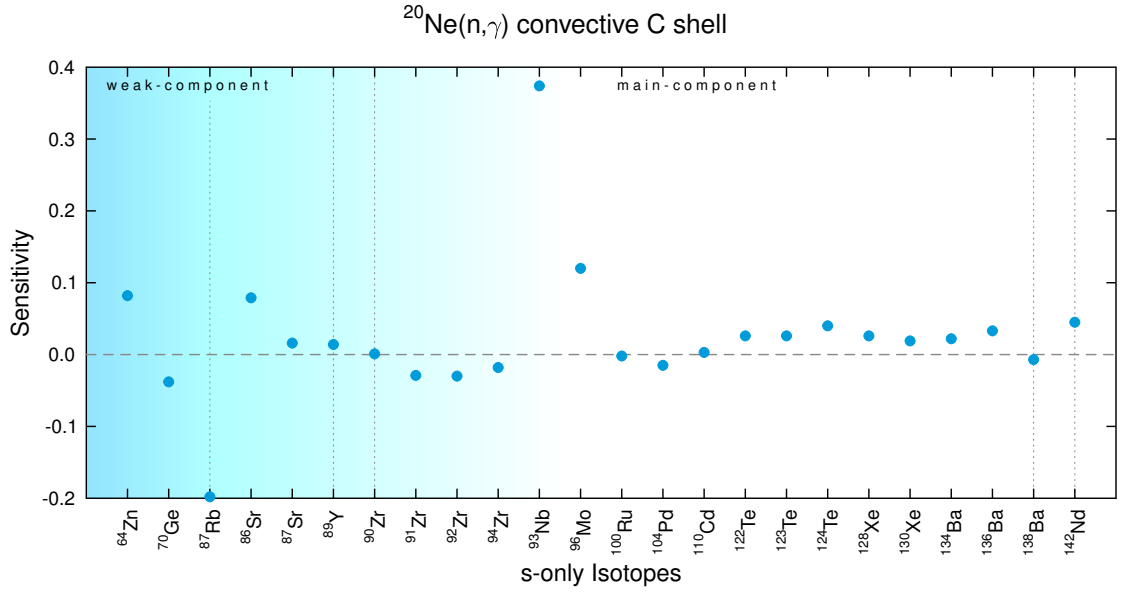

Figure A.124: Neutron poison reaction ^{20}Ne(n,γ) during the convective carbon shell burning (table 3.20).

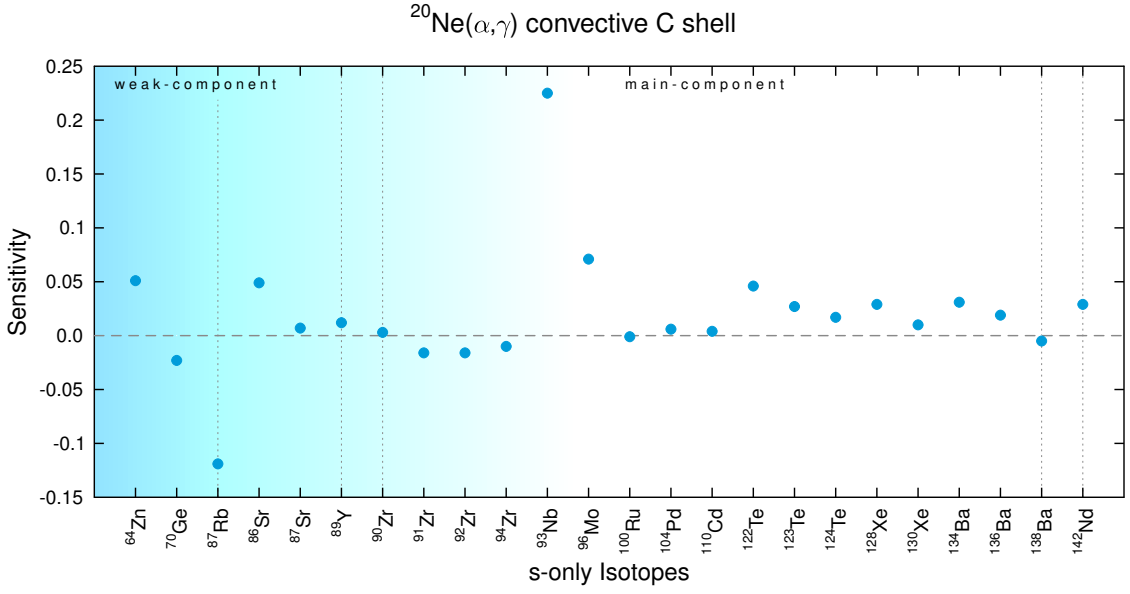

Figure A.125: Neutron poison reaction ^{20}Ne(α,γ) during the convective carbon shell burning (table 3.20).

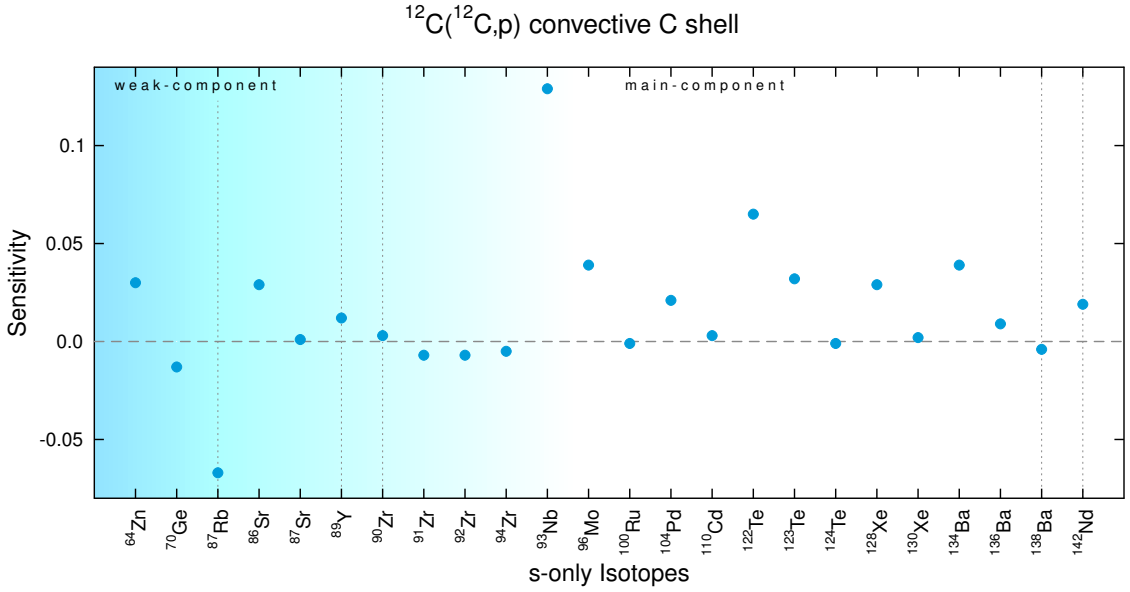

Figure A.126: Expected neutron poison reaction ^{12}C($^{12}C, p$) during the convective carbon shell burning (table 3.21). A small impact as neutron poison reaction can be recorded, but much less, than one would expect from a competing channel of a dominant neutron source.

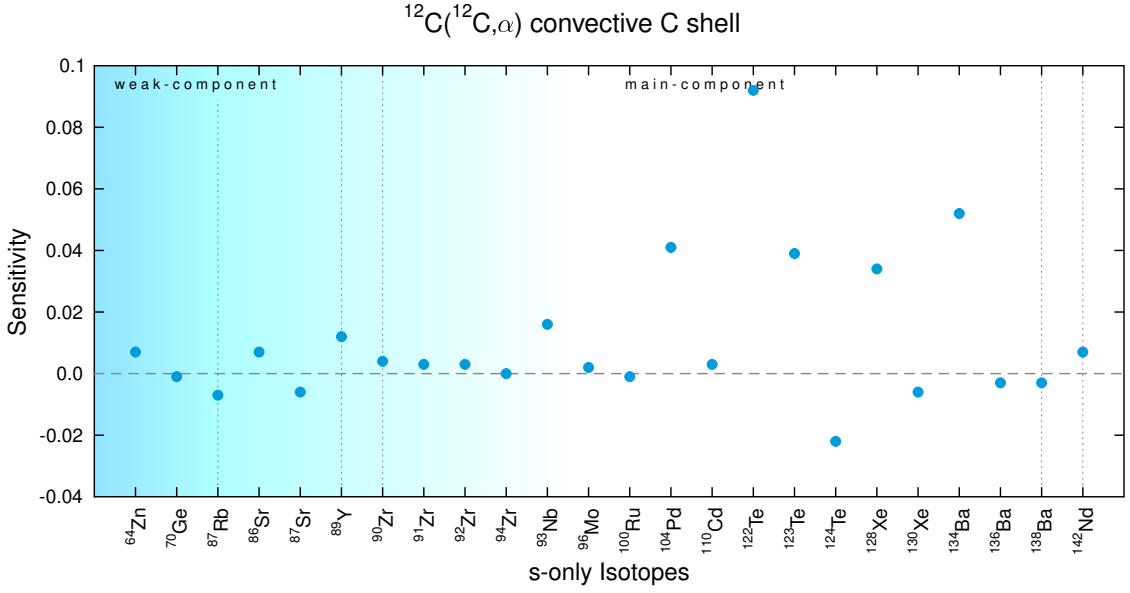

Figure A.127: Expected neutron poison reaction ^{12}C($^{12}C, \alpha$) during the convective carbon shell burning (table 3.21). A minimal impact as neutron poison reaction can be recorded, but much less, than one would expect from a competing channel of a dominant neutron source.

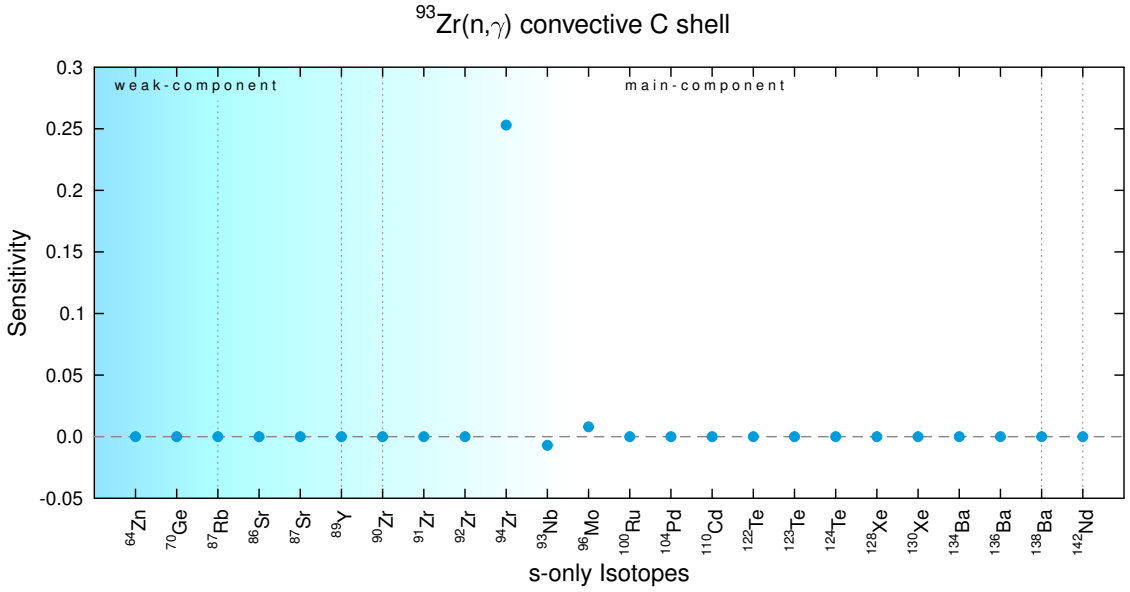

Figure A.128: Expected branching path ^{93}Zr(n,γ) during the convective carbon shell burning (table 3.22).

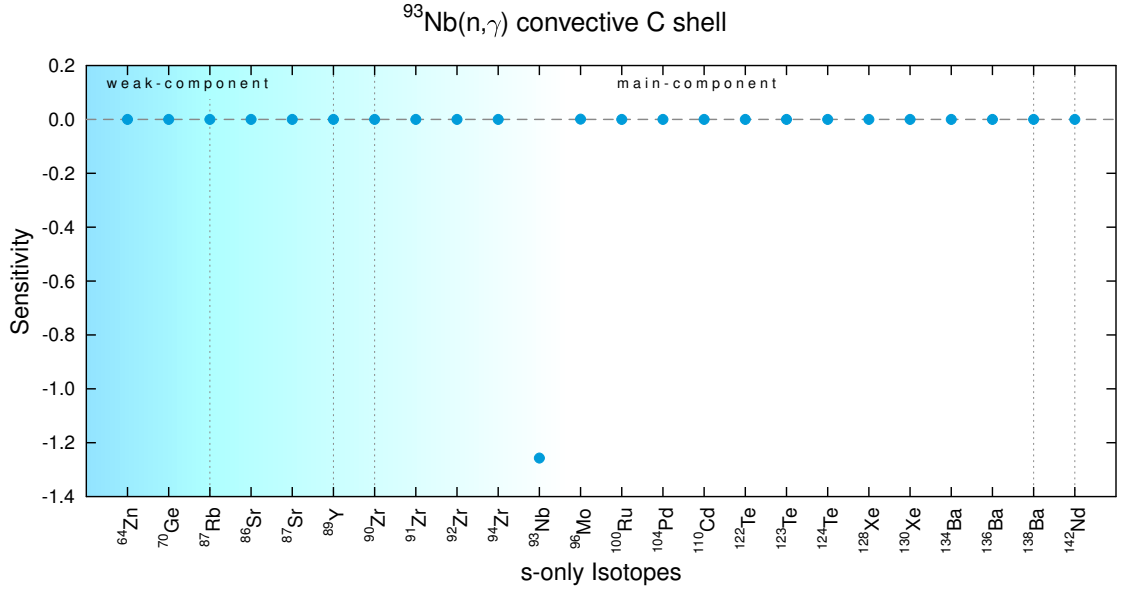

Figure A.129: Destruction path ^{93}Nb(n,γ) during the convective carbon shell burning (table 3.22).

A.3 *i* PROCESS

In this part of the appendix the local sensitivity table, initial abundances for the *i* process trajectories and remaining global sensitivity plots are listed for the *i* process.

LOCAL SENSITIVITIES DURING THE *i* PROCESS

Table A.8: Reactions with strongest local sensitivities during the *i* process. Filter criteria in chapter 2.3.3 on page 49.

Isotope	Most important reactions with respective sensitivities					
^{20}Ne	^{23}Na(p,γ)	-0.487	^{23}Na(p,α)	0.487	^{20}Ne(n,γ)	-0.440
^{21}Ne	^{21}Ne(n,γ)	-0.749	^{20}Ne(n,γ)	0.721	^{23}Na(p,γ)	-0.492
^{22}Ne	^{20}Ne(n,γ)	0.825	^{23}Na(p,γ)	-0.499	^{23}Na(p,α)	0.499
^{24}Mg	^{24}Na(β^-)	0.995	^{24}Na(n,γ)	-0.955	^{24}Mg(n,γ)	-0.853
^{25}Mg	^{25}Mg(n,γ)	-0.977	^{20}Ne(n,γ)	0.845	^{22}Ne(n,γ)	0.810
^{26}Mg	^{20}Ne(n,γ)	0.699	^{22}Ne(n,γ)	0.684	^{21}Ne(n,γ)	0.492
^{27}Al	^{27}Al(n,γ)	-0.951	^{26}Mg(n,γ)	0.697	^{20}Ne(n,γ)	0.679
^{28}Si	^{28}Si(n,γ)	-5.531	^{26}Mg(n,γ)	0.237	^{28}Al(β^-)	0.224
^{29}Si	^{28}Si(n,γ)	-1.984	^{29}Si(n,γ)	-1.023	^{26}Mg(n,γ)	0.489
^{30}Si	^{28}Si(n,γ)	-1.794	^{26}Mg(n,γ)	0.497	^{20}Ne(n,γ)	0.373
^{31}P	^{28}Si(n,γ)	-2.603	^{31}P (n,γ)	-1.454	^{31}Si(β^-)	0.972
^{32}S	^{28}Si(n,γ)	-2.767	^{32}S (n,γ)	-1.198	^{32}P (β^-)	0.999
^{33}S	^{33}P (β^-)	1.000	^{33}S (n,α)	-0.950	^{28}Si(n,γ)	-0.422
^{34}S	^{23}Na(p,γ)	0.150	^{23}Na(p,α)	-0.150	-	
^{36}S	^{23}Na(p,γ)	0.139	^{23}Na(p,α)	-0.139	-	
^{35}Cl	^{35}S (n,γ)	-1.027	^{35}S (β^-)	1.000	^{35}Cl(n,γ)	-0.882
^{37}Cl	^{37}S (n,γ)	-0.307	^{23}Na(p,γ)	0.140	^{23}Na(p,α)	-0.139
^{38}Ar	^{38}Cl(n,γ)	-0.981	^{38}Cl(β^-)	0.976	^{38}Ar(n,γ)	-0.968
^{40}Ar	^{40}Ar(n,γ)	-0.954	^{40}Cl(n,γ)	-0.464	^{40}Cl(β^-)	0.464
^{39}K	^{39}Ar(β^-)	1.000	^{39}K (n,γ)	-0.992	^{39}Ar(n,γ)	-0.815
^{41}K	^{41}K (n,γ)	-1.004	^{41}Ar(n,γ)	-0.985	^{41}Ar(β^-)	0.985
^{42}Ca	^{42}K (n,γ)	-1.008	^{42}K (β^-)	1.000	^{42}Ca(n,γ)	-0.995

Isotope	Most important reactions with respective sensitivities					
^{43}Ca	^{43}Ca(n,γ)	-1.007	^{43}K (n,γ)	-0.980	^{43}K (β^-)	0.979
^{44}Ca	^{44}Ca(n,γ)	-0.987	^{44}K (n,γ)	-0.969	^{44}K (β^-)	0.963
^{46}Ca	^{46}Ca(n,γ)	-0.986	^{46}K (β^-)	0.252	^{46}K (n,γ)	-0.249
^{48}Ca	^{23}Na(p,γ)	0.124	^{23}Na(p,α)	-0.124	-	
^{45}Sc	^{45}Sc(n,γ)	-1.006	^{45}Ca(n,γ)	-1.001	^{45}Ca(β^-)	1.000
^{47}Ti	^{47}Ti(n,γ)	-1.006	^{47}Sc(n,γ)	-1.004	^{47}Sc(β^-)	1.000
^{48}Ti	^{48}Ti(n,γ)	-1.002	^{47}Ca(β^-)	0.999	^{48}Sc(β^-)	0.819
^{49}Ti	^{49}Ti(n,γ)	-0.995	^{49}Sc(β^-)	0.934	^{49}Sc(n,γ)	-0.867
^{50}Ti	^{50}Ti(n,γ)	-0.892	^{50}Sc(β^-)	0.297	^{50}Sc(n,γ)	-0.283
^{51}V	^{51}V (n,γ)	-1.004	^{51}Ti(β^-)	0.719	^{51}Ti(n,γ)	-0.697
^{52}Cr	^{52}Cr(n,γ)	-0.959	^{52}V (n,γ)	-0.925	^{52}V (β^-)	0.925
^{53}Cr	^{53}Cr(n,γ)	-1.006	^{53}V (β^-)	0.465	^{53}V (n,γ)	-0.456
^{54}Cr	^{54}Cr(n,γ)	-0.970	^{54}V (β^-)	0.169	^{54}V (n,γ)	-0.167
^{55}Mn	^{55}Mn(n,γ)	-1.003	^{55}Cr(β^-)	0.768	^{55}Cr(n,γ)	-0.758
^{56}Fe	^{56}Mn(n,γ)	-1.001	^{56}Mn(β^-)	0.996	^{56}Fe(n,γ)	-0.964
^{57}Fe	^{57}Fe(n,γ)	-1.003	^{57}Mn(β^-)	0.659	^{57}Mn(n,γ)	-0.652
^{58}Fe	^{58}Fe(n,γ)	-0.990	^{34}P (n,γ)	0.127	^{34}P (β^-)	-0.123
^{59}Co	^{59}Co(n,γ)	-1.002	^{59}Fe(β^-)	1.000	^{59}Fe(n,γ)	-0.999
^{61}Ni	^{61}Ni(n,γ)	-1.005	^{61}Co(β^-)	0.995	^{61}Co(n,γ)	-0.992
^{62}Ni	^{62}Ni(n,γ)	-0.999	^{62}Co(n,γ)	-0.908	^{62}Co(β^-)	0.904
^{64}Ni	^{64}Ni(n,γ)	-0.976	^{34}P (n,γ)	0.140	^{34}P (β^-)	-0.136
^{63}Cu	^{63}Cu(n,γ)	-1.002	^{63}Ni(n,γ)	-1.000	^{63}Ni(β^-)	1.000
^{65}Cu	^{65}Cu(n,γ)	-0.996	^{65}Ni(β^-)	0.994	^{65}Ni(n,γ)	-0.992
^{66}Zn	^{66}Zn(n,γ)	-0.997	^{66}Cu(n,γ)	-0.986	^{66}Cu(β^-)	0.980
^{67}Zn	^{67}Zn(n,γ)	-1.005	^{66}Cu(n,γ)	-0.607	^{66}Cu(β^-)	0.603
^{68}Zn	^{68}Zn(n,γ)	-0.991	^{68}Cu(n,γ)	-0.952	^{68}Cu(β^-)	0.947
^{70}Zn	^{70}Zn(n,γ)	-0.991	^{70}Cu(n,γ)	-0.314	^{70}Cu(β^-)	0.313
^{69}Ga	^{69}Ga(n,γ)	-1.006	^{69}Zn(n,γ)	-1.002	^{69}Zn(β^-)	0.997
^{71}Ga	^{71}Ga(n,γ)	-1.007	^{71}Zn(n,γ)	-0.891	^{71}Zn(β^-)	0.890
^{70}Ge	^{70}Ga(n,γ)	-1.004	^{70}Ge(n,γ)	-1.003	^{69}Zn(n,γ)	-1.002
^{72}Ge	^{72}Ge(n,γ)	-1.003	^{72}Ga(n,γ)	-0.853	^{72}Ga(β^-)	0.845

Isotope	Most important reactions with respective sensitivities					
^{73}Ge	^{73}Ge(n,γ)	-1.008	^{73}Ga(n,γ)	-0.979	^{73}Ga(β^-)	0.975
^{74}Ge	^{74}Ge(n,γ)	-0.998	^{74}Ga(n,γ)	-0.951	^{74}Ga(β^-)	0.943
^{76}Ge	^{76}Ge(n,γ)	-0.992	^{75}Ga(β^-)	0.358	^{75}Ga(n,γ)	-0.347
^{75}As	^{75}As(n,γ)	-1.009	^{75}Ge(n,γ)	-1.005	^{75}Ge(β^-)	0.998
^{76}Se	^{76}As(n,γ)	-1.008	^{76}Se(n,γ)	-1.006	^{75}Ge(n,γ)	-1.005
^{77}Se	^{77}Se(n,γ)	-1.009	^{75}Ge(n,γ)	-0.971	^{75}Ge(β^-)	0.965
^{78}Se	^{78}Se(n,γ)	-1.001	^{78}As(n,γ)	-0.963	^{78}As(β^-)	0.955
^{80}Se	^{80}Se(n,γ)	-1.000	^{80}As(n,γ)	-0.756	^{80}As(β^-)	0.753
^{82}Se	^{82}Se(n,γ)	-0.972	^{34}P (n,γ)	0.164	^{34}P (β^-)	-0.158
^{81}Br	^{81}Br(n,γ)	-1.008	^{81}Se(n,γ)	-0.997	^{81}Se(β^-)	0.991
^{82}Kr	^{82}Br(n,γ)	-1.009	^{82}Kr(n,γ)	-1.004	^{82}Br(β^-)	1.000
^{83}Kr	^{83}Kr(n,γ)	-1.008	^{83}Br(n,γ)	-0.991	^{83}Br(β^-)	0.986
^{84}Kr	^{84}Kr(n,γ)	-0.996	^{84}Br(n,γ)	-0.989	^{84}Br(β^-)	0.981
^{86}Kr	^{86}Kr(n,γ)	-0.915	^{86}Br(β^-)	0.307	^{86}Br(n,γ)	-0.302
^{85}Rb	^{85}Rb(n,γ)	-1.007	^{85}Kr(n,γ)	-1.003	^{85}Kr(β^-)	1.000
^{87}Rb	^{87}Kr(β^-)	0.991	^{87}Kr(n,γ)	-0.982	^{87}Rb(n,γ)	-0.974
^{88}Sr	^{88}Rb(n,γ)	-1.001	^{88}Rb(β^-)	0.995	^{88}Sr(n,γ)	-0.933
^{89}Y	^{89}Sr(β^-)	1.000	^{89}Sr(n,γ)	-0.986	^{89}Y (n,γ)	-0.981
^{92}Zr	^{92}Y (n,γ)	-1.008	^{92}Y (β^-)	1.000	^{92}Zr(n,γ)	-0.993
^{94}Zr	^{94}Y (n,γ)	-1.000	^{94}Zr(n,γ)	-0.997	^{94}Y (β^-)	0.992
^{96}Zr	^{96}Zr(n,γ)	-0.964	^{96}Y (n,γ)	-0.633	^{96}Y (β^-)	0.632
^{97}Mo	^{97}Mo(n,γ)	-1.009	^{97}Nb(n,γ)	-1.007	^{97}Zr(β^-)	0.999
^{98}Mo	^{98}Nb(n,γ)	-1.007	^{98}Mo(n,γ)	-1.005	^{98}Nb(β^-)	0.998
^{100}Mo	^{100}Mo(n,γ)	-1.006	^{100}Nb(n,γ)	-0.530	^{100}Nb(β^-)	0.530
^{100}Ru	^{99}Mo(n,γ)	-1.008	^{100}Ru(n,γ)	-1.007	^{99}Mo(β^-)	1.000
^{101}Ru	^{101}Ru(n,γ)	-1.009	^{101}Tc(n,γ)	-1.004	^{101}Mo(n,γ)	-1.000
^{102}Ru	^{102}Ru(n,γ)	-1.007	^{102}Tc(n,γ)	-0.931	^{102}Tc(β^-)	0.922
^{104}Ru	^{104}Ru(n,γ)	-1.007	^{103}Tc(n,γ)	-0.890	^{103}Tc(β^-)	0.883
^{103}Rh	^{103}Ru(n,γ)	-1.009	^{103}Rh(n,γ)	-1.009	^{103}Ru(β^-)	1.000
^{106}Pd	^{106}Pd(n,γ)	-1.007	^{106}Rh(n,γ)	-0.971	^{106}Rh(β^-)	0.963
^{108}Pd	^{108}Pd(n,γ)	-1.007	^{108}Rh(n,γ)	-0.929	^{108}Rh(β^-)	0.920

Isotope	Most important reactions with respective sensitivities					
^{110}Pd	^{110}Pd(n,γ)	-1.007	^{110}Rh(n,γ)	-0.886	^{110}Rh(β^-)	0.878
^{109}Ag	^{109}Pd(n,γ)	-1.009	^{109}Ag(n,γ)	-1.009	^{109}Pd(β^-)	1.000
^{112}Cd	^{112}Cd(n,γ)	-1.007	^{112}Ag(n,γ)	-0.980	^{112}Ag(β^-)	0.972
^{113}Cd	^{113}Cd(n,γ)	-1.009	^{113}Ag(n,γ)	-0.794	^{113}Ag(β^-)	0.787
^{114}Cd	^{114}Cd(n,γ)	-1.006	^{114}Ag(n,γ)	-0.837	^{114}Ag(β^-)	0.832
^{116}Cd	^{116}Cd(n,γ)	-1.004	^{114}Ag(n,γ)	-0.638	^{114}Ag(β^-)	0.634
^{115}In	^{115}In(n,γ)	-1.009	^{115}Cd(n,γ)	-1.008	^{115}Cd(β^-)	1.000
^{116}Sn	^{115}Cd(n,γ)	-1.008	^{116}Sn(n,γ)	-1.003	^{115}Cd(β^-)	1.000
^{117}Sn	^{117}Sn(n,γ)	-1.008	^{115}Cd(n,γ)	-0.565	^{115}Cd(β^-)	0.561
^{118}Sn	^{118}In(n,γ)	-1.002	^{118}Sn(n,γ)	-1.001	^{118}In(β^-)	0.993
^{119}Sn	^{119}Sn(n,γ)	-1.007	^{119}In(n,γ)	-0.847	^{119}In(β^-)	0.839
^{120}Sn	^{120}Sn(n,γ)	-0.997	^{120}In(n,γ)	-0.985	^{120}In(β^-)	0.976
^{122}Sn	^{122}Sn(n,γ)	-0.992	^{122}In(n,γ)	-0.790	^{122}In(β^-)	0.784
^{124}Sn	^{124}Sn(n,γ)	-0.985	^{124}In(n,γ)	-0.345	^{124}In(β^-)	0.344
^{121}Sb	^{121}Sb(n,γ)	-1.009	^{121}Sn(n,γ)	-1.008	^{121}Sn(β^-)	1.000
^{123}Sb	^{123}Sb(n,γ)	-1.008	^{123}Sn(n,γ)	-1.002	^{123}Sn(β^-)	0.995
^{124}Te	^{124}Sb(n,γ)	-1.009	^{124}Te(n,γ)	-1.006	^{123}Sn(n,γ)	-1.002
^{125}Te	^{125}Te(n,γ)	-1.009	^{124}Sb(n,γ)	-1.008	^{123}Sn(n,γ)	-1.001
^{126}Te	^{126}Te(n,γ)	-1.003	^{126}Sb(n,γ)	-0.910	^{126}Sb(β^-)	0.901
^{128}Te	^{128}Te(n,γ)	-0.998	^{128}Sb(n,γ)	-0.993	^{128}Sb(β^-)	0.985
^{130}Te	^{130}Te(n,γ)	-0.981	^{130}Sb(n,γ)	-0.910	^{130}Sb(β^-)	0.906
^{132}Xe	^{132}Xe(n,γ)	-1.002	^{132}I (n,γ)	-0.999	^{132}I (β^-)	0.990
^{134}Xe	^{134}Xe(n,γ)	-1.013	^{134}I (n,γ)	-1.007	^{134}I (β^-)	0.995
^{136}Xe	^{136}Xe(n,γ)	-0.972	^{136}I (n,γ)	-0.326	^{136}I (β^-)	0.322
^{137}Ba	^{137}Ba(n,γ)	-1.009	^{137}Cs(n,γ)	-0.998	^{137}Cs(β^-)	0.990
^{138}Ba	^{138}Cs(n,γ)	-1.001	^{138}Cs(β^-)	0.991	^{138}Ba(n,γ)	-0.984
^{139}La	^{139}La(n,γ)	-1.006	^{139}Ba(n,γ)	-1.003	^{139}Ba(β^-)	0.995
^{140}Ce	^{140}La(n,γ)	-1.010	^{140}La(β^-)	1.000	^{140}Ce(n,γ)	-0.989
^{142}Ce	^{142}Ce(n,γ)	-1.004	^{142}La(n,γ)	-0.894	^{142}La(β^-)	0.885
^{145}Nd	^{145}Nd(n,γ)	-1.010	^{145}Pr(n,γ)	-1.009	^{145}Pr(β^-)	1.000
^{146}Nd	^{146}Nd(n,γ)	-1.008	^{146}Pr(n,γ)	-0.958	^{146}Pr(β^-)	0.948

Isotope	Most important reactions with respective sensitivities					
^{148}Nd	^{148}Nd(n,γ)	-1.009	^{148}Pr(n,γ)	-0.867	^{148}Pr(β^-)	0.858
^{150}Nd	^{150}Nd(n,γ)	-1.010	^{150}Pr(n,γ)	-0.801	^{150}Pr(β^-)	0.795
^{152}Sm	^{152}Sm(n,γ)	-1.010	^{152}Pm(n,γ)	-1.008	^{152}Pm(β^-)	0.998
^{154}Sm	^{154}Sm(n,γ)	-1.010	^{154}Pm(n,γ)	-0.825	^{154}Pm(β^-)	0.816
^{156}Gd	^{156}Eu(n,γ)	-1.010	^{156}Gd(n,γ)	-1.010	^{156}Eu(β^-)	1.000
^{157}Gd	^{157}Gd(n,γ)	-1.010	^{157}Eu(n,γ)	-0.605	^{157}Eu(β^-)	0.599
^{158}Gd	^{158}Gd(n,γ)	-1.009	^{158}Eu(n,γ)	-0.992	^{158}Eu(β^-)	0.982
^{160}Gd	^{160}Gd(n,γ)	-1.010	^{160}Eu(n,γ)	-0.953	^{160}Eu(β^-)	0.943
^{162}Dy	^{162}Dy(n,γ)	-1.010	^{162}Tb(n,γ)	-1.008	^{162}Tb(β^-)	0.998
^{163}Dy	^{163}Dy(n,γ)	-1.010	^{163}Tb(n,γ)	-0.792	^{163}Tb(β^-)	0.785
^{164}Dy	^{164}Dy(n,γ)	-1.009	^{164}Tb(n,γ)	-0.947	^{164}Tb(β^-)	0.938
^{165}Ho	^{165}Dy(n,γ)	-1.010	^{165}Ho(n,γ)	-1.010	^{165}Dy(β^-)	1.000
^{167}Er	^{167}Ho(n,γ)	-1.010	^{167}Er(n,γ)	-1.010	^{167}Dy(n,γ)	-1.002
^{168}Er	^{168}Er(n,γ)	-1.009	^{168}Ho(n,γ)	-1.004	^{168}Ho(β^-)	0.994
^{170}Er	^{170}Er(n,γ)	-1.009	^{170}Ho(n,γ)	-0.835	^{170}Ho(β^-)	0.827
^{173}Yb	^{173}Yb(n,γ)	-1.010	^{173}Tm(n,γ)	-1.009	^{173}Tm(β^-)	0.999
^{174}Yb	^{174}Yb(n,γ)	-1.009	^{174}Tm(n,γ)	-1.007	^{174}Tm(β^-)	0.997
^{176}Yb	^{176}Yb(n,γ)	-1.009	^{176}Tm(n,γ)	-0.810	^{176}Tm(β^-)	0.802
^{178}Hf	^{178}Lu(n,γ)	-1.009	^{178}Hf(n,γ)	-1.009	^{178}Lu(β^-)	0.999
^{179}Hf	^{179}Hf(n,γ)	-1.010	^{178}Yb(n,γ)	-0.630	^{178}Yb(β^-)	0.625
^{180}Hf	^{180}Hf(n,γ)	-1.009	^{180}Lu(n,γ)	-1.005	^{180}Lu(β^-)	0.995
^{181}Ta	^{181}Ta(n,γ)	-1.010	^{181}Hf(n,γ)	-1.009	^{181}Hf(β^-)	1.000
^{184}W	^{184}W (n,γ)	-1.009	^{184}Ta(n,γ)	-0.962	^{184}Ta(β^-)	0.952
^{186}W	^{186}W (n,γ)	-1.009	^{186}Ta(n,γ)	-0.933	^{186}Ta(β^-)	0.923
^{187}Re	^{187}W (n,γ)	-1.010	^{187}Re(n,γ)	-1.010	^{187}W (β^-)	1.000
^{190}Os	^{190}Os(n,γ)	-1.009	^{190}Re(n,γ)	-0.993	^{190}Re(β^-)	0.983
^{192}Os	^{192}Os(n,γ)	-1.009	^{192}Re(n,γ)	-0.922	^{192}Re(β^-)	0.914
^{193}Ir	^{193}Ir(n,γ)	-1.010	^{193}Os(n,γ)	-1.009	^{193}Os(β^-)	1.000
^{195}Pt	^{195}Pt(n,γ)	-1.010	^{195}Ir(n,γ)	-1.009	^{195}Os(n,γ)	-1.001
^{196}Pt	^{196}Pt(n,γ)	-1.008	^{195}Os(n,γ)	-0.593	^{195}Os(β^-)	0.587
^{198}Pt	^{198}Pt(n,γ)	-1.008	^{198}Ir(n,γ)	-0.821	^{198}Ir(β^-)	0.816

Isotope	Most important reactions with respective sensitivities					
^{200}Hg	^{200}Hg(n,γ)	-1.007	^{200}Au(n,γ)	-0.880	^{200}Au(β^-)	0.873
^{201}Hg	^{201}Hg(n,γ)	-1.009	^{201}Au(n,γ)	-1.001	^{201}Au(β^-)	0.993
^{202}Hg	^{202}Hg(n,γ)	-1.006	^{201}Pt(n,γ)	-0.896	^{201}Pt(β^-)	0.890
^{204}Hg	^{204}Hg(n,γ)	-1.008	^{204}Au(n,γ)	-0.515	^{204}Au(β^-)	0.514
^{203}Tl	^{203}Hg(n,γ)	-1.009	^{203}Tl(n,γ)	-1.009	^{203}Hg(β^-)	1.000
^{205}Tl	^{205}Tl(n,γ)	-1.007	^{205}Hg(n,γ)	-0.832	^{205}Hg(β^-)	0.831
^{206}Pb	^{206}Pb(n,γ)	-0.994	^{206}Tl(n,γ)	-0.911	^{206}Tl(β^-)	0.906
^{207}Pb	^{207}Pb(n,γ)	-0.989	^{207}Tl(β^-)	0.365	^{207}Tl(n,γ)	-0.346
^{208}Pb	^{207}Tl(β^-)	0.251	^{134}Te(n,γ)	0.229	^{208}Pb(n,γ)	-0.221
^{209}Bi	^{209}Pb(β^-)	0.983	^{209}Pb(n,γ)	-0.897	^{209}Bi(n,γ)	-0.881

INITIAL ABUNDANCES FOR THE *i* PROCESS

Table A.9: Initial abundances for the *i* process simulations. Added abundances give unity.

isotope	initial abundance	isotope	initial abundance	isotope	initial abundance
^{OT}Pr	$2.00000 \cdot 10^{-01}$	^{2}H	$5.33206 \cdot 10^{-06}$	^{3}He	$1.63537 \cdot 10^{-05}$
^{4}He	$9.85178 \cdot 10^{-02}$	^{7}Li	$1.64299 \cdot 10^{-11}$	^{11}B	$1.00063 \cdot 10^{-09}$
^{12}C	$5.00000 \cdot 10^{-01}$	^{13}C	$8.00237 \cdot 10^{-06}$	^{14}N	$1.90260 \cdot 10^{-04}$
^{15}N	$7.49449 \cdot 10^{-07}$	^{16}O	$2.00000 \cdot 10^{-01}$	^{17}O	$6.54344 \cdot 10^{-07}$
^{18}O	$3.72566 \cdot 10^{-06}$	^{19}F	$1.56159 \cdot 10^{-07}$	^{20}Ne	$2.91113 \cdot 10^{-04}$
^{21}Ne	$7.32738 \cdot 10^{-07}$	^{22}Ne	$2.35461 \cdot 10^{-05}$	^{23}Na	$7.70091 \cdot 10^{-06}$
^{24}Mg	$1.45415 \cdot 10^{-04}$	^{25}Mg	$1.91816 \cdot 10^{-05}$	^{26}Mg	$2.19471 \cdot 10^{-05}$
^{27}Al	$1.43277 \cdot 10^{-05}$	^{28}Si	$1.89166 \cdot 10^{-04}$	^{29}Si	$9.94835 \cdot 10^{-06}$
^{30}Si	$6.78413 \cdot 10^{-06}$	^{31}P	$1.60759 \cdot 10^{-06}$	^{32}S	$9.50101 \cdot 10^{-05}$
^{33}S	$7.73373 \cdot 10^{-07}$	^{34}S	$4.47807 \cdot 10^{-06}$	^{36}S	$1.91234 \cdot 10^{-08}$
^{35}Cl	$1.89839 \cdot 10^{-06}$	^{37}Cl	$6.41728 \cdot 10^{-07}$	^{36}Ar	$1.04342 \cdot 10^{-05}$
^{38}Ar	$2.00252 \cdot 10^{-06}$	^{40}Ar	$3.37139 \cdot 10^{-09}$	^{39}K	$9.89841 \cdot 10^{-07}$
^{40}K	$1.27041 \cdot 10^{-10}$	^{41}K	$7.50978 \cdot 10^{-08}$	^{40}Ca	$1.79218 \cdot 10^{-05}$
^{42}Ca	$1.25594 \cdot 10^{-07}$	^{43}Ca	$2.68297 \cdot 10^{-08}$	^{44}Ca	$4.24210 \cdot 10^{-07}$
^{46}Ca	$8.50417 \cdot 10^{-10}$	^{48}Ca	$4.14856 \cdot 10^{-08}$	^{45}Sc	$1.14295 \cdot 10^{-08}$
^{46}Ti	$6.82297 \cdot 10^{-08}$	^{47}Ti	$6.28506 \cdot 10^{-08}$	^{48}Ti	$6.36269 \cdot 10^{-07}$
^{49}Ti	$4.76570 \cdot 10^{-08}$	^{50}Ti	$4.66158 \cdot 10^{-08}$	^{50}V	$2.82620 \cdot 10^{-10}$

isotope	initial abundance	isotope	initial abundance	isotope	initial abundance
^{51}V	$1.15159 \cdot 10^{-07}$	^{50}Cr	$2.14681 \cdot 10^{-07}$	^{52}Cr	$4.30534 \cdot 10^{-06}$
^{53}Cr	$4.97555 \cdot 10^{-07}$	^{54}Cr	$1.26178 \cdot 10^{-07}$	^{55}Mn	$3.05616 \cdot 10^{-06}$
^{54}Fe	$2.01369 \cdot 10^{-05}$	^{56}Fe	$3.27814 \cdot 10^{-04}$	^{57}Fe	$7.70584 \cdot 10^{-06}$
^{58}Fe	$1.04350 \cdot 10^{-06}$	^{59}Co	$1.11088 \cdot 10^{-06}$	^{58}Ni	$1.51790 \cdot 10^{-05}$
^{60}Ni	$6.04852 \cdot 10^{-06}$	^{61}Ni	$2.67307 \cdot 10^{-07}$	^{62}Ni	$8.66264 \cdot 10^{-07}$
^{64}Ni	$2.27729 \cdot 10^{-07}$	^{63}Cu	$1.59992 \cdot 10^{-07}$	^{65}Cu	$7.35605 \cdot 10^{-08}$
^{64}Zn	$2.80478 \cdot 10^{-07}$	^{66}Zn	$1.65944 \cdot 10^{-07}$	^{67}Zn	$2.47556 \cdot 10^{-08}$
^{68}Zn	$1.14901 \cdot 10^{-07}$	^{70}Zn	$3.91114 \cdot 10^{-09}$	^{69}Ga	$7.12188 \cdot 10^{-09}$
^{71}Ga	$4.86362 \cdot 10^{-09}$	^{70}Ge	$1.27922 \cdot 10^{-08}$	^{72}Ge	$1.71408 \cdot 10^{-08}$
^{73}Ge	$4.84825 \cdot 10^{-09}$	^{74}Ge	$2.28908 \cdot 10^{-08}$	^{76}Ge	$4.86894 \cdot 10^{-09}$
^{75}As	$3.31036 \cdot 10^{-09}$	^{74}Se	$3.18381 \cdot 10^{-10}$	^{76}Se	$3.44494 \cdot 10^{-09}$
^{77}Se	$2.84521 \cdot 10^{-09}$	^{78}Se	$8.97376 \cdot 10^{-09}$	^{80}Se	$1.92064 \cdot 10^{-08}$
^{82}Se	$3.46491 \cdot 10^{-09}$	^{79}Br	$3.29101 \cdot 10^{-09}$	^{81}Br	$3.28299 \cdot 10^{-09}$
^{78}Kr	$1.21792 \cdot 10^{-10}$	^{80}Kr	$8.04007 \cdot 10^{-10}$	^{82}Kr	$4.12054 \cdot 10^{-09}$
^{83}Kr	$4.13499 \cdot 10^{-09}$	^{84}Kr	$2.06161 \cdot 10^{-08}$	^{86}Kr	$6.38401 \cdot 10^{-09}$
^{85}Rb	$5.52792 \cdot 10^{-09}$	^{87}Rb	$2.18232 \cdot 10^{-09}$	^{84}Sr	$8.77940 \cdot 10^{-11}$
^{86}Sr	$1.58958 \cdot 10^{-09}$	^{87}Sr	$1.20842 \cdot 10^{-09}$	^{88}Sr	$1.36282 \cdot 10^{-08}$
^{89}Y	$3.26741 \cdot 10^{-09}$	^{90}Zr	$4.07811 \cdot 10^{-09}$	^{91}Zr	$8.99424 \cdot 10^{-10}$
^{92}Zr	$1.38920 \cdot 10^{-09}$	^{94}Zr	$1.43877 \cdot 10^{-09}$	^{96}Zr	$2.36640 \cdot 10^{-10}$
^{93}Nb	$5.53729 \cdot 10^{-10}$	^{92}Mo	$2.56995 \cdot 10^{-10}$	^{94}Mo	$1.63653 \cdot 10^{-10}$
^{95}Mo	$2.84763 \cdot 10^{-10}$	^{96}Mo	$3.01416 \cdot 10^{-10}$	^{97}Mo	$1.74510 \cdot 10^{-10}$
^{98}Mo	$4.45297 \cdot 10^{-10}$	^{100}Mo	$1.81384 \cdot 10^{-10}$	^{96}Ru	$8.33205 \cdot 10^{-11}$
^{98}Ru	$2.86816 \cdot 10^{-11}$	^{99}Ru	$1.97801 \cdot 10^{-10}$	^{100}Ru	$1.97303 \cdot 10^{-10}$
^{101}Ru	$2.69845 \cdot 10^{-10}$	^{102}Ru	$5.04011 \cdot 10^{-10}$	^{104}Ru	$3.03285 \cdot 10^{-10}$
^{103}Rh	$3.07363 \cdot 10^{-10}$	^{102}Pd	$1.15349 \cdot 10^{-11}$	^{104}Pd	$1.28450 \cdot 10^{-10}$
^{105}Pd	$2.59951 \cdot 10^{-10}$	^{106}Pd	$3.21188 \cdot 10^{-10}$	^{108}Pd	$3.16831 \cdot 10^{-10}$
^{110}Pd	$1.42934 \cdot 10^{-10}$	^{107}Ag	$1.09359 \cdot 10^{-10}$	^{109}Ag	$1.03499 \cdot 10^{-10}$
^{106}Cd	$1.76616 \cdot 10^{-11}$	^{108}Cd	$1.28123 \cdot 10^{-11}$	^{110}Cd	$1.83134 \cdot 10^{-10}$
^{111}Cd	$1.89386 \cdot 10^{-10}$	^{112}Cd	$3.60238 \cdot 10^{-10}$	^{113}Cd	$1.84062 \cdot 10^{-10}$
^{114}Cd	$4.36571 \cdot 10^{-10}$	^{116}Cd	$1.15812 \cdot 10^{-10}$	^{113}In	$4.36664 \cdot 10^{-11}$
^{115}In	$9.91924 \cdot 10^{-10}$	^{112}Sn	$2.46179 \cdot 10^{-11}$	^{114}Sn	$1.70061 \cdot 10^{-11}$
^{115}Sn	$8.82494 \cdot 10^{-12}$	^{116}Sn	$3.81695 \cdot 10^{-10}$	^{117}Sn	$2.03299 \cdot 10^{-10}$
^{118}Sn	$6.47029 \cdot 10^{-10}$	^{119}Sn	$2.31260 \cdot 10^{-10}$	^{120}Sn	$8.85360 \cdot 10^{-10}$
^{122}Sn	$1.27838 \cdot 10^{-10}$	^{124}Sn	$1.62495 \cdot 10^{-10}$	^{121}Sb	$1.56709 \cdot 10^{-10}$
^{123}Sb	$1.19133 \cdot 10^{-10}$	^{120}Te	$4.03893 \cdot 10^{-12}$	^{122}Te	$1.11339 \cdot 10^{-10}$
^{123}Te	$3.91566 \cdot 10^{-11}$	^{124}Te	$2.09374 \cdot 10^{-10}$	^{125}Te	$3.12868 \cdot 10^{-10}$
^{126}Te	$8.37220 \cdot 10^{-10}$	^{128}Te	$1.42202 \cdot 10^{-09}$	^{130}Te	$1.54050 \cdot 10^{-09}$
^{127}I	$9.30289 \cdot 10^{-10}$	^{124}Xe	$6.74257 \cdot 10^{-12}$	^{126}Xe	$5.94843 \cdot 10^{-12}$

isotope	initial abundance	isotope	initial abundance	isotope	initial abundance
^{128}Xe	$1.20318 \cdot 10^{-10}$	^{129}Xe	$1.49315 \cdot 10^{-09}$	^{130}Xe	$2.40011 \cdot 10^{-10}$
^{131}Xe	$1.20377 \cdot 10^{-09}$	^{132}Xe	$1.46667 \cdot 10^{-09}$	^{134}Xe	$5.45627 \cdot 10^{-10}$
^{136}Xe	$4.51157 \cdot 10^{-10}$	^{133}Cs	$3.53725 \cdot 10^{-10}$	^{130}Ba	$4.60514 \cdot 10^{-12}$
^{132}Ba	$4.47269 \cdot 10^{-12}$	^{134}Ba	$1.08442 \cdot 10^{-10}$	^{135}Ba	$2.97965 \cdot 10^{-10}$
^{136}Ba	$3.57593 \cdot 10^{-10}$	^{137}Ba	$5.15219 \cdot 10^{-10}$	^{138}Ba	$3.31288 \cdot 10^{-09}$
^{138}La	$3.79975 \cdot 10^{-13}$	^{139}La	$4.24070 \cdot 10^{-10}$	^{136}Ce	$2.17704 \cdot 10^{-12}$
^{138}Ce	$2.98103 \cdot 10^{-12}$	^{140}Ce	$1.06570 \cdot 10^{-09}$	^{142}Ce	$1.35823 \cdot 10^{-10}$
^{141}Pr	$1.63694 \cdot 10^{-10}$	^{142}Nd	$2.46055 \cdot 10^{-10}$	^{143}Nd	$1.11213 \cdot 10^{-10}$
^{144}Nd	$2.18928 \cdot 10^{-10}$	^{145}Nd	$7.67821 \cdot 10^{-11}$	^{146}Nd	$1.59933 \cdot 10^{-10}$
^{148}Nd	$5.41986 \cdot 10^{-11}$	^{150}Nd	$5.37826 \cdot 10^{-11}$	^{144}Sm	$1.02517 \cdot 10^{-11}$
^{147}Sm	$5.10542 \cdot 10^{-11}$	^{148}Sm	$3.85359 \cdot 10^{-11}$	^{149}Sm	$4.76951 \cdot 10^{-11}$
^{150}Sm	$2.56412 \cdot 10^{-11}$	^{152}Sm	$9.41571 \cdot 10^{-11}$	^{154}Sm	$8.11623 \cdot 10^{-11}$
^{151}Eu	$5.41140 \cdot 10^{-11}$	^{153}Eu	$5.98539 \cdot 10^{-11}$	^{152}Gd	$9.20322 \cdot 10^{-13}$
^{154}Gd	$1.00224 \cdot 10^{-11}$	^{155}Gd	$6.84544 \cdot 10^{-11}$	^{156}Gd	$9.52753 \cdot 10^{-11}$
^{157}Gd	$7.33294 \cdot 10^{-11}$	^{158}Gd	$1.17093 \cdot 10^{-10}$	^{160}Gd	$1.04389 \cdot 10^{-10}$
^{159}Tb	$6.85822 \cdot 10^{-11}$	^{156}Dy	$2.72977 \cdot 10^{-13}$	^{158}Dy	$4.73961 \cdot 10^{-13}$
^{160}Dy	$1.16990 \cdot 10^{-11}$	^{161}Dy	$9.51331 \cdot 10^{-11}$	^{162}Dy	$1.29134 \cdot 10^{-10}$
^{163}Dy	$1.26824 \cdot 10^{-10}$	^{164}Dy	$1.44462 \cdot 10^{-10}$	^{165}Ho	$1.20864 \cdot 10^{-10}$
^{162}Er	$4.27612 \cdot 10^{-13}$	^{164}Er	$5.08410 \cdot 10^{-12}$	^{166}Er	$1.07496 \cdot 10^{-10}$
^{167}Er	$7.37793 \cdot 10^{-11}$	^{168}Er	$8.67154 \cdot 10^{-11}$	^{170}Er	$8.77477 \cdot 10^{-11}$
^{169}Tm	$3.82561 \cdot 10^{-11}$	^{168}Yb	$5.94383 \cdot 10^{-13}$	^{170}Yb	$1.40649 \cdot 10^{-11}$
^{171}Yb	$6.64566 \cdot 10^{-11}$	^{172}Yb	$1.02187 \cdot 10^{-10}$	^{173}Yb	$7.59442 \cdot 10^{-11}$
^{174}Yb	$1.50730 \cdot 10^{-10}$	^{176}Yb	$6.11192 \cdot 10^{-11}$	^{175}Lu	$4.43080 \cdot 10^{-11}$
^{176}Lu	$1.18200 \cdot 10^{-12}$	^{174}Hf	$4.84037 \cdot 10^{-13}$	^{176}Hf	$1.58673 \cdot 10^{-11}$
^{177}Hf	$5.65246 \cdot 10^{-11}$	^{178}Hf	$8.33954 \cdot 10^{-11}$	^{179}Hf	$4.18720 \cdot 10^{-11}$
^{180}Hf	$1.08442 \cdot 10^{-10}$	^{180}Ta	$3.38838 \cdot 10^{-15}$	^{181}Ta	$2.76974 \cdot 10^{-11}$
^{180}W	$6.28845 \cdot 10^{-13}$	^{182}W	$1.40639 \cdot 10^{-10}$	^{183}W	$7.63860 \cdot 10^{-11}$
^{184}W	$1.64419 \cdot 10^{-10}$	^{186}W	$1.54185 \cdot 10^{-10}$	^{185}Re	$2.02162 \cdot 10^{-11}$
^{187}Re	$4.50033 \cdot 10^{-11}$	^{184}Os	$2.32433 \cdot 10^{-13}$	^{186}Os	$1.88940 \cdot 10^{-11}$
^{187}Os	$1.96136 \cdot 10^{-11}$	^{188}Os	$1.59361 \cdot 10^{-10}$	^{189}Os	$1.95330 \cdot 10^{-10}$
^{190}Os	$3.19335 \cdot 10^{-10}$	^{192}Os	$5.01175 \cdot 10^{-10}$	^{191}Ir	$3.86572 \cdot 10^{-10}$
^{193}Ir	$6.57405 \cdot 10^{-10}$	^{190}Pt	$2.55971 \cdot 10^{-13}$	^{192}Pt	$1.48487 \cdot 10^{-11}$
^{194}Pt	$6.31968 \cdot 10^{-10}$	^{195}Pt	$6.51885 \cdot 10^{-10}$	^{196}Pt	$4.88864 \cdot 10^{-10}$
^{198}Pt	$1.40153 \cdot 10^{-10}$	^{197}Au	$4.56331 \cdot 10^{-10}$	^{196}Hg	$9.18351 \cdot 10^{-13}$
^{198}Hg	$6.02681 \cdot 10^{-11}$	^{199}Hg	$1.02532 \cdot 10^{-10}$	^{200}Hg	$1.41053 \cdot 10^{-10}$
^{201}Hg	$8.09019 \cdot 10^{-11}$	^{202}Hg	$1.84204 \cdot 10^{-10}$	^{204}Hg	$4.27646 \cdot 10^{-11}$
^{203}Tl	$1.07767 \cdot 10^{-10}$	^{205}Tl	$2.59782 \cdot 10^{-10}$	^{204}Pb	$9.15267 \cdot 10^{-11}$
^{206}Pb	$8.73650 \cdot 10^{-10}$	^{207}Pb	$1.05852 \cdot 10^{-09}$	^{208}Pb	$2.76352 \cdot 10^{-09}$

isotope	initial abundance	isotope	initial abundance	isotope	initial abundance
^{209}Bi	$2.11330 \cdot 10^{-10}$				

GLOBAL SENSITIVITIES DURING THE *i* PROCESS

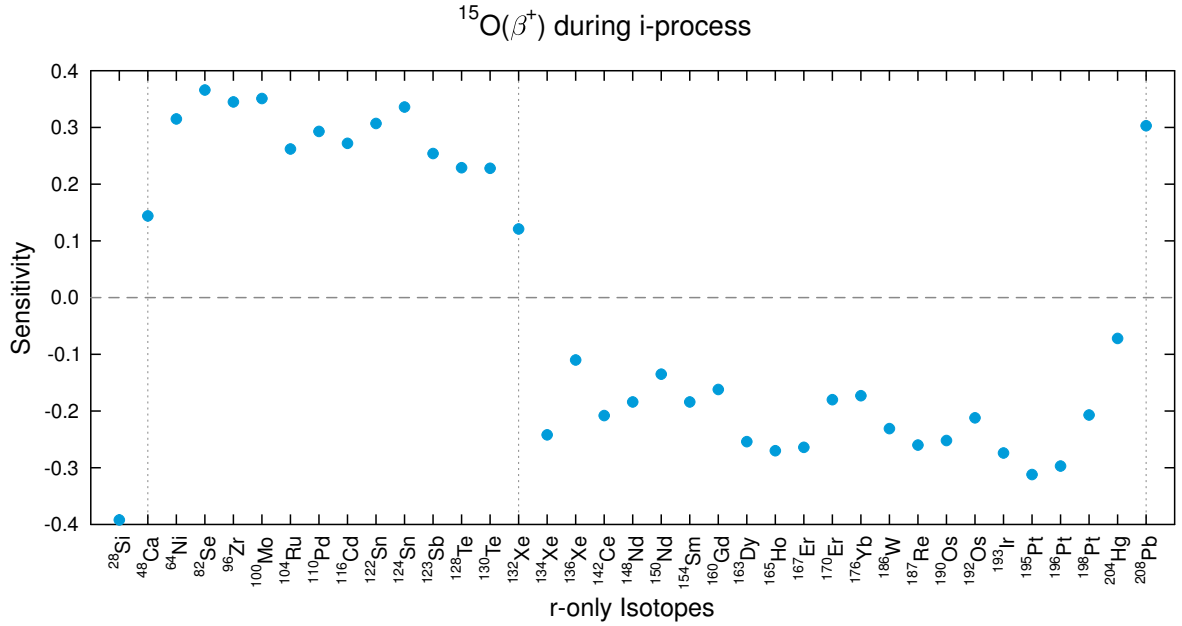

Figure A.130: Neutron donator reaction ^{15}O(β^+) during the *i* process (table 3.24). The β^+-decay is the second last step in the CNO cycle before an α-particle is released, which feeds the ^{13}C(α, n) reaction.

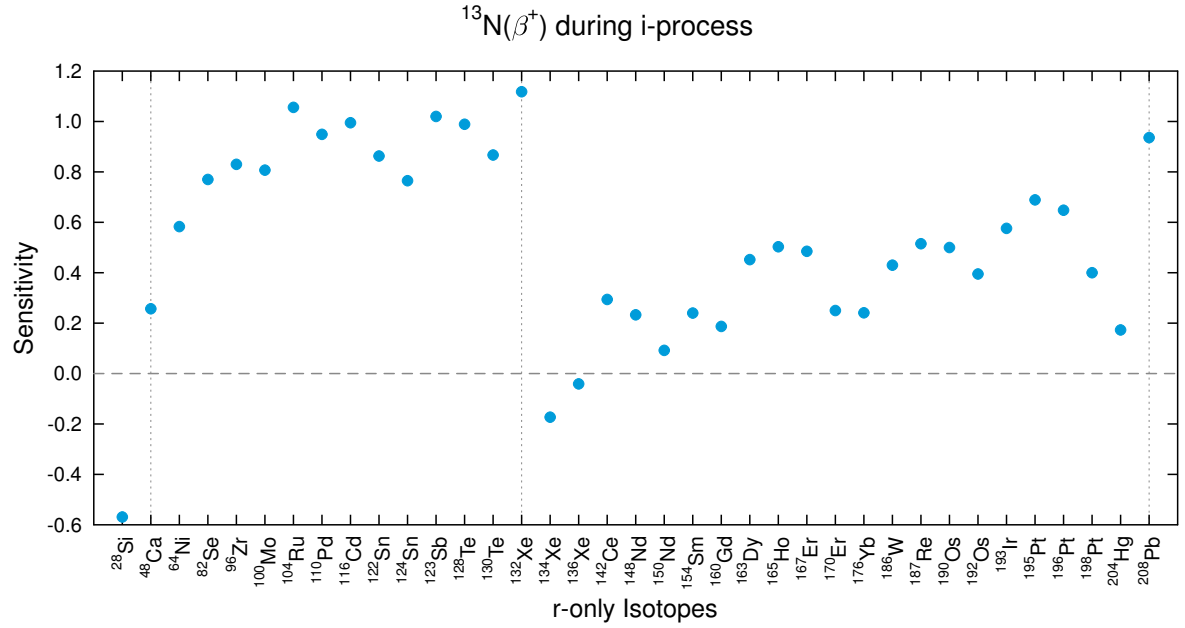

Figure A.131: Neutron donator reaction ^{13}N(β^+) during the *i* process (table 3.24). The β^+-decay of ^{13}N creates the neutron source ^{13}C. The effect from the neutron donator reaction ^{13}N(β^+) is not as strong as the ^{13}C(α, n) reaction. Therefore only ^{134}Xe and ^{136}Xe are depleted from the second plateau, whereas the other isotopes show still a positive sensitivity.

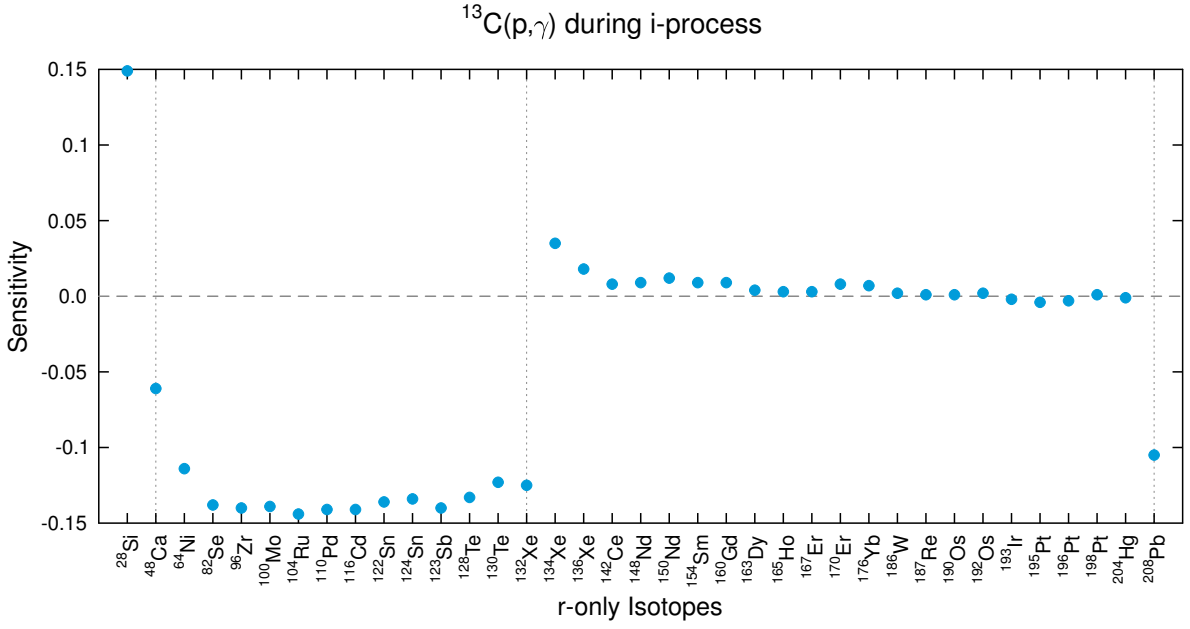

Figure A.132: Neutron poison reaction ^{13}C(p, γ) during the *i* process (table 3.25). The proton capture on ^{13}C competes with the α capture, which releases neutrons.

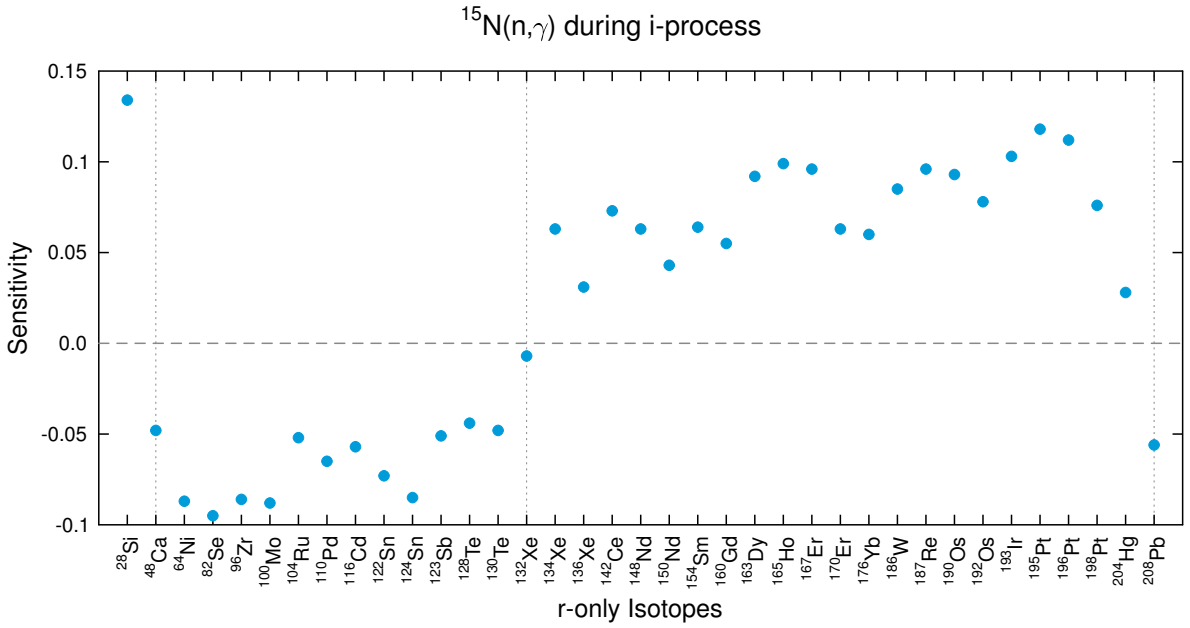

Figure A.133: Neutron poison reaction ^{15}N(n,γ) during the *i* process (table 3.25). The neutron capture on ^{15}N is not part of the *i* process path, since seed isotopes have mass numbers higher than 20. ^{15}N(n,γ) steals neutrons and is a breakout from the CNO cycle, which would otherwise release an α-particle.

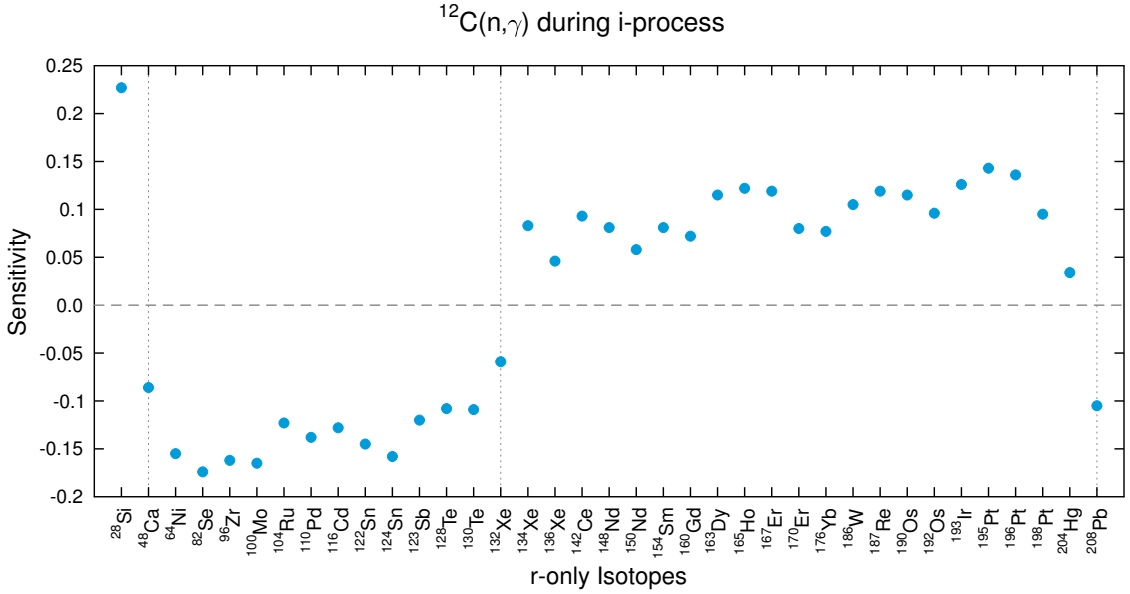

Figure A.134: Neutron poison reaction ^{12}C(n,γ) during the *i* process (table 3.25).

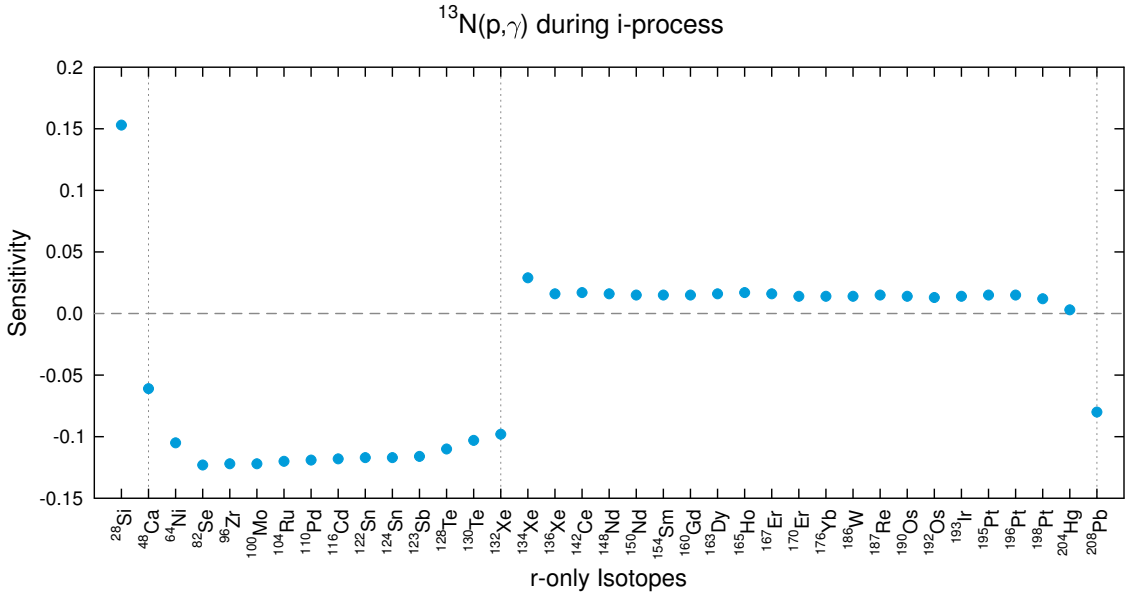

Figure A.135: Neutron poison reaction ^{13}N(p,γ) during the *i* process (table 3.25).

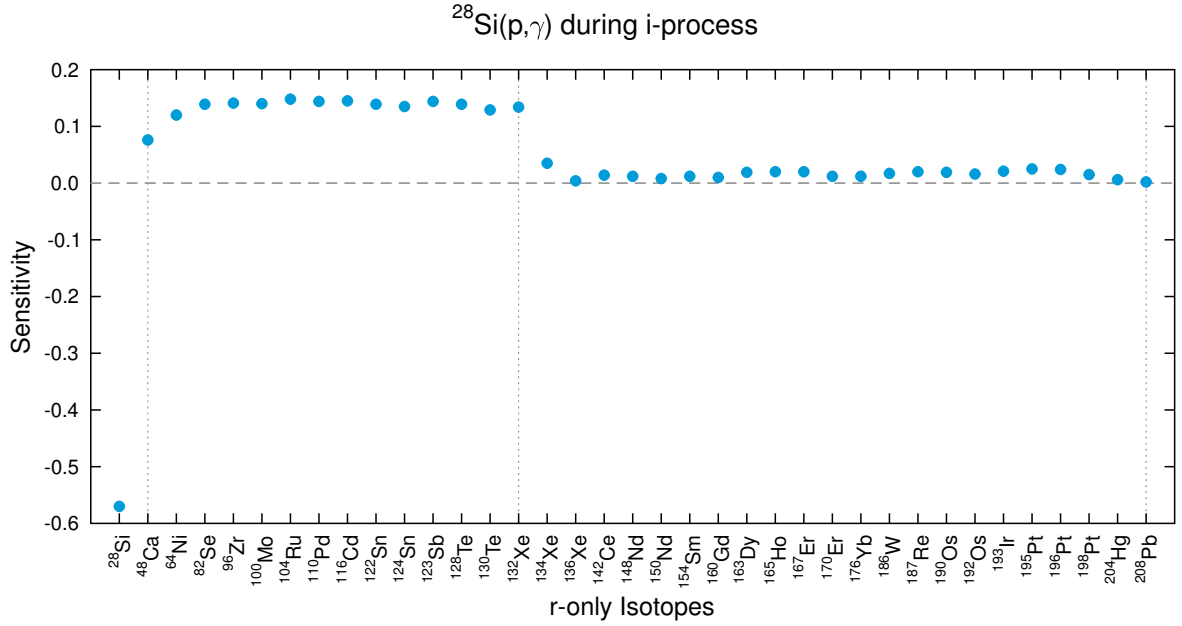

Figure A.136: Competing capture reaction ^{28}Si(p,γ) during the *i* process (table 3.26). The proton capture on ^{28}Si with subsequent β^+-decay produces ^{29}Si without the absorption of a free neutron.

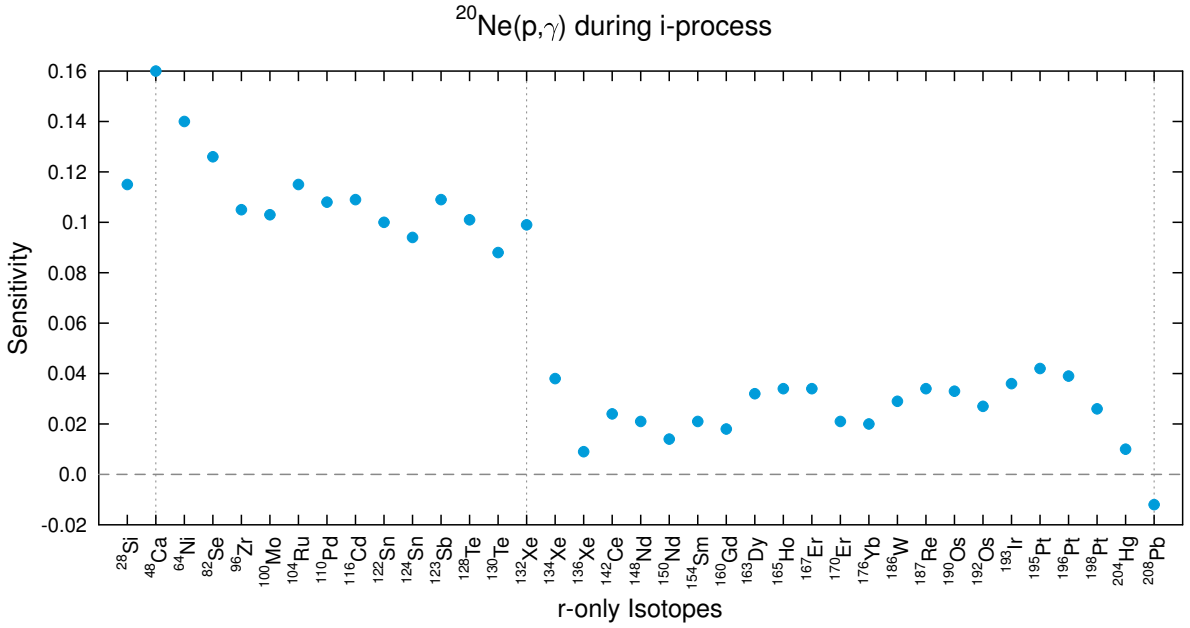

Figure A.137: Competing capture reaction ^{20}Ne(p,γ) during the *i* process (table 3.26). The proton capture on ^{20}Ne with subsequent β^+-decay produces ^{21}Ne without the absorption of a free neutron.

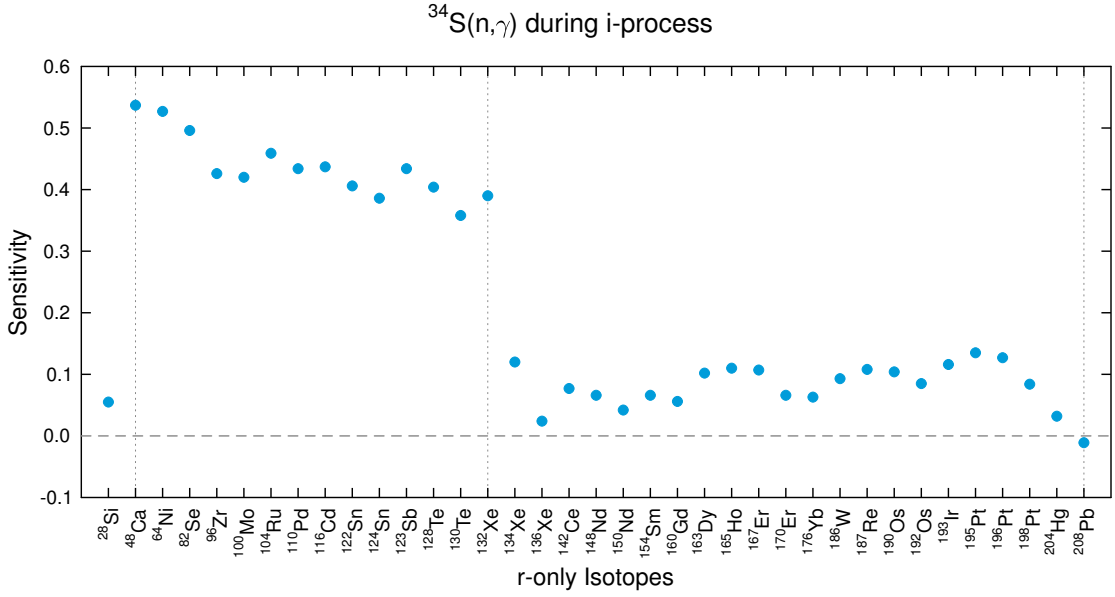

Figure A.138: Competing capture reaction ^{34}S(n,γ) during the *i* process (table 3.26).

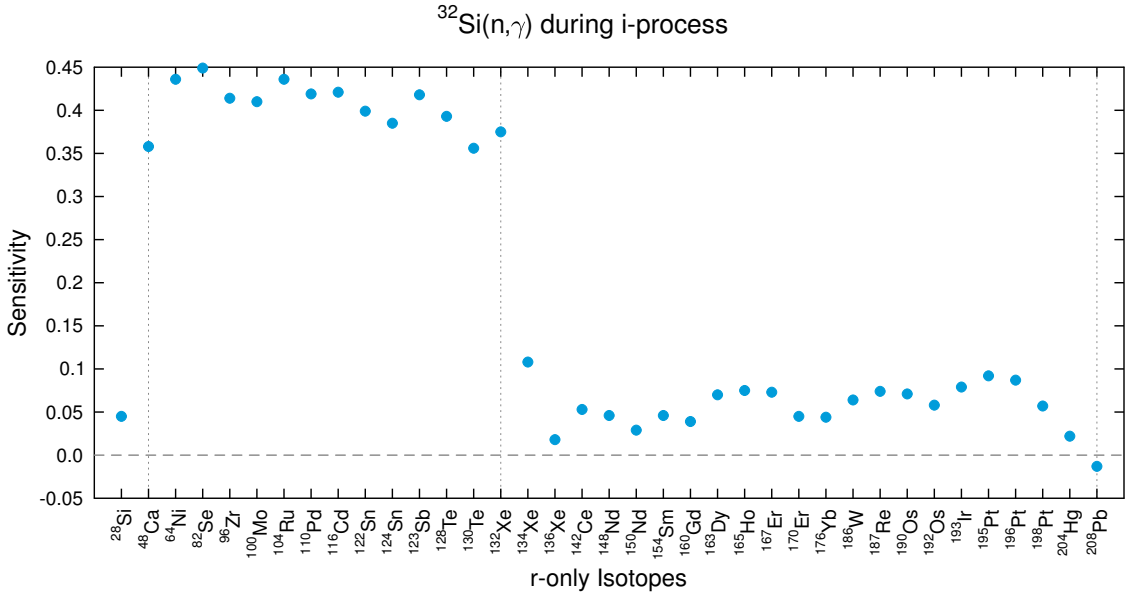

Figure A.139: Competing capture reaction $^{32}\mathrm{Si}(n,\gamma)$ during the *i* process (table 3.26).

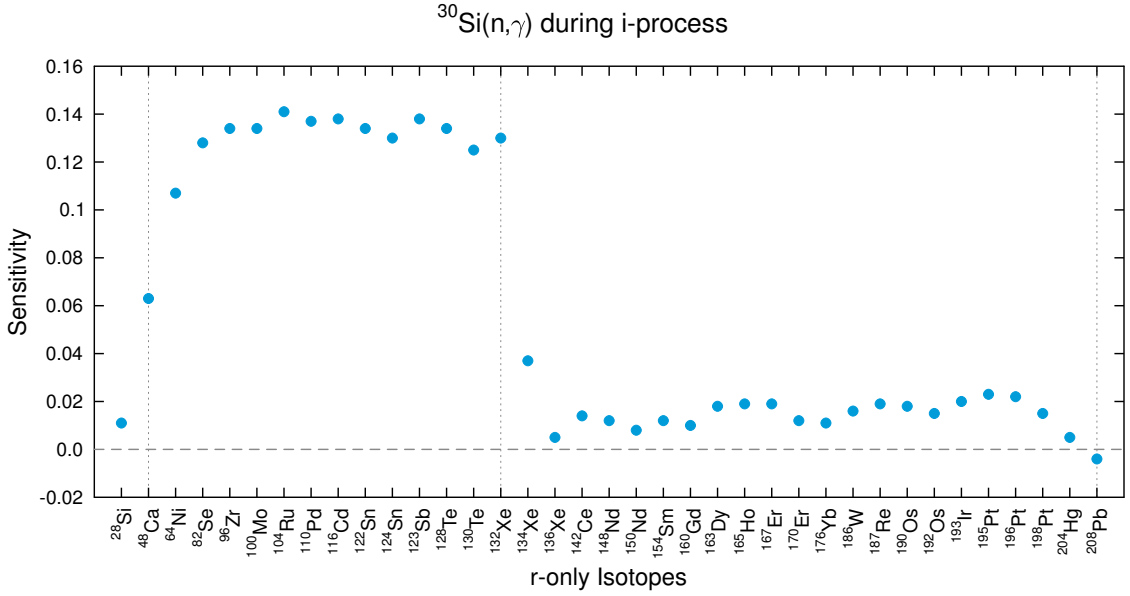

Figure A.140: Competing capture reaction $^{30}\mathrm{Si}(n,\gamma)$ during the *i* process (table 3.26).

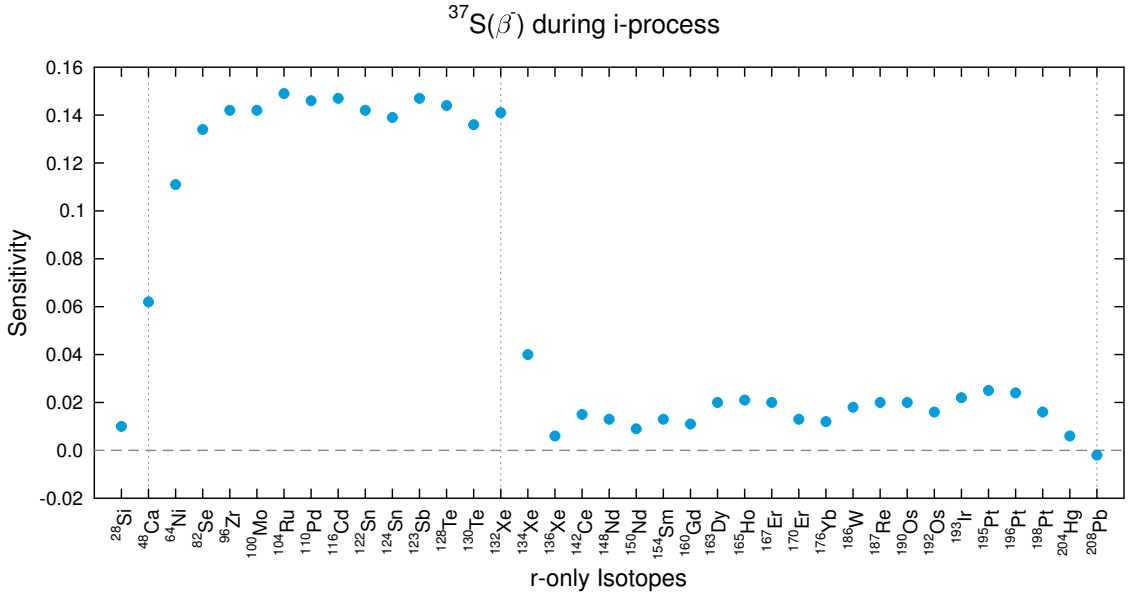

Figure A.141: Competing capture reaction ^{37}S(β^-) during the *i* process (table 3.26).

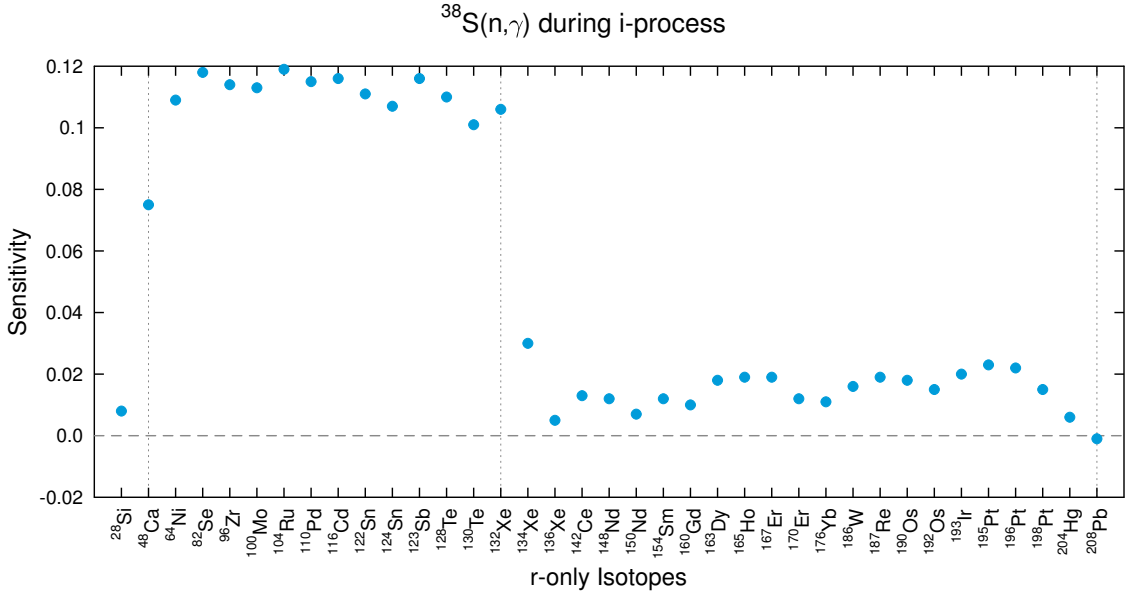

Figure A.142: Competing capture reaction ^{38}S(n,γ) during the *i* process (table 3.26).

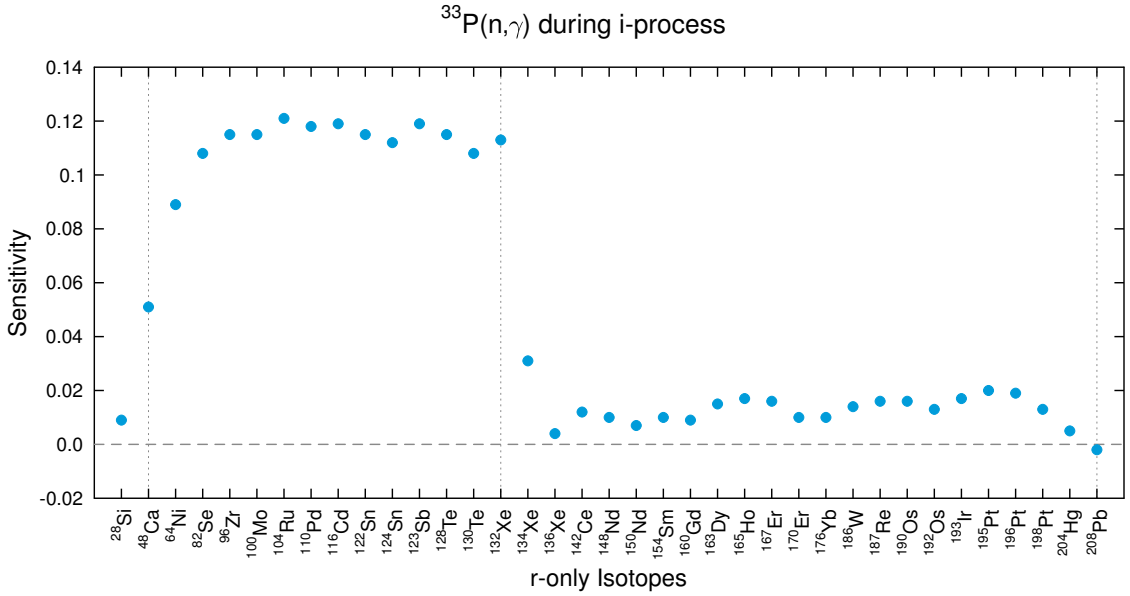

Figure A.143: Competing capture reaction $^{33}\mathrm{P}(n,\gamma)$ during the *i* process (table 3.26).

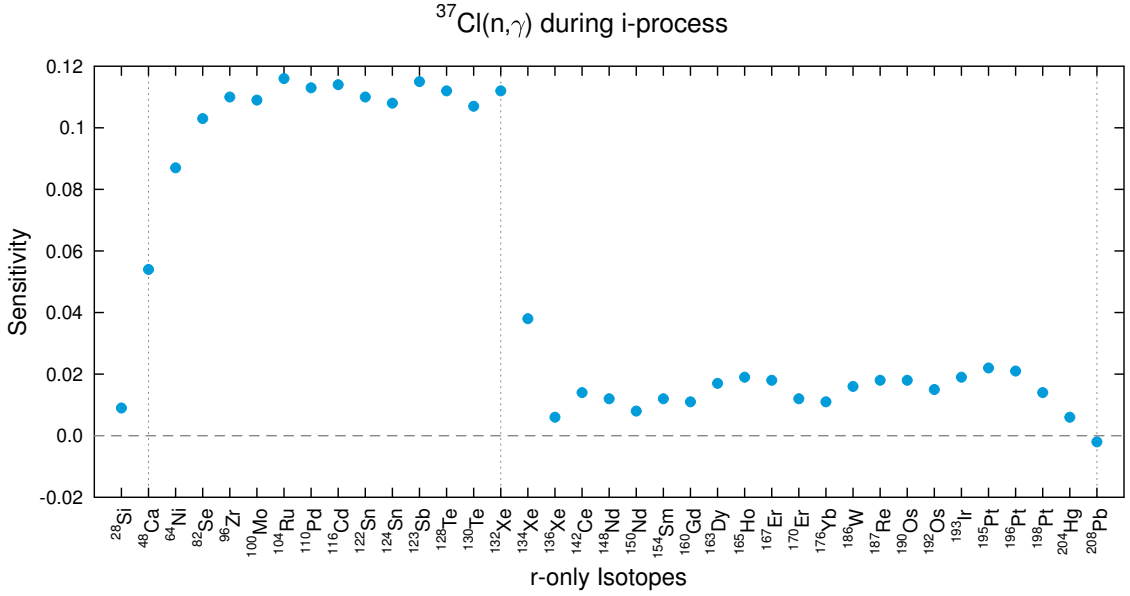

Figure A.144: Competing capture reaction $^{37}\mathrm{Cl}(n,\gamma)$ during the *i* process (table 3.26).

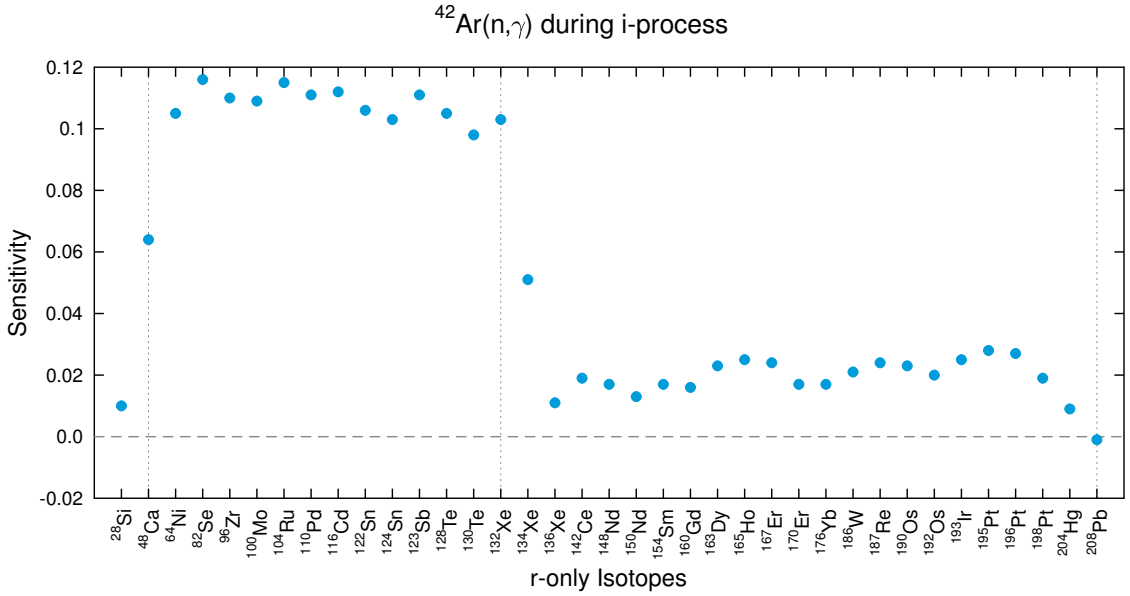

Figure A.145: Competing capture reaction ^{42}Ar(n,γ) during the *i* process (table 3.26).

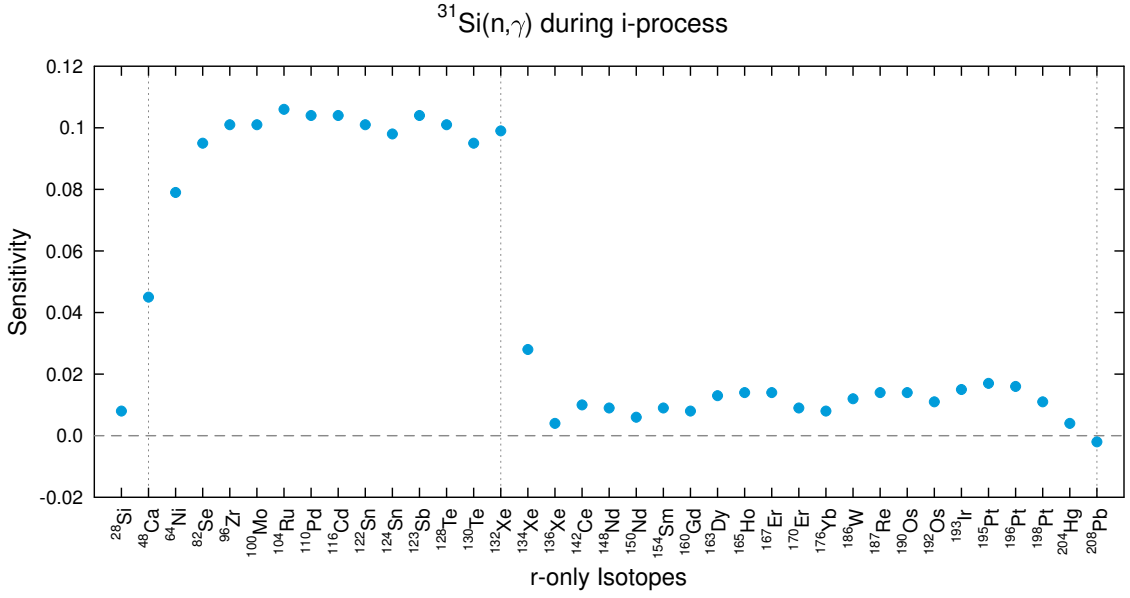

Figure A.146: Competing capture reaction ^{31}Si(n,γ) during the *i* process (table 3.26).

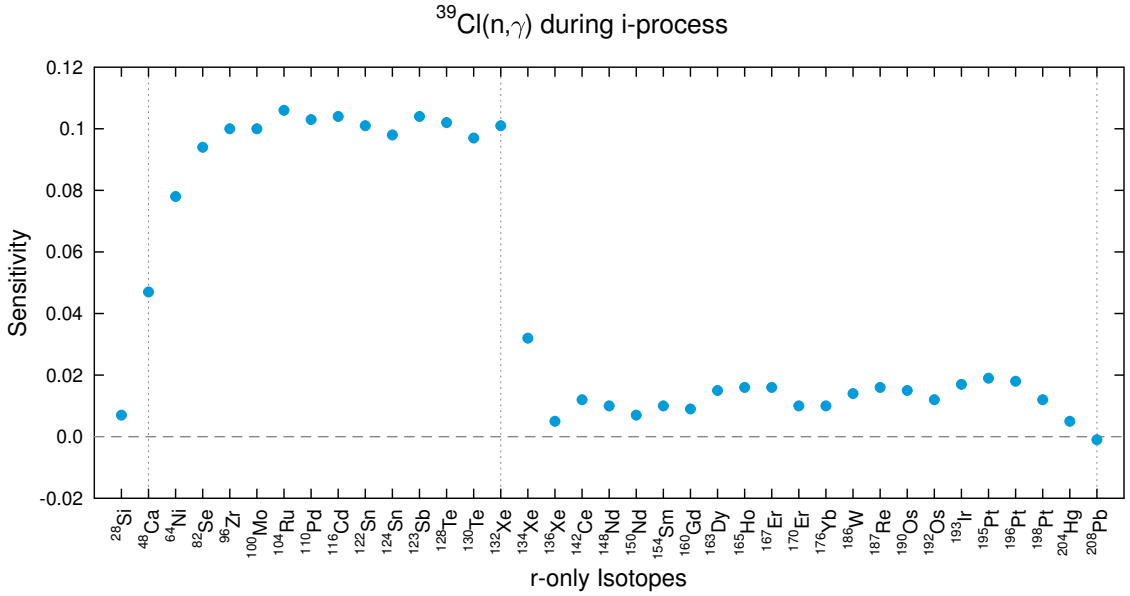

Figure A.147: Competing capture reaction ^{39}Cl(n,γ) during the *i* process (table 3.26).

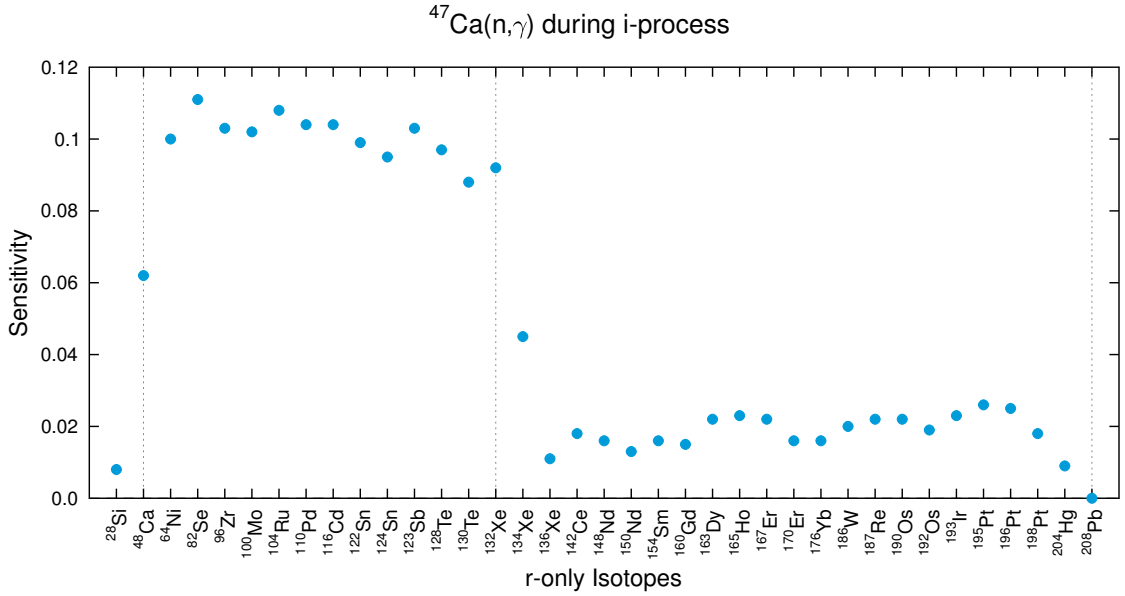

Figure A.148: Competing capture reaction $^{47}\mathrm{Ca}(n,\gamma)$ during the *i* process (table 3.26).

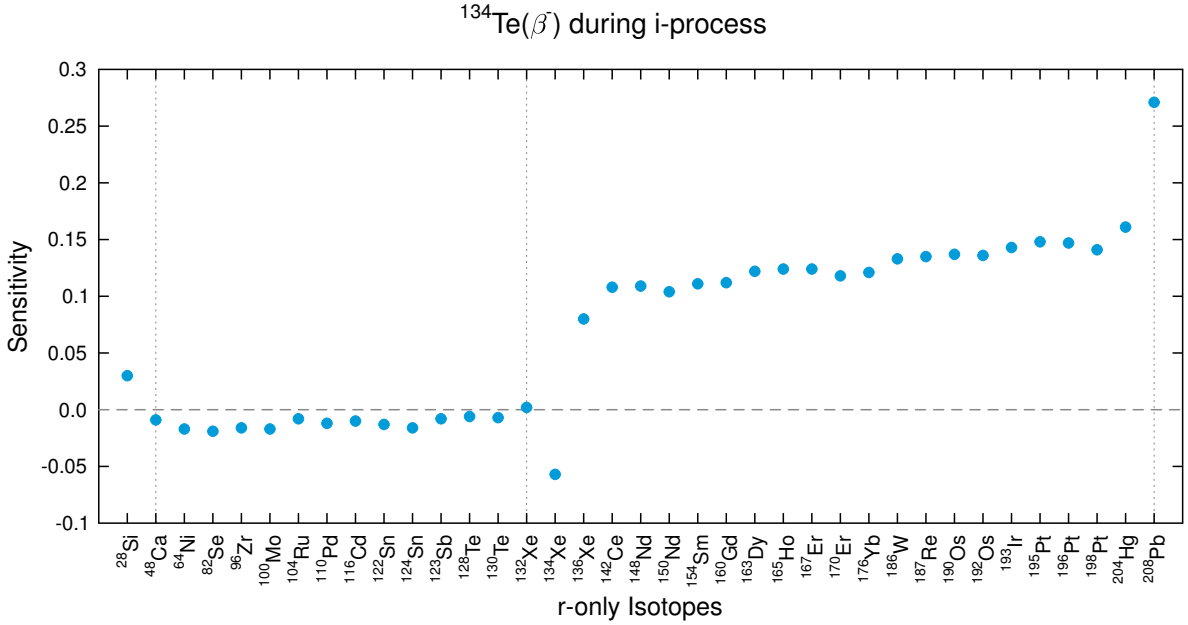

Figure A.149: Bottleneck reaction $^{134}\mathrm{Te}(\beta^-)$ during the *i* process (table 3.27). The β-decay of ^{134}Te feeds the $^{135}\mathrm{I}(n,\gamma)$ reaction (figure 3.37).

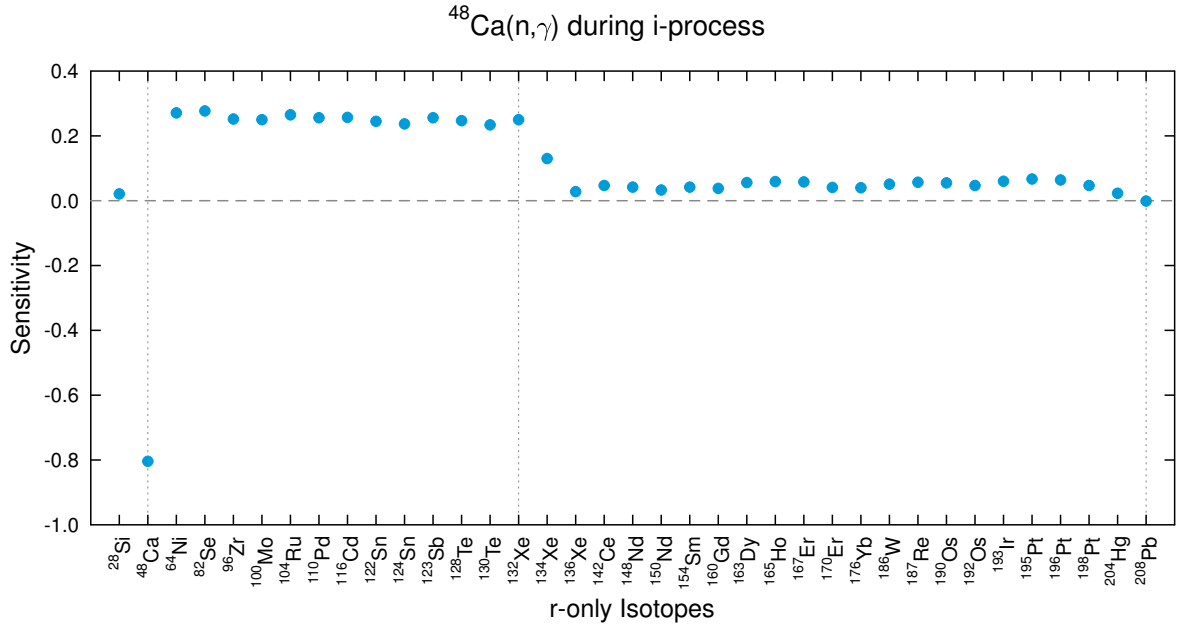

Figure A.150: Bottleneck reaction ^{48}Ca(n,γ) during the *i* process (table 3.27). The overcoming of the double magic nuclei ^{48}Ca is crucial for the evolution of the first *i* process plateau.

A.4 LEPP

In this part of the appendix the remaining sensitivity plots are listed for the LEPP isotopes.

LEPP SENSITIVITIES DURING THE WEAK *S* PROCESS

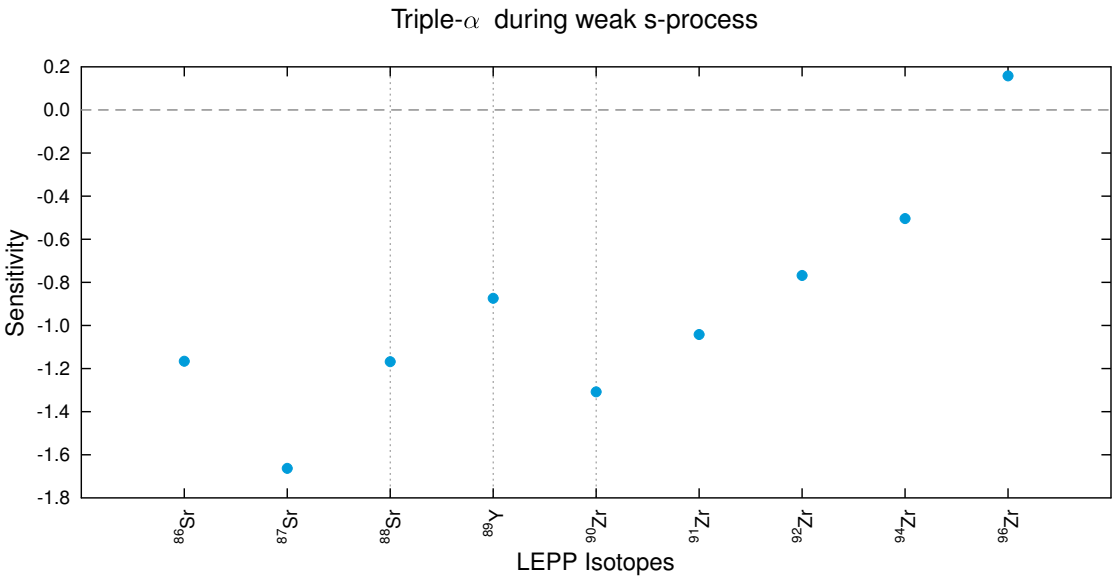

Figure A.151: Triple-α process during the weak *s* process on LEPP isotopes. (table 3.28). The sensitivities of the LEPP isotopes are plotted. The vertical dotted grey lines symbolize neutron magic nuclei.

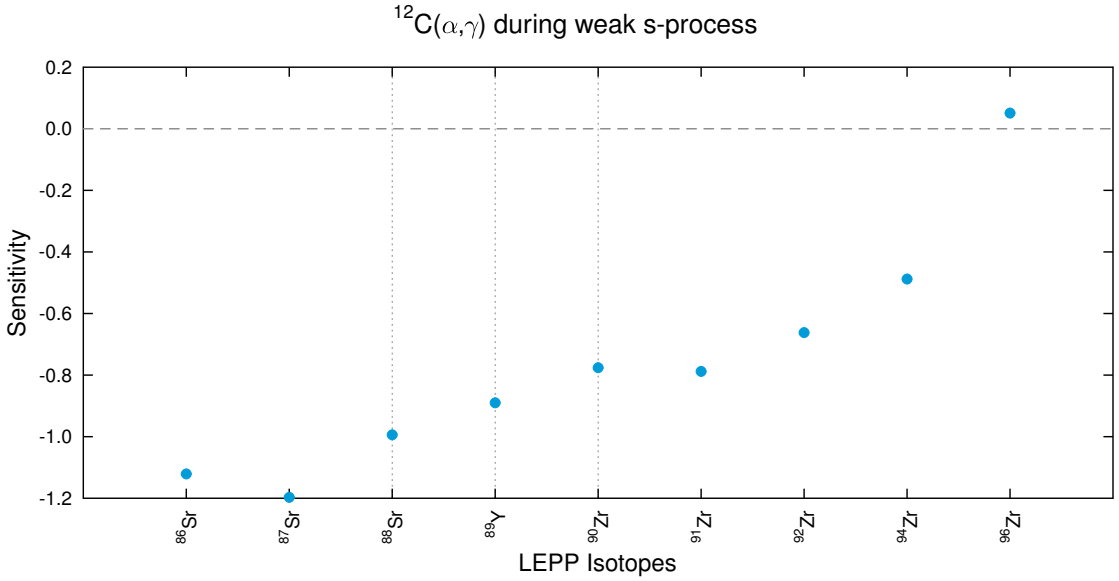

Figure A.152: ^{12}C(α,γ) during the weak *s* process on LEPP isotopes. (table 3.28). The sensitivities of the LEPP isotopes are plotted. The vertical dotted grey lines symbolize neutron magic nuclei.

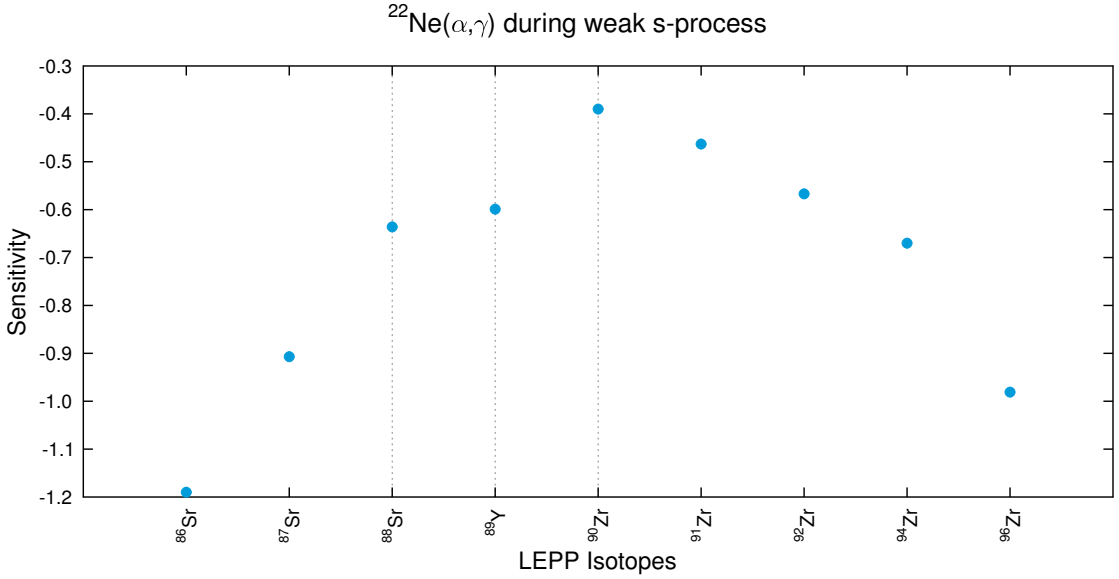

Figure A.153: ^{22}Ne(α,γ) during the weak *s* process on LEPP isotopes. (table 3.28). The sensitivities of the LEPP isotopes are plotted. The vertical dotted grey lines symbolize neutron magic nuclei.

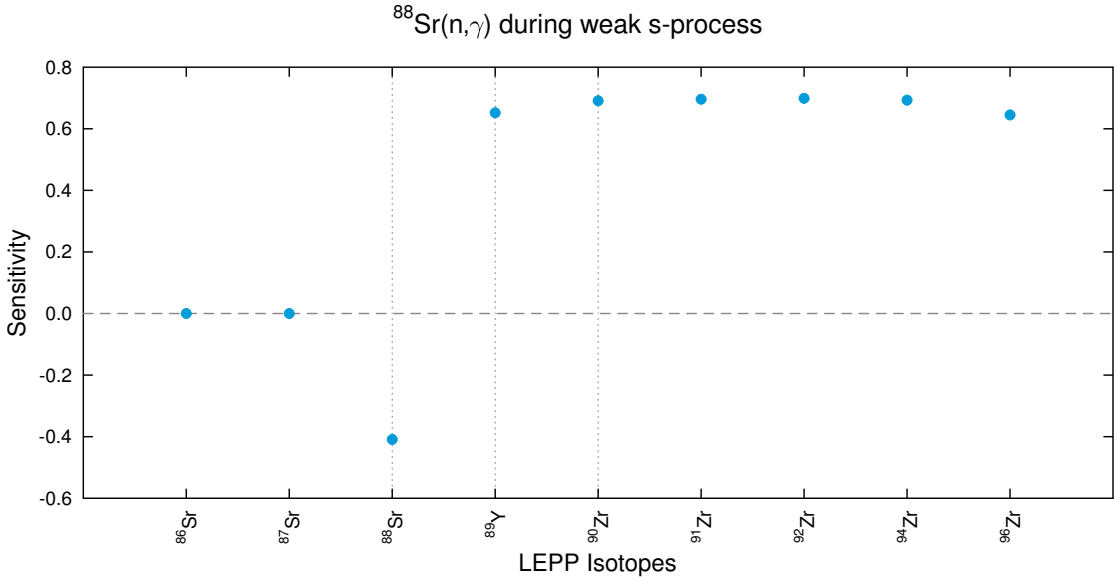

Figure A.154: Bottleneck reaction $^{88}\mathrm{Sr}(n,\gamma)$ during the weak *s* process on LEPP isotopes. (table 3.28). The sensitivities of the LEPP isotopes are plotted. The vertical dotted grey lines symbolize neutron magic nuclei.

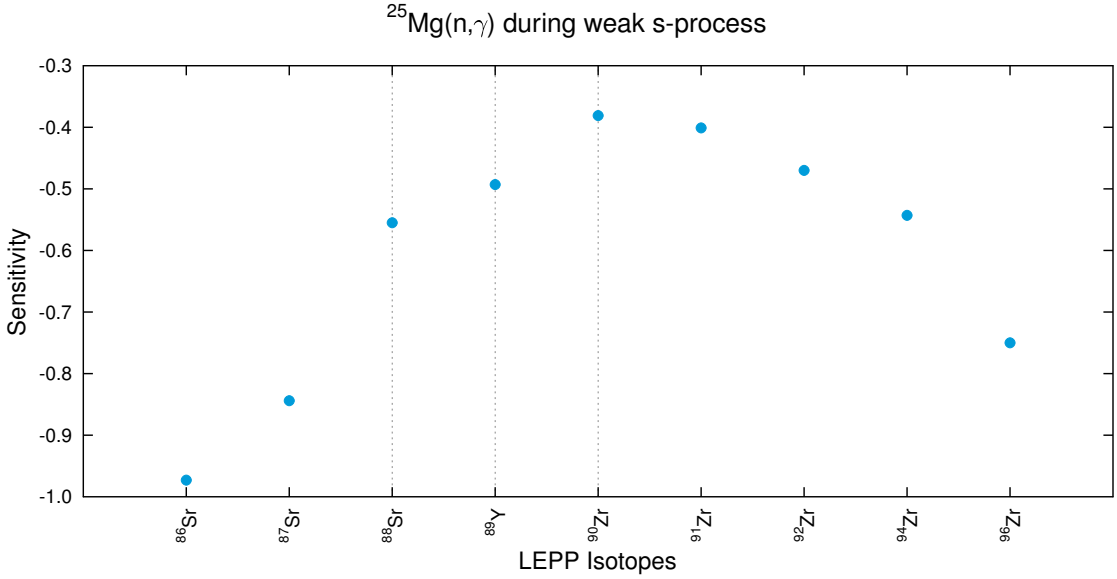

Figure A.155: Neutron poison reaction $^{25}\mathrm{Mg}(n,\gamma)$ during the weak *s* process on LEPP isotopes. (table 3.28). The sensitivities of the LEPP isotopes are plotted. The vertical dotted grey lines symbolize neutron magic nuclei.

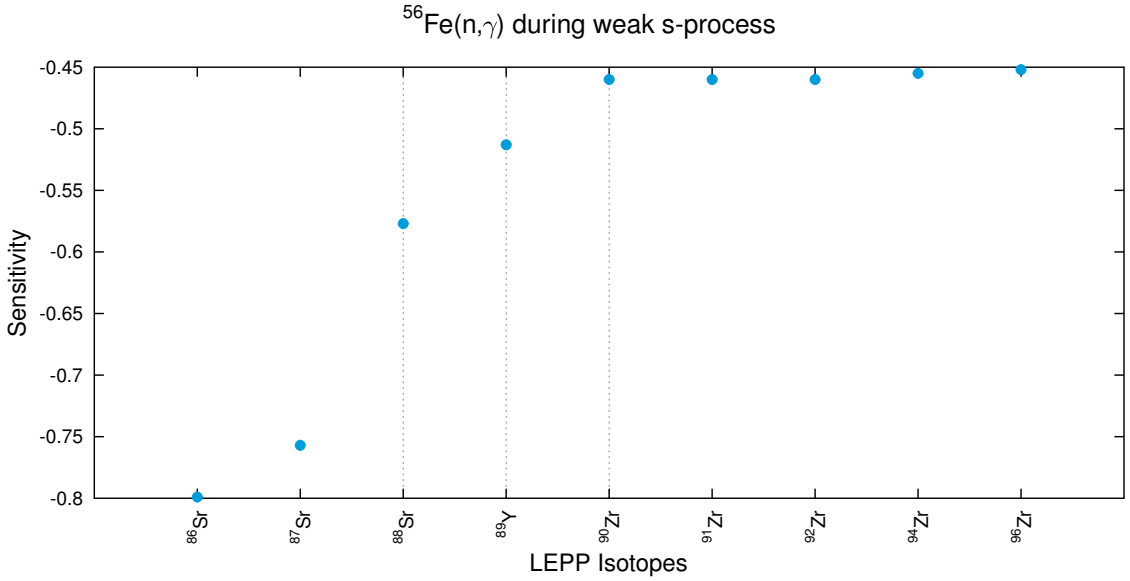

Figure A.156: Competing capture reaction $^{56}\mathrm{Fe}(n,\gamma)$ during the weak *s* process on LEPP isotopes. (table 3.28). The sensitivities of the LEPP isotopes are plotted. The vertical dotted grey lines symbolize neutron magic nuclei.

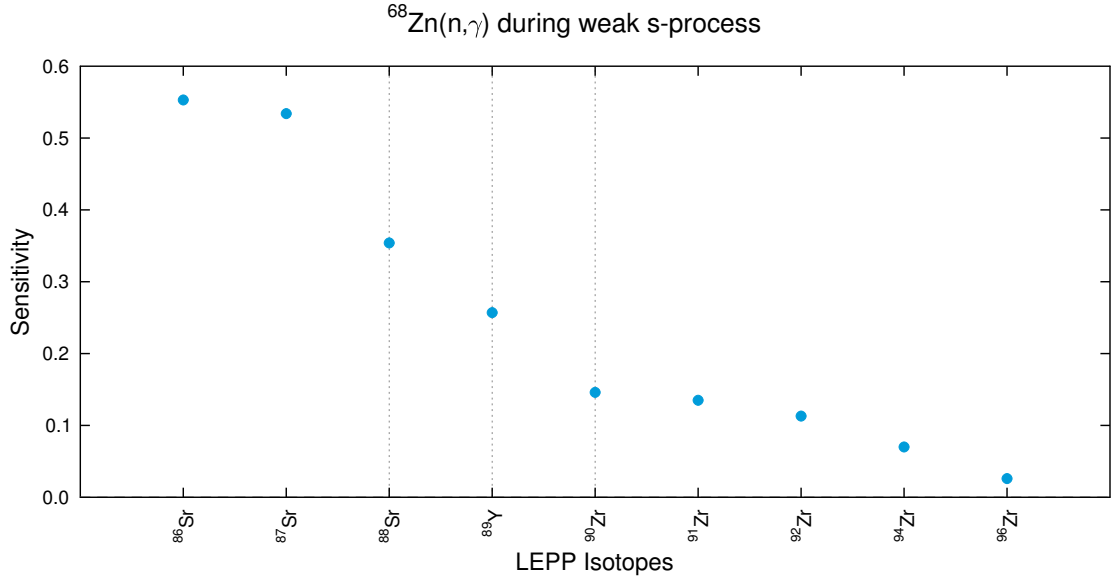

Figure A.157: $^{68}\mathrm{Zn}(n,\gamma)$ impact during the weak *s* process on LEPP isotopes. (table 3.28). The sensitivities of the LEPP isotopes are plotted. This rate produces a sensitivity pattern, which matches the LEPP characteristics and is therefore a candidate for the LEPP. The vertical dotted grey lines symbolize neutron magic nuclei.

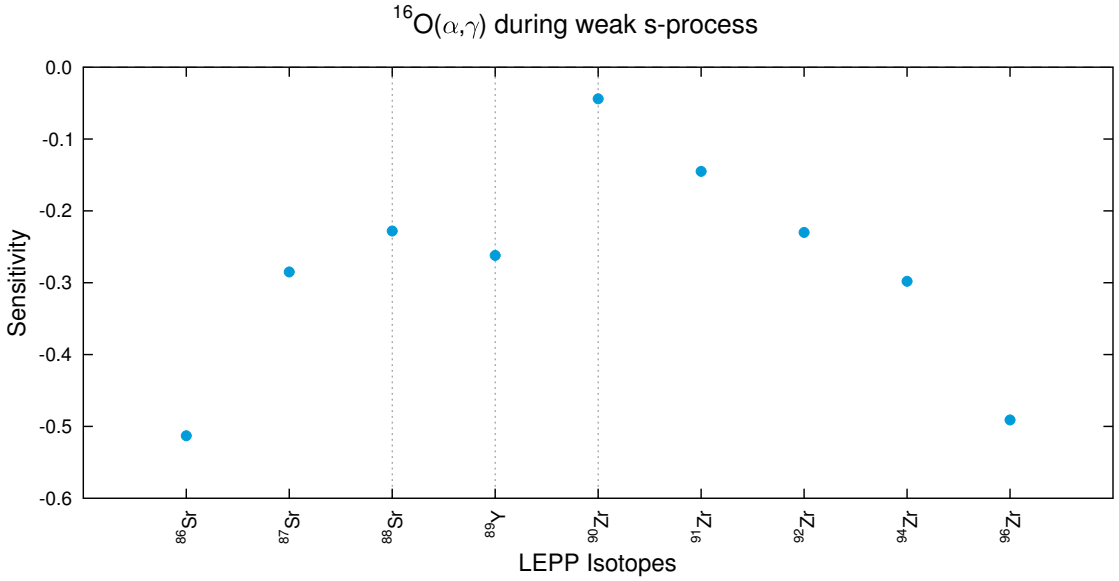

Figure A.158: ^{16}O(α, γ) during the weak *s* process on LEPP isotopes. (table 3.28). The sensitivities of the LEPP isotopes are plotted. The vertical dotted grey lines symbolize neutron magic nuclei.

LEPP SENSITIVITIES DURING THE *i* PROCESS

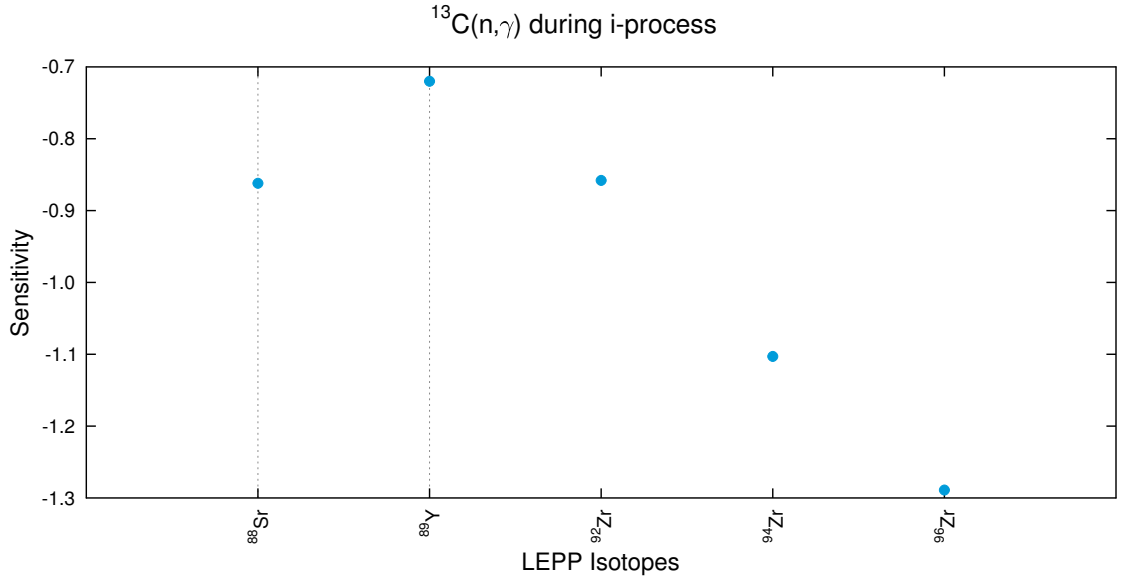

Figure A.159: Neutron poison reaction $^{13}C(n,\gamma)$ during the *i* process on LEPP isotopes. (table 3.29). The sensitivities of the LEPP isotopes are plotted. The vertical dotted grey lines symbolize neutron magic nuclei.

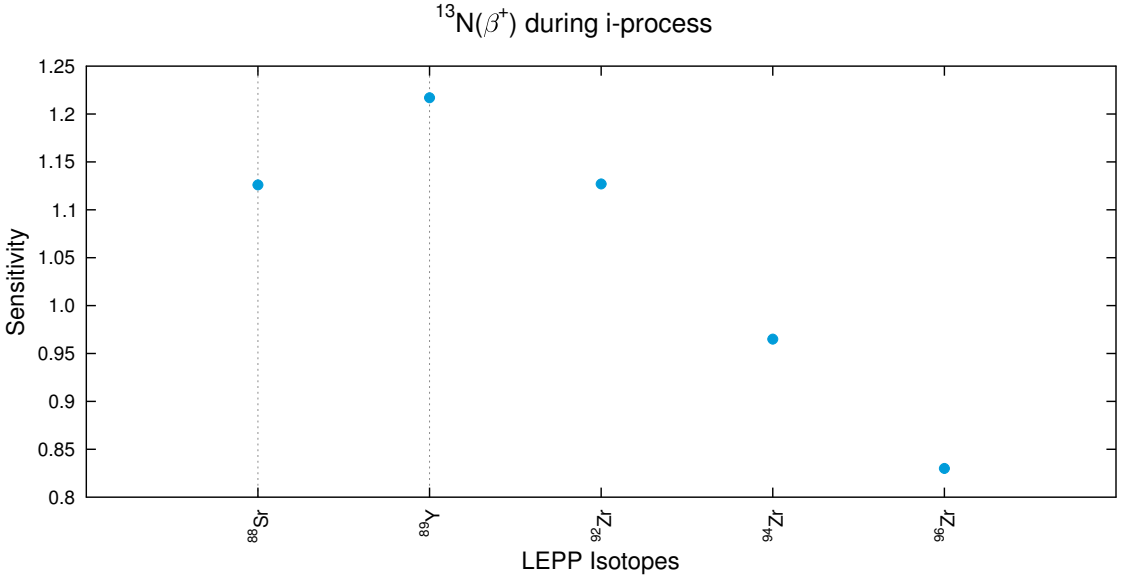

Figure A.160: $^{13}N(\beta^+)$ during the *i* process on LEPP isotopes. (table 3.29). The sensitivities of the LEPP isotopes are plotted. The vertical dotted grey lines symbolize neutron magic nuclei.

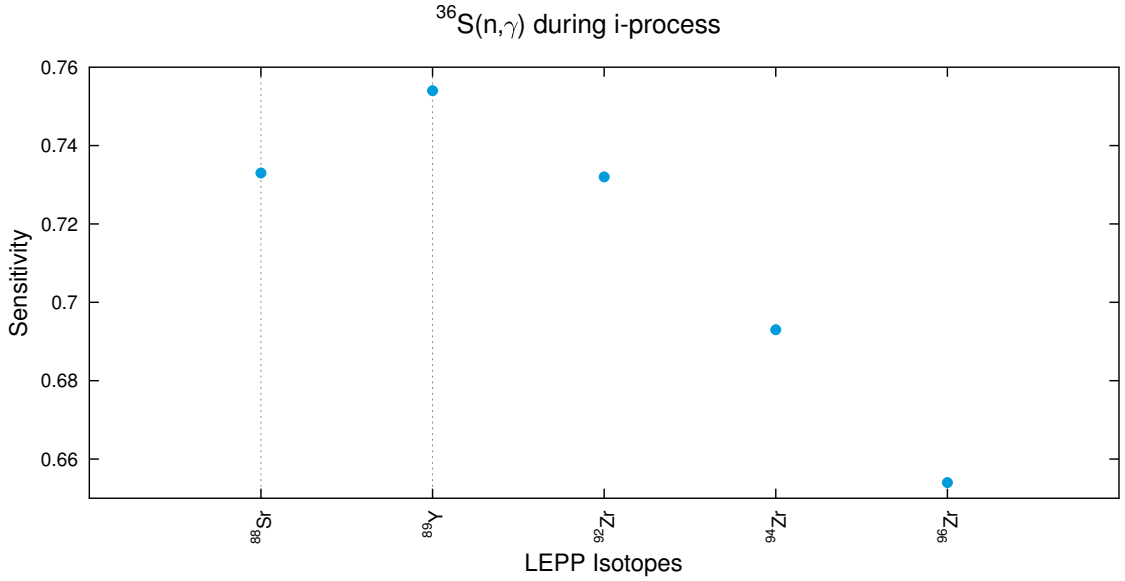

Figure A.161: Seed reaction $^{36}S(n,\gamma)$ during the *i* process on LEPP isotopes. (table 3.29). The sensitivities of the LEPP isotopes are plotted. The vertical dotted grey lines symbolize neutron magic nuclei.

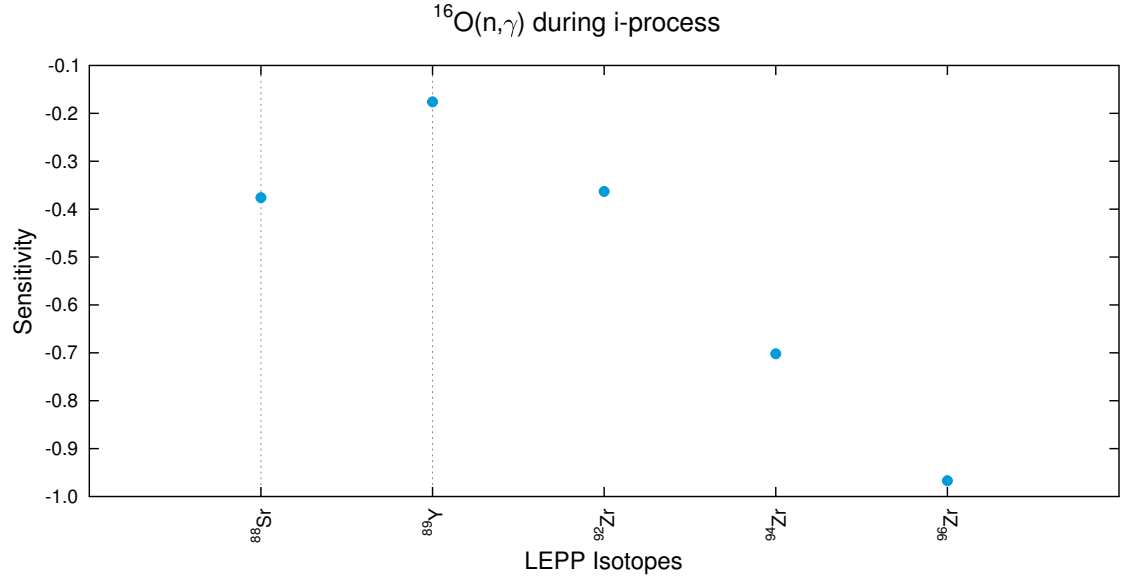

Figure A.162: Neutron poison reaction $^{16}O(n,\gamma)$ during the *i* process on LEPP isotopes. (table 3.29). The sensitivities of the LEPP isotopes are plotted. The vertical dotted grey lines symbolize neutron magic nuclei.

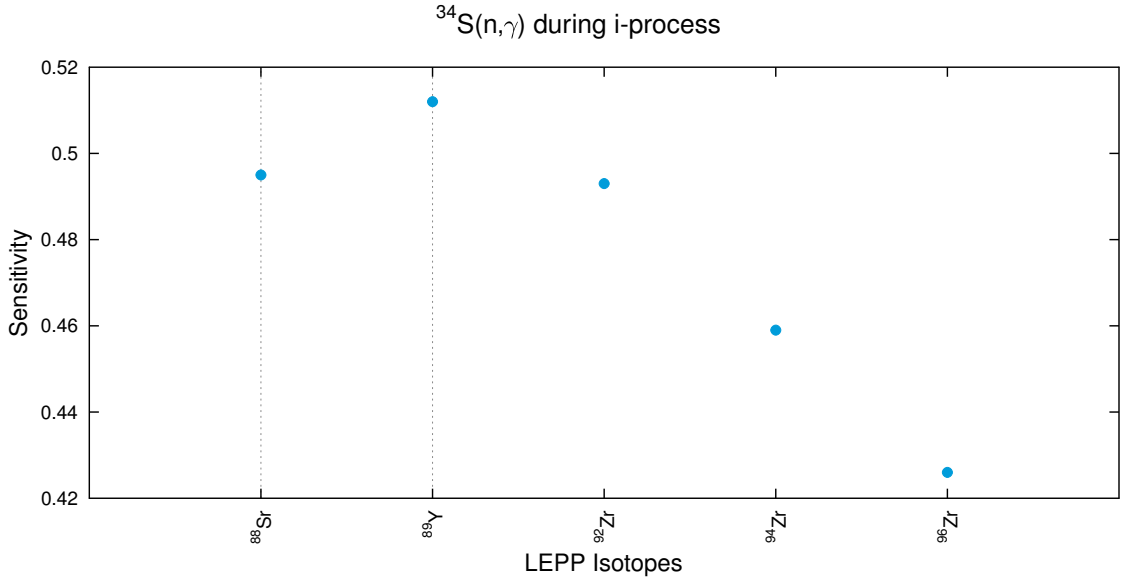

Figure A.163: Seed reaction ^{34}S(n,γ) during the *i* process on LEPP isotopes. (table 3.29). The sensitivities of the LEPP isotopes are plotted. The vertical dotted grey lines symbolize neutron magic nuclei.

Danksagung

An dieser Stelle möchte ich all jenen meine Dankbarkeit zum Ausdruck bringen, die mich auf verschiedenen Wegen während meiner Promotion unterstützt haben.

Mein erster Dank geht an Herrn Professor Dr. René Reifarth für die Aufnahme in seine Arbeitsgruppe und die Ermöglichung dieser Arbeit. Für seine vielfältigen Anregungen während der gesamten Promotionszeit und auch für das entgegen gebrachte Vertrauen eigene Ideen in die Arbeit einfließen zu lassen.

Einen besonderen Dank möchte ich an Frau Dr. Kerstin Sonnabend richten, die sich immer Zeit für meine Fragen und Probleme genommen hat. Vor allem aber für die zahlreichen Stunden, die Sie für Korrekturen dieser Arbeit aufgebracht hat und ohne die diese Arbeit in dieser Form nicht vorliegen würde.

Für die finanzielle Unterstützung möchte ich mich bei HIC for FAIR und HGS-HIRe bedanken.

Weiterhin bedanke ich mich bei der NuGrid für die Aufnahme in die Kollaboration und für die Bereitstellung der Programme und Sternmodelle. Insbesondere bei Dr. Marco Pignatari für die hervorragende Einführung und Einarbeitung in die Welt der Simulationen.

Bei Dr. Jan Glorius, meinem ehemaligen Bürogenossen, bedanke ich mich für die anregenden Diskussionen und Korrekturen, die mit dafür gesorgt haben, dass diese Arbeit den richtigen Schliff bekommen hat.

Ein großer Dank geht an Stefan Schmidt, der nicht nur jedes Computerproblem während meiner Dissertation gelöst hat, sondern mir auch privat immer eine große Hilfe war und mir mittlerweile ein sehr guter Freund geworden ist.

Ebenfalls danke ich Benedikt Thomas für die tolle Zusammenarbeit und die daraus entstandene Freundschaft.

Ein weiteres Dankeschön gilt Dr. Ralf Plag für die “After-Group-Meetings“ bei einem kühlen Bier, die dafür gesorgt haben, dass ich die nötige Portion Ablenkung erhalten habe.

Moritz Pohl danke ich mit den Worten: “What happens in Buchenau, ...“

Markus Reich, Ceyhun Arda, Philipp Erbacher danke ich für die freundschaftliche Büroatmosphäre, die dafür gesorgt hat, dass ich gerne zum Arbeitsplatz gekommen bin.

Besonderen Dank auch an die gesamte Arbeitsgruppe für das angenehme Arbeitsklima und die Bereitstellung aller Rechner für meine Simulationen und dem Verständnis, wenn ich mal wieder das gesamte Netzwerk lahm gelegt habe.

Meinen langjährigen Studienfreunden Robert Singh, Gunther Caspar und Thomas Schönenbach möchte ich für die schöne Zeit an der Uni danken.

Meiner Familie bin ich für die unentwegte Unterstützung, die mir immer den nötigen Rückhalt gegeben hat, sehr dankbar.

Abschließend bedanke ich mich bei meiner Freundin, Taniya Thomas, für ihre verständnisvolle Unterstützung und ihre aufmunternden Worte in jeder Phase meiner Arbeit.

Curriculum Vitae

Personal information

Name	Alexander Koloczek
Date of birth	February 12th, 1986
Place of birth	Frankfurt am Main, Germany
Nationality	German

Education

since 2011	PhD student at the Institut für Angewandte Physik, Goethe-Universität Frankfurt am Main Supervisors: Prof. Dr. René Reifarth, Dr. Kerstin Sonnabend
2010	Master thesis in physics: Sunyaev-Zeldovich observations of Abell 2744 (grade: 1.0) Supervisor: Prof. Dr. Cathy Horellou
2009 – 2010	Student of physics and astrophysics at Gothenburg University, Sweden
2009	Bachelor thesis in physics: Herkunft von UHECRs (grade: 1.0) Supervisor: Prof. Dr. Marcus Bleicher
2006 – 2009	Student of physics at Goethe-Universität Frankfurt am Main
2006	Allgemeine Hochschulreife (Abitur) at the Philipp-Reis-Schule, Friedrichsdorf (grade: 1.5)